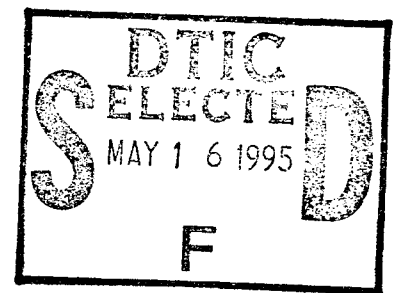


THE ADHESION SOCIETY

PROCEEDINGS

of the

Eighteenth Annual Meeting



1995

This document has been approved
for public release and sale; its
distribution is unlimited.

HILTON HEAD, SC
19-22 FEBRUARY, 1995
J. W. HOLUBKA, EDITOR

LIBRARY OF CONGRESS NUMBER: 95-75257

19950515 096

DTIC QUALITY INSPECTED 5

REPORT DOCUMENTATION PAGE		READ INSTRUCTIONS BEFORE COMPLETING FORM												
1. Report Number Library of Congress #95-75257	2. Govt Accession No.	3. Recipients Catalog Number												
4. Title (and subtitle) The Adhesion Society Proceedings of the Eighteenth Annual Meeting		5. Type of Report and Period Covered Final Nov. 15, 1994-Sept. 30, 1995												
7. Author (s) J.W. Holubka, Editor		6. Performing Org. Report Number												
9. Performing Organization Name and Address The Adhesion Society 2 Davidson Hall, Virginia Tech Blacksburg, VA 24061-0201		8. Contract or Grant Number (s) N00014-95-1-0216												
11. Controlling Office Name and Address Office of Naval Research, ONR 252 Ballston Tower One 800 North Quincy St., Arlington, VA 22217-5000		10. Program Element, Project, Task Area and Work Unit Numbers												
14. Monitoring Agency Name and Address (if different from Controlling office)		12. Report Date February 22, 1995												
		13. Number of Pages 370												
		15. Security Class (of this Report) Unclassified												
		15a. Declassification/Downgrading Schedule N.A.												
16. Distribution Statement (of this Report)														
<table border="0"> <tr> <td>Scientific Officer Code: 332</td> <td>Grant Administrator</td> <td>Defense Technical Info Center</td> </tr> <tr> <td>Peter P. Schmidt</td> <td>ONR Regional Office N66020</td> <td>Building 5, Cameron Station</td> </tr> <tr> <td>ONR, 800 N. Quincy St.</td> <td>101 Marietta St., Suite 2805</td> <td>Alexandria, VA 22314</td> </tr> <tr> <td>Arlington, VA 22217-5000</td> <td>Atlanta, GA 30323-0008</td> <td></td> </tr> </table>			Scientific Officer Code: 332	Grant Administrator	Defense Technical Info Center	Peter P. Schmidt	ONR Regional Office N66020	Building 5, Cameron Station	ONR, 800 N. Quincy St.	101 Marietta St., Suite 2805	Alexandria, VA 22314	Arlington, VA 22217-5000	Atlanta, GA 30323-0008	
Scientific Officer Code: 332	Grant Administrator	Defense Technical Info Center												
Peter P. Schmidt	ONR Regional Office N66020	Building 5, Cameron Station												
ONR, 800 N. Quincy St.	101 Marietta St., Suite 2805	Alexandria, VA 22314												
Arlington, VA 22217-5000	Atlanta, GA 30323-0008													
17. Distribution Statement (of abstract entered in block 20, if different from report)														
<div style="border: 1px solid black; padding: 5px; display: inline-block;"> This document has been approved for public release and sale; its distribution is unlimited. </div>														
18. Supplementary Notes														
19. Key Words (Continue on reverse if necessary and identify by block number)														
Adhesion Society, Annual Meeting, Eighteenth, Proceedings														
20. Abstract (Continue on reverse if necessary and identify by block number)														
This document is a collection of abstracts of papers presented at the 18th Annual Adhesion Society Meeting held at Hilton Head, SC on February 19-22, 1995. The program was chaired by Joseph W. Holubka.														

THE ADHESION SOCIETY

PROCEEDINGS

of the

Eighteenth Annual Meeting



1995

Accession For	
NTIS CRA&I	<input checked="" type="checkbox"/>
DTIC TAB	<input type="checkbox"/>
Unannounced	<input type="checkbox"/>
Justification	
By	
Distribution /	
Availability Codes	
Dist	Avail and/or Special
A-1	

HILTON HEAD, SC
19-22 FEBRUARY, 1995
J. W. HOLUBKA, EDITOR

LIBRARY OF CONGRESS NUMBER: 95-75257

SPONSORING ORGANIZATIONS

Ford Motor Company

Office of Naval Research

Loctite

Gordon and Breach

© 1995 The Adhesion Society

All rights reserved. Individual authors may reproduce their contribution for personal or company use provided that the source and The Adhesion Society copyright are acknowledged. Instructors are permitted to photocopy isolated articles for noncommercial classroom use only. Additional copies of the complete volume can be obtained by writing Joseph W. Holubka, Program Chairman, Ford Motor Company, Ford Research Laboratory, MD3198 SRL, Dearborn, MI 48121, USA.

LIBRARY OF CONGRESS NUMBER: 95-75257

18TH ANNUAL MEETING OF THE ADHESION SOCIETY

**FEBRUARY 19-22, 1995
HILTON HEAD, SC, USA**

PROGRAM CHAIR

**Joseph W. Holubka
Ford Research Laboratory
Ford Motor Company**

PROGRAM COMMITTEE

**Terry St Clair
NASA**

**Anna Balazs
University of Pittsburgh**

**Don Rimai
Eastman Kodak Company**

**John Dillard
Virginia Polytechnic Institute and State University**

**Marek Urban
North Dakota State University**

**Rose Ryntz
Ford Motor Company**

**Louis Sharpe
Consultant**

**Christopher Brown
Worcester Polytechnic Institute**

LOCAL ARRANGEMENTS

**Jenifer Marchesi
Polaroid Graphics Imaging, Inc.**

ADHESION SOCIETY EXECUTIVE COMMITTEE

J. P. Bell, President

H. M. Clearfield, Vice President

J. A. Fillbey, Secretary

G. D. Davis, Treasurer

D. R. Speth, Editor

J. Dillard, Member-at-Large

Al Pocius, Member-at-Large

PREFACE

Welcome to the Eighteenth Annual Meeting of the Adhesion Society! We hope the meeting will be especially enjoyable and informative for you. This year's program has been expanded and will be conducted with concurrent sessions. This has been done as a result of a successful testing of concurrent sessions at the last meeting in Orlando, as well as the contribution of an exceedingly large number of good papers. Approximately 165 papers were submitted for consideration for presentation at this meeting. Of these, a total of 130 papers will be presented this year in thirteen separate sessions over the two and one half days of the conference. Three areas of adhesion science will be emphasized in this year's meeting. These areas include: New Materials for Adhesives and Coatings; Small Particle Adhesion; and Chemical/Physical Characterization of Adhesive Interactions. Two sessions will be assigned to each of these areas of technical interest. In addition, "special topics sessions" on modelling adhesion processes; durability: environmentally induced adhesion reduction, pressure sensitive adhesives; mechanical characterization adhesion producing interphases; and applications of adhesion science will also be presented. These special topic sessions likely could form the basis of future, more intensive symposia in future meetings if enough interest is generated and communicated to the program organizers.

Although this meeting was not designed specifically to be an international conference, the papers that were contributed show very well the global nature of Adhesion Science. About 15% of the papers in this year's program have been contributed from outside of the United States. The papers came from as far as Japan, China, Taiwan and Australia and as close as Canada. Papers also were contributed from England, Germany, France, and Spain.

Financial support for this meeting came from Ford Motor Company, Office of Naval Research, Loctite, and Gordon and Breach Science Publishers. This support is sincerely appreciated because it allows us to provide support for travel, registration and accommodations to students and faculty members who have a need. The funds are also used to provide state-of-the-art AV facilities at the meetings and allow for more extensive publicity for the meeting. We also thank 3M for sponsorship of our annual Award for Excellence in Adhesion Science.

I would also like to thank members of the Program Committee for helping me review the large number of contributed papers. I would also like to acknowledge Jim Boerio, Lou Sharpe, Ray Dickie, and Jim Bell for their assistance in providing guidance and useful discussions related to organizing this program. I would also like to acknowledge the assistance of Jenifer Marchesi for her excellent work on Local arrangements, and to Kim Mills for her assistance at the Adhesion Society home office and in particular in her assistance in preparing and mailing the advertisements for the meeting.

I hope you have a enjoyable and informative meeting. Also be sure that you enjoy Hilton Head and its attractions. This meeting site is nice to very pleasant in the middle of the winter. Finally, I would greatly appreciate your feedback - both good and bad. I will forward your comments to the next program chair and hopefully the meeting next year will be even better.

Joseph W. Holubka
Program Chair - 1995 Meeting

TABLE OF CONTENTS

SPONSORING ORGANIZATIONS.....	ii
PROGRAM AND LOCAL ARRANGEMENTS COMMITTEES.....	iii
ADHESION SOCIETY EXECUTIVE COMMITTEE MEMBERS.....	iv
PREFACE.....	v
PROGRAM.....	vii
AUTHOR INDEX.....	365

THE ADHESION SOCIETY

PROGRAM OF THE 18TH ANNUAL MEETING

SUNDAY EVENING

- 4:00 - 6:00 REGISTRATION**
- 6:00 - 7:00 PRESIDENT'S RECEPTION**
- 7:00 - 7:45 BUSINESS MEETING**

MONDAY MORNING

- 8:00 - 8:15 MEETING OPENING REMARKS**
James P. Bell - President of Adhesion Society
Joseph W. Holubka - 1995 Program Chairman

MONDAY MORNING - SESSION 1

**The Adhesion Society Award for Excellence in Adhesion Science Session
Sponsored by the 3M Company. Awardee: Professor Jacques Schultz**

Session Chair: James P. Bell, University of Connecticut

- 8:15 - 8:30 3M Award Presentation to Dr. Jacques Schultz**
Al Pocius, 3M
- 8:30 - 9:00 "THE RELATIONSHIP BETWEEN SURFACE
ENERGETICS AND ADHESION STRENGTH", Professor
Jacques Schultz, University of Haute Alsace, Centre National de la
Recherche Scientifique, France. p. 1**
- 9:00 - 9:30 "THE ROLE OF ADHESION PROMOTERS ON THE
STRUCTURE OF THE INTERPHASE", M. Grunze, T.
Strunskus and C. Woll, Angewandte Physikalische Chemie der
Universitat Heidelberg, Germany. p. 5**
- 9:30 - 10:00 Break**
- 10:00 - 10:30 "VISCOELASTICITY AND KINETICS OF WETTING ON
RUBBERY MATERIALS", Alain Carre and Martin E. R.
Shanahan, Centre de Recherche Corning Europe and Centre National de
la Recherche Scientifique, France. p. 8**
- 10:30 - 11:00 "SURFACE AND INTERFACIAL STUDIES OF PLASMA-
MODIFIED COMPOSITES", Joannie W. Chin and James P.
Wightman, Department of Chemistry, Virginia Tech., USA. p. 11**

- 11:00 - 11:30** **"ANALYSIS OF THIN CYANURATE PREPOLYMER FILMS ON SOLIDS AS A MODEL OF THE ADHESIVE INTERPHASE"**, W. Possart, S. Dieckhoff, D. Fanter, T. Gesang, A. Hartwig, R. Hoper, V. Schlett, and O.-D. Hennemann, Fraunhofer Institute of Applied Materials Research, Germany. **p.15**
- 11:30 - 12:00** **"THE DIRECT MEASUREMENT OF SURFACE FORCES BETWEEN SOLID POLYMER FILMS AND ITS RELATIONSHIP TO POLYMER SURFACE AND ADHESION SCIENCE"**, Alphonsus V. Pocius, 3M Adhesive Technologies Center; and V. S. Mangipudi and M. Tirrell, Department of Materials Science and Chemical Engineering, University of Minnesota, USA. **p.18**

12:00 - 1:30 **LUNCH**

MONDAY AFTERNOON - SESSION 2A

NEW MATERIALS FOR ADHESIVES AND COATINGS #1

Session Chair: Terry St Clair, NASA, USA

- 1:30 - 1:40** **Opening Comments**
Terry St. Clair, NASA, USA
- 1:40 - 2:10** **"ADHESIVE PROPERTIES OF CURED PHENYLETHYNYL TERMINATED IMIDE OLIGOMERS"**, B. J. Jensen, R. G. Bryant, J. G. Smith, and P. M. Hergenrother, NASA Langley Research Center, USA.
- 2:10 - 2:40** **"ACRYLIC ADHESION TO POLYOLEFIN"**, Jeffrey T. Fields, Andrew Garton, and James P. Bell, University of Connecticut, USA.
p. 21
- 2:40 - 3:10** **"VINYLPHOSPHONIC ACID ANODIZING ALUMINUM FOR STRUCTURAL ADHESIVE BONDING"**, G. A. Nitowski, Aluminum company of America and K. Wefer and J. G. Dillard, Virginia Tech, USA. **p. 24**
- 3:10 - 3:30** **BREAK**
- 3:30 - 4:00** **"USING POLYMERIC BINDERS IN SUSPENSION PREPREGGING AND TAILORING FIBER/MATRIX ADHESION FOR CARBON-REINFORCED COMPOSITES"**, S. Gardner, A. Gonzalez, R. M. Davis, S. Case, J. J. Lesko, and K. L. Reifsnider, Department of Chemical Engineering, Virginia Tech, USA. **p.27**
- 4:00 - 4:30** **"FUNCTIONALIZED BLOCK COPOLYMERS AS ADHESION PROMOTERS"**, Michael S Kent, and Randall Saunders, Sandia National Labs, USA. **p. 29**

- 4:30 - 5:00** **"SYNTHESIS AND PROPERTIES OF THE PHENYLETHYNYL-TERMINATED POLYIMIDE LARC-PETI-5"**, Roberto J. Cano and Brian J. Jensen, NASA Langley Research Center, USA. **p. 32**

MONDAY AFTERNOON - SESSION 2B

MODELLING OF ADHESION PROCESSES

Session Chair: Anna Balazs, University of Pittsburg

- 1:30 - 1:40** **Opening Comments**
Anna Balazs, University of Pittsburg.
- 1:40 - 2:10** **"ADHESION AT METAL-CERAMIC INTERFACES: AN ELECTROSTATICS - BASED MODEL"**, J. W. Mintmire and F. H. Streitz, Naval Research Laboratory, USA. **p. 35**
- 2:10 - 2:40** **"A COMPUTER MODEL FOR WETTING HYSTERESIS"**, S. P. Wesson and A. Mahale, TRI Princeton, USA. **p. 38**
- 2:40 - 3:10** **"METALLIZATION OF POLYIMIDE SURFACES: STILL NO CONSISTENT MODEL"**, M. Grunze, T. Strunskus, and Ch. Woll, Angewandte Physikalische Chemie, and Technische Fakultat der Christian-Albrechts-Universität zu Kiel, Germany. **p. 41**
- 3:10 - 3:30** **BREAK**
- 3:30 - 4:00** **"SPECIAL ADHESIVE FINITE ELEMENTS FOR MODELLING ADHESIVELY BONDED JOINTS AND CRACK-PATCH REPAIRS IN TWO- AND THREE-DIMENSIONS"**, M. W. Taylor, Raul Andruet, and D. A. Dillard, Department of Engineering Science and Mechanics, Virginia Tech., USA. **p. 45**
- 4:00 - 4:30** **"ATOMIC SCALE ADHESION, FRICTION, AND WEAR IN HYDROCARBON SYSTEMS"**, J. A. Harrison, and M. D. Perry, Chemistry Department, United States Naval Academy; R. J. Colton and C. T. White, Naval Research Laboratory; and D. W. Brenner, Department of Material Science and Engineering, North Carolina State University, USA. **p. 47**
- 4:30 - 5:00** **"ADHESION MECHANICS DURING LOW SPEED NORMAL IMPACT OF SPHERICAL "ROCKS" INTO MULTILAYERED PAINTED STEEL SUBSTRATES"**, A. C. Ramamurthy and Joseph W. Holubka, Ford Motor Company; and Dennis Mihora, FM Analysts, USA. **p. 52**

MONDAY AFTERNOON - SESSION 2C

SMALL PARTICLE ADHESION #1

Session Chair: Don Rimai, Eastman Kodak Company

- 1:30 - 1:40 Opening Comments**
Don Rimai, Eastman Kodak Company
- 1:40 - 2:10 "TIME DEPENDENT ADHESION INDUCED
PHENOMENA: VISCOELASTIC CREEP OF A
POLYMERIC SUBSTRATE OVER RIGID PARTICLES", D.
S. Rimai, L. P. DeMejo, J. H. Chen, R. C. Bowen and T. H. Mourey,
Eastman Kodak Company, USA. p. 56**
- 2:10 - 2:40 "PARTICLE GENERATION IN CORROSIVE GAS
DELIVERY SYSTEMS", S. Krishnan, S. Grube, A. Tudhope and
O. Laparra, Ultra Clean Technology, and VLSI Technology, Inc. USA.
p. 59**
- 2:40 - 3:10 "ENHANCED REMOVAL OF RADIOACTIVE PARTICLES
FROM CIRCUIT BOARDS BY FLUORINATED
SURFACTANT SOLUTIONS", R. Kaiser, C. S. Yam and O. K.
Harling, Entropic Systems Inc, and Department of Nuclear
Engineering, MIT, USA. p. 62**
- 3:10 - 3:30 BREAK**
- 3:30 - 4:00 "EFFECT OF SURFACE MOISTURE ON THE
POLARIZATION OF INDIVIDUAL GLASS PARTICLES",
T. N. Tombs and T. B. Jones, Eastman Kodak Company and the
Department of Electrical Engineering, University of Rochester, USA.
p. 66**
- 4:00 - 4:30 "PARTICLE BOUNCE OR CAPTURE: THE ROLE OF
ADHESION FORCES", Bart Dahneke, Eastman Kodak Company,
USA.**
- 4:30 - 5:00 "MEASUREMENT OF ADHESION BETWEEN
POLYMERS: INFLUENCE OF INTERFACIAL
CHAINS", M. Deruelle, V. S. Mangipudi, M. Tirrell, Department of
Chemical Engineering and Materials Science, University of Minnesota,
and L. Leger, Laboratoire de Physique de la Matiere Condensee,
College de France, URA CNRS, France. p. 69**
- 5:00 - 5:30 "HYDROPHOBIC COAGULATION AND FLOATATION
OF ULTRA FINE COAL", Zhiwei Jiang, Yingjia Kang, and
Youzhu Li, China University of Mining and Technology, China. p. 72**

MONDAY EVENING - POSTER SESSION - 8:00 -10:00

Session Chair: John Dillard, Virginia Tech

1. **"A STUDY OF THE EFFECTS OF LOW POWER PLASMA TREATMENT ON CARBON BLACK, GRAPHITE AND HIGHLY ORIENTATED PYROLYTIC GRAPHITE (HOPG) STRUCTURES"**, S. O'Kell and C. Jones, Department of Materials, Science and Engineering, University of Liverpool, England. **p. 75**
2. **"A STUDY OF THE INTERPHASE REGION IN CARBON FIBRE EPOXY COMPOSITES USING DYNAMIC MECHANICAL THERMAL ANALYSIS"**, K. Atkinson and C. Jones, Department of Materials, Science and Engineering, University of Liverpool, England. **p. 77**
3. **"PLASMA-POLYMERIZED FILMS: ADHESIVE BONDING APPLICATIONS"**, L. Deshayes, M. Charbonnier, F. Gaillard, J. Baborowski, and M. Romand, CNRS, France. **p. 79**
4. **"PLASMA-PRETREATMENT OF POLYMERS: APPLICATION TO THEIR METALLIZATION BY AN ELECTRODELESS PROCESS"**, M. Alami, M. Charbonnier, and M. Romand, CNRS, France. **p. 83**
5. **"USE OF EVANESCENT WAVES FT-IR SPECTROSCOPY FOR IN-SITU STUDY OF THE DEGRADATION OF POLYMER-SUBSTRATE SYSTEMS"**, I. Linossier, F. Gaillard and M. Romand, CNRS, France. **p. 86**
6. **"INFLUENCE OF CHEMICAL ELECTROCHEMICAL AND PHYSICAL SURFACE TREATMENTS OF AISI 304L ON ITS REACTIVITY - CONSEQUENCES ON ADHESION TO EPOXY RESINS"**, F. G. Gaillard, E. Peilleux and M. Romand, CNRS, France. **p. 89**
7. **"ADHESION OF RUBBER TO STEEL: THE USE OF PLASMA POLYMERIZED PRIMER FILMS"**, Y. M. Tsai, F. J. Boerio, and W. J. van Ooij, Department of Materials Science and Engineering, University of Cincinnati; and Dong K. Kim, Goodyear Tire and Rubber Company, USA. **p. 92**
8. **"PLASMA POLYMERIZED SILICON CONTAINING PRIMERS FOR ALUMINUM"**, C. E. Taylor, I Segall and F. J. Boerio, Department of Materials Science and Engineering, University of Cincinnati; and D. J. Ondrus, R. A. Dickie and S. Ward, Ford Motor Company, USA. **p.95**
9. **"CARBON FIBER - POLYMER MATRIX ADHESION IN HIGH PERFORMANCE COMPOSITES"**, H. Zhuang and J. P. Wightman, Department of Chemistry, Virginia Polytechnic Institute and State University, USA. **p. 98**
10. **"TIME AND TEMPERATURE DEPENDENT FRACTURE OF STEEL/EPOXY JOINTS"**, K. L. Urban, M. D. Rakestraw, T. Chang, N. E. Shephard, D. A. Dillard, J. G. Dillard, and T. C. Ward, Department of Engineering Science and Mechanics, Virginia Tech, USA. **p. 100**

11. **"CONTROL OF TOUGHENED POLYCYANURATE MORPHOLOGY UTILIZING GRADIENT TEMPERATURE CURING"**, D. S. Porter, C. A. Williams, S. A. Srinivasan, J. E. McGrath and T. C. Ward, Department of Chemistry, Virginia Tech, USA. **p. 102**
12. **"INTERFACIAL CHARACTERIZATION OF CTRE AND CTFE BLENDS WHEN USED AS HOT MELT ADHESIVES AND THE IMPLICATIONS ON ADHESION AND FUNCTIONAL CHARACTERIZATION"**, J. L. Longhenry and B. J. Love, Department of Materials Science and Engineering, Virginia Tech, USA. **p. 104**
13. **"ASPECTS OF DENATURING IN ADHESIVE BONDING TO DENTIN"**, R. R. Hamandi and B. J. Love, Department of Materials Science and Engineering, Virginia Tech, USA. **p. 106**
14. **"ACCELERATED DEBONDING TEST TO EVALUATE DURABILITY OF METAL/ADHESIVE BONDS"**, T. Chang, Y. H. Lai, N. E. Shephard, E. A. Sproat and D. A. Dillard, Virginia Tech, USA. **p. 108**
15. **"NEW INVESTIGATIONS INTO FLUORINATED CELLULOSE FIBERS"**, Ulli Becker and Wolfgang Glasser, Wood Science and Forest Products Research, Virginia Tech, USA. **p. 110**
16. **"SPLICING OF SAPPHIRE AND SILICA FIBER"**, A. Barnes, S. Gollapudi, R. May, and R. Clais, Bradley Department of Electrical Engineering, Virginia Tech, USA. **p. 112**
17. **"DURABILITY OF ADHESIVELY BONDED TITANIUM"**, S. A. Risch, B. L. Holmes, G. S. Frick, J. P. Wightman, and J. G. Dillard, Department of Chemistry, Virginia Tech, USA. **p. 114**
18. **"AN EXTENSION OF THE JKR TECHNIQUE TO DESCRIBE ADHESION HYSTERESIS IN MODIFIED PDMS"**, Susanne Perutz, Pascal Silbersan, F. I. Kramer and C. Cohen, Cornell University, USA. **p. 116**
19. **"MODEL EXPERIMENTS ON ELASTOMER-SOLID ADHESION"**, Y. Marciano, M. Deruelle, M. Tirrell, H. Hervet, and L. Leger, CNRS, France; and Department of Chemical Engineering and Materials Science, University of Minnesota, USA. **p. 119**
20. **"INTERACTION OF FUNCTIONAL GROUPS IN POLYMERS WITH STEEL SURFACES"**, I. Sutherland, P. Carpenter, R. J. Heath and B. Pearson, Department of Chemistry, Loughborough University, England. **p. 121**
21. **"ADSORPTION OF POLYCYANURATE FILMES ON SILICON WAFERS AND ALUMINUM SUBSTRATES STUDIED BY XPS"**, S. Dieckhoff, V. Schlett, W. Possart, and O. D. Hennemann, Fraunhofer-Institut für Angewandte Materialforschung, Germany. **p. 123**
22. **"A COMPARISON OF SCANNING FORCE MICROSCOPY AND ELLIPSOMETRY FOR THICKNESS DETERMINATION OF ULTRATHIN POLYMER FILMS"**, T. Gesang, D. Fanter, R. Hofer, W. Possart, O. D. Hennemann, Fraunhofer Institut für Angewandte Materialforschung, Germany. **p. 126**

23. **"ADHESIVE SELECTION PROTOCOL"**, Gregory L. Anderson, Thiokol Corporation, USA. **p. 129**
24. **"CHEMISTRY AND REACTIVITY OF CARBOXYLIC ACID CONTAINING SURFACES"**, C. A. Fleischer, G. Apai, W. P. McKenna, Eastman Kodak Co., USA. **p. 132**
25. **"EFFECT OF PLASTICIZER CONTENT AND PHOTOAGING ON PVB/GLASS ADHESION"**, R. J. May and B. J. Love, Department of Materials Science and Engineering, USA. **p. 135**
26. **"EXPERIMENTAL STUDY OF KGR-1 ADHESIVE SHEAR SPECIMENS"**, M. Y. Tsai, and J. Morton, Department of Engineering Science and Mechanics, Virginia Tech and R. B. Krieger, Cytec Engineered Materials Inc. USA.
27. **"PHOTOELASTIC STUDY OF PROPAGATING CRACKS IN ADHESIVE JOINTS"**, Y. Y. Wang and F. P. Chiang, Department of Mechanical Engineering, State University of New York at Stony Brook, USA. **p. 137**
28. **"THE DIFFUSION OF ISODODECYL PELARGONATE WITHIN AN EPOXY ADHESIVE"** K. Kwan and T. C. Ward, Virginia Tech, USA. **p. 139**
29. **"FRACTURE TOUGHNESS TESTING OF ADHESIVELY BONDED SHEET STEEL"**, I. Ashcroft, P. Basu, and G. Spinks, Department of Materials Engineering, University of Wollongong, Australia. **p. 141**
30. **"ADHESION OF PAINT COATINGS TO ALLOY COATED SUBSTRATES"**, Youlai Zhang, I. Ashcroft, M. Binns and G. M. Spinks, Department of Materials Engineering, University of Wollongong, Australia. **p. 143**
31. **"MEASURING THE POWER LAW DEPENDENCE OF THE VAN DER WAALS INTERACTION USING ATOMIC FORCE MICROSCOPE TECHNIQUES"**, Ron Reifenger, B. Gady, and D. Schlee, Department of Physics, Purdue University, USA. **p. 145**
32. **"AEROSIZER PARTICLE SIZE DISTRIBUTION MEASUREMENTS OF FREE-FLOWING AND COHESIVE DRY POWDERS"**, Bart Dahneke, Eastman Kodak Company, USA.
33. **"EQUILIBRIUM INTERMOLECULAR DISTANCE AT THE FIBRE-MATRIX INTERFACE IN MODEL COMPOSITES"**, M. Nardin and J. Schultz, CNRS, France. **p. 147**
34. **"LOW ENERGY ION IMPLANTATION/DEPOSITION AS A FILM SYNTHESIS AND BONDING TOOL"**, Andre Anders, Simone Anders, Ian Brown and Igor Ivanov, Lawrence Berkeley Laboratory, University of California, USA. **p. 149**
35. **"SURFACE ANALYSIS, PEEL STRENGTH AND SEALANT ADHESION TO AGED OXYGEN PLASMA MODIFIED UNPLASTICIZED PVC FILMS"**, Mojgan Babaj-Cline and J. P. Wightman, Department of Chemistry, Virginia Tech, USA. **p. 151**

36. **"HUMIDITY AND TEMPERATURE DOUBLY SHIFTED FRACTURE ENERGY MASTER CURVES FOR THE PREDICTION OF SEALANT ADHESION"**, N. E. Shephard and J. P. Wightman, Department of Chemistry, Virginia Tech, USA. **p. 155**
37. **"ALTERING THE FIBER MATRIX INTERPHASE IN SEMICRYSTALLINE POLYMER MATRIX COMPOSITES"**, R. L. Clark and R. G. Kander, Department of Materials Science and Engineering, Virginia Tech, USA. **p. 157**
38. **"HIGH SPEED INFRA RED IMAGING OF FRACTURE IN THERMOPLASTIC OLEFINS"**, Y. Wang, S. Telenkov, Z. L. Wu, T. Ahmed, X. Wang, L. D. Favro, P. K. Kuo and R. L. Thomas, Wayne State University; A. C. Ramamurthy, Ford Motor Company; W. Brostow, N. D'Sousa and H. Galina, University of North Texas, USA. **p. 159**
39. **"FILM FORMATION OF LATEX COATINGS"**, C. A. Fleischer, H. R. Grashof, D. Schwark, K. Schlafer, and J. F. Elman, Eastman Kodak Company, USA. **p. 162**
40. **"THE WETTABILITY OF ROUGH SUBSTRATES BY VISCOUS POLYMER MELTS"**, S. A. Tschetter, N. Shephard and J. P. Wightman, Department of Chemistry, Virginia Tech, USA. **p. 165**
41. **"EFFECT OF ADHEREND TYPE UPON THE ADHESIVE MODE-I FRACTURE ENERGY OF DCB JOINTS"**, A. J. Bell, A.J. Kinloch and Y. Wang, Department of Mechanical Engineering, Imperial College of Science, Technology and Medicine, England. **p. 167**
42. **"POLYMERIC COUPLING AGENTS FOR ENHANCING THE ADHESION OF EPOXY TO STEEL"**, Karthik Vaideeswaran and James P. Bell, University of Connecticut, USA. **p. 171**
43. **"PHASE DIAGRAMS OF ACRYLIC PRESSURE SENSITIVE ADHESIVE"**, Hyun-Joong Kim and Hiroshi Mizumachi, University of Tokyo, Japan. **p. 173**
44. **"THE DESIGN OF COMPOSITE TO METAL TUBULAR LAP JOINTS FOR TORSIONAL LOADING"**, M. D. Roseman, and A. J. Kinloch, Department of Mechanical Engineering, Imperial College of Science, Technology and Medicine, England. **p. 176**
45. **"HEAT CYCLES LEAD TO IMPROVEMENTS FOR CHLORINATED POLYOLEFIN ENHANCED PAINT TO PLASTIC ADHESION"**, William L. Dechent and James O. Stoffer, University of Missouri-Rolla, USA. **p. 182**

TUESDAY MORNING - SESSION 3A

NEW MATERIALS FOR ADHESIVES AND COATINGS - #2

Session Chair: Terry St Clair, NASA, USA

- 8:00 - 8:10 OPENING COMMENTS**
Terry L. St. Clair
- 8:10 - 8:40 "RELATIONSHIP BETWEEN THE SILICA CONTENT OF SYNTHETIC VULCANIZED STYRENE-BUTADIENE RUBBER AND ITS ADHESION PROPERTIES",** A. Torro-Palau, J. M. Martin-Martinez, J. C. Fernandez-Garcia, and A. C. Orgiles-Barcelo, INESCOP and Adhesion and Adhesives Laboratory, University of Alicante, Spain. **(paper dedicated to honoring Professor Schultz). p. 185**
- 8:40 - 9:10 "DESIGN AND CHARACTERIZATION OF HIGH PERFORMANCE POLYIMIDE ADHESIVE",** G. W. Meyer, B. Tan, J. Heidbrink, and J. E. McGrath, Department of Chemistry, Virginia Tech, USA. **p. 189**
- 9:10 - 9:40 "THE FRACTURE EFFICIENCY OF TESTS FOR ADHESIVE BONDS",** Yeh-hung Lai and D. A. Dillard, Virginia Tech, USA. **p. 192**
- 9:40 - 10:00 BREAK**
- 10:00 - 10:30 "SURFACE-MODIFICATION OF STYRENE - BUTADIENE COPOLYMERS AND THEIR ADHESION TO COPPER AND TO GOLD",** Paul D. Mumbauer, and Gregory S. Ferguson, Department of Chemistry, Lehigh University. **p. 195**
- 10:30 - 11:00 "A THERMOPLASTIC POLYETHERIMIDE ADHESIVE",** Terry L. St. Clair and Donald J. Pogar, NASA Langley Research Center, USA. **p. 198**
- 11:00 - 11:30 "NEW COUPLING AGENTS FOR BONDING POLYMERS TO ALUMINUM",** Stephanie L. Nesbitt, J. P. Bell, and D. E. Nikles, Department of Chemical Engineering, University of Connecticut, and Center for Materials for Information Technology, and the University of Alabama, USA. **p. 199**

TUESDAY MORNING - SESSION 3B

CHEMICAL/PHYSICAL CHARACTERIZATION OF ADHESIVE INTERACTIONS #1

Session Chair: Marek Urban, North Dakota State University

- 8:00 - 8:10** **Opening Comments**
Marek Urban, North Dakota State University, USA
- 8:10 - 8:40** **"INFRARED AND RAMAN SPECTROSCOPY OF POLYMER/METAL INTERPHASES: APPLICATION TO ADHESION"**, F. J. Boerio, I. Segall, C. E. Taylor, Y. M. Tsai, J. T. Young, and W. W. Zhao, Department of Materials Science and Engineering, University of Cincinnati, USA. **p. 202**
- 8:40 - 9:10** **"RHEO-PHOTOACOUSTIC FT-IR SPECTROSCOPY AND INTERLAYER ADHESION OF POLYMERS"**, Brian D. Pennington and Marek W. Urban, North Dakota State University, USA. **p. 206**
- 9:10 - 9:40** **"THE DETERMINATION OF ADSORPTION ISOTHERMS BY XPS AND TOF-SIMS"**, J. F. Watts, J. E. Castle, M. M. Chehimi, and M-L Abel, Department of Materials Science and Engineering, University of Surrey, England; and Institut de Topologie et de Dynamique des Systemes, University of Paris, France. **p. 209**
- 9:40 - 10:00** **BREAK**
- 10:00 - 10:30** **"THE QUANTITATIVE EVALUATION OF ACID-BASE PROPERTIES BY XPS"**, S. R. Leadley, J. F. Watts and G. Beamson, Department of Materials Science and Engineering, University of Surrey, England. **p. 212**
- 10:30 - 11:00** **"DYNAMICS OF ADHESION PROMOTERS AND THE PHYSICAL PROPERTIES OF COMPOSITES"**, Timothy W. H. Wang and Frank Blum, Department of Chemistry and Materials Research Center, University of Missouri-Rolla, USA. **p. 215**
- 11:00 - 11:30** **"DETECTION OF SUBADHESIVE HYDRATION OF ALUMINUM ADHERENDS BY ELECTROCHEMICAL IMPEDANCE SPECTROSCOPY"**, G. D. Davis and P. L. Whisnant, Martin Marietta Laboratories, and J. D. Venables, Venables and Associates, USA. **p. 218**
- 11:30 - 12:00** **"THE ADSORPTION OF SILANE MOLECULES ON YTTRIUM TREATED STEEL SUBSTRATES: A ROUTE TO IMPROVED BOND PERFORMANCE"**, S. J. Davis and J. F. Watts, Department of Materials Science and Engineering, University of Surrey, England. **p. 221**

- 12:00 - 12:30** **"PENETRATION OF SILVER INTO SELF-ASSEMBLED ORGANIC MONOLAYERS"**, G. C. Herdt and A. W. Czanderna, Measurements and Characterization Branch, National Renewable Energy Laboratory, USA. **p. 224**

TUESDAY MORNING - SESSION 3C

SMALL PARTICLE ADHESION #2

Session Chair: Don Rimai, Eastman Kodak Company

- 8:00 - 8:10** **Opening Comments**
Don Rimai, Eastman Chemical Company
- 8:10 - 8:40** **"THE ADHESION OF GLASS PARTICLES TO SILICON SUBSTRATES"**, R. C. Bowen, D. S. Rimai, and L. P. DeMajo, Eastman Kodak Co., USA. **p. 227**
- 8:40 - 9:10** **"PARTICLE REMOVAL FROM SMOOTH AND ROUGH SURFACES UNDER SUBSTRATE ACCELERATION"**, Mehdi Soltani, and Goodarz Ahmadi, Department of Mechanical and Aeronautical Engineering, Clarkson University, USA. **p. 230**
- 9:10 - 9:40** **"A SIMPLE MODEL FOR THE EFFECTS OF TIME ON THE ADHESION OF SUBMICROMETER PARTICLES TO SUBSTRATES"**, F. Zhang and A. A. Busnaina, Clarkson University; and D. S. Rimai, Eastman Kodak Co., USA. **p. 233**
- 9:40 - 10:00** **BREAK**
- 10:00 - 10:30** **"PARTICLE ADHESION: A MOLECULAR DYNAMICS APPROACH"**, D. Quesnel, D. S. Rimai and L. P. DeMajo, Department of Mechanical Engineering, University of Rochester, USA.
- 10:30 - 11:00** **"TONER ADHESION: THE EFFECT OF NON-UNIFORM SURFACE CHARGE DISTRIBUTION"**, D. Hays, E. Eklund, W. H. Wayman and L. J. Brillson, Xerox, USA. **p. 237**
- 11:00 - 11:30** **"RELATIONSHIPS BETWEEN PARTICLE ROUGHNESS, PARTICLE-SURFACE ADHESION AND PARTICLE CHARGING"**, H. A. Mizes, M. L. Ott, E. A. Eklund and Dan Hays, Xerox Corporation, USA. **p. 240**
- 11:30 - 12:00** **"HUMIDITY SENSITIVITY OF THE ADHESION OF TONER PARTICLES TREATED WITH SURFACE-MODIFIED SURFACE ADDITIVES"**, Mary L. Ott and Scott M. Silence, Xerox Corporation, USA. **p. 243**

TUESDAY AFTERNOON FREE

TUESDAY EVENING - SESSION 4A

DURABILITY: ENVIRONMENTALLY INDUCED ADHESION REDUCTION

Session Chair: Rose Ryntz, Ford Motor Company

- 7:00 - 7:10** **Opening Comments**
Rose Ryntz, Ford Motor Company
- 7:10 - 7:40** **"MEASUREMENT OF WET ADHESION COATING SYSTEM ON STEEL: An EQUIVALENT CIRCUIT MODEL"**, Peter J. Moreland, Zeneca Resins, England. **p. 246**
- 7:40 - 8:10** **"A STUDY OF THE EFFECTS OF MOISTURE DIFFUSION ON THE STRENGTH AND FATIGUE RESISTANCE OF EPOXY BONDED ADHESIVE JOINTS"**, J. A. Harris Materials and P. A. Fay, Material Engineering Research Laboratory Ltd. and Ford Motor Company, England. **p. 249**
- 8:10 - 8:40** **"RELATIONSHIP BETWEEN ADHESION LOSS AND WATER AT THE POLYMER / SUBSTRATE INTERFACE"**, Tinh Nguyen, David Alsheh, Dale Bentz and Eric Byrd, National Institute of Standards and Technology, USA. **p. 252**
- 8:40 - 9:10** **"EFFECT OF PRECURE MOISTURE EXPOSURE ON A STRUCTURAL EPOXY ADHESIVE"**, S. M. Ward, M. A. DeBolt, G. L. Westerbeek, and R. A. Dickie, Ford Research Laboratory, USA. **p. 255**
- 9:10 - 9:40** **"ADHESIVE BONDING OF COATED STEELS"**, I. A. Ashcroft, P. Basu, and G. Spinks, Department of Engineering, University of Wollongong, Australia. **p. 258**
- 9:40 - 10:10** **"SILANE COUPLING AGENTS AS ADHESION PROMOTERS FOR BONDING THERMOPLASTIC POLYMERS TO ALUMINUM"**, Steven H. McKnight and John W. Gillespie, Center for Composite Materials, University of Delaware, USA. **p. 261**

TUESDAY EVENING - SESSION 4B

CHEMICAL/PHYSICAL CHARACTERIZATION OF ADHESIVE INTERACTIONS #2

Session Chair: Marek Urban

- 7:00 - 7:10** **Opening Comments**
Marek Urban, North Dakota State University, USA

- 7:10 - 7:40** **"CHARACTERIZATION OF INTERPHASES IN POLYMER - POLYMER JOINTS"**, M. F. Vallat, C. Spitteri, J. Schultz, A. Belgrine, G. Evrard, and A. Coupard, Centre de Rescherches sur la Physico-Chemie des Surfaces Solides and Laboratoire de Recherches et de Controle des Caoutchous et des Plastiques, France. **p. 264**
- 7:40 - 8:10** **"THE INFLUENCE OF SURFACE MORPHOLOGY ON THE ADHESION OF COATINGS TO THERMOPLASTIC POLYOLEFINS UNDER STRESS"**, Rose A. Ryntz, Ford Motor Company, USA. **p. 267**
- 8:10 - 8:40** **"IN SITU FTIR STUDY OF THE REACTION OF ORGANOSILANES AT THE FLAT SILICA SURFACE"**, M. J. Azzopardi and H. Arribart, Laboratoire CNRS/Saint Gobain, France. **p. 275**
- 8:40 - 9:10** **"ADHESION BETWEEN SEMICRYSTALLINE POLYMERS"**, E. Boucher, J. P. Folkers, H. Hervet and L. Leger, Laboratoire de la Matiere Condensee - URA CNRS, France. **p. 278**
- 9:10 - 9:40** **"CHARACTERIZATION OF INTERFACES BETWEEN VACUUM DEPOSITED SILICONE DIOXIDE FILMS AND POLYMETHYL METHACRYLATE SUBSTRATES"**, W. H. Tsai, J. T. Young, Y. M. Lian and S. L. Liao, Polymer Analysis and Characterization Department, Union Chemical Laboratories, Taiwan. **p. 281**
- 9:40 - 10:10** **"ADHESION MECHANISMS OF POLYURETHANES TO GLASS SURFACES"**, R. K. Agrawal and L. T. Drzal, Michigan State University, USA. **p. 285**

**TUESDAY EVENING - SESSION 4C
PRESSURE SENSITIVE ADHESIVES**

Session Chair: Louis Sharpe, Consultant, USA

- 7:00 - 7:10** **Opening Comments**
Louis Sharpe, Consultant, USA
- 7:10 - 7:40** **"SURFACE AND INTERFACIAL STRUCTURE OF RELEASE COATINGS FOR PRESSURE SENSITIVE ADHESIVES"**, David J. Kinning, 3M Adhesive Technologies Center, USA. **p. 288**
- 7:40 - 8:10** **"STRUCTURE-PROPERTY-PERFORMANCE RELATIONSHIPS IN EMULSION PRESSURE SENSITIVE ADHESIVES: EFFECT OF MATERIAL AND FORMULATING PARAMETERS"**, Krishan C. Sehgal and David R. Bassett, USCAR Emulsion Systems, Union Carbide Corporation, USA. **p. 292**

- 8:10 - 8:40** "IMAGING THE BONDING AND DEBONDING OF PRESSURE SENSITIVE ADHESIVES", Robert K. Galkiewicz, 3M Adhesive Technologies Center, USA. p. 296
- 8:40 - 9:10** "RATE - TEMPERATURE DEPENDENCE OF THE AUTOHESION OF CARBON BLACK-FILLED STYRENE-BUTADIENE RUBBER", G. R. Hamed and P. S. Wu, Polymer Science Department, University of Akron, USA. p. 300
- 9:10 - 9:40** "VISCOELASTIC PROPERTIES OF PRESSURE SENSITIVE ADHESIVES", E. P. Chang, Avery Research Center, USA. p. 303
- 9:40 - 10:00** "SILICONE PRESSURE SENSITIVE ADHESIVES WITH ENHANCED SURFACE WETTABILITY", Dr. Shaow B. Lin, Specialty Coatings Technology, GE Silicones, USA. p. 307
- 10:00 - 10:20** "MAXIMUM PEEL STRENGTHS OF PRESSURE SENSITIVE STYRENE BUTADIENE LATEX POLYMERS OVER WIDE TEMPERATURE AND PEEL RATE RANGES", J. J. Spitzer, J. Antonucci, A. E. Karabela, and K. P. Lok, BASF, USA. p. 310
- 10:20 - 10:40** "WATER WICKING RATE OF AN ABSORBANT PAPER LAMINATED BY PRESSURE SENSITIVE ADHESIVE", T. Yang, and R. J. Nelson, Abbott Laboratories, USA. p. 313

WEDNESDAY MORNING - SESSION 5A

MECHANICAL CHARACTERIZATION OF COATING/ADHESIVE-SUBSTRATE INTERPHASE

Session Chair: Christopher Brown, Worcester Polytechnic Institute

- 8:00 - 8:10** **Opening Comments**
Christopher Brown, Worcester Polytechnic Institute
- 8:10 - 8:40** "HERTZIAN INDENTATION TEST FOR MONITORING THE FRACTURE ENERGY OF POLYMER/GLASS INTERFACES IN SANDWICH GEOMETRIES", J. E. Ritter, T. J. Lardner, G. Bao, and P. Juntawongso, Department of Mechanical Engineering, University of Mass. USA. p. 316
- 8:40 - 9:10** "INTERFACIAL CRACK GROWTH IN POLYMER/GLASS SANDWICH SPECIMENS", J. E. Ritter, T. J. Lardner, G. C. Prakesh, and A. J. Stewart, Department of Mechanical Engineering, University of Mass. USA. p. 319
- 9:10 - 9:40** "RATE DEPENDENT INTERFACIAL AND COHESIVE FRACTURES IN CONVENTIONAL DOUBLE CANTILEVER BEAM SPECIMENS", M. D. Rakestraw, M. W.

Taylor, Y. H. Lai, T. Chang and D. A. Dillard, Department of Engineering Science and Mechanics, Virginia Tech. **p.322**

9:40 - 10:00 BREAK

10:00 - 10:30 "STUDY OF EFFECT OF THICKNESS ON MECHANICAL PROPERTIES OF ADHESIVE MATERIALS BY SIEM", Y. Y. Wang, Qing Wang and Fu-pen Chiang, Department of Mechanical Engineering, State University of New York at Stony Brook, USA. p. 325

10:30 - 11:00 "TOPOGRAPHY AND CAPILLARY BONDING OF WET POLYETHYLENE SURFACES", S. C. Colbeck, CRREL and J. B. Rossacci, E. M. Shipulski and C. A. Brown, Mechanical Engineering Department, Worcester Polytechnic Institute, USA. p. 328

11:00 - 11:30 "FRACTURE OF AN ADHESIVE SUBSTRATE INTERFACE IN SANDWICH SPECIMENS", J. G. Swadener and K. M. Liechti, Engineering Mechanics Research Laboratory, University of Texas, USA. p. 331

11:30 - 12:00 "ELASTOPLASTIC, THREE DIMENSIONAL STRESS ANALYSIS OF THE PENINSULA BLISTER TEST", A. Shirani and K.M. Liechti, Engineering Mechanics Research Laboratory University of Texas, USA p. 334

WEDNESDAY MORNING - SESSION 5B

APPLICATIONS OF ADHESION SCIENCE

Session Chair: Kimberly Chaffin, Ford Motor Company

8:00 - 8:10 Opening comments
Kimberly Chaffin, Ford Motor Company

8:10 - 8:40 "RF CURING IMPLEMENTATION IN AUTOMOTIVE PRODUCTION", Kimberly A. Chaffin, Chi Li, and R. A. Dickie Ford Research Laboratory, Ford Motor Company, USA. p. 337

8:40 - 9:10 "GUIDED WAVES FOR METAL TO COMPOSITE ADHESION BOND INSPECTION", Joseph L. Rose and Krishna Rajana, and Semyen Pelts, Department of Engineering, Science and Mechanics, Pennsylvania State University, USA. p. 340

9:10 - 9:40 "THE BOEING WEDGE TEST: FACT OR FICTION", R. D. Adams, University of Bristol, England.

9:40 - 10:00 BREAK

10:00 - 10:30 "INCREASED ADHESION AT THE FIBER INTERFACE FOR POLYETHYLENE FIBER PAPERS FOLLOWING

OXYFLUORATION TREATMENT", B. Riedl and H. Chtourou,
Centre for Research on Science and Engineering of Macromolecules,
Laval University, Canada. **p. 343**

**10:30 - 11:00 "PERFORMANCE TESTING OF COATED ALUMINUM
FOOD AND BEVERAGE PRODUCTS"**, R. A. Haaksma,
Corporate Research and Development, Reynolds Metals Company,
USA **p. 346**

WEDNESDAY MORNING - SESSION 5C

GENERAL PAPERS

Session Chair - Greg Anderson, Thiokol

8:00 - 8:10 Opening Comments
Greg Anderson, Thiokol

8:10 - 8:40 "BOND STENGTH OF THE FRP-WOOD INTERFACE", J.
F. Davalos and E. J. Barbero, Constructed Facilities Center, USA. **p. 349**

**8:40 - 9:10 "FAILURE ANALYSIS AND CHARACTERIZATION OF A
PHENOLIC ADHESIVE USED TO SEPARATE BRONZE
FROM A SULFUR CURED RUBBER"**, George Dallas, Eugene
Slagowski, Wayne Cheatile and Linda Shalkowski, Research and
Development, Beloit Manhattan, USA. **p. 352**

**9:10 - 9:40 "EFFECT OF CONTAMINATION AND ROUGHNESS OF
STAINLESS STEEL ON THE ADHESIVE BONDING
WITH A SILICONE ELASTOMER"**, M. Mantel, N. Shephard,
and J. P. Wightman, Virginia Tech and Uguine Research Center,
France. **p. 355**

9:40 - 10:00 BREAK

**10:00 - 10:30 "EFFECT OF ELECTRODEPOSITION OF POLYAMIC
ACID ON THE SURFACE PROPERTIES OF CARBON
FIBERS"**, W. Yuan and J. O. Iroh, Department of Materials Science
and Engineering, University of Cincinnati, USA. **p. 359**

**10:30 - 11:00 "BOND CHARACTERISTICS AT POLYMER-PIGMENT
INTERFACES"**, J. Lara, Shu-De Rong, and H. P. Schreiber,
Department of Chemical Engineering, Ecole Polytechnique, Canada. **p. 362**

THE RELATIONSHIP BETWEEN SURFACE ENERGETICS AND ADHESION STRENGTH

J. Schultz

University of Haute Alsace
Centre de Recherches sur la Physico-Chimie des Surfaces Solides - CNRS
68200 - Mulhouse, France

INTRODUCTION

One of the fundamental questions of adhesion is the following : Is it possible to predict the adhesive strength of an assembly as measured by any destructive test from the intrinsic properties of the solids in contact and more precisely from their surface properties ? This paper illustrates how we tried to answer this problem through a few pieces of work contributing to a better knowledge of the relationship between experimental work of separation and thermodynamical work of adhesion.

RESULTS

Our first work devoted to this problem was performed with A.N. Gent at the University of Akron [1, 2]. Using model adhesive assemblies made of slightly crosslinking SBR deposited on a rigid substrate, we could show that the energy of separation measured by peeling is much higher (10^2 to 10^4 times) than the reversible work of adhesion calculated from the surface

energies of the solids. By changing the nature of the substrate or by peeling in various liquid media, we could demonstrate that the experimental work of separation W can be expressed as a product of two terms :

$$W = W_0 \cdot f(R, T)$$

W_0 being the reversible work of adhesion and $f(R, T)$ a mechanical factor, depending on rate of peeling R and temperature T and representing the energy expended in deforming irreversibly the viscoelastic adhesive layer during fracture propagation.

In 1984, we developed with A. Carré [3] a more complete relationship (equation of the multiplying factors) including a third term $g(M_c)$ called molecular dissipation factor which depends on the molecular weight M_c between crosslinks according to a theory proposed by Lake and Thomas [4].

The role of surface properties on adhesive strength has been verified by studying extensively the effect of a liquid environment on peel energy [5]. When only physical interactions are being exchanged at the solid-solid interface and if the liquid does

not swell or react with the solids, the reduction in peel strength can be quantitatively predicted from the surface energies of the solids and the liquid. Moreover, a kinetical study of the potential rate of penetration into the crack front during peeling allowed us to calculate very precisely the transition peel rates corresponding to total or partial presence of the liquid at the crack tip on a microscopical level and hence its influence on peel strength [6, 7]. Along the same lines, we developed a method allowing us to evaluate the respective contribution of physical and chemical bonds to the energy of adhesion [5, 8].

However, there are many difficulties in predicting quantitatively the strength of adhesion from surface properties. Among them, let's mention the determination of undisputed values of the surface energy of solids, the phenomena of orientation of macromolecules at interfaces and the formation of interphase .

Part of our work has contributed to a better understanding and determination of surface properties of solids. Methods based on wetting by a two liquid phase system [9] and on inverse gas chromatography at infinite dilution [10, 11] are of particular interest in this field.

Another problem lies in the orientation and re-orientation of macromolecular chains at interfaces leading to a strong change of the

level of interactions at the solid-solid interface. To take this effect into account, we proposed to replace the static concept of surface energy by the dynamic concept of "potential" surface energy showing that the surface energy of a solid and hence the interfacial energy between solids is driven by thermodynamical considerations of energy minimization [12]. The adhesion of grafted polyolefins (acrylic acid grafted polyethylene or maleic anhydride grafted polypropylene) to aluminium substrates illustrate this phenomenon [12, 13]. The second example dealing with the grafted polypropylene sample also demonstrates the predominant role of interphase formation.

This aspect is specifically described by a study devoted to the fibre/matrix adhesion in composite materials [14]. In this case again, a quantitative relationship could be obtained between the adhesive strength or more precisely the shear strength of the fibre/matrix interface τ measured by a fragmentation test and the reversible energy of adhesion W_0 calculated from dispersive and acid-base interactions :

$$\tau \left(\frac{E_f}{E_m} \right)^{1/2} = \frac{W_0}{\lambda}$$

E_f and E_m are the elastic moduli of the fibre and the matrix and λ is a universal intermolecular distance.

This relationship has been quantitatively verified for many composite systems including glass and carbon fibres and thermosetting and thermoplastic matrices. However, when using semicrystalline polymers or elastomers, an important deviation is observed which could be attributed to the formation of an interphase due either to transcrystallisation or to the creation of a pseudo-glassy layer. These interfacial regions exhibit properties and more specifically mechanical properties different from the bulk matrices [14, 15]. We could demonstrate, that our general model relating stress transfer capacity and adhesion remains valid when such interphases are formed if the specific mechanical properties of there interphases are taken into account.

CONCLUSION

Given the great variety of materials to be bonded, the diversity of bonding and testing conditions, it is obvious that there is no unique or universal relationship between the surface properties of solids and the final performance of an adhesive system. However in simple cases or even in more complicated systems exhibiting interfacial or interphasial structuration, the role of surface energy or surface reactivity can be quantitatively demonstrated.

REFERENCES

1. A.N. Gent and J. Schultz, Proc. 162nd ACS Meeting 31 (2), 113 (1971).
2. A.N. Gent and J. Schultz, J. Adhesion 3, 281 (1972).
3. A. Carré and J. Schultz, J. Adhesion 17, 135 (1984).
4. G.J. Lake and A.G. Thomas, Proc. Roy. Soc., London A300, 103 (1967).
5. A. Carré and J. Schultz, J. Adhesion 18, 171 (1984).
6. MER Shanahan and J. Schultz, J. Polym. Sci. 18, 171 (1980).
7. A. Carré and J. Schultz, J. Adhesion 18, 207 (1985).
8. M.F. Vallat and M. Nardin, J. Adhesion (in press).
9. J. Schultz, K. Tsutsumi and J.B. Donnet, J. Coll. Interface Sci. 59 (2), 272 and 277 (1977).
10. J. Schultz, L. Lavielle and H. Simon, Proc. Intern. Symposium on "Science and New Applications of Carbon Fibres" Toyohashi University, Japan 3, 169 (1984).
11. J. Schultz, L. Lavielle and C. Martin, J. Chim. Phys. 84 (2), 231 (1987).
12. J. Schultz, A. Carré and C. Mazeau, Intern. J. Adhesion and Adhesives 4 (4), 163 (1984).
13. J. Schultz, L. Lavielle, A. Carré and P. Comien, J. Mat. Sci. 24, 4363 (1989).

14. M. Nardin, E.M. Asloun and J. Schultz, Polym. Adv. Technol. 2, 109, 115, 161 and 171 (1991).
15. M. Nardin, A. El. Maliki and J. Schultz, J. Adhesion 40 (2-4), 93 (1993).

The role of adhesion promoters on the structure of the interphase

M. Grunze, T. Strunskus, Ch. Wöll, University of Heidelberg, Applied Physical Chemistry, INF 253,
D-69120 Heidelberg, Germany.*

** Technische Fakultät der Christian-Albrechts-Univ. zu Kiel,
Kaiserstr. 2, 24143 Kiel-Gaarden, Germany.*

ABSTRACT

In this contribution we describe new experimental results on the molecular orientation of polyimide deposited by the Langmuir Blodgett technique onto SiO_x surfaces and SiO_x substrates pretreated with a variety of alkylsilanes. We found that on both silicon surfaces the third polyimide layer has an orientation close to the one expected for the bulk structure. Our previous studies on the structure of Langmuir Blodgett deposited polyimide films on etched Si(100) surfaces showed a strongly perturbed interphase region. Incomplete imidization in the first polyimide layer on the aminosilane treated surfaces gives direct evidence of chemical bonds between the two materials. Delamination experiments of spun-on polyimide films onto the silane films indicate that bond fracture occurs in the aminosilane/polyimide interphase. This indicates, that also in these systems the polyimide interphase is the "weak" link in the laminate structure.

INTRODUCTION

In this contribution we describe new experiments designed to test the hypothesis, that the mechanical properties of the "interphase" between polymer and inorganic substrate, as determined by molecular density, molecular orientation and molecular weight distribution, play an important (if not decisive) role in the stability of the bonding between the inorganic substrate and the polymer. Our previous studies on polyimide films deposited by the Langmuir-Blodgett technique onto SiO_x substrates, using Near Edge X-Ray Absorption Fine Structure measurements (NEXAFS) as a probe for molecular orientation revealed, that the orientation in the interphase depends on the chemical bond between the

substrate and the polymer, i.e. the nature and reactivity of the substrate surface [1]. Whereas on gold and silver surfaces a gradual transition of the interface polymer orientation into the polymer bulk structure was observed with increasing thickness, the strong reaction between the polymer and an etched silicon surface leads to a structurally and chemically ill defined substrate/polymer interphase.

Here we describe new experiments on the structure and chemical composition of Langmuir-Blodgett deposited polyimide films deposited onto silicon surfaces covered with a thin oxide layer and onto silane treated silicon surfaces. These experiments are complemented by delamination experiments of polyimide films prepared by spin coating onto silane pretreated silicon surfaces.

EXPERIMENTAL

The silicon wafers in this study were coated with a native oxide layer or were pretreated with 3-Aminopropyltriethoxysilane (APTMS), 17-Aminohexadecyl-trimethoxy-silane (AHTMS), n-Triacontyltrichlorosilane (TCTS), n-Octadecyltrichlorosilane (OTS), n-Octadecyltrimethoxysilane (OTMS) and n-Propyltrichlorosilane (PTS) following standard procedures [2,3] before polyimide deposition. The silane layers were characterized extensively with respect to homogeneity, molecular orientation and chemical interactions [2,3] using surface spectroscopies and Atomic Force Microscopy (AFM). Polyimide films were either deposited by the Langmuir Blodgett technique [1,3,5], or, for the delamination experiments, were prepared by spin coating.

RESULTS

A comparison of the growth kinetics and lateral order and of the orientation of the molecules in the self-assembled monolayers show that the amino-terminated silanes have a high degree of disorder and that some of the terminal amino groups interact with the substrate /3/. This is also evident from contact angle and ellipsometric measurements /6/. Contrary, the methyl-terminated silane films show a distinct nucleation behaviour via island growth which, however, depends critically on the experimental conditions. In this work only methylterminated silane films were used for the investigation of the polyimide interphase structure and chemistry.

We recall that Langmuir-Blodgett films of polyimide deposited onto etched silicon wafers show a high distortion and fragmentation over at least three monolayer thickness /1,4/. The respective Cls NEXAFS data for polyimide on Si(100) were shown in ref. /1/. We noted that the spectra exhibit a very different intensity ratio than expected for intact polyimide. Before thermal curing at 200 °C (30 minutes in high vacuum) the polyimide precursor (the octadecylammonium salt of polyamic acid) used in the Langmuir deposition technique showed spectra representative for the intact molecule. Only during imidization, fragmentation occurs leading to at least 3 monolayers of degraded polymer. Concurrent with the chemical reactions between polymer and the silicon surface, a high disorder in the molecular films is induced. On top of these (undefined) decomposition products at the interface intact polyimide is found, however, with a high degree of disorder.

Contrary to the presented results on etched silicon, the NEXAFS results in this study for the 1, 3 and 5 LB layer film on APS (of which itself the NEXAFS data indicate a high degree of disorder) show that essentially the second layer already corresponds to intact polyimide. (Note that the probing depth of NEXAFS in electron partial yield (> 150 eV) detection mode at the Cls edge corresponds to ca. 10 Å). In the first polyimide layer the NEXAFS and XPS experiments show a partial reaction between the

polyimide precursor and the aminosilane consistent with carbamide bond formation. A slight preferential orientation of the phenyl rings parallel to the substrate surface exists, similar to the NEXAFS results obtained on thick vapor deposited polyimide films on a silicon substrate. These results are very different to those obtained for polyimide Langmuir Blodgett layers on etched Si (100) /1/.

That delamination occurs in this structurally and chemically ill-defined "weak boundary layer" in the LB deposited polyimide films on a Si(100)/SiO_x surface was verified by us in crude fracture experiments /7/. For spun on polyimide films on SiO_x surfaces Oh et al. /8/ reported an increase in peel strength by a factor of 1,5 - 2,0 for the APS treated as compared to the untreated SiO_x surface. In both the experiments with spun on films and in our work on LB deposited polyimide layers microscopic evidence for a "slip-stick" behaviour was found, indicating a similar delamination mechanism /7/.

The question remains, where bond breaking occurs in polyimide films prepared by spin coating onto alkylsilane layers. We therefore investigated the chemical composition of the silicon- and polymer fracture side of such laminates. The SiO_x surfaces studied were pretreated with APTMS, AHTMS, TCTS, OTS, OTMS or PTS before a ca. 2µm thick polyamic acid film was spun on and subsequently imidized.

Attempts to delaminate these films with standard peel tests using Cr/Cu deposition onto the polymer surface for peeling failed on all samples due to the strong adhesion in the polyimide/silane/SiO_x interface. Therefore, the wafers were broken and partly peeled around the cleavage line. Small spot Si 2p, C 1s and N 1s XP data (using the VG ESCASCOPE photoelectron microscope) were recorded on the SiO_x side of the laminates to determine the locus of rupture.

The locus of failure in all cases was estimated from the intensity of the Si 2p XPS signal relative to the intensity of an untreated SiO_x surface to be 1,5 - 4 nm away from the silicon surface, i.e. somewhere in the vicinity to the silane/polyimide interface. In the XP spectra, however, we detect

some intensity characteristic for carbonyl carbon around $E_B = 289$ eV in the C 1s data and a small but significant N 1s intensity, the former originating from polyimide fragments. Whereas for the amino-terminated silanes the nitrogen signal could originate from the silane, this is not possible in the case of OTS or PTS. Hence, we conclude that for both aminosilane and methyl-terminated silane fracture occurs to some extent within the polyimide film.

Another possible explanation for the presence of polyimide residues on the SiO_x side of the laminate would be that the silane film de-wets the surface, desorbs or degrades otherwise during thermal treatment allowing a direct contact between polyimide and substrate. For two reasons we suggest that this is not the case: First, the observation that silane films without polyimide do not degrade during a thermal treatment identical to our imidization procedures, and secondly, that intact polyimide was observed in our NEXAFS experiments with Langmuir Blodgett deposited polyimide. That leaves, however, the possibility that the solvent or the spin coating process itself destroys the silane films and hence leads to the observed fracture behaviour. Further studies will have to clarify these possibilities in order to verify our present observation of good adhesion between polyimide and methyl-terminated alkylsilane films on silicon.

The major result of this work is that silanisation of silicon effectively avoids the chemically and structurally ill defined "weak boundary" layer observed on untreated silicon surfaces. The polyimide films deposited directly onto an etched silicon substrate exhibit an interphase region, where an interface induced orientation eventually changes to a bulk like orientation. We propose that this interphase region is the weak boundary layer where the cohesive failure in the polymer layer occurs. Its absence on the APS pretreated sample leads to an enhancement of the cohesive strength of the substrate/polyimide laminate as shown by the work of Oh et. al. /8/.

1. M. Grunze, G. Hähner, Ch. Wöll, W. Schrepp: "Interphase Orientation of Polyimide on Polycry-

stalline Gold, Silver and Si(100) ", Surface and Interface Analysis, Vol. 20, (1993), 393-401.

2. K. Bierbaum, G. Hähner, S. Heid, M. Kinzler, Ch. Wöll, F. Effenberger, M. Grunze: "A NEXAFS and XPS study on the film properties of self-assembled monolayers of organosilanes on oxidized Si (100)." Langmuir (1994), im Druck.

3. K. Bierbaum, M. Grunze: "Preparation and Characterization of thin Organosilane Films on Oxidized Substrates - A Surface Analysis Approach", The Adhesion Soc., Orlando (1994), 213-221.

4. A. Killinger, C. Thümmel, M. Grunze, W. Schrepp: "Interfacial Chemistry of Langmuir-Blodgett Deposited Polyimide Films on Si(100)", J. of Adhesion (1992), Vol. 36, 229-245.

5. M. Grunze, W. Meyer, R. Lamb, A. Ortega-Vilamil, W. Schrepp: "Langmuir-Blodgett Deposited Polyimide Films on Gold and Silver Surfaces", Surf. Sci. 273 (1992), 205-218.

6. K. Bierbaum, M. Grunze: "Growth of self-assembled n-alkyltrichlorosilane films on Si(100) investigated by Atomic Force Microscopy", Langmuir, submitted.

7. M. Grunze, M. Buck, Ch. Dressler und M. Langpape: "New experimental approaches for the study of polymer/metal interphases", J. of Adhesion (1994), 45:1-4, 227-43 .

8. T. S. Oh, L. P. Buchwalter and J. Kim, in Acid-Base Interaction, ed. by K. L. Mittal and H. R. Anderson, P. 287. VSP (1991).

ACKNOWLEDGEMENT

We thank M. Kinzler, W. Schrepp, and A. Schertel for their help in analyzing the NEXAFS data and J. Rogers for preparing some of the samples.

VISCOELASTICITY AND KINETICS OF WETTING ON RUBBERY MATERIALS

A. Carré¹ and M.E.R. Shanahan²

¹ Centre de Recherche Corning Europe,
7 bis Avenue de Valvins, 77210 Avon, France.

² Centre National de la Recherche Scientifique,
Ecole Nationale Supérieure des Mines de Paris, Centre des
Matériaux P.M. Fourn, BP 87, 91003 Evry, France.

ABSTRACT

The kinetics of spreading of a liquid drop is usually controlled by conversion of capillary potential energy into viscous dissipation within the liquid when the solid is rigid. However, if the solid is soft, a "wetting ridge" near the solid/liquid/vapor triple line can also be a dissipative sink as the wetting front moves. As a consequence, the kinetics of wetting of rubbery materials may be controlled essentially by viscoelastic losses in the polymer rather than by viscous losses in the liquid drops. Therefore, a direct analogy between the kinetics of wetting and adhesion respectively for a liquid and a solid on an elastomeric substrate has been recently proposed. In this paper, the superposition of viscoelastic braking and rubber swelling in the drop spreading phenomenon is also presented and discussed.

INTRODUCTION

Under classic conditions of wetting, in which a small axisymmetric sessile drop is deposited on a flat, horizontal, smooth, rigid, homogeneous and isotropic solid surface and allowed to spread to equilibrium, the kinetics of spreading is controlled essentially by a dynamic energy balance between the rate of restitution of capillary potential energy and viscous dissipation occurring due to shear motion within the liquid [1]. Nevertheless, when liquids are put into contact with soft solids, such as elastomers or gels, local deformation will result near the solid (S)/liquid(L)/vapor(V) triple line due mainly to the component of liquid surface tension, γ , perpendicular to the undisturbed substrate, $\gamma \sin \theta$ [2,3], θ being the conventional contact angle at the triple line. The resulting "wetting ridge", or elastic displacement of the solid has a height, h , of the order of magnitude $\gamma \sin \theta / G$, where G is the shear modulus of the solid.

When a small axisymmetric sessile drop is placed on a solid surface, the contact angle, $\theta(t)$, before equilibrium is attained, is greater than the static value, θ_0 , as predicted by the Young equation. This capillary imbalance leads to a spreading force of $\gamma [\cos \theta_0 - \cos \theta(t)]$ and as the S/L/V triple line advances at a rate U ($U = dr/dt$, where r is the drop contact radius), we may define

\dot{F} as the work done per unit time and per unit length of wetting front :

$$\dot{F} = \gamma U [\cos \theta_0 - \cos \theta(t)] \quad (1).$$

This work is consumed partially by viscous dissipation,

$T\dot{S}$, taking the form, for small contact angles [1],

$$T\dot{S} \approx \frac{3\eta l U^2}{\theta(t)} \quad (2)$$

where η is liquid viscosity and l is a logarithmic factor approximately constant involving cutoff distances to the dissipative zone of the drop.

However, when the solid is soft, the wetting ridge near the triple line is also a dissipative sink as the wetting front moves [4,5]

and a viscoelastic dissipation, $\dot{E}\Delta$, occurs at the wetting ridge:

$$\dot{E}\Delta \approx \frac{\gamma^2 U}{2\pi G \epsilon} \left(\frac{U}{U_0} \right)^n \quad (3),$$

where G represents the shear modulus of the solid, ϵ is a cutoff distance near the triple line, below which the behavior is no longer linearly elastic (a few nanometers [3]), and U_0 and n are constants related to the rate-dependent viscoelastic dissipation of the solid [6]. Considering the energy balance between equation (1) and equations (2) and (3) together, we obtain

$$\cos \theta_0 - \cos \theta(t) \approx \frac{3\eta l U}{\gamma \theta(t)} + \frac{\gamma}{2\pi G \epsilon} \left(\frac{U}{U_0} \right)^n \quad (4)$$

which is the basic equation governing spreading in the general case. Typically, $n \ll 1$, and thus at sufficiently high speeds, the first member on the right hand of eq.(4) dominates, while at lower speeds the second member governs behavior. This last situation corresponding to the experimental results reported here, equation (4) will be recast as

$$\log[\cos \theta_0 - \cos \theta(t)] \approx n \log U + \log \frac{\gamma}{2\pi G \epsilon U_0^n} \quad (5).$$

EXPERIMENTAL

The contact angle θ of small sessile drops of tricresylphosphate, TCP, (drop volume 2 μ l, viscosity $\eta = 70$ cP, surface tension, $\gamma = 40.9$ mN.m⁻¹), has been measured as a function of time after deposition, t , on flat, smooth, horizontal surfaces of soft and rigid solids at 20°C. Although TCP is a non-volatile liquid at 20°C, solid samples were placed in a closed glass box to obviate any interference from the room atmosphere. In the case of the relatively high modulus solids, (Teflon PFA, Du Pont de Nemours, $G \approx 250$ MPa, and fused silica, Quartz et Silice, $G \approx 30$ GPa), equilibrium contact angles are attained after only ca. 15 seconds as shown in Figure 1. In these cases, the kinetics of spreading are very similar, although the contact angle on the glass is small compared to that on Teflon PFA which confirms that viscous dissipation (Eq.(2)) is relatively minor. The rubbery substrate (a two-component silicone elastomer, RTV 630, General Electric Co., $G = 1.5$ MPa) possesses an equilibrium contact angle, θ_0 , between those of the rigid solids but spreading to equilibrium is much slower (Figure 1). This behavior is

attributed to local deformation of the soft solid – the wetting ridge – caused by the vertical component of the liquid surface tension [5].

The hypothesis of viscoelastic braking of the spreading of TCP on the rubbery material is corroborated by Figure 2 in which the difference between the cosines of equilibrium contact angle, θ_0 , and the instantaneous contact angle $\theta(t)$, is plotted as a function of the liquid spreading speed, U , according to equation (5). The speed, U , was deduced from the variation of the drop contact radius, r , as a function of time t . Verification of Eq.(5) suggests that the spreading dynamics of TCP on the silicone elastomer is effectively governed by the formation of a wetting ridge at the liquid drop periphery. However, the value of the gradient $n = 0.23$ is rather low in comparison, on one hand, with values typically found in kinetic adhesion experiments [6], and on the other hand, with kinetic wetting studies using preswollen elastomers [5], both leading to a value of n in the range of 0.5–0.6. It is considered that swelling of the rubber by TCP may influence the spreading behavior and be responsible for the low value of n . Further evidence for interference due to swelling in the spreading kinetics is a slow and very long decay of $\theta(t)$ for a few days before a stable equilibrium value θ_0 is reached. This period of time is reduced to about 1 hour or less when the rubber is preswollen.

To investigate the hypothesis of swelling interference, the elastomer was immersed in TCP for several days until equilibrium swelling was noted by gravimetry (swelling $\approx 1\%$ wt). The solid was then carefully wiped before placing drops of TCP on it. The time dependent variation of contact angle on the preswollen polymer is shown in Figure 3 where the shape of the $\theta(t)$ curve is basically unchanged compared to the other solids although the equilibrium value θ_0 is obtained after ca. 30 minutes instead of a few days as in the case of the non-swollen rubber. Using equation (5), it appears that the spreading kinetics is now controlled only by viscoelastic dissipation, the gradient n being 0.56 as shown in Figure 4 and as obtained in other experiments [5,6].

To dissociate purely viscoelastic effects from swelling effects in the first set of experiments with the non-swollen samples, it may be observed that the period corresponding to the major part of the contact angle variation – the contact angle changes by 20 degrees in the first 10 minutes for both types of samples – is over after 30 minutes of contact with the preswollen elastomer. In addition, after 30 minutes, the contact angle on the non-swollen rubber decreases slowly and approximately linearly up to 60 minutes of contact with a linear fit satisfying the equation $\theta(t) = 53.1 - \alpha t$ ($\alpha = 5.24 \times 10^{-3}$ deg.s $^{-1}$ for t between 30 and 60 minutes). This linear part can be derived from an exponential decay of $\cos \theta(t)$ with time when the viscoelastic braking regime is over.

Assuming that this mid term evolution of the contact angle is dependent only on the swelling effect, it becomes possible to separate the purely viscoelastic braking from the swelling effect by taking $\theta^*(t) = \theta(t) + \alpha t$ as being the virtual contact angle in the absence of rubber swelling.

The use of $\theta^*(t)$ in equation (5) is illustrated in Figure 4 where the "swelling free" linear fit (line 3) now has a gradient n of 0.59 and is situated parallel and near to the preswollen data line. This result indicates that the low gradient value for $n=0.23$ is very probably related to the swelling phenomenon.

Although all the mechanisms are not at present totally understood (for example, how the swelling affects quantitatively the damping properties of the elastomer), the wetting experiments conducted with preswollen and non-swollen elastomer samples demonstrate that the contact angle variation is mainly related to viscoelastic dissipation occurring in the wetting ridge but also to a possible swelling effect modifying the liquid-rubber molecular interactions with time when liquid-liquid interactions are superimposed on the original liquid-solid interactions. This secondary phenomenon increases the time necessary to attain a stable equilibrium value for θ_0 . Therefore, the value of the factor n is apparently reduced.

DISCUSSION AND CONCLUSION

The viscoelastic braking of a liquid spreading on a rubbery material can be considered to be similar to dissipation phenomena in the adhesion of elastomers. It is recognized that, during the separation process of an elastomer from a substrate, the apparent energy of adhesion often far exceeds the thermodynamic value and this excess corresponds essentially to viscoelastic dissipation [6,7]. The dissipative properties of the elastomer used in the present wetting study have also been determined using the rolling cylinder adhesion test [8,9] and the value of n found to be 0.55 which is in good agreement with the value of n obtained for TCP spreading when effects of rubber swelling do not interfere ($n \approx 0.5-0.6$).

Variation of interfacial interactions with time, in our case due to swelling, has a direct impact on θ_0 and on the Dupré work of adhesion at equilibrium, $W_0 = \gamma(1 + \cos\theta_0)$ or $W_0 = \gamma_1 + \gamma_2 - \gamma_{12}$ where γ_1 and γ_2 are the surface free energies of the materials in contact and γ_{12} is their interfacial free energy. An analogous situation may be encountered in the case of solid-solid contact involving a polymer or more specifically a rubbery material for which molecular rearrangements (in the rubber), above T_g , may modify the interfacial free energy, γ_{12} , with time as evoked in dwell time effects on rubber adhesion [10]. Although such processes may occur at liquid-polar polymer interfaces [11], it is thought that, in our experiments, interfacial energy variation results more from liquid diffusion than from molecular orientation, wetting liquid and solid substrate both being non-polar.

In conclusion, the present work shows that the kinetics of spreading of a liquid on a rubbery material may be largely dependent on viscoelastic dissipation in the wetting ridge of the substrate near the triple line. This behavior may, in practice, be slightly altered by swelling which modifies the liquid-solid interfacial interactions for long contact times.

REFERENCES

1. P.G. de Gennes, Rev. Mod. Phys. **57**, 827 (1985).
2. G.R. Lester, J. Colloid Sci. **16**, 315 (1961).
3. M.E.R. Shanahan and P.G. de Gennes, in Adhesion **11**, K.W. Allen Ed. (Elsevier Applied Science, London, 1987), p 71.
4. M.E.R. Shanahan, J. Phys. D : Appl. Phys. **21**, 981 (1988).
5. M.E.R. Shanahan and A. Carré, Langmuir **10**, 1647 (1994).
6. D. Maugis and M. Barquins, J. Phys. D : Appl. Phys. **11**, 1989 (1978).
7. A.N. Gent and J. Schultz, J. Adhesion **3**, 281 (1972).
8. A.D. Roberts and A.G. Thomas, Wear **33**, 45 (1975).
9. N. Zaghzi, A. Carré, M.E.R. Shanahan, E. Papirer and J. Schultz, J. Polym. Sci., Polym. Phys. **25**, 2383 (1987).
10. K.N.G. Fuller and G.J. Lake, in Adhesion **13**, K.W. Allen Ed. (Elsevier Applied Science, London, 1989), p 79.
11. A. Carré, S. Moll, J. Schultz and M.E.R. Shanahan, in Adhesion **11**, K.W. Allen Ed. (Elsevier Applied Science, London, 1989), p 82.

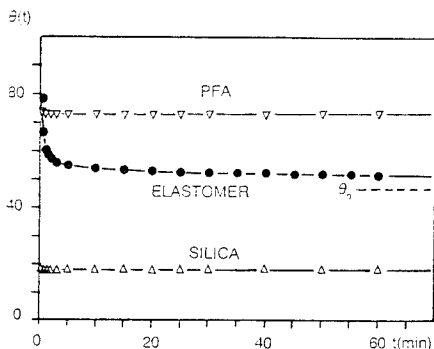


Figure 1 : Evolution of the contact angle, $\theta(t)$, of TCP on silicone rubber, Teflon PFA and silica glass.

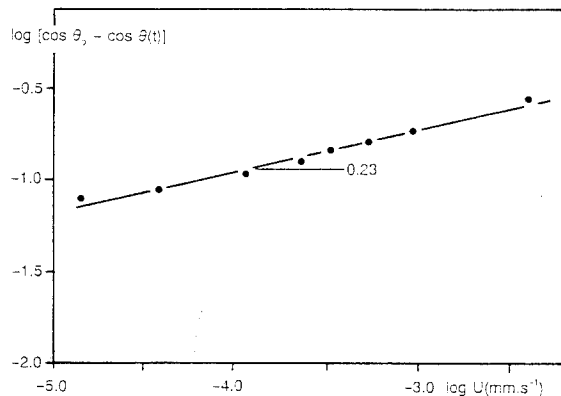


Figure 2 : Evidence of viscoelastic braking for TCP spreading on silicone rubber. The value 0.23 is the gradient n of Eq. (5).

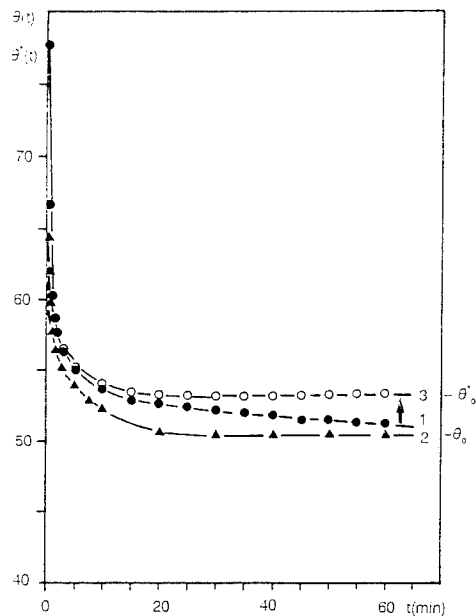


Figure 3 : Evolution of the contact angle, $\theta(t)$, of TCP on silicone elastomer (1), silicone elastomer preswollen with TCP (2) and on silicone elastomer after allowing for swelling effects (3).

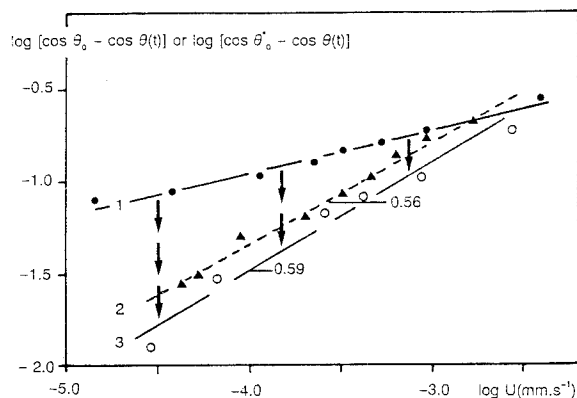


Figure 4 : Variation of the gradient n (Eq.(5)) with rubber swelling. After correction of swelling effect on θ_0 ($\theta_0 \rightarrow \theta'_0$) line 1 becomes 3. Line 2 refers to preswollen rubber.

SURFACE AND INTERFACIAL STUDIES OF PLASMA-MODIFIED COMPOSITES

Joannie W. Chin and James P. Wightman
Department of Chemistry
Center for Adhesive and Sealant Science
Virginia Polytechnic Institute and State University
Blacksburg, VA 24061

INTRODUCTION

In the adhesive bonding of carbon fiber-reinforced composites to form structures, surface preparation is necessary to optimize adhesive application. Oxygen plasma has been shown to be highly effective in removing contamination from and introducing polar functionality into composite surfaces [1,2]. These effects have been observed to improve the hot/wet resistance of adhesively-bonded composite joints relative to other pretreatment techniques. However, difficulties are encountered in the analysis of actual composite surfaces due to their heterogeneity, roughness and complex (and often undisclosed) resin chemistries, with the result that many aspects of the composite/adhesive interphase remain unknown.

The objective of this research was to study the changes in oxygen plasma-treated composite surfaces by using model compounds with known structures and stoichiometries. Detailed surface analysis of thin films made from these materials enabled molecular information on the plasma-treated surfaces to be obtained, as well as provided insight into the mechanism of interaction between the plasma-treated surfaces and adhesives.

EXPERIMENTAL

Materials

To prepare model composite surfaces, thin films were spin-cast from commercially available composite matrix resins. Araldite® MY 720 epoxy resin and a diaminodiphenylsulfone (DDS) curing agent from Ciba Geigy were utilized to simulate an epoxy composite system. A bismaleimide composite surface was represented by Matrimid® 5292, a commonly used starting formulation for many commercial BMI composites, also from Ciba Geigy.

Dilute resin solutions were prepared and spin-coated on chrome steel plates which had been cleaned in oxygen plasma. Coatings were thermally cured in a forced-air Blue M oven, using the manufacturer-recommended cure cycles.

Analysis of Plasma-treated Films

Polymer coatings were exposed to a 50 watt oxygen plasma in a March Instruments Plasmod¹⁶ Unit for 30 seconds. X-ray photoelectron spectroscopy (XPS) analysis of both the non-exposed and plasma-treated films was carried out on a Perkin Elmer PHI 5400 spectrometer. Photopeaks of interest were curve-resolved to obtain more detailed structural information on the plasma-treated surfaces.

Infrared reflection absorption spectroscopy (IR-RAS) was used to examine the molecular changes in the plasma-treated model composite surfaces and was performed on a Nicolet 510 Fourier transform infrared spectrometer utilizing parallel polarized incident radiation. Reflectance measurements were taken with a Seagull® variable angle reflection accessory from Harrick Scientific Corporation, set at an incidence angle of 75°. Although not generally considered to be a surface sensitive analytical technique, IR-RAS is highly suitable for the analysis of thin films on high refractive index substrates [3]. The strategy which is used involves making the films thin enough so that the surface and near-surface regions constitute a significant percentage of the entire coating thickness.

IR-RAS Epoxy Adsorption Studies

Immediately following treatment with a 30 second/50 watt oxygen plasma, the polymer coated plates were immersed in a bath of neat EPON® 830 (no crosslinking agent added) and heated at 180°C for one hour in a convection oven. Following this thermal treatment, excess EPON® 830 was drained from the sample surfaces and the

samples extracted thoroughly in methylene chloride.

RESULTS AND DISCUSSION

Surface Analysis of Model Epoxy

XPS analysis showed the expected increase in the oxygen concentration following plasma treatment. Curve-fitting of the carbon 1s photopeaks revealed increases in the intensities of the peaks at 286.0, 287.5 and 289.0 eV, indicative of an increase in the surface concentration of hydroxyl, carbonyl and carboxylate/ester species as a result of plasma treatment.

Infrared analysis of the plasma-modified epoxy surface served to complement the molecular information obtained from curve-fitting the XPS photopeaks. Figure 1 shows the IR-RAS difference spectrum obtained by subtracting the spectrum of the unmodified surface from the spectrum of the oxygen plasma-treated surface. Peaks are observed in the difference spectrum at 1770, 1438 and 1205 cm^{-1} . The peak at 1770 cm^{-1} can be assigned to C=O stretching in ester or carboxylic acid species, which is consistent with the observed increase in the XPS peak at 289.0 eV. The peak at 1205 cm^{-1} is identified as a C-O stretch, which corresponds to the increased intensity of the XPS photopeak at 286.0 eV. The peak at 1438 cm^{-1} can be tentatively assigned to either a ketonic methyl or methylene C-H bend or an O-H bend. It is easily seen that XPS and IR-RAS results are in agreement with each other in terms of the surface functional groups identified following oxygen plasma exposure.

Surface Analysis of Model Bismaleimide

XPS and IR-RAS were again used to study the changes which occurred in the surface of oxygen plasma-treated Matrimid[®] 5292 films. Curve-fitting the oxygen plasma-treated surface revealed increases in the intensities of peaks at 285.8 and 288.2 eV, corresponding to C-O and C=O functional groups. New peaks are observed at 286.9 and 289.7 eV, identified as C-O and O-C=O, respectively.

Figure 2 shows the IR-RAS difference spectrum for the oxygen plasma-treated bismaleimide surface. Peaks are observed in the difference spectrum at 1745, 1400 and 1206 cm^{-1} .

The peak at 1745 cm^{-1} can be assigned to C=O stretching in ester or carboxylic acid species. This assignment is consistent with the appearance of the XPS peak at 289.7 eV after plasma treatment. The peak at 1205 cm^{-1} is identified as a C-O stretch, which corresponds with the increased intensity of the XPS photopeak at 285.8 eV and the presence of the new photopeak at 286.9 eV. The peak at 1400 cm^{-1} can be tentatively assigned to either a ketonic methyl or methylene C-H bend or an O-H bend. It is again seen that the XPS and IR-RAS results are consistent with one another.

EPON[®] 830 Adsorption Studies

To determine potential interactions of the plasma-treated surface with adhesives, the oxygen plasma-treated MY 720/DDS and Matrimid[®] 5292 surfaces were immersed in liquid EPON[®] 830 after a 30 second, 50 watt oxygen plasma treatment. It was hypothesized that, following solvent rinsing of the immersed surfaces to remove physisorbed EPON[®] 830, a residual thin layer of more tightly bound or chemisorbed material would remain and should be detected by IR-RAS analysis. A similar study was carried out by Webster and Wightman, using plasma-treated poly(phenylene sulfide) as a substrate for EPON[®] 828 adsorption [4].

It was necessary to first carry out the IR-RAS analysis on neat EPON[®] 830 films so that infrared bands unique to this DGEBA epoxy could be identified. Significant peaks in the spectrum of uncured EPON[®] 830 include the C-O-C symmetric deformation at 1254 cm^{-1} and bands which correspond to the unopened epoxide ring at 864 and 917 cm^{-1} .

Figure 3(a) shows the IR-RAS spectrum of a nonplasma-treated MY 720/DDS film following EPON[®] 830 immersion and solvent rinsing. When compared to the original MY 720/DDS spectrum, a number of changes are evident. New peaks are observed at 1254 and 917 cm^{-1} , corresponding to EPON[®] 830 C-O-C stretching as well as epoxide ring vibrations. These changes observed in the MY 720/DDS spectrum following immersion in an epoxy bath confirm that adsorption of EPON[®] 830 has occurred on the surface of the MY 720/DDS film. However, the presence of the epoxide ring vibration at 917 cm^{-1} indicates that no reaction has taken place between the MY 720/DDS surface and the EPON[®] 830.

because the epoxide rings remain unopened and intact.

When the procedure is repeated using an oxygen plasma-treated MY 720/DDS substrate, the IR-RAS spectrum shown in Figure 3(b) results. This spectrum is virtually identical to the one shown in Figure 3(a) for the nonplasma-treated surface. Once again, the presence of the epoxide ring vibration at 917 cm^{-1} originating from the EPON[®] 830 indicates that no reaction has occurred between the surface and the neat epoxy resin. These preliminary results appear to indicate that the plasma-treated surface is not capable of initiating a reaction with an epoxy resin.

However, the experiment was repeated with one important change made to the procedure. The original method involved obtaining the IR-RAS spectrum of the plasma treated MY 720/DDS substrate *prior* to immersion in the EPON[®] 830 bath. This was an additional step which added 30-45 minutes between the plasma treatment and liquid epoxy exposure. Instead, the plasma-treated MY 720/DDS surfaces were *immediately* submerged into the EPON[®] 830 bath following plasma treatment. The IR-RAS spectrum of this surface is seen in Figure 3(c). The peak at 1254 cm^{-1} is evident, again confirming that adsorption of the EPON[®] 830 has indeed taken place. However, in this instance, *no peak* is seen at 917 cm^{-1} , indicating that the epoxide rings have indeed undergone a ring-opening reaction.

These results provide evidence for some type of interaction between the plasma-treated surface and the liquid epoxy resin. The fact that reaction is observed only when the elapsed time between plasma treatment and epoxy immersion is very short points to the instability of the plasma-treated surface. The surface is very likely quite reactive immediately following plasma exposure but quickly becomes deactivated upon exposure to the atmosphere.

Virtually identical results were obtained when the EPON[®] 830 adsorption procedure was carried out with the BMI model surfaces. It was once again observed that epoxy adsorption took place on both plasma and nonplasma-treated surfaces, but that epoxide ring opening occurred only when immediate contact was made between the plasma-treated BMI surface and the liquid epoxy resin.

CONCLUSIONS

XPS and IR-RAS analysis were shown to be complementary techniques for the investigation of changes in surface chemistry following plasma treatment. Adsorption of the liquid DGEBA epoxy resin, EPON[®] 830, was seen to take place on both epoxy and BMI thin films. Infrared bands characteristic of the liquid epoxy were observed in the spectra of nonplasma-modified and oxygen plasma-modified substrates after immersion and solvent rinsing. However, epoxide ring-opening reactions, as evidenced by the disappearance of the epoxide ring vibration at $917\text{--}920\text{ cm}^{-1}$, were only observed in the case of oxygen plasma-treated substrates immersed immediately into the liquid epoxy bath after plasma treatment.

Direct evidence for covalent interaction between a reactive, plasma-modified surface and a liquid epoxy resin can be correlated with the improved adhesion and hot/wet bond durability commonly exhibited by oxygen plasma-treated substrates. However, the fact that this interaction is only observed when a minimal of time elapses between plasma treatment and initial contact with the adhesive resin emphasizes the short-lived reactivity of the plasma-treated surface.

ACKNOWLEDGMENTS

Financial support and materials provided by BASF Structural Materials, Inc. is gratefully acknowledged. Additional financial support was provided by the Adhesive and Sealant Council, Inc. and the Center for Composite Materials and Structures at Virginia Tech.

REFERENCES

1. J.W. Chin and J.P. Wightman, *Composites Bonding*, ASTM STP 1227, 1994.
2. D.J.D. Moyer and J.P. Wightman, *Surf. Interface Anal.*, **14**, 492 (1989).
3. D.S. Dunn and D.J. McClure, *J. Vac. Sci. Technol.*, **A5**(4), 1327 (1987).
4. H.F. Webster and J.P. Wightman, *J. Adhesion Sci. Technol.*, **5**(1), 93 (1991).

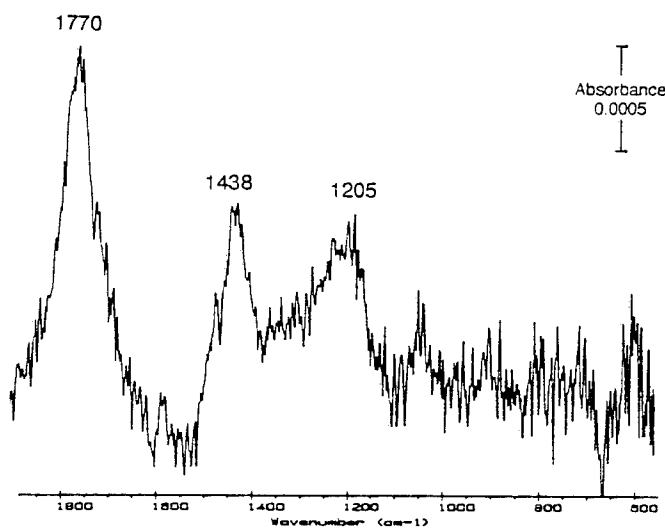


Fig. 1: IR-RAS difference spectrum for plasma-treated epoxy surface.

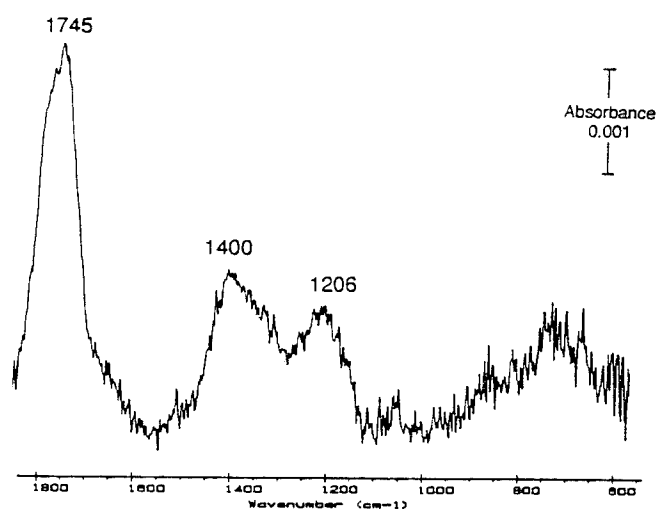


Fig. 2: IR-RAS difference spectrum for plasma-treated BMI surface.

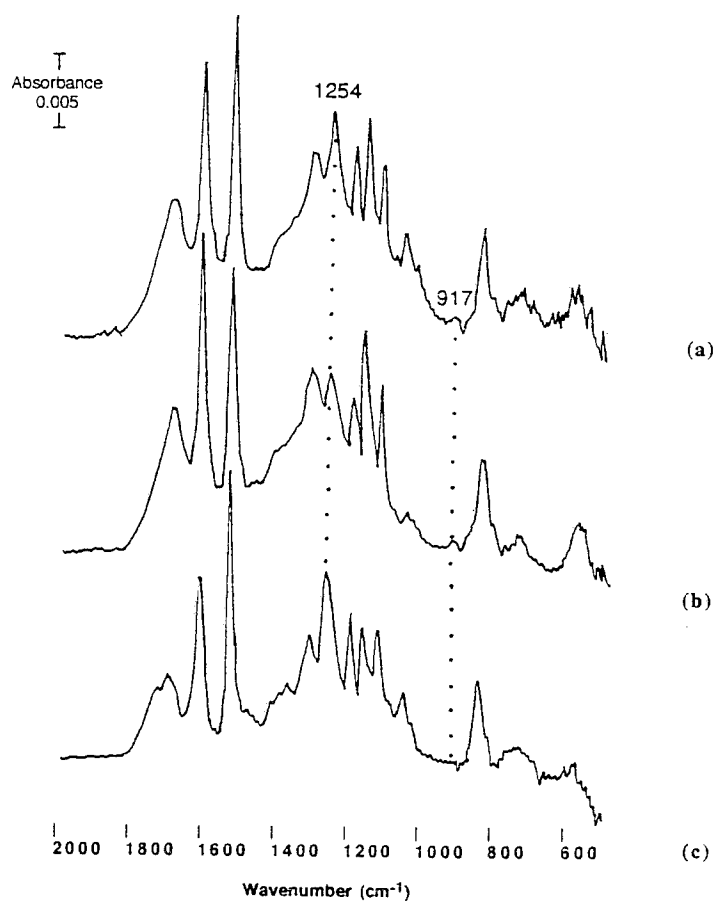


Fig. 3: IR-RAS spectra of epoxy model surfaces following EPON[®] 830 immersion and solvent rinse.

ANALYSIS OF THIN CYANURATE PREPOLYMER FILMS ON SOLIDS AS A MODEL OF THE ADHESIVE INTERPHASE

W. Possart, S. Dieckhoff*, D. Fanter, T. Gesang*, A. Hartwig*, R. Höper*, V. Schlett*, O.-D. Hennemann*
Fraunhofer Institute of Applied Materials Research, Branch Teltow, Kantstrasse 55, D-14513 Teltow, Germany

*) Fraunhofer Institute of Applied Materials Research, Neuer Steindamm 2, D-28719 Bremen, Germany

INTRODUCTION

The properties of adhering ultra-thin polymer films receive interest for an increasing number of technical applications. Moreover, an ultra-thin film may serve as a model for the investigation of the molecular structure and the interactions the three-dimensional interphase of a polymer adhesive on a solid substrate.

In this study, the model substrates are silicon wafers with extremely smooth surfaces and very smooth aluminium layers produced by electron beam evaporation on silicon wafers. A prepolymer of the dicyanate of the bisphenol A (DCBA) serves as a model for a curable adhesive. The cyclotrimerization reaction of cyanate groups was terminated at 45 Mol-% conversion of the cyanate into triazine rings according to IR spectroscopic determination. For that degree of conversion, the number distribution of prepolymer molecules consists of 75.6 % monomer, 12.5 % trimer, 4.6 % pentamer and 7.3 % larger network elements. The cyanate group and the triazine ring are typical features of cyanurate prepolymers. Moreover, the material contains a lot of aromatic carbon rings. Prepolymer and substrate are characterized individually to provide a reference. Uniform layers between about 3 nm and 100 nm thickness are prepared from a solution by spin coating or by dip coating.

The questions arise if these atom groupings take part in specific interactions and how they arrange in the interphase formed with the substrate.

For answers, several experimental techniques have been combined. AFM and ellipsometry provide the topography and the thickness of the prepolymer films. External reflection IR spectroscopy and XPS contain information about the energetic state and orientation of the organic molecules.

The paper summarizes the results obtained as a function of prepolymer thickness. It focuses on the film state immediately after preparation. The state of interpretation will be discussed and an outlook on further investigations will be presented.

EXPERIMENTAL

AES (Perkin Elmer PHI 660 SAM) reveals the chemical constitution of the substrates (lateral resolution ca. 0.1 μm). XPS (VG ESCALAB MK2 system with a polychromatic $\text{MgK}\alpha$ X-ray source or ESCALAB 220i XL with a monochromatic $\text{AlK}\alpha$ X-ray source) acquires the core level spectra.

An FTS 60A FTIR spectrometer (Bio-Rad) with a broad band MCT detector provides the IR spectra in combination with a SEAGULL reflection accessory (Harrick) and linearly polarized light. As a prerequisite of interpretation, high quality IR spectra of the prepolymer bulk are measured by ATR on a germanium hemispherical crystal in single reflection mode. For the ultra-thin prepolymer films, a background reflectance spectrum of each substrate sample is recorded just before coating with the prepolymer. Then the prepolymer layer is formed by spin or dip coating from solution. Immediately after preparation, the specimen is inserted into the spectrometer again for the reflectance spectrum of the coated sample.

Both the bare and the coated substrates are carefully controlled by ellipsometry in order to determine the oxide and the prepolymer layer thickness with high accuracy for the subsequent modelling of IR spectra. The ellipsometer is an AUTO EL II (Rudolph Res.).

The surface topography of the substrates and the prepolymer coatings are studied by AFM (Digital Instr. Nanoscope III). The contact mode is used for profile image. Simultaneous record of lateral force experienced by the AFM tip due to friction with the sample surface leads to a differentiation between surface profile and material inhomogeneities.

PROPERTIES OF THE SUBSTRATES AND THE PREPOLYMER

On both substrates, XPS and AES detect a carbon contamination of laterally uniform thickness. Aliphatic carbon of about 0.5 nm covers the Si-wafer. The aluminium has some 0.7 nm contamination. In the latter case, the carbon bonds are not purely aliphatic. ARXPS revealed (C-O)- and (C=O)-components at the interface to the substrate. The native oxide layers beneath that contamination are also uniform. Their chemical constitution is not the same on the two substrates, however. For silicon, it contains several bond states but we cannot resolve them because their chemical shifts are too small. The aluminium is not covered by a pure oxide. XPS reveals that more than 70 % of the oxygen form OH-like states.

Although both substrates visually show a surface finish like an optical mirror, AFM reveals pronounced distinctions on the microscopic level. The Si-wafer is flat even on the nanometer height scale (Root-Mean-Square roughness (RMS) 0.13 nm). The aluminium coating is less smooth (RMS roughness 5-10 nm). Nevertheless, adsorbing organic molecules will see a gently shaped profile.

In the prepolymer, the atoms exist in a manifold of chemical environments. XPS resolves only three of at least five carbon states. The first peak stems from all carbon atoms bound to nitrogen. The mathematical curve decomposition provides two components assigned to the triazine ring and to the cyanate group. The components are difficult to distinguish without curve fitting. The second peak is due to those aromatic carbons in the benzene rings that couple to the oxygen atoms. Again, there is no clear distinction whether it is the cyanate group or the triazine ring in the neighbourhood. The remaining aromatic and aliphatic carbons give rise to the most intense peak at the low-energy end of the C1s spectra. The expected two nitrogen bond states are not resolved in the N1s spectra at all. Fortunately, the two oxygen states are well separated in the O1s signal. Hence, only the O1s spectra provide unambiguous information about the state of cyanate groups and of the triazine rings.

ATR IR spectroscopy provides the data for a calculation of the optical function $n^*(\tilde{\nu}) = n(\tilde{\nu}) - i \cdot k(\tilde{\nu})$ ($\tilde{\nu}$ = wavenumber) for the prepolymer bulk in the mid infrared. The characteristic group frequencies are identified in accordance with the literature and IR catalogues. Hence, assignment rests upon analogy with known similar substances and the concept of localized vibrational modes. That common approach is rather qualitative. The detailed type of the molecular vibrations remains widely unspecified. In particular, this is true for the triazine ring and the cyanate group.

PROPERTIES OF THIN PREPOLYMER COATINGS

The prepolymer forms on Si continuous layers for all prepared thickness values larger than some 2 nm. These coatings are very smooth (RMS values \ll 1 nm in most cases) and show a granular structure. Dip coating produces granules of about 40 - 60 nm diameter for all thickness values. With spin coating, the granules are slightly larger and grow up to circa 250 nm with increasing layer thickness.

Things are quite different on Al. Dip coating produces prepolymer agglomerations around and among the highest substrate peaks. Spin coating fills the valleys of the Al substrate. It takes some 10 nm prepolymer (ellipsometric thickness) to get layers without holes.

For the core level XPS, spin or dip coating makes no difference in the spectra. The intensity ratio of the two O1s components is a function of prepolymer thickness indicating a growing deficit of cyanate groups with decreasing thickness on both substrates. Storage experiments in the vacuum revealed that the deficit results to a considerable extent from a substantial monomer evaporation. The dense prepolymer layers on Si are suitable targets for

ARXPS. Below circa 10 nm thickness, it reveals that the triazine rings become less concentrated in the outer surface layer. Obviously, these rings prefer the neighbourhood of the native silicon oxide.

The analysis of the IR reflection spectra reveals distinctions and similarities between the polymer films on the Si and on the Al. On both substrates, the cyanate valence vibrations retain their frequency positions. Therefore, the molecular force field experienced by the cyanate groups does not change significantly in the thin films. On Al, the valence vibrations of the (C-O-C)-bridge between the triazine and the benzene rings shift significantly to lower frequencies. Similar but less pronounced frequency shifts occur for the triazine and the benzene ring vibrations too. Surprisingly, this is true for the whole thickness range of about 100 nm. No such frequency changes are observed on Si. The cyanate band intensity reproduces the bulk value for all prepolymer films. Hence, the fresh films retain the prepolymer bulk composition. The intensity data of the triazine grouping and its surroundings show deviations from the bulk on Al only. Below circa 40 nm, the valence vibrations absorb less strongly than in a bulk-like film structure for the triazine and benzene rings as well as for the (C-O-C)-bridge between them. Since the prepolymer composition does not change, that thickness dependence indicates a preferred orientation of the triazine ring perpendicular to the plane of light incidence. That long range effect on Al is different from that what is observed with ARXPS in the vicinity to the Si substrate.

INTERPRETATION AND OUTLOOK

The combination of experimental methods described in that paper provides important information about the morphology and the molecular state of ultra-thin organic coatings on solids. Each method requires sophisticated tools for data processing. As a result, XPS and external reflection IR spectroscopy can reveal tiny changes in the energy and in the orientation of characteristic parts of the prepolymer molecules in the coatings just after preparation.

The AFM shows structural details of the ultra-thin prepolymer films with characteristic lateral dimensions from some 10 nm up to a few microns. In particular, it reveals whether films are discontinuous or continuous.

Up to now, our results show that the as prepared prepolymer layers do not undergo serious chemical changes or adhesive interactions where the molecule's electron system is strongly involved. The silicon wafer appears to be inert. The native aluminium surface induces slight changes in energy and orientation of the triazine rings. The cyanate groups are not involved at all. Hence, the good properties as an adhesive find no obvious explanation at this stage of film processing.

The spectral results are not easily explained by simple structural pictures. The observed long range effects are beyond the scope of traditional chemical adhesion models. Molecular orientation and interactions compete in influencing the spectra. Future interpretation should be supported by appropriate molecular modeling therefore. Moreover in practical applications, the adhesive prepolymer formulation is cured. In view of the so far obtained results we expect that curing will not only complete the network but also could contribute to the final adhesive interactions.

This study is the result of research projects funded by the Volkswagen - Stiftung in Germany. We thank Mrs. S. Jählig for valuable support by synthesizing the polymeric materials and Mr. H. Stuke for provision of the aluminium layers. It is also a pleasure to acknowledge the advice of Prof. M. Bauer in chemical synthesis.

Direct Measurement of the Forces of Adhesion between Solid Polymer Films: Relationship to Polymer Surface Energy and Adhesion Science

V. S. Mangipudi and M. Tirrell

Dept. of Materials Science and Chemical Engineering, University of Minnesota, Minneapolis, MN
and

A. V. Pocius

3M Adhesive Technologies Center, St. Paul, MN 55144-1000

ABSTRACT

The force of adhesion between a series of polymer films has been measured using the surface forces apparatus (SFA). Through the use of the Johnson, Kendall, Roberts theory of contact mechanics, we have been able to measure directly the work of adhesion between these films and this determination has been used to calculate the surface and interfacial energies of these films and film pairs. The polymer films which have been examined are poly(ethylene terephthalate) [PET], polyethylene [PE], poly(vinyl cyclohexane) [PVCH], polystyrene [PS] and polymethylmethacrylate [PMMA]. The SFA determined surface energies have been compared with the surface energies inferred from contact angle data. In addition, the surface forces data have been compared to the actual measurement of peel strength between PET and PE.

INTRODUCTION

The development of a relationship between the physical forces of adhesion and the practical measurement of adhesive bond strength has been a goal which has eluded adhesion scientists. The work of Gent and Schultz¹, Andrews and Kinloch² and Ahagon and Gent³ have shown that a simple mathematical expression captures the essence of the relationship between these two measureable quantities. The mathematical expression of this relationship is:

$$W_P = W_A + W_A \Phi \left(T, \frac{da}{dt} \right),$$

where W_P is the practical work of adhesion determined in a adhesive bond strength test, W_A is the work of adhesion and Φ is a function which describes the loss of energy in the adhesive and adherend by processes such as viscoelastic dissipation or permanent mechanical deformation. As such, Φ would be dependent upon the temperature, T , and the rate of crack propagation (or rate of bond strength determination), da/dt , where t is time and a is the radius of the crack. Even though this expression relates W_P and W_A in a phenomenological sense, the functional form of Φ is not available, *a priori*, and would be expected to be heavily dependent upon the type of test which was used to determine W_P .

In this paper, we describe work which is leading us to the basis for a connection between W_P and W_A . The work is

based upon the use of the Surface Forces Apparatus (SFA) to measure directly the W_A between solid polymer films by a mechanical method. The SFA has been used to probe the interactions between the surfaces of many different materials⁴, but only recently has it been applied to solid, self-supporting polymer films⁵. This paper will describe measurements on self-supporting polymer films as well as measurements on polymer films that were solvent cast onto mica. In earlier work, we have been able to show that the SFA measurement of W_A is reversible, reproducible and largely independent of rate⁵, which is to be expected of a thermodynamic quantity. Samples identical to those used in the SFA also were probed by contact angle measurement, which is the classical means of inferring the surface energy of a material. A comparison of the SFA data to the contact angle data shows that the two agree when the surface energies are dominated by dispersive interactions but disagree when the surfaces are able to display interactions other than dispersion forces. A comparison of peel strength data between poly(ethylene terephthalate) [PET] and polyethylene [PE] and the measurement of the W_A between these polymers will also be discussed.

EXPERIMENTAL

The details of the SFA have been described elsewhere and will not be repeated here^{4,5}.

The surface forces measurement has been analyzed by Johnson, Kendall and Roberts (JKR)⁶ as well as Derjaguin, Mueller and Toporov (DMT)⁷. We have found that the results of our measurements agree in a substantial fashion with the JKR theory and we will not consider the DMT analysis further in this paper. The primary equation which was used in this work is:

$$P_n = \frac{P_s}{R} = \frac{3}{2} \pi W$$

where P_n is the normalized pull-off force, P_s is the measured pull-off force and R is the radius of curvature in the contact zone. When the two surfaces in contact are the same then $W = W_C = 2\gamma$ but when the two surfaces in contact are dissimilar then $W = W_A = \gamma_1 + \gamma_2 - \gamma_{12}$ where the γ_i are surface and interfacial tensions and W_A and W_C are the works of adhesion and cohesion, respectively. Measurements were also made of the dependence of the contact radius with applied force

as well as measurements of the distance of separation of the two surfaces as a function of applied load.

The measurements of P_{ij} were conducted in an SFA which was kept at 25°C. The interior of the apparatus was kept at zero humidity through the use of a vial of sulfuric acid kept in the chamber. The rate of separation was varied by the rate at which the synchronous motor was run. While in contact, the distance of separation between the surfaces outside the contact zone could be measured.

PET films were prepared by methods previously described⁵. PE films were obtained from a multilayer PE/PET coextrusion. The samples were obtained by simply slowly peeling the layers apart. Surface analysis indicated that the PE was free from contamination from the PET. The other investigated polymers were dissolved in good solvents to yield clear solutions which were cast onto mica and then dried. PE film was also subjected to air corona treatment.

Contact angles were measured on the surfaces by means of a Rame-Hart contact angle goniometer. Advancing and receding angles were measured but only the results from recently advanced contact angle data are quoted. Both polar and non-polar liquids were used.

RESULTS AND DISCUSSION

Contact angle measurements have long been used to measure the wetting properties of solvents and have long been investigated as a method by which one can probe surface interactions. It has also been used to infer the surface energy of materials. The basis for the inference of surface energy from contact angle methods is the Young equation which states:

$$\gamma_{LV} \cos \theta = \gamma_{SV} - \gamma_{SL}$$

where θ is the contact angle, γ_{LV} is the liquid-vapor interfacial energy, γ_{SV} is the solid-vapor interfacial energy and γ_{SL} is the solid-liquid interfacial energy. With a single contact angle measurement, one can measure the difference between γ_{SV} and γ_{SL} . However, without an independent measurement of γ_{SL} , γ_{SV} cannot be determined directly. As a result, several methods of inferring surface energy have been proposed. Some of the well-known methods of inferring surface energy are listed in Table 1 along with the measured inferred surface energies for the polymer surfaces studied in this work. Table 1 also provides a listing of the surface energies of the polymers investigated in this work as they were determined through the use of the SFA

Examination of Table 1 shows the curious effect that the PE film and the PVCH coating which are dominated by dis-

persive force intermolecular bonding show relatively good agreement between the SFA determined surface energy and the contact angle inferred surface energy (depending upon the model chosen for inferring the surface energy). However, the SFA determined surface energy is markedly higher for those polymers which have a substantial component of non-dispersive intermolecular bonding (PET, PMMA, PS, corona treated PE). The results in this Table indicate that great care must be taken as it regards inferring surface energies from contact angle data as it depends substantially on the model. The source of the discrepancy is still being investigated but we believe that it is due to specific interactions between contact angle liquids and surfaces which do not mimic the actual intermolecular bonding in the solid polymer.

The SFA was used to determine the interfacial energy between PET and PE. The value was found to be 17 mJ/m². This high interfacial energy could be expected to predict poor interfacial bonding between these two polymers. Poor adhesion could be inferred from our earlier statement of the ease of removal of PE from PET and *vice versa* along with the surface analysis which showed clean interfacial failure between the two materials. Indeed, when peel measurements were carried out using a 90° peel apparatus, the peel strengths which we determined were quite low. The peel measurements were carried out as a function of peel rate and they are shown in Figure 1. As shown, the peel forces which we obtain are on the order of grams per centimeter width. We note, however, that when peeling PE from PET the peel forces are markedly higher than when PET is peeled from PE. Naturally, this is a manifestation of the absorption of energy by PE during the peeling process which is not available to the PET because of the glassy nature of the PET. It is also interesting to note that if one places the interfacial energy determined by SFA on this plot at the nominal separation rate used in the SFA, the lowest value of peel strength for PET from PE is only 0.5 orders of magnitude higher than the interfacial energy which was determined at a rate of about 0.1 microns per second. In addition, to the eye, it seems that the two curves of peel strength are converging and seemingly could be extrapolated to the SFA determined value of interfacial energy. This finding leads us to believe that we may in the future be able to directly relate practical adhesion measurement in this system to the SFA determined surface energy.

REFERENCES

1. A. N. Gent and J. Schultz, *J. Adhesion*, **3**, 281 (1972).
2. E. H. Andrews and A. J. Kinloch, *Proc. Royal Soc. A*, **332**, 385 (1973).

3. A. Ahagon and A. N. Gent, *J. Polym. Sci. Polym. Phys. Ed.*, **13**, 1285 (1975).
4. a. J. N. Israelachvili and G. E. Adams, *J. Chem. Soc. Faraday Trans.*, **174**, 975 (1978).
b. J. N. Israelachvili and D. Tabor, *Proc. Royal. Soc. London. A.*, **331**, 19 (1972).
c. R. G. Horn and D. T. Smith, *J. Non-Cryst. Solids*, **120**, 72 (1991).
d. Y. L. Chen, C. A. Helm and J. N. Israelachvili, *J. Phys. Chem.*, **95**, 1036 (1991).
5. a. W. W. Merrill, A. V. Pocius, B. V. Thakker and M. Tirrell, *Langmuir*, **7**, 1013 (1991).
b. V. S. Mangipudi, M. Tirrell and A. V. Pocius, *J. Adh. Sci. Tech.*, **9**, xx (1995), *in press*.
c. V. S. Mangipudi, M. Tirrell and A. V. Pocius, *Langmuir*, *accepted for publication*.
d. V. S. Mangipudi, M. Tirrell and A. V. Pocius, *Macromolecules*, *in preparation*.
6. K. L. Johnson, K. Kendall and A. D. Roberts, *Proc. Roy. Soc. London. A.*, **324**, 301 (1971).
7. B. V. Derjaguin, V. M. Muller and Y. P. Toporov, *J. Colloid Interface Sci.*, **53**, 314 (1975)
8. W. A. Zisman, *Adv. Chem Ser. #43*, R. F. Gould, Ed., American Chemical Society: New York, 1964, pp. 1-51.
9. S. Wu, *J. Colloid. Interface Sci.*, **71**, 605 (1979).
10. S. Wu, *J. Polym. Sci. Pt. C.*, **34**, 19 (1971).
11. S. Wu, *J. Adhesion*, **5**, 39 (1973).

Table 1
Listing of Surface Energies Determined by SFA and Comparison to Surface Energies
Inferred from Contact Angle Measurements (in mJ/m²)

Polymer	Polyethylene	Poly(vinyl cyclohexane	Polystyrene	Poly(methyl methacrylate)	Poly(ethylene terephthalate)	Corona Treated PE
Method						
SFA	33±1.6	28.2±0.7	44±2.1	53	61±1.9	55±2
Zisman Plot ⁸	25	32	27	40.2±0.2	38	38
Wu Equation of State ⁹	33	33	42	45±2.1	44	45±1
Geometric Mean ¹⁰	34±2	34±5.8	41±8	44±4.5	45±2	49±4
Harmonic Mean ¹¹	36±4	37±6.8	44±11	48±7.1	51±5	53±6

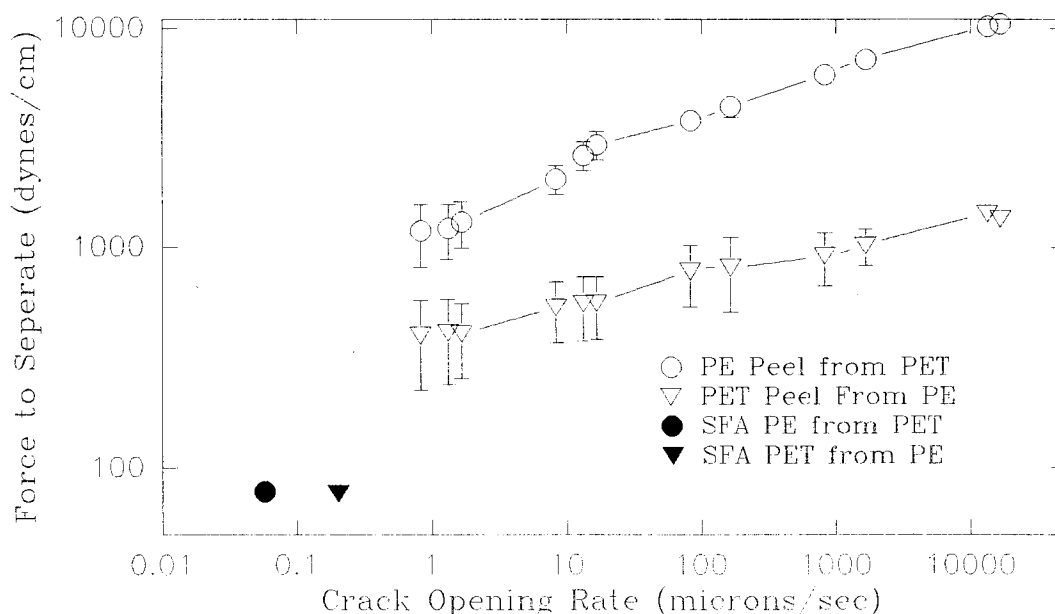


Figure 1. Practical adhesion measured as 90° peel strength as a function of the rate of crosshead separation. Also shown is the measurement of interfacial energy from SFA at the rate at which the crossed cylindrical lenses are separated.

ACRYLIC ADHESION TO POLYOLEFINS

Jeffrey T. Fields, Andrew Garton and James P. Bell

Institute of Materials Science, U-136

University of Connecticut

Storrs, CT 06269

INTRODUCTION

While polyolefins, i.e. low density and high density polyethylenes (LDPE & HDPE) and polypropylene (PP), have gained wide usage because of their low costs and high chemical resistance, it is often this resistance that has limited their implementation in applications that require adhesive bonding. Their inherent low surface tensions (<35 mN/m) and limited reactivities make it difficult for adhesives to wet or react with polyolefin surfaces.

In recent years, several authors have reported the formation of strong, durable bonds to polyolefins and other polymers through the use of reactive adhesives [1-4]. The mechanism of adhesion presented in these papers involves the interdiffusion of the monomeric adhesive or coating into the substrate, and subsequent polymerization of the adhesive within the substrate. The resulting entangled adhesives provide strong adhesion to the substrates with significant durability and resistance to the environment. This paper describes the development of an anaerobic acrylic adhesive for bonding polyolefins which functions in the same manner.

EXPERIMENTAL

An anaerobic curing system consisting of cumene hydroperoxide (CHP), saccharine (BS), N,N-dimethyl-p-toluidine (DMPT) and Cu(II)2-ethylhexanoate

(CuEH) was employed in this study. Methyl meth-acrylate (MMA) and triethylene glycol dimethacrylate (TRIEGMA) were used as the monomers in this adhesive. The formulation of this adhesive is shown in Table 1.

The reaction was initiated by adding 0.10 mL of the catalytic solution (part II) to part I (time 0). An exotherm was produced at 2-3 minutes reaction time with joints being formed from this point until the adhesive gelled, at about 45 minutes.

The polyolefin lap joints were tested in block shear according to ASTM D4501-91, and were formed from substrates that were Soxhlet extracted with acetone and wiped with toluene or a primer consisting of 1% CuEH in toluene. The joints were allowed to cure for at least 3 days and then each was cut into 3-2.5 cm wide bonds for testing.

Table 1: Formulation of anaerobic acrylic adhesive used in this study.

Chemicals	MW	Amount
<i>Part I</i>	--	--
MMA	100.1	8 mL
TRIEGMA	286.0	0.25 g
BS	183.2	0.34 g
DMPT	135.0	0.25 g
CHP	152.2	0.10 g
<i>Part II</i>	--	--
MMA	100.1	5.0 mL
CuEH	350.0	0.25 g

Fourier Transform Infrared Spectroscopy (FTIR) was used to

characterize the interpenetration of the adhesive and substrates. The uptake of the adhesive into the polyolefins was followed using transmission IR spectroscopy performed on films that had been soaked in the reacting adhesive at specific times. Infrared microscopy was used to observe the interphase formed by the interpenetration by sampling cross-sections cut from unstressed joints.

Durability testing was performed on selected LDPE/LDPE joints by placing them in boiling water and periodically checking for failure. After over 3 months time, the remaining unfailed joints were re-tested in block shear.

RESULTS AND DISCUSSION

LDPE/LDPE joints were formed from the reacting adhesive at 3, 10, 20, 30 and 40 minutes reaction time. Both primed and unprimed substrates were used to form joints for block shear testing. The results of this are included as Table 2. The joint strengths of primed HDPE/HDPE and PP/PP bonds formed at 3 minutes reaction time are also included in Table 2, although these values are the average of only 3 samples. HDPE and PP joints formed at other reaction times exhibited little to no strength. All of the joints that are represented in Table 2 displayed some degree of substrate failure, which was quite drastic in some cases.

The uptake-desorption experiments revealed that considerable adhesive entered the polyolefin films and remained there after curing. No significant evidence of unreacted species was detected using either transmission IR or surface sensitive internal reflection spectroscopy. The final concentrations that were detected in the films were then plotted against the joint strengths to show the relationship between

the extent of interpenetration and the joint strengths. This plot is included as Figure 1.

Table 2: Summary of LDPE/LDPE Block Shear Testing

Reaction Time	Treatment	Strength (MPa)	1 σ (MPa)
3 min.	unprimed	8.41	1.10
3 min..	primed	7.17	1.06
10 min.	unprimed	9.10	1.49
10 min.	primed	7.52	1.70
20 min.	unprimed	7.31	1.21
20 min.	primed	7.03	1.37
30 min.	unprimed	6.90	1.37
30 min.	primed	6.89	1.74
40 min.	unprimed	5.18	1.06
40 min.	primed	5.79	1.61
HDPE- 3 min.	primed	12.4	----
PP-3 min..	primed	2.82	----

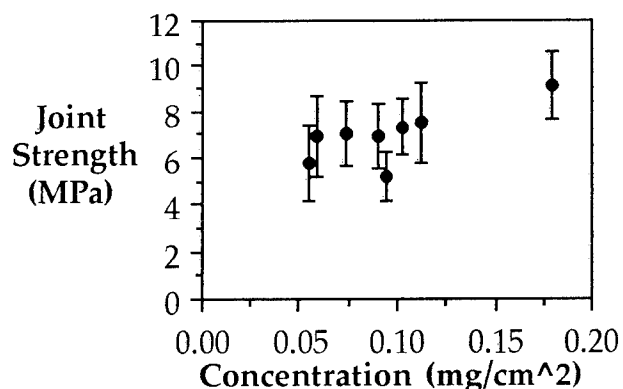


Figure 1: Plot of joint strengths versus adhesive uptake concentrations.

IR microscopy on joint cross sections revealed that the distance that the adhesive diffused was quite significant. Figure 2 presents a plot of the relative adhesive concentration versus the distance from the interface for the best LDPE joints (10 min. primed) and the worst joints (40 min. primed). This clearly showed that in the

best case the interphase was over 1.5 mm, while in the worst case the adhesive could only be detected ~300 μm into the substrate. It should be noted that substrate failure was observed in both of these cases, but the amount of substrate failure and the differences in the joint strengths was attributed to the varying degrees of interpenetration.

The result of the interpenetration mechanism was very strong joints that were extremely durable. This was exhibited in the durability testing that was performed on stressed, but unfractured joints. Several of these were soaked in boiling water for over 3 months. No failures were noted after this treatment, but it was evident that both the LDPE and adhesive had been degraded by the change in colors and opacity. Subsequent retesting did result in a drop in strengths, however, substrate failure was still present, indicating that the adhesion was still good.

The relative bondability of the three polyolefins was also investigated here. It was found that LDPE was the easiest to bond to followed by HDPE and PP which only formed strong bonds with this adhesive at the exotherm (~65-70°C). We related this phenomenon to the chain mobility of these substrates at the application temperature or to G'' , the log of which correlates inversely with the log of the diffusivity.

CONCLUSIONS

An acrylic adhesive was developed that formed strong, water resistant structural joints with polyolefins. This two component, anaerobic adhesive formed strong LDPE/LDPE joints that resulted in substrate failure upon block shear testing, and strong HDPE and PP joints when the adhesive was at its exotherm. The relative

trend in polyolefin bondability was related to the loss moduli of the polymers at the application temperatures. The interphase of mixed LDPE and adhesive was determined to be as large as 1.7 mm using IR microscopy, and it was concluded that this interpenetration was the mechanism of adhesion.

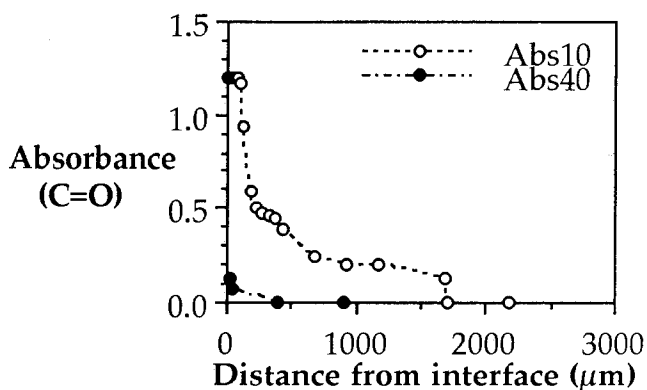


Figure 2: Plot of the carbonyl absorbance versus the distance from the interface for 10 and 40 minute primed bond cross sections.

We gratefully acknowledge financial support from the Connecticut Department of Higher education and the Plastics Institute of America. We also thank Loctite Corp. for their assistance, especially Dr. D. Billy Yang and David Wolf.

REFERENCES

1. L. N. Lewis and D. Katsamberis, J. Appl. Polym. Sci., 42, 1551 (1991).
2. J. Yang and A. Garton, J. Appl. Polym. Sci., 48, 359 (1993).
3. D. Jia, Y. Pang, and X. Liang, J. Polym. Sci.: Part B: Polym. Phys., 32, 817 (1994).
4. J. Yang and A. Garton, J. Adhesion, 46, 67 (1994).

VINYLPHOSPHONIC ACID ANODIZING ALUMINUM FOR STRUCTURAL ADHESIVE BONDING

G. A. Nitowski

Aluminum Co. Of America

Alcoa Technical Center, Alcoa Center, PA 15069

K. Wefers and J. G. Dillard

Department of Chemistry

Virginia Polytechnic Institute & State University, Blacksburg, VA 24061

INTRODUCTION

To obtain strong and durable adhesively bonded aluminum joints, costly surface pretreatments are required. Pretreatments are designed to remove residual mill lubricant and surface oxides, roughen the surface, and in certain instances, change the chemistry of the surface. Typically, for aerospace applications, these are lengthy anodizations that may require the use of environmentally deleterious chromates. For example, the phosphoric acid anodizing (PAA) process [1] requires a 20 min anodization. The typical chromic acid anodizing process [2] calls for a 40 min anodization, along with the use of solutions containing Cr(VI), a potential carcinogen. OSHA has targeted Cr(VI) for a 100x reduction in workplace exposure. The use of chromates also results in costly hazardous waste disposal problems. In order to expand the use of adhesively bonded aluminum structures, there is a need to develop short-term, chromate-free, environmentally benign aluminum surface pretreatments that enhance polymer adhesion. It was found [3] that when aluminum alloy is anodized in aqueous solutions of vinylphosphonic acid (VPA) {see Figure 1} for 30 s or less, and bonded with epoxy paste adhesives, the adhesive joint strength and durability, were comparable to joints with standard PAA adherends.

Within recent decades, the use of organophosphonic acids in treating aluminum has been reported in the literature. Gillich, et al., have patented the process

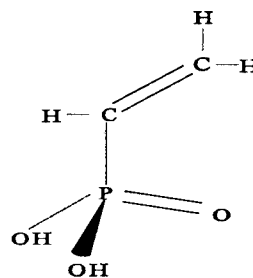


Figure 1
Vinylphosphonic Acid

of anodizing in polyvinylphosphonic acid to obtain a mixed organic/aluminum oxide film on the aluminum metal. [4, 5] They claim that the mixed film is highly wettable by polymers used in lithographic plates, and results in lithographic plates that exhibit improved performance. Venables, et al., describe the use of nitrilotris(methylene)triphosphonic acid (NTMP) to prevent hydration of aluminum oxide surfaces, with resulting improved adhesive joint durability. [6, 7, 8, 9] This process typically calls for immersion times of several minutes in solutions of NTMP in the ppm range. Gray, et al., describe the treatment of aluminum and galvanized steel with an activating agent such as HF followed with an organophosphonic acid treatment. [10] It is claimed that the treatment provides improved adhesion and resistance to humidity for polymeric coatings.

In this investigation, vinylphosphonic acid anodization (VPAA) of aluminum alloy, for 30 s or less, was shown to result in epoxy bonded joints with durability comparable to those formed with 20 min

PAA adherends. While the PAA adherends have a porous anodic oxide surface film, it was determined that the anodic oxide formed in VPA solutions is of the non-porous barrier type, and is covered with a layer of the reaction product and the aluminum oxide. It is proposed that the interfacial chemistry that occurs between the VPA surface layer and the epoxy adhesive is the primary mechanism of joint durability enhancement for this system.

EXPERIMENTAL

Aluminum alloy 6061-T6 and a dicyandiamide cured, epoxy paste adhesive {XA-3498, 3M Corp.} were used in this investigation. Technical grade VPA (65% w/w) was obtained from the Hoechst-Celanese corporation and diluted to 10%(w/w) with deionized water. The metal was initially degreased in the vapors of 1,1,1-trichloroethane, etched in a HNO_3 / HF solution, and rinsed with deionized water. Some etched metal was anodized in 10% phosphoric acid solution at 10 V for 20 min. Additional etched metal was treated with an Alcoa proprietary chrome phosphate (CrPO_4) chemical conversion coating for 10 s. Metal was also anodized in 10% VPA solution at 40 V for 10 s. Joints with a bond line thickness of 380 μm (0.015 in) were cured at 149°C (300°F) and 310 KPa (45 psi) pressure for 30 min. The joints were tested in the lap shear (ASTM D-1002) and the wedge test (ASTM D3762-79) configurations. The reported values are averages and standard deviations from at least 5 replicate joints.

RESULTS

The data in Table 1 show that there is no significant difference in the lap shear breaking strengths for any of the surface pretreatments. Furthermore, the apparent failure mode for all of the lap shear joints was cohesive in the adhesive. These data imply that for "dry" adhesion, the weakest link in these joints is the epoxy adhesive.

TABLE 1
Avg. Lap Shear Breaking Strengths

Pretreatment	Strength (MPa)	Strength (psi)
HNO_3 /HF etch	21.9 ± 1.2	3104 ± 174
PAA	21.9 ± 1.3	3176 ± 189
CrPO_4	20.3 ± 0.7	2948 ± 102
10% VPAA	21.4 ± 1.2	3104 ± 174

The wedge test data for the same treatments are found in Figure 2.

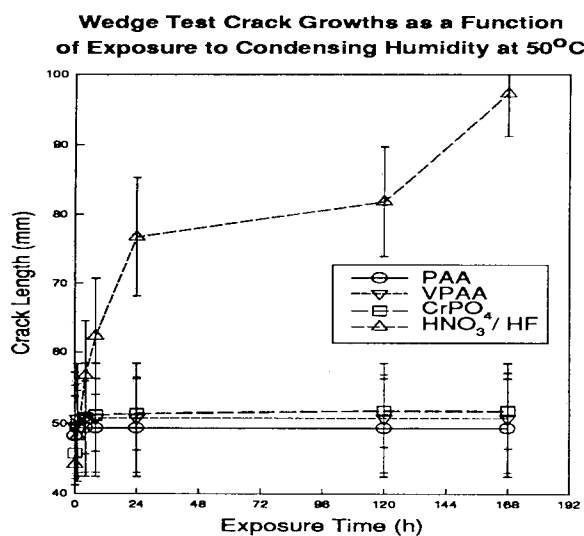


Figure 2

The wedge test data show that all of the pretreatments significantly improve the joint durability over the acid etched metal. Furthermore, there was no significant difference between performance of the chemical conversion coating (CrPO_4), the porous anodic oxide (PAA), or the barrier anodic oxide (VPAA) for these joints. The

failure mode of the joints with anodized or conversion coated adherends was cohesive in the adhesive; the apparent failure mode for the joints with etched-only adherends was interfacial.

DISCUSSION

Anodization of aluminum alloys for structural adhesive bonding was shown to be a short-term, chromate free alternative to current commercial pretreatment practices. The use of transmission electron microscopy (TEM) and Auger electron spectroscopy (AES) with depth profiling have shown

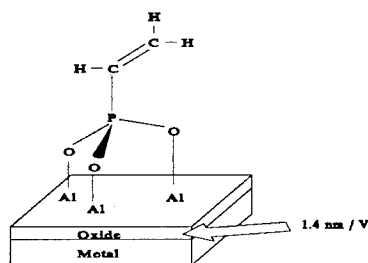


Figure 3

VPA Anodic Aluminum Oxide

that the anodic oxides formed in VPA solution are of the non-porous, barrier type. A duplex barrier layer is formed, with a dense layer of pure aluminum oxide adjacent to the metal, having a thickness corresponding to 1.4 nm/V, and a surface layer of the reaction product of VPA and Al_2O_3 . This is shown schematically in Figure 3.

The formation of the duplex barrier layer was unexpected due to the high solubility of Al_2O_3 in acidic solutions. It is postulated that during anodization, the organic portion of the VPA prevents the ingress of water and the dissolution of the Al_2O_3 , while allowing the diffusion of O^{2-} and OH^- ions into the forming oxide.

Due to the non-porous nature of the oxide, the mechanism of mechanical interlocking is not entirely

applicable to joints formed with VPA anodized adherends. The microscopic porosity observed with PAA oxides is not present. The VPA anodic oxide is made hydration resistant through the formation of hydrolytically stable Al-O-P bonds on the surface during anodizing. The vinyl group on the anodic oxide surface is available for chemical reaction with the functional groups in the epoxy resin. It is submitted that an Al-O-P-C-C-C~ molecular structure at the interface chemically couples the adhesive with the adherend, and is not easily hydrolyzed. Thus, a hydrolytically stable interphase is formed.

Furthermore, when an organophosphonate with a non-reactive group, such as phenylphosphonic acid, was substituted for VPA the adhesive joint durability was degraded. These data suggest that, in these systems, interfacial chemistry, rather than surface topography, plays the major role in determining adhesive joint durability.

REFERENCES

- [1] Boeing Aerospace Corp. Specification BAC555
- [2] Ministry of Defence, Specification DEF 151 (1965).
- [3] L. F. Wieserman, K. Wefers, G. A. Nitowski, and E. S. Martin, U. S. Patents 5,032,237 (1991 July); 5,126,210 (1992 June 30).
- [4] T. N. Gillich and J. E. Walls, U. S. Patent No. 4,381,226 (1983 April 26).
- [5] T. N. Gillich, J. E. Walls, S. F. Wanat, and W. J. Rozell, U. S. Patent No. 4,383,897 (1983 May 17); 4,399,021 (1983 August 16).
- [6] J. D. Venables, M. E. Tadros, and B. M. Ditchek, U. S. Patent No. 4,308,079 (1981 December 29).
- [7] D. A. Hardwick, J. S. Ahearn, and J. D. Venables, *J. Materials Science*, 19 (1984) 223-232.
- [8] G. D. Davis, J. S. Ahearn, L. T. Matienzo, and J. D. Venables, *J. Materials Science*, 20 (1985) 975-988.
- [9] D. A. Hardwick, J. S. Ahearn, A. Desai, and J. D. Venables, *J. Materials Science*, 21 (1986) 179-187.
- [10] R. C. Gray, M. J. Pawlik, P. J. Prucnal, and C. J. Baldy, U. S. Patent No. 5,294,265 (1994 March)

USING POLYMERIC BINDERS IN SUSPENSION PREPREGGING AND TAILORING FIBER/MATRIX ADHESION FOR CARBON FIBER-REINFORCED COMPOSITES

S. Gardner¹, A. Gonzalez¹, R.M. Davis¹, S. Case², J.J. Lesko², K.L. Reifsnider²

Center for Adhesive and Sealant Science

¹Department of Chemical Engineering, ²Engineering Science and Mechanics Department
Virginia Polytechnic Institute, Blacksburg, VA 24061-0211

INTRODUCTION

There is a great deal of interest in carbon fiber reinforced thermoplastic composites given their advantages over thermoset matrix composites. High performance thermoplastic polymers are preferred because of their indefinite shelf life (no curing occurs in contrast with thermosets), their excellent strength and lifetime at elevated temperatures and reprocessability. The manufacture of thermoplastic composites is complicated by high melt viscosity of matrix material which leads to poor wetting of the fibers. Powder-based techniques have received much attention because they circumvent this problem. In particular, aqueous suspension prepregging of thermoplastic polymer powders shows great promise and it is environmentally friendly. This method has become very important as it is especially useful for constructing composites with different interphases.

Suspension prepregging consists of passing a carbon fiber through an aqueous slurry of polymer powder and winding the powder-coated fiber on a drum. The polymer powder must be dispersed well and adhere to the fiber. Binders are needed to fasten the polymer particles to the carbon fibers during the prepregging step so that the powder coated fibers may be handled for further manufacturing steps. After consolidation of the composite, the presence of these binders alters the fiber-matrix interphase region.

EXPERIMENTAL

Materials. The matrix material was Victrex PEEK 380 Grade from ICI with a median particle diameter of 12 microns. The binders used were LaRC TPI polyamic acid (PAA) supplied by Mitsui Toatsu, and BisP-BTDA PAA which was synthesized in the Chemistry Department of Virginia Tech. An experimental control composite was established with APC-2 prepreg supplied by ICI. The APC-2 composites are assumed to be made solely of PEEK and carbon fibers with no other material in the interphase region.

Suspension Preparation. The PAA is dissolved in an aqueous solution of ammonium hydroxide. The PEEK powder is then mixed into this solution. The dissolved PAA acts as an electrostatic stabilizer for the PEEK particles providing a homogeneous suspension.

Prepregging and composite production. A schematic of the drum winder-prepregger is shown in Figure 1. The fiber was coated with the PEEK suspension in the resin pot. As seen in the detailed view in

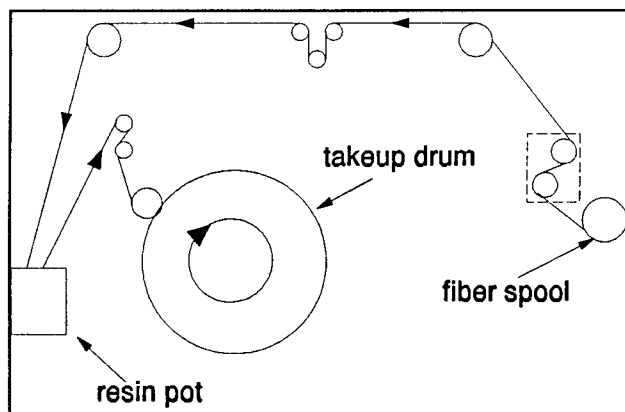


Figure 1. Schematic of drum winding prepregger for aqueous suspension prepregging.

Figure 2, the dissolved PAA serves as a binder during the prepregging step, adhering the powder to the fiber; and in the next step, the PAA was converted to the corresponding polyimide. After consolidation of the composite, this polyimide dominated the interphase between fiber

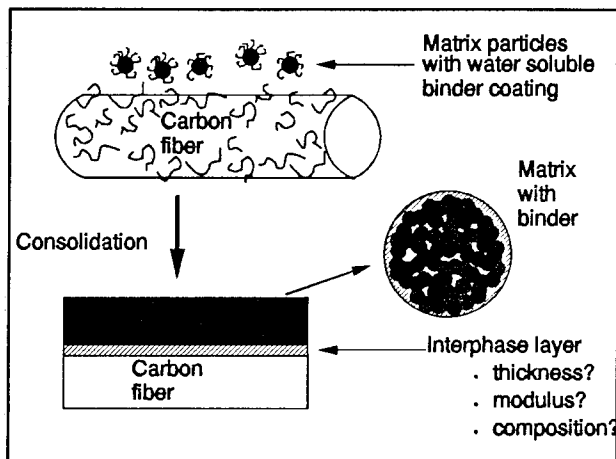


Figure 2. The role of the binder for aqueous suspension prepregging and the resulting composite.

and bulk matrix. An evaluation of composite quality was made, which includes acoustic C-scan, image analysis (for void volume) and fiber volume fraction measurement. Once composite quality was established, the panel was machined for mechanical testing.

Notched Fatigue Testing. The notched fatigue coupons were cut from [0/90]_{2s} panels and were 1.0" x 5.0" with a 0.25" diameter circular notch cut in the center of the coupon. The testing was done on an MTS, loading the specimen in tension/tension at a level of R=0.1 until failure or after 10⁶ cycles. The ultimate tensile strength (UTS) of a notched coupon was measured and the fatigue testing was done at two specific fractions (0.75 and 0.85) of UTS. The tested specimens were examined with X-ray to determine failure mode and extent of damage.

Impact Testing. The impact coupons were cut from a [0/90/±45]_{2s} panel and were 3" x 3" square. The impact testing was done with a gas gun apparatus which fired a steel impactor at various velocities. The tested specimens were evaluated with C-scan and X-ray to determine extent of damage. An image analysis computer program was used to determine the area of damage.

RESULTS

Notched Fatigue Testing. The notched fatigue test results are shown in Figures 3, 4. At 75 % UTS the two polyimide binder composites have a higher normalized stiffness than the APC-2 composite during fatigue. At 85% UTS, the LaRC-TPI binder composite maintains a slightly higher normalized stiffness than the BisP-BTDA binder composite. At this load level, the APC-2 composite failed after less than ten cycles of loading. A typical X-ray radiograph shows damage in the form of longitudinal split growth initiating at the stress concentrations of the notch edges and transverse crack growth near the notch, which is not as prevalent.

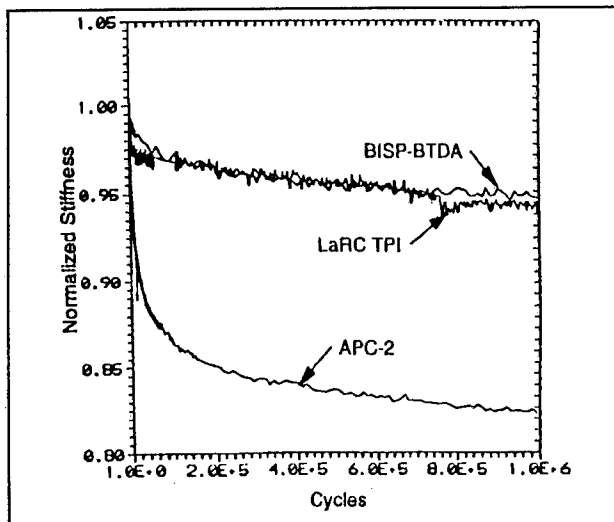


Figure 3. Normalized stiffness with fatigue cycles at 0.75 UTS.

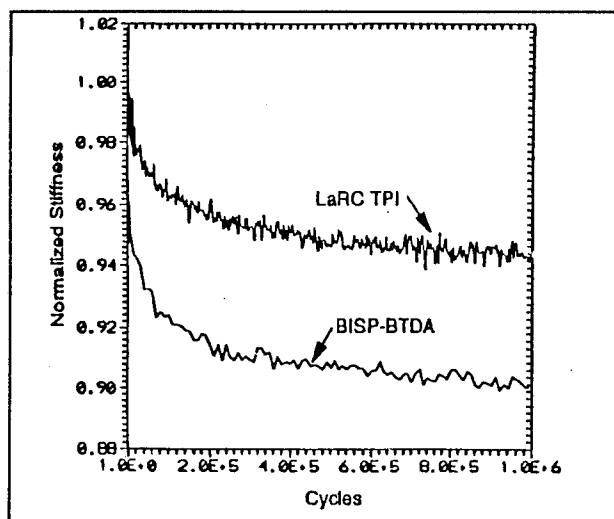


Figure 4. Normalized stiffness with fatigue cycles at 0.85 UTS.

Impact Testing. The impact test results are reported as two parameters in Table I; damage area growth rate and threshold velocity. The damage area growth rate is the rate which damage area increases with increasing impactor velocity. The threshold velocity is the lower limit of impactor velocity that creates damage detectable by C-scan. The threshold velocities for the APC-2 composite and BisP-BTDA composite are slightly higher than for the LaRC TPI binder composite. The damage area growth rate, however, is lower for both the polyimide binder composites.

Table I. Impact testing results.

	Threshold Velocity (m/s)	Damage Area Growth Rate (mm ² /(m/s))
APC-2	11.1	33.3
PEEK/BisP-BTDA	11.0	21.9
PEEK/LaRC TPI	9.9	23.9

DISCUSSION

Notched fatigue data is an indication of interphase strength. A strong interphase will prevent the split growth at the stress concentrations, hence damage will occur in the form of transverse cracks. A weaker bond will promote split growth.

At 0.75 UTS the APC-2 sample showed greater stiffness reduction than did both of the binder composites. X-ray radiographs showed that both binder composites had similar length splits which were shorter than for the APC-2 sample. This implies a weaker fiber-matrix bond for the APC-2. The LaRC TPI/PEEK composite had longitudinal splits but no transverse cracking above and below the notch. This indicates that the splits developed immediately after the start of loading, thus decreasing the stress concentration and preventing the formation of transverse cracks. The BisP-BTDA/PEEK composite had similar length splits but also had significant damage above and below the notch in the form of transverse cracks indicating the fiber-matrix bond was strong enough to prevent the development of the splits immediately after the start of loading. Thus the BisP-BTDA/PEEK composite had a stronger fiber-matrix adhesion than the LaRC TPI/PEEK composite and the APC-2 composite.

At 0.85 UTS the BisP-BTDA/PEEK composite had larger splits and more transverse cracks than the LaRC TPI/PEEK composite. This is consistent with the BisP-BTDA/PEEK composite having a stronger fiber-matrix bond. The APC-2 composite failed within the first 10 cycles which is consistent with the APC-2 composite having the weakest fiber-matrix bond.

Impact data showed that the LaRC TPI/PEEK composite had lower threshold velocities than APC-2 and BisP-BTDA composites. The threshold velocity for the BisP-BTDA/PEEK composite and APC-2 composite were almost the same. The lower damage area growth rates for the binder composites indicate that they had more resistance to higher levels of impact energy. The binder composites showed more fiber breakage in impact failure. This was noticed visibly and confirmed with residual compression tests, which indicated a stronger fiber-matrix adhesion for these composites over the APC-2 composite.

CONCLUSIONS

The BisP-BTDA/PEEK composites and the LaRC TPI/PEEK composites made by aqueous suspension prepregging had a stronger fiber-matrix bond than APC-2. A polyimide interphase region significantly affects the durability of the composite. The BisP-BTDA/PEEK composites had a stronger fiber-matrix bond than the LaRC TPI/PEEK composites as determined by notched fatigue testing. The fiber-matrix bond for the BisP BTDA/PEEK composite may be *too strong* for optimization of composite durability since split growth did not occur fast enough for the 0.85 UTS test.

ACKNOWLEDGEMENTS

Center for Adhesive and Sealant Science at Virginia Tech
National Science Foundation Science and Technology Center at VPI under contract No. DMR-8809714.

Virginia Tech Center for Composite Materials and Structures.

REFERENCES

1. Towell, T.W., Hirt, D.E., and Johnston, N.J., 35th International SAMPE Symposium, 22:1156 (1990).
2. Texier, A., and Davis, R.M., Proceedings of the Society of Plastic Engineers ANTEC'91 Conference, 37:2018 (1991).
3. Texier, A., Davis, R.M., Lyon, K.R., Gungor, A., McGrath, J.E., Marand, H., and Riffle, J.S., Polymer 34(4):897 (1993).
4. Yu, T.H., Davis, R.M., Journal of Thermoplastic Composites Materials, 6(1):62 (1993).
5. Gonzalez, A., "The Effects of Polymeric Binders on the Processability and Properties of Composites Made by Suspension Prepregging", M.S. Thesis, Chemical Engineering, VPI (1993).

FUNCTIONALIZED BLOCK COPOLYMERS AS ADHESION PROMOTERS

Michael S. Kent and Randall Saunders

Sandia National Labs. P.O. Box 5800
Albuquerque, NM 87185

INTRODUCTION

The goal of this work is to develop novel functionalized block copolymers to promote adhesion at inorganic substrate/polymer interfaces. We envision several potential advantages of functionalized block copolymers over small molecule coupling agents. Greater control over the structure of the interphase region should result through careful design of the backbone of the copolymer. The number of chains per area, the degree of entanglement between the copolymer and the polymer matrix, the number of sites per chain able to attach to the substrate, and the hydrophobicity of the interphase region can all be strongly affected by the choice of block lengths and the monomer sequence. In addition, entanglement between the copolymer and the polymer matrix, if achieved, should contribute significantly to adhesive strength.

Our program involves four key elements: the synthesis of suitable functionalized block copolymers, characterization of the conformation of the copolymers at the interface by neutron reflectivity and atomic force microscopy, characterization of the degree of bonding by spectroscopy, and measurement of the mechanical properties of the interface. In this paper we discuss block copolymers designed as adhesion promoters for the copper/epoxy interface. We have synthesized a diblock with one block containing imidazole groups to bond to copper and a second block containing secondary amines to react with the epoxy matrix. We have also prepared a triblock copolymer containing a hydrophobic middle block. Below we describe the synthesis of the block copolymers by living, ring-opening metathesis polymerization (ROMP) and the first characterization data obtained by neutron reflectivity.

EXPERIMENTAL

Synthesis

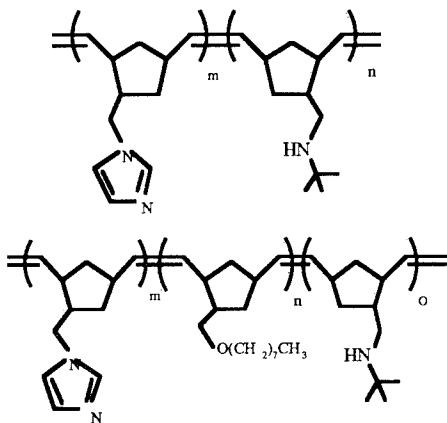
ROMP has been known for many years. However, the synthesis of block copolymers by ROMP became possible only recently when Grubbs [1] and Schrock [2] developed molybdenum and titanium based initiators capable of living polymerization. The molybdenum based initiator is capable of tolerating a wide variety of chemical functionalities on norbornene-type monomers, and thus lends itself to the synthesis of well-defined, functionalized block copolymers that can be tailored to a wide variety of interfaces.

All reactants were purchased from Aldrich Chemical Company. Tetrahydrofuran was used as the polymerization solvent, and was vacuum distilled from a sodium/benzophenone solution immediately prior to use. The molybdenum based initiator ((2,6-diisopropylimido)neophylidene-molybdenum-bis-*t*-butoxide) was purchased from Strem and used without further purification. All polymerizations were performed under an inert atmosphere in a Vacuum Atmospheres dry box.

The synthesis of the three monomers (5-(*n*-methylimidazole)-2-norbornene, 5-(*t*-butylaminomethyl)-2-norbornene, and 5-(octaoxymethyl)-2-norbornene) will be described in detail elsewhere. All three were dried by distilling from and storing over calcium hydride or sodium hydride, and filtering through activated neutral alumina immediately prior to use.

A partially deuterated form of the imidazole monomer, used in the neutron reflection experiments, was prepared following the same reaction scheme as that for the protonated imidazole monomer, but starting with a partially deuterated dicyclopentadiene precursor. This sample contained 4 to 5 deuterium atoms per repeat unit.

The two block copolymers synthesized for this study are shown below.



Typically a total of 1g of copolymer was formed in about 15 mls. dry THF. An appropriate amount of the first monomer was initially stirred with the molybdenum initiator. Upon complete consumption, the second monomer was then added. After the polymerization of the final block, the living chain ends were terminated by the addition of benzaldehyde. The copolymers were characterized by proton nmr, which showed complete consumption of all monomer except in the case of the imidazole monomer. This was the last block in the polymerization sequences, and thus did not destroy the continuity of the other blocks. The block copolymers were precipitated from acetonitrile, dried, and redissolved in chloroform for future use.

Each block in the copolymers had a targeted molecular weight of 15,000 g/mol. The actual molecular weight of the imidazole block is roughly 10,000 g/mol, whereas the other blocks are assumed to have the targeted molecular weight based upon the observation of total monomer consumption.

Characterization of adsorbed films by neutron reflectivity

Since both the imidazole and amine functionalities have an affinity for the copper surface, it is essential to determine whether the blocks order into layers upon adsorption to a copper substrate, with one block adsorbing preferentially, or whether they adsorb in a

disordered conformation with both blocks adsorbing at the surface. To address this question we prepared copolymer samples with partially deuterated imidazole blocks and examined adsorbed films of these copolymers by neutron reflectivity. With this technique the neutron refractive index profile normal to the surface is obtained with $\sim 5 \text{ \AA}$ resolution. The selective deuteration allows one to distinguish between the two blocks. The copolymers were adsorbed from solution onto silicon wafers which had been previously sputter-coated with smooth, thin ($\sim 250 \text{ \AA}$) copper films. Following the adsorption step, the samples were thoroughly washed with MeOH and THF to remove any copolymer not strongly adsorbed to the surface.

Results for the diblock copolymer (with targeted block lengths 15K-15K) adsorbed from 0.002 g/ml solution in MeOH are shown in Figure 1a. The main effect of the adsorbed copolymer on the reflectivity is to shift the fringes to lower q . This is consistent with the imidazole block selectively adsorbing to the surface, as shown in Figure 1b. The curves in Figures 1b-1d were calculated using the known atomic compositions of the blocks and assuming a 30 \AA thickness for the layers formed by each block, which is consistent with the size of the shift observed in Figure 1a. Thus, these data suggest that the copolymer adsorbs in a monolayer film, and that the blocks form separate layers with the imidazole block adsorbed to the surface. Work involving atomic force microscopy is in progress to further characterize the structure of the adsorbed films.

References:

1. R. H. Grubbs and W. Tumas, *Science* **243**, 902, 1989.
2. R. R. Schrock, *Acc. Chem. Res.*, **23**, 158, 1990.

Acknowledgments:

This work benefited from the use of the POSY II reflectometer at the Intense Pulsed Neutron Source at Argonne National Labs, and was supported by the U.S. Department of Energy under contracts DE-AC04-94AL85000 and W-31-109-ENG-38.

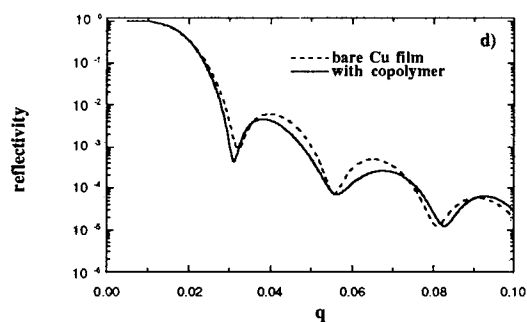
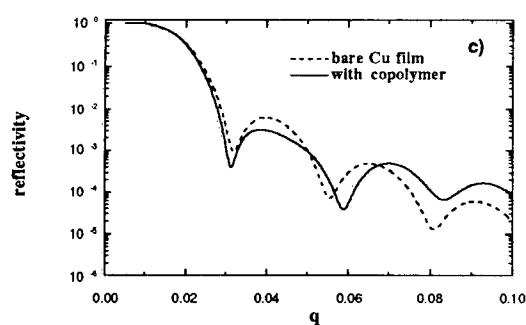
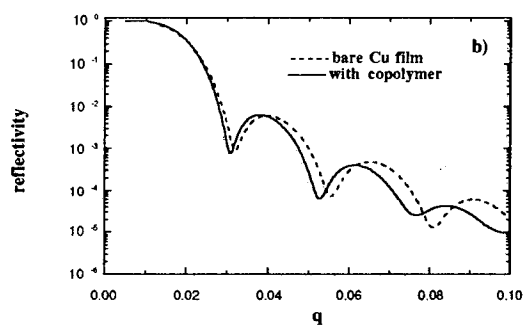
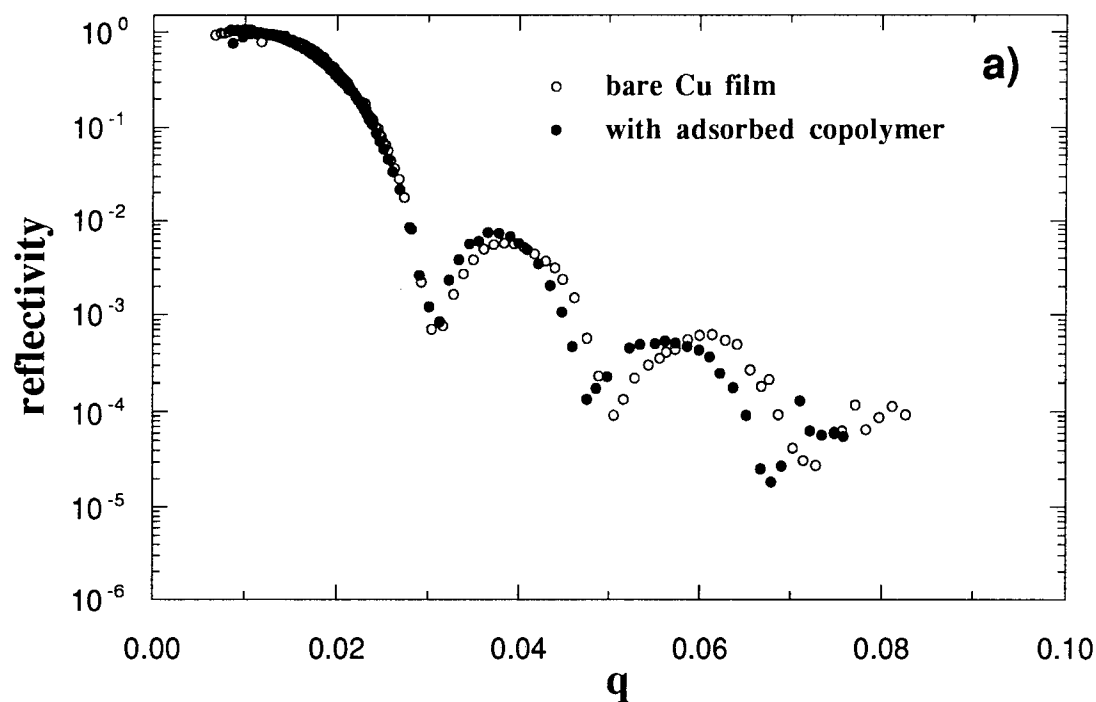


Figure 1. a) Neutron reflectivity for a bare Cu film and after adsorption of the block copolymer. Also shown are calculated reflectivity curves for the cases in which b) the imidazole block selectively adsorbs, c) the amine block selectively adsorbs, and d) the two blocks are randomly mixed in a single layer. These comparisons strongly suggest that the imidazole block selectively adsorbs.

EFFECT OF MOLECULAR WEIGHT ON ADHESIVE PROPERTIES OF THE PHENYLETHYNYL-TERMINATED POLYIMIDE LARCTM-PETI-5

Roberto J. Cano and Brian J. Jensen
NASA Langley Research Center
Hampton, VA 23681-0001

INTRODUCTION

Future civilian aircraft will require the use of advanced adhesive systems with high temperature capabilities. One such material has been developed at the NASA Langley Research Center, a phenylethynyl-terminated polyimide given the designation LARCTM-PETI-5.[1,2] Recent work has shown the advantages of similar phenylethynyl-terminated polyimides as films, moldings, adhesives, and composite matrix resins.[3-8] Phenylethynyl-terminated oligomers provide greater processing windows than materials which incorporate simple ethynyl endcaps. Since these low molecular weight, low melt viscosity oligomers thermally cure without the evolution of volatile by-products, they provide an excellent means of producing polymers with high glass transition temperatures, excellent solvent resistance, and high mechanical properties.

Three different versions of LARCTM-PETI-5 with theoretical number average molecular weights (M_{ns}) of 2500, 5000, and 10000 g/mol were synthesized in this work. Differential Scanning Calorimetry (DSC) measurements were performed on the dry powder form of these materials to establish cure conditions which result in high glass transition temperatures (T_g s). Lap shear specimens were prepared from adhesive tape made from each material and with the thermal cure conditions determined from the DSC data. The tensile shear data established processing conditions which provided the best adhesive strengths. Further testing was performed to establish the properties of LARCTM-PETI-5 as an adhesive material and to determine its solvent resistance.

EXPERIMENTAL

Polymer Synthesis

The three different molecular weight oligomers were prepared as previously reported [1,2] by offsetting the monomer ratio (Table 1)

in favor of the diamines and endcapping with the appropriate amount of 4-phenylethynyl phthalic anhydride (Equation 1).

Characterization

Inherent viscosities were measured at 25°C on 0.5% solutions in N-methylpyrrolidinone (NMP). DSC was performed on a Shimadzu DSC-50 calorimeter at a heating rate of 20°C/min with the T_g taken at the inflection point in the heat flow vs. temperature curve.

Adhesive Specimens

Oligomer solutions (15-20% solids in NMP) were used to coat 112 E-glass (A-1100 finish). Each coat was dried in a circulating air oven for one hour each at 100 and 225°C to provide adhesive tapes with volatile contents of ~1-2 %. Twelve to fifteen mil thick tape was produced by applying several coats of the solution. Titanium (Ti-6Al-4v) treated with Pasa-Jell 107™ surface treatment was bonded under varying conditions of temperature and pressure. Four tensile shear specimens of each material type for each condition were tested at either room temperature (RT) or 177°C according to ASTM-1002.

RESULTS AND DISCUSSION

Powdered versions of the 2500, 5000, and 10000 g/mol molecular weight materials cured at various conditions were subjected to DSC analysis to determine T_g . The cure conditions evaluated and the corresponding T_g s are shown in Table 2. All three materials showed the similar results of increasing T_g s with increasing cure temperature. Since all three materials produced similar T_g s, the 5000 g/mol material was chosen to perform further analysis. As shown in Table 3, a T_g as high as 274°C was determined for this material cured for 1/2 hr at 325 and 1/2 hr at 375°C. The results also indicate that a hold at 375°C is required since the ramp to 375°C with no hold produced a T_g

of only 234°C. A processing temperature as low as 316°C resulted in a T_g of 263°C when held for 2 hours. Several cure conditions produced T_gs in a similar range. Four cure conditions were then chosen to make Ti lap shear specimens to evaluate their adhesive properties.

The results from the Ti tensile shear tests are presented in Table 4. As shown by the results, the highest tensile shear strengths were obtained by different processing condition for each material. For the low molecular weight version, a low processing temperature of 316°C for two hours provided the best adhesive properties. The tensile shear results for the 10000 g/mol material were all low, which indicated the need for increased pressure. As evidence by the results is Table 5, increased pressure provides higher strengths for the 10000 g/mol material while pressures as low as 25 psi provide good strengths for the 2500 g/mol material. Overall, excellent adhesive properties were obtained with each of these materials.

These materials also showed excellent solvent resistance. As shown in Table 6, all three materials were essentially unaffected (strength retention between 92 and 100%) by a 48 hour hydraulic fluid soak.

CONCLUSIONS

LARCTM-PETI-5 displays excellent adhesive properties. Ti tensile shear strengths as high as 7630 psi at RT and 5100 psi at 177°C were determined. Processing temperatures as low as 316°C and pressures as low as 25 psi resulted in good adhesive properties. The tensile shear properties of these materials are also unaffected by hydraulic fluid. The molecular weight of LARCTM-PETI-5 has an important effect on the bonding pressures required to obtain good tensile shear strengths.

REFERENCES

1. P. M. Hergenrother, R. G. Bryant, B. J. Jensen, J. G. Smith, Jr. and S. P. Wilkinson, *Soc. Adv. Matl. Proc. Eng. Series*, **39**(1), 961(1994).
2. R. G. Bryant, B. J. Jensen, J. G. Smith, Jr. and P. M. Hergenrother, *Ibid.*, (Closed Papers), **39**, 273(1994).
3. C. W. Paul R. A. Schultz and S. P. Fenelli U. S. Pat 5,138,028 (1992) (to National Starch and Chemical Co.).
4. C. W. Paul, R. A. Schultz and S. P. Fenelli in *Advances in Polyimide Science and Technology*, (C. Feger, M. M. Khojasteh and M. S. Htoo, ed.) Technomic Pub. Co., N.Y., 1993, p 220.
5. R. G. Bryant, B. J. Jensen and P. M. Hergenrother, *Polym. Prepr.*, **34**(1), 566 (1993).
6. B. J. Jensen, R. G. Bryant and S. P. Wilkinson, *ibid.*, **35**(1), 539 (1994).
7. S. J. Havens, R. G. Bryant, B. J. Jensen, and P. M. Hergenrother, *ibid.*, **35**(1), 553 (1994).
8. J. G. Smith, Jr. and P. M. Hergenrother, *ibid.*, **35**(1), 353 (1994).

Table 1. Theoretical Molecular Weights, Inherent Viscosities, and Monomer Offset Ratios for Three Molecular Weight Versions of PETI-5.

Theoretical Molecular Weight	Inherent Viscosity, dL/g	Monomer Offset Ratio
2500 g/mole	0.22	0.8276
5000 g/mole	0.38	0.9098
10000 g/mole	0.44	0.9539

Table 2. Glass Transition Temperatures for Three Molecular Weight Versions of PETI-5.

PETI-5, 2500g/mol	Glass Transition Temp., °C
Cure Condition	
1 hr @ 300	219
1 hr @ 325	253
1 hr @ 350	254
1 hr @ 375	275
PETI-5, 5000g/mol	Glass Transition Temp., °C
Cure Condition	
1 hr @ 300	239
1 hr @ 325	257
1 hr @ 350	263
1 hr @ 375	270
PETI-5, 10000g/mol	Glass Transition Temp., °C
Cure Condition	
1 hr @ 300	258
1 hr @ 325	259
1 hr @ 350	266
1 hr @ 375	271

Table 3. T_g s of PETI-5, 5000 g/mol After Several Cure Conditions.

Cure Condition	Glass Transition Temperature, °C
1 hr @ 300°C	239
1 hr @ 325°C	257
1 hr @ 350°C	263
1 hr @ 375°C	270
1/2 hr @ 375°C	268
1/4 hr @ 375	262
Ramp to 375°C, no hold	234
1/2 hr @ 350°C, 1/2 hr @ 375°C	272
1/2 hr @ 325°C, 1/2 hr @ 375°C	274
2 hr @ 316°C	263

Table 4. Tensile Shear Strengths for PETI-5 at RT and 177°C for Various Cure Temperatures Bonded at 75 psi.

PETI-5, 2500g/mol	Tensile Shear Strength ,psi	
Cure Condition	RT	177°C
1 hr @ 350	5470	4520
1 hr @ 375	5760	4330
1/2 hr @ 325,	6490	4720
1/2 hr @ 375		
2 hr @ 316	6460	5100
PETI-5, 5000g/mol	Tensile Shear Strength ,psi	
Cure Condition	RT	177°C
1 hr @ 350	7630	5000
1 hr @ 375	5290	3840
1/2 hr @ 325,	6370	3710
1/2 hr @ 375		
2 hr @ 316	5130	4970
PETI-5, 10000g/mol	Tensile Shear Strength , psi	
Cure Condition	RT	177°C
1 hr @ 350	4260	2840
1 hr @ 375	N/A	3160
1/2 hr @ 325,	4260	3050
1/2 hr @ 375		
2 hr @ 316	4250	3830

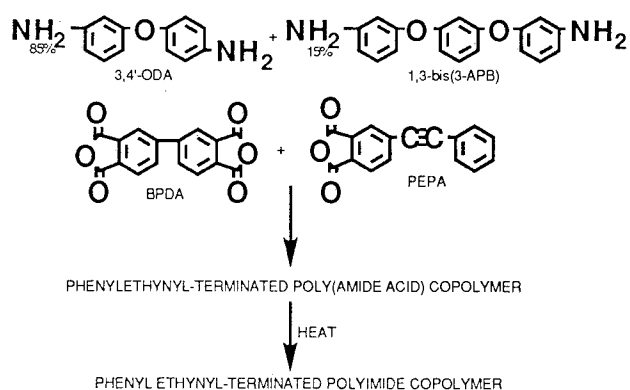
Table 5. Effects of Processing Pressure on Tensile Shear Strength Bonded at 350°C for 1 Hour.

Material	Processing Pressure, psi	Tensile Shear Strength, psi
PETI-5, 2500 g/mol	75	5470
	25	6030
PETI-5, 10000 g/mol	75	4260
	100	6350
	200	6380

Table 6. Tensile Shear Strength After 48 Hour Soak in Hydraulic Fluid With Bonding Conditions of 75 psi, and 350°C for 1 Hour.

Material	Tensile Shear Strength, psi	Strength Retention, %
PETI-5, 2500 g/mol	5430	99
PETI-5, 5000 g/mol	6990	92
PETI-5, 10000 g/mol	4260	100

Equation 1. Polymer Synthesis of PETI-5.



ADHESION AT METAL-CERAMIC INTERFACES: AN ELECTROSTATICS BASED MODEL

J. W. Mintmire and F. H. Streitz

Chemistry Division, Code 6179
Naval Research Laboratory
Washington, DC 20375

INTRODUCTION

The metal-oxide/metal-oxide and metal/metal-oxide interfaces are ubiquitous in the adhesion of ceramics and metals. A range of technologically important materials applications are critically dependent on the properties of these interfaces: ceramic-metal composite materials, conductive metals on metal-oxide substrates in electronic devices, and anticorrosive surface oxide layers on structural metals are just a few representative examples. Atomic-scale simulations of metal-oxide materials can be important in understanding and predicting the effect of the interface region on materials properties. Such simulations are difficult, however, both at the first-principles level and at the empirical level. For first-principles methods, the unit cell sizes—particularly for defect supercell simulations—tend to be large, increasing the computational requirements of the simulation. Empirical potentials for these materials are also difficult because of the complexity of the bonding interactions in metal/metal-oxide systems.

One primary objective we have in our current research effort is to simulate the atomic-scale dynamics and energetics of technologically important metal/metal-oxide interfaces. To do this we need an empirical method that allows the local cation valence to vary according to the local environment and which includes the Coulombic electrostatic interaction among the anions and cations. We have investigated the use of a model based on long-range electrostatic interactions and local atomic electronegativity-based properties for a direct calculation of charge transfer in metal-oxide systems, and incorporated the resulting electrostatic potential into an overall model potential for the titanium dioxide (rutile) and α -alumina systems. [1,2] We present herein a brief outline of our approach for modeling the electrostatic component of the potential energy of ionic systems, and how standard empirical potential techniques can be effectively merged with this approach. We then describe results for a simulation of adhesive failure at a model metal-ceramic interface between an

aluminum (111) face and an α -alumina (0001) face. [3] Our results indicate that this approach will be able to provide physically realistic empirical potentials for future simulations on mixed metal/metal-oxide systems.

APPROACH

One of the dominant interactions in the metal-oxides is the Coulombic interaction between anions and cations. Earlier models using empirical potentials included such effects by incorporating fixed atomic charges and polarizability functions into the energetics of metal-oxides. Because our ultimate goal in this work is to develop relatively simple empirical potentials for studying the adhesion of metal-oxides with metal substrates, any new approach must include an ability to calculate the local atomic charge (or equivalently, the valence) based on the local environment of each atom. The long-range nature of the Coulomb interaction will lead to this "local" environment typically being relatively large-scale, of the dimensions of the screening length in the metal oxides.

Conceptually then, what is needed is a description of the total electrostatic energy of an array of atoms as a function of atomic charges (valences) and position. We define an atomic energy term E_i in terms of the local charge q_i on atom i

$$E_i(q_i) = E_i(0) + \chi_i^0 q_i + \frac{1}{2} J_i^0 q_i^2 \quad (1)$$

where χ_i^0 and J_i^0 correspond to local atomic properties traditionally denoted as the electronegativity [4,5] and hardness. [6]

The electrostatic energy, E_{es} , of a set of interacting atoms with total atomic charges q_i is then given by the sum of the atomic energies E_i , and the electrostatic interaction energies between all pairs of atoms,

$$E_{es} = \sum_i E_i(q_i) + \frac{1}{2} \sum_{i \neq j} V_{ij}(\mathbf{R}_{ij}; q_i, q_j) \quad (2)$$

where \mathbf{R}_{ij} denotes the vector $\mathbf{R}_i - \mathbf{R}_j$. The Coulomb pair interaction $V_{ij}(\mathbf{R}_{ij}; q_i, q_j)$ is given by the classic electrostatic interaction between two charge distributions $\rho_i(\mathbf{r}; q_i)$ and $\rho_j(\mathbf{r}; q_j)$, where $\rho_i(\mathbf{r}; q_i)$ is the charge distribution about atom i (including the nuclear point charge) for total charge q_i and r_{12} is the distance between two atoms. The simplest model for $\rho_i(\mathbf{r}; q_i)$ is as a point charge of charge q_i ; this leads to $V_{ij}(\mathbf{R}_{ij}; q_i, q_j) = q_i q_j / R_{ij}$. Rappé and Goddard [7] have suggested the use of spherically symmetric exponential functions to generate a $\rho_i(\mathbf{r}; q_i)$ linear in q_i . We then choose the values of q_i as those that minimize E_{es} subject to the constraint that the sum of the q_i be constant.

The electrostatic energy is just one component of the total energy of a metal-oxide (or metal) system. Indeed, the electrostatic interaction between cations and anions will be strictly attractive at any internuclear separation, so that in the short-range limit a repulsive potential will be needed to maintain physically reasonable internuclear separations in any empirical potential constructed using the above described electrostatic potential. What is needed for a complete potential is a description of the non-Coulombic part of the interatomic interactions. This remaining interaction could be modeled using any standard empirical potential, such as a sum of pair potentials, an embedded atom method (EAM) approach, [8-11] or a many-body potential such as that developed by Abell and others for covalent systems. [12-14] We have chosen to merge our above described electrostatic model with an EAM potential. [1,2]

ALUMINUM-ALUMINA INTERFACE

Another principal goal of our current research effort is to simulate the processes of adhesion and adhesive failure of metal/metal-oxide interfaces that are important in composite materials. We describe herein an initial simulation of the rupture under tensile stress of an interface between an α -alumina (0001) face and an aluminum (111) face. A preliminary report of this data has been presented elsewhere. [3] The simulation described herein used 675 atoms in a unit cell with two-dimensional periodic boundary conditions. The two-dimensional unit cell was constructed starting with two separate slabs: a 5×5 supercell of an aluminum (111) slab with 9 layers (225 atoms), and a 3×3 supercell of a (0001) slab of α -alumina with 5 layers of the conventional Al_2O_3 crystalline unit cell (450 atoms). These supercells were chosen because both have hexagonal symmetry in the plane of two-dimensional

periodicity, with lattice constants within 0.6% of each other. Because our simulations require a unique set of periodic boundary conditions, we have forced the composite system to share common translational vectors with a length of 1.428 nm, which is the average of the unit cell dimensions in the surface plane of 1.424 nm for (0001) alumina and 1.432 nm for (111) aluminum.

Upon juxtaposition of aluminum and α -alumina slabs the oxygen atoms at the interface diffuse rapidly into the aluminum, disordering the alumina surface and oxidizing the adjacent aluminum surface. This process has the effect of shifting the interface several layers into the aluminum. We allow this composite system to equilibrate to a temperature of 100 K for about 1-2 ps of simulation time. We then applied a tensile stress to the composite slab system using the following procedure. Two exterior planes of atoms (one of the exterior aluminum surface, one of the exterior alumina surface) were held rigid and all other atoms were allowed to relax using a Broyden-Fletcher-Goldfarb-Shanno (BFGS) scheme [15,16] so that the total energy was minimized, with forces calculated directly from our model. The separation of the two exterior planes was incremented in steps of 0.05 Å in a series of calculations.

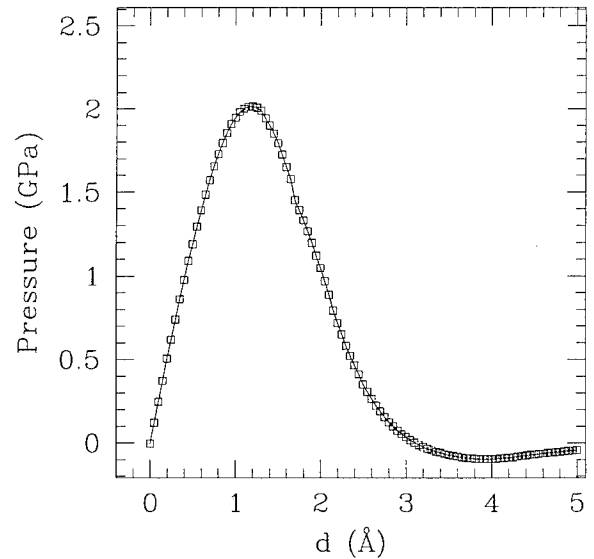


Figure 1. Tensile stress on composite aluminum (111)/ α -alumina(0001) slab versus total change in distance between two exterior planes.

This first simulation resulted in a relatively weak interface with a well-defined interphase region. Three major regions can be assigned to our slab system: a

metal region consisting of the remaining undisturbed aluminum not immediately adjacent to the interface, a metal-oxide region consisting of alumina (0001) layers not substantially disordered, and an interface (or interphase) region of surface aluminum and alumina that are substantially disordered by the presence of the interface. Of the total slab thickness of about 4.0 nm, these three regions correspond to 29%, 39%, and 32% of the total thickness, respectively, roughly one-third for each region. The tensile stress was calculated by summing over the forces on the atoms in the rigid planes. Figure 1 depicts the change in tensile stress as strain is introduced into the system. We note an elastic region near the equilibrium strain, increasing to a maximum tensile stress of 2 GPa, and then rapidly decreasing with strain as the interface ruptures. For comparison, we have performed similar simulations with pure α -alumina, resulting in a yield stress limit of about 40 GPa. We note that these are small unit cells with no grain boundaries or other crystalline defects other than those introduced by the supercell conditions, so that these numbers correspond to the theoretical limit of yield stresses for materials. Examination of the energy versus strain behavior (not depicted) reflects the same behavior as the pressure curve with an ideal work of adhesion of about 0.3 J/m².

SUMMARY

In summary, we have developed an electrostatic model for metal oxides which calculates both a local atomic charge and the electrostatic potential as a function of nuclear coordinates. We have constructed an overall empirical potential that merges the electrostatic potential with an embedded atom method potential. Our current simulation of adhesive failure at a model metal/metal-oxide interface provides physically reasonable values for the work of adhesion and tensile strength expected for the interface, and indicates that this method is capable of describing the physical processes of adhesion and adhesive failure at a metal/oxide composite interface. We are currently investigating more complex interphase regions and dynamics simulations of the formation of a native oxide layer on bulk aluminum.

This work was supported by the U.S. Office of Naval Research (ONR). FHS acknowledges support through the NRC-NRL Postdoctoral Associateship Program.

REFERENCES

1. F. H. Streitz and J. W. Mintmire, *J. Adhes. Sci. Technol.* **8**, 853 (1994).
2. F. H. Streitz and J. W. Mintmire, *Phys. Rev. B* **50**, 11996 (1994).
3. F. H. Streitz and J. W. Mintmire, *Composite Interfaces*, in press.
4. R. P. Iczkowski and J. L. Margrave, *J. Am. Chem. Soc.* **83**, 3547, (1961).
5. R. G. Parr, R. A. Donnelly, M. Levy, and W. E. J. Palke, *J. Chem. Phys.* **68**, 3801 (1978).
6. R. G. Parr and R. G. Pearson, *J. Am. Chem. Soc.* **105**, 7512 (1983).
7. A. K. Rappé and W. A. Goddard, *J. Phys. Chem.* **95**, 3358 (1991).
8. M. S. Daw and M. I. Baskes, *Phys. Rev. Lett.* **50**, 1285 (1983).
9. M. S. Daw and M. I. Baskes, *Phys. Rev. B* **29**, 6443 (1984).
10. S. M. Foiles, M. I. Baskes and M. S. Daw, *Phys. Rev. B* **33**, 7983, (1986).
11. M. W. Finnis and J. E. Sinclair, *Phil. Mag. A*; **50**, 45 (1984).
12. G. C. Abell, *Phys. Rev. B* **31**, 6184 (1985).
13. J. Tersoff, *Phys. Rev. Lett.* **61**, 2879 (1988); *Phys. Rev. Lett.* **56**, 632 (1986).
14. D. W. Brenner, *Phys. Rev. B* **42**, 9458 (1990).
15. J. E. Dennis, Jr. and R. B. Schnabel, *Numerical Methods for Unconstrained Optimizations and Non-linear Equations* (Prentice-Hall, Englewood Cliffs, NJ, 1983).
16. J. D. Head and M. C. Zerner, *Chem. Phys. Lett.* **122**, 264 (1985).

A COMPUTER MODEL FOR WETTING HYSTERESIS

S. P. Wesson and A. Mahale

TRI/Princeton, 601 Prospect Avenue, Princeton, NJ 08542

INTRODUCTION

A liquid meniscus that encounters a heterogeneous surface will behave differently in advancing and receding modes, producing wetting hysteresis. A model that demonstrates the effect of surface heterogeneity on the shape of the wetting trace is presented. The model assumes that features in a wetting trace obtained by the Wilhelmy method arise from three processes occurring simultaneously: portions of the meniscus slide over energetically uniform areas, become fastened to low energy sites, and slip from low energy sites to higher energy regions.

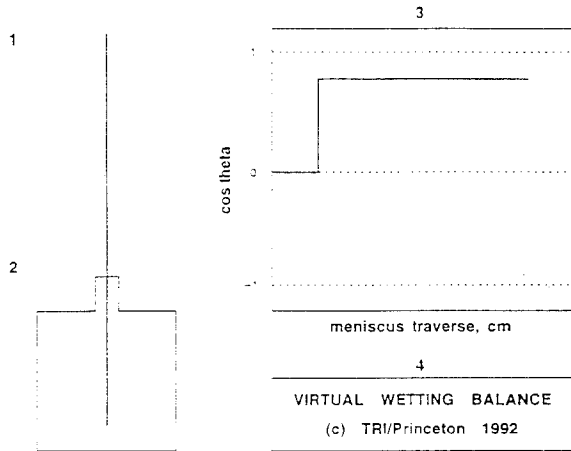


Fig. 1: Program VB, the virtual wetting balance.

Fig. 1 shows the elements of the virtual wetting balance: (1) the virtual solid, an array of 1 to 50 vectors of contact angle values θ read in from an ASCII file, (2) the virtual liquid, embodied as a lookup table of meniscus height values vs. θ , where each vector in the virtual surface is wetted with an individual meniscus segment, and (3) a virtual XY recorder that computes $\cos\theta$ from the average height of all the meniscus segments as the liquid traverses up and down the solid surface.

RESULTS AND DISCUSSION

Table 1 lists twelve virtual surfaces in terms of constituent domain sizes and their respective contact angle values, the number of repeat units of domain combinations, and the number of vectors. Virtual hysteresis loops were computed for these surfaces using properties for water in the meniscus height equation, saved to disk as ASCII files and presented in Figure 2.

Figure no	No. of vectors	Surface description
Contact angle/length of domain		
(a)	1	$10^\circ/2.4 \text{ cm}$
(b)	1	$120^\circ/2.4 \text{ cm}$
(c)	1	$(10^\circ/0.5 \text{ cm} + 120^\circ/0.1 \text{ cm}) \times 4$
(d)	1	$(10^\circ/0.1 \text{ cm} + 120^\circ/0.5 \text{ cm}) \times 4$
(e)	1	$(10^\circ/0.2 \text{ cm} + 120^\circ/0.2 \text{ cm}) \times 6$
(f)	1	$(10^\circ/0.1 \text{ cm} + 120^\circ/0.1 \text{ cm}) \times 12$
(g)	1	$(10^\circ/0.001 \text{ cm} + 120^\circ/0.001 \text{ cm}) \times 1200$
(h)	1	$10^\circ\text{--}120^\circ$ random
(i)	50	$10^\circ\text{--}120^\circ$ random
(j)	1	30° or 70° random
(k)	5	30° or 70° random
(l)	50	30° or 70° random

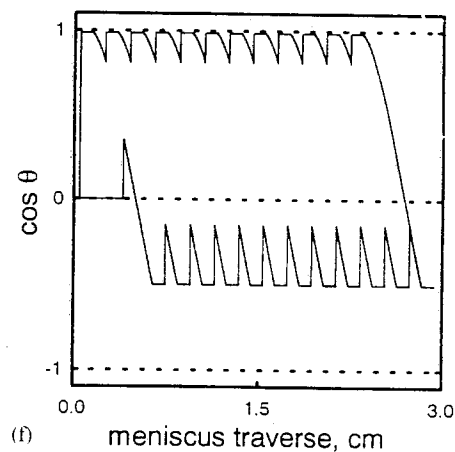
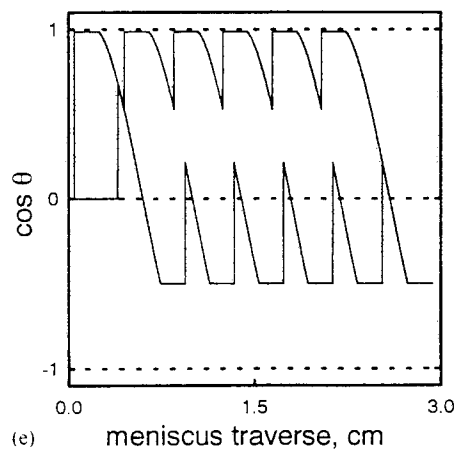
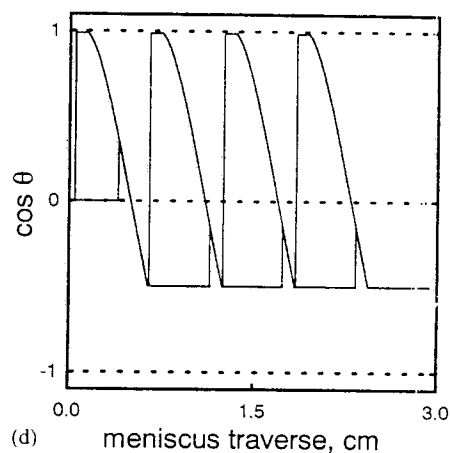
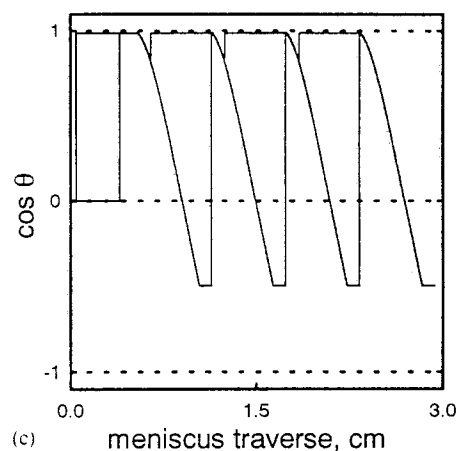
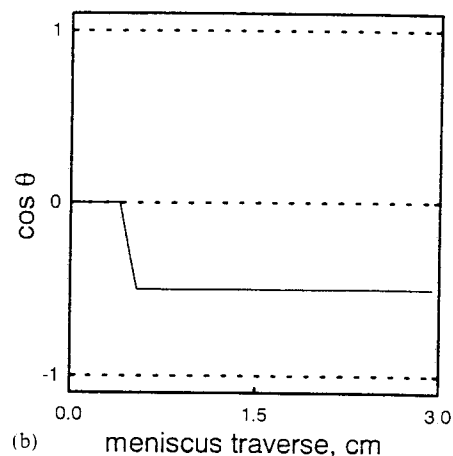
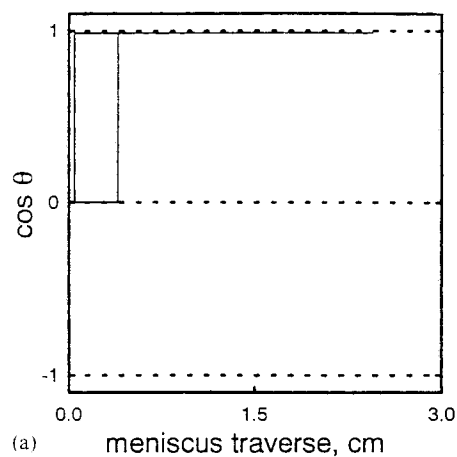
Table 1: Configuration of virtual surfaces for wetting traces in Figure 2.

Fig. 2(a) shows the hysteresis loop from wetting a uniformly high energy surface. The advancing mode wettability value is the same as that in the receding mode. This absence of hysteresis is seen in Fig. 2(b), which displays the trace from wetting a uniformly low energy surface.

Fig. 2(c) is the wetting trace from a surface with long high energy domains that alternate with short low energy domains. The advancing mode shows large oscillations as the meniscus is pinned by the low energy sectors, but the receding mode is relatively constant. The reverse situation, that of a surface with long low energy domains alternating with short high energy sections, is shown in Fig. 2(d). The advancing mode is relatively constant, but the receding mode shows major oscillations as the meniscus is stretched to maximum by high energy domains emerging from the liquid.

Figures 2(e) to 2(g) show the effect of diminishing domain size with respect to meniscus height.

The hysteresis loop in Fig. 2(h) results from wetting a surface with wettabilities randomly assigned between 10° and 120° , but we can discern only that there are at least two site energies. Increasing the solid perimeter from 1 vector to 50 vectors diminishes the amount of chatter in the advancing and receding branches: contrast Figures 2(h) and 2(i).

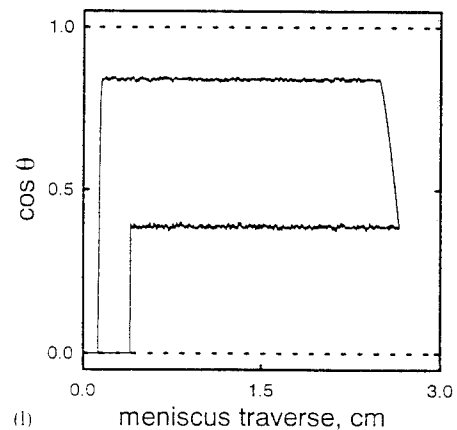
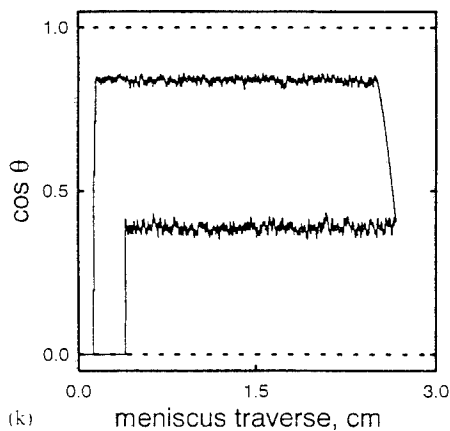
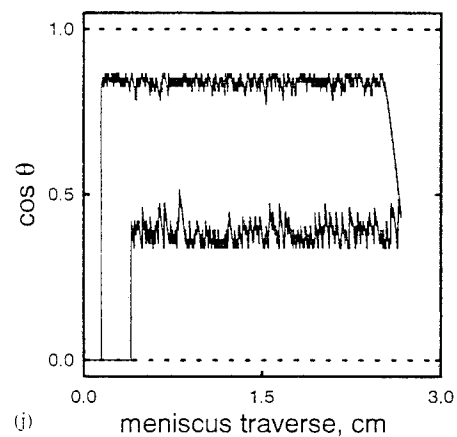
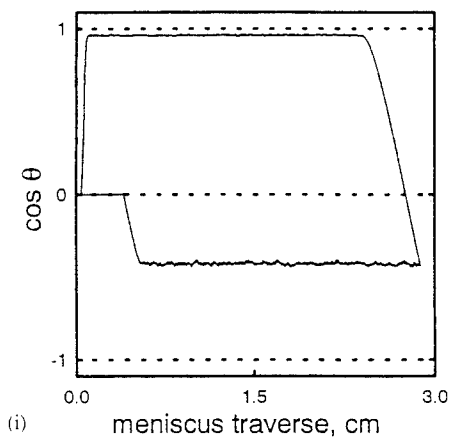
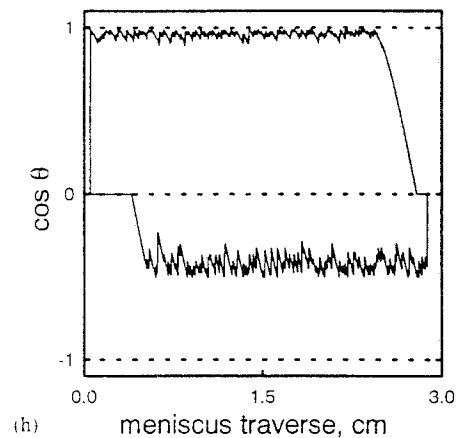
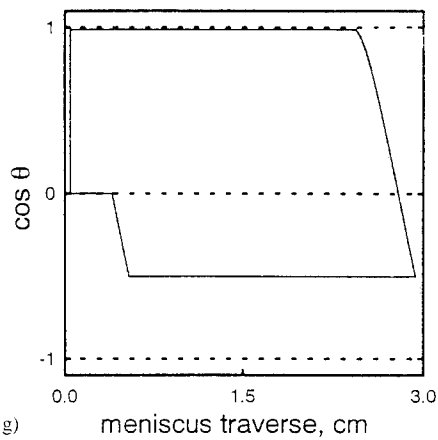


Figures 2(a) to 2(f): Virtual hysteresis loops. Surfaces are represented schematically by thick lines (high energy) and thin lines (low energy).

A model for a bienergetic polymer shows the chatter characteristic of wetting fibers with small perimeters (Fig. 2(j)) in contrast to the smooth trace from wetting a film sample with a large perimeter (Fig. 2(l)).

CONCLUSIONS

1. Surface heterogeneity can cause wetting hysteresis on an otherwise perfect solid.
2. There is no wetting hysteresis on energetically uniform solids.



Figures 2(g) to 2(l): Virtual hysteresis loops. Surfaces are represented schematically by thick lines (high energy) and thin lines (low energy).

3. Chatter in the wetting trace is controlled by the ratio of meniscus height to domain size.

4. Chatter in the wetting trace is controlled by the ratio of meniscus height to surface perimeter.

REFERENCES

1. A. D. Mahale and S. P. Wesson, *Colloids and Surfaces A: Physicochem. and Eng. Aspects* **82**, 117 (1994).
2. S. P. Wesson, Y. K. Kamath and A. D. Mahale, *Colloids and Surfaces A: Physicochem. and Eng. Aspects* **82**, 133 (1994).

Metallization of Polyimide Surfaces: Still no consistent Model

M. Grunze, T. Strunskus*, Ch. Wöll

Angewandte Physikalische Chemie, Im Neuenheimer Feld 253, 69120 Heidelberg, Germany

*Technische Fakultät der Christian-Albrechts-Universität zu Kiel, Kaiserstr. 2, 24143 Kiel-Gaarden, Germany

ABSTRACT

In this communication we summarize our previous results on the metallization (with Pd, Au, Ag, Cr, Cu, K) of vapor phase deposited polyimide films studied by x-ray photoelectron spectroscopy and Infrared Reflection Absorption Spectroscopy (IRRAS). Although these metals are believed to react very differently with the polyimide surface, only potassium shows the expected behaviour, i.e. reduction of polyimide and charge transfer. There is no clear distinction between the other metals at very low metal coverages, only at the higher metal coverages chemical reactions between chromium and the polyimide surfaces are detected. The lack of chemical reactivity of chromium atoms is very surprising. Additional NEXAFS experiments were conducted to understand the reaction between individual chromium atoms and small chromium clusters with the polyimide surface. The results are not consistent with any presently proposed model.

INTRODUCTION

Following our studies of the metallization of vapor deposited polyimide films with Pd, Au, Ag, Cr, Cu, and K using IRRAS and XPS /1,2/, we recently conducted Near-Edge-X-Ray-Absorption Fine Structure (NEXAFS) measurements using synchrotron radiation to study the deposition of Cr and Cu on vapor deposited polyimide films. From our infrared measurements we concluded, that for lowest metal coverages all metals (except K) physically interact with the polymer surface. Whereas for K deposition the formation of a charge transfer complex is clearly evident in the IRRAS and XPS data, there is no qualitative difference in the IRRAS data for the other metals. However, it is very obvious that the degree of

spectroscopic changes induced by metal deposition heavily depends on the metal, i. e. whereas chromium at the smallest coverages causes remarkable spectral changes, these are only observed at a later stage for the other metals. The quantitative difference in the IRRAS and XPS data could therefore be ascribed to different diffusion and cluster formation rates and hence in a difference in metal dispersion in the polymer surface. At higher metal coverages clear evidence for chemical reactions between chromium and the polyimide layer is observed in the XPS data, in quantitative agreement with previous reports /3,4/.

RESULTS AND DISCUSSION

The observation, that chromium seems not to react with the polymer at the lowest coverages contradicts the present models, where it is proposed that chromium chemically reacts with the polymer. In order to probe the local changes in electronic structure caused by the metal/polymer interaction, NEXAFS experiments were performed for chromium and copper deposited onto polyimide at room temperature. The experiments were performed at the synchrotron storage ring BESSY in Berlin at the HE-TGM 2 monochromator. The polyimide films were prepared "in situ" by coevaporation of pyromellitic dianhydride (PMDA) and 4,4'-oxydianiline (ODA) following established procedures /5/. After curing at 250 °C for 30 minutes in vacuum, the respective metals were evaporated from a tungsten basket onto the polymer surface. Metal coverages were estimated from the XPS data, the NEXAFS spectra were recorded in the electron partial yield mode (> 150 eV).

In figure 1 we show the C 1s, N 1s and O 1s NEXAFS data recorded for the clean polyimide surface (a) and the surface covered with a submonolayer chromium (b) coverage. Strong effects

are observed in the O1s NEXAFS spectra. The spectrum of the clean polyimide surface is dominated by the intense π^* O 1s $\rightarrow \pi^*$ transition in the polyimide carbonyl group at 531 eV, and a strong σ^* absorption around 540 eV. The π^* transition corresponds to the excitation of the O 1s electron into the carbonyl π^* orbital located at the oxygen atom. After chromium deposition, the spectrum is drastically changed: The original π^* transition is significantly reduced in intensity and appears to be shifted to higher photon energies (524 eV and 526 eV).

Contrary to the very profound changes in the O1s NEXAFS data, the changes in the C1s and N1s NEXAFS data are minute. In the C1s data, only the transition associated with the C 1s \rightarrow CO π^* transition in the carbonyl group of the polyimide ring system is affected. In the N 1s data, the transition from the N1s orbital into the π^* orbital located at the carbonyl group (414 eV) is reduced in intensity. These results indicate, that the effect of chromium is localised, only the π^* orbital at the carbonyl oxygen atom is severely effected by chromium. The transitions corresponding to the excitation of N1s and C1s electrons in the CO π^* level are still present and only marginally attenuated. This proves that the extended π -electron system of the pyromellitimide (unit including the carbonyl) must be still intact. Any chemical reaction involving breaking or forming of chemical bonds should severely affect the conjugated π -electron system of the pyromellitimide unit and should result in drastic changes in the NEXAFS spectra at the nitrogen and carbon edge. Hence, we have to conclude that chromium atoms interact only locally with the carbonyl oxygen atom and raises the energy of the CO π^* orbital (as evidenced by the shift to higher photon energies), but that the double bond character in the carbonyl group is preserved.

In the case of copper, the interaction with the unoccupied polymer orbitals is not localised. This is evident from a uniform attenuation of the C1s, O1s and N1s adsorption fine structure features as a function of copper coverage.

We can only speculate about the nature of interaction between individual chromium atoms and the carbonyl oxygen atom in polyimide. Bond breaking or bond formation can be ruled out from the

NEXAFS data. Charge transfer from or to the chromium atom should lead to a change in the infrared reflection absorption data, which, however, is not observed. Similarly, formation of a chromium π -arene complex /4/ should also lead to shifts in the vibrational frequencies, which is not observed in the experimental data. We therefore conclude, that at lowest chromium coverages the changes observed in the XPS and NEXAFS spectra are not due to a chemical reaction with the polymer, but are to a large extent related to a final state screening effect in the photo-excitation process.

Metal deposition and all measurements in this study were performed at room temperature. Therefore, we can not rule out, that the system is in a metastable state and chemical reactions between the metal atoms and the polymer would occur if sufficient energy is provided by heating the sample. This should be kept in mind when comparing experimental results and theoretical calculations /4,6/, since in the theoretical work the lowest energy state of the system is calculated.

In conclusion, the results from IR, XPS and NEXAFS experiment itself do not allow to derive a general model for the interaction of chromium atoms with polyimide surfaces, but reveal that present models are not adequately describing the local chemical interactions.

ACKNOWLEDGEMENT

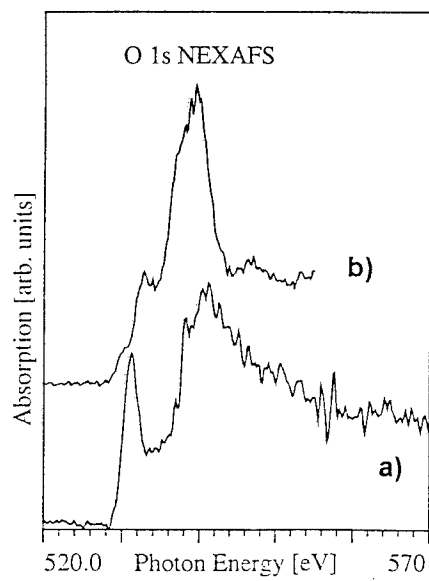
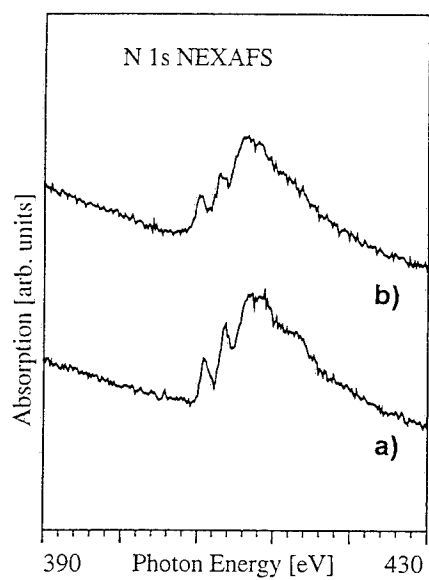
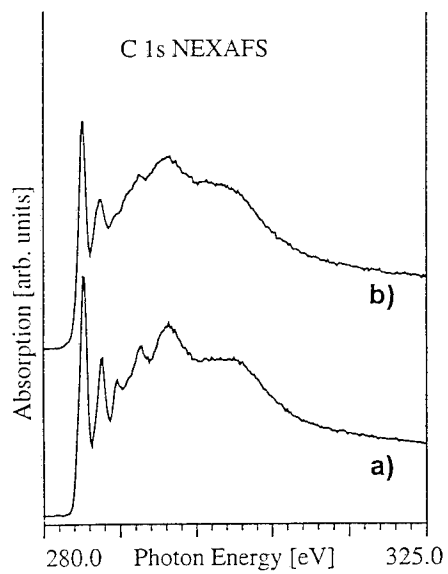
We gratefully acknowledge the help of A. Schertel and C. Mainka for assistance at the synchrotron measurements.

Figure caption:

fig. 1

C1s, O1s and N1s NEXAFS spectra for the clean polyimide surface (a) and a submonolayer chromium coverage (b). Metal evaporation and the measurements were performed at room temperature.

1. T. Strunskus, Ph. D. dissertation, University of Heidelberg 1993 and T. Strunskus, M. Grunze, B. Kochendorfer, submitted.
2. T. Strunskus, C. Hahn, D. Frankel, and M. Grunze, J. Vac. Sci. Technol. A **9**(3) 1272, (1991).
3. N. J. Chou and C. H. Tang, J. Vac. Sci. Technol. A **2**, 751 (1984)
4. a) R. Haight, R. C. White, B. D. Silverman, and P. S. Ho, J. Vac. Sci. Technol. A **6**, 2188 (1988).
b) R. C. White, R. Haight, B. D. Silverman and P. S. Ho, Appl. Phys. Lett. **51**, 481 (1987).
5. R. N. Lamb, J. Baxter, M. Grunze, Langmuir **4** (1988), 249.
6. S. G. Anderson J. Leu, B. D. Silverman, and P. S. Ho, J. Vac. Sci. Technol. A **11** (2), 368 (1993).



SPECIAL ADHESIVE FINITE ELEMENTS FOR MODELLING BONDED JOINTS AND CRACK-PATCH REPAIRS IN TWO- AND THREE-DIMENSIONS

M.W. Taylor, R. Andruet, and D.A. Dillard

Center for Adhesive and Sealant Science
Department of Engineering Science and Mechanics
Virginia Polytechnic Institute and State University
Blacksburg, Virginia 24061-0219

INTRODUCTION

In the design and analysis of adhesively bonded joints including crack-patch repair configurations accurate methods are required to predict the response of a bonded system under various load conditions. Finite elements have been traditionally used to model complicated joint configurations and yield accurate adhesive stresses within the bonded region away from stress singularities. A 'strength of materials' approach in the calculation of adhesive stresses ignores singularities and have been used with much success especially in closed-form solutions to simple joint geometries.

Incorporating the generality and accuracy of the finite element method with the simplicity of 'strength of materials' adhesive stress calculations has been the focus of research of Carpenter and Barsoum, and Amijima and Fujii [1,2]. In the present work two displacement-based finite elements were derived with specific applications to the modelling of adhesively bonded joints in two- and more importantly three-dimensions, to give 'strength of materials' stresses in the adhesive.

ADH2D and ADH3D Adhesive Elements

The twelve degree of freedom ADH2D element is a four-node plane-elasticity element which satisfies C^0 displacement continuity at boundaries between itself and two standard plane-frame elements. The nodes of this element are offset from its geometric corners to the nodes of the plane-frame elements themselves (Figure 1). Similarly the 18-node ADH3D element satisfies C^0 displacement continuity at boundaries between itself and two shear deformable plate elements which are capable of modelling laminated composite plates. The nodes of this element are offset from its geometric corners to the nodes of the plate elements themselves (Figure 2).

Figure 1: The ADH2D Element

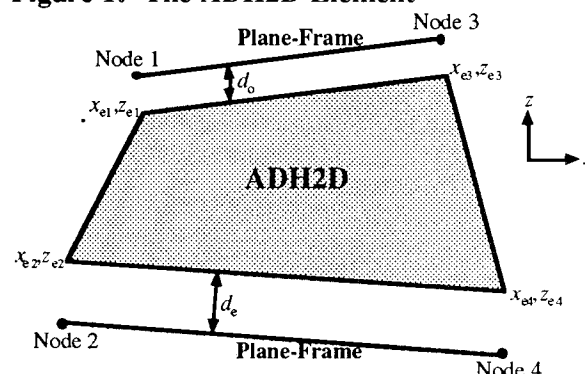
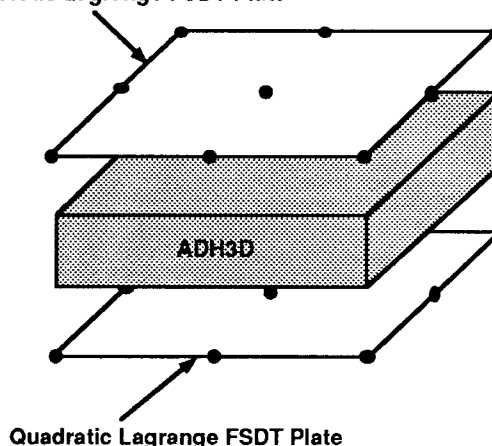


Figure 2: The ADH3D Element
Quadratic Lagrange FSDT Plate



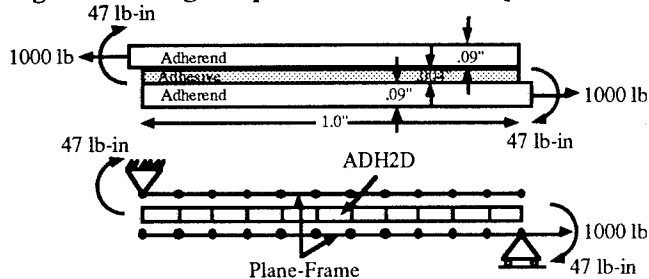
Tapering of the adhesive, thermal and moisture expansion of both adherends and adhesive, and the ability to model stepped adherends are included in the derivations.

RESULTS

The following example illustrates the use of the ADH2D and ADH3D elements to model a typical aluminum-epoxy single-lap-shear bonded joint which represents one of the more complicated joint

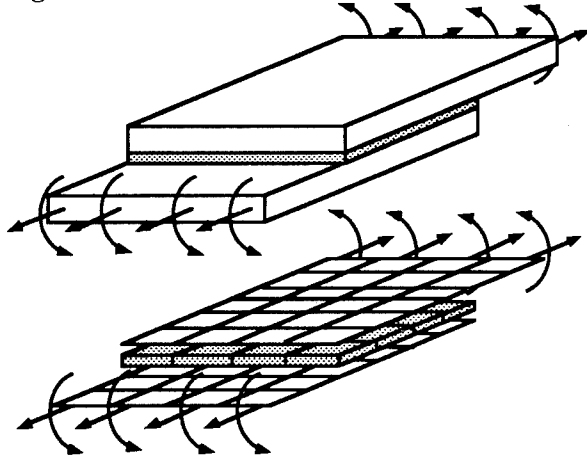
geometries to analyze. Several closed-form solutions for adhesive stresses are used for comparison purposes.

Figure 3: Single-lap-shear Joint Example



The results from the current ADH2D-plane-frame model depicted in Figure 3 are within 1.5% of the best closed form solutions [3,4,5]. A convergence study was showed that this method was more efficient at analyzing adhesive stresses than an incompatible method used in [1]. This same one inch wide single lap shear configuration was modelled in three dimensions using the ADH3D elements similar to the model in Figure 4.

Figure 4: ADH3D Model of SLS Joint



The normal (peel) stresses in three dimensions are depicted in Figure 5. Clearly the stress distribution of this joint is very three dimensional.

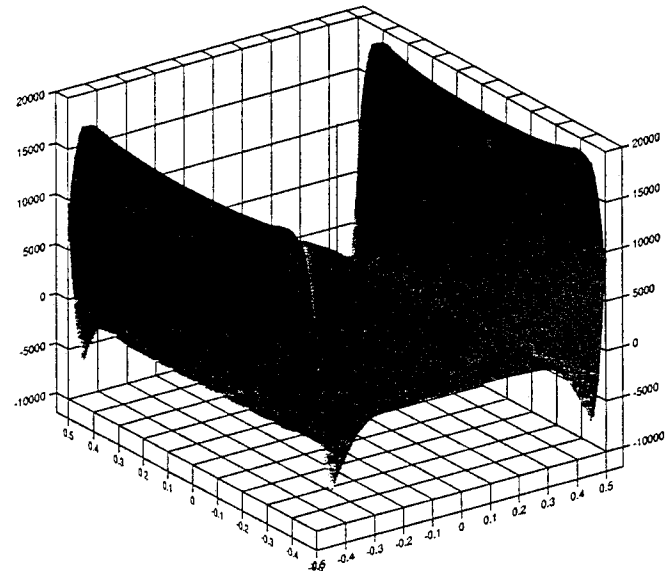
A typical crack-patch repair scenario comprised of an adhesively bonded carbon/epoxy patch over top of a cracked aluminum plate was modelled using the ADH3D elements and three-dimensional stresses in the bonded region were obtained.

CONCLUSION

A plane-stress element, ADH2D, and a brick-type element ADH3D have their nodal degrees-of-freedom offset to those of the adherend elements. A numerical example using the ADH2D and ADH3D

elements to model a single-lap-shear joint corresponded well with closed-form adhesive stress solutions. This method holds much potential for the modelling of general adhesive joints. Future work includes incorporating geometric non-linearity into the formulation. A typical crack-patching adhesively bonded repair configuration will be further modelled using ADH3D elements, under static and fatigue loading.

Figure 5: 3-D Peel Stresses in SLS Joint



ACKNOWLEDGMENTS

We would like to gratefully acknowledge the Virginia Institute for Material Systems and the Center for Adhesive and Sealant Science for funding this work.

REFERENCES

1. W.C. Carpenter and R. Barsoum, *Journal of Adhesion*, **30** (1989), 25-46.
2. S. Amijima and T. Fujii, *Int. J. of Adhesion and Adhesives*, **7** (1987), 199-204.
3. M. Goland and E. Reissner, *Journal of Applied Mechanics*, **77** (1944), A17-A27.
4. F. Delale and F. Erdogan, *Journal of Applied Mechanics*, **48** (1981), 331-338.
5. W.C. Carpenter, *Journal of Adhesion*, **35** (1991), 55-73.

ATOMIC-SCALE ADHESION, FRICTION, AND WEAR IN HYDROCARBON SYSTEMS

J.A. Harrison¹² and M.D. Perry

Chemistry Department

United States Naval Academy, Annapolis, MD 21402, USA

R.J. Colton and C.T. White

Naval Research Laboratory

Surface Chemistry Branch, Washington, DC 20375, USA

D.W. Brenner

Department of Material Science and Engineering

North Carolina State University, Raleigh, NC

27695, USA

INTRODUCTION

Advances in experimental technology have recently allowed for the investigation of a number of phenomena at the atomic scale. For instance, atomic-scale hardness and adhesion can be investigated using an atomic force microscope (AFM) configured as an indenter [1]. When the AFM tip is moved laterally across a sample surface, atomic-scale friction, wear, and adhesion can be investigated [2]. If the relationship between nanometer-scale properties of materials and their bulk properties was understood, information obtained from these experiments could ultimately be used to design better adhesives, lubricants, and friction and wear resistant materials. In order to elucidate the relationship between nanoscale and bulk properties we have used molecular dynamics (MD) simulations to investigate and visualize atomic-scale processes.

In this paper we review our work which has focused on the atomic-scale indentation, adhesion, friction and wear of diamond (111) surfaces [3-8]. Our studies have focused on diamond surfaces because of diamond's extreme hardness and its wear resistance.

MODELING METHOD

The MD simulations were carried out in the usual way [5,6]. Once the positions and velocities of the atoms were specified, the

atoms evolve in time according to classical equations of motion. The interatomic forces, which govern the motion of the atoms, were derived from a many-body classical potential energy function, originally developed to model diamond deposition, that is unique in its ability to model *chemical reactions* [9]. This potential consists of pair-additive repulsive and attractive terms coupled to a many-body analytic bond-order function. This function includes angle bending, torsional, and short-range repulsive terms needed to model hydrocarbon interactions, e.g., adhesion and compression. The potential does not contain long-range forces such as van der Waals interactions; therefore, this study of adhesion only deals with covalent bond formation.

In this work, two starting configurations for the MD simulations have been used. For the friction and wear studies configurations similar to the one shown in Figure 1 were used [5-8]. These systems are composed of two diamond lattices oriented so that their (111) surfaces were in contact. The two lattices contained 10 layers of carbon atoms, each layer contained 16 atoms. The composition of the contacting (111) surfaces was varied to examine the effect of surface state on friction and wear [6]. The system shown in Figure 1, where the lower surface has been terminated with hydrogen only and the upper with hydrogen and ethyl groups, is one type of system that was investigated. In a typical friction simulation, sliding was simulated by moving the two

outermost (upper) layers of the upper lattice at a constant velocity, usually 100 m/s, in the chosen sliding direction. Periodic boundary conditions were applied in the plane of the (111) surfaces to simulate an infinite sliding surface. The temperature of the system was maintained at 300 K and the simulations lasted 30 ps unless otherwise noted.

The adhesion and indentation of diamond systems were examined by using larger lattices, typically 64 atoms per layer, and replacing the upper surface with a diamond tip [3,4]. Indentation was achieved by moving the rigid layers of the upper lattice toward the lower lattice, allowing the system to equilibrate, then decrementing the distance between the rigid layers of the tip and the surface, equilibrating, and so on. The rigid layers were decremented in 0.015 nm increments, followed by equilibration steps of approximately 50 to 120 fs (see reference [6] for details). Indentation rates faster than this produced heating of the lattices despite the application of a thermostat to the middle layers of each lattice.

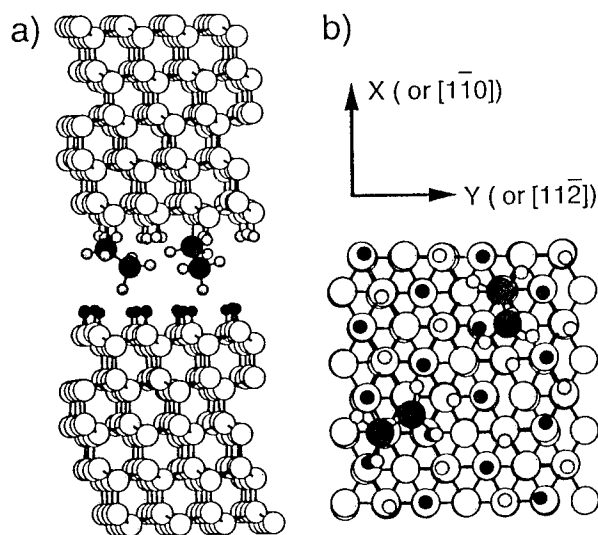


Fig. 1: Typical starting configuration showing (a) side-view of two hydrogen- and ethyl-terminated diamond (111) surfaces (for friction simulations) and (b) top view of same system with all but the interface layer of the upper surface not shown.

RESULTS AND DISCUSSION

Indentation and Adhesion

In standard indentation experiments, using macroindentors or an AFM, plots of applied normal load versus indentation depth are referred to as indentation curves [1]. If the geometry of the contact region is known and the indentation is elastic, the slope of these curves can be used to extract the elastic modulus of the material being indented [1,3]. Diamond (111) tips were used to indent a number of hydrocarbon substrates. We found the proper elasticity order, i.e., diamond (111) > diamond (100) > > graphite, and traced the origin of the elasticity to the molecular structure of the diamond lattices [3]. Diamond (111) has a larger modulus than diamond (100) because its indentation mainly involved the compression of carbon-carbon bonds; conversely, compression of the diamond (100) lattice involved both compression of carbon-carbon bonds and bending of bond angles. It is easier to change a bond angle than it is to compress a bond; therefore, diamond (100) appears softer.

Since the position and velocity of each atom was known as a function of time in MD simulations, the indentation mechanism can be elucidated from MD simulations. For instance, when diamond (111) surfaces were terminated with hydrogen, the diamond (111) tip *twisted* as it indented the opposing substrate to reduce repulsive interactions between hydrogen atoms on the tip and those on the substrate. This was not the case when the hydrogen atoms were removed from the substrate prior to indentation [4].

Large values of applied load on the diamond (111) tip resulted in large contact pressures and large localized stresses. These large stresses resulted in the breaking and subsequent reforming of covalent bonds, connecting the tip and the substrate. This adhesion between the surfaces resulted in irreversible damage to the tip and the surface upon separation (Figure 2).

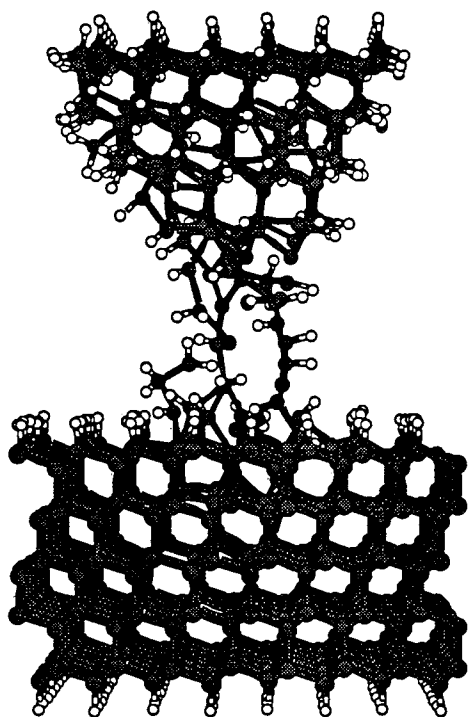


Fig. 2: Simulation of indentation that resulted in adhesion between a hydrogen-terminated diamond (111) tip and surface. The maximum value of applied load prior to retraction was 250 nN [4].

Friction and Wear

Microscopic friction is usually accompanied by wear, and energy is dissipated in the bulk material by movement of dislocations. In contrast, atomic-scale friction may occur *with or without* wear [5,10]. Indeed, wearless atomic-scale friction has been demonstrated experimentally [11] and there are several simple, analytic models which describe the principles of wearless friction [10]. The MD simulations described here have demonstrated the validity of these earlier models and yielded insight into the detailed mechanisms of friction and wear which were not previously known.

For instance, consider two diamond lattices, similar to those in Figure 1, except both are hydrogen terminated. When the upper surface was slid in the [112] crystallographic direction, video sequences of the simulations revealed that hydrogen atoms on opposing surfaces "collided", then "revolved" around each other in the sliding plane. This motion

resulted in mechanical or vibrational excitation of the interface atoms. This excitation takes the form of heat which was transferred to the bulk crystal and ultimately dissipated. This vibrational excitation and subsequent dissipation of energy was shown to be the essence of atomic-scale friction [8]. Furthermore, this motion and, therefore, the excitation was exacerbated as the load was increased. Thus, the friction increased as the applied load increased (Figure 3).

Replacing some of the hydrogen atoms on the upper surface with hydrocarbon groups (e.g., methyl, ethyl, or *n*-propyl) simulates boundary lubrication. The presence of the longer chain alkyl groups, both ethyl and *n*-propyl, on the upper diamond surface dramatically reduced the friction at moderate to high normal loads (Figure 3). The size and flexibility of these larger hydrocarbon chains in conjunction with the conformation they adopt when sliding were responsible for the observed reduction [6].

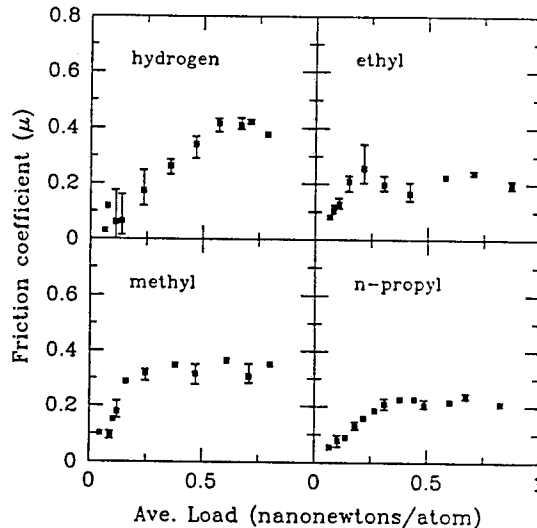


Fig. 3: Average friction coefficients versus average applied (normal) load for sliding in the [112] crystallographic direction on diamond (111). The lower diamond surface is hydrogen terminated in all cases and the upper surface was either hydrogen, methyl, ethyl, or *n*-propyl terminated.

It was previously shown [8] that friction is the result of vibrational excitation of the interface atoms when sliding. This energy was then dissipated into the lattice. The more vibrational excitation, the more energy dissipation, thus the higher the friction coefficients. The flexibility of the hydrocarbon groups allowed them to detour around high potential energy regions on the lower surface. High regions of potential energy corresponded to the lower surface hydrogen atoms. Therefore, avoiding the lower surface hydrogen atoms resulted in less vibrational excitation and thus, lower friction at larger loads.

At very large loads, approximately 1.1 nN/atom, it was possible to initiate wear of the diamond surfaces upon sliding when ethyl groups were present on the upper surface. These simulations were the first simulations which observed tribochemical reactions, that is, reactions which are initiated by, and occur during, sliding [7]. We observed complex, nonequilibrium radical chemistry that was initiated by the loss of hydrogen atoms from the attached ethyl groups. The observed chemistry consists of the abstraction of hydrogen from both the upper and lower surfaces, radical recombination, transient adhesion of the two surfaces, and formation of molecular wear debris. Each of these observations was shown to be consistent with conclusions inferred (but not directly measured) from experimental studies of the friction and wear of diamond.

SUMMARY

MD simulations have become a powerful tool to study atomic-scale processes. When coupled with modern scanned probe microscopies, the mechanisms of phenomena such as adhesion, indentation, friction and wear can be directly studied. Information gleaned from these studies may ultimately lead to the design of better adhesives or materials with desired friction and wear characteristics.

ACKNOWLEDGEMENT

This work was supported by the Office of Naval Research (ONR) under Contract No. N00014-95-WR20014. Figure 1 was generated with the program XMol (XMol, version 1.3.1 Minnesota Supercomputer Center, Inc., Minneapolis, MN, 1993).

REFERENCES

1. N.A. Burnham and R.J. Colton, *Force Microscopy in Scanning Tunneling Microscopy and Spectroscopy: Theory, Technique, and Applications*, edited by D.A. Bonnell, (VCH Publishers, 1993), p. 191-250 and references therein.
2. G.J. Germann et al., *J. Appl. Phys.* **73**, 163 (1993).
3. J.A. Harrison, C.T. White, R.J. Colton, and D.W. Brenner, *Mat. Res. Soc.* **239**, 573 (1992).
4. J.A. Harrison, C.T. White, R.J. Colton, and D.W. Brenner, *Surf. Sci.* **271**, 57 (1992) and references therein.
5. J.A. Harrison, C.T. White, R.J. Colton, and D.W. Brenner, *Phys. Rev. B* **46**, 9700 (1992).
6. J.A. Harrison, C.T. White, R.J. Colton, and D.W. Brenner, *J. Phys. Chem.* **97**, 6574 (1993).
7. J.A. Harrison and D.W. Brenner, *J. Am. Chem. Soc.* **116**, 10399 (1994).
8. J.A. Harrison, C.T. White, R.J. Colton, and D.W. Brenner, *Thin Solid Films* in press.
9. D.W. Brenner, *Phys. Rev. B* **42**, 9458 (1990); D.W. Brenner, J.A. Harrison, C.T. White, and R.J. Colton, *Thin Solid Films* **206**, 220 (1991).

10. G.M. McClelland and J.N. Glosli, NATO ASI Proc. on Fundamentals of Friction: Macroscopic and Microscopic Processes, ed. I.L. Singer and H.M. Pollock, (Kluwer Academic Publishers, Dordrecht, 1992) p. 405-26 and references therein.

11. C.M. Mate et al., Phys. Rev. Lett. 59, 1942 (1987).

12. To whom correspondence should be addressed.

Adhesion Mechanics During Low-Speed Normal-Impact of Spherical "Rocks" into Multilayer Painted Steel Substrates

A. C. Ramamurthy¹ and J. W. Holubka²

¹ :Automotive Components Division, Ford Motor Company, Detroit, MI

² : Scientific Research Laboratories, Ford Motor Company, Dearborn, MI

and

Dennis J. Mihora

FM Analysts, Santa Barbara, CA

INTRODUCTION

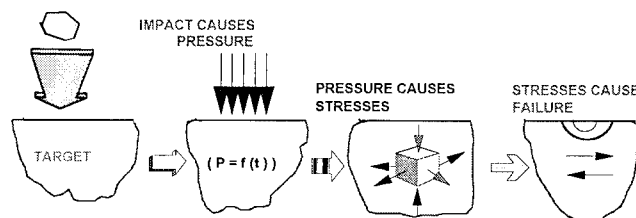
Stone impact damage to automotive paint finishes has been a matter of concern over the past decade, focused mainly on the substrate/paint system response to the external load. Impact damage can result in paint loss and possible corrosion problem due to loss of adhesion at the polymer-metal interface. Recent work in the area of stone impact damage have addressed various issues such as phenomenology and impact induced corrosion [1,2], post impact damage analysis [3], advanced instrumentation for laboratory simulations [4] and data analysis [5]. This paper is a preliminary report which is a part of a larger effort currently underway to address this complex problem. We report the use of DYNA2D, an explicit finite element code to simulate several low velocity impact scenarios for automotive paint finishes. Of particular focus in this paper are impact scenarios akin to painted sheet steels. Several projectile types ranging from stones to steel ball bearings have been considered in these simulations. Preliminary results reported here demonstrates the power and sensitivity of numerical simulations to substrate/Paint systems, type of projectile, geometry and impact parameters such as velocity and angle of impact.

PHENOMENOLOGY OF STONE IMPACT DAMAGE

A schematic illustration of impact phenomenon is shown on this page. For impacts normal to the surface, a compressional stress wave propagates through the paint layers and the projectile at approximately the acoustic wave speed in the respective media. This wave will be reflected in tension from free surfaces of the target and projectile. When the tensile wave reaches the impact surface the projectile and target will separate and further reflections occur. This process continues and gives rise to "ringing" in the projectile-target interaction, thus resulting in a time dependent pressure distribution at the impact surface. This process is significant on the order of microseconds.

As stress waves propagate through the coated substrate, local stresses which can far exceed the yield stresses develop, thus resulting in fracture, delamination, internal spallation or void

initiation and permanent "denting" of the sheet metal substrate.



As the projectile-target interaction continues larger sections of the target may be involved in describing the dynamic responses such as the gross deflection of the sheet metal substrate. These phenomenon are significant in the order of milliseconds. Eventually the dynamic response will tend asymptotically to a static response, perhaps involving the entire target.

NEED FOR NUMERICAL SIMULATION, AND ADVANTAGES OF NUMERICAL SIMULATION

In stone impact research, despite advances in experimental techniques, impact phenomenon are inherently very difficult to study due to their transient nature typically lasting a few hundred microseconds. Measurement of dynamic stresses without significantly altering fixture geometry is very complicated and will be addressed elsewhere (6). Thus assessment of dynamic information via post impact investigations is virtually impossible. Closed form solutions of impact phenomenon are available but only for a few simple cases. Numerical simulation (NS) of impact events via the use of appropriate wave propagation codes are a major step towards understanding this complex phenomenon within the paint layers.

Numerical simulation involves the application of shock physics principles and material behavior (based on carefully designed experimental data) to describe an impact event. In the present work, impact of projectiles onto automotive paint finishes have been assessed using an explicit time integration finite element design tool DYNA. A detailed

description on the DYNA engine can be found in Reference 7.

Implementation and advantages of NS in stone impact research are summarized below:

- For any given material model (with or without failure criteria), it is possible to visualize the impact event which can include sophisticated animation and zoom mechanisms as a function of time and thickness into the target material.
- Evaluate pressure, stress, strain and displacement fields as a function of time and thickness for further analysis or experimental validations.
- Alter material models, failure criteria, material properties, impose geometric constraints, change geometry of the system.
- Understand damage for various impact conditions (velocity, angle of impact and ambient temperature) including different projectile types.
- Optimize material properties to minimize damage (a primary goal).

CHOICE OF PROJECTILES FOR NUMERICAL SIMULATIONS

Many rock geometry's, masses, velocities and impact angles are considered in the impact of painted automotive surfaces. The important component of the rock is the shape that produces the initial "indentation" of the painted surface. There are many possible rock materials, orientations and curvatures of the impacting rock. The curvature of the impact site also depends on the selected "rock" projectile. Clearly, the geometry of an impacting stone projectile is variable. The present work examines the mechanics of the impact event of the most basic rock shape -- the sphere.

DYNA 2D SIMULATION : RESULTS AND DISCUSSION

In this section we present a brief overview of our simulation results. A more detailed account of this work is currently under preparation [8]. With 2D modeling, a very high number of elements are used for the four paint layers, metal substrate and spherical rock. Figure 1 shows the discretization of the components. The target is composed four paint layers and the sheet metal. A variable proportional zoning was used in the target to provide the highest fidelity near the centerline where the shear stresses are the largest. All the elements use simple 4 node bricks. Because of symmetry, only one half the model must be represented. The target is a shell structure as defined by the large diameter to thickness ratio of 81. This "thin" shell is supported at the perimeter with a vertical (z-axis) deflections constraint. Rotations along the perimeter are allowed.

Table shown on this page summarizes the 2D axisymmetric discretization, the layer thickness and assumed properties of the target.

There are large normal forces transmitted during the two body contact between the spherical stone and the paint. Friction is known to induce significant damage during oblique impacts. Friction between the sphere and paint was ignored only in these normal impact cases. To properly transmit forces between the two bodies, a set of contact "slide surfaces" was attached to the exterior of the sphere and the exposed surface layer of the clear coat.

Layer Type	# discrete elements	Thickness (mm)	E (Ksi)	ν	Specific Gravity ρ_{SG}
"Stone"	288				
Steel			30000	0.28	7.89
Granite			8000	0.25	2.6
Clear Coat	5000	0.06	409.	0.35	1.18
Base Coat	5000	0.05	306.	0.43	1.691
Stone Guard	10, 000	0.11	306.	0.40	2.03
Electrocoat	2500	0.025	423.5	0.44	1.54
1008 AK Steel	7000	0.813	30000	0.28	7.89

The substrate is represented as an elastic perfectly plastic material with kinematic hardening ($\beta = 0.$) during the plastic flow stage. In the oscillating mode, there is hysteretic energy dissipation. Simulations will show significant plastic flow after the yield stress of 50.8 Ksi is reached. The tangent modulus subsequent to the yield point is 56 Ksi.

Impact mechanics between a 4.75 mm diameter stone traveling at 50 Km/hr and the 1008 steel is a complex event as shown in **Figure 2**. The response is non-linear both during the short impact time (up to 15 μ s) and the longer term bending period ($>200 \mu$ s). Element **a** is the contact face of the clear coat while **b** represents the compression side of the 1008 steel (under the paint) and element **c** (top) the back side of 1008 steel. There is plastic flow occurring on the tensile side of the 1008 steel. There are different levels of contact including rebound of the stone off the paint at about 100 μ s and recontact at 140 μ s. Possible adhesion damage to paint relates to the maximum compression stresses in the initial 20 μ s as the later time bending deflections are not important.

In Fig 3, the four paint layers and the steel face are represented with lines (**a, bottom**) as the clear coat to line (**e, top**) as the steel face. The dispersion of axial momentum results in a reduction in axial stress through the paint layers. The paint is not damaged with these compression stresses. This short time pulse can induce other forms of damage at locations away from this centerline compression.

In Fig 4 , the radial (in-plane) stresses in the steel layer show a non-symmetry of stress response from rock of 4.75 mm diameter travelling at 50 Km/hr. Lines **a(bottom)** shows the steel is in compression directly under the paint. Line **b(top)** shows the steel on the side opposite the rock contact and is in tension with significant yielding. At impact speeds as low as 20 Km/hr, the steel shows some yielding. With a sphere impact, there are many situations where the paint remains intact, does not delaminate or chip but the metal displays a permanent "dent".

The most likely cause of paint damage from spherical rocks is shear delamination. The maximum shear strains are not at the impact centerline but near the edge where the rock and paint separate from contact. Shown in **Figure 5** is the response case for a 2.54 mm diameter stone impacting at 100 Km/hr which induces a moderate level of shear in the paint. The shear contours are the largest in the Electrocoat layer (mat 5) at about $15\mu s$. By comparison, the radial tensile (+) stress/strains in the paint layers are relatively small.

CONCLUSIONS

The largest mismatch in physical properties occurs at the polymer-metal interface as a results of largest shear and delamination stress. (The mismatch in strain states is less between the four paint layers. The maximum linear elongation is relatively small however, the shear is shown as the most likely inducement of adhesion delamination.

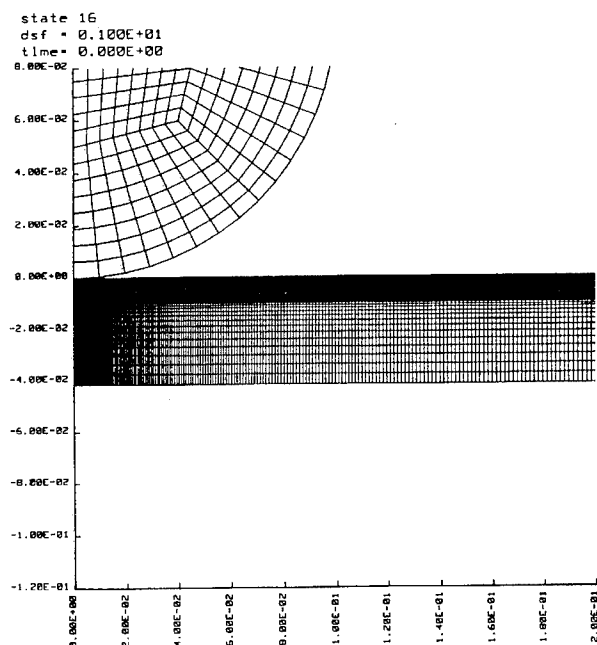


Figure 1

Maximum compression stresses and strains in the paint are at the centerline in the clear coat. The maximum compression bending stresses and the maximum tension strains are also at the centerline. The tension strains are quite large because of plastic flow on the tension side. The largest tension strains exceed 10 percent. The time at compression is associated with maximum compression stress in the paint and compressive stresses in the sheet metal.

REFERENCES

- 1) A. T. Zehnder, A. C. Ramamurthy, S. J. Bless and N. S. Brar, *Int. J. Impact Eng.*, 13 (1993) 133.
- 2) A. C. Ramamurthy, W. I. Lorenze and S. J. Bless, *Prog. Org. Coatings.*, 25(1994)43.
- 3) A. C. Ramamurthy, T. Ahmed, L. D. Favro, R. L. Thomas, D. K. Hohnke and R. Cooper, SAE Tech Paper No. 930051, Detroit, MI 1993.
- 4) A. C. Ramamurthy, W. Isbell, V. Venditto and T. Jennings, SAE Tech Paper No. 932331, Dearborn, MI, 1994.
- 5) A. C. Ramamurthy, W. I. Lorenzen and Mirna Macdonald, *Electrochim. Acta.*, 38(1993)2083.
- 6) A.C. Ramamurthy, J. A. Charest and D. J. Mihora, Manuscript in preparation.
- 7) J. O. Hallquist, *Theoretical Manual for DYNA*, University of California, Lawrence Livermore National Laboratory, Rept No. UCID-19401, 1982.
- 8) A. C. Ramamurthy, J. Holubka and D. J. Mihora, Manuscript in preparation.

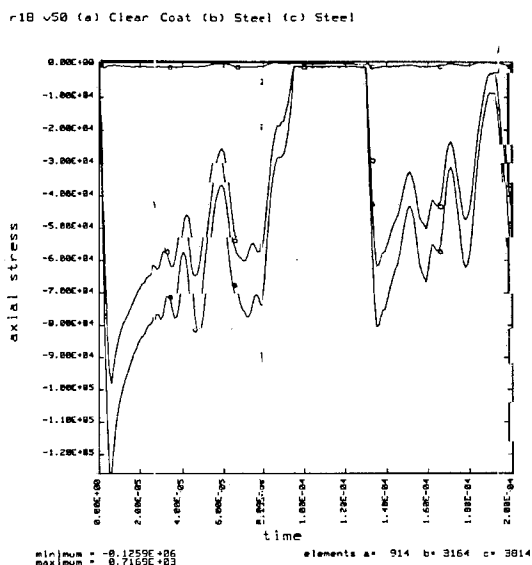


Figure 2

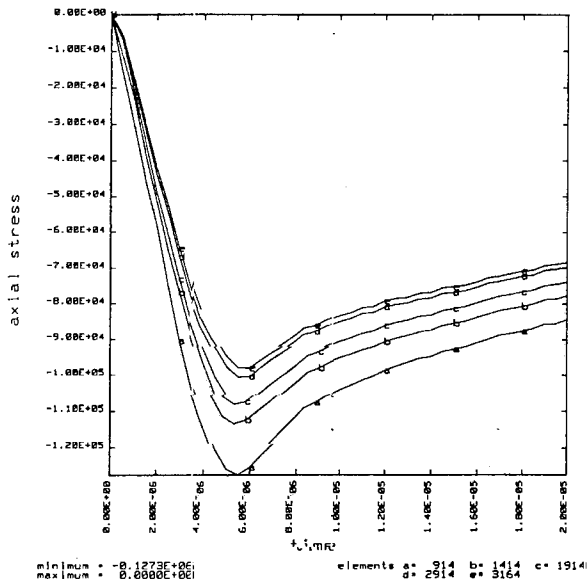


Figure 3

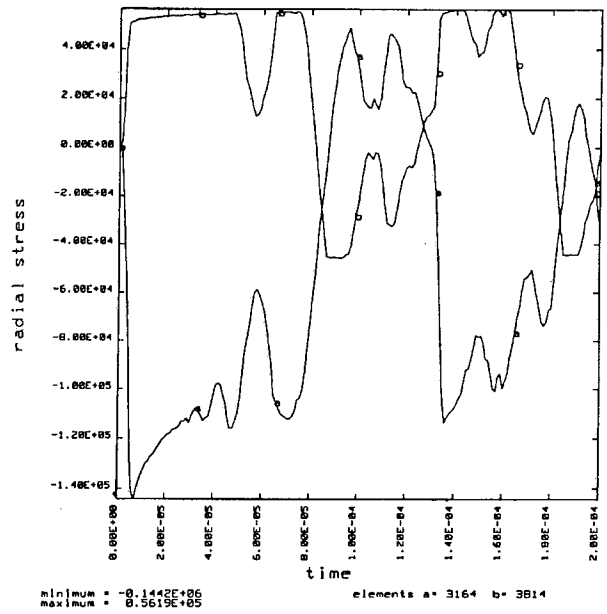


Figure 4

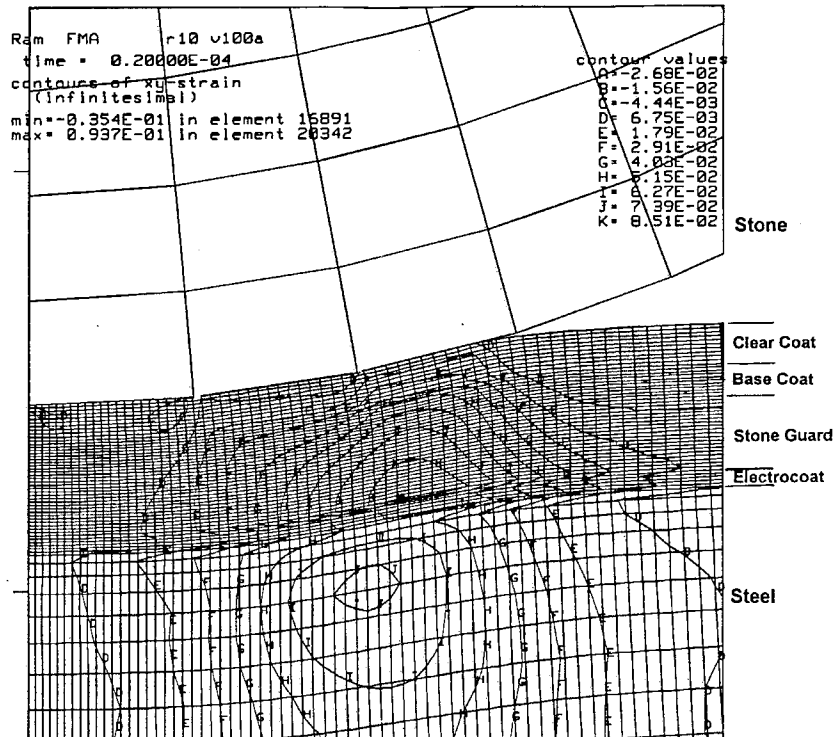


Figure 5

TIME DEPENDENT ADHESION INDUCED PHENOMENA: VISCOELASTIC CREEP OF A SUBSTRATE POLYMER OVER RIGID PARTICLES

D. S. Rimai, L. P. DeMejo, J. Chen, R. C. Bowen, and T. H. Mourey
Eastman Kodak Company
Rochester, NY 14653-6402, U.S.A.

ABSTRACT

The adhesion of micrometer size particles to an alternating block copolymer composed of polydimethylsiloxane and polyester was found to be accompanied by substantial viscoelastic flow of the substrate polymer. This flow gave rise to contact radii which were substantially larger than those predicted by the JKR theory. The flow of the material occurred over a period of days and, in some instances, the observed contact radii were greater than a critical radius for substantial engulfment of the particles by the substrate. Size exclusion chromatography has identified the presence of at least three different molecular weight polydimethylsiloxane rich copolymer species in the *n*-hexane soluble mobile phase responsible for the unexpected behavior exhibited by this polymer substrate.

INTRODUCTION

Particle adhesion to surfaces has been the subject of investigation for over sixty years. Derjaguin¹ and Bradley^{2,3} originally postulated, independently, that significant stresses can result from surface forces and give rise to the deformations observed between contacting materials. Derjaguin¹ calculated the contact radius between a particle and a substrate by assuming that the particle could be treated as a Hertzian indenter. The fact that surface force induced stresses could be large enough to exceed the elastic limit of at least one of the interacting materials was first recognized by Krupp.⁴ He introduced a phenomenological model which subdivided the contact zone into a plastically deformable high stress inner circular region and a lower stress elastic outer annular region. Plasticity was described by a time dependent hardness parameter and only compressive stresses were assumed. Johnson, Kendall and Roberts⁵ measured the contact radius between macroscopic gelatin and rubber spheres and found it to be approximately double that predicted by Derjaguin's model. Assuming linear elastic response of the materials, they proposed a model (hereafter referred to as the JKR theory) which characterized the nature of the interaction between contacting bodies as compressive toward the center of the contact zone and tensile in the outer regions of contact. Again, assuming only tensile interactions and a Hertzian shaped contact zone, Derjaguin, Muller and Toporov⁶ invoked a molecular model (DMT model) that

equipartitioned such interactions inside and outside the contact zone. This approach yielded a contact radius which Tabor⁷ recognized to be approximately half the JKR prediction. After protracted debate in the literature, Tabor⁸, Derjaguin and coworkers⁹, and Muller and coworkers¹⁰ finally demonstrated that both models had validity for materials falling within different ranges of surface energies and moduli (the JKR theory holding for high surface energy, compliant materials and the DMT model pertaining to low surface energy, rigid substances). Maugis and coworkers¹¹⁻¹⁴ introduced a material hardness parameter, *H*, which they equated to three times the yield strength, *Y*, of the material in their approach to expand the JKR theory to include non-recoverable plastic flow.

Experimental observations of adhesion induced deformations between micrometer size particles and substrates, using a scanning electron microscope (SEM) have led to the determination of the power law dependence of the contact radius on particle radius or on Young's modulus.¹⁵⁻²⁰ These results viewed in the context of the forementioned models have enabled Rimai and coworkers to distinguish between elastic and plastic deformations for different particle/substrate systems. The surface force apparatus and the atomic force microscope have also been utilized to measure surface forces, adhesion induced contact radii and meniscus heights to complement the SEM studies.²¹⁻²³ Anomalous large contact menisci, interparticle bridging and particle encapsulation, due to the adhesion induced flow of a soft polyester/PDMS copolymer substrate over micrometer and submicrometer size spherical particles, have been observed by DeMejo and coworkers^{24,25} with a scanning electron microscope. The observations were usually made at least one week after the particles were deposited on the substrate. The height of the menisci and the size of the contact radii were well in excess of those predicted by small deformation linear elastic theories such as the JKR theory.^{5,7} Owing to the size of the deformation, it was hypothesized that the substrate deformed plastically. Permanent substrate deformations (craters), resulting from the surface forces between the polyester/PDMS copolymer substrate and gold or tin particles, were observed by Vrtis and coworkers²⁶ after these particles were removed by amalgamation with mercury. These observations further supported the plastic flow mechanism proposed to explain the original results.

In this paper, the major observations and conclusions of the previous investigations of particles contacting the polyester/PDMS substrate are reviewed. In addition, more detailed analytical data are presented which characterize the chemical and molecular structure of the mobile phase in the substrate. This hexane soluble, PDMS rich phase was shown previously to give rise to the anomalous adhesion induced viscoelastic creep behavior.²⁵

EXPERIMENTAL PROCEDURE

The measured average radii²⁴⁻²⁶ and Young's moduli^{27,28} (literature values) of the particles investigated in connection with the polyester/PDMS substrate and the modulus of the substrate (as determined using an Instron tensile tester)²⁴ are listed in Table I.

TABLE I
Particle and substrate characteristics

Materials	Average Particle Radius (μm)	Young's Modulus (N/M^2)
Gold	1.3	8×10^{10}
Glass	3.6	6×10^{10}
Tin	1.5	4×10^{10}
Polystyrene	2.2	3×10^9
PVF ₂	0.2	1×10^9
Polyester/PDMS	-	9×10^6

Detailed descriptions of the particles and substrate copolymer are given in previous studies.²⁴⁻²⁶ The Young's moduli of all the particles listed in Table I are at least two orders of magnitude larger than that of the substrate. Assuming material homogeneity, this large modulus difference implies that only the substrate material would be expected to deform in the contact zone.

The polyester/PDMS copolymer substrate film was cast out of a 14.5% solution in methylene chloride onto a Teflon surface. Each set of particles listed in Table I were deposited on the smoother (air/polymer interface) side of the film from a height of approximately 1 cm, to avoid gravitational contributions to the observed deformations.^{29,30}

One gram of polyester/PDMS film was extracted with four 20 ml portions of high pressure liquid chromatography(HPLC)-grade 97% n-hexane. The extracts were combined, blown to dryness with a stream of nitrogen and weighed. The average weight percent extracted for two trials was $6.7 \pm 0.3\%$.

The copolymer substrate before and after n-hexane extraction as well as the n-hexane extract were analyzed by size-exclusion chromatography (SEC). The SEC eluent was HPLC-grade toluene continuously sparged with helium. Three 7.5 x 300 mm Mixed-B columns from Polymer Laboratories, Ltd. thermostated at 30.0°C were used with a nominal eluent flow rate of 1.00 mL/min. The actual flow rate was calculated from the retention volume of a flow marker, 1-chloro-2,4-dinitrobenzene, that was added at a concentration of 0.01% to each sample. Polymer samples were injected in 100 mL at a concentration of 1.5 mg/mL. Ultraviolet (UV) absorption and differential refractive index (DRI) detectors were coupled in series after the columns.

The SEM equipment and procedures used to prepare the samples for viewing at high magnification and high tilt angles have already been described.²⁴⁻²⁶ These instruments and procedures allowed the careful examination of the particle/substrate interface both prior to and post particle removal or solvent extraction of the substrate.

RESULTS AND DISCUSSION

SEM Studies

Large menisci, interparticle bridging and particle encapsulation were observed when 3.6 micrometer radius glass particles, 2.2 micrometer radius polystyrene particles and 0.2 micrometer radius polyvinylidene fluoride particles were deposited on the polyester/PDMS copolymer cast film substrate.²⁴

In this early study, the "adhesive" material originating from the substrate was observed to flow up several particle heights. Also, the smaller polyvinylidene fluoride beads appeared to be completely encapsulated by the substrate material and the individual particles appeared to sink even deeper into the substrate. In essence, the observed contact radii were greater than a critical radius for substantial engulfment of the particles by the substrate.²⁴

When the same polystyrene and PVF₂ particles were deposited on the n-hexane extracted substrate and the samples were viewed by SEM, the anomalously large menisci and other time dependent creep phenomena were no longer evident. Instead, the extracted substrate surface displayed numerous cavities.

SEC Analysis

Hexane is a good solvent for PDMS and a poor solvent for the polyester. An extraction of a film of the block copolymer substrate with n-hexane is expected to selectively remove PDMS-rich material from the surface. Further removal of soluble material from the bulk of the film depends on the conditions of hexane extraction, film thickness and the degree of swelling. In this study, the film maintained its integrity and exhibited little swelling in n-hexane. Therefore, it is presumed that

analysis of the extract qualitatively identified the composition of the material primarily at the surface of the free-standing film. Surface material that is chemically different from the bulk may be anticipated for compositionally heterogeneous copolymers.

A straightforward SEC procedure was developed in our laboratory which takes advantage of the unique and selective responses of the DRI and UV detectors for each block component. The specific refractive index increment (dn/dc) of polyester is positive in toluene, whereas the dn/dc of PDMS in toluene is negative. The dn/dc of a copolymer of the two components is to a first approximation, linearly proportional to the weight fractions and specific refractive index increments of the individual components. The dn/dc of the copolymer is slightly negative in toluene and the DRI response is therefore negative. Molecular size decreases with increasing retention volume in SEC chromatograms and the low molecular weight material produces a negative DRI response. After extraction with n-hexane, the low molecular weight region of the chromatogram has a slightly positive DRI response, indicating an enrichment of the polyester component in this fraction. The material extracted by n-hexane produces a negative DRI response, confirming that the material removed from the film is PDMS rich and the shift to longer retention volumes is consistent with low molecular weight material.

The composition of the extract is confirmed by the UV chromatograms. The polyester component absorbs UV light at 313 nm but the PDMS segment is transparent. The area under the UV chromatogram of the extract is much smaller than the UV response for a comparable amount of the block copolymer. The UV absorption of the extract is small but significant since it distinguishes the soluble material as PDMS-rich copolymer rather than PDMS homopolymer.

CONCLUSIONS

Similar time dependent creep phenomena, as reported in earlier studies, were observed by SEM after polymeric microparticles were deposited on the unextracted polyester/PDMS copolymer substrate. However, these phenomena were conspicuously absent after the same particles were deposited on the n-hexane extracted substrate. The hexane soluble polymer (approximately 7% of the copolymer substrate) was analyzed to primarily consist of low molecular weight PDMS rich copolymer fractions. The surface cavitation morphology of the extracted substrate suggests that the silicone rich extract was the discontinuous phase of a polymer blend.

REFERENCES

1. B. V. Derjaguin, *Kolloid Z.* **69**, 155 (1934).
2. R. S. Bradley, *Philos. Mag.* **13**, 853 (1932).
3. R. S. Bradley, *Trans. Faraday Soc.* **32**, 1088 (1936).
4. H. Krupp, *Adv. Colloid Interface Sci.* **1**, 111 (1967).
5. K. L. Johnson, K. Kendall and A. D. Roberts, *Proc. Royal Soc. Lond. A* **324**, 301 (1971).
6. B. V. Derjaguin, V. M. Muller and Yu P. Toporov, *J. Colloid Interface Sci.* **53**, 314 (1975).
7. D. Tabor, *J. Colloid Interface Sci.* **58**, 2 (1977).
8. D. Tabor, *J. Colloid Interface Sci.* **67**, 380 (1978).
9. B. V. Derjaguin, V. M. Muller and Yu P. Toporov, *J. Colloid Interface Sci.* **67**, 378 (1978).
10. V. M. Muller, V. S. Yushchenko and B. V. Derjaguin, *J. Colloid Interface Sci.* **77**, 91 (1980).
11. D. Maugis and M. Barquins, *J. Phys. D* **11**, 1989 (1978).
12. D. Maugis, in: *Microscopic Aspects of Adhesion and Lubrication*, J. M. Georges (Ed.), p. 221. Elsevier, Amsterdam (1982).
13. D. Maugis and M. Barquins, *J. Phys. D* **16**, 1843 (1983).
14. D. Maugis and H. M. Pollock, *Acta Metal.* **32**, 1323 (1984).
15. L. P. DeMejo, D. S. Rimai and R. C. Bowen in: *Particles on Surfaces* 2 (K. L. Mittal Ed. 1989).
16. D. S. Rimai, L. P. DeMejo and R. C. Bowen, *J. Appl. Phys.* **68**, 6234 (1990).
17. R. C. Bowen, L. P. DeMejo, D. S. Rimai and W. B. Vreeland, *J. Appl. Phys.* **70**, 3360 (1991).
18. L. P. DeMejo, D. S. Rimai and R. C. Bowen, *J. Adhesion Sci. Technol.* **5**, 959 (1991).
19. D. S. Rimai, L. P. DeMejo, W. Vreeland, R. C. Bowen, S. R. Gaboury and M. W. Urban, *J. Appl. Phys.* **71**, 2253 (1992).
20. D. S. Rimai, L. P. DeMejo, W. B. Vreeland, R. C. Bowen, S. R. Gaboury, and M. W. Urban, *J. Appl. Phys.* **73**, 668 (1993).
21. R. G. Horn, J. N. Israelachvili and F. Pribac, *J. Colloid Interface Sci.* **115**, 480 (1987).
22. W. M. Merrill, A. V. Pocius, B. V. Thakker and M. Tirrell, *Langmuir* **7**, 1975 (1991).
23. D. M. Schaefer, M. Carpenter, R. Reifengerger, L. P. DeMejo and D. S. Rimai, *J. Adhesion Sci. Technol.* **8**, 197 (1994).
24. L. P. DeMejo, D. S. Rimai, J. Chen, and R. C. Bowen, *J. Adhesion* **39**, 61 (1992).
25. L. P. DeMejo, D. S. Rimai, J. Chen, and R. C. Bowen, *J. Adhesion* (in press).
26. J. K. Vrtis, C. D. Athanasiou, R. J. Farris, L. P. DeMejo and D. S. Rimai, *J. Adhesion Sci. Technol.* **8**, 929 (1994).
27. D. W. Van Krevelen, Ed., *Properties of Polymers* (Elsevier, Amsterdam, 1990).
28. ASM Handbook **2** (2nd Ed. 1992).
29. L. N. Rogers and J. Reed, *J. Phys. D* **17**, 677 (1984).
30. S. Wall, W. John and S. L. Goren, in *Particles on Surfaces* 2 (K. L. Mittal, Ed. 1989).

Particle generation in corrosive gas delivery systems

S. Krishnan, S. Grube, Ultra Clean Technology, Menlo Park, CA,
A. Tudhope, O. Laparra, VLSI Technology, Inc., San Jose, CA

Introduction

Stainless steel tubing is widely used in gas delivery systems in the semiconductor industry. As this industry moves to smaller device geometries the focus on minimizing contamination from all possible sources has gained high priority. Consequently, in the area of gas delivery for semiconductor processes the quality of the gas delivery system is constantly being improved to meet the industry's requirements.

Typical electropolished stainless steel tubing has a surface composition consisting of a Cr/Fe ratio of ~ 1.5 and a $\text{Cr}_2\text{O}_3/\text{Fe}_2\text{O}_3$ ratio of ~ 2.5 . It has desirable surface characteristics like rapid moisture desorption and a chromium passivation layer and is well suited for inert gas delivery. However, corrosive gas delivery [1-3] poses problems of contamination. In a previous study [1] corrosion in tubing delivering HCl gas occurred in a region known as the heat-affected-zone (HAZ) near the welded portions of the tubing. The HAZ typically extends from the weld site to approximately 2-5 mm downstream of the weld as seen in Fig. 1. Manganese (Mn) which outgasses during the welding process and re-deposits in the HAZ was found to cause localized corrosion of the stainless steel surface in the presence of HCl and moisture. In this study the corrosion-induced particles generated in the HAZ near the weld sites of tubing, supplying HCl gas to a gate oxidation furnace, are characterized. The effects of the metallurgical composition of the stainless steel tubing, welding techniques, and post-weld rinsing on the extent of corrosion is investigated.

Experimental Procedure

Single melt, conventional stainless steel tubing with a high Mn content (~ 1.6 -2 wt %), and ultraclean, double-melt processed stainless steel with a low Mn content (~ 0.6 wt.%) were used in these experiments. Conventional welding which involved orbital tungsten inert gas (TIG) welding at a speed of 4 rpm was used to weld the conventional tubing material. Ultraclean welding, involving orbital TIG welding in a Class 100 cleanroom at a speed of ≥ 10 rpm was used to manufacture the low Mn weldments. The ultraclean welding was followed by a post-weld rinse in a hot DI water bath at 60°C . Both weldments were installed on a gas delivery system supplying purified HCl gas to a gate oxidation furnace.

Each weldment was exposed to a total of ~ 4 hours of semiconductor grade HCl gas (< 10 ppb H_2O). After exposure, the weldment was cut open to expose the heat-affected-zone (HAZ) near the weld site and observed with a scanning electron microscope (SEM, Hitachi-2400). Energy dispersive spectroscopy (EDS) was used to perform an elemental analysis of the tubing surface as well as the corrosion by-products in the HAZ. Electron spectroscopy for chemical analysis (ESCA) of the HAZ in the conventional high Mn and ultraclean low Mn weldments was also performed.

Results and Discussion

Figure 2 shows the corrosion in the HAZ in the conventional high Mn stainless steel tubing exposed to HCl. Extreme corrosion is evident with large "boulder-like"

particulate ranging up to 5 μm being generated due to corrosion of the tubing surface. EDS (Fig. 3) of the particulate revealed the presence of a prominent chlorine peak in addition to the background stainless steel matrix elements. (Mn is obscured by the more predominant Ni peak). Thus, excessive amounts of chlorine were detected in the corrosion induced particulate observed on the high Mn conventional weldment. This indicates that local HCl attack in the HAZ near the weld sites in the conventional tubing has resulted in chloride structure formation on the stainless steel. All of the corrosion by-products were detected in the HAZ near the weld while the overall stainless steel surface away from the weld region showed essentially no evidence of corrosion. Figure 4 shows the HAZ of the low Mn ultraclean weldment. The small ring-like structures observed on the surface indicate the onset of corrosive attack of the stainless steel surface by HCl. However, very little corrosion is evident on this surface compared to the high Mn conventional weldment. EDS on this weldment showed only a small amount of chlorine and oxygen in the faint ring-like structures. The amount of chlorine present was significantly smaller than that on the high Mn weldment observed under identical conditions. Based on the SEM observations and the EDS analysis, the low Mn ultraclean weldment shows significantly less corrosion than the high Mn conventional weldment for identical conditions of exposure to HCl.

ESCA analysis was performed in the HAZ in the high Mn conventional weldment and the low Mn ultraclean weldment after exposure to HCl. The Mn content in the HAZ of the conventional weldment was ~ 3 times greater than that in the ultraclean weldment. Since ESCA is confined to the top 50-100 Å of the

sample surface, these values should reflect the Mn content on the sample surface rather than the Mn content in the bulk stainless steel. These results combined with the SEM and EDS results indicate a direct link between the extent of corrosion and the Mn re-deposition in the HAZ.

Manganese has a higher vapor pressure (at welding temperatures) than Fe, Cr, Ni, Mo, or other elements in the stainless steel matrix. As a result, during the welding process Mn selectively vaporizes due to the high local temperatures, and re-deposits downstream of the weld in a portion of the HAZ where the chromium passivation layer is mostly intact. Deposited Mn in the downstream HAZ acts as a catalyst and causes enhanced corrosion of the stainless steel tubing in the presence of halogen gases.

Based on the extent of corrosion in the HAZ and the formation of corrosion induced particles on the tubing surface, Mn contamination, due to its outgassing, is an important factor for the corrosion of stainless steel exposed to HCl. The extent of Mn outgassing during welding is dependent on the welding speed and the concentration of Mn in the stainless steel alloy. Minimizing the Mn content in the alloy, maximizing the welding speed, and performing post-weld rinsing are approaches that reduce the extent of the Mn re-deposition phenomenon, consequently, reducing corrosion in gas delivery systems.

References

- [1] S. Miyoshi, T. Kojima, T. Suenaga, T. Ohmi, U. Mizuguchi, *Proceedings of Microcontamination Conference*, pp. 606-615, Sep. 93.
- [2] H. Wang, G. Doddi and S. Chesters, *J. of IES*, pp. 28-31, Jul/Aug. 94.

[3] J. Wei, R. Brooksby, S. Lewkowitz and B. Mohammed, *Semiconductor International*, pp. 70, Oct. 93.

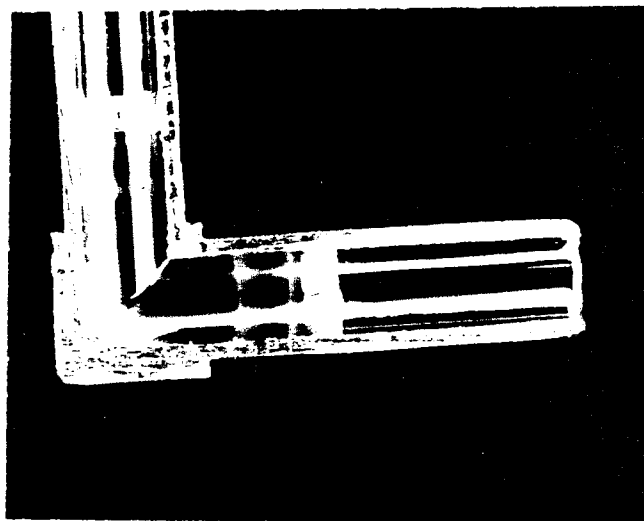


Fig. 1. Cross-section of a weldment with visible discoloration due to Mn deposition in the heat-affected-zone (HAZ)

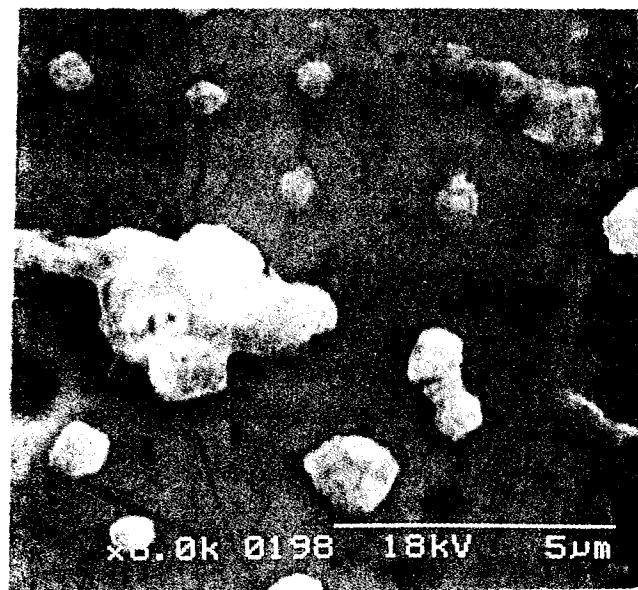


Fig. 2. SEM of the corrosion particulate in the HAZ in the conventional weldment

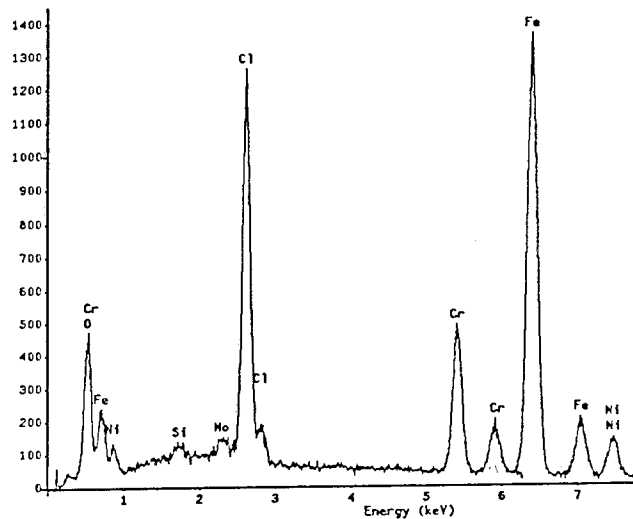


Fig. 3. EDS on the corrosion particulate in the conventional weldment



Fig. 4. SEM of the corrosion in the HAZ in the ultraclean weldment

ENHANCED REMOVAL OF RADIOACTIVE PARTICLES FROM CIRCUIT BOARDS BY FLUORINATED SURFACTANT SOLUTIONS

C. S. Yam¹, R. Kaiser² and O. K. Harling¹

[1] Department of Nuclear Engineering, Massachusetts Institute of Technology, Cambridge, MA 02139

[2] Entropic Systems Inc., P.O. Box 397, Winchester, MA 01890-0597

INTRODUCTION

A laboratory scale ultrasonic decontamination system has been developed to demonstrate the application of ESI's enhanced particle removal process [1] to the decontamination of radioactive electronic circuit boards [2]. The process uses inert perfluorinated liquids as the working media; the liquids have zero ozone depletion potential, are non-toxic, nonflammable, and are generally recognized as non-hazardous materials. The parts to be cleaned are first sonicated with a dilute solution of a high molecular weight fluorocarbon surfactant in an inert perfluorinated liquid. The combination of ultrasonic agitation and liquid flow promotes the detachment of the particles from the surface of the part being cleaned, their transfer from the boundary layer into the bulk liquid, and their removal from the cleaning environment, thereby reducing the probability of particle redeposition [3]. The process is operated in a closed flow loop, therefore minimizing the consumption of the process liquid. After the cleaning process, the parts are rinsed with the pure perfluorinated liquid to remove residual surfactant, and dried. This ultrasonic cleaning process does not affect the performance of the electronic circuit boards being decontaminated.

DECONTAMINATION SYSTEM

A laboratory scale decontamination system has been designed and constructed with a process layout as outlined in Fig. 1. There are two separate cleaning loops in this system; loop #1 is a washing loop which contains a mixture of surfactant solution in perfluorinated liquid as the working medium; and loop #2 is a rinsing loop which contains pure perfluorinated rinse liquid. As shown in Figure 1, the cleaning liquid is drawn from storage tank (T-1) by pump (P-1) through a closed flow loop #1 consisting of a flow meter (FM-1), a 0.2 μm membrane filter assembly (F-1), a test cell (S), a 0.2 μm membrane particle capture filter (F-3), a redundant 0.2 μm membrane filter assembly (F-4), and finally returns to the storage tank (T-1). The test cell, containing the test part to be cleaned, is placed in a temperature controlled ultrasonic bath, filled with two gallons of water as a coupling liquid for ultrasonic propagation. Ultrasonic agitation in the bath is generated by a square wave generator with a power range of from 15 watts to 285 watts. The "detached" radioactive particles are removed from the cell by the fluorocarbon perfluorinated liquid, and then captured on a disposable 0.2 μm membrane filter (F-3).

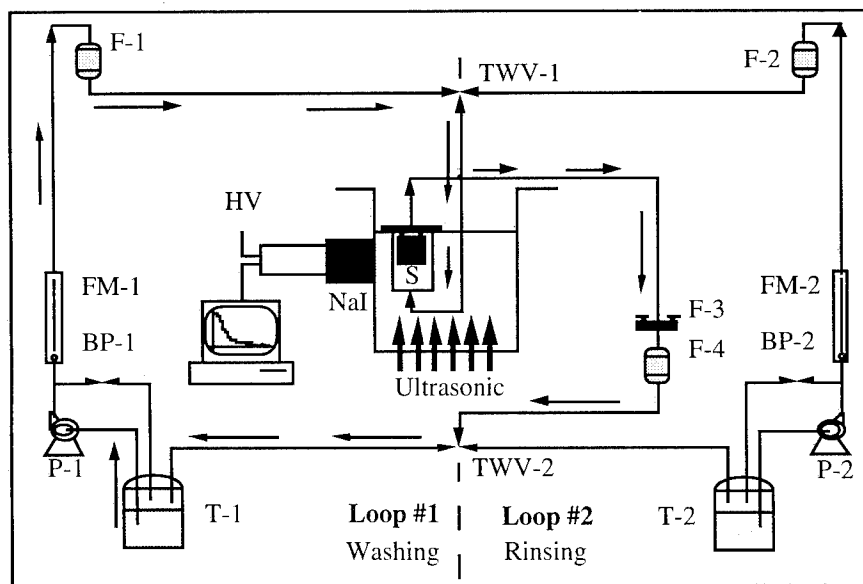


Fig. 1 Schematic of the Decontamination System

SYNTHESIS OF RADIOACTIVE MODEL CIRCUIT BOARDS

Model Circuit Boards

In this laboratory scale cleaning system, the radioactive parts are placed in a small test cell as shown in Fig. 1. This test cell is a thin walled, electropolished, stainless steel cylindrical chamber, 6 cm in diameter and 10 cm deep. The cylinder has an internal volume of 250 ml. Small circuit boards, 3.81 cm square, were designed and built to fit into the test cell. These boards are functional and are tested before and after each decontamination run. The circuitry of these boards is shown in Fig. 2.

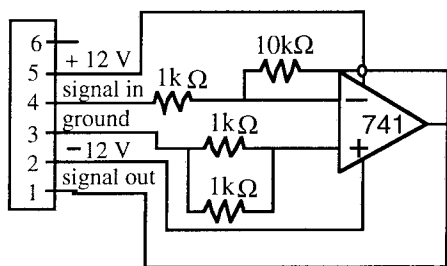


Fig. 2 Circuitry of the Model Circuit Boards.

Contamination Of Circuit Boards

Natural iron oxide (Fe_2O_3) powder samples were (principal isotope= Fe-59) irradiated at the MIT 5 MW reactor. Particle size distribution curves of two iron oxide samples used in the experiment are shown in Fig. 3. The mean diameter D_{50} for the fine and coarse powders is 0.75 and 1.54 μm , respectively. After irradiation the sample powder was suspended in isopropanol. The test circuit boards were contaminated by dipping them in this suspension.

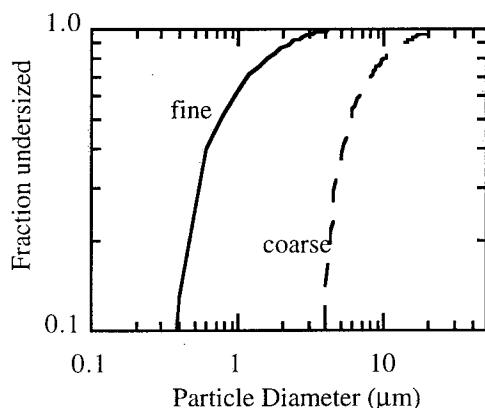


Fig. 3 Particle Size Distribution of the Iron Oxides

The solution was first sonicated at 120 Watts for 15 min. to ensure homogeneity of the suspension. A

circuit board was then dipped into the suspension for 15 min. and air dried for 15 min. The activity of the board increased as the number of "dips" increases. The contamination level of the boards ranged from 60,000 dpm to 480,000 dpm of Fe-59 .

CAPTURE OF RADIOACTIVE PARTICLES

Filtration Efficiency

Before initiating the particle removal studies, it was necessary to demonstrate that any suspended particles could be captured by simple filtration. The purpose of these experiments was to determine suitable filters for capturing the contaminants. The filtration efficiency of a series of 47 mm diameter membrane filters was evaluated. Seven filters with pore size range from 0.05 to 5.0 μm (0.05, 0.1, 0.2, 0.45, 0.65, 1.0 and 5.0 μm) were tested. 100 ml of the isopropanol which contained irradiated iron oxide powder was filtered by each membrane filter. The activity of the Fe-59 isotope was measured before and after each filtration. Filtration efficiency was obtained by comparing these two measurements. Fig. 4 shows the filtration efficiency versus filter pore size.

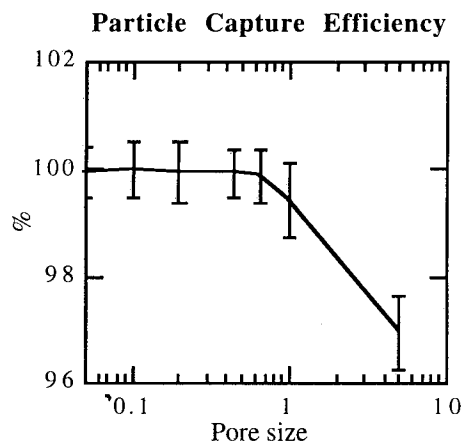


Fig. 4 Filtration Efficiency of the Iron Oxides

The results presented in Figure 4 show that a capture efficiency of 99.95 % can be obtained with a 0.2 μm filter. To ensure adequate capture of the contaminants during the actual experiments, two 0.2 μm membrane filters were placed in series and therefore resulting in a 99.9975 % capture efficiency.

Permeability

Filtration times were also recorded during the filtration experiments. The permeability was observed to increase with increasing pore size as shown in Fig. 5. At 0.2 μm , the permeability of the

fluid is about 0.0083 ml/cm²/sec/psi. At a flow rate of 300 ml/min., this results in a pressure drop across a 47mm diameter filter of about 25 psi, which interfered with the ultrasonic agitation. For this reason, a large surface area cartridge filter (1000 cm²) was used, resulting in negligible pressure drop at experimental flow rates.

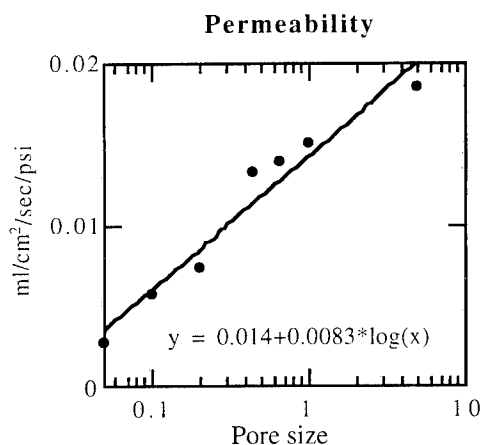


Fig. 5 Filter Permeability Results

ON-LINE ACTIVITY MONITORING SYSTEM

A radiation detection system consisting of a 3"x3" NaI scintillation gamma detector, a pre-amplifier, an amplifier, a high voltage power supply, a counter and a computer data acquisition system, was used to monitor the radioactivity level of the test parts during the decontamination process, as shown in Fig. 6. The Fe-59 emits gamma rays with energy 1.09 and 1.29 MeV, so the attenuation due to the process liquid, the thin steel wall or the water bath is insignificant. The percent of removal or the decontamination factor (DF), was calculated as shown below.

$$DF = \frac{\text{Initial Activity at time 0}}{\text{Final Activity at time t}}$$

The background radioactivity has to be minimized to reduce errors in calculating DF. To reduce the radiation background, a 2 inch thick lead shield was installed around the system surrounding the water bath and the gamma detector. Furthermore, when the final count rate is comparable to the background level (when a high DF was achieved), a long post-cleaning counting was also required. In calculating the final DF, the net activity of the circuit was used.

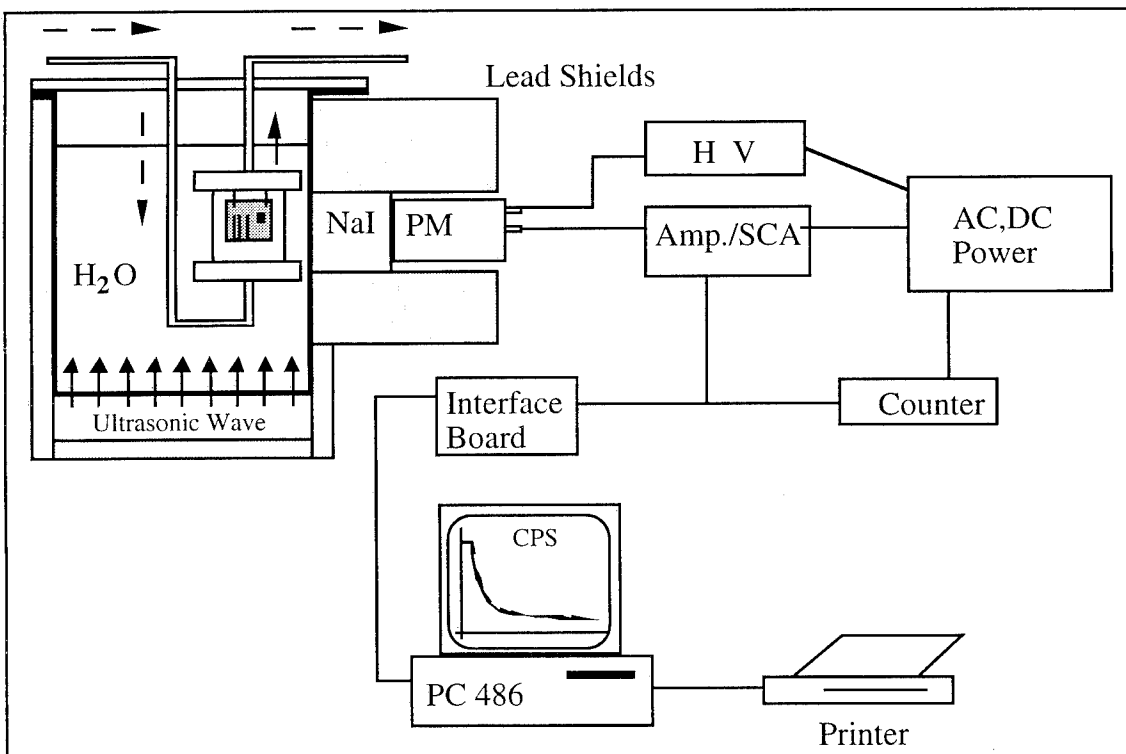


Fig. 6 An On-line Radiation Detection System For Monitoring The Decontamination Level

RESULTS

Characteristics of Particle Removal Rate

More than 100 cleaning experiments were performed with different operating conditions - liquid type, flow rate, temperature, particle size, sonication power, etc. Typical results are presented in Fig. 7. As can be seen in this figure, a combination of ultrasonic agitation and flow is required to achieve particle removal. As is evident from Fig. 7, no significant change in activity is noted during the first 5 min. of the experiment when no ultrasonic power was applied. Once the ultrasonic power was applied (60 watts), a very rapid change in activity was then noted, decreasing rapidly during the first 5 min. of sonication. After the first 5 min., the rate of change of activity decreases.

The removal rate is also a function of flow rate. Initially, the rate of particle removal is higher at a higher flow rate of 150 ml/min. than at 75 ml/min. However, after approximately 60 min., flow rate has little further effect on the continuing rate of decontamination. At the end when most of the particles are removed, removal is no longer a function of mass transfer, but is a probabilistic surface event independent of fluid flow. At 60 min., at both flow rate, DF's greater than 1000 were obtained.

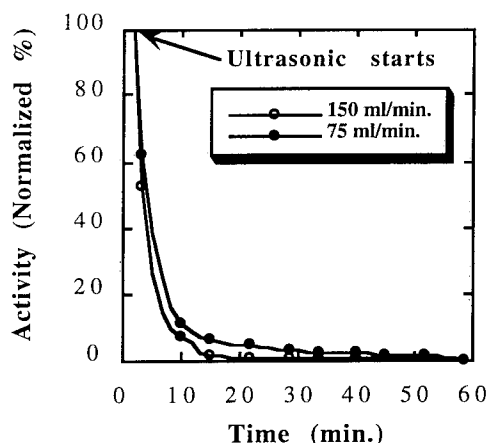


Fig. 7 Ultrasonic Cleaning Of Radioactive Circuit Boards with Perfluorocarbon Surfactant Solution.

The particle removal rate at the end of the 1 hr experiment is not zero. With the perfluorinated solutions used, the DF increases from 1200 after 1 hr to 1800 after 2 hrs.

Process Liquid

Particle removal is also a function of liquid properties. Different process liquids were used in the cleaning experiments. The results show that perfluorinated liquids have better particle removal

capability than CFC-113 (Freon). Addition of 0.3 % of a fluorinated surfactant further enhances the cleaning capability of the perfluorinated liquids. A summary of DFs results obtained with different process liquids in 1 hr is presented in Table 1. This table presents the best results obtained under the following process conditions: sonication power 60 W, flow rate 75 ml/min. and temperature 110 °F.

Table 1 Comparison of DF for different process liquids.

Process Liquid	DF	Error
CFC-113	64	5 %
PFC-Vetrel	93	8 %
PFC-3M's PF-5070	250	15 %
PFC-3M's PF-5070 + 0.3 % surfactant	1213	30.5%

PFC : Perfluorocarbon

Surfactant : Dupont's 157 FSL Lot-12

CONCLUSIONS

Based on the experimental data obtained it is concluded that: i) particle removal ability of perfluorinated liquids is better than that of CFC-113 (Freon); ii) enhanced removal is obtained with addition of 0.3 % of perfluorinated surfactant ; iii) high DFs greater than 1000 are obtained in 1 hr; iv) removal rate after 1 hr is non-zero; and v) this cleaning process is non-destructive to electronic circuit boards.

The data obtained indicate that this process, once implemented on a large scale, will offer users in the nuclear industry a practical and cost effective means of decontaminating and recovering a wide variety of tools and instruments.

ACKNOWLEDGMENT

The authors acknowledge the support of this work by the Nuclear Regulatory Commission under Contract No. NRC-04093-106.

REFERENCES

1. R. Kaiser, U.S. Patent 4,711,256, "Method and Apparatus for Removal of Small Particles from a Surface", December 8, 1987.
2. R. Kaiser and O.K. Harling, "Enhanced Removal of Radioactive Particles by Fluorocarbon Surfactant Solutions", Draft Final Report NRC-04-92-109, Prepared for U.S. Nuclear Regulatory Commission, Washington, DC 20555, March 1993. NUREG/CG 6081.
3. R. Kaiser, "Enhanced Particle Removal from Inertial Guidance Instrument Parts by Fluorocarbon Surfactant Solutions", "Particles on Surface 4: Detection, Adhesion and Removal", K.L. Mittal, Editor, Plenum Press, New York, 1993.

EFFECT OF SURFACE MOISTURE ON THE POLARIZATION OF INDIVIDUAL GLASS PARTICLES

T. N. Tombs* and T. B. Jones**

*Office Imaging, Research and Technology Development
Eastman Kodak Company
Rochester, NY 14653-6402

**Department of Electrical Engineering
University of Rochester
Rochester, NY 14627

INTRODUCTION

When glass particles adsorb water from humid environments their low frequency dielectric properties change drastically. An increase in the effective polarization of a particle in an electric field can increase the force of attraction and adhesion to a surface. To investigate the polarization mechanism, variable frequency measurements upon individual glass particles (50-100 μm diam) suspended in silicone oil were performed with a computer-controlled dielectrophoretic (DEP) levitator. The dielectric surface properties of individual particles have been measured in the frequency range between 10 Hz and 100 kHz. A relaxation in the dipole moment of moistened glass particles suspended in silicone oil is clearly evident in measured DEP spectra. Depending on the type of surface treatment, the characteristic relaxation times of soda-lime glass particles change by more than 4 orders of magnitude. The effect on particle relaxation time is shown as a function of relative humidity and resting time (in the silicone oil). A model based on ohmic surface conduction is used to explain the phenomenon. This research has implications with respect to the controversy surrounding the influence of moisture on the performance of electrorheological (ER) fluids, where the electrostatic force between particles affects fluid viscosity.

THEORY [1]

One approach to modeling surface polarization of dielectric particles is to consider "normal" conduction in a thin ohmic surface layer. This concept of surface conductivity was first applied to particles by Murphy and Lowry [2] and theoretically developed by Miles and Robertson [3], and O'Konski [4]. By solving Laplace's equation for a spherical particle having a thin conducting shell, Miles and Robertson showed that the dielectric behavior of the coated sphere is equivalent to a homogeneous sphere with a modified volume conductivity. The model, therefore, can be considered as an extension of Maxwell's [5] and Wagner's [6] theories of heterogeneous dielectrics. In the Maxwell-Wagner model, charge migration through the bulk of a lossy dielectric particle was shown to cause a relaxation in its polarization. The

relaxation is due to the finite response time of the charge that accumulates at the surface of the particle. This surface charge screens the applied electric field from the bulk of the particle. Miles and Robertson showed that a nonconducting particle will exhibit a similar relaxation if an ohmic surface layer is present. O'Konski reworked the original theory and presented a more physical interpretation than Miles and Robertson while achieving similar results.

Consider a single uniform sphere of radius R , permittivity ϵ_2 , and conductivity σ_2 , suspended in a fluid of permittivity ϵ_1 , and conductivity σ_1 . The induced dipole moment of the sphere due to an alternating electrical field \mathbf{E} of radian frequency ω is given by the Maxwell-Wagner theory as

$$\mathbf{p} = 4\pi\epsilon_1 R^3 \mathbf{E} \underline{K} \quad (1)$$

where the complex Clausius-Mossotti factor is

$$\underline{K} = (\underline{\epsilon}_2 - \underline{\epsilon}_1)/(\underline{\epsilon}_2 + 2\underline{\epsilon}_1), \quad (2)$$

and $\underline{\epsilon}$ represents complex permittivity: $\underline{\epsilon} = \epsilon - j\sigma/\omega$ (underscore $\underline{}$ signifies a complex quantity, and $j = \sqrt{-1}$). Following O'Konski, a thin ohmic surface layer with surface resistivity λ can be accounted for by letting

$$\underline{\epsilon}_2 = \epsilon_2 - j(\sigma_2 + 2\lambda/R)/\omega. \quad (3)$$

The frequency spectrum of the particle's dipole moment is conveniently represented by the Debye equation [7]. Expressed in terms of the high frequency (K_∞) and low frequency (K_0) limits of K , the Debye equation is

$$K = K_\infty + (K_0 - K_\infty)/(1 + (\omega\tau)^2) \quad (4)$$

where

$$K_\infty = (\epsilon_2 - \epsilon_1)/(\epsilon_2 + 2\epsilon_1), \quad (5)$$

$$K_0 = (\sigma_2 + 2\lambda/R - \sigma_1)/(\sigma_2 + 2\lambda/R + 2\sigma_1), \quad (6)$$

and the characteristic relaxation time, given by O'Konski, is

$$\tau = (\epsilon_2 + 2\epsilon_1)/(\sigma_2 + 2\lambda/R + 2\sigma_1). \quad (7)$$

RESULTS

The experiments described here were conducted with individual spherical particles (50-100 μm diam) suspended

in silicone oil (Dow Corning 200®). A constant relative humidity, used to control the amount of physically adsorbed water on the particles, was established in sealed chambers with saturated aqueous salt solutions containing excess solids. Particles were heat-dried at 250° C for 20 minutes before being placed in the humidity chambers. An effective relative humidity of 0% was achieved by heat-drying the particles in this manner then quickly covering them with oil.

The electrical characteristics of individual particles were measured with the DEP levitator by observing the DEP force over a range of frequencies (more information on the experimental apparatus can be found in Ref. [8]). The DEP spectrum is defined as the square of the levitation voltage versus frequency, from which the particle's relaxation time τ , surface conductivity λ , and dielectric permittivity ϵ_2 can be determined.

The wide range in relaxation times exhibited by otherwise identical glass spheres was quickly confirmed to be due to water adsorption. Consistency in the relaxation times of measured DEP spectra was attained by careful control of the humidity to which particles were exposed. The water adsorbed on the surface of the glass particles was altered by heat and humidity treatments. Heat-drying particles at 250° C for 20 minutes to remove physically adsorbed water consistently decreases the measured relaxation frequency ($f_r = 1/2\pi\tau$) to less than 10 Hz. Exposing the particles to a water-saturated environment increases the relaxation frequency several orders of magnitude (Fig. 1).

A nonlinear least-squares curve fit of the DEP spectra (K versus frequency), based on the Debye equation yields the measured relaxation times of the levitated particles. The effective permittivity of a particle ϵ_2 is obtained from the measured value of K_∞ and knowledge of the permittivity of the medium ϵ_1 . Similarly, K_0 determines the effective surface conductivity λ . However, for the system studied here, that is when σ_1 and σ_2 are much less than $2\lambda/R$, the surface conductivity can not be accurately determined in this manner because K_0 is very insensitive to λ/R . Instead, we use the relaxation time (Eq. (7)), which is adequately sensitive to λ/R , to calculate the surface conductivity

$$\lambda = (\epsilon_2 + 2\epsilon_1)R/2\tau. \quad (8)$$

DEP spectra obtained for particles exposed to various values of fixed relative humidity (after heat-drying at 250° C for 20 minutes) show an increase in relaxation frequency with increasing relative humidity. Figure 1 shows representative DEP spectra for particles treated at various relative humidities (rh), while Fig. 2 graphs the relaxation frequency versus $\%rh$ for all the data. A large increase in f_r occurs between 15% and 32% rh , while a smaller increase, one order of magnitude, occurs between 32% and 90% rh . The 6 data points at 0% rh in Fig. 2 represent particles that were heat-dried at 250° C for 20 minutes. The spectra of these particles do not exhibit any relaxation

phenomena within the frequency range of the DEP levitator. A somewhat arbitrary relaxation frequency of 5 Hz was assigned to these data and to the 15% rh data; this value represents an upper limit, actual values may be much lower.

Although stringent measures were taken to assure that the particles were all treated the same, some scatter appears in the data. In addition to the precautions described above, particle size and shape were strictly monitored by visual inspection with a microscope. Only particles that appeared clean and perfectly spherical were tested. Samples having shape deformities or surface contamination were discarded. Apparently, undetectable particle to particle differences in the surface structure are responsible for the scatter shown in Fig. 2. The surface characteristics of alkali glass, known to vary greatly from sample to sample, strongly influence the effect that

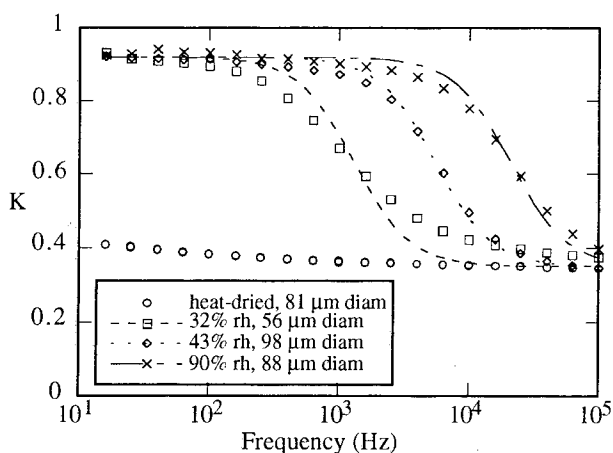


Fig. 1. Representative DEP spectra for soda-lime glass particles treated at various rh . Curves are fitted to the Debye equation.

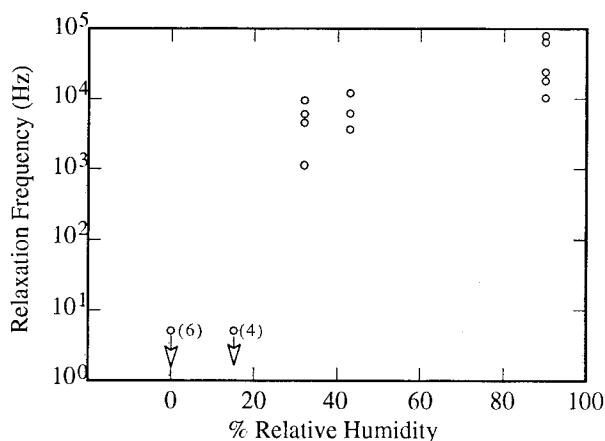


Fig. 2. Relaxation frequencies of soda-lime glass particles (54-78 μ m diam) treated at different relative humidities.

moisture has upon surface conductivity. According to O'Konski's conducting film model these influences are reflected in the relaxation time (see Eq. (7)).

When left in the silicone oil for more than 2 hours the measured relaxation frequencies of moisture-treated particles begin to shift gradually to lower values. The relaxation frequency of the particle decreased slowly over time until, after approximately 330 minutes, f_r had changed by an order of magnitude. The "time-in-oil" effect is shown in Fig. 3 for particles treated at different rh . Note that each data point in the figure represents a complete DEP spectrum; a Debye curve fit of the spectrum yields f_r . In addition, each matching symbol on the plot is the same particle at different times, that is, all the data presented in Fig. 3 represent only 2 different particles.

Silicone oil is capable of absorbing significant amounts of water (up to 0.1 % by weight) and, apparently, the oil slowly absorbs the surface moisture on the particles. The curves in Fig. 3, which are identical in shape, show that the absorption of water occurs at the same rate in each case. According to the conductive film model, a decrease in the thickness of a particle's water layer causes a proportional decrease in its relaxation frequency. The scatter in the data that appears after 2×10^4 seconds (about 6 hours) is most likely due to absorption of water from surrounding air and to changes in ambient conditions in the laboratory; the relative humidity of the laboratory was not controlled and the levitation chamber was not sealed.

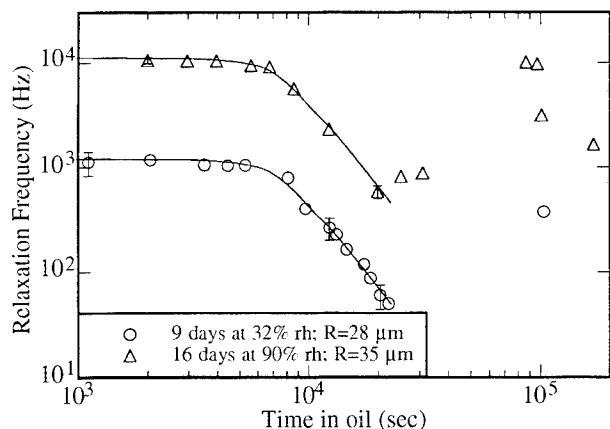


Fig. 3. Time of particle exposure to oil versus the relaxation frequency, which is obtained from curve fitting the particle's spectra. Error brackets indicate 99% confidence intervals that result from the Debye curve fits.

The conducting film model may be used to calculate the effective surface conductivity from the measured values of relaxation frequency (Eq. (8)). Unfortunately, no published values of surface conductivity for moist glass particles in oil are available. However, DEP measurements were found to be roughly comparable to published DC measurements performed in air on glass plates [9,10] and glass fibers [11]. These encouraging results lend support to the hypothesis that the conductive film model may, to a first approximation, describe the surface polarization phenomena of the particles.

ACKNOWLEDGMENTS

This work was supported in part by grants from the Particulate and Multiphase Processes Program of the National Science Foundation (USA). Funding was also provided by the Office Imaging, Research and Technology Development organization of Eastman Kodak Company, Rochester, New York. Donation of the frequency synthesizer, digital multimeter, and power amplifier by the John Fluke Manufacturing Company is gratefully acknowledged. Silicone oil was supplied by Dow Corning Corporation, Midland, Michigan. Glass particles were provided by Potters Industries Inc., Parsippany, New Jersey.

REFERENCES

1. T. N. Tombs and T. B. Jones, *IEEE Trans. Industry Appl.* **29** (1993), pp. 281-285; T. N. Tombs, Ph.D. Thesis (University of Rochester, Rochester, NY, 1992).
2. E. J. Murphy and H. H. Lowry, *J. Phys. Chem.* **34** (1930), pp. 598-620.
3. J. B. Miles and H. R. Robertson, *Phys. Rev.* **40** (1932), pp. 583-591.
4. C. T. O'Konski, *J. Chem. Phys.* **23** (1955), p. 1559; C. T. O'Konski, *J. Phys. Chem.* **64** (1960), pp. 605-619.
5. J. C. Maxwell, *A treatise on electricity and magnetism*, third edition, Clarendon Press, Oxford (1891).
6. K. W. Wagner, *Arch. Elektrotech.* **3** (1914), p. 83.
7. P. Debye, *Polar molecules*, Chemical Catalogue Co., New York (1929).
8. T. N. Tombs and T. B. Jones, *Rev. Sci. Instrum.* **62** (1991), pp. 1072-1077.
9. N. G. Gutkin, K. S. Yesvtropev, and D. Y. Kuznetsov, *Zh. Tekhn. Fiz.* **22** (1952), p. 1318.
10. M. Kantzer, *Bull. Inst. Verre* **5** (1946), pp. 11-14.
11. W. Hinz and V. Havlicek, *Glast. Ber.* **31** (1958), p. 422.

Measurement of Adhesion Between Polymers: Influence of Interfacial Chains

M. Deruelle, V.S. Mangipudi, M. Tirrell

Department of Chemical Engineering and Materials Science, University of Minnesota,
Minneapolis, Minnesota 55455

L. Léger

Laboratoire de Physique de la Matière Condensée, Collège de France, URA CNRS 792,
11, Place Marcelin Berthelot, 75231 Paris Cedex 05, France

ABSTRACT

The influence of polymer chains grafted near the interface on the adhesion between an elastomer and a solid has been studied. The adhesion between cross-linked poly(dimethylsiloxane) [PDMS] brought into contact with a silicon wafer covered by a grafted layer of monodisperse PDMS was measured. The influence on the adhesion of the molecular weight and the surface density of the grafted chains was examined by modifying them independently. The mechanical test we used was the JKR method which measures the variation of the radius of the contact area, a , between the wafer and the lens as a function of applied load, P . This technique gives the dependence of the interfacial adhesion energy or strain energy release rate, G , on the crack propagation speed, V . Our results show that G still depends on V , even in the lowest range of speeds. If we refer to the low velocity values of strain energy release rate as adhesion energies, G_o , we find that G_o is affected strongly by the grafted layer and apparently governed by the ability of the chains from the grafted layer to penetrate the network. The adhesion energies we measure are invariably higher than that expected from accounting for only the surface energy of PDMS. Layers grafted from the melt state over a range of molecular weights, where the grafted chains have their unperturbed dimensions, show less adhesion enhancement than do layers of the same thickness, produced by grafting high molecular weight polymers from a range of solution concentrations, which results in compressed configurations of the grafted chains when the solution grafted layers are dried. There appears to be a thickness for the grafted layers which is optimum in generating adhesion enhancement between the lens and the wafer.

In our recent studies, we have coated the PDMS cap with glassy polymers like polystyrene, and measured the adhesion between PS coated cap and a PS coated flat surface. From these measurements, the surface energy of PS can be determined. These experiments constitute a suitable alternative to the studies done using the surface forces apparatus (SFA).

INTRODUCTION

Interfacially anchored chains are effective in promoting the adhesion between rubbers and other solids.¹ Interfacial mechanical properties, such as sliding friction, between elastomers and solids may also be manipulated by interfacial chains. Means of attaching chains to interfaces and our understanding of the structures of such interfacial layers have increased substantially recently. Our aim is to use this structural knowledge to enhance mechanistic understanding of interfacial properties.

The current situation regarding solid-elastomer adhesion has been well-summarized recently by Brown.^{2,3} At interfaces involving elastomeric polymers, the measured adhesion energy is always a strong function of the rate of crack propagation. Interfacial chains, or connectors, that cross the interface (for example, polymer chains grafted by their ends to an otherwise impenetrable solid) and couple physically by interpenetration and possible entanglement (for example, with a elastomer), and raise the strength of the interfacial bond further. In this work, we confine ourselves to conditions well above the glass transition temperature of the elastomeric component and where the mechanism of interfacial failure does not involve any chain scission. The failure occurs predominantly by chain pullout.

The objective of this work is to experimentally determine the dependence of interfacial adhesion energy or fracture toughness (G) on the number density (Σ) and length of connecting chains (related to the degree of polymerization, N), and on the rate of crack propagation (V). There are theoretical models available predicting these dependencies, which have as yet had little confrontation with experimental data. As discussed by Brown,^{2,3} all these models assume that a threshold stress exists below which chain pullout does not occur. In this view, a threshold adhesion energy, G_o is obtained at crack propagation velocities less than a critical speed, V^* . The interfacial adhesion energy, (G) increases above G_o for V greater than V^* . The models differ in what they assume about the state of the chains after pullout and in the details of the analysis of the elastic fracture problem. The rate of growth of G

above V^* is predicted to depend on the nature of the intermingling among the interfacial chains. The experimental dependencies of G and G_o on Σ are yet to be established definitively. The models of de Gennes and coworkers predict ^{4,5}

$$G_o - W \approx kTN\Sigma \quad (1)$$

where W is the Dupré energy, or the thermodynamically reversible work of adhesion between two surfaces A and B , ($W = \gamma_A + \gamma_B - \gamma_{AB}$), and N is the degree of polymerization of the connector chains.

Brown recently examined the adhesion of crosslinked polyisoprene to surfaces to which linear polyisoprene connector chains are tethered. He obtained G_o experimentally by extrapolation of his G versus V data (which appeared to be reasonably linear) to zero velocity. The interfacial adhesion energy, both at zero velocity (G_o) and at finite velocity (G), increased the areal density (Σ) of connector chains, appearing to reach a plateau values around a density of 0.05 to 0.1 nm⁻², for a particular connector length (N).

In this work, we examine the influence of PDMS connector chains on the adhesion of PDMS to a solid. We particularly examine the effect on adhesion of two alternative ways of grafting chains on the solid surface, from melt and from solution state.

In a different set of experiments, we coat the PDMS caps with glassy polymers, and measure the thermodynamic work of adhesion and surface energies of the polymers.

THEORY AND EXPERIMENTS

Adhesion between the solid and the elastomer was measured in the JKR type experiments.⁶ In this experiment, only a small volume of the sample experiences any deformation. Due to this, the bulk dissipative effects, which are extensive in volume of material deforming, become negligible. In a typical experiment, the lens is compressed against the flat surface at constant imposed displacement (δ), and the load (P) and contact radius (a) are measured. δ is the displacement by which the lens is squeezed from the position of an undeformed tangential contact between the spherical and flat surfaces. The fracture toughness, G , is related to P and a through the following relation.

$$G = \frac{\left(P - \frac{a^3 K}{R} \right)}{6 \pi K a^3} \quad (2)$$

$$\text{and } \delta \text{ is given by } \delta = \frac{a^2}{3R} + \frac{2P}{3aK} \quad (3)$$

where P is load, a is contact radius, R is radius of the undeformed sphere, and K is the bulk modulus. Equation (2) is extension of the JKR theory due to Johnson, Kendall and Roberts. In a true equilibrium situation, $G = W$. This is the classical Griffith criterion of fracture mechanics. In that limit, equation (2) becomes the original JKR expression. By measuring the variation of a and P with time (t), at constant imposed δ , we can get $V = \frac{da}{dt}$ and $G(t)$ from eq. (2).

In the case of adhesion measurements between surfaces of glassy polymers, since there are no time dependent effects, we can measure the thermodynamic work of adhesion. In that case, equation 2 becomes the original JKR equation, i.e. $G = W$.

The experimental set up was rather simple. The PDMS cap was placed on a rigid support that was mounted on a translating stage. The stage could be displaced vertically using a micrometer, imposing a constant δ . The lens was compressed on the flat surface that was put on analytical balance, which reads the load (P). The radius of the deformed zone (a) was measured using a microscope.

Sample preparation

The PDMS chains, used to modify the surface of the silicon wafer by grafting, were α,ω hydroxyl-terminated with polydispersity of approximately 1.1. The chains were grafted onto the native oxide of a silicon wafer at 120°C from solution or from melt. The grafting density was controlled by varying the degree of polymerization, N and concentration Φ of polymer in the solution. $\Phi = 100\%$ corresponds grafting from the melt. It has been shown that⁷ Σ scales like $N^{-1/2} \Phi^{7/8}$. Two different series of substrates were studied, one was obtained by maintaining N fixed, and in the other Φ was varied (from 5% to 100%) in the solution from which the PDMS was grafted; the other one was obtained by keeping $\Phi = 100\%$ (reaction from the melt) and varying the molecular weight of the polymers grafted (from 17,000 to 500,000). The thicknesses of all dried, grafted layers were determined by ellipsometry.

Preparation of the elastomeric lenses

The PDMS lenses were prepared by crosslinking α,ω vinyl-terminated chains of different molecular weights. The cross linker was an oligomer consisting of hydromethylsiloxane monomers. Crosslinking is effected via hydrosilation catalyzed by a platinum complex. Lens for the JKR adhesion experiments were prepared by placing droplets of the uncured mixture onto a microscope slide that had previously been treated with chlorosilane so that

the PDMS does not wet the glass, thereby producing a small spherical cap. The reaction was carried out for one hour at 70°C. The details can be obtained from elsewhere.⁸

RESULTS AND DISCUSSION

The contact radius (a) and load (P) have been measured during loading and unloading. G and $V = \frac{da}{dt}$ are determined using eq.2. In the simple case of crosslinked PDMS cap in contact with a bare wafer or a wafer covered with crosslinked PDMS, the loading and unloading data superimpose, *i.e.* there is no hysteresis. However, hysteresis has been observed as a general feature when PDMS cap is in contact with grafted PDMS layers, *i.e.* the contact area at a given load is higher while unloading than during loading. This is due to the increase in adhesion energy or fracture toughness owing to the intermingling between grafted chains and the network. Figure 1 shows the typical variation of G with V . As it can be seen, the data do not appear to have reached a low speed asymptote, certainly not one in the neighborhood of $W = 2\gamma$. The variation G with contact time has been measured to investigate the evolution of interactions in the contact zone. Figure 2 illustrates the influence of Σ on G in the case of solution-graft and melt-grafted chains. Both types enhance the adhesion of the lens to the solid surface above the PDMS surface energy. Interestingly, the enhancement is significantly higher in the case of solution-graft chains compared to the melt-graft chains. This could be due to the difference in configurations of the solution-graft and melt-graft chains. It can also be noted that there is optimum thickness of the grafted layer at which the enhancement in adhesion is maximized.

Figure 3 shows the results of adhesion measurements between two PS surfaces. The surface energy obtained from these measurements ($\sim 45\text{ mJ/m}^2$) agrees well with the SFA measurements.⁹

REFERENCES

1. Reichert, W., Brown, H.R. *Polymer*, **1993**.
2. Brown, H.R. *Annu. Rev. Mater. Sci.*, **1991**, 21, 463.
3. Brown, H.R. *Macromolecules*, **1993**, 26, 1666.
4. Raphael, E., de Gennes, P.-G. *Macromolecules*, **1992**, 96, 4002.
5. Ji, H., de Gennes, P.-G. *Macromolecules*, **1993**, 26, 520.
6. Johnson, K.L., Kendall, K., Roberts, A.D. *Proc. R. Soc. London. A* **1971**, 324, 301.
7. Auroy, P., Auvray, L. *J. Phys. II*, **1992**, 2, 1133.
8. Duell, M., Léger, L., Tirrell, M. *Macromolecules* (submitted) and *Faraday Discussions* (in press).
9. Mangipudi, V.S., Tirrell, M., Pocius, A.V. *Macromolecules* (submitted)

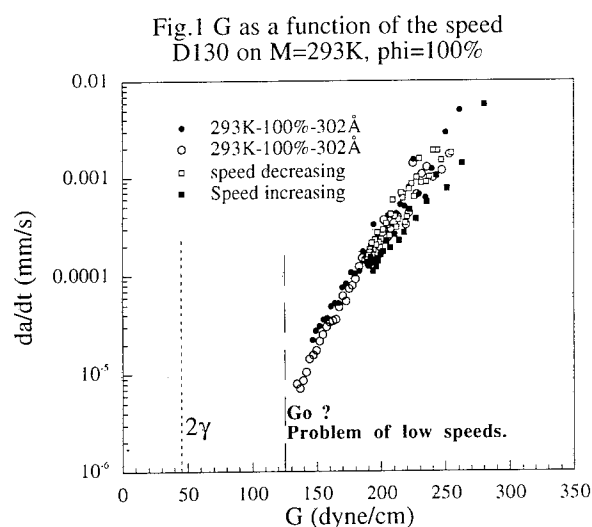


Fig. 2. Effect of thickness of the grafted layer on fracture toughness

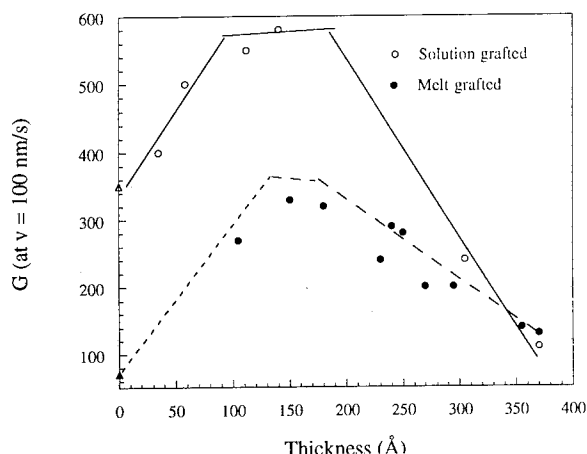
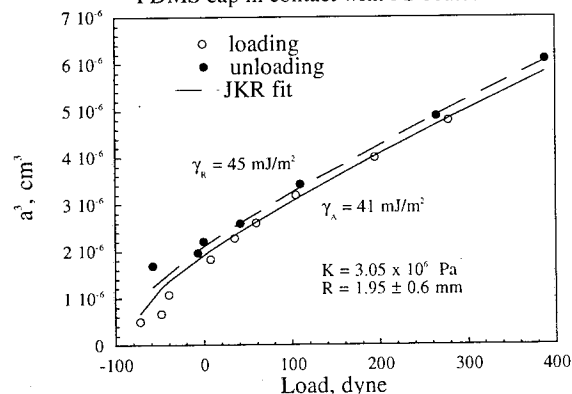


Fig. 3. Adhesion between PS surfaces. PS coated PDMS cap in contact with PS coated wafer



HYDROPHOBIC COAGULATION AND FLOTATION OF ULTRA FINE COAL

Zhiwei Jiang*, Yingjia Kang+ and Youzhu Li*

* Beijing Graduate School, China University of Mining and Technology

D11 Xueyuan Rd, Beijing 100083, CHINA

+ Zhuzhou Coal Preparation Plant, Zhuzhou, Hunan, CHINA

INTRODUCTION

Coal is one of the most important resources of primary energy of the world. The importance of clean coal technology has increased considerably as more people realize that coal combustion produces one of the largest sources of the environmental pollution. Pre-combustion cleaning of coal is an effective and economic approach for better and cleaner utilization of coal. Physical cleaning of coal such as froth flotation requires that coal feed be ground to very fine size first to liberate the fine-grained mineral matter. However ultra fine coal has poor floatability. The problems associated with ultra fine coal flotation in current understanding are very low flotation rate, poor selectivity as results of slime coatings on particles and entrainment of ultra fine gangue in the froth, excess reagents consumption, increased froth stability and poor recovery. Although our understanding of the behavior of fine particles in flotation is still limited, it is clear that particle size is a key factor here. Fundamental studies on the collision and adhesion between particles and bubbles in flotation suggested that one applicable method for the improvement of micronized coal flotation was to enlarge the effective particle size of coal before flotation^[1].

Some recent studies have showed that hydrophobic surfaces exhibit an attractive interaction energy which was not considered in the classical DLVO theory^[2,3]. Unoxidized coal particle surface has a degree of hydrophobicity, primarily depending on coal rank. Adsorption of hydrophobic reagents, such as diesel on coal surface can change its hydrophobicity. The attractive energy of hydrophobic surface can be used as the driving force for coal particles coagulation. Based on this theory a coal cleaning process called Selective Hydrophobic Coagulation and Flotation (SHCF) has been developed.

In the SHCF process, micronized coal is pulped with water under suitable condition. Ultra fine hydrophobic coal particles form coagula which have much larger effective size than individual coal particle, while hydrophilic particles of mineral matter are kept in dispersion in the pulp. Therefore the coagulation is a selective process based on hydrophobicity of particle surface. In the following stage of froth flotation, material being floated is mainly the hydrophobic coal coagula rather than those highly dispersed hydrophilic mineral particles.

EXPERIMENTAL STUDIES

Coal Sample

Coal sample used in this study is a medium rank bituminous coal. Its proximate and ultimate analysis results are shown in Table 1. The size distribution of the micronized coal sample was measured using a Microtrac particle size analyzer and the results is shown in Fig.1. The volume mean diameter of the coal sample was about 5 micron and 90% of the material was in the minus 10 micron size range.

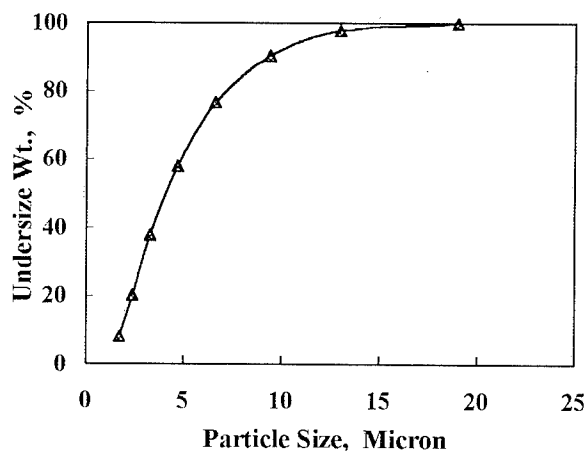


Fig.1 Particle size distribution of the micronized coal sample

Table 1
Proximate and Ultimate Analysis of Coal Sample

Ash	8.10 %
Volatile Matter	29.8 %
Fixed Carbon	56.1 %
Carbon	83.6 %
Hydrogen	5.16 %
Oxygen	7.80 %
Nitrogen	1.91 %
Sulfur	1.55 %

Comparison of SHCF and Conventional Flotation

In laboratory SHCF tests, diesel which is a common collector for coal flotation was used at a dosage of 10kg/t of coal to enhance the hydrophobicity of coal particle surface. There is no frother was used in SHCF process. For conventional flotation, dosage of diesel (collector) and octanol-2 (frother) were 5.0 kg/t and 1.0 kg/t respectively. Fig.2 shows the ash-yield curves calculated from the test results of SHCF process and that of conventional flotation. SHCF was significantly better than conventional flotation with regard to both ash content and yield of the clean coal product. With SHCF process, a premium quality clean coal with 1.74% ash and 0.15% inorganic sulfur was produced at 81% recovery of combustible matter. A 84% ash reduction and 91% inorganic sulfur rejection was achieved. At the same recovery of combustible matter, conventional flotation had only 53% ash reduction and 69% inorganic sulfur rejection. As flotation rate constant increases with particle size, pre-treatment of ultra fine coal slime with selective hydrophobic coagulation can also speed up the flotation process. For the coal sample tested, the flotation time required by SHCF process was only 3 to 5 minutes, while that required by the conventional flotation was as long as 8 to 10 minutes.

Effect of Oil Additions

In the conventional oil agglomeration process for coal cleaning, typical dosage of diesel or kerosene is 100 kg/t of coal. SHCF process requires much less oil. In the case that the natural hydrophobicity of solid particle surface is very good, oil may not be required.

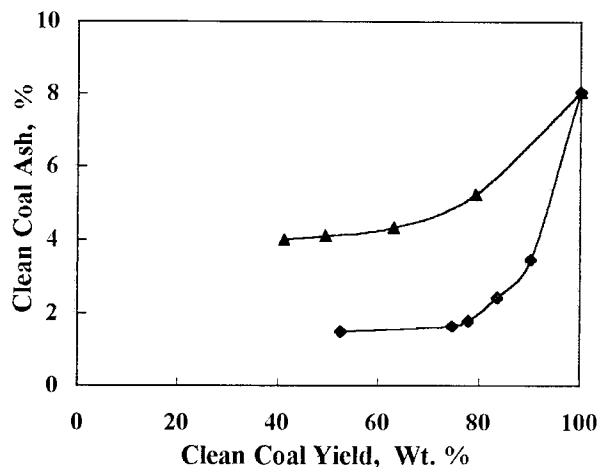


Fig.2 Comparison of SHCF and conventional flotation of micronized coal.

However as adsorption of oil on coal surface dose significantly increase its hydrophobicity, additions of oil is an important factor affecting the efficiency of SHCF process. A series of laboratory SHCF tests were carried out to quantify the effect of oil additions. Fig.3 shows the results. When the additions of oil increased from 2kg/t to 20kg/t ash content of the clean coal product has no significant change, however, yield of clean coal increased from only 48% to 78%. These results suggested that for the coal sample tested, an oil addition of about 10kg/t of coal would be adequate. Dosage of oil also affect flotation rate. The required flotation time decreased with increase of diesel dosage,

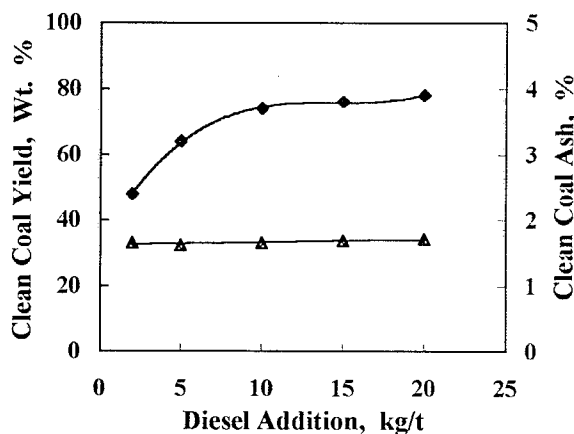


Fig. 3 Effect of diesel additions in the selective hydrophobic coagulation and flotation of the micronized coal sample.

as shown in Fig. 4. When dosage of oil increased from 2 kg/t to 15 kg/t, flotation time reduced from 10 minutes to 3 minutes.

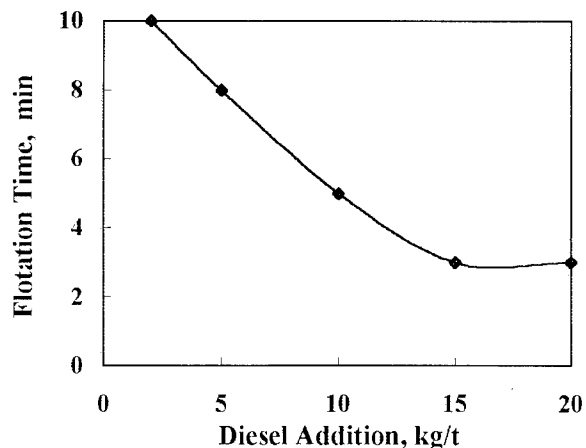


Fig. 4 Effect of diesel additions on flotation time in the SHCF process.

Effect of Dispersant Additions

A key feature of the SHCF process is that hydrophilic particles would be kept in high degree of dispersion in the pulp and not be trapped into the coagula formed by hydrophobic particles. This would ensure the good selectivity of SHCF as a separation process. A number of dispersant were tested to find out their effectiveness for dispersion of hydrophilic mineral particles presented in feed coal. Fig.5 shows the effect of addition of Dispersant 102 on both clean coal yield and ash content. These results suggested that an adequate addition of dispersant would improve the process by increasing clean coal yield and decreasing its ash content. However, the effectiveness is limited and over dose of dispersant could lead a considerable loss in clean coal yield without further reduction of its ash content.

CONCLUSION

For micronized coal cleaning, the results obtained with SHCF process were significantly better than those obtained with conventional flotation, with regard to both clean coal yield and ash and sulfur

rejection. Additions of hydrophobic oil is an important factor affecting the efficiency of SHCF process for ultra fine coal cleaning. Appropriate selection and adequate addition of dispersant would also improve the performance of SHCF process. As the amount of oil required by SHCF process was only about 10 percent of that required by the conventional oil agglomeration process, SHCF would be a technically and economically more acceptable process for cleaning of micronized coal.

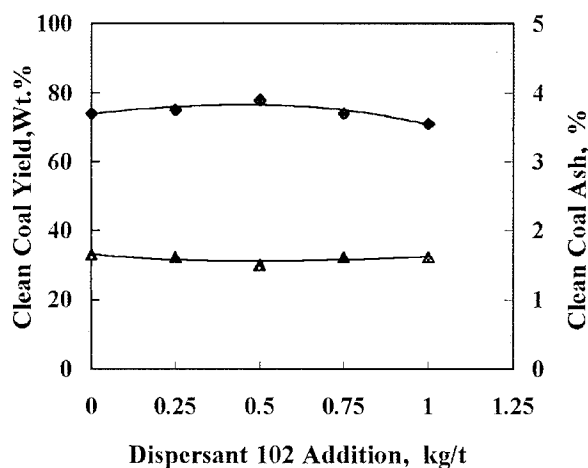


Fig. 5 Effect of Dispersant 102 in the selective coagulation and flotation of the micronized coal sample.

REFERENCE

1. Jiang, Z. and Holtham, P., In: K.S. Forsberg (ed.), Proceedings of the XVI Int. Min. Processing Congress, Stockholm, Elsevier, Amsterdam, 1988, pp.651 -663.
2. Israelachvili, J.N. Intermolecular and Surface Forces: With Applications to Colloidal and Biological Systems, Academic Press Inc. London, 1985.
3. Xu, Z. and Yoon, R.H., J. Colloid Interface Sci., 132(2), 532(1989).

A STUDY OF THE EFFECTS OF LOW POWER PLASMA TREATMENT ON GRAPHITE AND HIGHLY ORIENTATED PYROLYTIC GRAPHITE(HOPG)SURFACES.

S.O'Kell and C.Jones.

Department of Materials Science and Engineering,
The University of Liverpool,
PO Box 147, Liverpool,
L69 3BX. Great Britain.

INTRODUCTION

Plasmas have been widely used to improve the adhesive properties of surfaces [e.g. 1-3]. One such application is the treatment of carbon fibres in an attempt to improve their adhesion to epoxy resins [e.g. 4]. Although such treatments are successful the interaction of the plasma with the fibre surface is not yet fully understood. Carbon fibre surfaces consist of basal plane graphite, edge sites and defect sites. Instead of using carbon fibres, we have chosen two different graphitic surfaces for our experiments, namely graphite and highly orientated pyrolytic graphite (HOPG). This will allow us to understand how plasma interactions occur at the edge sites and on the basal planes.

When a carbon surface is treated with a plasma it becomes activated and on exposure to air will absorb contaminants from the environment, typically moisture. This may overshadow the surface chemical changes introduced by the plasma itself. For this reason chemical characterisation of selected samples has been carried out *in situ* using X-Ray Photoelectron Spectroscopy (XPS). Auger Electron Spectroscopy (AES) has also been used to determine the location of the chemical groups and topographical alterations have been monitored by means of Atomic Force Microscopy (AFM).

EXPERIMENTAL

Plasma treatments were performed using a novel low power system built in house, operating at powers of less than 1W [3].

In situ XPS analyses were performed by directly attaching the plasma cell onto the preparation chamber of the Scienta ESCA300 Spectrometer. This enabled us to study the effects of the plasma on carbon substrates before and after exposure to air. AES chemical mapping was carried out on a VG Microlab with a field emission electron gun. Topographical changes were studied using the Nanoscope II AFM, operated in constant force mode.

RESULTS

Using XPS to characterise the plasma treated surfaces, we found that a nitrogen plasma chemically interacted with the graphite but not with the HOPG. The atomic concentration of nitrogen on the graphite was 5% after a treatment time of one minute. However, analysis of HOPG before exposure to air shows virtually no nitrogen containing functionality present on the treated basal surface, implying that the reaction only occurs at the edge sites and not on the basal plane. After exposure to air the HOPG adsorbs moisture onto the basal planes, indicating their activation during plasma treatment. Auger

mapping of the O, N and C KLL signals of a scored HOPG sample, enabling us to detect signals from both the edge sites and basal planes. The nitrogen functionality does indeed confine itself to the edge sites, which can be seen in figure 1. The light areas show the high concentration of nitrogen at the edge sites. The adsorbed oxygen covers the whole surface, indicating that not only does the nitrogen plasma react with edge sites but treatment also activates the basal planes.

In contrast, an air plasma oxidises both graphite and HOPG surfaces. This implies that in this case, chemical reactions occur at both the edge sites and basal planes. The atomic concentration of oxygen is slightly greater for graphite (18%) than for HOPG (12%) after 1 minute of treatment.

For both the air and nitrogen plasma treatment, the introduction of functional groups occurs within the first few seconds of exposure, reaching a maximum within 60 seconds of treatment.

Changes in the topography of these surfaces is not visible with scanning electron

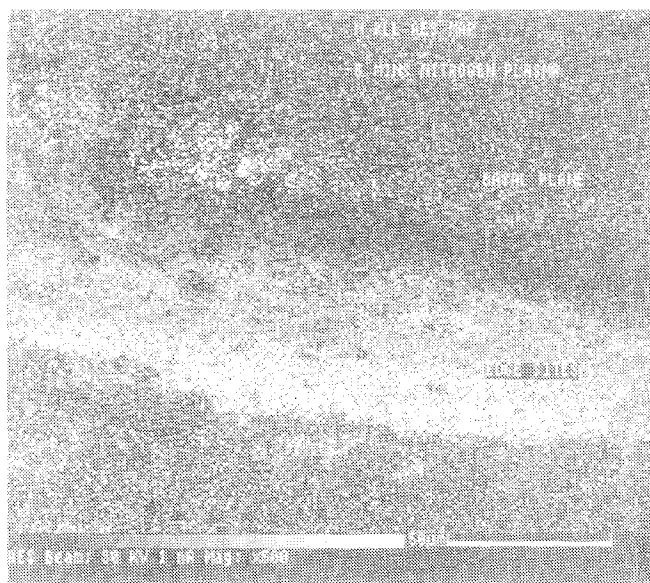


Figure 1: Auger N KLL Map of HOPG treated with a N_2 plasma for five minutes.

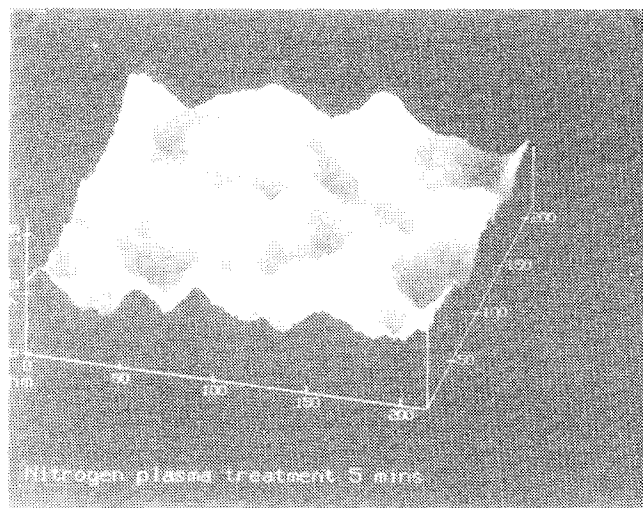


Figure 2: AFM of HOPG treated with an N_2 plasma for five minutes.

microscopy. However, using atomic force microscopy significant changes are detected. Figure 2 show a typical AFM image of an HOPG surface treated with a nitrogen plasma for five minutes. The peak to trough distance averaged 7nm. A similar roughening on samples treated with an air plasma was also observed, although, the average peak to trough distance was only 3nm.

CONCLUSIONS

It has been shown that a nitrogen plasma can only chemically interact with the edge sites of graphite. However, there is evidence that this plasma also leads to activation of the basal planes. This is evident by the adsorption of oxygen onto the treated surface after exposure to air. Even with the low power level used to generate both plasmas, each treatment results in a roughening of the HOPG surface.

REFERENCES

1. J.R.Hall et al, J. of Appl. Polymer Sci. 13, 2085 (1969).
2. R. Foerch and D. H. Hunter J. Poly. Sci. 30, 279 (1992).
3. S. O'Kell et al, Surface and Int. Analysis, in press. (1994).
4. C. Jones, Surface and Interface Analysis, 20, 357 (1993).

A STUDY OF THE INTERPHASE REGION IN CARBON FIBRE EPOXY COMPOSITES USING DYNAMIC MECHANICAL THERMAL ANALYSIS.

K. Atkinson and C. Jones

Department of Materials Science and Engineering,
The University of Liverpool,
PO Box 147, Liverpool,
L69 3BX. Great Britain.

INTRODUCTION

One of the main challenges to scientists studying interfacial phenomena in carbon fibre/epoxy composites is the ability to promote chemical bonding between fibre and resin. It is thought that chemical bonds exist between electrochemically treated fibres and epoxy resins, however their concentration is too low to play a major role in fibre/resin adhesion¹. Using a low power air plasma significantly increases the concentration of chemical functionality. In this case the presence of these chemical groups *has* been shown to play a major role in fibre/resin adhesion². If chemical bonding is more prominent in composites made from air plasma treated fibres, then surely the 'interphase' region in these materials will be affected.

The attraction of one of the resin components to the fibre surface will almost certainly influence the localised curing of the resin and hence its glass transition temperature (T_g). One method commonly used to measure T_g in both resin and composite samples is dynamic mechanical thermal analysis (DMTA).

Results obtained from DMTA depend heavily on the type of resin used, the curing cycles, and the mode of testing. This may account for the apparent conflicting data presented by different research groups in the literature. In general it has been shown that the presence of fibres increases the measured T_g (eg^{3,4}), however Harris et al⁵ observed no such increase. The value of T_g in their case was

approximately 128°C irrespective of surface treatment. Other groups^{eg 6} detected a small difference in T_g with fibre surface treatment.

In this study we compare samples made using fibres with a well characterised surface i.e. untreated (XAU), commercially treated (XAS) and air plasma treated fibres (as described previously²).

All samples have been made from the same batch of resin and have undergone identical curing cycles. The dynamic response of the samples are explained.

EXPERIMENTAL

Unidirectional bars were made up using the 'leaky mould' technique. The resin system used was Ciba Geigy MY750/NMA/K61B. The curing schedule was 2 hours at 120°C followed by a post cure of at least 15 hours at 180°C to ensure a fully cross-linked structure.

DMTA was carried out on a polymer labs. analyzer using both dual and single cantilever testing modes at a frequency of 1Hz, an oscillation amplitude of 64µm and a heating rate of 2°C/min.

RESULTS

Initial experiments were performed using the dual cantilever mode as used by Harris et al⁷. An increase in the T_g was observed from 135°C for the resin to 177°C for the untreated fibre composite. To maximise the sample response, a single cantilever regime was used. This allowed

us to compare results using different sample free lengths.

Figure 1 shows the $\tan\delta$ data obtained for a series of carbon fibre/epoxy samples with a free length of 19mm. The volume fraction, cure cycle and DMTA heating rate were identical, which excludes any thermal conductivity differences as mentioned by Thomason³. However, thermal conductivity differences may account for the increase in the T_g on the addition of fibres.

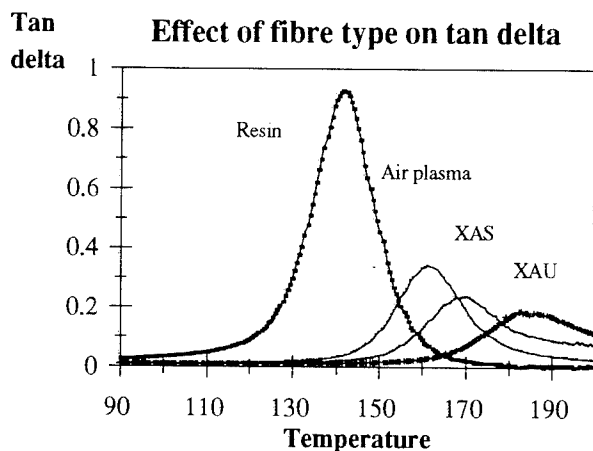


Figure 1

Even using untreated carbon fibres there is some degree of interfacial adhesion in the composite. The strain amplitudes incurred by the samples during the DMTA are such that interfacial failure does *not* occur. It is therefore proposed that the rise in T_g is due to the restriction imposed by the fibres on the mobility of the resin.

Very little, if any, chemical interactions occur between untreated fibres and epoxy resins. In contrast there is thought to be chemical interactions between both XAS and air plasma treated fibres and epoxy resins. If one of the components of the resin were attracted towards the fibre then the stoichiometry of the resin would be altered, thus affecting the degree of cure. Garton⁷ proposed that the catalyst is preferentially adsorbed onto the oxidised sites of commercially treated fibres which leaves the bulk resin deficient in catalyst, thus affecting the curing rate. Both of these phenomena would

result in a lowering of the T_g of the resin. Commercial oxidation (XAS) *does* lead to a decrease in the measured T_g , as shown in Figure 1.

Plasma treated surfaces are thought to have a much greater potential for chemically reacting with the resin. Our results show a more pronounced effect than that seen for commercially treated fibres and therefore supports this proposal.

Table 1 compares the T_g data from single cantilever tests, using different span lengths. The trends in the data are similar. The decrease in T_g for the air plasma treated fibre sample is slightly more pronounced for the longer free length.

	RESIN	XAU	XAS	AIR
Free length				
12mm(T_g °C)	143.5	176	167	165.5
Free length				
19mm(T_g °C)	143	174	169	161.5

Table 1

CONCLUSIONS

We have clear evidence that fibre surface treatment affects the properties of the resin. It is proposed that this is not simply an interphase or localised phenomena since broadening or secondary peaks are *not* observed in the $\tan\delta$ curve.

We are, however, uncertain as to whether these changes are due to the removal of the catalyst or a stoichiometric imbalance of the resin. This is a subject of further study.

REFERENCES

- [1]LT Drzal, MJ Rich & PF Lloyd. J Adhesion 16 (1982),1
- [2]GJ Farrow, KE Atkinson, N Fluck, C Jones submitted to Surface and interface analysis (1994)
- [3]JL Thomason. Poly. Comp. 11,2 (1990), 105
- [4]Yoon Suk Ko. Poly. Eng. Sci. 2213 (1982), 805
- [5]B Harris,O G Braddell & D P Almond, J. Mat. Sci. 28, 12, (1983),3353
- [6]J F Gerard . Poly. Eng Sci. 28, (1988),568
- [7]A Garton & WTL Stevenson J.Poly.Sci: Pt A 26 (1988)

PLASMA-POLYMERIZED FILMS : ADHESIVE BONDING APPLICATIONS

L. Deshayes, M. Charbonnier, F. Gaillard, J. Baborowski, M. Romand

Département de Chimie Appliquée et Génie Chimique (CNRS, ERS 069)
Université Claude Bernard - LYON 1, 69622 VILLEURBANNE CEDEX, FRANCE

ABSTRACT

Plasma polymerized tetraethoxysilane (PPTEOS) films were deposited on stainless steel substrates from a liquid TEOS monomer in a diode-type reactor inductively coupled to a power source operating at 13.56 MHz. XPS, FTIR and x-ray emission (LEEIXS) analyses have allowed to obtain information on composition, structure and thickness of PPTEOS films. The latter are mainly constituted of siloxane chains with a methyl group at their end. Practical adhesion measurements using a three point flexure test show that film adhesion on the corresponding substrates is greater than film cohesion.

INTRODUCTION

Plasma polymerization is a plasma assisted chemical vapor deposition (PACVD) process which may be used to deposit organic or inorganic thin solid films on various substrates. This process takes place under non-equilibrium thermodynamic conditions when the material surface is exposed to an electrical discharge in a gas at low pressure. Depending on the nature of the starting monomer and on the deposition conditions, the so-synthesized layers have generally very different chemical and physical properties relative to conventionally prepared films. More particularly plasma polymers (PP) have been shown, in most cases, to be highly branched and cross-linked and therefore more resistant to aggressive environments. It is the reason why PP films on metallic substrates have been investigated for use as corrosion inhibiting barrier and adhesion promoting underlayer capable of improving long term performances of adhesive/metal or paint/metal systems [1-6].

In the present work, tetraethoxysilane (TEOS) was used as a precursor and PPTEOS films were deposited on stainless steels and their composition, thickness, structure and adhesion properties were studied as a function of some experimental parameters (deposition time for example).

EXPERIMENTAL

The stainless steel substrates used were industrial quality F17 sheets, 0.5 mm in thickness. Coupons 50 x 10 mm were stamped out, cleaned ultrasonically in acetone, subjected to surface pretreatment and PP film deposition, and employed to prepare specimens for adhesion testing. Plasma treatments in an Ar, O₂ or NH₃ medium and PPTEOS films deposition were carried out in a capacitively coupled reactor fitted with two parallel electrodes operating in the RIE mode at a frequency of 13.56 MHz. In this work the deposition conditions were the following (gas pressure: 100 mTorr, power density: 0.5 W.cm⁻²). The tetraethoxysilane (TEOS) precursor was supplied by Fluka (purity > 98 %). PPTEOS films were obtained with or without argon as a carrier gas. The thicknesses of the PPTEOS films studied in this work were always less than 200 nm.

XPS analyses were carried out using a RIBER SIA 200 spectrometer equipped with a non-monochromatic Mg x-ray source. LEEIXS analyses were performed with a home-made wavelength dispersive x-ray spectrometer operating with a cold cathode tube as an electronic excitation source. FTIR spectra were recorded on a Nicolet 710 spectrometer. PPTEOS film structure characterization was carried out by transmission on films polymerized onto KBr pellets. Delamination location was

characterized by microspectrometry on PPTEOS films deposited onto stainless steels. These measurements were performed in the reflection mode with a Nic-Plan device equipped with a grazing incidence (84°) objective. So-analyzed areas were $250\ \mu\text{m}$ in diameter.

Adhesion measurements were carried out using a three point flexure test according to T 300 10 AFNOR specifications [7].

RESULTS AND DISCUSSION

As expected, the characterization of PPTEOS films by XPS only shows the presence of C, O and Si. The atomic concentrations of these elements determined by XPS are compared with those of the precursor inferred from its chemical formula. Results are given in Table 1. As can be seen the O content does not change significantly while the Si content increases of about 20 % and the C content accordingly decreases. Clearly, some volatile hydrocarbon products (CO , CO_2) resulting from decomposition processes within the plasma are evacuated into the vacuum system and therefore are not available to the film growth. In addition, the Si 2p spectrum indicates that silicon from the film is in an oxidized form [E_b (Si 2p) = 103.8 eV] while the C1s peak presents a main component at 285 eV associated with C-H and C-Si bonds, and a slight broadening towards higher binding energies probably due to some hydroxyl and carbonyl functionalities which were formed after air exposure of the sample surface.

Table 1. Composition of TEOS and PPTEOS

	at. % in TEOS	at. % in PPTEOS
C	61	41
O	31	28
Si	8	31

Figure 1 represents the IR spectrum characteristic of the TEOS precursor used in this work. Bands near 2980, 2896 and $1390\ \text{cm}^{-1}$ are due respectively to the stretching and deformation modes of C-H bonds in CH_2 , CH_3 groups. In addition, the bands attributed to Si-O

bonds in Si-O-C groups are observed near $1103\ \text{cm}^{-1}$ and $1082\ \text{cm}^{-1}$ (asymmetric stretching) and near $970\ \text{cm}^{-1}$ (symmetric stretching). All these IR bands are in agreement with those expected for the monomer structure even though bands located near $796\ \text{cm}^{-1}$ (bonding mode) and $456\ \text{cm}^{-1}$ (rocking mode) could be attributed to the existence of siloxane (Si-O-Si) bonds and therefore to the presence of some sort of polymerization. It should also be noted that the corresponding asymmetric stretching band is probably included in the bands near $1082\ \text{cm}^{-1}$. For comparison, figures 2a and 2b represent IR transmission spectra of PPTEOS films deposited on KBr pellets for 30 and 60 s, respectively. In both cases, some striking differences with respect to the TEOS deposit spectrum can be observed. A broad and intense band due to the asymmetric stretching of Si-O bonds in Si-O-Si groups is observed at $1046\ \text{cm}^{-1}$. Moreover, formation of siloxane bridges is also supported by a band near $794\ \text{cm}^{-1}$ due to the Si-O symmetric bonding mode and by a band near $442\ \text{cm}^{-1}$ which is assigned to the deformation mode (rocking) of this same bond. CH_3 groups are also evidenced via the stretching of their C-H bonds at $2930\ \text{cm}^{-1}$. The presence of the band near $885\ \text{cm}^{-1}$ (stretching of Si-C bonds) should prove that CH_3 groups are linked to terminal silicium atoms as $\text{Si}(\text{CH}_3)_3$. It should also be noted that the band of the $\text{Si-OC}_2\text{H}_5$ groups which is present at $970\ \text{cm}^{-1}$ in the IR spectrum of the precursor is no longer identified for the PPTEOS films. From this result it appears that,

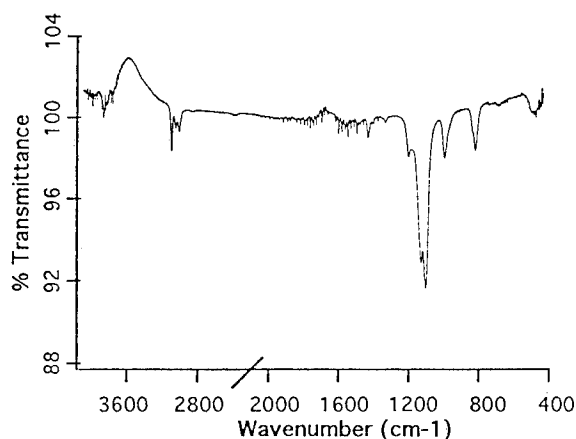


Fig. 1: IR transmission spectrum of a TEOS precursor deposit.

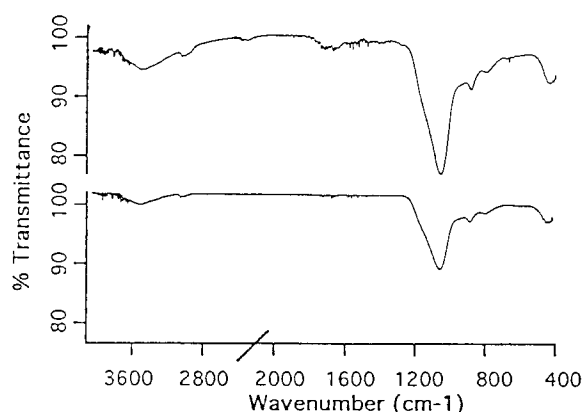


Fig. 2: IR transmission spectra of PPTEOS films deposited for (a) 30 and (b) 60 secondes.

in the experimental conditions used for the RF plasma, the TEOS non dissociated molecules [8] are not condensed as such in the growing film. Under these conditions it can be suggested that PPTEOS films are structurally formed of siloxane bridges Si-O-Si and of Si-(CH₃)₃ groups. Taking now into account the intensity change of the main band at 1046 cm⁻¹ as a function of deposition duration, film thickness is shown to increase linearly vs. time (Table 2). Similar results are obtained by LEEIXS by dispersing and detecting SiK_α radiations from the film and FeL_α radiations from the substrate. In addition, some PPTEOS films were deposited with argon as a carrier gas. IR analysis of such films does not show significant changes of the PPTEOS structure and of the deposit rate.

Table 2. Absorbance percentage of the band at 1046 cm⁻¹ vs. plasma duration

Plasma duration (s)	Absorbance (%)
30	12
60	21
90	30

Adhesion measurements

In this study, PPTEOS films were deposited on stainless steel substrates. Figure 3 shows the changes in adhesion properties of adhesive/PPTEOS/metal systems as a function of deposit duration i.e. of film thickness. As can be seen the measured parameter (maximal

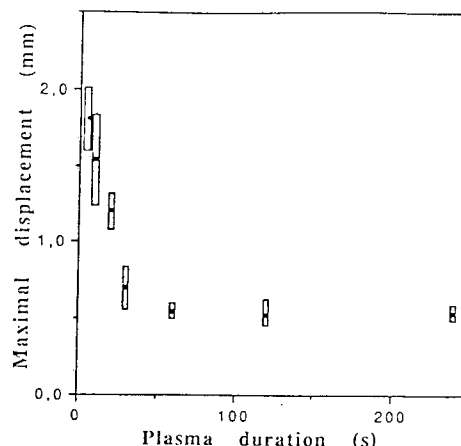


Fig. 3: Effect of plasma duration on adhesion properties of adhesive / PPTEOS / metallic substrate joints.

displacement d_{max} at failure initiation) is greater for ultra-thin films (thickness < 10 nm) then decreases for deposit duration between 5 and 20 s (film thicknesses < 100 nm) and remains constant for thicker films. In order to identify the initiation failure location and therefore to interpret these results, FTIR microscopy analyses were carried out. Whatever the film thickness, failure always occurs cohesively within the PPTEOS films. Indeed the band at 1046 cm⁻¹ associated with the Si-O-Si bonds is always present. However its intensity changes in relation with the initial film thickness. Roughly, the failure takes place near the adhesive/PPTEOS interface in the case of very thin films (thickness < 10 nm) and more deeply within the PPTEOS films when the latter are thicker. In all cases, adhesion measurements using the three point flexure test prove that adhesion at the PPTEOS / substrate interface is stronger than PPTEOS film cohesion. It should also be noted that a similar conclusion can be drawn whatever the substrate pretreatment (degreasing, degreasing + Ar, O₂ or NH₃ plasma).

CONCLUSION

This work shows that PPTEOS films present strong adhesion properties on stainless steel substrates, the failure of an adhesive / PPTEOS / metal system occurring cohesively

within the PTEOS film. XPS and FTIR analyses indicate that such films are mainly constituted of siloxane chains. Works in progress aim to characterize the thermal and chemical behaviour of such films in order to use them as strong and durable intermediate layers in adhesive / metal joints.

REFERENCES

1. H.P. Schreiber, M.R. Wertheimer, A.M. Wrobel, *Thin Solid Films*, 72, 487 (1980).
2. M.R. Wertheimer, J.E. Klemberg-Sapieha, H.P. Schreiber, *Thin Solid Films*, 115, 109 (1984).
3. Y. Matsuda, H. Yasuda, *Thin Solid Films*, 118, 211 (1984).
4. C.E. Taylor, F.J. Boerio, D.B. Zeik, S.J. Clarson, *Proceed. of the 16th Annual Meeting, The Adhesion Society Ed., Williamsburg, 21-26 February 1993*, p. 294.
5. Y.M. Tsai, U. Aggarwal, F.J. Boerio, D.B. Zeik, S.J. Clarson, W.J. Van Ooij, *Proceed. 17th Annual Meeting, The Adhesion Society Ed., Orlando, 20-23 February 1994*, p. 135.
6. L. Deshayes, M. Charbonnier, N.S. Prakash, M. Romand, *J. Adhesion*, 43, 209 (1993).
7. A. Roche, F. Gaillard, M. Romand, M. Von Fahnestock, *J. Adh. Sci. Technol.*, 1, 145 (1987).
8. C. Charles, P. Garcia, B. Grolleau, G. Turban, *J. Vac. Sci. Technol.*, A 10 (4), 1407 (1992).

PLASMA PRETREATMENT OF POLYMERS: APPLICATIONS TO THEIR METALLIZATION BY AN ELECTROLESS PROCESS

M. Alami, M. Charbonnier, M. Romand

Department of Applied Chemistry and Chemical Engineering (CNRS, ERS 069)
Université Claude Bernard - LYON 1, 69622 VILLEURBANNE CEDEX, FRANCE

ABSTRACT

Polycarbonate metallization by the "electroless" process was performed on samples previously treated by plasma. For the reaction to be initiated on the polymer surface, a catalyst (Pd) of this reaction must be chemisorbed on the surface in question. This is carried out in this work by the conventional two step process which consists of immersing the sample successively in an SnCl_2 then a PdCl_2 solution. This process allows studying the reaction mechanisms after each step of the treatment. It is shown that NH_3 plasma treatment of the polymer surface grafts nitrogenated groups which have the interesting property of chemisorbing palladium directly, making the SnCl_2 step useless. Under these conditions a new simplified process is proposed for making a polymer surface catalytic.

INTRODUCTION

The "electroless" metallization of polymers which works in aqueous solution is interesting because of its low cost. It consists of a redox reaction between the ions of the metal to be deposited and reducing ions. Such a solution is in a metastable state and the reaction takes place on contact with a catalyst (Pd). If the latter is adsorbed on the polymer surface the reaction starts on the catalyst islands, then continues by itself, the metal deposited (Ni or Cu) playing the role of catalyst for the reaction which is therefore an autocatalytic one.

The overall operating process includes a surface treatment of the polymer to activate its functional groups or to create new ones [1] and a treatment in aqueous solution to make the surface catalytic. The latter may be performed by either a one step or two step process [2-4]. In this work we have chosen the two step process in order to study the reaction mechanisms by XPS analysis. This process consists of immersing the sample successively in an SnCl_2 solution (sensitization step) then in a PdCl_2

solution (activation step) with an intermediary water rinsing.

In this work, polycarbonate substrates were treated by reactive gas (O_2 , NH_3) plasma, then sensitized by SnCl_2 and activated by PdCl_2 prior to being subjected to the actual metallization. XPS analyses were performed after each of the different steps of the whole procedure so as to understand their respective effects.

EXPERIMENTAL

The plasma treatments were performed in a capacitive R.F. reactor working in the Reactive Ion Etching (RIE) mode. The experimental conditions were the following: gas flow (100 sccm), pressure (100 mTorr), generator power density (0.5 W.cm^{-2}), treatment duration (30 s to 1 min).

The sensitization step consisted of immersing the sample for 3 min in a solution containing 0.1 g.l^{-1} of SnCl_2 and 0.1 ml.l^{-1} of HCl . The activation step worked in the same way with a solution containing 0.1 g.l^{-1} of PdCl_2 and 3.5 ml.l^{-1} of HCl .

XPS analyses were performed in a RIBER SIA spectrometer with a non-monochromatic $\text{MgK}\alpha$ excitation source and a MAC 2 analyser. Spectra were recorded using a take off angle of 25° with respect to the sample surface.

RESULTS AND DISCUSSION

The polycarbonate used in this work was of industrial quality. Before the sensitization / activation process, two surface treatments were performed on the substrate, viz. O_2 and NH_3 plasma treatments. Table 1 gives the surface

composition of the corresponding samples compared to that of an only-degreased sample. The O₂ plasma treatment increases the oxygen content, reveals silicon present in the substrate and brings out aluminium which comes from the sputtering of the reactor cathode on which the samples lie during the plasma treatment. The C1s core level spectrum (not presented here) shows a widening of the peak towards the high energy side. Its curve-fitting allows to characterize, in addition to carbonate groups, the presence of O=C-OH functions. The NH₃ plasma treatment grafts nitrogenated functions and increases oxygen surface concentration probably by a post-oxidation phenomenon on exposure to air.

Surface treatment	C %	O %	N %	Si %	Al %
Ethanol degreasing	88.7	11.3			
O ₂ plasma (1 min)	65.4	31.0		1.1	2.5
NH ₃ plasma (1 min)	69.3	18.7	11.4	0.6	0

Figure 1 represents the survey spectra of a polycarbonate sample treated by O₂ plasma for 1 min (a), the same treated by SnCl₂ (b), SnCl₂ / PdCl₂ (c), PdCl₂ (d). The Sn²⁺ ions adsorb easily on the surface freshly grafted with oxygenated functions. The activation treatment by PdCl₂ carried out immediately after the SnCl₂ one leads to palladium chemisorption and weakens the tin surface concentration. Finally merely the PdCl₂ treatment is inefficient for palladium chemisorption.

Figure 2 characterizes a polycarbonate sample treated by NH₃ plasma for 1 min (a), the same treated by SnCl₂ (b), SnCl₂ / PdCl₂ (c), PdCl₂ (d). The SnCl₂ treatment (b) does not leave any Sn²⁺ ions on the surface, but the whole treatment by SnCl₂ / PdCl₂ involves palladium chemisorption (c) just as does the mere PdCl₂ treatment (d). So, in this case the sensitization step by SnCl₂ is useless ; this therefore allows to simplify the process.

These results clearly show that Sn²⁺ ions adsorb on oxygen, but never on nitrogen. It agrees with the well-known affinity of Sn for oxygen. Conversely tin is not known to have the least affinity for nitrogen. Indeed no tin nitrogenated compound is mentioned in the literature.

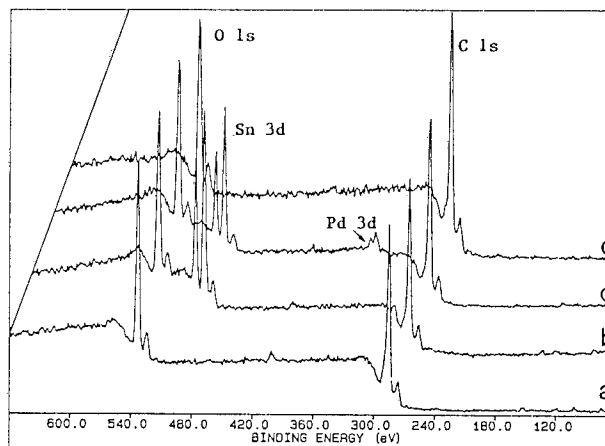


Fig. 1 - Survey spectra of polycarbonate samples treated by O₂ plasma (a), then by SnCl₂, SnCl₂ / PdCl₂ (c), PdCl₂ (d).

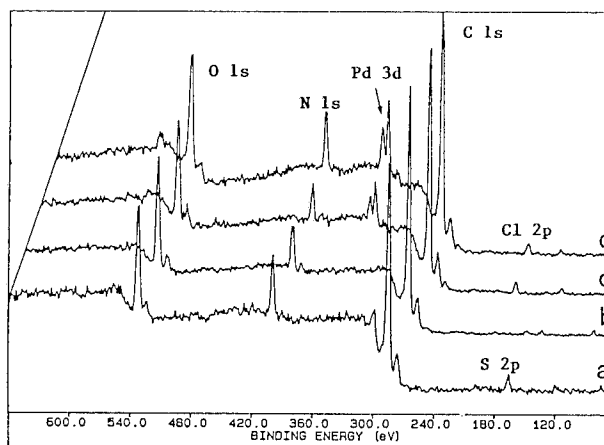


Fig. 2 - Survey spectra of polycarbonate samples treated by NH₃ plasma (a), then by SnCl₂ (b), SnCl₂ / PdCl₂ (c), PdCl₂ (d).

However, it does not completely explain the absence of tin on a polycarbonate surface grafted with nitrogenated groups because, besides these, there are oxygenated functions capable of reacting with Sn²⁺ ions. It appears that, in the reactive competition between oxygen and nitrogen atoms, the latter control the reaction and inhibit Sn²⁺ adsorption on the neighbouring oxygen atoms.

The above-mentioned results show, on the other hand, that palladium adsorbs either onto Sn²⁺ ions with which it is likely to form intermetallic compounds or complexes, or onto

nitrogen atoms for which it presents strong affinity. Indeed, many complexes of palladium II with 2 or 4 ammonia ligands are mentioned in the literature. Let us note that Hamaya et al. [5] have shown that palladium adsorbs on nitrogenated groups brought to a surface by an aminosilane treatment.

To determine the nature of the chemical bonds formed at the time of tin and palladium adsorption, C1s, O1s, N1s, Sn3d and Pd3d spectra were recorded for two samples respectively subjected to the following treatments: (a) O₂ plasma, (b) NH₃ plasma, (c) sample (a) followed by a sensitization / activation treatment by SnCl₂ / PdCl₂, (d) sample (b) followed by an activation treatment by PdCl₂. C1s and N1s spectra do not show any change after the sensitization / activation treatment or after the activation one when O1s spectra (Fig. 3) present a significant widening.

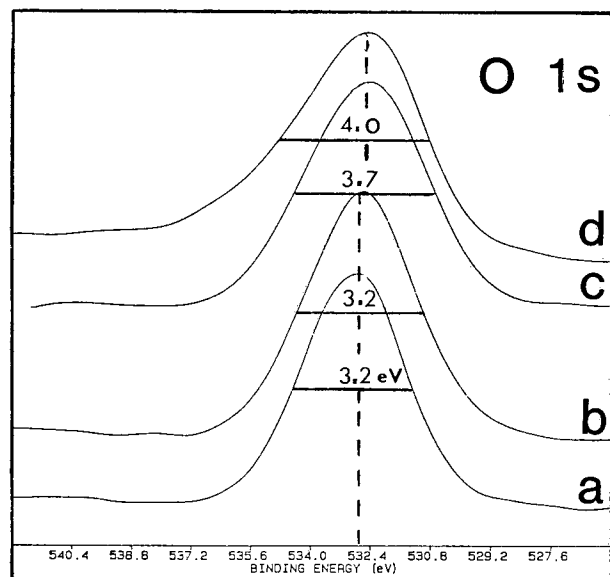
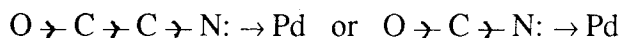


Fig. 3 - O1s spectra of polycarbonate samples treated by O₂ plasma (a), NH₃ plasma (b), sample (a) treated by SnCl₂ / PdCl₂ (c), sample (b) treated by PdCl₂.

Spectrum (b) which corresponds to Sn adsorption on oxygen atoms and to Pd adsorption on Sn shows a widening on the low binding energy side. The latter can be attributed to the O-Sn bond formation in which oxygen strongly attracts the bonding electrons. Spectrum (d) due to palladium chemisorption onto nitrogen

atoms after NH₃ plasma is widened towards the high binding energy side. It is an indirect evidence of N-Pd bond formation. Indeed, nitrogen atoms transfer their free pair of electrons to palladium resulting in a charge transfer which can be represented as follows:



Under these conditions, the electron density around oxygen is modified and the oxygen atoms attract the electrons of the O-C bond less strongly which results in the widening observed on the O1s peak.

XPS analyses show that tin is adsorbed on the oxygen atoms in the Sn²⁺ oxidized form. In the same way, palladium is chemisorbed, in all the cases, in the Pd²⁺ oxidized form.

CONCLUSION

This work shows the interest of modifying the polycarbonate surface by an NH₃ plasma prior to its metallization by the "electroless" process. This treatment grafts nitrogenated functions which are able to fix palladium directly on the nitrogen atoms by a one step process. The latter uses an acidic PdCl₂ solution which is stable and does not oxidize in air. Furthermore, the surface density of palladium is higher and its lateral distribution more homogeneous than those obtained by using a conventional two step process. This results in low-stressed metal / polymer interface and thick adhering metal films. The new simplified process described here for adsorbing palladium must give rise to a new interest for "electroless" metallization.

REFERENCES

1. E.M. Liston, L. Martinu, M.R. Wertheimer, J. Adhesion Sci. Technol., **7**, 10, 1091 (1993).
2. R.L. Cohen, J.F. D'Amico, K.W. West, J. Electrochem. Soc., **118**, 2042 (1971).
3. C.H. de Minjer, P.F.J.V.D. Boom, J. Electrochem. Soc., **120**, 1644 (1973).
4. R.L. Meek, J. Electrochem. Soc., **122**, 1478 (1975).
5. T. Hamaya, Y. Kumagai, N. Koshizaki, T. Kanbe, Chemistry Letters, 1461 (1989).

USE OF EVANESCENT WAVES FTIR SPECTROSCOPY FOR IN-SITU STUDY OF THE DEGRADATION OF POLYMER-SUBSTRATE SYSTEMS.

I. Linossier, F. Gaillard and M. Romand.

Département de Chimie Appliquée et Génie Chimique (CNRS, ERS 069), Université Claude Bernard LYON-1, 69622 Villeurbanne Cedex, France.

INTRODUCTION

The non-destructive analysis of buried interphases between solid substrates and polymers is gaining great interest in adhesion sciences but spectroscopic tools suitable for such studies are rare. The use of in-situ analysis by multiple internal reflection FTIR (MIR) has been suggested recently in order to carry out such analyses [1]. The MIR technique is interesting because of the low penetration (about one μm) of the evanescent infrared waves [2], which allows to analyse a strongly absorbing polymer in contact on the one side with a solid and on the other side with an aggressive medium such as water. In order to obtain chemical information on a polymer in the vicinity of a metal, an ultrathin (some nm) metallic layer can be deposited onto the reflection element.

This paper reports the capabilities of a home-made MIR cell for the in-situ determination of the water diffusion coefficient through thin PMMA films and for the study of water uptake at the interface of an adhesive-substrate system. Such investigations are carried out in order to assess the adhesion loss and therefore the durability of the corresponding joints.

EXPERIMENTAL

The cells used for horizontal and vertical MIR experiments are represented in Figures 1 and 2. These geometries allow to investigate respectively water diffusion through the thin

polymer film and at the polymer-substrate interface.

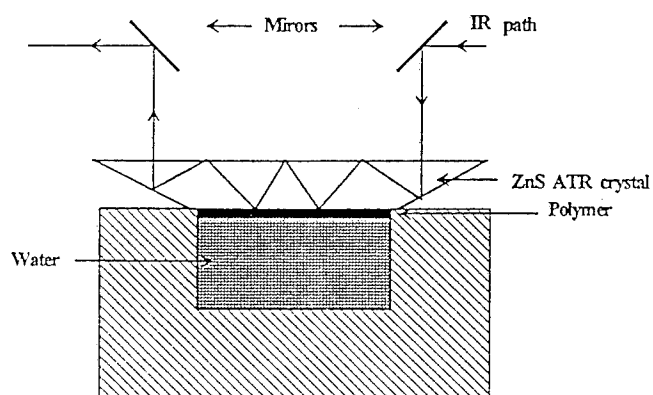


Fig 1. Horizontal MIR cell.

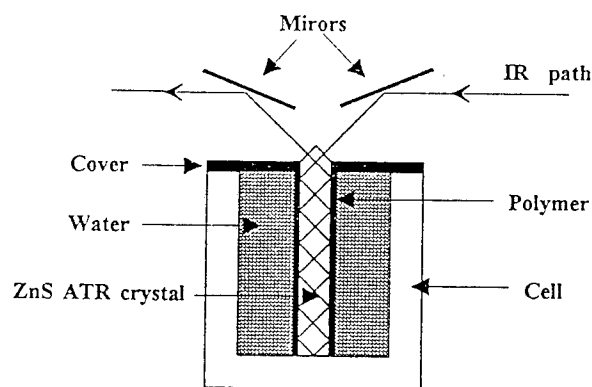


Fig 2. Vertical MIR cell.

The internal reflection element is made of ZnS ($n = 2.26$) bevelled at 22.5 degrees in order to obtain reflections under 45 degrees. The cell body is made of PTFE and mirrors of gold-coated silicon. For the applications reported here the cell is placed in a Nicolet 710 FTIR spectrometer equipped with a LN_2 -cooled MCT detector.

Typically 128 scans are collected to obtain a spectrum at a resolution of 4 cm^{-1} . The polymer films are obtained by casting PMMA ($M_w = 120000\text{ g.mol}^{-1}$, dissolved in chloroform) directly onto the internal reflection element.

RESULTS

Spectra in Figure 3 are relative to the water uptake by a PMMA film ($380\text{ }\mu\text{m}$ thick) studied at $25\text{ }^\circ\text{C}$ using the horizontal MIR configuration. The first recorded spectrum is taken as a reference (background). Subsequent results account for the progressive changes in the PMMA film near the internal reflection crystal. The water uptake of the interfacial zone can be studied by considering the band at about 3300 cm^{-1} , corresponding to $\nu(\text{O-H})$ vibration.

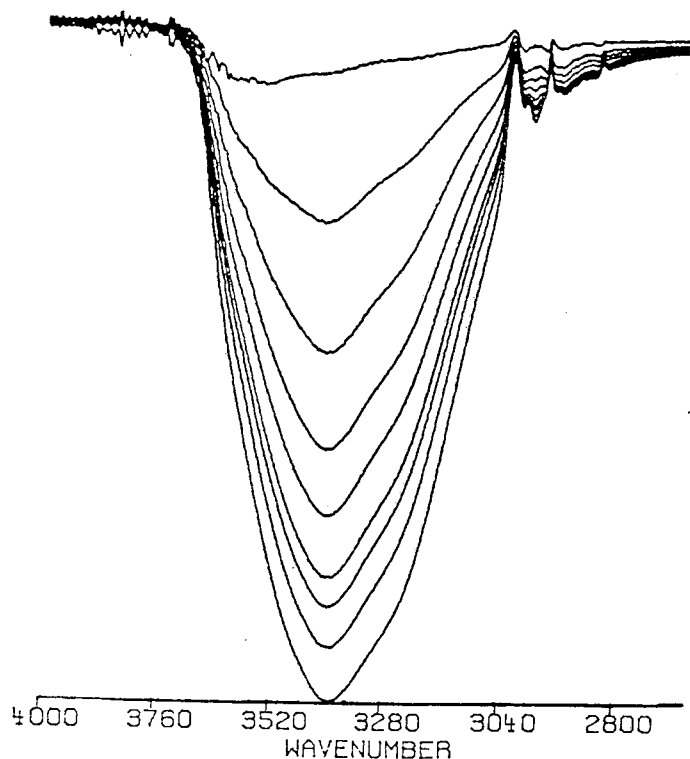


Fig. 3 Water uptake by a $380\text{ }\mu\text{m}$ -thick PMMA film (horizontal MIR cell).

In order to study by ATR the diffusion of water in polymer films, we use a simplified form of the Fick law as proposed by Fieldson and Barbari [3]:

$$\ln(1 - A_t / A_\infty) = \ln(4 / \pi) - (D \pi^2 t / 4 L^2)$$

where A_t and A_∞ are the values of the infrared absorbance at time t and at equilibrium, respectively, L the thickness of the polymer film and D the diffusion coefficient.

The value of D calculated from experimental results using this equation is $1.22 \cdot 10^{-8}\text{ cm}^2.\text{s}^{-1}$ which is close to literature data obtained on bulk PMMA by a gravimetric method [4].

The interfacial zone is known to be the weak part of a polymer-substrate assembly with respect to damage due to water diffusion. Then MIR investigations are carried out in the vertical operating mode in order to expose the interfacial zone directly to water penetration. The corresponding data are plotted in Figure 4 for films which are (a) $380\text{ }\mu\text{m}$ and (b) $1180\text{ }\mu\text{m}$ thick. The small change between the two curves corresponding to films of rather different thicknesses indicates that water diffusion along the interface is the prevalent phenomenon in such systems. The curve (c) in Figure 4 is calculated using the value of D determined previously and assuming only an 1D Fickian water diffusion through the thinnest film. This last phenomenon is much slower than diffusion at interface. These results highlight the necessity to take into account the water diffusion at the interface to assess the resistance of such assemblies to hostile environments.

The degradation of interphases in polymer-substrate assemblies has been proved to be largely dependent upon the surface treatment and therefore upon the resulting chemical reactivity of the substrate. In this case, results obtained by MIR in the vertical mode should be influenced by a chemical surface treatment of the internal reflection element. This has been confirmed by

the authors [5] who treated the ZnS crystal by an NH_3 radio-frequency plasma in order to improve its bondability. The vertical MIR experiments performed with a so-treated crystal resulted in an improved durability of the interfacial zone with respect to water diffusion. This can be related to a better adhesion resulting in the formation of a stronger and more resistant interphase.

CONCLUSION

The results presented here show that MIR FTIR spectroscopy is a tool well suited to determine the water (or other compound) diffusion coefficient in thin polymer films bonded to a substrate. The use of both vertical and horizontal MIR modes enables to distinguish between one-dimensional diffusion through the polymer layer and diffusion at (or near) the polymer-substrate interface. This last phenomenon has been shown to be far faster and dependent upon surface treatment of the substrate. The use of this technique could be of great help to assess the durability of polymer-substrate systems in hostile environments and to study in-situ chemical mechanisms involved in the interphase degradation.

REFERENCES

- [1] T. Nguyen, E. Byrd, C. Lin, *J. Adhesion Sci. Technol.*, **5** (9), 697 (1991).
- [2] N.J. Harrick, *International Reflection Spectroscopy*, (J. Wiley and Sons, New York, 1967).
- [3] G.T. Fieldson, T.A. Barbari, *Polymer*, **34** (6), 1146 (1993).
- [4] F. Bueche, *J. Polym. Sci.*, **14**, 414 (1954).
- [5] I. Linossier, F. Gaillard, M. Romand, European Conference on Adhesion, EURADH '94, September 12-15, 1994, Mulhouse, France. *Le Vide, les Couches Minces*, **272**, 346 (1994).

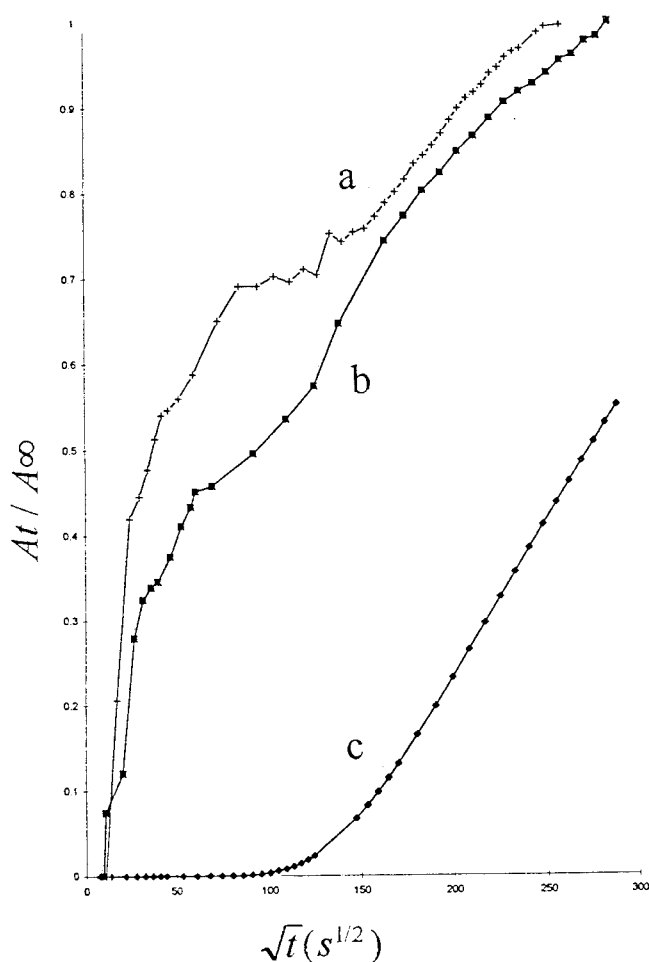


Fig. 4 Water uptake by (a) 380 and (b) 1180 μm thick PMMA films (vertical MIR cell). Simulation of water diffusion through the thinnest film (curve c).

INFLUENCE OF CHEMICAL, ELECTROCHEMICAL AND PHYSICAL SURFACE TREATMENTS OF AISI 304L ON ITS REACTIVITY - CONSEQUENCES ON ADHESION TO EPOXY RESINS.

F. Gaillard, E. Peillex and M. Romand.

Département de Chimie Appliquée et Génie Chimique (CNRS, ERS 069) Université Claude Bernard LYON-1, 69622 Villeurbanne Cedex, France.

INTRODUCTION

A wide range of treatments can be used to modify the surface of stainless steels prior to bonding [1,2]. The aim of this paper is to compare the effects of chemical (passivating), electrochemical (anodising) and physical (O₂ rf-plasma oxidising) treatments on the superficial composition of a stainless steel (SS). An attempt is made to correlate these results with the practical adhesion in epoxy/ treated SS systems, determined by a mechanical test.

Practical adhesion was determined using a three point flexure test [3].

Plasma treatments were performed in a reactor fed by an inductively coupled power source operating at a radio frequency of 15.56 MHz. Treatment gas was O₂ at a pressure of 100 mTorr, with a flow rate of 100 sccm. Power density was 0.53 W.cm⁻².

The surface treatments used are listed in Table I.

EXPERIMENTAL

Stainless steel sheets (1mm thick) used for this study were AISI 304L provided by Ugine, France. They were bonded to an epoxy resin AY103 with hardener AW134 (cured for 2 hours at 80°C) from Ciba Geigy.

The XPS data were recorded on an RIBER SIA 200 multitechnique (XPS, AES, ISS) spectrometer, equipped with a MAC2 analyser. The take-off angle of analysed photoelectrons was 30 degrees (near-grazing emission). Non-monochromatised MgK α radiation, from a dual anode (Mg/Al) system was used. Survey spectra were recorded at a resolution of 2 eV and narrow range spectra at better resolution i.e 0.9 eV. The maximum of the C1s peak envelope corresponding to carbon atoms bonded to other carbon and hydrogen atoms was assumed to be at 285.0 eV.

Name	Duration (t in s)	Treatment
ACET	300	Acetone degreasing in ultrasonic bath.
NFE	300	Etching in 15% HNO ₃ , 5% HF solution at 25°C
POt	5-300	Oxidising in rf O ₂ plasma 100 mTorr, 100 sccm
NPt	30 - 3600	Passivating in 65% HNO ₃ at 60°C
NAt	60 - 3600	Anodising in 65% HNO ₃ at 25°C under 0.5 mA cm ⁻²
SC	1800	Oxidising in concentrated H ₂ SO ₄ -K ₂ Cr ₂ O ₇ solution at 85 °C [1,2].
SCA	900	Anodising in concentrated H ₂ SO ₄ -K ₂ Cr ₂ O ₇ solution at 70 °C under 1.0 mA.cm ⁻² [1,2].

Table I. Surface treatments of AISI 304L.

RESULTS

The data given in Figure 1 are the results of XPS analyses of 304L samples treated as mentioned above. The main features reported here are : the area of C1s and O1s photoelectron peaks and the Cr / Fe atomic ratio. These results show that surface composition of AISI 304L can be varied over a wide range. Oxygen plasma treatments lead to a decrease of Cr/Fe ratio for treatments durations higher than 10s, as previously reported for another SS [4]. NA, SC, and SCA treatments produce the larger surface chromium enrichment. Such results confirm previous studies using AES [1] and x-ray emission spectrometry [5].

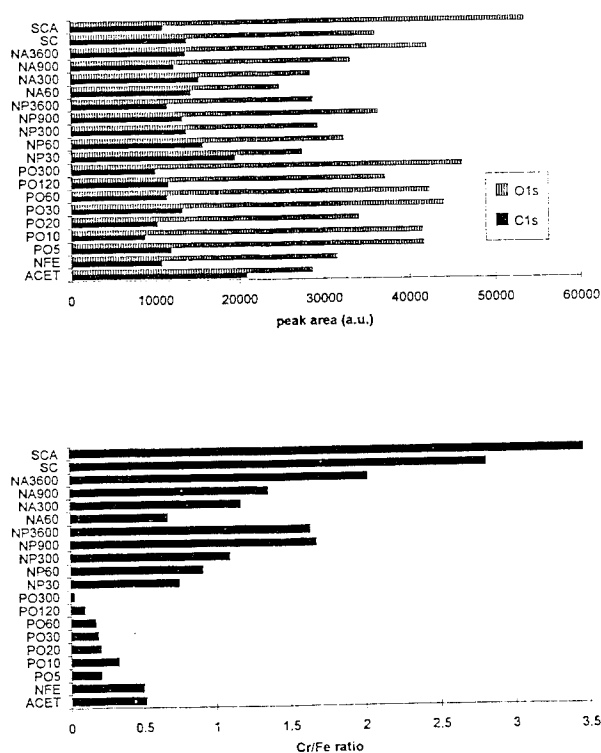


Fig. 1 Results of XPS analysis of surface treated 304L samples.

In order to determine the influence of the surface chromium enrichment on the strength of the bonded joints, some selected samples were glued with the epoxy resin, exposed 72 hours to 70°C, 95% HR, and tested mechanically. The parameter characteristic of the resistance of the bonded joint is here the maximal displacement (d_{max}) after sample failure. The variations of this parameter with the Cr / Fe ratio determined by XPS are plotted in Figure 2.

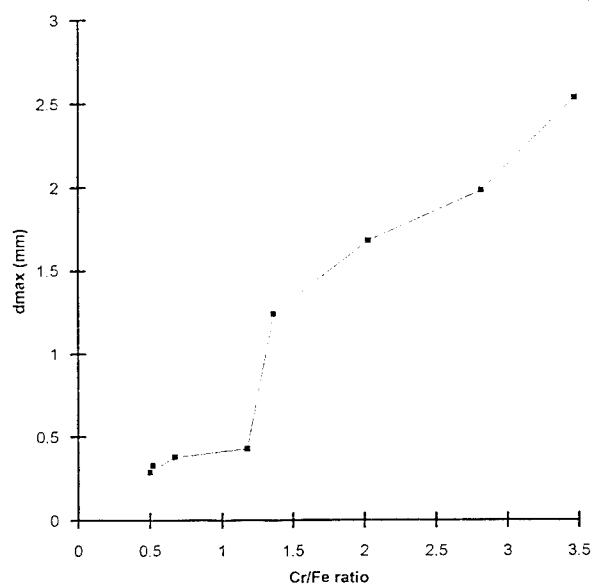


Fig. 2 Variations of d_{max} versus Cr / Fe ratio determined by XPS for various treated 304L samples.

Chromium-enriched SS surfaces lead to increased performances, as previously pointed out by R.P. Haak and T. Smith [1] using a wedge test. This change can be attributed to a modification of acid-base properties of the SS treated surfaces. An increased affinity of such chromium-enriched surfaces for basic probe molecules such as pyridine and ammonia has been shown by the authors using FTIR and thermal desorption analyses [6]. Of course, such surface treatments

can also influence some other parameters such as wettability, as recently shown in the literature [7].

CONCLUSION

This study allows a better understanding of the influence of stainless steel surface treatment on adhesion. Further work should consist in a quantitative approach using a monolayer-sensitive method such as ISS and model samples prepared by sputtering Cr and Fe with controlled proportions on perfectly flat silicon surfaces.

REFERENCES

- [1] R.P. Haak, T. Smith, *Int. J. Adhesion Adhesives*, **3** (1), 15 (1983).
- [2] F. Gaillard, Thesis, Lyon, France, 1987.
- [3] A. Roche, F. Gaillard, M. Romand and M. von Fahnestock, *J. Adhesion Sci. Technol.*, **1** (2), 145 (1987).
- [4] L. Deshayes, M. Charbonnier, N.S. Prakash, F. Gaillard, M. Romand, *Surf. Interface Anal.*, **21**, 711 (1994).
- [5] F. Gaillard, M. Romand, *Surf. Interface Anal.*, **12**, 491 (1988).
- [6] E. Peillex, F. Gaillard, M. Romand, J.P. Joly, D. Verchère, *J. Adhesion*, under press.
- [7] M. Mantel, J.P. Wightman, *Surf. Interface Anal.*, **21**, 595 (1994).

ADHESION OF RUBBER TO STEEL: THE USE OF PLASMA POLYMERIZED PRIMER FILM

Y.M. Tsai, F.J. Boerio and W.J. van Ooij
Department of Materials Science and Engineering
University of Cincinnati, Cincinnati, Ohio 45221-0012

Dong K. Kim
The Goodyear Tire & Rubber Company
Technical Center, Akron, Ohio 44316

INTRODUCTION

Adhesion of rubber to steel is of considerable practical importance in many areas of technology. For example, rubber is bonded to steel in the manufacture of steel-belted radial tires and engine mounts. However, direct adhesion of rubber to steel is very poor. As a result, steel tire cords are usually plated with brass, to which rubber adheres very strongly. But there are still some problems in bonding rubber to brass-plated steel. For example, the chemical waste of plating process is difficult to dispose of. Furthermore, brass-plated steel is vulnerable to corrosion because of the galvanic coupling of brass and steel.

The purpose of this paper is to describe results we have obtained in developing plasma polymerized primer films to enhance rubber-to-steel bonding. It is shown that plasma polymerized acetylene films are especially promising primers. Results obtained using a model rubber system to simulate reactions in the rubber/primer "interphase" are also described.

EXPERIMENTAL

A. Materials.--1010 cold-rolled steel (CRS) sheets of 0.5 mm thickness were obtained from The Goodyear Tire & Rubber Company (Akron, Ohio). The as-received substrates were mechanically polished to a mirror finish. Rubber compounds were also supplied by Goodyear. Laboratory-grade squalene ($C_{30}H_{50}$) was obtained from Aldrich.

B. Plasma polymerization.--Plasma polymerization and etching were carried out in a tubular reactor which was inductively coupled to an RF (13.56 MHz) power supply. Prior to plasma polymerization, the polished substrates were etched in an argon plasma at 1 Torr pressure, 20 W power, and 20 sccm flow rate for 10 minutes.

C. Adhesion measurements.--Miniature lap joints were prepared by using rubber as an "adhesive" to bond together pairs of steel adherends primed with plasma polymerized acetylene films. Ten joints could be prepared simultaneously in a specially designed mold in which the rubber "adhesive" was cured at 155°C under 133.44 kN

pressure for 35 minutes. The joint strengths (in N/64 mm²) were determined in an Instron at a strain rate of 20 mm/min.

D. Rubber model system.--A model rubber compound was prepared from squalene (100 parts per hundred parts of rubber, or phr), zinc oxide (10 phr), carbon black (10 phr), sulfur (5 phr), stearic acid (2 phr), DCBS, antioxidant, and cobalt naphthenate (each 1 phr). Polished steel substrates primed with plasma polymerized acetylene films were immersed into a stirred mixture of these materials at a temperature of 155 ± 5°C to simulate the curing of rubber against a primed steel substrate. At appropriate times between 1 and 100 minutes, substrates were removed from the mixture, rinsed ultrasonically with hexane, dried and examined using techniques such as XPS, SIMS and AES.

E. Analytical techniques.--A Perkin-Elmer Model 5300 XPS spectrometer with Mg K α X-rays, operating at 300 W and 15 kV DC, was used to obtain XPS spectra. Time-of-flight (TOF) SIMS analyses were performed on a KRATOS Prism instrument equipped with a reflectron-type mass analyzer and a 25 kV liquid metal ion source of ⁶⁹Ga⁺ ions, with a minimum beam size of 500 Å. Element depth profiling was done on a Perkin-Elmer 590A Scanning Auger Microprobe, sputtering with a beam of 1.5 keV Ar⁺ ions. The sputtering rate was 5 Å/minute calibrated for a Ta₂O₅ film of known thickness.

RESULTS AND DISCUSSION

A. Adhesion measurements

The breaking strength of lap joints prepared from polished substrates primed with PP acetylene films using argon as a carrier gas was 2007.8 N/64 mm² (standard deviation, σ =50.6 N) and was comparable to that of joints prepared from polished brass substrates, a average breaking strength of 2000 N/64 mm² (σ =67.8 N). When nitrogen was used as a carrier gas, the breaking strength of lap joints was still as high as 2014.5 N/64 mm² (σ =60.2 N) (see Figure 1). These strengths again compared well with the breaking strength of the joints from brass substrate. On the other hand, when oxygen was used as a carrier gas, the breaking strength of the lap joints prepared from plasma-

polymerized acetylene was only 1142.0 N/64 mm² (σ =298.3 N), a lower strength by a factor of two. The major reason for this low breaking strength was attributed to large amounts of oxygen incorporation in the plasma polymers which reduced the numbers of >C=C< bonds. It caused low breaking strengths due to the interfacial failure at rubber-plasma film interface and/or cohesive failure of plasma film which was evident from the low rubber coverage (about 30%) on the metal failure surface.

B. Rubber Model System

In an effort to determine the nature of reactions occurring in the "interphase" between rubber and plasma polymerized acetylene films, surface analysis techniques were used to examine primed steel substrates after reaction with a "model" rubber system in which natural rubber was replaced by squalene. This approach has been used previously by Van Ooij¹⁻².

XPS survey spectra showed strong Zn and S adsorption on the surface (see Figure 2), while only a small amount (about 0.5%) of cobalt was also observed. Although both cobalt and zinc accelerator complex were intermediates to the crosslinking of the plasma polymer with squalene, XPS surface analysis demonstrated clearly that the Zn adsorption was more intense than cobalt adsorption on the surface.

High resolution XPS S(2p) spectra obtained from a PP acetylene film after 35 minutes reaction time within squalene-based mixtures are shown in Figure 3. A peak attributed to cobalt and zinc sulfide was observed at a binding energy near 161.9 eV. The broad peaks centered around 163.5 eV and 164.3 eV in S(2p) spectra were assigned to -S_n- which was present in the forms of ineffective or pendant sulfur as well as effective or crosslinked sulfur. However, the relative ratio of peaks at 163.5 to 164.3 eV was much larger for experiments conducted in cobalt-containing mixtures than in mixtures without cobalt³. This seemed to indicate that the presence of Co resulted in shorter bridges as it has been found that the more polysulfidic bonds, the higher the observed binding energy¹.

From TOF-SIMS investigations, it was observed that the intensity of peaks at -24 and -25 amu assigned to mono-substituted and di-substituted acetylene, the intensities of peaks at +12, +26, +27, +39, +50/51, +77, +91, and +128 amu *etc.*, which are typically formed by unsaturated or aromatic hydrocarbons, were much lower in the PP acetylene film after reaction in squalene mixtures than in the as-prepared plasma polymer film. These were indications of the reaction between squalene mixtures and PP acetylene film. Some other interesting features were also noted. They are summarized as follows:

- Evidence of crosslinking was observed by the presence of peaks at -64 amu (due to S₂⁻), -96 (S₃⁻) and -128 amu

(S₄⁻) as well as the absence of a peak at -97 amu (due to HSO₄⁻);

- Peaks related to the sulfenamide part of the accelerator were seen at -134 and -166 amu in all samples after reaction in the squalene-based mixture. The amine part (+182 amu) was also strongly adsorbed;

- The intensity of Co on the surface was very high after 15 minutes of reaction and then dropped after this time. On the other hand, the Zn concentration was more intense after 35 minutes reaction than after 15 and 65 minutes reaction. This result was confirmed by XPS analysis;

Auger depth profiles of PP acetylene films before and after reaction in squalene mixtures revealed the continuous nature of the films prepared by the plasma deposition method. The very sharp profile between iron and carbon in the interface region showed that the pretreatments (including polishing and argon plasma etching) of the steel resulted in a clean steel surface. This prevented plasma polymer film from reacting with the low molecular weight impurities to form weak boundary layers.

Figure 4 is an expanded Auger depth profile of a plasma polymer film after 65 minutes in squalene mixture. Auger analysis revealed that the first few surface layers consisted of carbon, zinc, cobalt, and sulfur. The high sulfur concentrations on the surface were attributed to the metal sulfides (*i.e.*, zinc sulfide and cobalt sulfide). The sulfur concentration was higher on the surface than dropped in the plasma polymer film, but increased again at the plasma polymer/steel interface. On the other hand, the oxygen peak at the interface decreased with increasing reaction time in squalene mixtures. It appeared that the iron oxide had, in part, been converted to iron sulfide. An interesting feature about the reaction sequence of the zinc and cobalt can also be clarified from this figure. Zn was observed on top of Co in the outermost surface, indicating that the cobalt salt reacted with the accelerator first to form a cobalt perthiomeraptide intermediate which promoted the crosslinking reaction of plasma polymer film with squalene. Then, a zinc complex was formed and further promoted the crosslinking reaction between plasma polymer film and squalene on the top of the squalene/plasma polymer film promoted by cobalt complex.

CONCLUSION

Plasma polymerized acetylene films using argon or nitrogen as a carrier gas were excellent primers for rubber-to-steel bonding. Miniature lap joints prepared by using rubber as an "adhesive" to bond together pairs of steel adherends primed with plasma polymerized acetylene films were as strong as similar joints prepared using polished brass substrates. Failure of such joints was 100% cohesive in the rubber. Plasma-polymerized acetylene film

using oxygen as carrier gas would not be a good choice for adhering rubber to steel. It caused the low bonding strength at rubber-plasma film interface.

However, because of the excellent adhesion of rubber-to-plasma polymerized acetylene film, cohesive failure of rubber occurred in most instances. This made the study of the plasma polymer/rubber interface more difficult. Hence, a simulation, using a rubber "model" system, was conducted to investigate the possible interaction between rubber and plasma polymer film. The results obtained using XPS, SIMS, and AES showed that sulfur diffused through the primer, forming a layer of sulfide at the primer/substrate interface. Zinc and cobalt sulfides and perthiomeraptides, which formed at the interface between squalene and the plasma polymerized acetylene primer, catalyzed the reaction between squalene and primer. Crosslinks between squalene and the primer were mostly mono-sulfidic although some evidence for di- and tri-sulfidic crosslinks was observed.

ACKNOWLEDGMENT

This research was supported in part by a grant from the Edison Materials Technology Center (EMTEC) and National Science Foundation.

REFERENCES

1. W.J. van Ooij and A. Kleinhesselink, *Appl. Surf. Sci.*, **4**, 324 (1980).
2. W.J. van Ooij, W.E. Weening, and P.F. Murray, *Rubber Chem. Technol.*, **54**, 227 (1981).
3. Y.M. Tsai, F.J. Boerio, W.J. van Ooij, D.K. Kim, and T. Rau, paper presented at the Third International Conference on Adhesion and Surface Analysis, Loughborough, UK, April 12-14, 1994. To be published in *Surf. Interf. Anal.*

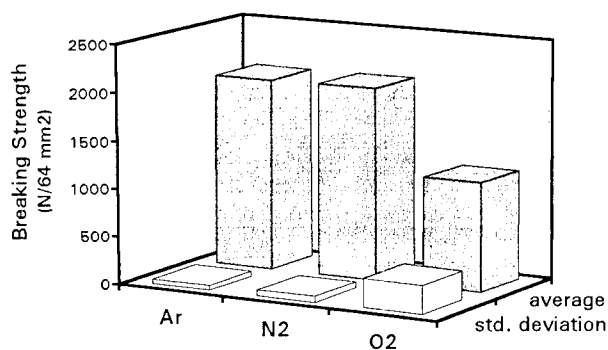


Figure 1. Comparison of breaking strengths of joints prepared from plasma-polymerized acetylene films using various carrier gases.

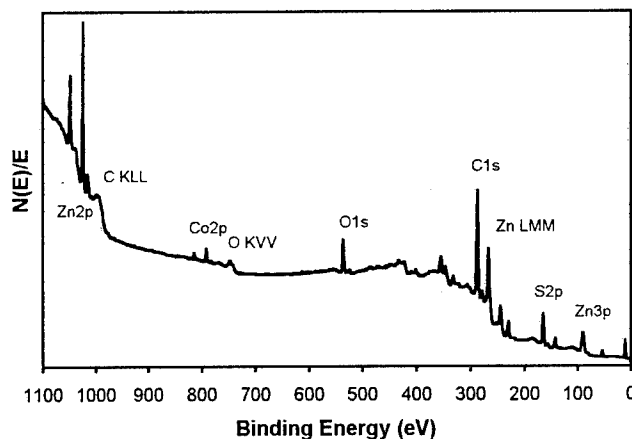


Figure 2. XPS survey spectrum obtained from plasma polymerized acetylene film after 35 minutes reaction in the squalene-based mixtures.

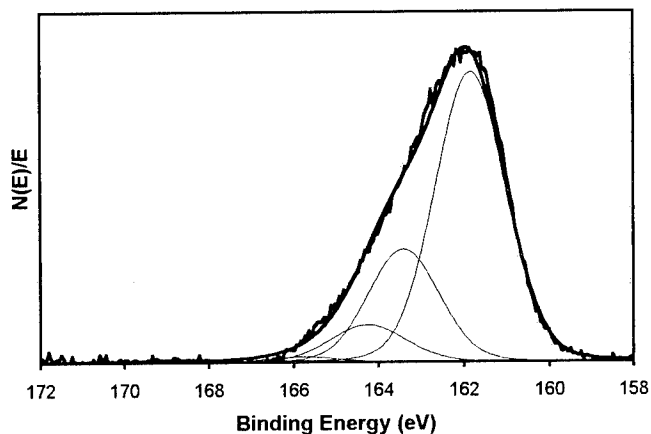


Figure 3. High resolution S(2p) XPS spectrum obtained from plasma polymerized acetylene film after 35 minutes reaction in the squalene-based mixtures.

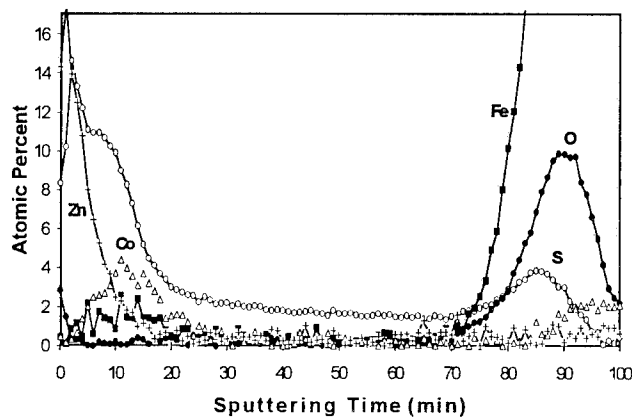


Figure 4. Expanded Auger depth profile of plasma-polymerized acetylene film after 65 minutes reaction in squalene-based mixtures.

PLASMA POLYMERIZED SILICON CONTAINING PRIMERS FOR ALUMINUM

C.E. Taylor, I. Scgall, and F.J. Boerio
Department of Materials Science and Engineering
University of Cincinnati, Cincinnati, Ohio 45221-0012

D.J. Ondrus
Ford Motor Company, AMDC
24500 Glendale Ave.
Detroit, MI 48239

S.M. Ward and R.A. Dickie
Polymer Science Department, Ford Motor Company
Dearborn, Michigan 48121-2056

INTRODUCTION

Plasma polymerization can produce continuous, pinhole free organic or inorganic polymer films that adhere well to a variety of different substrates.[1,2] The objective of this research was to develop plasma polymerized hexamethyldisiloxane films for use as corrosion inhibiting primers in the adhesive bonding of aluminum (Al). Hexamethyldisiloxane (HMDS) was deposited on to Al coupons in a radio frequency (RF) plasma reactor. Reflection-absorption infrared spectroscopy (RAIR) was used to characterize the bulk plasma polymer. X-ray photoelectron spectroscopy (XPS) and scanning electron microscopy (SEM) were used to study the film surfaces and the interface between the plasma polymerized film and the Al. The thickness of the plasma polymerized films was measured with ellipsometry. Lap shear joints were used to measure the durability of the Al/plasma primer/adhesive system.

EXPERIMENTAL

For lap joints Al alloy 6111 was cut into coupons and cleaned ultrasonically in acetone or degreased in acetone, etched in a solution of chromic and sulfuric acid and rinsed with distilled deionized water. For RAIR and ellipsometry, Al coupons were mechanically polished to a mirror finish with silicon carbide paper, aluminum oxide slurries and a magnesium oxide slurry. Plasma treatments and deposition were all carried out in a glass tubular reactor that was inductively coupled through external electrodes to an RF power source controlled by an impedance matching network.[3] Al coupons were placed in the afterglow region of the plasma. Coupons that were only acetone cleaned were also etched in an argon plasma at 25 Watts of power, a pressure of 0.5 Torr and an argon flow rate of 25 sccm. All films were less than 1000 Å thick. Depositions were carried out at 50 Watts of power, a pressure of 0.5 Torr and an oxygen/HMDS flow rate of 20/0.5 sccm.

For stress durability testing, lap joints were prepared using a modification of ASTM standard D1002-72. A 3" x 1" Al coupon primed with a plasma polymer was bonded with a proprietary automotive adhesive to a 3" x 1" Al coupon that had received a proprietary inorganic pretreatment. These joints were placed under load and exposed to cycles of corrosive environments. Each 24 hr cycle consisted of 15 min in a 5% aqueous solution of sodium chloride, 1 hr and 45 min drying at room temperature and 22 hrs in a humidity chamber at 90% RH and 50°C. The time to failure was compared to the time to failure for lap joints prepared without a primer and with the industry standard treatment (about 30 cycles).

The approximate thickness of plasma films deposited on polished substrates was determined using a Rudolph Research 436 ellipsometer.

RAIR spectra were obtained at grazing angle using a Perkin-Elmer 1800 Fourier-transform infrared spectrophotometer equipped with an external reflection accessory from Harrick Scientific. RAIR spectra of plasma polymerized coatings on polished Al were obtained by averaging 128 scans. The spectra reported here are difference spectra obtained by subtracting the baseline spectra of the polished metal from spectra of the plasma polymerized film on the polished Al.

XPS spectra were obtained using a Physical Electronics 5300 X-ray photoelectron spectrometer. Mg K α radiation at a power of 300 Watts was used as the excitation source. The pass energy was 44.75 eV and 17.90 eV for the survey and multiplex spectra respectively. The multiplex spectra were corrected for charging by referencing the C(1s) hydrocarbon peak to 284.6 eV. Alternating depth profiling was performed with a differentially pumped ion gun using argon gas.

SEM micrographs of the surfaces of plasma polymerized films deposited onto acid etched Al were obtained from an Amray field emission scanning microscope model 1845FE.

RESULTS AND DISCUSSION

The RAIR spectrum of a plasma polymerized HMDS film that was deposited with oxygen as a carrier gas showed a strong band related to Si-O-Si stretching vibrations near 1220 cm^{-1} . A band due to vibrations of non-bridging Si-O bonds (Si-OH) was observed at 938 cm^{-1} . Bands due to O-Si-O and Si-O-Si bending were seen at 800 and 490 cm^{-1} , respectively. A broad band located near 3360 cm^{-1} was assigned to O-H stretching. Since bands due to carbon containing functional groups or siloxane structures of the monomer were not observed, the plasma polymerized film was thought to be inorganic, consisting of silicon oxides.[4,5]

In the XPS survey spectra of a plasma polymerized HMDS film the peak assigned to carbon near 285 eV was very weak and the O 1s peak near 534 eV was very strong. Peaks due to Si were seen near 154 and 103 eV . The elemental composition of the film surface was 3% C, 71% O and 26% Si. The high resolution Si2p spectrum revealed one peak located near 102.6 eV , indicating that the silicon was oxidized. Confirming RAIR results, XPS data showed that the structure of the plasma polymerized film was silica-like. The high Si:O ratio (1 to 2.7) suggested the presence of nonbridging Si-O bonds as seen in the RAIR spectrum.

The durability of Al/epoxy joints constructed using this plasma polymer as a primer was of practical importance. Joints made of clean Al adherends without a primer failed after an average of 18 cycles of stress durability testing. Adhesive joints made from adherends primed with the silicon oxide primer, but not acid pretreated, failed after only 2 to 3 cycles. Since Al and Mg were seen with XPS on at least one failure surface of each joint, it was concluded that the interface between the primer and the Al substrate was weak and unstable in corrosive environments. Magnesium oxide is known to preferentially form at the surface of Al alloys with a high content of Mg. Magnesium oxide has also been shown to be detrimental to the durability of the oxide/metal interface.[6,7] Al substrates were etched in a chromic sulfuric acid solution to remove the magnesium oxide layer from the surface. Excellent stress durability test results were obtained from joints prepared from acid etched Al, primed with a plasma polymerized silicon oxide film. These joints failed after approximately 90 cycles in corrosive environments. However, the Al/primer/adhesive interfaces remained intact, but the Al failed due to galvanic corrosion around the bolt that held the joint in tension.

A scanning electron micrograph of a plasma polymerized HMDS silica-like film deposited on acid etched Al are shown in Figure 1. From the micrograph of the plasma polymer on Al, the film was seen to be continuous and pinhole free. The entire substrate surface was covered

with spherical particles including the etch pits that resulted from the Al acid etching pretreatment. The polymer film was formed of sphere shaped particles deposited next to each other and impinging upon one another.

Wertheimer and coworkers [1,2] have seen similar sphere structures in plasma polymerized HMDS siloxane films deposited at low (25°C). These spheres were thought to begin as nucleation sites for growth in the gas phase. The resulting film structure consisted of powder particles imbedded in a continuous film matrix. These plasma polymerized siloxane films did not protect Al coated glass slides from delamination in alkaline solutions. However, smooth silica films deposited at high substrate temperatures (400°C) did perform well as protective coatings. Contrastingly, our silica films which contained many particles performed exceptionally well as corrosion resistant primers for Al. Because of the excellent performance of silica-like films as primers, it was thought that the spherical structures were not merely weakly bound powder particles but were cohesively strong structures that could provide surface roughness for mechanical keying of the adhesive to improve adhesion.

In order to determine the chemical structure and bonding at the interface between the plasma polymerized film and the Al, a model system was used. A 100 \AA thick plasma polymerized silica film was deposited on an evaporated Al film supported by a glass slide. XPS was used to alternately sputter and acquire C1s, Al2p, Si2p and O1s spectra. This resulted in a profile of C, Al, Si and O concentrations as a function of distance through the primer to the Al. A plot of preliminary data shown as atomic concentration as a function of sputtering time is displayed in Figure 5. The Si and O concentrations decreased and the Al concentration increased as the plasma film was sputtered. Several changes in the O1s region were observed as a function of sputtering time. Initially, one peak was observed characteristic of the plasma polymerized silicon oxide primer. As the interface was approached, this peak became broad and asymmetric. After approximately 200 minutes of sputtering the O1s peak had shifted 1.4 eV to a lower binding energy possibly indicating a shift from silicon oxide to Al oxide. Before sputtering the Si2p region was characterized by one peak due to oxidized silicon that broadened and shifted to lower binding energy as the interface was approached. This suggested the presence of less oxidized silicon at the interface. High resolution Al2p spectra also showed that at the interface the Al was in the form of Al oxide. However, as sputtering continued into the evaporated Al film, metallic Al was observed. No carbon was seen at the interface suggesting that when the Al was first exposed to the HMDS and oxygen plasma, hydrocarbon contamination on the surface was removed. Oxygen plasmas have been shown to effectively remove organic

contamination from metal surfaces [8]. Free radical reactions of atomic oxygen and organic material form volatile CO, CO₂ and H₂O that are removed by vacuum pumping [9]. The interface between a plasma polymerized silica film and an evaporated Al film was free of carbon and contained Si and Al oxides. Further investigations of the interface are in progress

CONCLUSIONS

Plasma polymerized films from HMDS and oxygen have been shown to perform very well as primers for the adhesive bonding of Al. Lap joints prepared with silica-like primers deposited onto acid etched Al have shown exceptional durability in corrosive environments. The plasma deposition itself has been shown to effectively remove hydrocarbon contamination from the Al surface and to create a stable interface consisting of Al and silicon oxides.

ACKNOWLEDGMENTS

This work was supported by grants from the EPRI Center for Materials Fabrication, Ford Motor Company, the National Science Foundation and the Environmental Protection Agency.

REFERENCES

1. H.P. Schreiber, J.E. Klemberg-Sapieha, E. Sacher, and M. R. Wertheimer, in *Polymeric Materials for Corrosion Control*, ed. R.A. Dickie and F.L. Floyd, American Chemical Society, Washington, D.C., (1986).
2. M.R. Wertheimer, J.E. Klemberg-Sapieha and H.P. Schreiber, *Thin Solid Films*, **115**, 109, (1984).
3. F.J. Boerio, C.E. Taylor, S.J. Clarson, D. B. Zeik, W.J. van Ooij, and A. Sabata, paper presented at ASM/ESD Advanced Coatings Technology Conference, Chicago, IL, November 3-5, 1992.
4. N.B. Colthup, L.H. Daly and S.E. Wiberly, *Introduction to Infrared and Raman Spectroscopy*, Academic Press, San Diego, California, (1991).
5. N.P. Bansal, *Journal of the American Ceramic Society*, **71**, 666 (1988).
6. A.J. Kinloch, *Journal of Materials Science*, **17**, 617 (198).
7. A.J. Kinloch and N.R. Smart, *Journal of Adhesion*, **12**, 23 (1981).
8. D. Korzec, J. Rapp, D. Theirich and J. Engemann, *Journal of Vacuum Science and Technology A*, **12**(2), 369 (1994).
9. D.M. Manos and D.L. Flamm, *Plasma Etching: An Introduction*, Academic Press, 167-169 (1989).

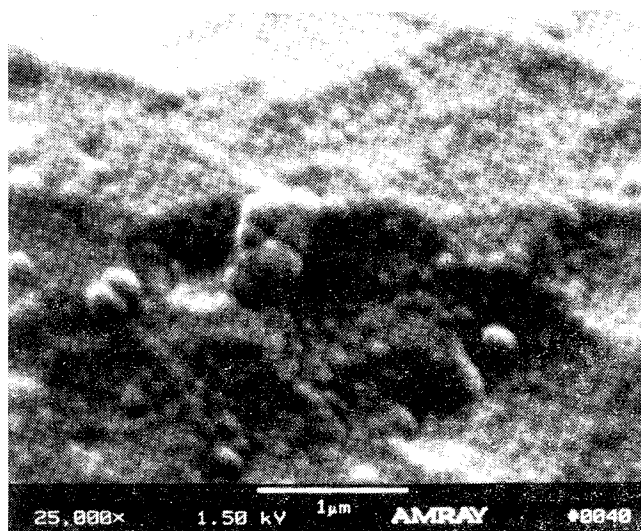


Figure 1. SEM micrograph of a plasma polymerized HMDS film deposited on acid etched aluminum using oxygen as a carrier gas.

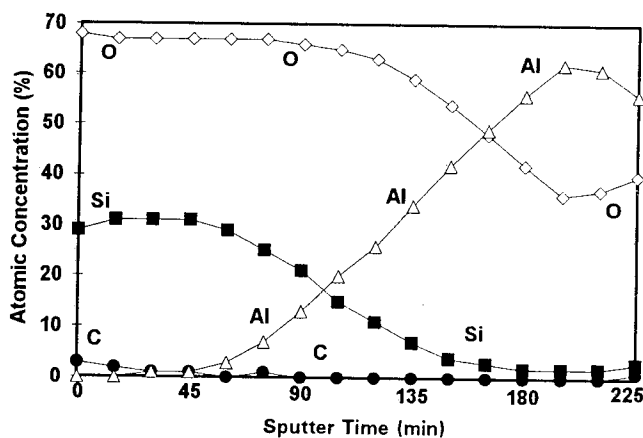


Figure 2. XPS depth profile of 100 Å thick plasma polymerized silica film deposited on evaporated aluminum supported by a glass slide.

CARBON FIBER/ MATRIX ADHESION IN HIGH PERFORMANCE COMPOSITES: THE INFLUENCE OF CARBON FIBER SURFACE PROPERTIES

H. Zhuang and J. P. Wightman

Chemistry Department
NSF Science & Technology Center
Center for Adhesive & Sealant Science
Virginia Polytechnic Institute & State University
Blacksburg, VA 24061

INTRODUCTION

Fiber reinforced composites are multi-phase systems in which the nature of fiber-matrix adhesion is a very important parameter in controlling the strength and toughness of composites. In order to improve interfacial adhesion, a better understanding of the effects of physical-chemical surface properties is critical. In the present work, carbon fibers with different surface morphology, surface chemistry, and surface energy were incorporated with epoxy resins. The strength, as well as the temperature dependence of interfacial adhesion was evaluated.

EXPERIMENTAL

Materials

The carbon fibers and their sources used for this study are summarized in Table 1.

Table 1. Carbon fibers and sources

Fiber	Producer	Surface Oxidative Treatment
AS-4	Hercules	Treated
AU-4	Hercules	Untreated
Panex 33	Zoltek	Treated

Epon828(Shell) epoxy resin cured with amine curing agents, meta-phenylenediamine (mPDA) (Aldrich) and Jeffamine DU-700 (Texaco), was used as matrix.

Surface Analysis

Carbon fiber surface topography was examined by scanning electron microscopy (SEM). Imaging was performed at 20 eV .

Fiber surface chemical characterization was performed with X-ray photoelectron spectroscopy (XPS). Spectra were collected with a Perkin-Elmer PHI 5300 spectrometer employing a Mg K α X-ray source operated at 15 kV with a power of 400 watts and a take-off angle of 45°.

Fiber surface energy was determined using a series of immiscible two liquids in a CAHN dynamic contact analysis system. Both dispersive and polar components of the surface free energies were obtained via the method developed by Schultz *et al.*^[1]

Fiber/Matrix Adhesion Measurement

Single fiber fragmentation test proposed by Kelly and Tyson^[2] and employed by Drzal *et al.*^[3] was conducted to evaluate the fiber/matrix adhesion. Dogbone shaped single fiber composite was pulled in tension at a cross head speed of 1 mm/min. and fiber break length was measured under transmitted cross polarized light. Interfacial stress transfer coefficient τ is calculated by:

$$\tau = \frac{\sigma_f d}{2l_c}$$

where d is the fiber diameter and σ_f is the tensile strength of the fiber at the critical length, l_c .

RESULTS AND DISCUSSION

Surface Analysis

Fiber surface topography by SEM showed that Panex 33 fibers had a rather rough surface with striations parallel to its

length, whereas AS-4 and AU-4 fibers were essentially featureless and smooth at 10K magnification.

The chemical composition of fibers obtained by XPS analysis is given in Table 2. It was observed that commercial surface treatment increased the surface oxygen content. A considerable amount of sodium was detected on the Panex 33 fiber surface.

Table 2: fibers surface concentrations (atomic %)

Fiber	C	O	N	Na
AU-4	94.4	3.1	2.5	0.04
AS-4	84.1	12.0	3.6	0.34
Penex 33	80.3	9.1	7.6	3.0

The dispersive (γ^d) and polar (γ^p) components of the surface free energy for the as received fiber are shown in Table 3. The commercially surface treated fibers (AS-4 and Panex 33) exhibited both a large total surface energy and a large polar component. This result parallels the high oxygen concentration observed by XPS.

Table 3: Surface energies of carbon fibers (mJ/m²)

Surface Energy	AU-4	AS-4	Panex 33
γ^{total}	53.2	73.2	70.4
γ^d	46.4	56.9	50.9
γ^p	6.86	16.3	19.5

Fiber/Matrix Adhesion

The single fiber composites were prepared by imbedding single fibers in the epoxy resins. Values of interfacial stress transfer coefficient (ISTC) calculated from single fiber fragmentation test are listed in Table 4. Compared with the AU-4 fiber, the AS-4 and Panex 33 fibers with high surface oxygen content and high surface energy produced stronger interfacial adhesion in both matrixes. Panex 33 fibers did not give larger ISTC values because of mechanical interlocking formed on the rough fiber surface.

Table 4: Interfacial stress transfer coefficients (MPa)

Fiber	Epon828-mPDA	Epon828-DU700
AU-4	34.3	22.9
AS-4	56.6	37.4
Panex 33	48.4	32.1

The temperature dependence of interfacial adhesion was also measured. Interfacial stress transfer coefficients decreased with elevated temperature. The Panex 33 fiber system showed enhanced durability at high temperature implying that improvement in temperature durability may be realized by surface roughness.

SUMMARY

Surface analysis has shown that significant changes in surface chemistry are produced by commercial surface treatment. Surface compositional changes were observed to manifest themselves in changes of fiber surface energy and subsequent changes in the strength of interfacial adhesion. Preliminary findings indicate that improved temperature durability may be achieved through the fiber surface roughness, although the initial interfacial strength appears not to be improved.

ACKNOWLEDGMENTS

Research support by McDonnell Douglas Aerospace is gratefully acknowledged.

REFERENCES

1. J. Schultz, C. Cazeneuve, M. E. R. Shanahan and J. B. Donnet, J. Adhesion **12**, 221 (1981).
2. A. Kelly and W. R. Tyson, J. Mech. Phys. solids **13**, 329 (1965).
3. L. T. Drzal and P. J. Herrera-Franco in Engineered Materials Handbook, v.3, Adhesives and Sealants, ASM International (1990), pp. 394.

TIME AND TEMPERATURE DEPENDENT FRACTURE OF A MODEL RUBBER TOUGHENED EPOXY: FAILURE ANALYSIS

K. L. Urban, M. D. Rakestraw, T. Chang, N. E. Shephard, D. A. Dillard
T. C. Ward and J. G. Dillard

*The Center for Adhesive and Sealant Science, Virginia Polytechnic Institute and State University
Blacksburg, VA 24061-0201*

INTRODUCTION

Theories of viscoelasticity predict that the mechanical properties of adhesives are affected by temperature and loading rate. Therefore to fully understand an adhesive's properties, one needs to characterize the material's mechanical behavior at different temperatures and loading rates. Five model rubber toughened epoxy systems were prepared with different levels of rubber toughener. Single-edge-notch bend (SENB) specimens were tested to characterize the critical-stress intensity factor, K_{IC} , as a function of the rate and temperature of loading. Previous research has demonstrated the usefulness of relating the fracture energy to the topology of the failed surface[1]. The failure surfaces were analyzed by using scanning electron microscopy (SEM).

MATERIALS

Five model epoxy systems with various amounts of rubber toughener were prepared as described by Rakestraw et. al.[2]. The five levels of rubber are 0, 4.2, 8.1, 11.6 and 15.0%, and the epoxy systems are labeled A, B, C, D and E respectively. The rubber toughener phase separates during cure to form micron size rubber domains in the epoxy matrix.

METHODS

Single-edge-notch bend specimens were fabricated of the five model epoxies. Each was tested according to ASTM D 5045 standard using a three point bend apparatus in an Instron 4505 [3]. The loading rate was 1 mm/min. Another study was performed on formulation C. The loading rate and temperature were varied. At 20°C the rates of loading were .001, .01, .1, 1 and 10 mm/min. , and at 60°C the rates of loading were .001, .01 and 10 mm/min.

Scanning electron micrographs (SEM's) were taken using an International Scientific Instrument model SX-40 with a beam voltage of 20 kV. The fracture surfaces of the SENB specimens were nonconducting. Therefore, a layer of gold was sputter coated on the surfaces to prevent surface charging during the experiment. An Edwards Sputter Coater model S150 was used with 40 mA current at 0.9 kV. The gold layer was sputtered for 3 min. and was approximately 300-500 Å thick.

EXPERIMENTAL RESULTS

In general the K_{IC} values increase as the rubber toughener level increases (Fig. 1). The increase in

toughness can be directly related to the size of the craze zone at the crack tip (Fig. 2). Numerous holes can be seen in the craze zone. This can be attributed to the rubber toughener (Fig. 5a). In the crack region past the craze zone, the holes are indistinct (Fig. 5b). This is the region of brittle fracture. Failure occurs through the rubber domains instead of around them.

The K_{IC} values decrease as the loading rate increases (Fig. 4). Again, the craze zone size correlates directly with the K_{IC} values (Fig. 3). This is in good agreement with the expected viscoelastic response. K_{IC} values measured at 60°C were essentially the same at 1.9 MPa(m)^{1/2}. This independence of fracture energy with respect to rate can be attributed to the significant crazing which occurs throughout the fracture plane (Fig. 5c). In addition, the number of holes left by the rubber toughener has increased with respect to the same sample fractured at room temperature (Fig. 5d).

SUMMARY AND CONCLUSIONS

The fracture energy of a model rubber toughened epoxy system has been related to the rubber content, loading rate and test temperature. The fracture surfaces have been analyzed by scanning electron microscopy. The fracture energy increases whenever there is an increase in the size of the craze zone. The extent of crazing can be increased by increasing the rubber toughener concentration, increasing the testing temperature or by decreasing the loading rate.

ACKNOWLEDGMENTS

The authors would like to thank the National Science Foundation Science and Technology Center: High Performance Polymeric Adhesives and Composites for their financial support. We also appreciate the support of the Center for Adhesive and Sealant Science and acknowledge The Dow Chemical Company for supplying the materials.

REFERENCES

1. Liechti, K. M. "Fracture Testing and Failure Analysis," in *Engineered Materials Handbook Vol 3.*, C. A. Dostal, Ed. ASM International, 1990, pp. 335.
2. Rakestraw, M. D.; Taylor, M. W.; Lai, Y. H.; Chang, T. and Dillard, D. A., abstract in this document.
3. *Annual Book of ASTM Standards*, Vol. 15.06 Adhesives, ASTM, Philadelphia, (1994).

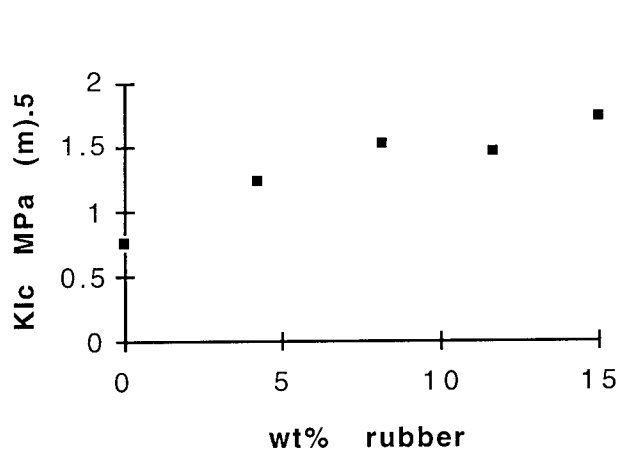


Fig. 1--Fracture Energy versus Wt % Rubber, 20°C, 1 mm/min.

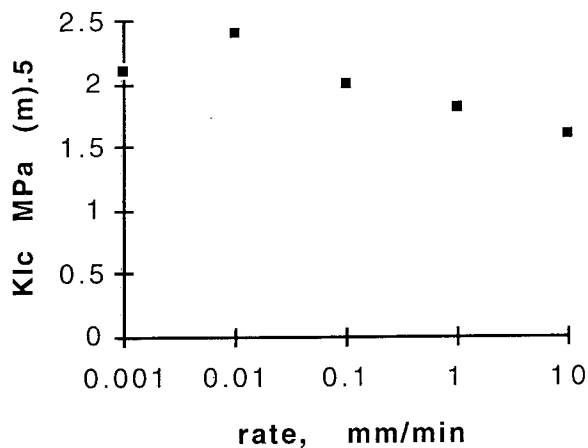


Fig. 4-- Fracture Energy versus Loading Rate of Formulation C, 20°C.

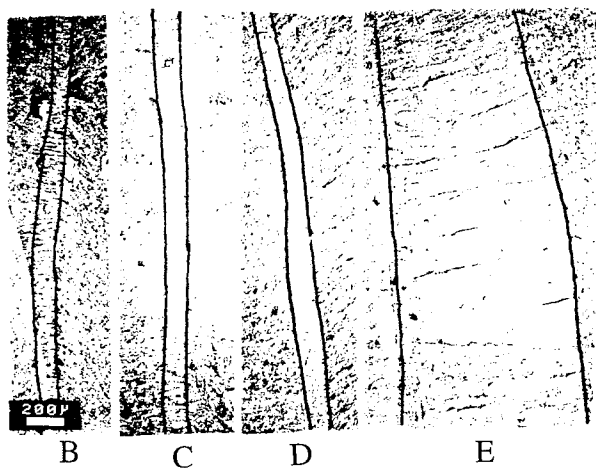


Fig. 2--SEM Images, Formulation B, C, D and E are shown width of the craze zone indicated. Crack growth is from left to right. No craze in formulation A.

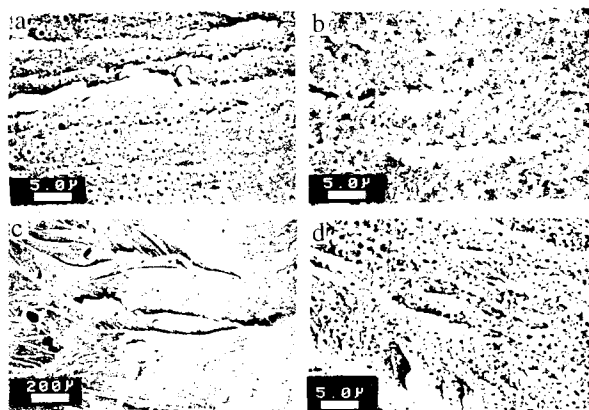


Fig. 5--SEM Images. a-Typical craze zone 20°C. b-Typical brittle fracture zone. c & d-60°C craze zone.

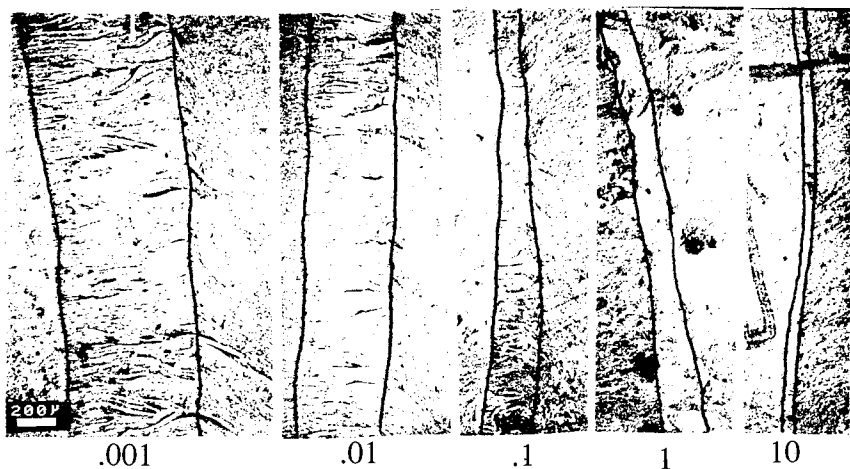


Fig. 3--SEM Images, Formulation C. Crack growth left to right. Loading rate indicated on the bottom. Craze is outlined. Fracture at 20°C.

CONTROL OF TOUGHENED POLYCYANURATE MORPHOLOGY UTILIZING GRADIENT TEMPERATURE CURING

D. S. Porter, C. A. Williams, S. A. Srinivasan, J. E. McGrath and T. C. Ward

Department of Chemistry

Center for Adhesive and Sealant Science

NSF Science and Technology Center:

High Performance Polymeric Adhesives and Composites

INTRODUCTION

It is difficult to overstate the importance of cure cycle variation on the performance of thermosetting resins and adhesives. Mechanical properties depend not only the completeness of the crosslinking reaction, but on the particular cure regimen used to obtain the cured material. [1]

One proposed high performance material and adhesive, trimerized bisphenol-A dicyanate ester (Ciba-Geigy AroCy B-10), has desirable thermal and mechanical properties. An attractive mechanism of toughening the material is incorporating a thermoplastic, as several classes of thermoplastic are soluble in the molten monomer. As gelation occurs, microphase separation takes place, effectively toughening the material.

Efforts by Srinivasan [2] and Brown [3] have focused on toughening the material through inclusion of a reactive thermoplastic, a hydroxyl-functionalized phenolphthalein-based amorphous polyarylene ether sulfone ($M_n = 15000$ g/mol). This particular toughening agent possesses the desirable property of a comparable T_g (about 259°C , the T_g of the unmodified cyanate ester material being 265°C), and has reactive functionalities on the polymer chains. These functionalities react with the cyanate ester material at the interface between toughener and thermoset, providing improved solvent stress cracking resistance.

The objective of this study was to elucidate exact cure condition/property relationships by

studying a continuum of morphologies produced utilizing a continuum of conditions across a single sample. Examination of the nature of the phase separation and the relative size of the domains should confirm the correlation between phase size and toughness in this material, and predictive models of toughness produced from a specific cure cycle can be developed.

EXPERIMENTAL

The material under study was a bisphenol-A based cyanate ester resin, Rhone Poulenc's AroCy B-10, toughened with 25 percent of a reactive thermoplastic, hydroxyl functionalized phenolphthalein-based amorphous polyarylene ether sulfone ($M_n = 15000$ g/mol). The thermoplastic was dissolved in the liquid dicyanate monomer at 104°C , and 250 ppm of aluminum acetyl acetonate with 2 pph nonyl phenol was added to catalyze the reaction. The mixture was stirred and degassed to remove entrapped air and other volatiles.

The resin was placed in a temperature gradient mold consisting of a block of thermally conductive material such that when placed between two temperature sources, the temperature at any given point would be proportional to the displacement from the temperature sources. A convenient source of regulated temperature was a platen press with independently controllable heated top and bottom platens. Thermocouples were inserted in the mold in various locations to map the temperature gradient. The resin was

cured to gelation or beyond, then postcured at 250 °C for two hours.

Samples were removed and fractured to reveal a clean surface. Fracturing was performed at one-half inch intervals down the length of the sample, corresponding to the points at which temperatures of the mold were measured. The specimens were vapor stained with ruthenium tetroxide for examination using a Philips 420T electron microscope at 12500 times magnification.

RESULTS AND DISCUSSION

The linear temperature gradient across the mold produced a gradient of morphologies corresponding to the increase in temperature, as shown by electron microscopy. A typical sample's electron micrographs are shown in figure 1. This system has been shown to produce a 0.5 to 1.0 micron interlocked phase morphology when cured ramped to a cure temperature of 200 degrees C for two hours and then postcured at 250 °C. [4]

ACKNOWLEDGMENTS

The authors would like to acknowledge the Center for Adhesive and Sealant Science, The Adhesive and Sealant Council Education Foundation and the National Science Foundation Science and Technology Center for Polymeric Adhesives and Composites at Virginia Tech.

REFERENCES

1. C. K. Riew, E. H. Rowe & A. R. Siebert in 'Toughness and Brittleness of Plastics', R. D. Deanin & A. M. Crugnola, Eds., ACS Adv. in Chem. Ser. 154, Washington, D.C., 1976, p. 326-343.
2. S. A. Srinivasan. Ph. D. Dissertation, VPI&SU, 1994.

3. J. M. Brown. Ph.D. Dissertation, VPI&SU, 1994.
4. Y. T. Chen and C. W. Macosko, 24th International SAMPE Technical Conference, October 1992 Preprint.

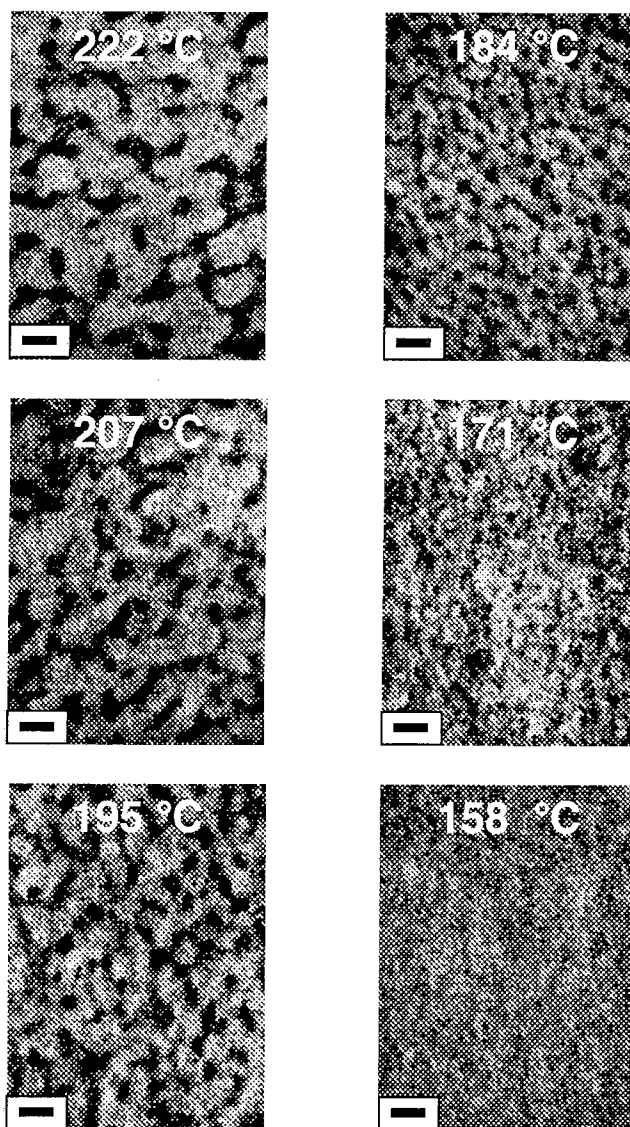


Figure 1
(0.5 μ bar)

CHARACTERIZATION OF CTFE AND CTFE COPOLYMERIC HOT-MELT ADHESIVES

J. L. Longhenry and B.J. Love

Dept. of Materials Science and Engineering

Center for Adhesive and Sealant Science

Virginia Polytechnic Institute and State University

Blacksburg, VA 24061-0237

INTRODUCTION

The crystallization of thin films of thermoplastic polymers adjacent to characteristic substrates is not well known. The crystallization conditions and the subsequent crystallinity may affect mechanical properties and solvent resistance. Polychlorotrifluoroethylene (CTFE) and CTFE copolymers have been used as hot melt adhesives for laminating low dielectric circuit boards together. For such high speed electronic devices, crystallization may also affect the dielectric characteristics of the polymer, thus, affecting the performance of the device. Furthermore, processing variables such as the cooling rate and the ensuing crystallization may also affect the adhesion of the formed interfaces.

In addition, bulk crystallized CTFE and CTFE copolymers may not be representative of the crystallinity at the interface. Crystallization next to a substrate may produce a transcrystalline region, a region of highly oriented crystallites which have nucleated from sites along the substrate [1,2]. Transcrystallinity is especially important as an interfacial phenomenon in these thermoplastic hot melt adhesives. Previous work by Folkes *et al* have already indicated that these type of crystallites may affect mechanical properties and adhesion of these interfaces [3,4]. This could be especially important in the electronic packaging industry given that dielectrics are moving toward thinner and thinner adhesive bond lines. Thus, there is the potential of having an entirely transcrystalline region acting as the dielectric insulating layer between microwave circuit boards.

The objective of this study is to understand the effects of processing variables such as cooling rate and substrate surface chemistry on the crystallization of CTFE and CTFE copolymers. Ultimately, we want to determine their effect on adhesion.

MATERIALS AND METHODS

Films of CTFE and CTFE copolymers known as Aclar films were supplied from Allied Signal. These included a CTFE homopolymer, CTFE/PVDF copolymers; and a CTFE/PVDF/PTFE terpolymer. Thicknesses range from 15 to 51 microns.

Samples were processed in a LINKAM THMS 600 hot stage preparation chamber. Homopolymer samples were heated to 250°C and held for 30 minutes while copolymers and terpolymer samples were heated to 230°C and held for 30 minutes. Samples were subsequently cooled at rates of 1, 20, and 30°C/min using a LINKAM TP91 control unit to at least 80°C below the crystallization temperature. These samples were used for X-ray Diffraction. Separate, much larger samples for blister testing and peel testing are being processed using a hot press at a low pressure of approximately 10 psi at elevated temperatures.

Wide Angle X-ray Diffraction using a Scintag XDS 2000 was performed with these samples. 20 scans of 10 to 22° were used for each sample at a rate of 1 °/minute. For each sample, two scans were obtained - one for the substrate-crystallized side and one for the free-crystallized side.

Differential Scanning Calorimetry (DSC) using a Mettler TA3000 unit is being used to determine the level of crystallinity present. Samples were made using the as-received films, and weigh between 7.0 and 8.0 mg. The thermal cycle being used is the same as that used for the hot stage processing, ie, holding for 30 minutes at elevated temperature and cooling at 1, 10, 15, 20, and 30°C/min.

Blister testing using the unconstrained, radial blister test will be performed in the future to look at the adhesion between these films and a glass substrate. The surface energy of the glass substrate will also be changed using a surface treatment of 3-aminopropyltri-

methoxysilane and the effect on adhesion will be evaluated using this blister test.

RESULTS AND DISCUSSION

X-ray diffraction is being used to determine the percent crystallinity present in each sample. A typical plot is shown below in Figure 1 for the CTFE homopolymer cooled at 1°C/min.

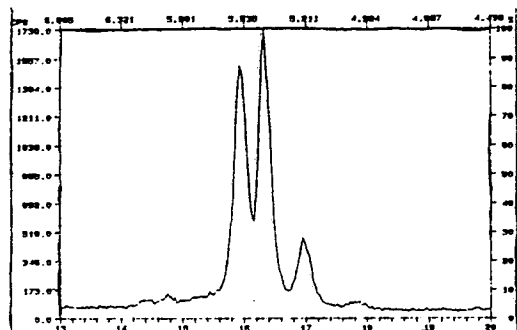


Figure 1: X-ray diffraction pattern of CTFE homopolymer.

An absolute method was used in the analysis of these plots to obtain the percent crystallinity. The results for the CTFE homopolymer are listed below in Table I. As expected, the general trend indicated is a decrease in the percent crystallinity with increasing cooling rate. Slight differences in the percent crystallinity between the freely crystallized and the substrate crystallized sides are seen.

Table I: Percent Crystallinity of CTFE

Cooling Rate	Free Side	Substrate Side
1°C/min	42.3	43.5
20°C/min	36.4	44.2
30°C/min	21.7	30.5

Differential Scanning Calorimetry is also being performed in order to corroborate the x-ray diffraction results. A representative DSC scan is shown below in Figure 2 for the CTFE homopolymer cooled at a rate of 20°C/min. Analysis of the percent crystallinity of all of the samples is currently being performed.

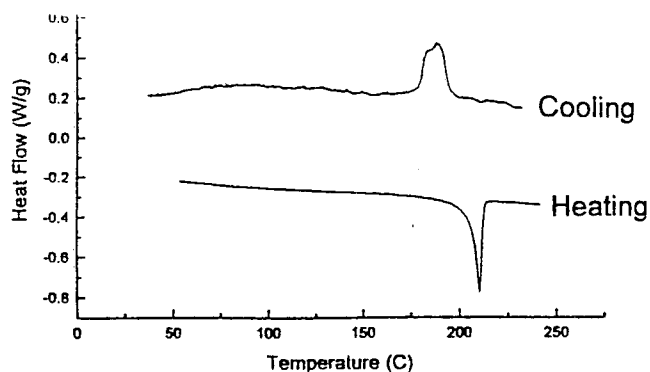


Figure 2: DSC scan of CTFE homopolymer.

CONCLUSIONS

The characterization results thus far show a decrease in the level of crystallinity present as the cooling rate increases. Further characterization efforts such as DSC are being performed and these results will be available presented. In addition, adhesion testing is currently being performed and it is expected that such data will be reported as well.

REFERENCES

1. H. Schonhorn, *Macromolecules*, 1, 145 (1968).
2. V. P. Privalko and Y. S. Lipatov, *Doklady Akademii SSSR*, 251, 152 (1980).
3. M. J. Folkes and S. T. Hardwick, *Journal of Materials Science Letters*, 6, 656 (1987).
4. M. J. Folkes and S. T. Hardwick, *Journal of Materials Science*, 25, 2598 (1990).

ACKNOWLEDGEMENTS

We would like to thank T. Messa, S. Murthy, and Y.P. Khanna at Allied Signal for the samples they supplied, and R. Verma for help in the analysis of the x-ray diffraction data.

Aspects of Denaturing in Adhesive Bonding to Dentin

R. R. Hamandi and B.J. Love

Center for Adhesive and Sealant Science

Department of Materials Science and Engineering

Virginia Polytechnic Institute and State University

Blacksburg, Virginia 24061-0237

Introduction

Adherence to dentin remains significantly more difficult than enamel adhesion since dentin contains more water and is more heterogeneous varying with tooth type and preparation method. In addition, dentin microleakage is still a clinical consideration (1,2). Leakage around dentin bonded restorations often occurs during thermal exposure, because of destabilization of collagen. The effect of temperature on the survival of a dentinal bond *in vivo* is not known. However, for *in vitro* studies, dentin bonding strength measurements have been overestimated compared to the *in vivo* measurements (1,3). A new *in vitro* approach may be more accurate measurements of adhesion.

The goal of this research is to evaluate dentin quality during processing like thermal aging prior to adhesive bonding. Furthermore infrared spectroscopy is used to detect the vibrational modes of dentin, before and after denaturing dentin. Torsional adhesive testing is used to evaluate bonding to dentin under these modified process conditions.

Experimental:

Extracted human teeth were stored in water for approximately six months. The dentin samples were collected by diamond saw sectioning using two parallel cuts. The first cut removed the root, and the second cut removed the occlusal enamel. Dentin surface energy was measured via contact angle of water and methylene iodide

droplets on the dentin surface. The samples were mounted with resin and mechanically polished. Several samples were heated at 65°C for varying lengths of time. Dentin reflectance IR spectra were collected using a Nicolet 740 FTIR equipped with a SpectraTech IR microscope attachment. A Leco Vickers microprobe measured the hardness of the dentin surfaces. The same samples, following thermal exposure, were rehydrated (86% RH) for two days at 45°C, and their hardness and IR spectra were re-recorded. Freshly extracted bovine teeth were also prepared but this time, dentin surfaces were further exposed to heating at 80°C.

Torsional adhesive testing is currently progressing on several bovine samples. A hole is prepared in the dentin by drilling to a standard depth and reaming each sample to yield a well prepared, 0.128" diameter hole. A light cured glass ionomer cement (Vitrebond, 3M) was then placed in the hole and a 0.125" diameter steel rod was inserted into the cavity while the cement cured. Each rod is attachable to a chuck which can be joined to the torsion meter for adhesion testing. The samples were allowed to sit for at least one hour prior to testing.

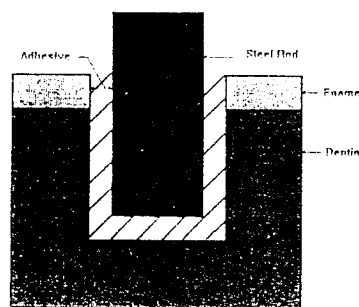


Fig. 1 Torsional Joint Construction

Results

The surface energy of dentin was determined to be 56 dyne/cm. By exposing dentin samples to higher temperatures (65°C) dentin hardness decreased with time. Table 1 shows how the room temperature hardness of human dentin is affected by increasing time at elevated temperature and in Table 2 for how room temperature hardness is affected by rehydration.

Vickers test	Denaturing Time	Av.Vickers Hardness	Load (g)	Exposure Temp.
Sample 1	0	68.83	300	27
Sample 2	1	63.37	300	65
Sample 3	2	53.88	300	65
Sample 4	3	54	300	65

Table 1

Vicker test	% Humidity	Hardness	Load (g)	Temp.
Sample1	86%	83.35	300	45
Sample 2	86%	80	300	45
Sample3	86%	76.73	300	45
Sample4	86%	67.49	300	45

Table 2

The water loss in dentin increased brittleness. We are investigating when water loss is occurring in dentin. Following exposure to the humid environment (86% RH) for two days at (45°C) hardness was recoverable. Rehydration restored human dentin's toughness. When the bovine samples were exposed to (80°C), their hardness was not recoverable after re-exposure to humidity. The infrared results indicated that the region between 1200-1450cm⁻¹ in human dentin was relatively unaffected by denaturing. After denaturing the bovine samples at higher temperatures, the IR results indicate a loss in this region, attributed by Silverstein to be related to C-H bending and C-N stretching in collagen were destroyed during thermal exposure (4). These IR results are shown in Figure 2 for the denatured human dentin at 65°C and in Figure 3 for the bovine dentin at 80°C.

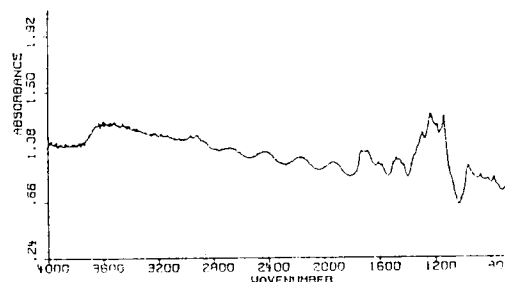


Fig. 2: Reflectance IR of human dentin denatured at 65°C

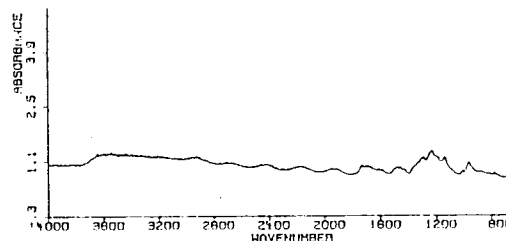


Fig.3: Reflectance IR of bovine tooth denatured at 80°C

Results from the torsional adhesion experiments will be presented at the meeting.

References

- 1-K. -J. M. Soderholm, "Correlation of *in vivo* and *in vitro* Performance of Adhesive Restorative Materials: A Report of the ASC MD156 Task Group on Test Methods on the Adhesion of Restorative Materials", *Dental Materials*, **7**, 74-83 (1991).
- 2-J. R. Weickzkousky, Y. U. Xy, E. L. Davis, and R. B. Joynt, "Microleakage in Various Dentin Bonding Agent/Composite Resin Systems", *Operative Dentistry*, **5** Supplement, 62-67 (1992).
- 3- I. Watanabe, N. Nakabayashi, "Measurement Methods for Adhesion to Dentine: Current Status in Japan", *J. Dent.*, **22**, 67-71 (1994).
- 4-R. M. Silverstein, C. G. Bassler, and T. C. Morrill, *Spectrometric Identification Of Organic Compounds*, 5th Ed., pp.93, 103-124 (1991).

ACCELERATED DEBONDING TEST TO EVALUATE DURABILITY OF METAL/ADHESIVE BONDS

T. Chang, Y. H. Lai, N. E. Shephard, E. A. Sproat, and D. A. Dillard

Center for Adhesive and Sealant Science
Virginia Polytechnic Institute and State University
Blacksburg, Virginia 24061-0201

INTRODUCTION

It is well documented that the interfacial regions of structural adhesives are those most susceptible to environmental attack by water[1]. Unfortunately, the diffusion process is very slow for conventional metal/adhesive test specimens of laminated beam types. Typical specimens of one inch width may require several years to reach a saturated moisture content because the moisture must diffuse throughout the adhesive layer from the exposed edges. It would be beneficial to determine the degraded strength of bonds when equilibrium saturation levels of moisture are reached quickly.

The objective of this research is to develop an experimental technique with which the rate of obtaining moisture equilibrium at the interface of metal/adhesive bonds is accelerated so that the effects of relative humidity on the strength of the bond can be quickly determined. The accelerated debonding test was developed. The specimens consist of a thin coating of adhesive bonded to a single substrate. These specimens equilibrate quickly because of the short diffusion path. The technique yields strain energy release rates (SERR) for mixed mode fracture. The technique is expected to be inexpensive and easy to conduct.

SPECIMEN ANALYSIS

The proposed debonding test specimen is depicted in Figure 1. Specimens consist of a thin layer of adhesive (≈ 0.10 mm) bonded to a thin substrate ($10 \times 12.5 \times 1.5$ mm).

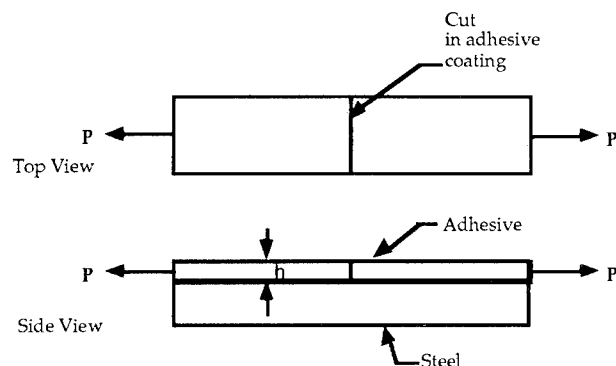


Fig. 1: Tensile Debonding Specimen (Not drawn to scale).

The specimens can be exposed to different types of environmental conditions. The adhesive layer is thin; the conditioning can be accomplished in hours. A cut is then introduced into the adhesive layer by cutting the adhesive across with a razor blade. Using a loading device (e.g., Instron loading frame), the specimen is slowly loaded perpendicular to the cut. The stress generated causes the crack to initiate at the cut. This crack initiation can be easily visually verified. The strain that initiates the crack movement is recorded.

The SERR (G) can be derived by taking into account the residual stress components and the stress caused by the load.

$$G = \frac{h}{2E} [(\sigma_t + \sigma_m + \epsilon E)^2 + (\sigma_t + \sigma_m - \nu \epsilon E)^2] \quad (1)$$

Where: σ_t is residual stress due to curing (Positive, bi-axial),

σ_m is residual stress due to moisture swelling (Negative, bi-axial),

ϵ is applied tensile strain (uni-axial),

E is modulus of the adhesive, and

h is adhesive thickness.

The SERR obtained in Equation 1 is a total SERR of Modes I and II.

The tensile debonding specimen can be modeled as a layered bi-material (Fig. 1) where the adhesive is a thin layer lying on top of the thicker substrate.

According to Hutchinson and Suo[2], such layered bi-material has a SERR ratio of:

$$\frac{G_{II}}{G_I} \approx (\tan 52^\circ)^2 \approx 1.6 \quad (2)$$

The plastic deformation of the substrate may not be an issue since the SERR is determined from the strain energy of the coating. If however, the adhesive deforms plastically, the equation above is no longer valid and SERR values obtained would be higher than the actual values.

PRELIMINARY EXPERIMENT RESULTS

Several preliminary experiments conditioned in different environments were conducted on steel/epoxy specimens. Cold rolled 1018 steel of 1.5 mm thick was used as the substrate. The adhesive was a model Dow Chemical epoxy system. The adhesive was cast on the steel panel to a thickness of 0.1 mm. The panel was

then cured at a temperature of 155°C for 90 minutes. After curing, the specimens were cut out of the panel. These specimens were conditioned at different relative humidity levels at 60°C until moisture saturation. Previous moisture ingress tests showed that the specimens achieved moisture saturation in less than three hours.

It was previously determined that the bulk adhesive's coefficient of thermal expansion (α) was $78 \times 10^{-6}/^{\circ}\text{C}$. Knowing that the adhesive was cured at 155°C, the thermal residual stress was estimated. The swelling of the bulk adhesive due to moisture ingress was measured. Hence the moisture residual stresses could be obtained. The modulus of the adhesive under different humidity levels were also determined.

The adhesive was cut across as illustrated in Figure 1 with a sharp razor blade and then loaded in tension at a cross head speed of 1 mm/min until the crack initiated. An extensometer was attached to the specimens to monitor the strain. Some preliminary results were obtained and analyzed. Figure 2 shows the critical strain to initiate cracks plotted against percent relative humidity.

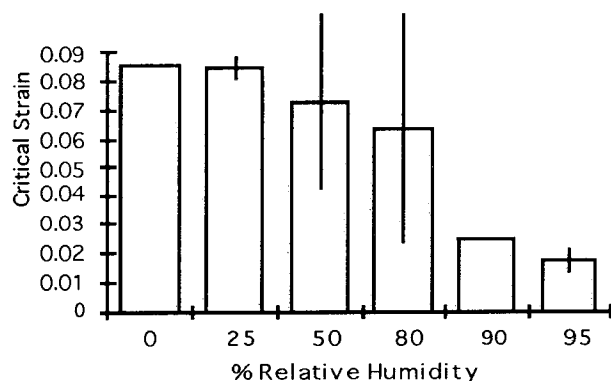


Fig. 2: Strain versus exposed percent relative humidity for tensile debonding tests.

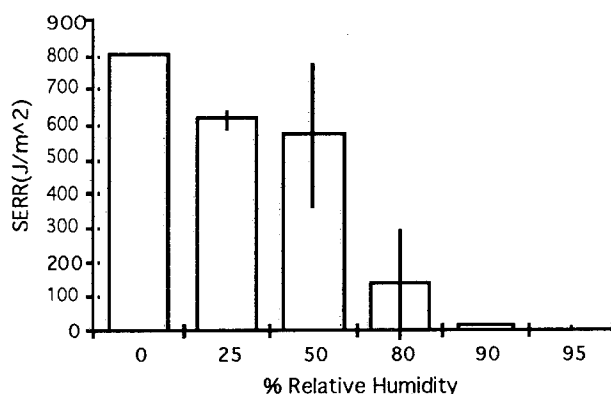


Fig. 3: SERR versus exposed percent relative humidity for tensile debonding tests.

Figure 2 show the qualitative results; the critical strain is a function of adhesive thickness. Using Equation (1), SERR was obtained. Figure 3 shows the SERR values plotted against percent relative humidity. This figure is more quantitative. The results show a decrease in SERR as the conditioning relative humidity increases. The figure also shows evidence of a critical relative humidity between 50 and 80 percent. That is, the adhesive strength drastically decreased between 50 and 80 percent relative humidity.

SUMMARY AND CONCLUSIONS

More tests with specimens conditioned at several different environments and time periods will be conducted to justify the methodology. The future goal is to be able to use this test methodology to measure SERR for both Mode I and II. A high speed video camera will be used to monitor crack initiation and propagation in an attempt to determine critical SERR. Theoretically, the specimen can also be bent or can undergo thermal loading to cause the crack to initiate. Analysis will be made to these types of loading to determine SERR values.

The tensile debonding test described above is an inexpensive and fast method to determine metal/adhesive bond durability. Efforts are underway to improve the testing methods so that the results can be even more accurate. Because of the simple geometry, and fast moisture ingress time, this test could be used to obtain preliminary results on environmental effects on the adhesive system in bonded joints. Conceivably, the test could be used to study moisture, redried, and hygrothermal effects on the bond durability. The test method could also be applied to coated specimens.

ACKNOWLEDGMENTS

The authors wish to thank the Center for Adhesive and Sealant Science and The Dow Chemical Company for supporting this research. We also appreciate the help of Dr. Didier Lefebvre and Mr. Mark Taylor for valuable suggestions and discussions.

REFERENCES

1. R. A. Gledhill, A. J. Kinloch, and S. J. Shaw, *J. Adhesion*, **11**, 3, (1980).
2. J. W. Hutchinson and Z. Suo, *Advances in Applied Mechanics*, **29**, 63, (1992).
3. H. M. Jensen and M. D. Thouless, *Int. J. Solids Struct.*, **30**, 779, (1993).
4. G. D. Vaughn, B. G. Frushour, and W. C. Dale, *J. Adhesion Sci. Technol.*, **8**, 635, (1994).

NEW INVESTIGATIONS INTO FLUORINATED CELLULOSE FIBERS

Ulli Becker and Wolfgang Glasser

Department of Wood Science and Forest Products

Center for Adhesive and Sealant Science

Virginia Tech

Blacksburg, VA 24061

Introduction

Cellulosic materials have increasingly become important as reinforcements and biomaterials (implants). Necessary features demanded by these applications include strength and stiffness as well as wettability and good adhesion properties towards the surrounding medium. The goal of the research is to engineer cellulosic materials with improved surface properties that at the same time provide strength and stiffness. A stiffer and stronger fiber can be produced by spinning from the liquid crystalline state, whereas surface properties can be influenced by introducing fluorine into the system.

Experimental

Cellulose acetate butyrate fibers with varying degree of substitution (DS) with acetyl (ac) or butyryl (bu), DS_{ac} and DS_{bu} , were spun from anisotropic and isotropic solutions in DMAc/LiCl via dry jet/wet spinning method with different take-up speeds by Davé et al (1). Strength and modulus properties were determined by single fiber tests after ASTM D 3822. Trifluoroethoxy acetates of cellulose were prepared as described elsewhere (2). Briefly, cellulose or cellulose acetate was reacted with trifluoroethoxy acetic acid and tosyl chloride in homogeneous phase. Trifluoroacetic acid was prepared by reacting trifluoroethanol with chloroacetic acid (3). Solubility tests were conducted using a solvent to solid ratio of 9 to 1, by weight. After stirring at room temperature for 24 hr., samples were examined visually to determine the solubility. Partially soluble samples were labeled as insoluble in that solvent. The dispersive component of the surface free energy was determined using inverse gas chromatography according to Garnier, Glasser (4). Contact angle measurements were conducted on solvent cast films of derivatives having DS_F of 0.2 and 0.6. Contact angle measurements were conducted with a Geniometer. Each data point reported represents the average of 5 measurements.

Results and Discussion

Cellulosic fibers spun from the anisotropic state show dramatically improved strength properties as compared to isotropic fibers (Fig. 1) (1). Also, the influence of the substitution pattern on the critical volume fraction (V_p^c) was examined. Contrary to Flory's theory, V_p^c was found to decrease with decreasing aspect ratio (5).

Fluorine is known for its effect of reducing the surface free energy. Surface fluorination of cellulose spheres produced results by inverse gas chromatography (Fig. 2) which showed that the total enthalpy of adsorption (ΔH_s) is remarkably independent of the nature of the substituents, regardless of the type of ester substituent (with F or not) and only dependent on the number of unmodified hydroxyl groups [3]. The ΔH_s was found to decrease with increasing substitution. On the other hand, the T_m of trifluoroethoxyacetylated cellulose derivatives with different DS_F was examined following homogeneous phase modification. The T_m was found to decrease with increasing DS_F . Surprisingly, the comparison of cellulose trifluoroethoxyacetate and cellulose acetate trifluoroethoxyacetate reveals that the T_m depends only on the DS_F and is independent of the remaining functionality (hydroxyl or acetyl). Solubility tests of the same materials reveal increased solubility in carbonyl containing solvents like acetone, DMSO (6). To further investigate the influence of fluorine on the surface properties, contact angle measurements were conducted using cellulose acetate trifluoroethoxyacetate having two different F-contents. These materials were synthesized using homogeneous phase modification of cellulose acetate in pyridine. Thus use of DMAc could be avoided. The results

indicate that the contact angle for water is independent of the fluorine content (Fig. 3). Formamide, a liquid with a lower surface free energy shows a slight (but significant) decrease in contact angle with a rising F-content.

Conclusions

1. Cellulose acetate butyrate fibers spun from liquid crystalline solutions show improved strength properties over corresponding fibers from isotropic solution.
2. The ΔH_s is a function of unmodified hydroxyl groups.
3. The T_m of trifluoroethoxyacetylated cellulose depends only on DS_F .
4. The influence of F-content on the contact angle depends on the surface free energy of the liquid used.

Acknowledgments

The authors gratefully acknowledge the help of J. Todd and J. Sealey for performing the cellulose derivatizations. The authors would like to thank Prof. J.P. Wightman (Chemistry Department, Virginia Tech) for his help in the field of surface chemistry.

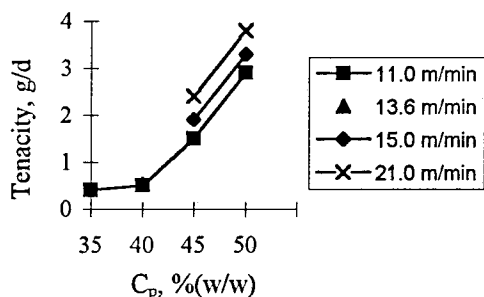


Fig. 1: Tenacity vs. polymer concentration of cellulose ester fibers spun at different take-up speeds. The ester was a commercial cellulose acetate butyrate with 39.4% acetyl content and 4.0% butyryl content. Source: reference 1.

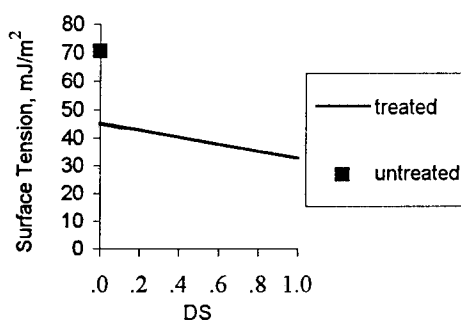


Fig. 2: Contact angle vs. DS_F . The material used was cellulose acetate trifluoroethoxy-acetate with varying DS_F . Source: Reference 4.

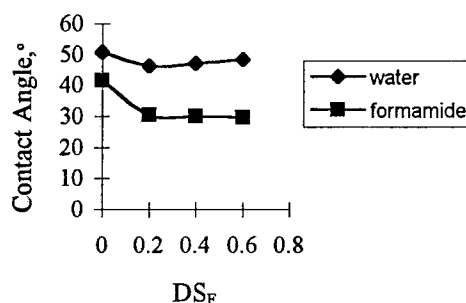


Fig. 3: Surface tension of unmodified cellulose and cellulose esters with different substituents and DS. The cellulose derivatives were cellulose laurate and cellulose acetate trifluoroethoxy acetate.

References

1. V. Davé, W.G. Glasser, and G.L. Wilkes, *J. Polym. Sci.: part B: Polym. Phys.*, **31**, 1145 (1993)
2. Y. Shimizu and J. Hayashi, *Cell. Chem. Technol.*, **23**, 677 (1989).
3. Beacham Research Laboratories (no author), Patent Brit. 873244.
4. G. Garnier and W.G. Glasser, *J. Adhesion*, **46**, 165 (1994)
5. V. Davé and W.G. Glasser, *ACS Symposium Series*, No. 489, (1992)
6. J. Sealey, *Novel cellulose ester*, Master Thesis (Wood Science and Forest Products) VPI & SU (1994)

SPLICING SAPPHIRE AND SILICA OPTICAL FIBERS

Adam E. Barnes, Russel G. May, Sridhar Gollapudi, Richard C. Claus
Fiber & Electro-Optic Research Center, Department of Electrical Engineering
Virginia Polytechnic Institute and State University, Bradley, Blacksburg, VA 24060

INTRODUCTION

Sapphire fiber sensors hold great promise for high temperature sensing applications because of their small size, their immunity to electromagnetic interference, and their high melting temperature, which exceeds 2000 °C. Unfortunately, sapphire fibers are expensive and have a high optical attenuation, which limits the length of sapphire fiber that can be used. Consequently, a practical sapphire sensor will only have sapphire fiber in the sensor head and use silica fiber for transmitting signals to and from the test region. To realize such a sensor system, a suitable method for splicing sapphire to silica is needed that would provide good adhesion between the fibers and low optical losses. This was no small task, since sapphire and silica fibers are radically different; having widely varying indices of refraction, coefficients of thermal expansion (CTE), waveguiding properties, melting behaviors, and molecular structures. Additionally, because of the small surface area involved when dealing with optical fibers, any bonding method requires very high adhesion per unit of surface area. Many splicing methods were examined, including diffusion enhanced splicing, splicing with coated fibers, and splicing inside of capillary tubes.

DIFFUSION SPLICES

The diffusion enhanced splice was initially fabricated using sapphire and silica rods, which were easier to handle than fibers. The splice was made by aligning the sapphire and the silica endfaces with micropositioners and heating them gradually with an oxy-propane torch to promote diffusion between the interface. This procedure was subsequently performed using fibers, but the heating in this instance was done in a small, ceramic oven. Although scanning electron microscopy (SEM) did indicate that diffusion may have occurred, there was also formation of mullite crystals (an intermediate mixture of silica and alumina) at the interface. These crystals were not conducive to good optical transmission, and compromised bond strength.

COATED FIBER SPLICES

Several sapphire-silica splices were made with one or both of the fibers coated with fused silica or aluminosilicate glass (ALG), and then spliced on an arc fusion splicer. Initially, uncoated sapphire and silica were attempted, and although the resulting splices were slightly stronger than the diffusion enhanced splices, there was still evidence of mullite crystal formation, which resulted in unacceptably high optical losses, around 10 dB. To prevent mullite formation, the sapphire fiber was coated with silica using chemical vapor deposition. The two fibers were then spliced together on the arc fusion splicer as before. Although this resulted in a strong splice, the optical losses were still on the order of 10 dB, likely due to misalignment of the sapphire and silica fibers. A SEM did not reveal evidence of mullite crystal formation. ALG was also used as a coating. ALG has a lower softening point than fused silica, and its intermediate refractive index between that of silica and sapphire reduces Fresnel reflections in the splice, making it a good choice for a binder. The ALG was melted in a crucible, and the fibers to be coated were dipped into the molten glass. Although coatings were attempted on both the silica and the sapphire, the coated silica fiber tended to crack upon cooling, probably due to the different CTEs between the silica and ALG. Initial attempts achieved splice losses of around 5 dB, and the adhesion between the fibers was poor. To lower the splice losses, attempts to improve the alignment were made by injecting light through the fibers to be spliced, and adjusting the fibers on the arc fusion splicer's micropositioners until maximum light transmission was obtained. This approach was unsuccessful, however, because it was found that the fibers shifted inside the molten ALG as it was heated and cooled. Subsequently, the ALG was polished parallel to the endface of the sapphire fiber, down to a thickness of a few microns, to allow better alignment of the fibers, as shown in Figure 1. Thinner ALG coatings resulted in lower optical losses. The lowest loss achieved with this method was 1.5 dB. To

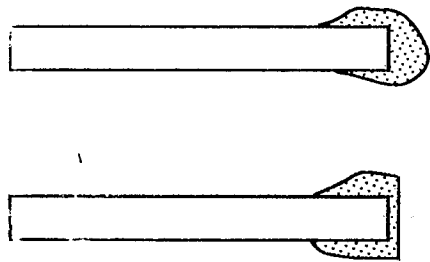


Figure 1. Sapphire fiber coated with ALG, before and after polishing

strengthen these splices, silica tubes were epoxied in place over the splice, which resulted in reasonably robust splices. Although this technique was capable of producing good splices, it was lengthy, involved, and difficult to perform.

CAPILLARY TUBE SPLICES

To improve the alignment of the fibers, which had up to this point proved to be the most critical parameter for low loss splices, splicing was attempted inside of capillary tubes that had inner diameters closely matched to the outer

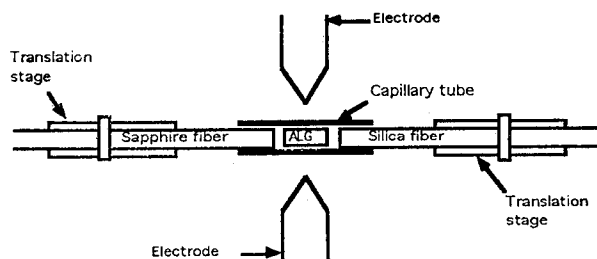


Figure 2. Set-up for capillary tube splice technique

diameters of the fibers to be spliced. A short piece of ALG was used as a binder inside the tube, and the whole assembly was spliced together on an arc fusion splicer, as shown in Figure 2. As the fibers are pushed together, the molten ALG flows in the small space between the capillary tube and the fibers. This effect dramatically increases the surface area used in the bond between the fibers, resulting in a much stronger splice. Initial attempts were made using fused silica tubing. This proved inadequate, as the different CTE between the tube and the ALG caused the tube to crack. Stainless steel tubing was also used in this approach. Unfortunately, because the steel tubing was opaque, the splice could not be monitored during the splicing

procedure. This resulted in either the fiber endfaces not being close enough together or the binder being overheated, which produced bubbles in ALG. In either case, the optical qualities of the splice were poor. Finally, a sapphire tube was used which did not have the problems of either the silica or steel tubes. The tube was produced by Saphikon using an edge-defined film fed growth technique. Splices with optical losses consistently below 1 dB were produced in this fashion. The exposed silica fiber proved to be the weakest part of the splice, so this was encased in a silica tube. The final splices were mechanically very strong. The sapphire capillary tube splices have the additional advantage of being relatively easy to fabricate.

CONCLUSION

Endeavoring to create mechanically strong, optically low loss splices between sapphire and silica fibers, three basic approaches were taken. Diffusion enhanced splicing displayed neither good adhesion nor low optical losses. Coated fiber splices achieved reasonable strength and optical loss, but only for sapphire fibers coated with ALG that had been polished to within a few microns of the sapphire fiber endface. The most successful splicing technique was the capillary tube splice with the use of a sapphire tube. The tube allowed a much larger surface area on the fiber to be utilized for good bond strength, and also provided a good method of aligning the fibers for low optical losses.

ACKNOWLEDGEMENTS

This work was sponsored by NASA LaRC under the NASA Research Grant NAG-1-1275. Initial splice work was done by Dr. Kent Murphy and Shari Feth at Virginia Tech with suggestions from Dr. David R. Clarke at University of California Santa Barbara.

REFERENCES

1. Gollapudi, Sridhar. Sapphire Optical Fibers: Splicing and Sensing Applications, Master's thesis, Virginia Polytechnic Institute and State University, 1992.

DURABILITY OF ADHESIVELY BONDED TITANIUM

S. A. Risch, B. L. Holmes, G. S. Frick, and J. G. Dillard

Center for Adhesive and Sealant Science
Virginia Tech, Chemistry Department, Blacksburg, VA 24061-0212

INTRODUCTION

The use of titanium as an adherend is widely accepted in industry due to its high strength to weight ratio and ability to maintain its intrinsic mechanical properties at elevated temperatures (1). Industrial applications require knowledge about the bond strength and adhesive durability, which depends greatly on the surface chemistry of the treated adherend.

In this study, silane surface treatments for titanium 6,4 were implemented, and the durability of the treated titanium when bonded with a polyimide adhesive was investigated by exposing the bonded sample under stress to various environments (2). The effects of the pretreatments on the titanium surface chemistry were evaluated using surface analysis techniques.

EXPERIMENTAL

Titanium adherends were pretreated by cleaning in 3% (w/w) sodium hydroxide solution, followed by neutralization in 3.33 M sulfuric acid solution. Phenylethynyltrimethyl, allyltriethoxy and vinyltriethoxy silane samples were prepared by soaking the titanium panels in 5% (w/v) silane in 95% ethanol at 50 C. All titanium panels were rinsed with 95% ethanol and

then dried for 1 hour in an 130 C oven following treatment.

Samples were bonded using a wedge type geometry with LARC-PETI-5 polyimide adhesive by heating the materials under 75 psi to the cure temperature of 350 C for 1 hour. The samples had a bond thickness of 0.25 mm, and a total bond length of 100 mm. Bond durability was monitored by measuring crack growth as samples were exposed to air and submerged in boiling water.

The failure modes of all samples were evaluated using x-ray photoelectron spectroscopy (XPS) and scanning electron microscopy (SEM).

RESULTS

Treated, non-bonded titanium surfaces characterized using XPS were comprised primarily of nitrogen, sulfur, and aluminum. Representative data are provided in Table 1 for allyltriethoxy silane-treated surfaces. The 8% silicon detected on all samples was independent of the silane used. The zinc detected on the samples exposed to boiling water is thought to come from the stainless steel wedge. The titanium was present only in the form of titanium dioxide, and no peak attributed to metal was observed in the Ti 2p spectra. The detection of both titanium and silicon may be due to

either a thin layer of silicon or incomplete coverage of the silicon.

A plot of crack propagation versus time in boiling water for samples of all three silane treatments is provided in Figure 1. The average initial crack length was similar for all samples, and averaged 28 mm. Two of the three bonded samples failed during the test for both allyltriethoxy silane and vinyltriethoxy silane pretreatments. The phenylethynyltrimethyl silane treatment resulted in the best durability. None of these samples failed during the test, and the average final crack length of 60 mm.

The failure mode, as determined visually and by XPS, was independent of the particular silane used. Cohesive failure was observed upon insertion of the wedge, prior to submersion. The region of the sample which failed during the test appeared to have failed interfacially. XPS analysis revealed silicon on both metal and adhesive failure surfaces, indicating that failure had occurred within the silane layer.

CONCLUSIONS

Samples treated with phenylethynyltrimethyl silane showed better durability in air and boiling water than did allyltriethoxy silane and vinyl triethoxy silane-treated samples. Other possible titanium preparatory methods are being explored, including transition metal anodization and plasma sprayed coatings.

ACKNOWLEDGEMENTS

Thanks are expressed to the Center for Adhesive and Sealant Science and Adhesive and Sealant Council, Inc. for their support of this research.

REFERENCES

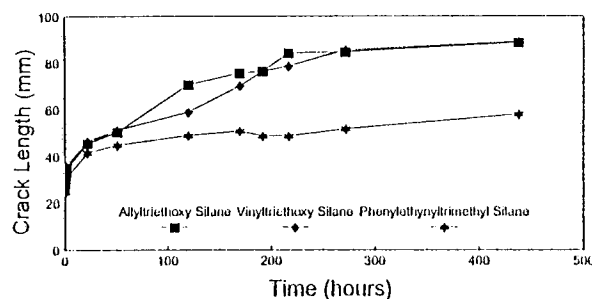
1. H. M. Clearfield, et. al., "Surface Preparation of metals" in Adhesives and Sealants, vol. 3., H. F. Brinson, ed., Applied Science Publishers, London, 1983, p. 85.
2. R. D. Rossi, "Polyimides" in Adhesives and Sealants, vol. 3., H. F. Brinson, ed., Applied Science Publishers, London, 1983, p. 85.

Table 1: Atomic Concentrations for Allyltriethoxy Silane-Treated Specimens

	%C	%O	%Ti	%Si	%N	%Al	%Zn
nonbonded	43.9	38.2	6.0	8.4	1.1	1.2	nd
init crack	82.7	11.7	nd	2.7	2.9	nd	nd
H2O crack-m	32.4	45.3	1.4	11.3	1.8	4.6	3.2
H2O crack-a	37.5	42.4	nd	11.6	1.2	4.4	2.9

m=metal side a=adhesive side nd=not detected (<0.2%)

Figure 1
Crack Propagation of Silane-Treated Titanium Bonded Specimens in Boiling Water



An Extension of the JKR Technique to Describe Adhesion Hysteresis in Modified PDMS

S. M. Perutz, P. Silberzan, E.J. Kramer, and C. Cohen

Dept of Materials Science and Engineering

Cornell University, Ithaca, NY 14853

INTRODUCTION

Recently, a new method for measuring the work of adhesion (W) of elastomers, developed by Johnson, Kendall and Roberts (JKR) [1] has been implemented by various laboratories to yield accurate and reproducible results [2-5]. Utilizing a sphere on sphere, or sphere on plane geometry, the JKR theory balances mechanical deformation of the elastomers with their inherent surface energy to derive W of the system. Based on work done originally by Hertz [6], they found that when a load (P) is applied to the system, the elastomers deform in such a way that the radius of the area of contact (a) is given by:

$$a^3 = R/K (P + 3\pi WR + (6\pi WRP + (3\pi WR)^2)^{1/2}) \quad (1)$$

$$K = 2E / (3(1-\nu^2)) \quad (2)$$

where R is the radius of curvature of the undeformed system, E and ν are the Young modulus and the Poisson ratio, respectively, of the elastomer. Using the JKR technique, one increases, and then decreases the applied load while measuring the resulting radius of contact. We have used this method to investigate the adhesive properties of poly(dimethylsiloxane) (PDMS) networks. All of our experiments study self-adhesion. Once the JKR method was found to accurately describe W in model PDMS networks [7], we then proceeded to synthesize modified PDMS networks to study cases of adhesion hysteresis; that is, cases where the W measured during loading of the two elastomers (W_l) is different from that measured during unloading (W_u). By adding a controlled amount of excess crosslinker molecules (a tetrafunctional silane), we introduced a source of chemical hysteresis.

EXPERIMENTAL

The apparatus used to measure W via the JKR technique is similar to that used by Chaudhury and Whitesides described in [3]. An elastomeric lens is lowered by a micromanipulator (Nikon) onto the second sphere or plane of elastomer that rests on a lever which is connected to an electrobalance (Mettler). As the sphere is lowered, the resulting applied load is read off of the balance and the area of deformation is measured with an optical microscope (Nikon, Diaphot). We typically loaded our samples at rates of approximately 4, 1 and 0.3 $\mu\text{N/s}$. The maximum load applied varied from 0.368 to 2.45 mN. All experiments were done at room temperature with relative humidity < 60%.

PDMS chains with molecular weights of 30,000-36,000 g/mol, and PDI of 1.03-1.18, were synthesized via a ring-opening polymerization. The polymer chains were endcapped with vinyl groups and formed into networks via a hydrosilylation reaction using tetrakis(dimethylsiloxy)-silane as a crosslinker. Model networks contained a ratio of 1.7 silane functionalities per vinyl group. Samples were also made in which an excess of the crosslinker molecule was added so that the silane to vinyl group ratios (r) were 1.9 and 2.5.

The PDMS networks were formed into lenses by depositing uncured droplets onto fluorinated glass slides. After curing, the gels were soaked in toluene to extract the sol-fraction and then dried in a 60°C vacuum oven for 24 hours before testing. We believe that this treatment also converts excess silane, Si-H, into silanol, Si-OH.

RESULTS

It was found that our model networks followed the JKR theory very closely and yielded values of approximately 0.048 (+/- 0.002) J/m² for

W_{ul} and W_l ; this corresponds well to twice the surface energy of PDMS ($\gamma_{PDMS} = 0.022 \text{ J/m}^2$) as measured by techniques such as contact angle measurements. The fraction of extracted material in these samples was between 0.7% and 0.9% by weight, showing that these are, in fact, model networks.

As the amount of excess crosslinker was increased in the PDMS networks, the amount of sol-extracted material also increased. And, though the W_l remained constant at values of $0.045 (+/- 0.004) \text{ J/m}^2$ in these samples, the measured W_{ul} was seen to increase to values of $0.076 (+/- 0.003) \text{ J/m}^2$ for samples with $r=1.9$, and to $0.106 (+/- 0.005) \text{ J/m}^2$ for those with $r=2.5$. Thus an adhesion hysteresis was realized. We believe that this increase in W_{ul} is due to hydrogen bonding between excess crosslinker molecules that have been hydrolyzed into silanol groups.

As the adhesion hysteresis increased, it was also observed that the fit of the JKR equation became worse, and, the predicted pull-off force (force at which the two elastomers finally separate) began to deviate from that observed experimentally. Also, the value for K , a bulk property of the material, was calculated by the JKR equation to be up to 50% greater during the unloading regime than that given for the loading regime; this is a non-physical result. Considering these discrepancies, we began to re-evaluate the application of the JKR theory in our experiment.

The pressure profile for the area of contact between the two elastomers is predicted by the JKR theory to be compressive at the center and tensile at the edges. From this description, we would expect that towards the edge of contact, chemical bonding is less likely to occur because the silanol groups are not forced into contact. However, under compressive stress, the silanol end groups are more likely to migrate and form hydrogen bonds across the interface. Hence we would predict that this bonding (the source of chemical hysteresis), and therefore W_{ul} , is not constant over the entire area of contact, but increases as we approach the center of contact.

To test this hypothesis, we inverted eqn (1) to determine the value of W at every contact area

radius using the K found during the loading experiment (K_l):

$$W(a) = (6\pi a^3 K_l)^{-1} * ((a^3 K_l / R) - P(a))^2 \quad (3)$$

Figures 1 and 2 show evaluation of the results from samples that display adhesion hysteresis using this modified JKR equation. While W_l remains constant, the variation of W_{ul} over the contact area is clearly seen.

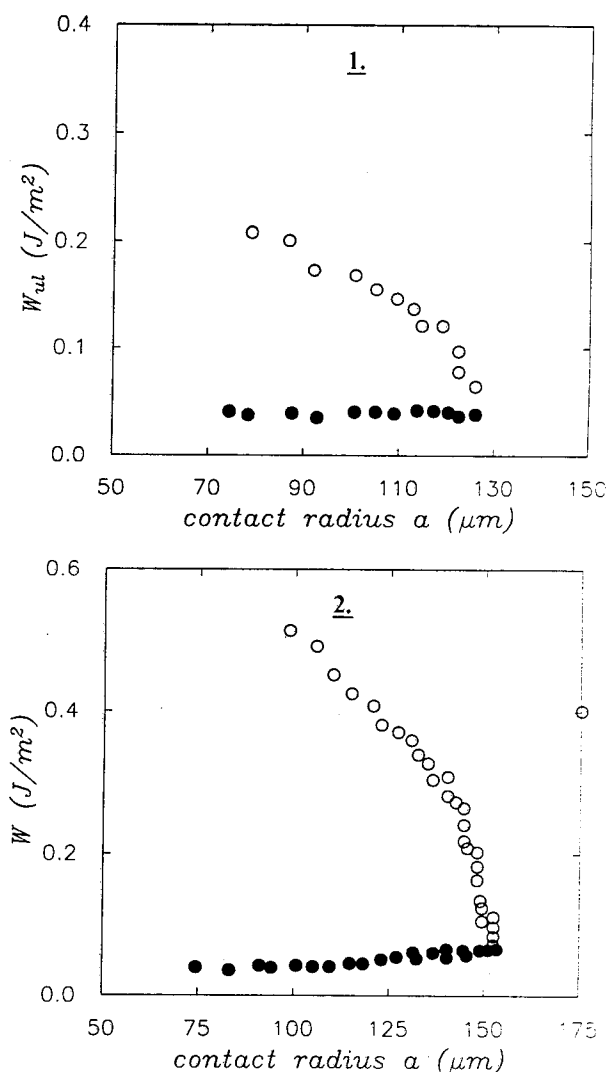


Fig 1 and 2. Evaluation of experimental data from 1.9r and 2.5r (respectively) materials using eqn (3). Filled circles correspond to loading regime, open circles correspond to unloading regime. While W_l is constant, W_{ul} increases as the contact radius shrinks. The 2.5r sample has a greater amount of excess crosslinker and its W_{ul} is seen to be greater.

We have also investigated the dependence of the local value of W_{ul} on the maximum local applied stress. As the maximum applied load increases, we expect that the degree of pressure-sensitive bonding will increase due to an expanded compressive region. Our data, shown in Table 1, confirms this trend. We then calculated the maximum stress (σ) experienced at every radius in the area of contact by eqn (4):

$$\sigma(r) = ((3KW_1) / (2\pi a_{\max}))^{1/2} * (1-r^2/a_{\max}^2)^{-1/2} -$$

$$((3Ka_{\max})/(2\pi R)) * (1-r^2/a_{\max}^2)^{1/2} \quad (4)$$

If the chemical bonding is pressure-sensitive, then the W_{ul} at each radius should be a function of the maximum stress experienced there. In figure (3) this is seen to be true irrespective of the maximum overall load applied.

Another aspect of the JKR theory that was modified to reflect the varying W_{ul} over the area of contact was the predicted pull-off force. By calculating the pull-off force based on the W_{ul} at the minimum area of contact, we were able to predict the pull-off force to within 5% of that observed experimentally (as opposed to up to a 50% error from the classical JKR theory).

Table 1. W_{ul} (J/m^2) a function of Maximum Load

Sample	Maximum Load (mN)		
	0.368	1.35	2.45
1.9r	0.086	0.140	0.161
2.5r	0.348	0.452	0.739

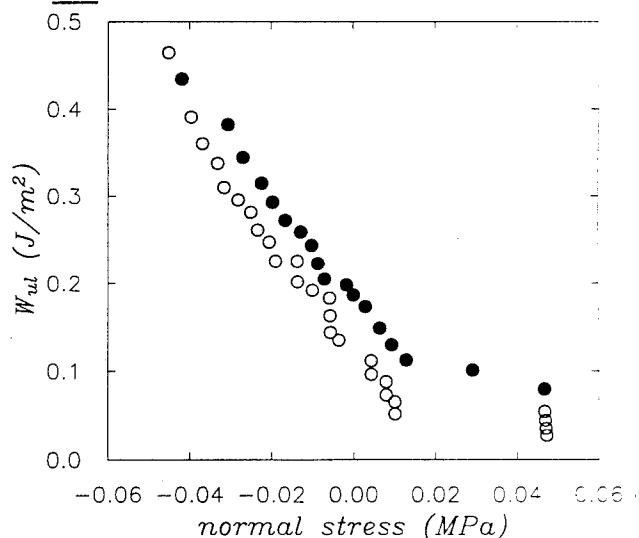


Fig. 3. 2.5r samples with 1.35 mN (filled circles) and 2.45 mN (open circles) maximum applied loads are evaluated to show the W_{ul} at every max σ experienced at every a (by equation (4)). Note the great similarity in the curves and their low constant value in regions of tension as compared to increasing W_{ul} in compressive regions.

CONCLUSION

The JKR technique was shown to be a reliable means to determine W of PDMS networks. We have found, however, that in cases where chemical adhesion hysteresis occurs, the JKR theory must be modified to correctly predict W_{ul} . We believe that due to the JKR pressure-profile, the chemical reaction causing this adhesion hysteresis is not constant over a , but is stronger in the center. We attribute the chemical hysteresis to a pressure-dependent, hydrogen bonding by the excess crosslinker added to the PDMS networks. Therefore we have extended the classical JKR theory to more accurately describe the case where W_{ul} is not constant over a . Not only did this better predict the experimentally observed pull-off force, but it also confirmed our hypothesis of the direct influence of the pressure profile on W_{ul} . For two different applied loads, the W_{ul} as a function of a was different; but, when the data were replotted as W_{ul} as a function of maximum normal stress they superimpose, verifying that the chemical reaction is dependent on the local pressure.

1. Johnson, Kendall, and Roberts, Proc. R. Soc. London, **324**, 301, (A 1971).
2. Horn, R.G., Israelachvili, J., Pribac, F., J Colloid Interface Sci, **115**, 480 (1987).
3. Chaudhury, M., Whitesides, G., Langmuir, **7**, 1975, (1991).
4. Merrill, W., Pocius, A., Thakker, B., Tirrell, M., Langmuir **7**, 1975 (1991).
5. Brown, H., Macromolecules, **26**, 1666 (1993).
6. Hertz, H. In Miscellaneous papers; McMillan & Co., London, 1896.
7. Silberzan, P., Perutz, S., Kramer, E.J., Chaudhury, M., Langmuir, **10**, 2466, (1994).

INFLUENCE OF INTERFACIAL CHAINS ON THE ADHESION BETWEEN A SOLID AND AN ELASTOMER.

M. Deruelle, J.P. Folkers, H. Hervet, L. Leger.

Laboratoire de Physique de la Matière Condensée
Collège de France
11, place Marcelin Berthelot 75231 Paris Cedex 05, FRANCE
U.R.A. C.N.R.S. 792

INTRODUCTION

In order to understand the mechanism of adhesion between elastomeric materials, model systems are often used. In some model systems, an elastomer is placed in contact with a surface on which polymeric chains have been deposited. The chains from the surface can then act as connectors to bind the elastomer to the surface (1). Recently, several studies have addressed the role of the length and the surface density of connectors in the adhesion to elastomers of different molecular weights (2,3,4).

In this study we varied the nature of the interfacial layers. We compared the adhesion to an adsorbed layer of polymer to that to a grafted layer of connectors.

EXPERIMENTAL

Materials and Sample Preparation.

The elastomers were made by cross-linking divinyl-terminated polydimethylsiloxane (PDMS) ($M_n=7300$, $I=2$) to 1,3,5,7-tetramethylcyclotetrasiloxane (D'4) using Karstedt's catalyst. The networks were allowed to cure at room temperature for 18 hours under an atmosphere of nitrogen. Different networks were obtained by varying the ratio of Si-H groups to vinyl groups ($R = \text{SiH/Vinyl}$) -- that is, the ratio of Si-H groups from D'4 to the vinyl groups from the PDMS. The networks were washed in toluene overnight to remove any non-reacted material.

Different types of layers were used in this study: The adsorbed layers were obtained by adsorption from solutions in octane with varying concentrations of dihydroxyl-terminated PDMS. All of these layers were formed on the native oxide layer of test-grade silicon wafers. The grafted layers were obtained by chemical grafting of mono-functionalized PDMS onto oxide layers for silicon that had been previously treated to inhibit adsorption but still allow chemical grafting. The free extremity of the chains from these layers were methyl-terminated. The thicknesses of all layers were measured with either ellipsometry or X-ray reflectivity.

Measurement of Elastic Moduli and Adhesion Energies.

For all measurements, we used the Johnson, Kendall, Roberts (JKR) technique. The experimental set-up is similar to that described in ref. (4). Because the magnitude of the adhesion energy G depends on the velocity at which the surfaces are separated, all of the energies are given for the velocity $0.1 \mu\text{m/s}$. W is the thermodynamic work of adhesion for an interface PDMS-PDMS, $W=2\gamma$, and was found to be $43 \pm 1 \text{ mJ/m}^2$. Although often used for measuring adhesion energies, the JKR apparatus can also be used for measuring elastic moduli. Figure 1 plots the elastic moduli of the different networks against the ratio SiH/vinyl. These results suggest that the elastomers are most highly cross-linked near a ratio 1.2, which we term the "optimum composition" for that particular PDMS.

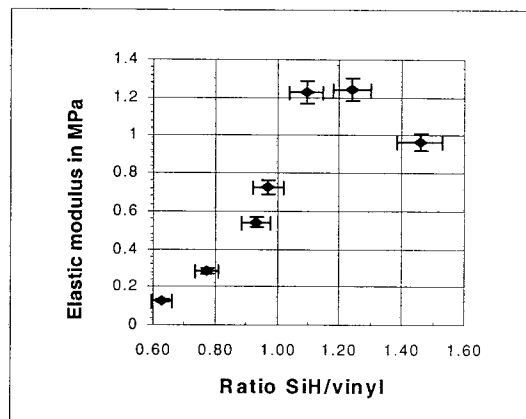


Figure 1: Variation of the elastic modulus with the chemical composition of the elastomer.

RESULTS AND DISCUSSION

Adhesion to Adsorbed Layers.

Using ratios close to the optimum composition for the network, we studied the adhesion to adsorbed layers of α, ω -OH PDMS. We have shown previously that the adhesion passes through a maximum with increasing surface density of chains (ref. 3,4). Figure 2 shows the maximum when an elastomer of molecular weight 10K between crosslinks was placed in contact with adsorbed layers of PDMS of molecular weight 412K with different surface densities.

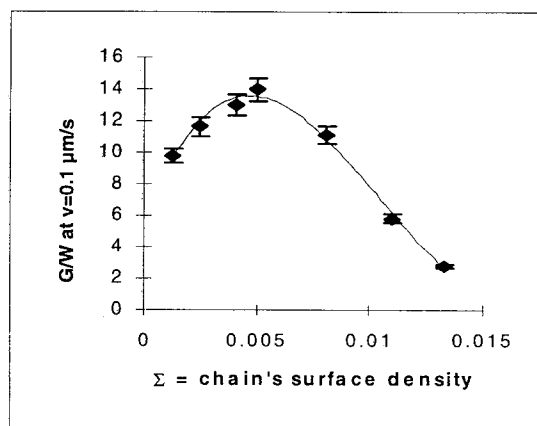


Figure 2: Adhesion to adsorbed layers of PDMS of molecular weight 412000 with different surface coverages.

In the theoretical models that describe the maximum (5), the elastic energy for stretching the network limits the amount of polymer that can penetrate into it, implying a surface density of chains above which interdiffusion is thermodynamically unfavorable. The elasticity of the interfacial layer of the network is thus an important parameter.

We then studied the adhesion against the layer with $\Sigma=0.0045$ from the previous series using elastomers with different chemical compositions. Figure 3 shows that the elastomer with the optimum composition gave the highest value of adhesion. This would imply that too many pendant chains on the elastomer are unfavorable to maximizing the interaction with the adsorbed layer. Another interesting result from Figure 3 is that the softer networks (i.e., those with the lower elastic moduli) formed weaker joints to the adsorbed layer. In principle, the softer networks should allow for increased interdiffusion of polymer chains relative to that for the stiffer networks. This effect was, however, not observed, implying a complex mechanism of adhesion between elastomers and adsorbed layers of polymer.

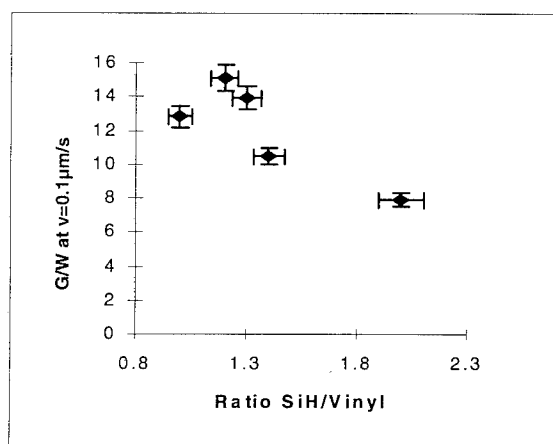


Figure 3 : adhesion against adsorbed layer of PDMS as a function of the chemical composition of the elastomer.

Adhesion to Grafted Layers.

The results obtained for the grafted connectors, given in Figure 4, are quite puzzling. In this experiment an elastomer of molecular weight 7K between crosslinks realized at the optimum composition was placed in contact with grafted layers of PDMS chains of molecular weights 17K and 300K. The contact time was 1 hour. (Experiments carried out overnight showed the same trend with a slight increase in the magnitude of the adhesion energies at low surface coverages.) These results show that very little adhesion is obtained with these systems compared to the case of adsorbed layers. The higher energies at low surface densities could potentially have been due to interactions between the elastomer and the underlying surface, as they extrapolate at zero density to the energy obtained when the elastomer is placed in contact with the treated silica.

Investigations are still underway to understand fully the difference between adsorbed and grafted connectors. One possible explanation of the results in Figure 2-4 could be "knitting" of the elastomer to the surface by the connectors, if the connector can "stitch" through the elastomer to the surface many times. For the

adsorbed layer, the connectors can readsorb to the silica after penetrating into the elastomer, thus forming stitches that would increase the adhesion; for the grafted layers, stitched connectors cannot readsorb, because of the inhibition of non-specific adsorption of the polymer to the silica. Following this train of thought, it is possible to surmise how less cross-linked elastomers were less strongly adhered to adsorbed layers: The introduction of non-crosslinked or "pendant" chains decreased the "grip" of the elastomer to stitched connectors.

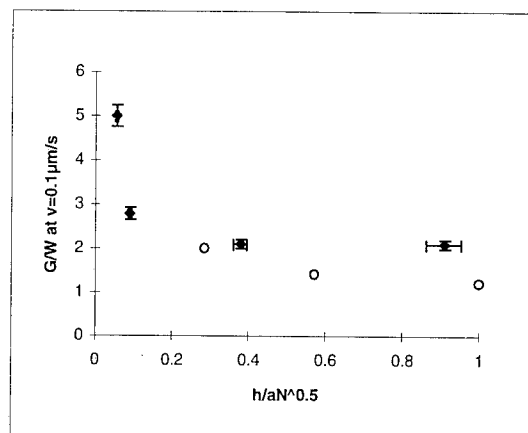


Figure 4 : Adhesion to grafted layers of PDMS given as a function of the fractional thickness, where $aN^{0.5}$ is the maximum thickness. Diamonds are for 300K grafted layers and circles for 17K.

CONCLUSION

In this study, we showed that adhesion to grafted layers of PDMS on non-adsorbing surfaces is very low compared to the adhesion to adsorbed layers of dihydroxyl terminated-PDMS on silica. We also studied the influence of the stoichiometry of the elastomer and showed the elastomer with the stoichiometry that gave the highest modulus also gave the highest value of adhesion to an adsorbed layer of PDMS. These results will help us understand the relationship between the structure of an elastomer and its adhesive properties.

REFERENCES

- [1] Raphaël E.; de Gennes P.G. *J. Phys. Chem.* 1992,96,4002.
- [2] Brown, H.R. *Macromolecules*, 1993,26,1666
- [3] Faraday discussion. 1994. 98 to appear.
- [4] Deruelle, M.; Leger L.; Tirrell, M., *Macromolecules*, to appear.
- [5] Brochard-Wyart, F. *et al. J. Phys. Chem.* 1994,98,9405.

Acknowledgments: We thank RHONE-POULENC for advice, materials and financial support.

INTERACTION OF FUNCTIONAL GROUPS IN WATER SOLUBLE POLYMERS WITH STEEL SURFACES

I Sutherland[†], PP Carpenter[†], RJ Heath[†], BR Pearson^{*}

[†]Loughborough University of Technology
Leicestershire, England LE11 3TU

^{*}IDAC, Hemel Hempsted, Herts, England

INTRODUCTION

Epoxy based electrocoat primers [1,2] are applied to steel body shells in the automotive industry to provide a barrier and impart a degree of corrosion resistance to the steel. If the interaction between the paint and the steel can be understood at the molecular level it may be improved, hence the onset of corrosion of the steel may be retarded. Commercial electrocoats are very complex and to probe these interactions we have used simple polymers each containing only a single active functional group. A study of the nature of the interaction between polymers containing specific functional groups and a mild steel substrate has been undertaken using reflection spectroscopy [3,4]. Here we report some preliminary results. Changes have been observed in infrared spectra as a function of polymer film thickness enabling us to identify interactions specific to the interphase region.

EXPERIMENTAL

The steel tokens (Pyrene 8074 mild steel) were cleaned with 5% sodium hydroxide solution at 40°C in an ultrasonic bath, and washed with distilled water. SEM showed typical surface roughnesses of the order of microns on the steel surface. Whilst such samples are not ideal for reflection spectroscopy they are representative of steels used industrially.

Two polymers were chosen for study, each containing a single functional group. Poly (acrylic acid) (PAA) and poly (vinyl alcohol) (PVA) were both supplied by Aldrich. These polymers are water soluble and were dissolved in triple distilled water in a range of concentrations between 1% and 0.001% weight / volume. Approximately equal amounts of each polymer solution (0.17 g cm⁻²) were coated onto cleaned mild steel tokens and dried at 80°C for approximately an hour. If the polymer was deposited uniformly then the most dilute solution used would produce a polymer layer, after drying, of approximately 0.02 microns.

IR spectra were collected at an angle of incidence of 80° using a Nicolet 20DXC spectrometer with a Spectratech specular reflection attachment. For each polymer the transmission spectrum was recorded to aid to assignment

of IR bands. XPS spectra were recorded on a VG ESCALAB spectrometer.

Polymer layers of approximately 150 microns were deposited from solution onto the steel surface. Adhesion was measured using a one square inch composite butt test with a crosshead speed was 1mm min⁻¹.

RESULTS

Poly (acrylic acid)

Spectra from coated tokens are shown in figure 1, and the peaks detected are assigned in table 1.

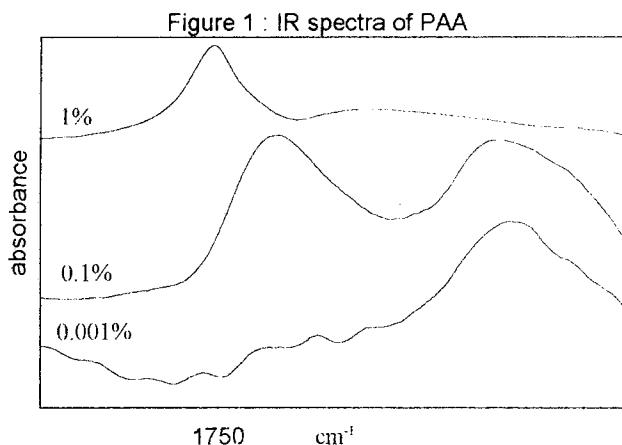


Table 1: Assignment of peaks for samples coated with poly (acrylic acid) (cm⁻¹)

	C=O v, non H bonded	FeOOC iron salt	C=O v, H bonded	C-H v
1%	1752	/	1665	1468
0.1%	1720	1592	/	1453
0.001%	/	1585	/	1453

/ : not detected

Carbonyl peaks at 1752 cm⁻¹ and 1665 cm⁻¹ were detected for samples coated with concentrated solution and were assigned to non-H bonded and H bonded carboxyl groups respectively. As the layer becomes thinner these two

peaks shift and reduce in amplitude, and a third peak at 1585 cm^{-1} is clearly visible. This peak may be assigned to CO_2^- groups [5].

Thus, there is strong evidence for chemical bonding occurring between metal atoms and the polymer. Since the minimum possible thickness of a coating, if uniform, would be approximately 20 nm, and under these conditions the dominant IR peaks are due to the carboxylic acid salt, this suggests that there is probably some diffusion of iron atoms into the adsorbed polymer producing an interphase region of appreciable thickness.

XPS measurements taken from a peeled side of a PAA film and the metal from which it came (table 2).

Table 2 : XPS compositions (atom %)

	polymer side (%)	Steel side (%)
Carbon	72.2	52.9
Oxygen	25.3	37.5
Iron	2.5	9.6

These results show the presence of a significant concentration of iron on the polymer side of the interface but it was not possible to unambiguously confirm its presence as carboxylate.

Poly (vinyl alcohol)

The peaks of interest are the OH stretch at 3331 cm^{-1} , the CH + OH deformations at 1445 and 1326 cm^{-1} and the C-O stretch at 1195 cm^{-1} . The spectra obtained are shown in figure 2 and data summarised in table 3.

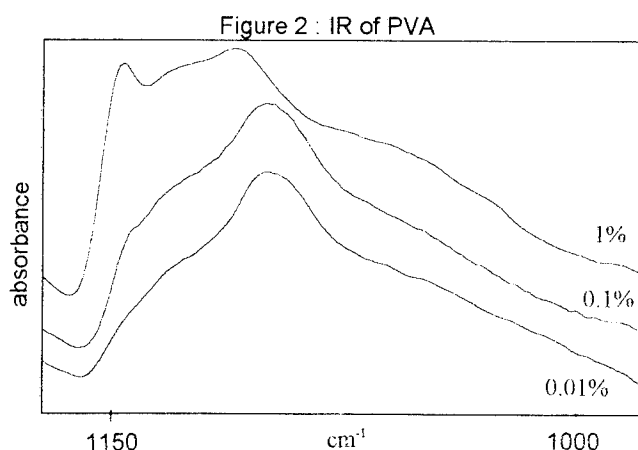


Table 3 : Assignment of peaks for samples coated with poly (vinyl alcohol) (cm^{-1})

	OH v	(OH+CH) δ	CO v	C-C v
1%	3395	1449 1332	1108	1144
0.1%	3267	1432 1334	1095	weak shoulder
0.01%	3316	1451 1332	1096	/

/ : not detected

It can be seen that the peaks associated with (OH + CH) deformations do not appear to shift to any great extent and nor does the OH stretching mode. The films are too thick to allow resolution of hydrogen bonding interactions with the substrate. The peak related to crystallinity (1144 cm^{-1}) [6] is common to both the transmission and 1% coated samples and is missing from the 0.1% and 0.01% tokens. This is attributed to a decrease in the crystallinity of the polymer as the thickness decreases and would result in a polymer layer having different mechanical properties in comparison to the bulk polymer.

Adhesion

Table 4 : Joint strength

	mean (N)	error (N)
PAA	3727	+/- 400
PVOH	1800	+/- 300

Visual inspection showed that failure occurred at or near the interface. The higher value observed for PAA may be due to chemical reaction with the surface, but further work is required to confirm this.

CONCLUSIONS

Thin layers of water soluble polymers on steel surfaces have been studied by FTIR and XPS. From studies of thin layers of PVA, there is some evidence for a change in the morphology of the polymer as we approach the surface. PAA reacts with the steel surface. There is good evidence for the formation of an interphase region in excess of 20nm thick containing iron carboxylate. Higher bond strengths were observed for PAA on steel compared to PVA.

It is proposed to extend the work to include water soluble polymers containing basic as well as acidic groups and to study interfacial interactions in more detail on flat substrates.

REFERENCES

1. D.Pletcher and F.C. Walsh, *Industrial Electrochemistry* 2nd edn. (Chapman and Hall, London, 1990), p441.
2. C.K. Mital, *Paintindia* Dec. 1992, 29-33
3. T. Nguyen, E. Byrd and A. Tsao, *J. Appl. Poly. Sci.* **32**, 6339-6352 (1986)
4. L. Ulren, T. Hjertberg, H. Ishida *J. Adhesion* **31**, 117-136 (1990)
5. A.R. Brodskii et.al. *J. Organomet Chem.* **178**, 325-31 (1979)
6. H. Tadokoro et.al. *J. Poly. Sci.* **26**, 379-82 (1957)

Adsorption of polycyanurate films on silicon wafers and aluminium substrates studied by XPS

S. Dieckhoff, V. Schlett, W. Possart*, O.-D. Hennemann

Fraunhofer-Institut für Angewandte Materialforschung
Lesumer Heerstraße 36, D-28717 Bremen

*Fraunhofer-Institut für Angewandte Materialforschung, Außenstelle Teltow
Kantstraße 55, D-14513 Teltow

ABSTRACT

We have investigated thin films of a DCBA prepolymer on silicon and aluminium substrates. Angle resolved x-ray photoelectron spectroscopy reveals some thickness-dependent features, which lead to an adsorption model for the DCBA prepolymer molecules. The adsorption of the first layer is governed by the interaction of the triazine rings with the substrate surface.

INTRODUCTION

The fundamental understanding of the chemical and physical phenomena of the adhesion at substrate/polymer interfaces is of great interest in order to solve and control adhesion problems.

We had used a prepolymer of the diandicyanato bisphenol A (DCBA) as a model of a network forming polymer, which has a potential as a high temperature adhesive. With regard to their importance in technical applications silicon wafers and aluminium has been used as substrates. We have studied the prepolymer-substrate interaction by the characterization of the prepolymer interphase. In order to identify differences between the prepolymer bulk and its interphase we have varied the film thickness which in turn changes the ratio of the analysed bulk and interphase volume.

We employed the spectroscopic techniques XPS, FTIR, AES and the imaging techniques AFM, STM, as well. AES and STM were only used for substrate characterization. This publication presents mainly the XPS results, those from AFM and FTIR can be found elsewhere [1, 2].

EXPERIMENTAL

One main part of our study was the characterization of the DCBA films by x-ray photoelectron spectroscopy (XPS) using a VG Scientific ESCALAB MK II with a MgK_{α} x-ray source typically operated with a power of 120 W. The base pressure of the analysis chamber was about 2×10^{-8} Pa. High resolution spectra were taken with 10 eV and survey spectra with 50 eV pass energy (CAE). The analysed area was $2 \times 5 \text{ mm}^2$ and angle resolved measurements were performed at two different

take-off angles, $\Theta = 0^\circ$ and $\Theta = 80^\circ$ with respect to the surface normal. Bulk-spectra in this publication are taken with a VG ESCALAB 220i XL (monochromated AlK_{α} x-ray source, XL-mode) which was available at the end of our investigation.

In addition, several other techniques were used to characterize substrates and films: Substrates were also investigated by AES using a Perkin Elmer PHI 660 SAM. Ellipsometry (SD 2002, Plasmos and Auto El II, Rudolph Res.) was employed in order to determine the thicknesses of the prepolymer layers. We used FTIR (FTS 60A, Bio-Rad) as a second spectroscopic technique to complement the XPS investigations. The surface topography of the substrates and the prepolymer coatings were studied by AFM (Omicron Vakuumphysik GmbH and Nanoscope III, Digital Instruments).

Silicon wafers ($\langle 100 \rangle$ -orientation, n-doped (Sb)) and thin evaporated aluminium films (thickness of about 500 nm) on silicon wafers served as substrates, both covered by their native oxides or hydroxides.

DCBA prepolymer films with thicknesses between 3 nm and 50 nm were deposited on the Si and Al substrates by spin and dip coating. The substrates were coated without any further pretreatment and 1,1,1-trichloroethan was used as the solvent for the prepolymer. The prepolymer was synthesized by a cyclotrimerisation reaction of cyanate groups of the DCBA. The reaction was terminated at 45 mol% conversion of the cyanate groups into triazine rings. The composition of the prepolymer was determined by HPLC (Tab.1).

Tab. 1: Composition of the DCBA prepolymer

Composition	number %
monomer	75.6
trimer	12.5
pentamer	4.6
heptamer	2.3
nonamer	1.3
higher oligomers	3.7

Hence the prepolymer consists of two different sorts of molecules. The monomer contains cyanate groups only.

whereas the oligomers have as potential reactive species cyanate groups as well as triazine rings. Both of them are supposed to interact with the substrate surface.

RESULTS AND DISCUSSION

The Si and Al substrates are covered by their native oxides or hydroxides, respectively. The silicon oxide layer (thickness of about 1 nm, determined by XPS and AES) is formed by Si in several intermediate oxidation states. Due to the limited energy resolution of the $\text{MgK}\alpha$ -source only the SiO_2 oxidation state is well separated. The aluminium surface layer consists of oxide and hydroxide states, as well. From the XPS O1s spectra it can be concluded that about 70% of the oxygen is in a hydroxide state. As determined by XPS and AES, the thickness of this surface layer is about 2.8 nm. In addition, both substrates are covered by an atmospheric contamination due to the ex-situ preparation. While the contamination layer on the Si wafer is purely aliphatic with a thickness of about 0.5 nm, the contamination on the Al substrates contains a (C-O)- and a (C=O)-component. Angle resolved XPS measurements reveal that the (C=O)-component is located at the interface of the contamination and the oxid layer. The thickness of the contamination layer on the Al substrates has been determined to about 0.7 nm (XPS, AES).

AFM reveals [1] the almost atomic smoothness of the silicon wafers. The roughness averaged over one batch of wafers amounts to 0.13 nm RMS. Prepolymer films on silicon wafers are completely covered, already with a mean film thickness of only 3 nm.

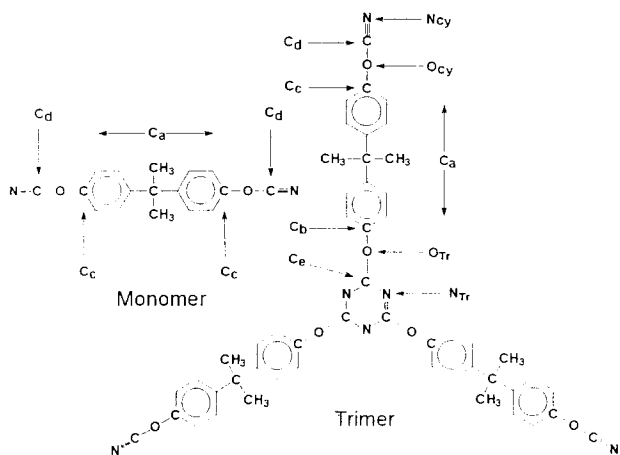


Fig. 1: Structure of the DCBA monomer and trimer. Higher oligomers have no additional chemical components

The roughness of the evaporated aluminium substrates is about 10 nm RMS. AFM results of the coated aluminium substrates proof that the thinnest prepolymer

films consist of isolated droplets with a height of about 15 nm. Only films with thicknesses of more than 13 nm are closed. Therefore, an unambiguous XPS characterization of the interphase is not possible and conclusive results are only obtained from films on silicon wafers.

The chemical structure of the trimer molecules displays all possible components (Fig. 1), which are also part of all other oligomers. From that, at least five different carbon states can be distinguished.

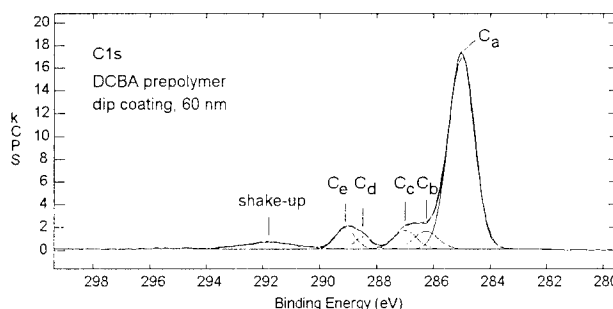


Fig 2: High resolution XPS C1s spectrum of a 60 nm DCBA prepolymer film.

In the C1s XPS spectra (Fig. 2) of the DCBA prepolymer these five states are clearly resolved. The first C1s peak (C_a) is caused by the emission of the aromatic and aliphatic C-atoms. The second and the third peak (C_b , C_c) correspond to those aromatic carbon atoms in the benzene rings which are bonded to the oxygen atom close to the triazine ring (C_b) or the oxygen atoms in the cyanate group (C_c). The fourth and the fifth peak are formed by the emission of those C-atoms bonded to the nitrogen in the cyanate group (C_d) and in the triazine ring (C_e), respectively. The components C_b - C_e were identified by comparison with the C1s spectra of the DCBA monomer where only the C-components C_a , C_c and C_d are present (Fig. 1). The sixth peak in the C1s-spectra is a shake-up structure caused by the $\pi \rightarrow \pi^*$ -transition in the aromatic rings [3].

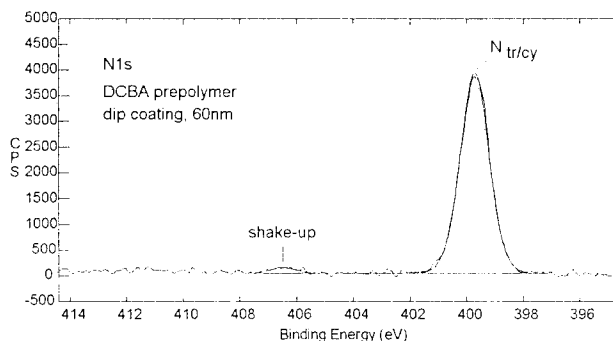


Fig. 3: High resolution XPS N1s spectrum of a 60 nm DCBA prepolymer film.

In the N1s-spectra (Fig. 3), the two expected nitrogen states (N_{tr} , N_{cy}) are not resolved, whereas the two oxygen states (O_{tr} , O_{cy}) can be distinguished in the O1s-spectra (Fig. 4). Therefore, the O1s spectra are ideally suited for the characterisation of cyanate groups and triazine rings.

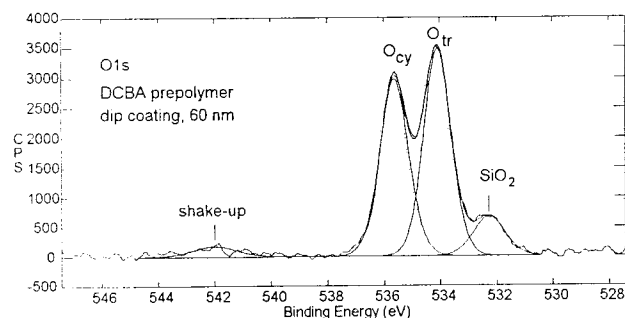


Fig. 4: High resolution XPS O1s spectrum of a 60 nm DCBA prepolymer film. The SiO_2 -Peak originates from a contamination caused by milling the prepolymer.

The energy optimisation of the DCBA trimer molecule has been determined by a quantum mechanical AM1 calculation [4, 5]. As a result the conformation with the lowest total energy ($E_{tot} = 1.59$ kJ / mol) is shown in Fig. 5. The conformation looks similar to a basket where the bottom is formed by the triazine ring.

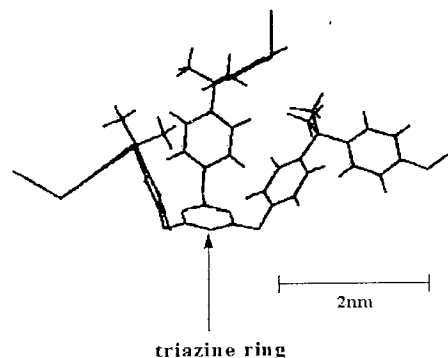


Fig. 5: Conformation with the lowest total energy of the trimer of the DCBA

Angle resolved XPS measurements proof a specific adsorption of the first DCBA prepolymer layer. Fig. 6 displays the shake-up intensity of films with thicknesses between 3 nm and 20 nm for two different take-off angles. At 80° take-off angle (information depth about 1.7 nm), the shake up intensity of the benzene rings increases significantly for those films with thicknesses less than 5 nm. These films are comparable with the spacial dimension of the DCBA trimer (Fig. 5). At 0° (normal emission, information depth about 10 nm) the

shake-up intensity is independent of the thickness, as expected.

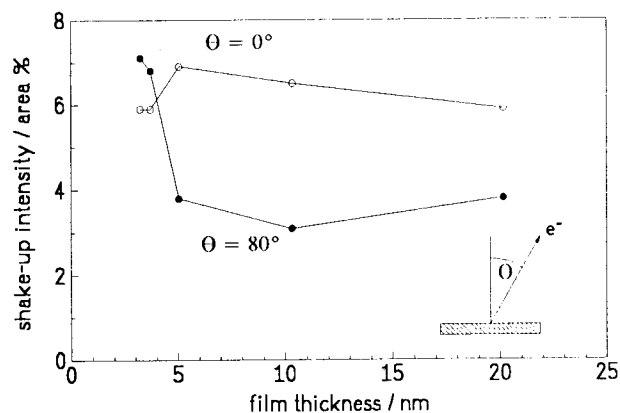


Fig. 6: XPS C1s shake-up intensity for two different take-off angles Θ .

These findings can be interpreted that the outer surface of the first layer consists mainly of benzene containing branches while triazine rings are mostly located near the substrate surface. It seems that there is a certain molecular arrangement in the first layer, while in thicker films the molecules are distributed more randomly. This adsorption model is supported by the calculated conformation of the DCBA trimer (Fig. 5), where the triazine ring is located opposite the benzene containing branches. These results are strong hints that mainly triazine rings are interacting with the surface of the substrates.

We gratefully acknowledge the financial support of the Volkswagen-Stiftung.

REFERENCES

1. T. Gesang, R. Höper, S. Dieckhoff, A. Hartwig, W. Possart, O.-D. Hennemann, submitted for publication in *Surf. Sci.*
2. W. Possart, submitted for publication in *J. Adhesion*
3. A. Dilks, *Electron Spectroscopy - Theory, Techniques and Application* (Eds. C.R. Brundle and A. B. Baker) Vol 4. Academic Press, London, 1981
4. U. Höweler, *MOBY - Molecular Modelling, Vers 1.5*. Springer, Heidelberg Berlin, 1992
5. M. J. S. Dewar et al., *J. Am. Chem. Soc.* **107**, 3902, (1985)

A Comparison of Scanning Force Microscopy and Ellipsometry for Thickness Determination of Ultrathin Polymer Films

T. Gesang, D. Fanter*, R. Höper, W. Possart*, O.-D. Hennemann

Fraunhofer Institut für angewandte Materialforschung, Bereich Klebtechnik,

Neuer Steindamm 2, D - 28719 Bremen, *Kantstr. 55, D-14523 Teltow

INTRODUCTION

Atomic force microscopy (AFM) is a high resolution imaging technique which can also be exploited for thickness measurements. A comparison of AFM [1] and ellipsometry [2] for thickness determination is presented.

EXPERIMENTAL

The samples used for the thickness measurements were films of a dicyanate of bisphenol A [3] spin cast onto silicon wafers. The films are continuous even with only 2 or 3 nm ellipsometric thickness.

AFM FOR THICKNESS DETERMINATION

Film thickness was determined by formation and evaluation of scanning squares. A scanning square of $(500 \text{ nm})^2$ area could be induced by increasing the scanning force. A subsequent $1 \mu\text{m}^2$ image with reduced force incorporating the scanning square is shown in the AFM image Fig. 1.

The rear exhibits the unperturbed polymer film, the front displays the scanning square.

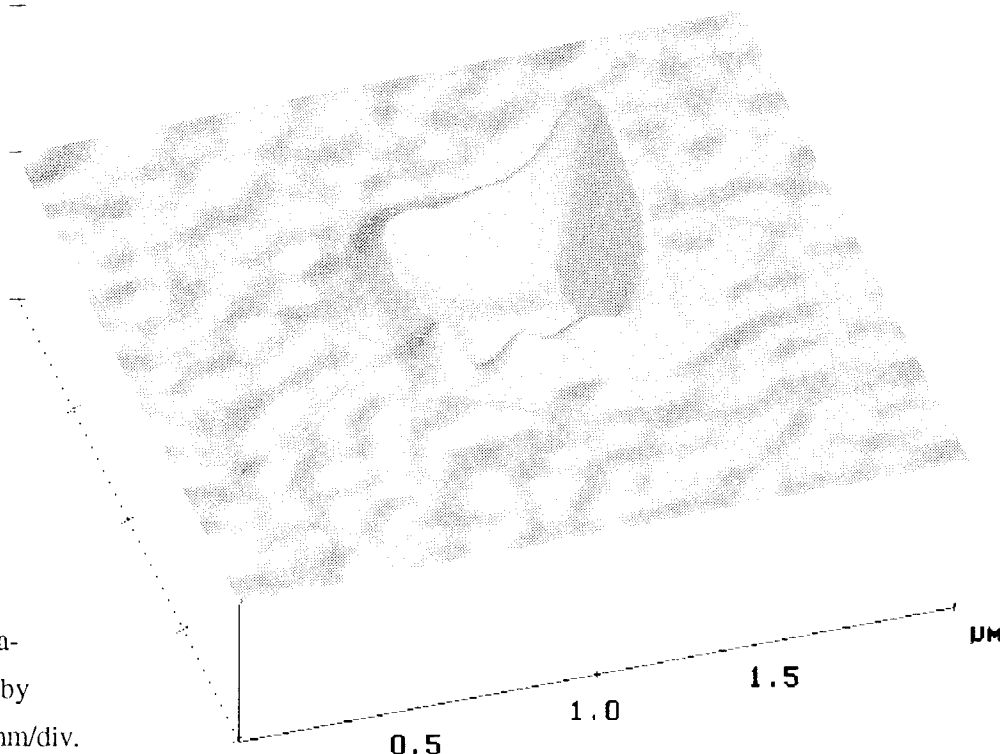
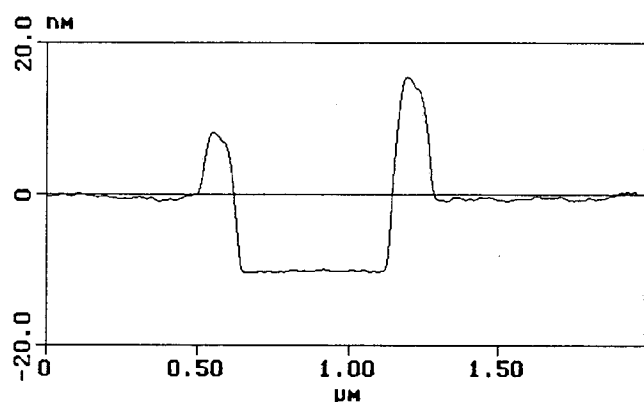


Fig. 1: AFM induced scanning square in the ultra-thin polymer layer imaged by AFM. Scaling: z-axis: 50 nm/div.



A cross section, **Fig. 2**, across scanning square (left) and polymeric film (right), reveals the flatness of the scanning square.

Fig. 2: Software cross section of Fig. 1 displaying scanning square (left) and polymer (right).

With the AFM all height levels $z(x,y)$ of the imaged area are stored and the film thickness can be determined by means of the AFM software. The software allows averaging over an area large compared to morphological structures and thus evades the necessity of subjectively defining height levels inherent in the measurement of a step height by a cross section (**Fig. 2**).

Further issues checked concerning accuracy include :

- AFM height calibration
- reproducibility of AFM measurements
- homogeneity of film thickness
- possibility of film deformation while imaging
- possibility of polymeric residue on the bottom of the scanning square

Considering all possible errors a confidence interval of ± 0.5 nm (1σ) was determined.

ELLIPSOMETRY FOR THICKNESS DETERMINATION

Every substrate is characterised (complex refractive index of the substrate and thickness of oxide/contamination layer) by employing a one layer model. For the thickness determination of the ultrathin polymer films a simple two layer model (silicon plus oxide/contamination plus polymer film) was used. Moreover, the complex refractive index of the ultrathin polymer film has to be known [4]. This entity is not directly accessible. Therefore, the value for thick (50 to 100 nm) films was utilised, which equals the bulk value.

The determination of the polymer thickness results in an error up to 0.1 nm due to measurement inaccuracies of the one angle of incidence and one wave length equipment.

RESULTS AND DISCUSSION

Fig. 3 shows the comparison of the film thicknesses as determined by AFM and ellipsometry at the same location on the sample.

Deviations from the solid line are due to *systematic* methodical errors of one or both methods. For thicknesses larger than some 10 nm AFM leads to significantly smaller values than ellipsometry. For about 10 nm thickness there is excellent agreement between both methods. For less than 10 nm there is a steadily growing deviation: AFM leads to larger values than ellipsometry.

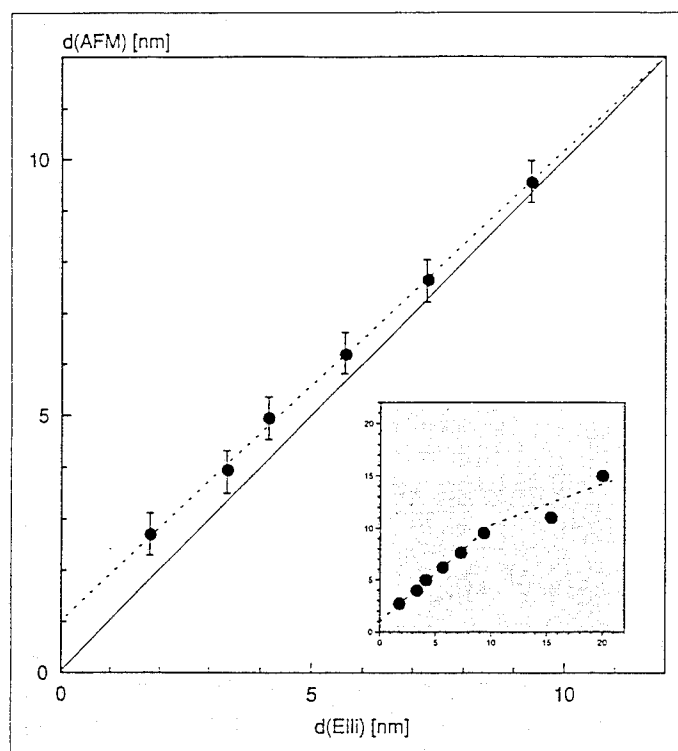


Fig. 3: Comparison of the film thicknesses as determined by AFM and ellipsometry at the same location on the sample.

----- : positions on which all points would fall, if both methods led to identical thickness values.

The most likely reason for the discrepancy in the regime above 10 nm (inset in **Fig. 3**) is, that the AFM tip can not penetrate the film fully during scanning square formation. The other possible reason, that the tip can not reach the bottom of the scanning square during imaging, can be excluded due to the large size of the scanning square.

The deviation below 10 nm in **Fig. 3** is a systematic one as can be concluded from the very good linearity of the measured points (which appears to be much better than the AFM error bar) and from the steadily increasing deviation with decreasing thickness. The most probable reason of this deviation is the utilisation of a constant refractive index for the polymer in ellipsometric evaluation. It is likely, that for ultrathin films the refractive index becomes modified due to the interaction of the polymer molecules with the substrate. This modification is expected to be the larger the more the film thickness decreases. This tendency is consistent with the steadily increasing deviation between AFM and ellipsometry with decreasing film thickness.

In addition, a second factor might influence the ellipsometric thickness evaluation. The two layer model assumes perfectly flat sample interfaces and surfaces. However, AFM images reveal that both substrate and polymer surfaces have a specific morphology, resulting in non zero roughnesses. Strictly, this should be included in the ellipsometric model [5], [6]. The fact that in the 1 to 10 nm range AFM measures bigger film thicknesses than ellipsometry will be even more pronounced, if the possible residual polymer layer in the scanning square is considered. This error probably retains the slope of the straight line and only leads to a small downward shift of the line. However, this residual layer presumably is much thinner than the polymer thickness to be determined.

References

1. Binnig, C. F. Quate, Ch. Gerber, Phys. Rev. Letts., 56(9), 930 (1986)
2. G. Tompkins, A User's Guide to Ellipsometry, (Academic Press, San Diego 1993)
3. M. Bauer, J. Bauer in I. Hamerton (Ed.): The Chemistry and Technology of Cyanate Ester Resins, (Chapman and Hall, Glasgow, 1994), in press
4. M. A. Azzam, N. M. Bashara, Ellipsometry and Polarized Light, (North Holland, Amsterdam, 1992)
5. E. Aspnes, J. B. Theeten, F. Hottier, Phys. Rev. B20, 3292 (1979)
6. J. M. M. Raaymakers, Verkerk, M. J., Appl. Optics 25, 3610 (1986)

ADHESIVE SELECTION PROTOCOL

G. L. Anderson

Thiokol Corporation, Science and Engineering
M/S 243, P.O. Box 707, Brigham City, UT 84302-0707

INTRODUCTION

In order to develop a methodology for selecting adhesive systems which will result in reliable bondlines, historical failure causes were examined: material/process sensitivities, improper material characterization and insufficient analysis. The material and bonding process must be controlled sufficiently; however, controlling process parameters which do not affect bond performance or reliability creates unnecessary recurring expenses. Bond system performance testing must be done in a manner which is representative of the surface preparation to be used in the production area and in a stress state which represents that induced in the production hardware. Bondline analyses must be performed using accurate constitutive properties of the selected adhesive system. Each of these factors must be taken into account throughout the adhesive selection. By eliminating the causes of the majority of the historical bondline failures, bondline reliability will be greatly enhanced.

APPROACH

The adhesive selection methodology is divided into three phases: adhesive candidate selection, process sensitivity studies and down selection, and system implementation. Adhesive candidate selection includes establishing selection criteria, selecting adhesive candidates, performing screening tests and performing a preliminary down selection. Process sensitivity studies and down selection entails evaluating the production process and defining experimental test matrices to identify critical process and material parameters, performing tests on intentionally induced variations, performing an aging study and making a down selection. Finally, system implementation involves characterization testing and process control.

DISCUSSION

Adhesive Candidate Selection

Design requirements for the selection of a bond system come from the interaction of design engineering, manufacturing engineering and structural analysis. Basically, the design group develops the design and determines the operational specifications and failure criteria

(e.g., maximum principal stress, strain energy density, etc.). The manufacturing group determines the necessary requirements to aid in the manufacture of the component bonds (e.g., pot-life). Structural analysis involving a parametric finite element analysis (FEA) of the component bondlines is needed to obtain the structural requirements. A preliminary analysis is performed on all bondlines in order to identify the bondlines which are the most highly stressed. Input material properties of a typical room-temperature cure epoxy adhesive may be used for the preliminary analysis. The FEA output should be in terms of the failure criteria previously determined.

Once the preliminary analyses are complete and the critical bondline is determined, the parametric study can be performed on the critical bondline using typical modulus/Poisson's ratio combinations for the various groups of adhesives which are compatible with the substrate materials and the process. The parametric study establishes the relationship between the modulus and Poisson's ratio of the adhesive and the required capabilities of elongation and strength. The analytical results can be used to plot response curves in which the responses are stress and strain and the parameter is adhesive modulus/Poisson's ratio combinations.

In summary, the adhesive requirements, pot-life, cure temperature, rheology, operational temperature range, strength and elongation, are now defined. Suitable adhesive candidates can now be identified for the screening tests. Regardless of the source used to identify preliminary candidates, the information desired is adhesive formulations whose properties exceed the defined requirements.

Once preliminary candidates have been selected, samples of the candidates are tested for screening. Screening tests include pot-life, rheology, uniaxial tension, adhesion strength, fracture toughness, dynamic mechanical analysis, and differential scanning calorimetry. To reduce the cost of the screening tests, candidates which do not meet a requirement should be eliminated from further testing. If no candidates remain after these eliminations, the selection requirements and FEA must be reviewed. It is quite possible that slight changes in the local geometry will significantly reduce the stresses in stress concentration regions. Points of geometric discontinuity (corners, bond

termini, etc.) must be examined carefully. The processing requirements, especially those which eliminated promising candidates, can also be reviewed to see if they can be relaxed.

The pot-life of an adhesive can be measured by continuously monitoring the viscosity throughout cure. The pot-life measurement begins with the combination of the resin and curative and ends at the point where the viscosity doubles from its initial reading. The continuous viscosity measurement may also be the rheological information needed for processing. In other applications where the adhesive is required to stay on a non-horizontal surface, a slump or fluid yield point may be needed. The slump can be measured following ASTM D-2202. The fluid yield point is a measure of the maximum shearing stress which does not cause flow, and can be measured using a vane rheometer.

Adhesive bulk material uniaxial tension tests should be performed using void-free specimens cut in such a way as to avoid flaws along the edge of the specimen, perpendicular to the line of the load. This is especially crucial when failure properties are desired. Additional information concerning the tensile testing is available in ASTM D-638. Testing should be performed using axial and transverse extensometers to measure axial and transverse strains. This will allow calculation of both the adhesive modulus and Poisson's ratio. The use of strain gages bonded to the specimen should be avoided, because the polyimide backing of the strain gage and the adhesive used to bond the gage to the test specimen can significantly stiffen the test article, leading to erroneous results.

Tensile adhesion testing should be performed using representative substrate material. The bond thickness should be representative of the mean of the expected range. For preliminary screening, it is suggested that a high-quality surface preparation be used in order to obtain the absolute capability of the bond systems in the screening tests. The effect of lesser surface preparation is examined in further testing.

Adhesion testing in shear should be performed using torsion ring specimens^{1,2}. All lap shear geometries induce large peel stresses (normal to the plane of the bondline) during loading^{3,4}. These peel stresses tend to cause failure at loads significantly lower than the shear capability of the adhesive. By loading the specimen in torsion, with the axial load controller set to zero in order to control the axial displacement, a state of simple shear stress in the bondline results. The actual shear testing should be performed similarly to the tensile testing.

Bondline fracture toughness should be obtained using tapered double cantilever beam (TDCB) specimens (ASTM D-3433) for metal substrates, width tapered double cantilever beam specimens⁵ for laminated composite materials and peel specimens for elastomeric substrates⁶. High-quality surface preparation is again suggested for this testing.

Two additional tests are suggested as part of the screening process: bondline fracture toughness, dynamic mechanical analysis (DMA) and differential scanning calorimetry (DSC). DMA characterizes the glass transition temperature (T_g), the storage and loss moduli in the glass and rubber states and high temperature degradation temperature regions. Adhesives with glass transition temperatures near ambient temperature should be avoided in most cases, where possible, because of the dramatic property changes at slightly elevated temperature. DSC aids in understanding the cure kinetics which is important for understanding the state of cure as a function of time and temperature. This is helpful in determining cure times at temperatures other than those reported by the vendor. The state of cure can be calculated from the vendor recommended cure conditions and used to determine the time required to cure the adhesive to the same extent at other temperatures.

At this point it is necessary to reduce the number of candidates to the two or three most promising candidates in order to reduce the cost of the Process Sensitivity Studies. Thus, the screening of the remaining candidates will be done on the basis of the system robustness. A preliminary indication of the robustness can be obtained by testing TDCB specimens contaminated reproducibly at low levels with the most probable contaminant from the manufacturing area. The candidates with the highest fracture toughness values when bonded to the contaminated surfaces should serve as the candidates used in further testing.

Process Sensitivity Studies and Down Selection

There are two processes which should be assessed for sensitivities: the vendor adhesive formulation process and the bond production process. Both processes are assessed using a three step process: evaluate the process to identify possible critical parameters, induce variations with respect to the identified parameters, and evaluate the variations to assess needed control. In addition, raw material variation can occur at the vendor level. These effects should also be determined.

In evaluating the processes, process parameters and their extreme operating limits are required. If the limits are unrealistically large, the test results will not give a true

distinction between critical and non-critical parameters. Perhaps a worse case results from underestimating the breadth of the process parameter limits. During production, the process parameters which are determined to be non-critical during this study must be controlled within the tested limits in order to ensure reliable bonds. If the limits are too small, production expenses and the number of discrepancies will be large. Unfortunately, combining the effects of possible vendor process/material variation with the effects of the production process variation results in test matrices which are too large to perform cost-effectively. It is suggested that the two sources of variation be decoupled, testing the effects of vendor process/material variation with the typical production process and vice versa.

Two experimental test matrices can now be designed with the cost of evaluation greatly reduced by statistical design of experiments. The maximum number of parameters which will allow reduction (fractioning) of the test matrices without confounding the primary cause-effect relationships with secondary relationships is eight (for sixteen test conditions). The criticality of the identified parameters must now be estimated from adhesion theory and experience. Only the eight most critical parameters will be tested. These eight parameters from each process are used to create L16 fractional factorial matrices.

The variations are then induced in materials and processes in accordance with the designed matrices. Tests to be performed on the variations are those used in screening the preliminary candidates. Analysis of variance is performed to determine the parameters which affect the performance of the bond system and the overall robustness of the bond system.

The last information needed to perform the down selection is an understanding of bondline aging. A large amount of information is available regarding long-term aging studies⁷ and complete characterization can be costly and time-consuming. For many applications, real-time testing with typical and worst-case environmental storage is sufficient. Test times should be arranged on a logarithmic scale, increasing the time interval between each set of tests. Accelerated aging studies (aging at elevated temperature) are useful to allow a timely down selection, but should be followed with an abbreviated real-time study, as different reaction mechanisms may be important at elevated temperatures.

At this point, the down selection is made using quality functional deployment (QFD) process. Important qualities of the bondline (e.g., pot-life, robustness, etc.) are weighted on a numeric scale with higher weights given to

the more important qualities. Next, the adhesive candidates are ranked on the numeric scale per the important qualities. Finally, the bond system candidates are given an overall ranking by summing the products of the quality weights and the respective candidate rankings. The candidate with the highest overall ranking is the best overall choice for the bondline.

System Implementation

Prior to production start-up with the new adhesive, process control limits must be set. In the previous section, critical process parameters and sensitivities were identified. By testing for response at various levels of the critical parameters, sensible control levels can be selected. Note that only those bondline qualities which were shown to be sensitive to the variation from the previous results need be tested.

Final characterization testing is often needed prior to system implementation. The final characterization testing is performed in conjunction with the established failure criteria in order to establish a reportable bondline reliability. For example, A-basis values of tensile adhesion strength can be compared with the maximum tensile stress expected in a given bondline loaded primarily in tension in order to determine the safety factor.

CONCLUSIONS

Many benefits are expected from employing a systematic method for selecting adhesives. By examining and eliminating causes of historical failures, increased reliability will result. Costs involved in selecting adhesives will also be reduced over the long term as databases containing the information required to select an adhesive are gathered from previous uses of the protocol. Finally, the number of adhesives used in a structure can be reduced once the requirements are determined for each bondline by grouping bondlines with similar requirements.

BIBLIOGRAPHY

1. R.W. Bryant and W.A. Dukes, *Brit. J. of Appl. Phys.*, **16**, 101 (1965).
2. W.T. McCarvill and J.P. Bell, *J. Adhesion*, **6**, 185 (1974).
3. R.D. Adams and W.C. Wake, *Structural Adhesive Joints in Engineering*, (Elsevier Applied Science Pub., New York, 1984), ch. 2.
4. J.K. Stozier et al., *J. Adhesion*, **3**, 209 (1987).
5. G. Liu and A.N. Gent, *J. Adhesion*, **38**, 79 (1992).
6. R.L. Patrick, ed., *Treatise on Adhesion and Adhesives*, Vol. 6, (Marcel Dekker, New York, 1989), chs. 1, 2.
7. R.D. Adams and W.C. Wake, *Structural Adhesive Joints in Engineering*, (Elsevier Applied Science Pub., New York, 1984), ch. 7.

CHEMISTRY AND REACTIVITY OF CARBOXYLIC ACID CONTAINING SURFACES

C.A. Fleischer, G. Apai, and W.P. McKenna
Eastman Kodak Company, Rochester, NY 14650-2104

INTRODUCTION

Polymer surface modifications, such as corona, plasma, and ultraviolet treatments, promote adhesion at polymer/polymer interfaces through introduction of specific functional groups which interact with subsequent coating layers. The mechanism of adhesion to such treated surfaces is difficult to understand due, in part, to the large number of different function groups which are formed.^{1, 2} Therefore, it is necessary to fabricate and characterize model surfaces containing specific functional groups of interest to provide insight into possible adhesion mechanisms. Carboxylic acid groups formed during corona and plasma treatments may play a significant role in adhesion promotion at polymer/gelatin interfaces, so such groups have been chosen for model surface studies.

Thin films of the potassium salt of poly(acrylic acid) (PAA) are analyzed before and after surface protonation by dilute acid solution. Conversion of acid functional groups to anhydride groups and further surface reaction of anhydride and/or acid groups with *n*-butyl amine are followed as a function of temperature for PAA and poly(vinyl methyl ether-co-maleic acid) (VME-MA), using infrared reflection absorbance spectroscopy (IRRAS) to analyze the thin film and high resolution electron energy loss spectroscopy (HREELS) to analyze the outer 10-20 Å.

EXPERIMENTAL

Materials. PAA and VME-MA (50-50) were used as received from Scientific Polymer Products, Inc. Sample substrates consisted of silicon wafers which were evaporatively coated with chromium and gold in house. Butylamine was used as received from Eastman Fine Chemicals.

Sample Preparation. PAA was neutralized with KOH in deionized water to form the potassium salt (PAAK). Solutions of 0.5% PAAK in water/ethanol (2/1) and 1% VME-MA in ethanol were spin coated at 1000 rpm for 60 s on a Headway Research Inc. (Garland, TX) photoresist spinner, model 1-EC101-R485. PAAK surfaces were protonated (PAAH) using a 10 mM HCl rinse. PAAH and VME-MA surfaces were

exposed to butylamine vapors by placing the coated wafers over a beaker containing butylamine for 30 s. Polymer coatings were heated to 100°C, 130°C, or 160°C for varying times and IRRAS and HREELS spectra were obtained. Some additional HREELS annealing experiments were carried out in ultrahigh vacuum (UHV).

IRRAS. The infrared data was obtained on a Bio Rad Digilab FTS-60A spectrometer. The angle of incidence for the reflection experiment was 85° relative to the perpendicular axis of the film and *p*-polarization was used. The reflection-absorption spectra were referenced to a blank gold mirrored silicon wafer. The typical spectrum was collected with 256 co-added scans at 4 cm⁻¹ resolution.

HREELS. HREELS data were acquired with a Vacuum Generators LEELS 400 spectrometer employing a sample transfer system that has been described previously.³ Experiments were carried out in an UHV system at pressures in the mid 10⁻¹⁰ mbar range. Annealing of samples in UHV was precisely monitored using a nonmagnetic N-type thermocouple spot welded to the back of the sample holder. A specular geometry of ~120° was used and resolutions of ~80 - 100 cm⁻¹ and peak locations of ± 5 cm⁻¹ were typical. No auxiliary charge neutralization was necessary for the HREELS experiments.

RESULTS AND DISCUSSION

The IRRAS results for PAAK and PAAH are presented in Figure 1. The potassium salt is identified by the strong carboxylate vibration at 1582 cm⁻¹. After HCl washing the carboxylate groups throughout the film are fully protonated, resulting in a shift in the carbonyl vibrational band to 1740 cm⁻¹. In the HREELS spectra the low frequency carboxylate vibration is not clearly observed for PAAK (Figure 2), whereas the carbonyl band at ~1730 cm⁻¹ is quite pronounced for the protonated acid. This suggests that the neutralized acid groups are perhaps buried below the HREELS sampling depth and after the acid wash the surface reorganizes to expose the protonated acid groups at the surface. An increase in the OH out-of-plane bending mode near 800 cm⁻¹ is also observed in the HREELS spectra after

protonation.

The acid groups of both PAAH and VME-MA condense to form anhydride groups upon heating. For PAAH, temperatures of $\geq 160^{\circ}\text{C}$ are needed to form anhydride groups, as is clear from the IRRAS spectra in Figure 1 and the HREELS spectra in Figure 3. In the IRRAS spectra, two distinct anhydride bands at 1808 cm^{-1} and 1764 cm^{-1} are observed after 4 h at 160°C ; however, the reaction is incomplete. Anhydride formation between 160°C and 180°C is observed clearly in the HREELS spectra by a shift of the carbonyl vibration from 1730 cm^{-1} to a broader feature centered at $\geq 1770\text{ cm}^{-1}$ and a reduction in the OH out-of-plane bending mode at 800 cm^{-1} . The surface reaction of carboxylic acids to anhydrides appears to go to completion.

It is interesting to note that for annealing temperature as high as 130°C , no significant restructuring of the polymer surface takes place. This is in marked contrast to a previous report⁴ of surface restructuring at 100°C . However, at 160°C a reduction in carbonyl intensity accompanies the onset of anhydride formation. Differences in the PAAH HREELS spectra of Figures 2 and 3 can be attributed to changes in the contribution of resonance scattering mechanism.⁵

The VME-MA copolymer forms anhydride readily at 100°C as is clear from the strong peaks at 1861 cm^{-1} and 1791 cm^{-1} in the IRRAS spectra in Figure 4. HREELS spectra (not shown) confirm these findings. The large difference between the temperature for anhydride formation in PAA and VME-MA may be a result simply of the adjacent acid group available for forming anhydride in VME-MA, or the high T_g of PAA (105°C) relative to that of VME-MA (80°C).

Exposure of VME-MA and PAA to butylamine results in formation of an ammonium salt as is shown in the IRRAS spectra in Figures 4 and 5, by bands at 1583 cm^{-1} and 1563 cm^{-1} , respectively. Upon heating PAA at 160°C , anhydride forms, as shown by increasing intensities of vibrations at 1762 cm^{-1} and 1804 cm^{-1} , which is complete in 2.5 h. In addition, the increase in intensity of the 1672 cm^{-1} vibration (shoulder after 1 h and a sharp band after 2.5 h) attributed to amide carbonyl, results from the reaction of anhydride or carboxylic acid groups with primary amine to form amic acid or amide, respectively. The HREELS spectra for the same sample after 1 h at 160°C (Figure 6c), also shows the vibration for amide at 1665 cm^{-1} . In addition, anhydride is not detected within the HREELS sampling depth (i.e., the carbonyl

band is observed at 1730 cm^{-1} , so has not shifted to higher wave number), suggesting that the anhydride groups at the surface reacted with butyl amine to form amide linkages.

VME-MA also forms an ammonium salt with butylamine, but the result of further heating is quite different (Figure 4). Anhydride forms again, and additional bands at 1705 cm^{-1} , $\sim 1400\text{ cm}^{-1}$, and $\sim 750\text{ cm}^{-1}$ appear, which can be assigned to imide carbonyl, CN and imide ring vibrations, respectively, which are observed in aliphatic polyimides.⁶ In addition, vibrations at 2880 cm^{-1} , 2930 cm^{-1} , and 2970 cm^{-1} , associated with the butyl amine methylene groups are observed after 2.5 h at 130°C confirming that butylamine remains on the surface.

CONCLUSIONS

HREELS results show that it is possible to obtain surfaces enriched in carboxylic acid groups. Anhydride formation, followed as a function of temperature, goes to completion quickly at the surface (5 min), whereas complete conversion does not occur in the bulk thin film after 4 h. HREELS and IRRAS shows that acid-containing surfaces are good candidates for reaction with primary amine groups in gelatin.

REFERENCES

1. T. Ohmichi, H. Tamaki, H. Kawasaki, S. Tatsuta, *Physicochem. Aspects Polym. Surf.*, Mittal, K., Ed. (Plenum: New York, NY, 1983), p. 793.
2. J.M. Pochan, L.J. Gerenser, J.F. Elman, *Polymer*, **27**, 1058 (1986).
3. B.G. Fredrick, G. Apai, T.N. Rhodin, *Surf. Sci.*, **244**, 67 (1991).
4. Y. Novis, N. Degosserie, M. Chtaib, J.J. Pireaux, R. Caudano, P. Lutgen, G. Feyder, *J. Adhesion Sci. Technol.*, **7**, 699 (1993).
5. G. Apai, W.P. McKenna, *J. Phys. Chem.*, **98**, 9735 (1994).
6. K. Itoya, K. Yoshihiro, M. Kakimoto, Y. Imai, *Macromolecules*, **27**, 4101 (1994).

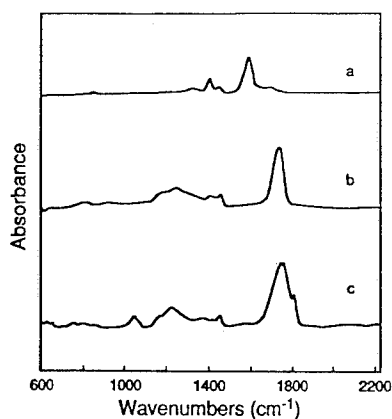


Figure 1. IRRAS spectra of PAA: (a) potassium salt; (b) protonated by HCl rinse; (c) heated 4 h at 160°C.

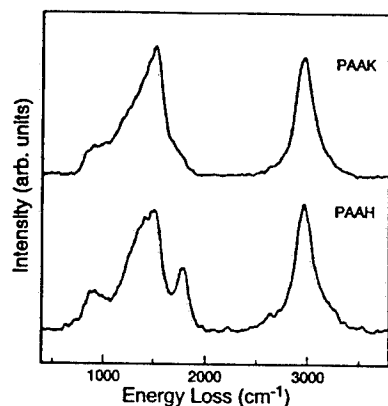


Figure 2. HREELS vibrational spectra of PAA: potassium salt (PAAK); protonated by HCl rinse (PAAH).

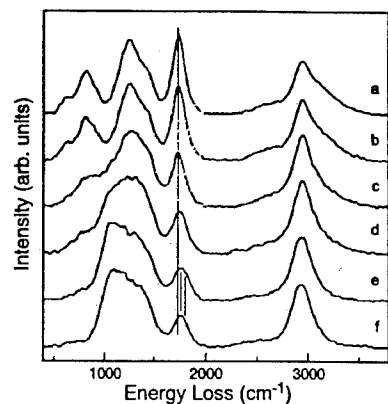


Figure 3. HREELS vibrational spectra of PAAH following heat treatments: (a) room temperature; (b) 130°C; (c) 160°C; (d) 170°C; (e) 180°C; (f) 190°C.

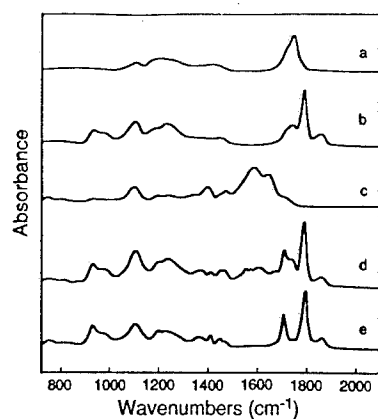


Figure 4. IRRAS spectra of VME-MA copolymer: (a) as coated; (b) heated 2.5 h at 100°C; (c) exposed to butylamine; (d) heated at 130°C for 1 h; (e) heated at 130°C for 2.5 h.

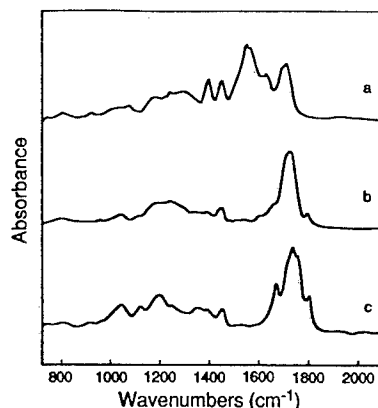


Figure 5. IRRAS spectra of PAA: (a) following butylamine exposure; (b) heated at 160°C for 30 min; (c) heated at 160°C for 4 h.

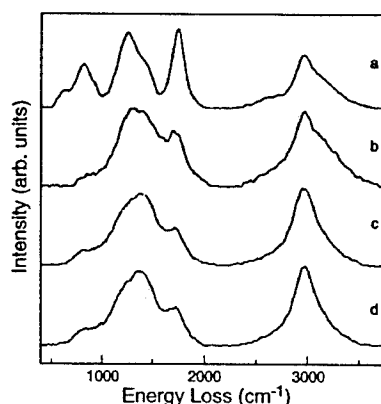


Figure 6. HREELS vibrational spectra of PAA: (a) as protonated; (b) exposed to butylamine; (c) exposed to butylamine and heated 1 h, 160°C; (d) sample (c) heated 130°C in UHV.

EFFECT OF PLASTICIZER CONTENT AND PHOTOAGEING ON PVB/GLASS ADHESION

May, R. J. and Love, B. J.

Center for Adhesive and Sealant Science

Department of Materials Science and Engineering

Virginia Polytechnic Institute and State University

Blacksburg, VA 24061-0237

INTRODUCTION

Polyvinylbutyral, PVB, has been used as the adhesive interlayer in automotive safety glass for the past six decades. The performance of this laminated glass construction is heavily dependant on the properties of the interlayer material[1,2] and the interlayer/glass adhesion. The mechanical properties of PVB have been studied in an attempt to model the behavior of laminated glass composites and determine its applicability to architectural and other uses.[3] Similarly, researchers have studied the adhesion of PVB to glass to understand and control the properties of these composites.[2,4] Mikhaliuk *et al*[5] and others[6] have discovered that PVB undergoes chemical changes due to UV radiation present in sunlight. Since PVB plays such a large role in determining the overall composite properties of the laminate, these changes which occur due to sunlight may effect the durability of laminated glass constructions. The focus of this work is to determine the effect these chemical changes caused by photoageing have on the mechanical properties of PVB and the glass/PVB interface in an attempt to understand laminate durability.

PVB is a terpolymer made from the reaction of polyvinylalcohol with butyraldehyde. The resulting polymer contains approximately 80% polyvinylbutyral, up to 20% of polyvinylalcohol and a residual amount of polyvinylacetate. Plasticization of PVB results in a pliable, tacky material that bonds well to glass and tends to absorb large amounts of energy on impact. UV radiation has been shown to degrade PVB, forming of free radicals at low temperatures and crosslinks at room temperature.[5] These chemical changes will change the mechanical properties of PVB and may affect the adhesion between PVB and glass, ultimately affecting the laminated composite.

There are a number of theories to explain PVB/Glass adhesion. Chehimi and Watts⁷ have speculated that the adhesion is due to Acid-Base interactions present. Chugunov *et al*⁸ investigated the effect of surface roughness on PVB/Glass adhesion and concluded that mechanical interlocking is not a significant factor. Huntsberger³ studied the effect of water at the interface and concluded that water greatly lowers the adhesion of PVB to glass. This adhesion research has generally been limited to commercially available PVB compounds which

contain varying amounts of plasticizer content depending on the manufacturer and the application. Anywhere from 20-40% of plasticizer may be added to the polymer to control its properties. This large variation in plasticizer content is likely to have a significant effect, not only on adhesion but on the mechanism of photoageing.

Peel and lap shear testing have been a common form of mechanically testing adhesion, however, neither can distinguish the force required to cause yielding in the adherends and the strength of the bond. This problem can be circumvented by the use of a properly run radial blister test.

The radial blister test involves bonding a film of adhesive onto a substrate and applying pressure using air or other gas through a hole in the substrate. This pressure causes a blister to form in the film which transfers the stress to the bond interface. If the test is designed properly, debond occurs prior to yielding in the film. From the pressure and the resultant volume changes, a critical strain energy release rate, G_c , can be calculated. (Equation 1)

$$(1) \quad G_c = \frac{3(1-\nu^2)}{32E} \cdot P_c^2 a^4$$

where ν = poisson's ratio P = pressure
 E = Young's modulus a = Radius of debond
 H = Height at the center of the debond

Lai and Dillard⁷ have proposed a method of designing the blister test such that yielding does not occur. By adjusting the initial debond radius and thickness of the film, the stress in the film membrane can be lowered below the yield stress of the polymer. Thus accurate measurement of the strength of an adhesive interface between the film and the substrate is possible without introducing errors caused by gross yielding of the adherends.

EXPERIMENTAL METHOD

PVB was obtained in granular form from PolySciences with a published Mw of 180,000 to 270,000 g/mol. Butyl benzyl phthalate was used as the plasticizer. Sample films were solution cast onto glass using a mixture of polymer and plasticizer dissolved in a solution of Toluene/Ethyl Alcohol.

The surface quality of the films and the possibility of residual stresses prompted the use of a hot press to obtain some of the required films. The films were pressed between either Kapton or Teflon release film at a temperature between 140°C and 200°C and 30 psi load.

Glass transition measurements were done using Dynamic Mechanical Spectroscopy (DMS) on a Seiko Dynamic Mechanical Analyzer. A temperature sweep at a frequency of 0.1 hz was run from -150°C to 100°C. The temperature where the Tan δ peak occurred was identified as T_g. The stress relaxation and tensile test experiments were performed on a Polymer Laboratories Miniature Materials tester with either a 200 N or a 20N load cell depending on the plasticizer content. The required dogbone samples were cut using a die conforming to ASTM D1708-84.

Mechanical property measurements were performed using thick films, 0.2 to 0.8 mm. Thin films, 0.04 mm, were used to for FTIR Spectroscopy. For the photoageing experiments, samples were exposed to the radiation from a Spectroline R-51 UV lamp emitting at 254, 313 and 365 nm. Chemical changes in the material as a result of UV exposure were tracked using a Nicolet Fourier Transform Infra-Red Spectrometer.

RESULTS

During the initial tensile tests, it was discovered that PVB containing from 0-10% plasticizer exhibited typical plastic behavior with yielding and crazing occurring at low strain followed by necking and eventual failure. However, at plasticizer content of 20-40%, the polymer exhibits typical nonlinear elastomeric behavior with small amounts of yielding.

In order to represent the two very different mechanical behaviors and limit the number of experiments, the remaining tests were done using the neat polymer and PVB with 30% plasticizer added.

The results of the stress relaxation measurements can be seen in Figures 1 and 2.

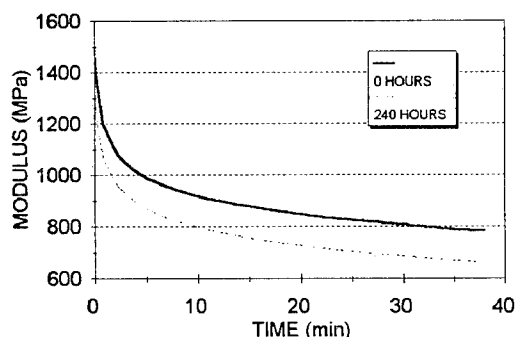


Figure 1. Stress Relaxation of Neat PVB, aged and unaged

As expected, the neat polymer had significantly longer relaxation

behavior than plasticized PVB. Only small changes were seen with ageing, however.

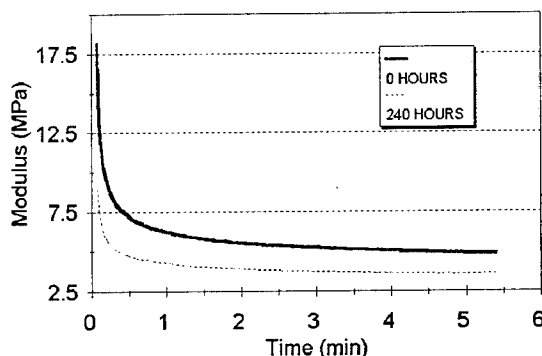


Figure 2. Stress Relaxation 30% Plasticized PVB, aged and unaged

The neat polymer has an initial modulus of approximately 1450 MPa when measured at $\dot{\epsilon} = 0.45 \text{ min}^{-1}$. After 240 hours of UV ageing, that modulus drops to approximately 1280 MPa. Similarly PVB plasticized with 30% butyl benzyl phthalate has an initial modulus of 18 MPa at $\dot{\epsilon} = 4.5 \text{ min}^{-1}$. After 240 hours of ageing that modulus drops to approximately 9 MPa. Obviously the chemical changes caused by the UV radiation have led to corresponding loss in stiffness of PVB.

Using DMS, no changes were seen in the T_g behavior of either the plasticized or neat polymer due to the photoageing. Currently we are running radial blister tests on both the aged and unaged material and will be presenting results of that work at the conference.

ACKNOWLEDGEMENTS

We would like to thank Dr. G. Wilkes, Dr. Dave Dillard, Dr. Yai-Hung Lai and Mr. S. Srinivas for their assistance.

REFERENCES

- 1) C. V. G. Vallabhan, Y. C. Das, and M. Ramasamudra, *J. Mat. Civil. Eng.*, **4** (1) 71 (1992).
- 2) B. J. Love, *ASCE J. Mat. Civil. Eng.*, **5** (4) 546 (1993)
- 3) J. R. Huntsberger, *J. Adhesion*, **13**(2) 107 (1981).
- 4) A. M. Chugonov, A. I. Kaprov, and V. N. Gusel'nikova., *Steklo i Keramika*, **3** 11 (1985).
- 5) V. Reinohl, J. Sedlar and M. Navratil, *Polymer Photochemistry*, **1**(3) 165 (1981).
- 6) O. M. Mikhailik, Y. N. Seropegi, M. Y. Melnikov, and N. V. Fock, *Eur. Polym. J.*, **17**(9) 1011 (1981).
- 7) M. M. Chehimi and J. F. Watts, *J. Adhesion*, **14**, No 1-4, p 81-91, (1993).
- 8) Y. Lai and D. A. Dillard., Submitted to *Intl. J. Solids and Structures*. (1994).

PHOTOELASTIC STUDY OF PROPAGATING CRACKS IN ADHESIVE JOINTS

Y.Y. Wang and F.P. Chiang

Department of Mechanical Engineering
State University of New York at Stony Brook
Stony Brook, NY 11794-2300

INTRODUCTION

The stress distribution around interfacial cracks in adhesive joints with different adhesives are investigated by photoelastic method. Our experimental study reveals that the singular elastic stress field exists around an interfacial crack in an adhesive joints. The disturbance of the adhesive layer to this singular stress field is localized. For a propagating crack, when the adhesive material is very ductile, the new crack is bridged by some fibrils and the global stress concentration losses. The elastic fracture stress field around the new crack tip is disturbed for this ductile crack extension. When the material properties of the adhesive is very similar to the adherend, stress field near the new crack tip remains self similar.

EXPERIMENTAL CONFIGURATION

An artificial crack is made by embedding a piece of very thin plastic film ($5\mu\text{m}$) between the adhesive and the adherend. The crack initially stays in the interface. The specimen geometry is shown in Fig.1. The isochromatic fringes obtained by photoelasticity are multiplied and processed digitally. Fig.2 displays the isochromatic fringe patterns of specimen 1 and 2 before and after the crack propagating.

STRESS BEFORE CRACK PROPAGATING

The isochromatic fringe patterns (Fig.2) describe the distributions of the maximum shear stresses of the specimens. The fringe patterns before the crack propagating indicate that the singular stress fields exist, if they are viewed at a macro scale and the adhesive layer is regarded as a small scale feature. The disturbance is constrained near the layer and the stress field away from the disturbance area could be characterized by homogeneous stress intensity factors as if the adhesive layer were absent. These remote stress intensity factors can be deduced from the isochromatic fringes [1]. The shapes of the fringe loops (Fig.2(a) and (c)) agree well with the singular stress field even near the adhesive layer, while the fringes inside a sector of $-60^\circ < 60^\circ$ depict some deviation. An interesting point is that the distributions of the maximum shear stress in front of the crack tip along the interface are different for different specimens. Fig.3 is the plot of the distributions of the maximum shear stresses of the three bonded specimens. The distribution of specimen 1 is similar to that of the homogenous specimen; which is expected, since the material of the adhesive is the same as that of the adherend. The maximum shear stresses of specimens 2 and 3 first decrease to a minimum value and then increase and approach to a constant value. This disturbance of the singular stress field is caused by the material mismatch of the adhesive and the adherend.

STRESS AFTER CRACK PROPAGATING

A photoelastic technique is used to observe the stress field of a propagating crack along the adhesive layer. The change of the isochromatic fringes as the damage processes is observed under a polariscope. Since the material of the adhesive of specimen 1 is the same as that of the adherend, it behaves just like a homogeneous specimen. A brittle fracture damage is observed. When the crack is arrested, the stress field around the new crack tip remains self similar (see Fig.2(a) and (b)). Specimen 2 and 3 manifest totally different damage processes than that of specimen 1. Under a load of prescribed displacement, cavities form within the adhesive layer ahead of crack tip. Then the cavity extends very close to the crack tip and the stress at the original crack tip is released. As the appearance of this damage process, the isochromatic fringe order at the point of the cavity increases but the fringe order at the original crack tip decreases. Then other cavities form in front of the new crack tip and extends to the crack tip, and so on. With the damage extends, the stress concentration around the old crack tip disappears. The process of the cavity forms and extends is recorded by some half-circle fringes, because the cavity forms each time, the localized stress concentration makes the fringe order increases at that particular point. After the cavity extends, the out side fringe circle coalesces with the main fringe loop while the inside fringe circle remains. It should be pointed out that the "new crack" is bridged by some fibrils and it may not be regarded as a real crack. As a result, the fracture surface is rough and the fringe loops that represent stress concentration disappear. The "new crack" is contained inside of the adhesive layer. This fracture process is different from that of a bulk polymeric material [2]. The cavities formed inside of the adhesive layer do not coalesce together due to the constrained deformation of the adhesive layer. It is because these unbroken fibrils still transmit loads across the crack faces, the stress concentration losses at the "new crack" tip.

ACKNOWLEDGEMENT

The sponsorship of AFOSR, No. F.496209310218 and ONR, No. N000149J1380 is greatly acknowledged.

REFERENCES

1. R.J. Sanford, *Experimental Mechanics*, 3, p.241 (1989).
2. A.J. Kinloch and R.J. Young, *Fracture Behavior of Polymers*, (Applied Science Publishers, London and New York, 1983), p.147.

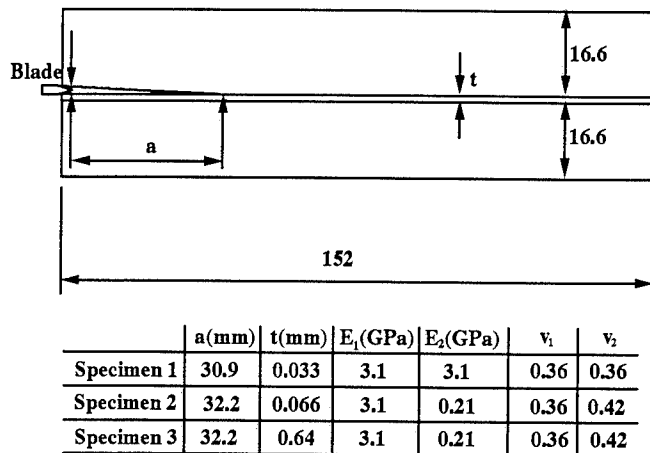


Fig.1 Geometry of Specimens. The dimension in the figure is in mm.

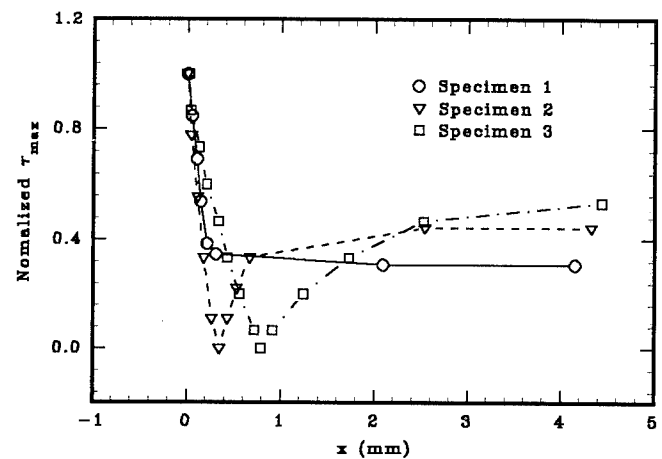
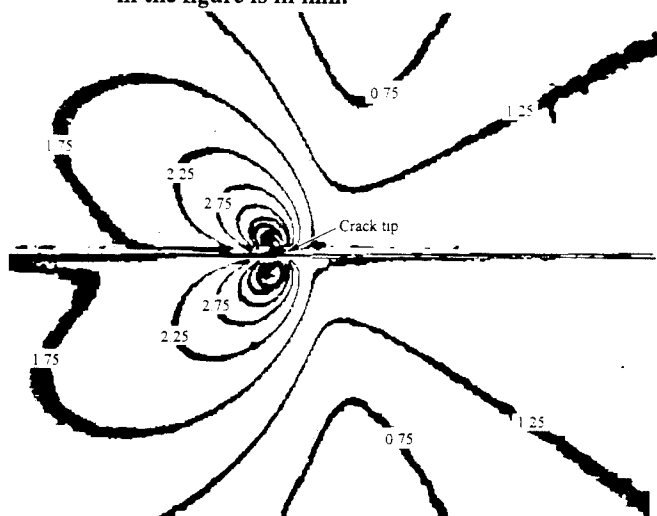
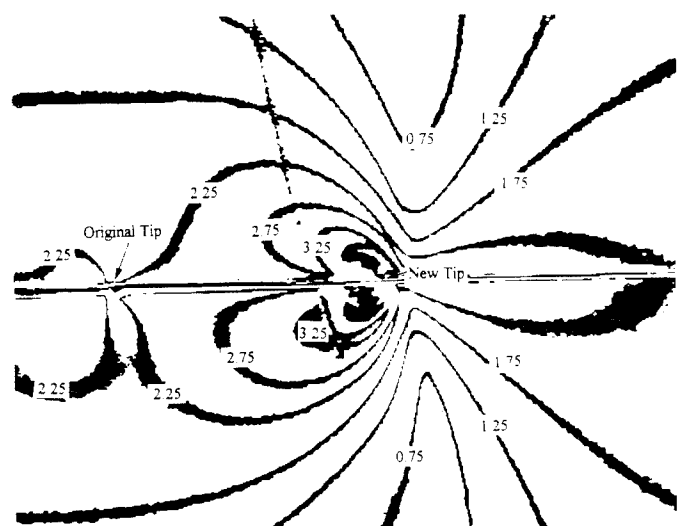


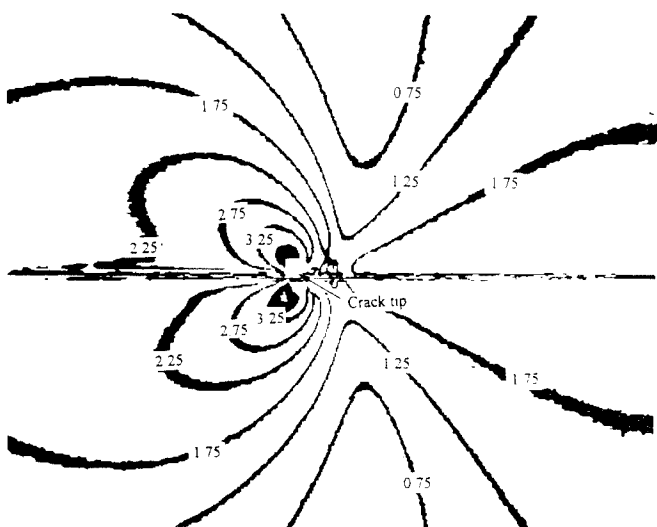
Fig.3 Distribution of Maximum Shear Stress in Front of the Crack Tip along the Interface.



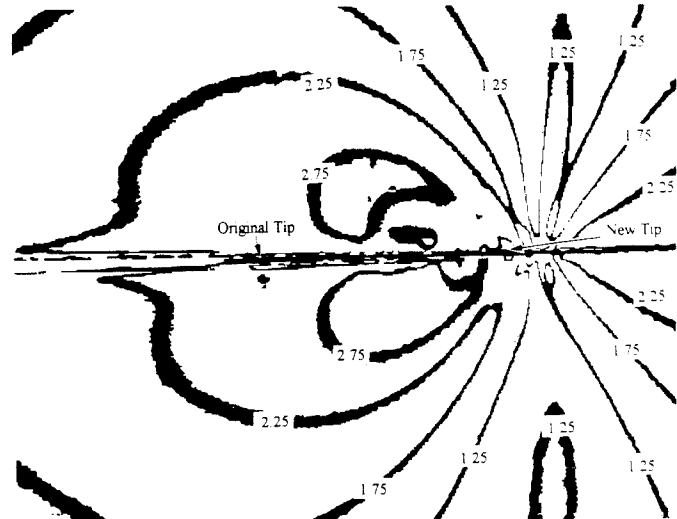
(a) Specimen 1, before crack propagating.



(b) Specimen 1, after crack propagating.



(c) Specimen 2, before crack propagating.



(d) Specimen 2, after crack propagating.

Fig.2 The isochromatic fringe patterns before and after the crack propagating.

DIFFUSION OF ISODECYL PELARGONATE IN AN EPOXY ADHESIVE

K.S. Kwan and T.C. Ward

Virginia Polytechnic Institute and State University
Department of Chemistry and NSF Technology Center
Center for Adhesive and Sealant Sciences
Blacksburg, VA 24061

INTRODUCTION

A gradient in concentration of a small molecular weight species results in a driving force for molecular diffusion. [1,2] There are four different classes of diffusion [2] of which concentration-dependent diffusion, for example, can be described with Fick's First Law for an isotropic material: $J = -D(\nabla C)$

where J =mass diffusion flux, C is the concentration, and D is the diffusion coefficient.

High performance adhesives are often subject to such environmental conditions. For instance, a concentration gradient in humidity and/or some small foreign penetrant may result in mass diffusion into the sample and prove detrimental to a polymer adhesive's expected lifetime. Therefore, it is very important to study the diffusional properties of a polymeric adhesive under these types of conditions.

MATERIALS

The diffusant to be investigated is a plasticizer known as isodecyl pelargonate (IDP) which is the ester of isodecyl alcohol and pelargonic acid. From the molecular formula, $(CH_3)_2CH(CH_2)_6 OCO(CH_2)_6CH_3$, one can see that it is a relatively linear, aliphatic molecule with a characteristic ester linkage.

The adhesive system under investigation is a thermoset epoxy manufactured by Rogers, Corp. based upon Epon 828™.

EXPERIMENTAL

Epoxy Preparation

The material, itself, exists as a B-staged film. The curing conditions used are:

=> 100°C for 1 hr.

=> 175°C for 2 hr.

=> 200°C for 2 hr.

Kinetic Adsorption Tests

Perkin-Elmer AD-6 Autobalance
27°C, 63°C, and 93°C

Infrared Analysis

Design an in-situ monitoring configuration for the Nicolet 800 FTIR and a horizontal ATR flat-plate.

RESULTS

Kinetic adsorption tests have been performed in an effort to obtain qualitative diffusional behavior of IDP in an epoxy film. Tests have been performed at three different temperatures in an effort to see the temperature dependence.

Analysis of the data has been done via a Fickian model for a 2-dimensional semi-infinite plate,

$$\frac{Mt}{M_\infty} = 1 - \sum_{n=0}^{\infty} \frac{8}{(2n+1)^2 \pi^2} \exp \left[\frac{-D(2n+1)^2 \pi^2 t}{4L^2} \right]$$

where M is the mass at time (t) and/or the mass at equilibrium (∞), $2L$ is the thickness, n is the number of arbitrary composite slices, and D is the diffusion coefficient.

Using both a long-time approximation and a short-time approximation, one can see in Figures 1-3, that the weight uptake data qualitatively gives a linear fit characteristic of Fickian behavior. From the slopes of these lines, approximate diffusion coefficients have been evaluated, respectively, for each temperature as follows: 3.0×10^{-9} , 4.0×10^{-9} , and 2.70×10^{-8} cm^2/sec .

Simultaneously, a design of an in-situ monitoring technique has been chosen based upon an FTIR method analogous to that of Fieldson and Barbari [3]. An actual schematic of the setup is shown in Figure 4. Currently, tests of this setup are underway.

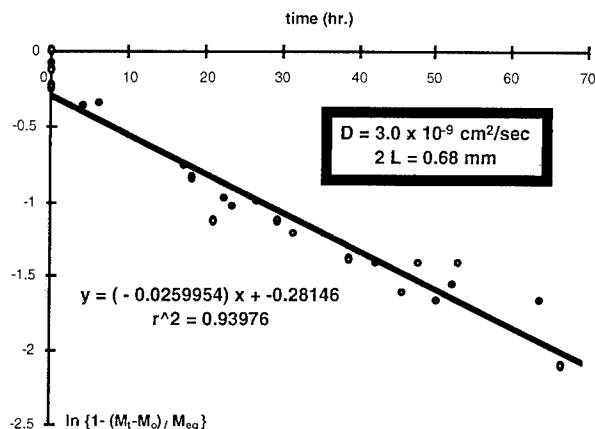


Figure 1: Wt. Uptake Data of 100% IDP at 27°C (long-time approximation)

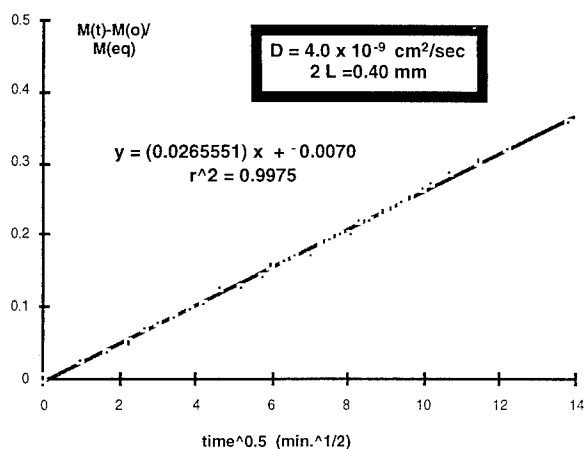


Figure 2: Wt. Uptake Data of 100% IDP at 63°C (short-time approximation)

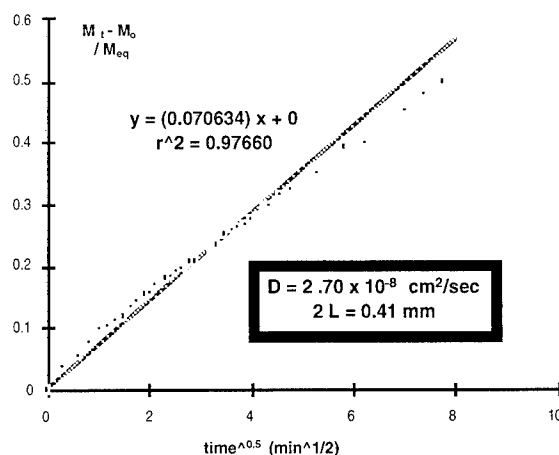


Figure 3: Wt. Uptake Data of 100% IDP at 93°C (short-time approximation)

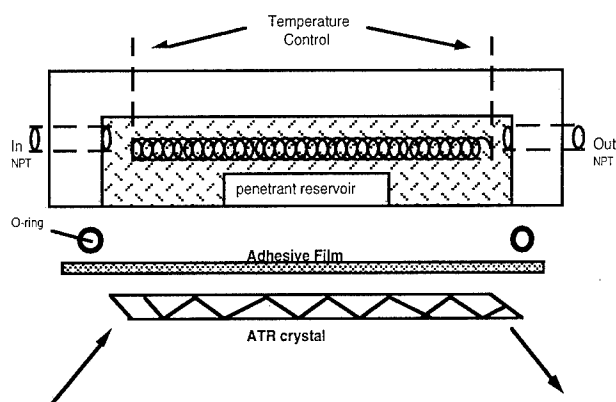


Figure 4: Horizontal ATR Setup

CONCLUSIONS

Upon completion and testing of this design, appropriate diffusion equations must be chosen for relating IR absorption to mass transport. Preliminary kinetic adsorption tests seem to imply a Fickian-type behavior with diffusion coefficients typical of glasses which increase with temperature (10^{-9} cm^2/sec). This finding is very important because appropriate diffusion equations can now be utilized for in-situ monitoring of IDP.

[1] Wolf R. Vieth, *Diffusion In and Through Polymers: Principles and Applications* (Oxford University Press, New York, 1991).

[2] D. Lefebvre, T.C. Ward, D.A. Dillard, and H.F. Brinson, *Adhesion Science Review*, ed. H.F. Brinson, J.P. Wightman, and T.C. Ward (Commonwealth Press, Inc., Radford, VA, 1987).

[3] G.T. Fieldson and T.A. Barbari, *Polymer* **34**, 6, 1146 (1993)

FRACTURE TOUGHNESS TESTING OF ADHESIVELY BONDED SHEET STEEL

Ian Ashcroft, Prosenjit Basu and Geoffrey Spinks
Department of Materials Engineering, University of Wollongong,
Northfields Ave, Wollongong, NSW, 2522, Australia.

INTRODUCTION

A wide variety of mechanical tests have been used to measure the "strength" of adhesively bonded joints. The selection of a test method is dependent on the experimental materials and the aim of the test: whether this is to aid in the design of joints, evaluate the effect of material properties or environmental degradation on joint strength, or to investigate the intrinsic mechanisms of failure in a particular system.

We have been working on the latter aspect for adhesively bonded sheet steel. As with many other workers, we prefer to use a fracture mechanics tests to provide a reliable failure criterion. However, many fracture test geometries rely on linear elastic behaviour occurring within the test material, and this is difficult to achieve with thin sheet steel due to yielding within the adherend. For this reason, we have attempted to generate fracture toughness data for adhesively bonded sheet steel using the width tapered cantilever beam (WTCB-Fig. 1) test and the wedge test.

The WTCB enables the calculation of fracture toughness without the need to measure crack lengths (equation 1) [1-3]:

$$G_{1c} = \frac{12P^2}{Eh^3} \frac{a}{b} \quad (1)$$

where E is the adherend modulus, h is the thickness of adherend, P is the failure load, and a/b is a constant dependent upon the specimen width taper.

The aim of this work was to determine whether the WTCB geometry was suitable for various sheet steel grades. To test the validity of the test a compliance calibration was performed and the fracture energy values calculated were compared with those obtained from another test method (Wedge test [4]).

EXPERIMENTAL

WTCB test pieces were made from various coated steels supplied by BHP Steel Pty Ltd. These were either alloy coated (zinc or zinc/aluminium) or organic coated. The steel had a guaranteed yield strength of 550MPa, 170MPa or 130MPa and was supplied in sheets of thickness ranging from 0.55 mm to 1.00 mm. Epoxy adhesives were supplied by Ciba Geigy (AV3131: one part and K138: two part) and a polyurethane was supplied by Sika (Sikaflex 360HC).

RESULTS

The WTCB test was found to be suitable for sheet steels only if the yield strength of the steel was > 500MPa. Lower yield strength steel (e.g. 170MPa) plastically yielded within the adherend.

Compliance calibrations for the high yield strength steel joints confirmed that the geometry had a "linear change of compliance" with crack area (Fig 2), which indicates that equation 1 is valid. The fracture toughness values calculated from the compliance calibration agreed with the value obtained from equation 1.

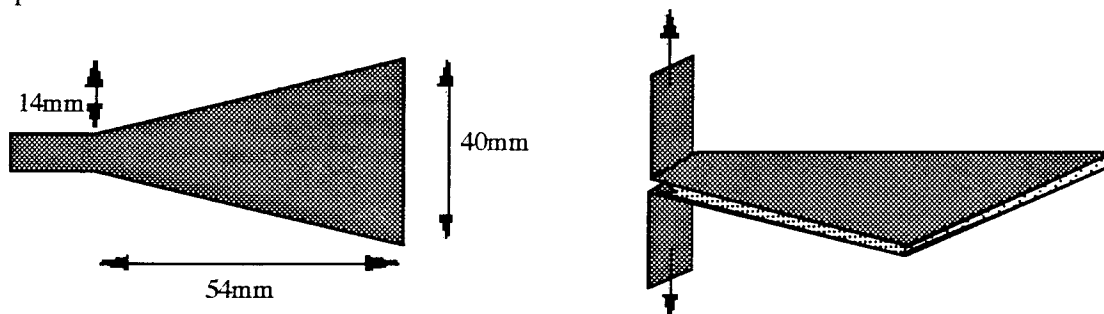


Figure 1: Schematic diagram of WTCB specimen geometry.

Bondline thicknesses were varied by incorporating glass beads of different diameters into the adhesive. In the range tested (0.25 - 1.20 mm) the bondline thickness had no effect on fracture energy (Fig. 3). Interestingly, the weight fraction of glass beads added to the adhesive had a significant effect on the fracture energy (Fig. 4). At high glass bead contents the fracture was interfacial and SEM analysis of the fracture surface showed poor wetting of the substrate in this instance. At lower glass bead contents the fracture was cohesive. However the bonding between the epoxy and the glass beads was poor, which is believed to cause the initial decrease in the fracture toughness of the composite.

The wedge test was also found to be suitable only for high yield strength steel sheet. With low yield strength sheet the adherend was plastically deformed upon the insertion of the wedge, and crack growth was not observed. The fracture energy was calculated from equation 2:

$$G_{1c} = \frac{3h^3Ev^2}{16a^4} \quad (2)$$

where v is the wedge height. Accurate measurements of crack length (a) are required, however the G_{1c} values obtained with the wedge test were consistent with those obtained using the WTCB test: $761 \pm 13\%$ (J/m²) (WTCB) and $793 \pm 17\%$ (J/m²) (Wedge) for zinc coated steel bonded with AV3131.

CONCLUSIONS

The results have shown that the fracture energy of adhesively bonded sheet steel joints can be successfully obtained from both the WTCB test and the wedge test. A minimum yield strength of the steels must be exceeded, however, to avoid plastic deformation within the adherend. Bondline thicknesses greater than 0.25 mm had no effect on the fracture energies obtained, however glass beads should be avoided as a means of fixing the bondline thickness.

REFERENCES

1. G.Liu and A.N. Gent, *J.Adhesion* **38** 1992 79.
2. K.S. Han and J. Koutsky, *Composites* Jan **1983** 67.
3. W.D. Bascom, J.L. Bitner, R.J. Moulton and A.R. Siebert *Composites* Jan **1980** 9.

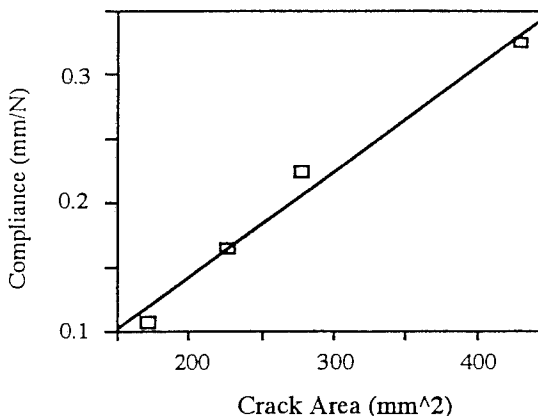


Figure 2: Compliance calibration chart for zinc coated steel bonded with one part epoxy adhesive.

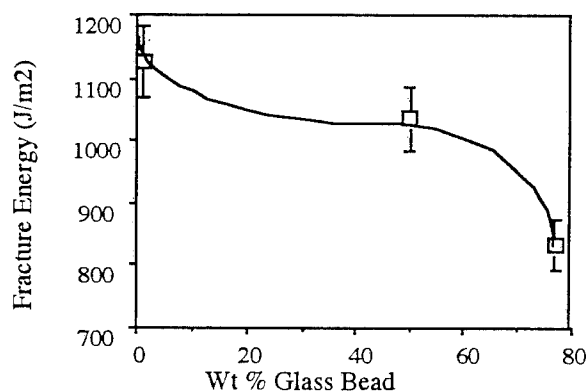


Figure 3: Fracture energy as a function of bondline thickness for zinc coated steel bonded with one part epoxy adhesive.

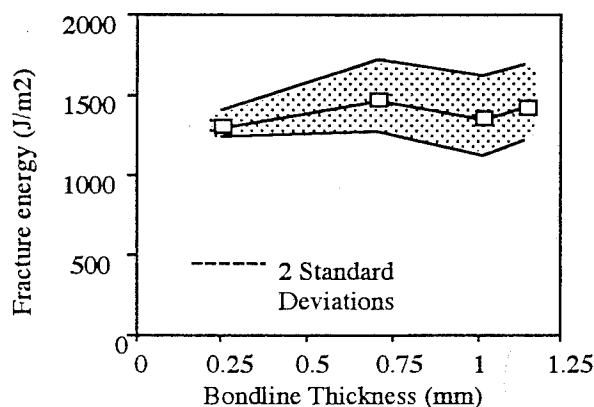


Figure 4: Fracture energy as a function of weight fraction of glass beads added to one part epoxy adhesive for bonding zinc coated steel.

Adhesion of Paint Coatings to Alloy Coated Substrates

Youlai Zhang, **I. Ashcroft**, M.R. Binns and G.M. Spinks
Department of Materials Engineering, University of Wollongong,
Northfields Ave, Wollongong, NSW, 2522, Australia.

INTRODUCTION

The aim of this study has been to understand the effect of processing conditions on the adhesion of organic coatings to alloy coated steel substrates. Adhesion of organic paint layers to the metal alloys is critical to the successful use of composite metal/polymer products. For example, the corrosion protection of the underlying metal is believed to be influenced by the polymer/metal adhesion [1]. An increase in the strength and stability of the adhesion may produce improved product performance in terms of increased service life in harsh environments. In addition, painted products are sometimes bonded to particle board and other materials, and information on the limits of adhesion in these circumstances is required for its successful use.

Most high durability paint systems for metallic substrates are heat cured to ensure maximum wetting and crosslinking of the polymer. The paint baking conditions will be affect the extent to which these processes can occur, and hence will affect adhesion. This study has investigated the effects of cure temperature, time and atmosphere on the adhesion.

EXPERIMENTAL

Pigmented epoxy based paints were applied to a zinc/aluminium coated steel sheet to give a dry film thickness of $5\mu\text{m}$. Coatings were cured at a peak metal temperature (PMT) in the range 150°C to 350°C . This was conducted both in air and under an argon atmosphere. Other coatings were cured at a fixed temperature but for different lengths of time.

Adhesion was measured by a pull-off test in which a steel stud was adhered to the coating surface and removed using an Instron tensile testing machine at a crosshead speed of 30 mm/min . The properties of the coatings were determined using a thermomechanical analyser (TMA) and an ultramicroindentation testing machine (UMIS-2000). The morphology of the coating/ metal interface was examined using a scanning electron microscope (SEM).

RESULTS

A peak in adhesion was observed for coatings cured in air at different temperatures (Fig 1). SEM analysis showed that the coating wetted the substrate better at higher temperatures (Fig 2). Discolouration of the samples at higher temperatures suggested that oxidation of the coating may have caused brittleness which reduced the adhesion. Tests conducted in argon (Fig 3) confirmed this, since the adhesion steadily increased with increasing temperature and the polymer was not discoloured.

Similar results were observed for coatings cured at a constant temperature for different times (Fig. 4). Initially the adhesion increased which can be attributed to better wetting and increased crosslinking. At longer cure times the adhesion decreased which may be attributed to oxidation.

DISCUSSION

The results highlight the importance of the fracture process to determining adhesion. The observations may be explained by equation 1, which relates the adhesion strength to material parameters: E , Young's modulus; ∂_c , critical crack opening displacement; and a , crack length.

$$\sigma_c = \frac{\partial_c E}{Y^2 \pi a} \quad (1)$$

(Y is a geometric constant)

With increased cure temperature and cure time both the crosslink density and wetting of the substrate increase. Thus, E increases and a decreases, which both increase the adhesion strength. At longer cure times and/or higher temperatures in air the adhesion decreases since the polymer becomes embrittled.

This can be explained by a decrease in ∂_c . In argon oxidative embrittlement does not occur and the adhesion increases with further improvements in wetting (i.e. further reductions in a).

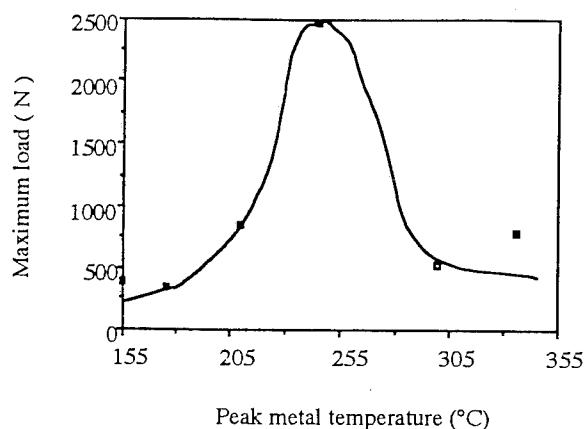
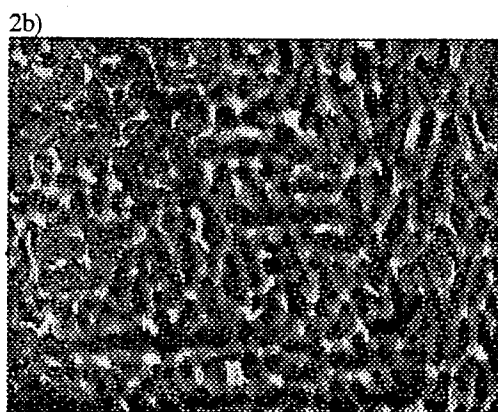
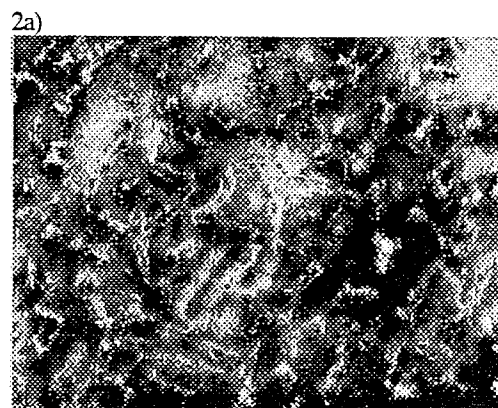


Figure 1: Effect of cure temperature on coating adhesion (in air).



2c)

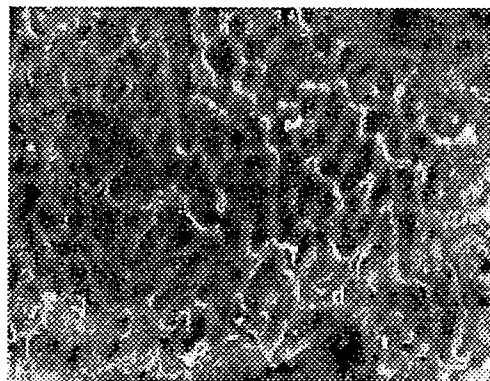


Figure 2: SEM micrographs (x500) of coating side of polymer/metal interface: a) 155°C PMT; b) 245°C PMT; and c) 336 °C PMT.

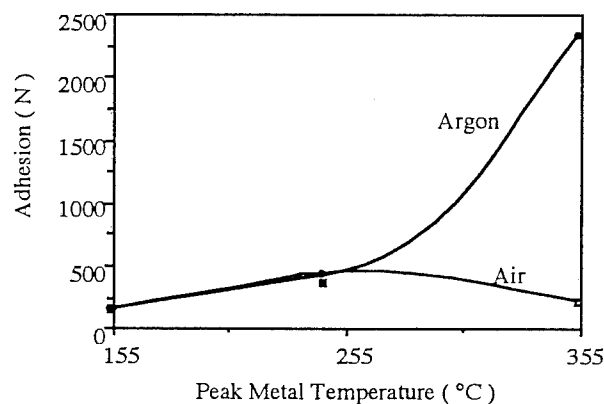


Figure 3: Effect of cure temperature on coating adhesion

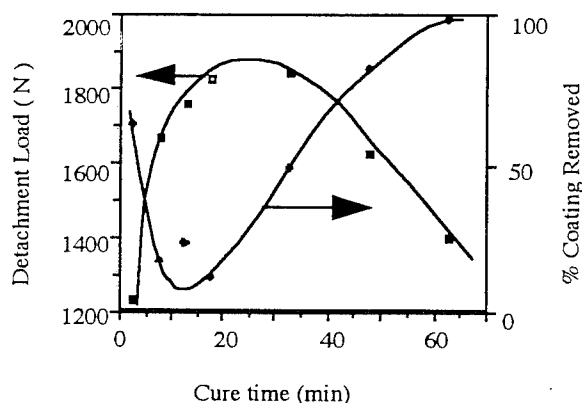


Figure 4: Effect of cure time on coating adhesion (in air).

CONCLUSIONS

The results show that the adhesion of epoxy coatings to the metal substrate is significantly affected by the processing conditions. An increased cure temperature promotes better wetting and increased degree of cure, which increase the adhesion. Oxidation of the polymer tends to decrease the adhesion. The results have been adequately explained by a fracture mechanics approach.

REFERENCE

1. C.M. Hendry, *J. Protective Coatings Linings* March 1993 51.

Measuring the Power Law Dependence of the Interaction Force Gradient using Atomic Force Microscope Techniques

B. Gady, D. Schleef, and R. Reifenberger

Department of Physics, Purdue University West Lafayette, In 47907-1396

ABSTRACT

The shift in the resonance frequency of an oscillating cantilever was measured as a function of position above an atomically flat substrate. This data determines the power law dependence of the force gradient that governs the long range interaction between an object attached to the cantilever and the substrate. Results for both a bare SiO₂ tip (commonly used in non-contact atomic force microscopy) and a 3.5 μm radius polystyrene sphere are presented.

I. INTRODUCTION

Determining the interaction force between a micron-size object and a flat surface as a function of separation is useful since this interaction ultimately governs many important properties including the attraction and adhesion of small particles to substrates. Preliminary measurements of this interaction using atomic force microscope (AFM) techniques are described.

Identifying the origin of the interaction force is of fundamental importance. A discussion of the long-range van der Waals contribution to the interaction force is available in the literature.¹⁻⁶ However, in the case of insulating objects, an electrostatic contribution due to trapped charges may be important. With the recent development of AFM, it is possible to study the interaction force as a function of distance and assess the relative contribution of these two mechanisms.

Although there is considerable discussion of the interaction between macroscopic objects of different shapes, there are relatively few experimental techniques for measuring these forces. Early experimental work has been reported by Israelachvili and Tabor⁷ using the surface force apparatus (SFA) and later by others such as by Derjaguin et al.⁸ Both studies found results consistent with the Hamaker¹ and Lifshitz² models, respectively. In both cases, however, the measurements were restricted to a crossed cylinder geometry.

In what follows we discuss measurements of the force gradient between a polystyrene sphere with radius $R = 3.5\mu\text{m}$ and an atomically flat carbon surface. The data are analyzed to determine the power law ansatz appropriate for the interaction force gradient as a function of surface-to-surface separation.

II. EXPERIMENTAL

The AFM apparatus used in this study is a custom-built instrument described elsewhere.⁹ In order to measure the long range interactions, an ac modulation technique was employed.

Two probe geometries were used in this study: the tip of a silicon ultralever,¹⁰ and a nominal 3.5 μm radius polystyrene sphere mounted on the end of an ultralever. The procedure for mounting the polystyrene sphere has been discussed elsewhere.^{11,12} The substrate chosen was HOPG because it is atomically flat and is electrically conductive. The substrate was grounded to minimize effects due to static charges. To minimize contamination due to water vapor and eliminate hydrodynamic effects between the ultralever and substrate, the AFM was mounted in a small stainless steel chamber which was first purged with dry nitrogen and then evacuated to a pressure below ~ 400 mTorr.

Knowledge of d , the surface-to-surface separation between the sphere and substrate, is important when determining the power law dependence of the interaction force and the force gradient. If the spring constant of the ultralever is known, an estimate of the absolute separation distance can be made from the measured jump to contact distance. Measuring the jump to contact distance in this way served as an absolute calibration for our measurements.

III. RESULTS AND DISCUSSION

The force gradient governing the interaction can be determined by measuring the shift in resonance frequency $\omega(d)$ of the ultralever as a function of the surface-to-surface separation distance d . The force gradient is given to first order approximation by¹³

$$\frac{\partial F}{\partial d} \simeq k \left[1 - \left(\frac{\omega(d)}{\omega_o} \right)^2 \right] \quad (1)$$

where ω_o is the resonant frequency of the ultralever far from the substrate and k is the known spring constant of the ultralever (in this case 1.9 N/m). Figure 1 shows a logarithmic plot of the force gradient as a function of the surface-to-surface separation distance for both the ultralever tip and a polystyrene sphere oscillating above

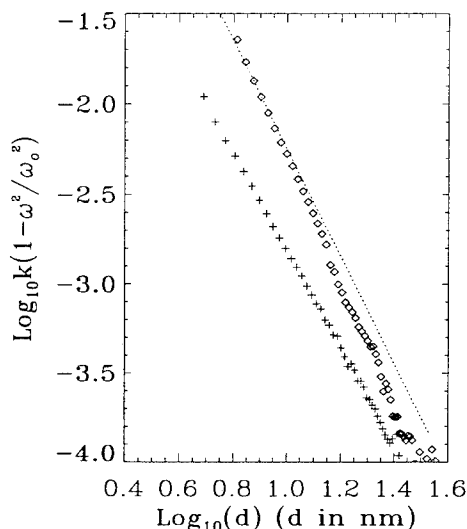


FIG. 1. The logarithm of the measured force gradient plotted as a function of the logarithm of the surface-to-surface separation distance d (in nanometers) for a bare Si ultralever (+’s) and a $3.5\ \mu\text{m}$ radius polystyrene sphere (boxes). The dashed line shows a d^{-3} dependence.

an HOPG substrate. The dashed line shows a $1/d^3$ dependence for the sake of comparison. A least squares fit to all the data plotted gives a power law of $d^{-(3.4 \pm 0.05)}$ for the sphere and $d^{-(2.6 \pm 0.09)}$ for the AFM tip.

According to the van der Waals model, a sphere very near a flat surface should be governed by a force gradient which obeys $1/d^3$ dependence for $d \ll R$ in the nonretarded regime.⁵ For a tip, the exact geometry is important. If the tip is approximated as a cone, a $1/d^2$ behavior is expected. If the tip is approximated by a cylinder, $1/d^4$ power law should apply.

The power law dependence of the force gradient for the sphere interacting with the flat substrate is in rough agreement with expectations based on a retarded van der Waals interaction and requires a Hamaker constant of $\sim 0.1 \times 10^{-19}\ \text{J}$ for a quantitative match to the data. On the other hand, an electrostatic force between sphere and substrate can also be considered. Two limiting cases can be discussed. In one limit, charge might be uniformly distributed throughout the sphere. A force gradient proportional to $1/(d+R)^3$ is expected,¹⁴ a result that does not agree with this experiment. In the other limit, charge might be trapped at the bottom of the sphere, triboelectrically produced during the initial measurement of the jump to contact distance. If this is the case and the charge is localized over the contact region which is small compared to R , a $1/d^3$ force gradient might be expected from elementary considerations. Under these circumstances, a trapped charge of order ~ 10 electrons would

be required to approximately explain the measured force gradient.

The interpretation of the data for the tip is not as clear due to uncertainties in the exact probe geometry. Future work will improve the accuracy in measuring the small shifts in frequency for large surface-to-surface separations, a further reduction in the ambient pressure by another factor of ten, and an assessment of the surface roughness of the polystyrene spheres which may become important at small separations.

This work was funded in part by a grant from the Research and Technology Division of Office Imaging at Eastman Kodak. The authors are indebted to D. S. Rimai and L.P. DeMejo for their continued interest and support and to D.M. Schaefer and D. Krause for helpful discussions during the initial stages of this work.

- ¹ H.C. Hamaker, *Physica* **4** **58**, 1058 (1937).
- ² E. M. Lifshitz, *JETP* **2**, 73 (1956).
- ³ I. E. Dzyaloshinskii, E. M. Lifshitz, and L. P. Pitaevskii, *JETP* **37**, 161 (1960).
- ⁴ D. Langbein, *J. Phys. Chem. Solids* **32**, 1657 (1971).
- ⁵ J.N. Israelachvili and D. Tabor, Van der Waals forces: Theory and experiment, in *Progress in Surface and Membrane Science*, Vol. 7, edited by J.F. Danielli, M.D. Rosenberg, and D.A. Cadenhead, pages 2-53, Academic Press, New York, 1973.
- ⁶ U. Hartmann, Theory of non-contact atomic force microscopy, in *Scanning Tunneling Microscopy III*, edited by R. Weisendanger and H.J. Guntherodt, pages 293-360, Springer Series in Surface Science, New York, 1993.
- ⁷ J. N. Israelachvili and D. Tabor, *Proc. R. Soc. Lond. A* **331**, 19 (1972).
- ⁸ B. V. Derjaguin, Y. I. Rabinovich, and N. V. Churaev, *Nature* **272**, 313 (1978).
- ⁹ W. Mahoney, D. M. Schaefer, A. Patil, R. P. Andres, and R. Reifenberger, *Surf. Sci.* **316**, 383 (1994).
- ¹⁰ Available from Park Scientific Instruments, Sunnyvale CA 94089.
- ¹¹ D.M. Schaefer, M. Carpenter, R. Reifenberger, L.P. DeMejo, and D.S. Rimai, *J. Adhesion Sci. Technol.* **8**, 197 (1994).
- ¹² D.M. Schaefer, M. Carpenter, B. Gady, R. Reifenberger, L.P. DeMejo, and D.S. Rimai, *J. Adhesion Sci. Technol.* (in press) (1995).
- ¹³ W.A. Ducker, R.F. Cook, and D.R. Clarke, *J. Appl. Phys.* **67**, 4045 (1990).
- ¹⁴ W.R. Smythe, *Static and Dynamic Electricity*, McGraw-Hill Book Company, Inc., New York, 1950.

EQUILIBRIUM INTERMOLECULAR DISTANCE AT THE FIBRE-MATRIX INTERFACE IN MODEL COMPOSITES

M. Nardin and J. Schultz

Centre de Recherches sur la Physico-Chimie des Surfaces Solides, CNRS,
24, Avenue du Président Kennedy,
F-68200 Mulhouse, France.

In a recent work [1,2], concerning fibre-matrix interfaces in model composites, the following simple relationship between the interfacial shear strength τ and the reversible work of adhesion W established at these interfaces, has been proposed and its validity extensively discussed :

$$(1) \quad \tau = \left(\frac{E_m}{E_f} \right)^{1/2} \frac{W}{\delta} .$$

In this equation, E_m et E_f are elastic moduli of the matrix and the fibre respectively and δ is, to a first approximation, a distance equal to about 0.5 nm, thus corresponding to a mean interatomic distance at the interface. The interfacial shear strength was measured by a fragmentation test on single fibre composites, whereas W was estimated from the surface properties of both constituents in contact. It was considered that only two major types of intermolecular interactions are involved : pure dispersive interactions (London) and electron acceptor-donor interactions (Lewis' acid-base interactions). Defining the ratio W/δ as an adhesive pressure p [3], the form of equation (1) is equivalent to Amonton's law corresponding to friction phenomena, i.e. :

$$(2) \quad \tau = \mu \cdot p ,$$

where μ could be considered as a static friction coefficient (static means that μ is relative to the state of deformation of the system just before sliding between fibre and matrix). Moreover, the most important parameter in this equation appears to be the equilibrium intermolecular distance at the interface. However, it is found that this distance is almost kept constant whatever the level of

intermolecular forces existing at the interface, in contradiction with literature data [4] especially when strong acid-base interactions are involved.

The aim of the present study is first to examine the validity of equation (1) from a theoretical point of view and to analyse more precisely the role of the interfacial intermolecular distance. First, the mathematical form of equation (1) is justified in terms of static friction. It is considered, in agreement with Tabor [5], that displacement between both materials in contact, fibre and matrix, during the fragmentation test, can effectively occur when the molecular forces at the interface are overcome. Therefore, from a simple force balance equation and a shear lag analysis [6] of the state of deformation, it appears that τ is directly related to W through equation (3), similar to equation (1), in which an interfacial intermolecular distance λ depending on the level of W is now involved :

$$(3) \quad \tau \approx \kappa(g,m) \left(\frac{E_m}{E_f} \right)^{1/2} \frac{W}{\lambda} ,$$

where $\kappa(g,m)$ is a function of geometrical and mechanical parameters of the systems.

The second part of the study is devoted to the determination of the intermolecular distance λ at the interface for various systems (glass or carbon fibres in thermosetting or thermoplastic matrices), previously studied [1,2]. All the parameters involved in equation (3) are known. Figure 1 shows that λ decreases from about 0.5 nm when only weak London's interactions are being established between fibre and matrix (in the case of glass fibres in polyethylene matrix for example), to

about 0.2 nm when strong acid-base interactions are also involved at the interface, in addition to dispersive interactions (like for carbon fibres in epoxy resins).

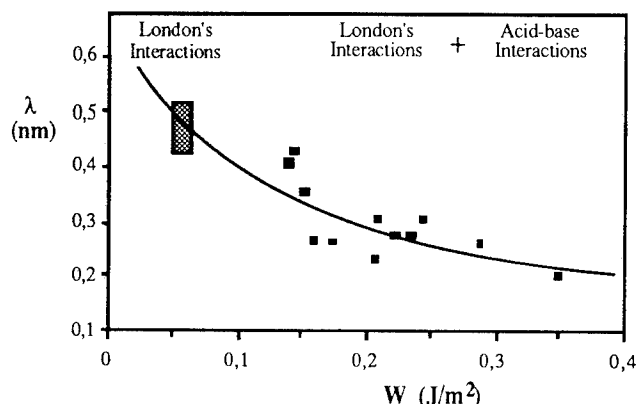


Fig. 1 : Variation of the intermolecular distance λ at the interface versus the reversible work of adhesion W .

Such a variation is in good agreement with data available in the literature [4]. Concerning acid-base interactions only, this agreement is clearly confirmed in Figure 2, where the values of enthalpy variations of these interactions for our systems, $-\Delta H^{ab}$, are compared, as a function of λ , with interaction energies, E_{int} , for different acid-base adducts or hydrogen bonds given in the literature [4].

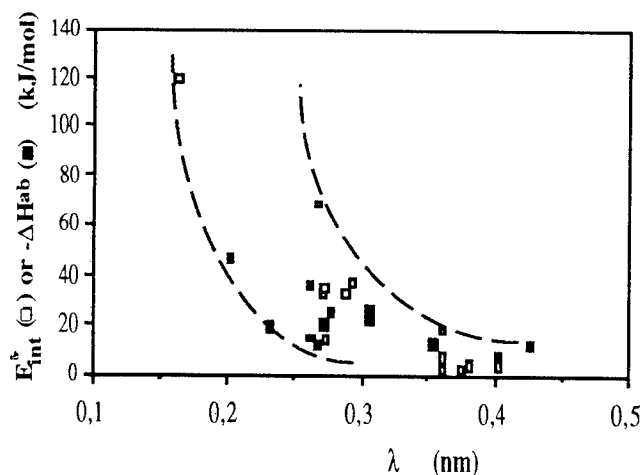


Fig. 2 : Comparison, versus λ , between the enthalpies of acid-base interactions for the systems studied, $-\Delta H^{ab}$, and the interaction energies, E_{int} , for various acid-base adducts or hydrogen bonds [4].

Although interactions established at the interface are different in nature, it can be observed, to a first approximation, that W varies like λ^{-2} . By analogy with the theoretical expression of the interaction energy U between a fibre embedded in an infinite matrix, i.e. :

$$(4) \quad |U| \approx \frac{A_{fm}}{8\lambda^2},$$

a consistent value of the Hamaker constant A_{fm} for given interfaces ($1.4 \cdot 10^{-19}$ Joules for graphite-polymer interfaces for example) are then estimated [3,7]. Moreover, considering that an exponential variation of λ versus W can be used, a threshold intermolecular distance, equal to about 0.7 nm, beyond which no adhesion phenomena could be considered, is defined in good agreement with results available in the literature [8].

Finally, the new interpretation of the results of the fragmentation test on single fibre composites, proposed in the present study, could lead to the estimation of fundamental parameters in adhesion science, such as adhesive pressure and intermolecular distance at the fibre-matrix interface, as well as values of Hamaker constants for the given systems.

1. M. Nardin and J. Schultz, C. R. Acad. Sci. Paris **311**, Série II, 613 (1990).
2. M. Nardin and J. Schultz, Composite Interfaces **1**, 177 (1993).
3. J. N. Israelachvili, Intermolecular and Surface Forces, (Academic Press, London 2nd ed., 1991).
4. L.-H. Lee, J. Adhesion Sci. Technol. **7**, 583 (1993).
5. D. Tabor, in Microscopic Aspects of Adhesion and Lubrication, J. M. Georges ed., (Elsevier, New York, 1982), p. 651.
6. H. L. Cox, British J. Appl. Phys. **3**, 72 (1952).
7. J. Lyklema, Fundamentals of Interface and Colloid Science. Volume 1 : Fundamentals, (Academic Press, London, 1991).
8. K. H. Chung, J. Appl. Polym. Sci. **42**, 1319 (1991).

IMPROVED THIN FILM ADHESION BY METAL PLASMA IMMERSION ION IMPLANTATION AND DEPOSITION

Simone Anders, André Anders, and Ian G. Brown
Lawrence Berkeley Laboratory, University of California, Berkeley, CA 94720

INTRODUCTION

Plasma Immersion Ion Implantation using gaseous plasmas has been developed as a means of ion implantation by Conrad and co-workers [1]. The substrate which is immersed in a plasma is pulse biased to a negative voltage. An electric sheath is formed around the substrate, and ions are accelerated through this sheath and implanted into the substrate. If the plasma is not gaseous but of a condensable nature such as metal or carbon plasma, low energy deposition takes place between the pulses while ion implantation occurs during the pulses. This method, which combines high energy ion implantation and low energy plasma deposition in an alternating manner, is called Metal Plasma Immersion Ion Implantation and Deposition (MePIIID) [2]. In the present paper we describe the method and give examples for its application.

PLASMA PRODUCTION

The plasma is produced by a cathodic arc discharge which forms a plasma of the cathode material. The cathode can be any solid, conducting material such as metals, graphite and highly doped semiconductors. The solid or liquid micron-size particles which are created along with the plasma at the cathode are separated from the plasma using bent magnetic filters. Sources and filters of various size and design can be used depending on the application; films of thicknesses between monolayers and many microns can be deposited. The sources can also operate in a gaseous atmosphere to form compound films such as oxides and nitrides, and they can be clustered in order to deposit multilayers or co-deposit various materials. Plasma sources and filters are described in detail in [3, 4].

The cathodic arc plasma is highly ionized with a mean ion charge state between 1 and 3 depending on the cathode material. The ions have a directed kinetic energy of 20-200 eV, also depending on the cathode material. This is the

ion energy during the low-energy deposition phase, whereas the ion energy during the implantation phase is given by the ion charge state and the applied pulsed bias voltage.

FILM FORMATION

It is possible to form a wide variety of implantation/deposition depth profiles by varying the pulse bias voltage, the ratio between pulse on and off time and the total implanted/deposited dose. High bias voltage leads to a deep intermixing between film and substrate. At high pulsed bias duty cycle, sputtering during the implantation phase can remove the amount of material deposited between the pulses. In this case no film is formed, but a sputter-limited implantation depth profile with a maximum retained dose higher than achievable using conventional ion implantation is obtained. Lower bias voltage leads to a shallow intermixing and the formation of a film. The film properties can also be tailored by varying the biasing during film growth, e.g. starting with a high bias voltage for strong intermixing and continuing with a lower bias voltage for film growth. The film properties depend on the biasing regime. We have investigated this, in particular for amorphous hard carbon films [5]. Hardness, stress, mass density, and other film parameters can be influenced greatly by substrate biasing.

This method has been developed for conducting substrates. Biasing (using a metal electrode on which the insulator is mounted) is problematic for insulating substrates because of a space charge build-up at the substrate surface by high-energy ion bombardment and secondary electron emission caused by ion bombardment. The same is valid for the deposition of insulating films such as oxides on conductive substrates. The voltage drop across the insulating substrate or film which reduces the potential of the substrate surface and therefore the ion energy increases with insulator thickness. For thin insulating substrates or films a remarkable influence of the pulsed bias on the adhesion and

film properties can be observed, whereas for thick substrates or films the effect of the pulsed bias is marginal or negligible. It can be assumed that the space charge accumulated during the ion implantation phase is removed during the deposition phase. Therefore short bias pulses are preferable to minimize surface charge-up.

Well-adherent films of metals on metals, of nickel on carbon-carbon fiber material, and of metal oxides on metal have been formed [3]. In the next section we describe the deposition of amorphous hard carbon on various substrates and of platinum on Teflon in more detail.

TWO EXAMPLES

Deposition of amorphous hard carbon films on silicon, stainless steel, copper and nickel

Amorphous hard carbon films have been deposited on a variety of metal substrates and silicon. The films exhibit a high hardness up to 60 GPa but also a very high internal compressive stress of up to 10 GPa. This high stress causes the film to delaminate when a certain film thickness is reached. Biasing of the substrate to high negative voltages leads to a considerable intermixing at the interface which in turn improves the adhesion. Fig. 1 shows a comparison between an Auger depth profile and a simulation of a carbon implantation/deposition on Si with a dose of $1.2 \times 10^{17} \text{ cm}^{-2}$ using a pulsed

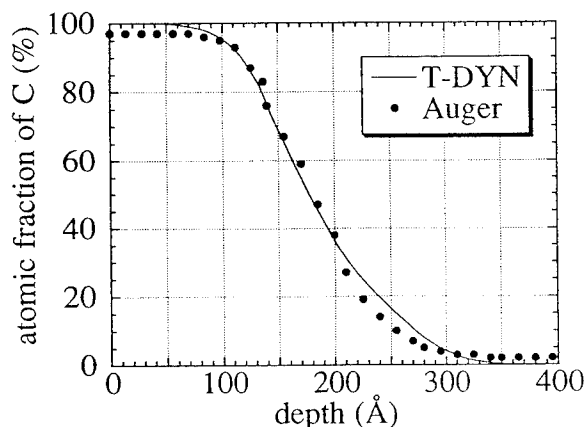


Fig. 1: Auger depth profile and simulation (using the code T-DYN 4.0) of a carbon implantation/deposition film on Si. Dose $1.2 \times 10^{17} \text{ cm}^{-2}$, pulsed bias voltage of -1.5 kV with a duty cycle of 25%.

bias voltage of -1.5 kV with a duty cycle of 25%.

A thin film of about 100 Å is intermixed into the Si substrate over a depth of almost 200 Å. The code T-DYN 4.0 [6] has been used to simulate the implantation/deposition process.

The adhesion of amorphous hard carbon films on Si was measured using a pull tester. We found no failure of the film adhesion up to a pull strength of 70 MPa which was the maximum tensile strength of the epoxy used to glue the pin of the pull tester to the substrate.

Platinum films on Teflon

Teflon films of 250 micron thickness were mounted on a large metallic sample holder with good contact between the Teflon and the holder. Platinum films of up to 2000 Å thickness were deposited on the Teflon using a pulsed bias of -2 kV and 25% duty cycle applied to the holder. The adhesion of the films was tested using the "scotch tape test". The film adhesion exceeded the internal strength of the Teflon.

ACKNOWLEDGMENTS

We are indebted to Dr. Dao Duong for valuable discussions regarding the metallization of polymers. This work was supported by the U. S. Department of Energy, Division of Advanced Energy Projects, under Contract NO. DE-AC03-76SF00098.

REFERENCES

- [1] J. R. Conrad, J. L. Radtke, R. A. Dodd, F. J. Worzala and N. C. Tan, *J. Appl. Phys.* **62**, 4591 (1987)
- [2] A. Anders, S. Anders, I. G. Brown, M. R. Dickinson and R. A. MacGill, *J. Vac. Sci. Technol.* **B12**, 815 (1994)
- [3] A. Anders, S. Anders, I. G. Brown and I. C. Ivanov, *Mat. Res. Soc. Symp. Proc.* **316**, 833 (1994)
- [4] S. Anders, A. Anders and I. G. Brown, *J. Appl. Phys.* **74**, 4239 (1993)
- [5] S. Anders, A. Anders, I. G. Brown, B. Wei, K. Komvopoulos, J. W. Ager III and K. M. Yu, *Thin Solid Films*, to be published
- [6] J. P. Biersack, S. Berg and C. Nender, *Nucl. Instrum. Meth. Phys. Res.* **B59/60** 21 (1991)

SURFACE CHARACTERIZATION OF AGED PLASMA MODIFIED UNPLASTICIZED POLY(VINYL CHLORIDE)

M. Babai-Cline and J.P. Wightman

Center for Adhesive and Sealant Science

Department of Chemistry

Virginia Tech

Blacksburg, VA 24061

INTRODUCTION

The use of radio frequency plasmas for surface modification of polymeric surfaces has been well documented over the past 50 years [1]. The most significant effect of plasma treatment is surface chemistry modification of polymeric surfaces. The surface layer of a polymer is changed, creating chemical groups which can generally improve chemical and physical interactions at the bonding interphase[2-5]. By introducing polar functional groups, plasma treatment increases the wettability of the polymeric surface, thereby affecting adhesion characteristics. As a result, plasma modification has the potential for widespread use in adhesive bonding. A problem arises, however, in industrial environments, where conditions may require that the treated materials be stored for lengthy periods of time prior to bonding.

In the present study, the aging of oxygen plasma treated unplasticized poly (vinyl chloride) (UPVC) was investigated through x-ray photoelectron spectroscopy (XPS), contact angle analysis (CAA), and 180° peel test measurements using an acrylic-based pressure sensitive adhesive (PSA).

EXPERIMENTAL

Materials.

Unplasticized poly(vinyl chloride) was purchased from Goodfellow in 30 cm x 30 cm x 0.1 cm sheets. These sheets were then cut into appropriate dimensions: 1.5 cm x 1.5 cm for XPS analysis; 5 cm x 1.5 cm for contact angle analysis; and 2.5 cm x 5.0 cm for 180° peel test.

Sample Preparation.

Oxygen plasma treatment was carried out in a March I Instruments solid state Plasmod® unit at 13.56MHz and 50 watts of power. The pressure inside the chamber was regulated to 1 torr by a March GCM - 200 Gas Control Module. Plasma treatments were carried out for 1 minute. Samples were analyzed and tested following various aging times. 180° peel test samples were prepared by manually

applying a 1.9 cm wide piece of Scotch Magic® tape on the UPVC and rolling a 40 kg cylinder five times over the surface of the PSA.

Sample Analysis.

XPS analysis was carried out on a Perkin-Elmer PHI 5300 spectrometer equipped with a magnesium achromatic x-ray source ($K_{\alpha} = 1253.6$ eV) operated with a power of 400 watts and a take-off angle of 45°. Survey scans were taken in the range of 0 - 1100 eV. Narrow scan were obtained on any significant peaks noted in the survey scan. Carbon 1s scans were curve-fit using the Apollo Version 4.0 ESCA software in order to obtain information on the bonding state of carbon.

Contact angle analysis was performed on a Rame-Hart Model 100-00 115 NRL contact angle goniometer equipped with a video monitor. Using distilled deionized water, changes in wettability of the UPVC surfaces as induced by the oxygen plasma treatment were assessed. By using diiodomethane in addition to water, surface energy data was calculated by the method of Owens and Wendt[7].

180° peel tests of Scotch Magic Tape® against the polymer were performed on an Instrumetors, Inc. Model 3M90 slip/ peel tester at ambient conditions using a peel rate of 10 cm per minute.

RESULTS

The semi-quantitative results for surface composition are listed in Table I. The XPS survey scan show that the plasma modified surfaces contain carbon, oxygen, chlorine, nitrogen, and tin.

Nitrogen and tin are unique to the plasma modified surfaces. It is believed that nitrogen is due to atmospheric exposure following plasma treatment. The nitrogen photopeak consists of two peaks at around 401.7 eV and 400.0 eV. These binding energies correspond to nitrogen species such as $-NH_3^+$ and C-N, respectively. The small amount of tin present is presumably due to organotin stabilizers used in processing the polymer[6].

The presence of tin indicated that the plasma treatment not only changed the surface composition of the UPVC, but also etched or eroded the surface, revealing small amounts of the stabilizer. With one week of aging, however, the amount of tin decreases from about 1% to 0.4% and remain at this level over the next nine weeks. This may be indicative of some aging process whereby the etched UPVC surface is being covered by organic contamination.

Oxygen plasma treatment of UPVC decreases the carbon content while increasing the oxygen content. This result is consistent with previous work in our laboratory with plasma modification of LARC-TPI (a thermoplastic polyimide) which showed a decreased carbon concentration accompanied by an increase in oxygen content of the surface[9]. The oxygen to carbon as well as the chlorine to carbon ratios of the untreated and plasma treated and aged samples are included in Table I. The lower than expected Cl/C ratio(0.27) and high O/C ratio (0.07) of the untreated sample is indicative of some carbonaceous surface contamination. The O/C ratio of the treated samples increased significantly as would be expected for a surface rich in oxygen-containing groups. The surface composition of the plasma treated UPVC does not change significantly as the samples age. A more detailed description of the plasma modified UPVC surfaces is possible by curve-fit analysis of carbon 1s photopeak. The curve-fit peak assignments are listed in Table II. The carbon 1s photopeaks remained fairly constant through eight weeks of aging. The presence of the high-binding energy carbon species indicates that the oxygen plasma has induced some chain scission in the UPVC.

The effects of the oxygen plasma on the surface energy of the UPVC surface before and after treatment are shown in Figure 1. As expected, an oxygen plasma treatment initially increases the surface energy significantly. The rise and fall in the surface energy follows closely the behavior of the polar contribution, which decreases from 40 mJ/m² to almost zero. The dispersive component remains fairly constant throughout the aging time and closely matches the surface energy of the aged samples. These observations seem to contradict the XPS results which show that the polar functionalities remain on the surface of the polymer after eight weeks of aging. Initially, the surface energy is high because the plasma treatment cleaned the surface of any organic contamination. As the samples age, however, carbon contamination covers the surface, thus reducing the surface energy of the PVC. Contact angle analysis probes the very top surface while the sampling depth of the XPS is on the order of five to ten nanometers at take-off angles of 45° to 90°. Therefore, the carbon

contamination must be a very thin layer which cannot be sampled by XPS. A take-off angle of 15°, which allows shallower sampling depth than a take-off angle of 45°, did not detect the thin organic layer. Since contact angle analysis is limited to the top few angstroms of the surface, monitoring the surface energy via this method will indicate thin surface contamination.

The 180° peel test was used for assessing the extent of adhesion between two materials. Here, Scotch Magic Tape® PSA was utilized to compare the peel strength of different aged samples. The results are illustrated in Figure 5. For the samples which were not aged and aged up to five weeks, the adhesion of the tape to the plasma treated UPVC was strong enough so that the adhesive tore away from the tape backing. After eight weeks of aging, however, not only did there appear to be regions of interfacial failure between the PSA and plasma modified UPVC, but the peel strength decreased below that of the control sample. This behavior also held true for the samples which were aged for twelve weeks. It was noted above that the polar component of the surface energy decreased significantly. A possible explanation of the contact angle analysis and peel test results may be found in the weak boundary layer concept. Although the plasma-induced changes were still present in the near-surface region (as indicated by the presence of high binding energy carbon species), a weak region formed which easily tore away from the bulk polymer.

SUMMARY

Oxygen plasma modification of UPVC creates a surface rich in oxygen species which has a higher surface energy compared to the untreated surface. In the case of UPVC, the total surface energy is initially increased due to an increase in the polar component of the surface energy. However, after twenty-four hours of aging, the total surface energy decreases as organic contamination begins to cover the very outermost surface. This thin coverage is undetected by XPS, which shows an unchanged surface after twelve weeks of aging. Peel test measurements indicate that the plasma modification increases adhesion. Aging results show that the plasma treatment is beneficial to adhesion up to five weeks after treatment, but after eight weeks, peel strength is decreased to below the value obtained for the untreated sample, suggesting the formation of a weak boundary layer.

ACKNOWLEDGMENTS

The support of the Center for Adhesive and Sealant Science and the Adhesive and Sealant Council, Inc. is gratefully acknowledged.

REFERENCES

1. Liston, E.M., *J. Adhesion*, **30**, 199 (1989).
2. Hook, T.J., Gardella, J.A., and Salvati, L. *J. Mater. Res.*, **2**, 132 (1987).
3. Everhart, D.S., and Reilly, C.N., *Anal Chem*, **53**, 665 (1981).
4. Yasude, H. *et al. J. Polym Sci*, **15**, 991 (1977).
5. Hollahan, J.R. and Carlson, G.L., *J. Appl. Polym Sci*, **14**, 2499 (1970).
6. Tester, D.A. in *Degradation and Stabilization of PVC*, E.D. Own, ed. Elsevier Applied Science Publishers, New York (1984).
7. Owens, D.K., and Wendt, R.C., *J. Applied Polymer Sci.*, **13**, 1741 (1969).
8. Webster, H.F. and Wightman, J.P., *Langmuir*, **7**, 3099 (1991).
9. Chin, J.W. and Wightman, J.P., *J. Adhesion*, **41**, 23 (1993).

TABLE I.

Atomic concentrations of UPVC surfaces before and after plasma treatment and after aging.

Sample	Photopeak						
	C	O	Cl	Sn	N	C/Cl	O/C
Untreated	73.7	7.8	18.5	nsp	nsp	0.28	0.07
<u>Plasma Treated</u>							
<u>Aging time</u>							
<u>(weeks)</u>							
0	60.6	21.0	16.9	1.0	0.5	0.35	0.28
12	59.3	18.7	20.8	0.4	1.8	0.35	0.32

nsp denotes "no significant peak"

TABLE II.

XPS Carbon 1s curve-fit peak assignments

Sample	BE (eV)	%	Assignment
Untreated	285.0	61.6	C-C, C-H
	286.5	35.2	C-O, C-Cl
	288.6	3.2	C=O
<u>Plasma Treated</u>			
<u>Aging time (weeks)</u>			
0	285.0	45.2	C-C, C-H
	286.3	37.7	C-O, C-Cl
	288.1	8.2	C=O
	289.5	8.9	O-C=O
12	285.0	46.8	C-C, C-H
	286.4	37.5	C-O, C-Cl
	287.9	7.5	C=O
	289.1	8.2	O-C=O

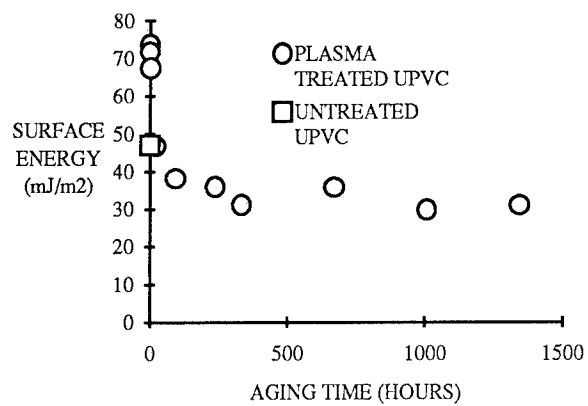


Figure 1. Total surface energy for plasma treated UPVC after aging.

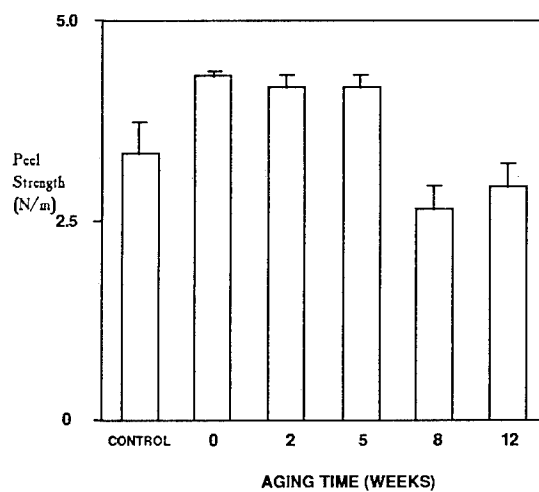


Figure 2. Peel strength of plasma treated UPVC before and after aging

Humidity and Temperature Doubly Shifted Fracture Energy Master Curves for the Prediction of Sealant Adhesion.

N. E. Shephard and J. P. Wightman

Department of Chemistry and Materials Engineering Science, Center for Adhesive and Sealant Science, Virginia Tech, Blacksburg, VA 24061

INTRODUCTION

This research attempts to construct fracture energy master curves for the sealant/aluminum interphase. The shifting variables are humidity and temperature. The fracture energy was measured using a 45° peel test. The location and mechanism of the failure zone will be related to the shifting variables. The master curves will be used to predict crack growth for a sealant joint exposed to outdoor cyclic conditions of temperature, humidity and load.

EXPERIMENTAL

Materials.

A model "acetoxycure" silicone sealant was used in this research. The primary ingredient was polydimethylsiloxane α , ω -diol with 42 000 g/mol number average molecular weight and with a viscosity of 14 000 centistoke. Ethyl-triacetyloxysilane was used to endlink the polymer. The ratio of end-linker reactive sights to reactive polymer ends was 16.5:1. Excess end-linker is used to reduce the cure rate and improve the shelf life of the uncured sealant. 6 part per hundred parts polymer of fumed silica was added to the sealant to control the rheology and increase the modulus of the sealant.

T-6061 T6 aluminum alloy was the adherend used for adhesion testing. The aluminum surface was polished with alumina buffing compound then solvent degreased and argon plasma cleaned. The argon plasma treatment was carried out in a March I unit. The power output was 50 watts and the treatment time was 15 minutes.

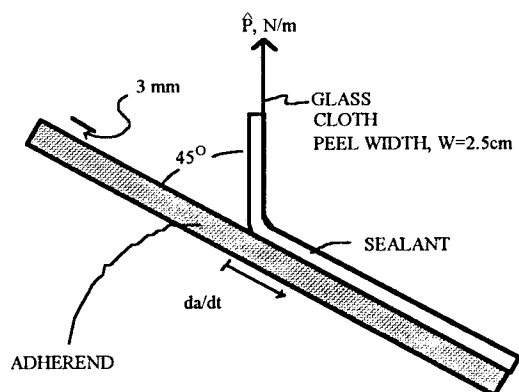


FIG. 1--45° Peel Test Configuration.

Durability Testing.

The 45° peel test was conducted under constant load using a lever arm and fulcrum bearing. (FIG. 1) The fracture energy can be estimated by the following equation which assumes no strain occurs in the peeling member.

$$G = \frac{P}{w}(1 - \cos\theta)$$

Where P is the peeling force, w is the peel width and θ is the peeling angle. The crack length was measured to the nearest 5 micrometers with a linear variable displacement transducer. The fracture energy was measured over the range of relative humidity between 0 and 90 (+/- 0.5) %rh. It was also measured over a range of temperature from 0 to 90 (+/- 0.5) C°. The temperature and humidity were controlled using a small forced air oven with humid and dry air inlets.

X-ray photoelectron spectroscopic analysis was performed using a Perkin Elmer PHI 5400 spectrometer employing a Mg K_{α} (1253.6 eV) achromatic X ray source operated at 15 kV with a power of 400W. Angle dependent

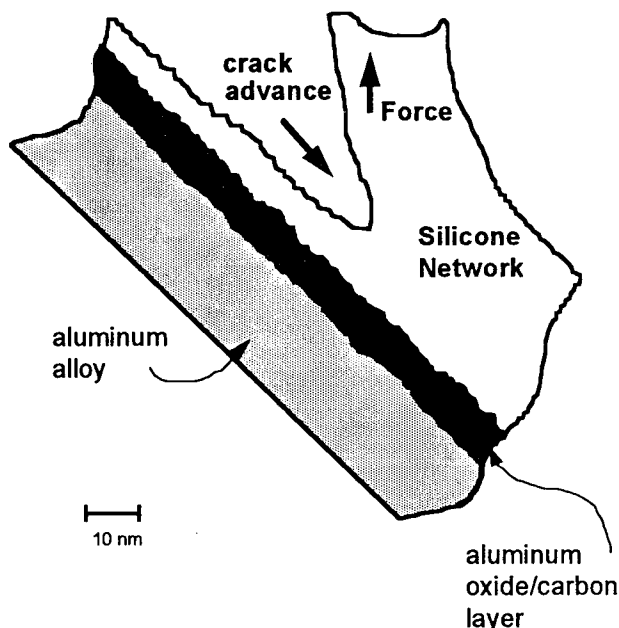


FIG. 2--Interfacial failure zone. %rh greater than 35.

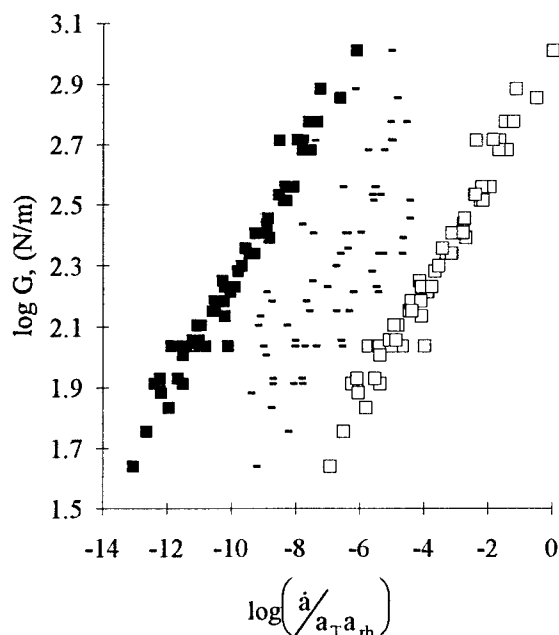


FIG. 3--Logarithmic plot of fracture energy vs. crack growth rate. Where - equals unshifted data, ■ is the master curve for 30 °C and 36.6 % rh, and □ is the master curve for 90 °C and 85.6 % rh.

analysis was done by varying the take off angle between the surface and direction of electron detection. Values between 15° and 90° were typically used.

RESULTS AND DISCUSSION

XPS analysis of the peeled surfaces indicated fracture occurred very near the surface of the aluminum whenever the relative humidity was greater than 35%. The fracture surface of the aluminum side contained silicon as well as aluminum and oxygen. This suggests the fracture surface occurs in the sealant but within 40 nm of the aluminum oxide.(FIG. 2) This phenomenon was independent of temperature. When failure occurred cohesively, the crack would propagate along the fiberglass/sealant interphase.

Only data taken above 35% relative humidity was used to prepare the master curves. Doubly shifted master curves of the crack growth rate vs. fracture energy were constructed for the aluminum/sealant joint.(FIG. 3) Shift factor plots form smooth monotonic curves suggesting no change in mechanism of fracture.(FIG. 4) After shifting, the fracture energy has been measured over a range of fourteen decades of crack growth rate. The fracture energy is strongly dependent on the relative humidity and temperature. A linear fit to the fracture data of FIG. 3 can

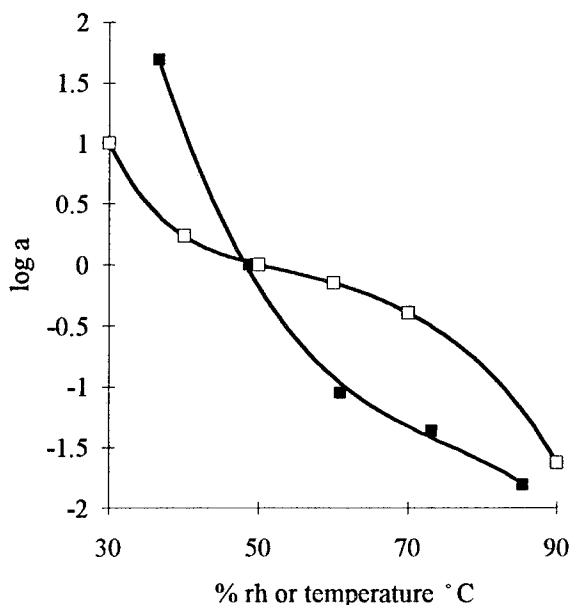


FIG. 4--Shift factor plot for %rh and temperature. ■ is a_{rh} and □ is a_T .

be used to relate the crack speed to the fracture energy, temperature, and relative humidity through the following equation:

$$G = 3974 \left(\frac{\dot{a}}{a_{rh} a_T} \right)^{0.1841}$$

Where a_{rh} and a_T can be taken from FIG. 4.

CONCLUSION

The method of shifting variables has been demonstrated for the sealant joint. Many decades of fracture energy and growth rate can be measured with relatively simple equipment. The strong dependence of temperature and relative humidity on fracture energy can easily be seen by the shift factor plot. The failure mode changes to cohesive in the sealant when the relative humidity is less than 35%. Future work will input climate data into the above equation and compare crack growth to real growth in an outdoor testing device.

ACKNOWLEDGMENTS

The financial support of the Dow Corning Corporation and the Center for Adhesive and Sealant Science at Virginia Polytechnic Institute and State University is gratefully acknowledged.

ALTERING THE FIBER-MATRIX INTERPHASE IN SEMICRYSTALLINE POLYMER MATRIX COMPOSTIES

R. L. Clark, Jr. and R. G. Kander

Department of Materials Science and Engineering and Center for Adhesive and Sealant Science, Virginia Polytechnic Institute & State University, Blacksburg, VA 24061-0237

INTRODUCTION

Crystallization of polymer blends in which an uncrystallizable polymeric diluent is added to a crystallizable polymer host have been the focus of numerous studies. For instance, early work combined isotactic and atactic isomers of the same polymer, and recently, completely dissimilar polymers have been blended. In general, both the nucleation and growth of spherulites are suppressed with the addition of a diluent. Keith, et al. [1] extended this phenomenon of blending dissimilar polymers by adding certain diluents to aliphatic polyesters and nylons, but only in trace amounts (~1%). This particular work showed that the incidence of nucleation was acutely sensitive to the presence of the diluent, whereas the growth rates of the spherulites were not.

More recently, this concept was further investigated with blends involving nylons. Srinivas [2] added various concentrations of poly(vinyl pyrrolidone) (PVP) to a series of nylons. His results were in agreement with those of Keith, et al. Banding was introduced in the spherulites at crystallization temperatures where this didn't normally occur in the crystallization of the host polymer, and this banding was very regular in the spherulites. In addition, there was a reduction in the nucleation density. Finally, the nucleation density suppression seemed to plateau after a given concentration of diluent was achieved.

Not only can additions of diluents alter the morphology of semicrystalline thermoplastic polymers, but also foreign surfaces can have a dramatic effect on the microstructure of the system. For example, when high modulus carbon fibers are added to nylon, profuse crystallization formation is seen at the surface of the carbon fiber. The impingement of the closely nucleated spherulites on the fiber surface only allows growth unidirectionally from the fiber. This produces what is

known as the "transcrystalline" region. This morphology is extremely different from that of the bulk polymer, and it introduces orientation and new boundaries to the system. The formation of such a region can alter the mechanical and physical properties of the composite system. For instance, Lee and Porter [3] reported an approximate factor of two increase in the transverse tensile strength for highly transcrystalline, versus highly spherulitic, materials.

Since this region can ultimately influence the properties of the composite, attempts were made to replace the transcrystalline region with an interphase having a morphology similar to that of the bulk polymer. This new interphase should have properties closely resembling that of the bulk polymer. Poly (vinyl pyrrolidone) [PVP], an amorphous diluent proven to alter the bulk morphology of nylon by reducing the nucleation density, was coated onto high modulus carbon fibers which were, in turn, added to nylon and blends of nylon/PVP matrices. The experimental parameters that were varied are the molecular weight and amount of diluent used to coat the carbon fibers, and the concentration and molecular weight of PVP added to the matrix resin.

Previous studies focused on producing samples with varying interphasial regions, while the current study focuses on completing these samples and determining the interfacial property changes due to the various interphases.

As a further indication as to what effect the transcrystalline region has on adhesion in semicrystalline polymer matrix composites, additional systems from which samples with and without transcrystallinity can be produced are being studied. In particular, poly (ether ketone ketone) (PEKK) reinforced with several different fibers is being examined. In this system, the transcrystalline region is

altered not by a blending technique but by changing the crystallization history of the composite sample.

EXPERIMENTAL

For this study, nylon 66 was used as the host polymer, and PVP was used as the diluent. The blends of nylon 66 and low molecular weight poly(vinyl pyrrolidone), PVP_l (MW \approx 10,000), were produced by adding PVP_l at concentrations of 1%, 3%, 5%, and 7%.

In order to study the morphological characteristics in the nylon 66/PVP_l blends, films were formulated by melt casting. Drops of solution containing either nylon 66 or one of the blends were placed on a hot stage for three minutes at 300°C. The temperature was then reduced to 235°C at a cooling rate of 90°C/min. to allow for crystallization. The crystallization time was kept constant at fifteen minutes for each sample, after which each sample was quenched in air to room temperature.

Next, unsized carbon fibers were added to the melt prior to crystallization. In pure nylon 66 and in all the blends, the transcrystalline region was produced. Finally, carbon fibers sized with PVP, were added to the melt in an attempt to alter the interphase region and produce a region having morphology similar to that of crystallization of the bulk polymer. In this series of tests, the unsized carbon fibers were sized with PVP_l.

In addition to determining what effect the concentration of solution (or the amount of PVP on the fibers) has on the system, the effect of molecular weight in both the blend and on the fiber was studied. A high molecular weight PVP, PVP_h (MW \approx 1,000,000), was used as the diluent and was added to nylon 66 using the above concentrations. Furthermore, the unsized carbon fibers were sized with PVP_h. Finally, using these systems and those previously made, fibers sized with PVP_l were added to the blends of nylon 66 and PVP_h, and fibers sized with PVP_h were added to the blends of nylon 66 and PVP_l.

RESULTS AND CONCLUSIONS

The results from the melt cast films of the matrix material are as follows. The addition of PVP_l introduced banding to the system and reduced the

nucleation density of the nylon, thus allowing the spherulitic size to increase up to five-fold. Furthermore, although not shown here, the spherulitic size did plateau at a given concentration of PVP_l, i.e. 3% PVP_l blend. When 'unsized' high modulus carbon fibers were added to nylon, the transcrystalline region which is produced caused by the large number of spherulites growing from the fiber surface. When these fibers were added to a 7% blend of PVP_l in nylon, the transcrystalline region grows in size, and the nucleation density on the fiber surface is slightly decreased by the migration of the PVP_l in the blend to the surface of the fiber. When PVP_l-sized fibers were added to pure nylon, the sizing dramatically reduced the nucleation density on the fiber surface, and when these fibers were added to a 7% PVP_l blend, almost a complete removal of the transcrystalline region is achieved.

Current work is being performed on determining the interfacial shear strength changes due to the different interphase morphologies produced. The sensitive nature of nylon 66 to water has produced difficulties in producing valid samples for microbead or standard fiber pull-out testing, therefore, a modified fiber pull-out test is being constructed to eliminate these problems. The results from these tests will be presented at the conference. Meanwhile, fiber pull-out tests have been performed on PEKK/glass fiber composites where samples with and without transcrystallinity were produced. Again, this data will be presented at the conference, and from these data, inferences regarding the role of the transcrystalline region in adhesion in semicrystalline polymer matrix composites can be made.

REFERENCES

- [1] H.D. Keith., F. J. Padden, T.P. Russell, *Macromolecules*, 1989, **22**, 66.
- [2] S. Srinivas, *Crystallization Behavior of Nylon 66 and its Blends with Poly(vinyl pyrrolidone)*, Virginia Tech, March 1992.
- [3] Y. Lee and R.S. Porter, *Polym. Eng. Sci.*, 1986, **26**, 1183.

HIGH-SPEED INFRARED IMAGING OF FRACTURE IN THERMOPLASTIC OLEFINS

Yingxia Wang, S. Telenkov, Z. L. Wu, T. Ahmed, Xun Wang, L. D. Favro, P. K. Kuo and R. L. Thomas

Department of Physics
Wayne State University
Detroit, MI 48202
and
A. C. Ramamurthy

Plastics and Trim Products Division
Ford Motor Company
Detroit, MI 48202

and

Witold Brostow, Nandika Anne D'Souza and Henryk Galina

Laboratory for Polymers and Composites
Center for Materials Characterization
University of North Texas
Denton, TX 76203-5308

INTRODUCTION

In reviewing a multicoated system as identified in the schematic shown in Figure 1, it was determined that failure occurred not in the interface between the components but rather within the base material itself. Since the base material consisted of a polymeric blend of polypropylene (PP) and EPDM, we have decided to study both the failure mechanism and the morphological nature of the blend. Material fracture in polymeric systems is determined by intrinsic material properties as well as properties introduced during processing or post-processing as well as time and temperature effects in field environments. The area of failure analysis of polymers has borrowed from the existing framework determined under Linear Elastic Fracture Mechanics. (LEFM). Applications to polymeric systems fail due to the invalid assumptions of linearity (as opposed to non-linearity apparent readily in stress-strain curves of semicrystalline systems) and elasticity (as opposed to viscoelasticity). While great progress has been made towards improving the fracture determination, the problem of the non-linearity in the systems is still very much present. One assumption in testing polymeric components is the presumption of the crack rate being the deterministic quantity. This work includes an examination of zones of deformation through temperature mapping around the crack tip.

METHOD

Morphology-Crystallinity Determination for the Blend

The possibility that the delamination of the coating might be due to thermally induced morphology during subsequent processing operations has been investigated in terms of the differences of recrystallization temperatures of the blend in comparison to its crystallizing component, PP.

Since the polymeric transitions are associated with an enthalpic change in the material, this technique is useful in determining polymeric transitions.

Failure Analysis and Thermal Mapping

The tool for the fracture toughness evaluation consists in the use of thermal images. A primary basis for evaluation is a modification of existing photoelasticity techniques to incorporate thermoviscoelastic experiments. The concept of stress analysis in photoelasticity arises from fringe patterns formed when a polarized monochromatic light goes through a material under load. The fringe represents a region where the differences between principal stresses are constant. Prior to the widespread use of computers, analysis was limited to establishing isoclinic fringes to determine the value of the principal stresses from tabulation of their differences. However, computers now permit analysis via digital image processing. While the image consists of an infinite number of points with differing light (emissivity) for each point in the material under stress, it is possible to discretize the image into a finite number of small segments called pixels whose light intensity values are the average of the set of real points constituting each one to them [1].

Infrared thermal mapping is based on the principle that infrared (IR) energy is emitted by all materials above 0 K; this is the part of the electromagnetic spectrum with wavelengths between 10^{-3} and 10^{-6} m. A parameter useful in bridging the gap between temperature measurement and the infrared measurements is the *emissivity*. Different materials have different emissivities and will therefore emit IR at different intensities for a given temperature. It is important to note that the emissivity is a function of the

molecular structure and surface characteristics of the material [2].

EXPERIMENTAL

Differential Scanning Calorimetry (DSC)

The DSC used was a Perkin Elmer DSC-7 operating on a UNIX platform. Thermal runs were conducted between 30°C and 180°C to mirror the experiments on the TSD. Isothermal annealing at the upper and lower temperatures was conducted to ensure equilibration of the thermal analyzer. Two consecutive runs were conducted at 20 K/min. to note changes in transition characteristics of the material.

Thermal Imaging

Tensile tests on notched tensile samples were carried out at Wayne State University. The infrared emission from the sample was monitored over time using either a Inframetrics IR Camera (8 -12 mm spectral band at 30 Hz frame rate) or a Santa Barbara 128 X 128 InSb focal plane array camera (3 - 5 mm spectral band up to 244 Hz frame rate [3]. The images obtained are imported into digital imaging software and x, y, pixel value, time readings are noted by recording the values at the fringe edges of the sample and measuring the changes in the isothermal contours. In addition, crack tip x, y coordinate-time data are recorded to track the crack growth rate. Measurements on two different strain rates, 4 and 8 mm/min, are noted to evaluate the effect of strain rate on the crack growth rate.

RESULTS

The effects of repetitive heating of the blend are shown in Figure 2 while the corresponding cooling curves are shown in Figure 3. As can be seen, the thermal history effect is eliminated in the system after one heat since subsequent heating and cooling curves overlay on each other. This is true of the polypropylene component in the blend system too - as can be seen in Figures 4 and 5. Of greater importance is the fact that there are two melting transitions in the blend with only a single recrystallization peak, indicating multiple crystalline structures in the system with similar recrystallization kinetics [4]. This is frequently seen in systems which have a broad molecular weight distribution and the presence of the second component (EPDM) causes the formation of two different crystals with different melting points. A sampling of the thermal images is shown in Figure 6. Two inferences can be viewed: the crack tip absolute x, y coordinate does not change; instead, the temperature field around the tip changes. A surface plot of the crack tip-temperature profile is shown in Figure 7. As can be seen, the highest temperature occurs at a distance away from the crack tip. This implies that we need to reconsider the equation relating the crack growth rate to the stress intensity factor [5]:

$$\log K_I = (1/2) \cdot \log (a^*{}^2 G E) + (1/2) \cdot \log [1 + (1/bh_{cr}) \cdot dh/dt] \quad (1)$$

here K_I is the stress intensity factor, a^* is a factor dependent on the geometry, G is the surface energy per unit area, E is the elastic modulus, b is a time-independent factor related to the chain relaxation capability (CRC) [6-8] of the material, h is the crack length, h_{cr} the largest value of h at which the crack will not propagate and t is time. Eq. (1) now needs to be amplified by inclusion of a term representing the effects of the plastic zone radius. Work done on this problem will be presented at the 3rd International Conference on Polymer Characterization [9]. The maximum temperature occurrence at a distance from the tip can be caused by two effects. First, returning to the preliminary concept of fracture as related to the energy G required to form two new surfaces, we infer that the energy must come from an energy transfer from the surrounding matrix to the crack front. This would explain the cooling in front of the crack tip. A second hypothesis might be a cooling due to crystallization, and could be explained by the occurrence of stress induced crystallization.

CONCLUSIONS

The blend system used in the coating shows large scale effects arising from the crystallinity in the system. The crystallization kinetics of the blend differs from that of its major component - even while maintaining its melting characteristics. The rubber component also influences the expansion capabilities of the blend. Therefore, direct correlation between the temperature maps of the propagating crack in the system must take into account the changing expansivity of the system over wide temperature ranges. The thermal maps of the blend system indicate that the temperature fields influence catastrophic failure more than a change in the absolute crack tip position - this in contrast to the situation in metallic systems.

Acknowledgments

Equipment donation to our Laboratory by the Perkin-Elmer Corp. is appreciated.

References

1. S. Levialdi, *Digital Image Analysis*, Marshfield, London, 1984.
2. J. Merchant, *Thw Infrared Temperature Handbook*, Omega Engineering, 1994.
3. R. L. Thomas, L. D. Favro, P. K. Kuo, Z. L. Wu, T. Ahmed, X. Wang, Y. Wang, L. C. Jiang and H. Van Oene, Ford Motor Company report.
4. V. A. Bershtein and V. Abramovich, *Differential Scanning Calorimetry of Polymers*, Ellis Horwood, 1994.
5. W. Brostow, M. Fleissner and W. F. Müller, *Polymer* **32**, 419 (1991).

6. W. Brostow, Mater. Chem. & Phys. **13**, 47 (1985).
7. W. Brostow and R.D. Corneliussen, editors, Failure of Plastics)Hanser - SPE, Munich - Vienna - New York 1986).
8. W. Brostow, J.Kubát and M.J. Kubat, Mechanical Properties and Reliability of Polymeric Materials, to be published in 1996.
9. W. Brostow, N.A. D'Souza, L.D. Favro, A.C. Ramamurthy, R.L. Thomas and Y. Wang, to be presented at the 3rd International Conference on Polymer Chaaracterization, University of North Texas, Denton, January 11-15, 1995.

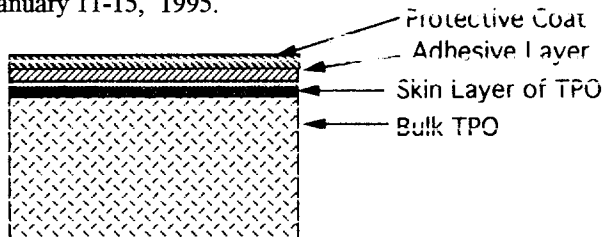


Figure 1: Schematic of the system

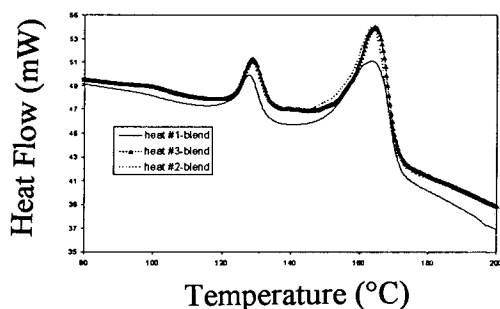


Figure 2: Heating curves for the blend

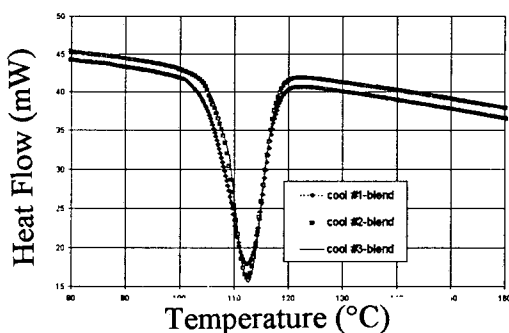


Figure 3: Cooling curves for the blend system

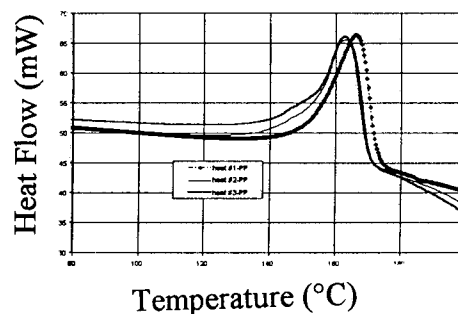


Figure 4: Heating Curves for the polypropylene (PP)

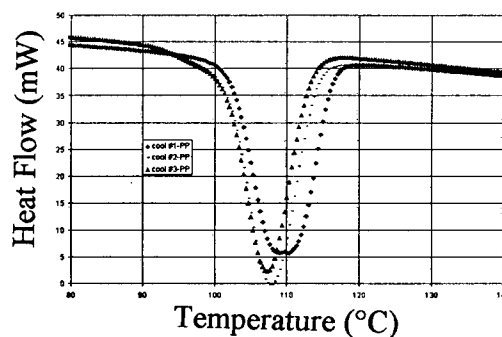


Figure 5: Cooling curves for the polypropylene (PP)

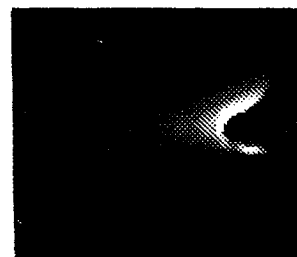


Figure 6: Infrared thermal image of the blend

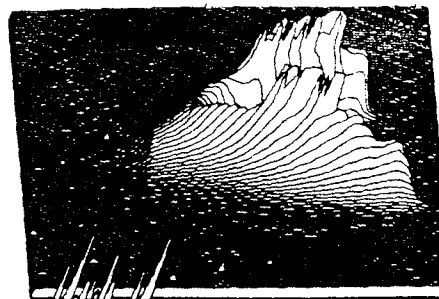


Figure 7: Surface plot of the temperature field around the growing crack

FILM FORMATION OF LATEX COATINGS

C. A. Fleischer, H. R. Grashof, D. Schwark, K. Schlafer, and J. F. Elman
Eastman Kodak Company, Rochester, NY 14650-2104

INTRODUCTION

Latex film formation, the process by which a latex polymer dispersion forms a transparent, void-free film, is typically divided into three steps.¹ Following water evaporation (stage I), the particles deform into a void-free film (stage II), and then interdiffusion occurs between the particles at temperatures above the glass transition temperature (T_g), resulting in a homogeneous, strong film. Small-angle neutron scattering (SANS)^{2,3,4,5,6} and fluorescence non-radiative energy transfer methods^{6,7} have been used to monitor latex film coalescence. However, such techniques require polymer labels (deuteration or fluorescence labels), which are not always practical. Transmission electron microscopy (TEM) of stained cross-sections has been used for qualitative comparison of latex coatings.⁸ Variable-angle spectroscopic ellipsometry (VASE) is a non-destructive method for determining film thickness and optical constants. VASE is used to monitor the first two stages of latex coalescence as a function of time in coatings of poly(styrene-co-methacrylic acid) (95/5) lattices. Through comparison of the refractive index of the film, at a given time, with that of a void-free film, the percent void is determined as latex film formation proceeds.

EXPERIMENTAL

Materials. Poly(styrene-co-methacrylic acid) (PSMA) was synthesized as follows. 15 g of Rhodocal A-246/L (Rhône Poulenc surfactant consisting of a 40% aqueous solution of sodium C_{14} - C_{16} olefin sulfonate) was mixed with 416 ml distilled water in a 2 l, 4 neck round bottom flask equipped with a stirrer, condenser, and nitrogen inlet. The resulting solution was stirred under a nitrogen blanket at 90°C in a constant temperature bath for 30 min. A monomer dispersion of 184 g styrene, 16 g methacrylic acid, 15 g Rhodocal A-246/L in 240 ml of distilled water and an initiator solution consisting of 3.87 g $Na_2S_2O_8$ in 59.11 g of distilled water were simultaneously metered into the stirred reaction flask over a period of 175 min. The reaction was then stirred an additional 8 h at 90°C, and then cooled to room temperature, filtered, and purified by dialysis against distilled water for 23 h. The composition was determined by NMR to be 95.2 wt% styrene and 4.8 wt% methacrylic acid. The precipitated polymer had a M_n of 27,200, M_w of 76,800, and T_g of 117°C. The latex polymer had a T_g of 100°C, as a result of 4% residual styrene. The median particle size measured with a Microtrac ultrafine particle analyzer was 34.3 nm, and 80%

of the particles were between 25.7 and 48.1 nm. Type p, 2" diameter, 12.0-14.0 μm thick silicon wafers with <100> orientation were used as substrates for spin coating.

Sample Preparation. PSMA latex was spin coated onto silicon or polyester (for TEM cross-sectioning) from 2-4% latex solids solution in deionized water. Isolated PSMA was spin coated onto silicon from a 2% dichloroethane solution. Spin coating was preformed on a Headway Research Inc. (Garland, TX) photoresist spinner, model 1-EC101-R485 at 1000 rpm for 60 s. VASE was preformed on a bare silicon wafer, the films as coated, and the films after subsequent heat treatments at 110°C or 125°C for varying times.

Ellipsometry. Data was acquired from 250 to 1000 nm and incident angle was varied between 45° and 85° \pm 0.005° using a J.A. Woollam Co. VASE system. Data at three or four angles of incidence was acquired over the full spectral range for each sample to improve statistics. Samples were mounted vertically and held by vacuum. Amplitude attenuation (Ψ) and phase shift (Δ) values were acquired with a simultaneous measurement of the standard deviation associated with each datum.

Optical Constant Modeling. Before extracting a full ellipsometric understanding of a new system, the complex refractive index of the solvent cast film was obtained. The Δ and Ψ values were fit with a simple Cauchy layer on an appropriate silicon (Si) model (KOH etched Si had previously been modeled by placing about 11 Å of SiO_2 on top of an infinite Si layer). The Cauchy equation is a polynomial that relates the real refractive index, η , to wavelength in microns, λ :

$$\eta = a + b/\lambda^2 + c/\lambda^4 \quad (1)$$

where a , b , and c are the Cauchy parameters. Initially the imaginary part of the refractive index (k) is assumed to be zero and the error between model and data is minimized to obtain the three Cauchy parameters and the film thickness. If the material absorbs in the UV and/or visible region, then k values must be incorporated into the model. Models of uncoalesced films were described by use of an effective medium approximation (ema) layer. Such an approach mixes the complex refractive indices for two known materials with a given morphology. In this case the optical constants for the void-free film were mixed with the constants for void ($\eta=1.0$, $k=0$) using a spherical (as opposed to lamellar or columnar) morphology.

Transmission Electron Microscopy (TEM). The coating side of the polyester/coating samples were sputter-

coated with gold prior to ultramicrotomy to insure that the coating was not removed during sectioning. Using a Reichert-Jung Ultracut E ultramicrotome, ~90 nm thick cross-sections were cut at room temperature with a diamond knife and floated onto the surface of a distilled water bath. The sections were collected onto grids covered with a carbon-coated thin Formvar film.

RESULTS AND DISCUSSION

Figures 1 and 2 present an example of the model and experimental results for ψ and Δ , respectively, for PSMA immediately after spin coating. The model used to obtain the best fit profile contains 17.2% void and has a thickness of 3362 Å. The results show excellent correlation between the model and experiment for three different incident angles. The optical constants, η and k , are presented in Figure 3 as a function of wavelength. The resulting values are essentially identical to that of pure poly(styrene) (PS).

Figure 4 presents normalized thicknesses and void percents for PSMA as a function of time at 110°C, as determined by ellipsometric modeling. Normalized thicknesses were obtained by referencing thickness to that of the final, fully densified latex film. The results show that the thickness and void percent decrease as a function of time at 110°C, resulting in a void-free film after 12 min. At 125°C, a void-free film was obtained in 30 s. As is clear from the TEM micrograph in Figure 5, after 15 min at 110°C discrete particle boundaries are observed, suggesting that minimal interdiffusion between particles has occurred. After 15 min at 140°C, some interdiffusion has occurred, but still structure is observed in the film (TEM not shown). When highly hydrophilic comonomers, such as methacrylic acid, are incorporated in emulsion polymerizations, the polymerization is often not homogeneous, with the more polar monomers accumulating at the particle surface.⁸ Therefore, the PSMA latex may have a shell that is enriched in methacrylic acid and a core that is mainly PS. The T_g of pure poly(methacrylic acid) is 228°C,⁹ so a shell that is enriched in methacrylic acid could act as a barrier to coalescence at temperatures in excess of the overall polymer T_g (100°C).

Figure 6 presents the relationship between the measured void percent and the reduced thickness, measured separately by ellipsometry. The relationship that is predicted by geometric space filling considerations, assuming conservation of mass, is developed as follows. Assuming that the length and width of the coating is constant during the heat treatment, the normalized thickness at any time, t_n , can be described as:

$$t_n = t/t_f = V/V_f \quad (2)$$

where t , t_f , V , and V_f are the actual and final thicknesses and volumes, respectively. Percent void, P , is defined as:

$$P = 100 V_v/V = 100V_v/(V_v + V_f) \quad (3)$$

where V_v is the void volume. Combining equations (2) and (3) results in the following relationship:

$$P = (100t_n - 100)/t_n \quad (4)$$

The results follow the predicted curve closely, with a correlation coefficient of 0.996, as is shown in Figure 6. This confirms the validity of this ellipsometric method for monitoring the first two stages of latex film formation.

CONCLUSIONS

PSMA forms a void-free coating in 12 min at 110°C and in less than 1 min at 125°C. When extended to coatings on film support, VASE provides a non-destructive method for determining the extent of film formation, thus providing a means for defining optimal drying conditions for latex coatings. TEM cross-sections suggest that although the PSMA forms a void-free coating at 110°C, higher temperatures are required for interdiffusion to occur between latex particles.

REFERENCES

1. Y. Wang, M.A. Winnik, J. Phys. Chem., **97**, 2507 (1993).
2. Y. Chevalier, C. Pichot, C. Graillat, M. Joanicot, K. Wong, J. Maquet, Lindner, B. Cabane, Coll. Polym. Sci., **270**(8), 821 (1992).
3. M. Joanicot, K. Wong, J. Richard, J. Maquet, B. Cabane, Macromolecules, **26**, 3168 (1993).
4. L.H. Sperling, A. Klein, J.N. Yoo, K.D. Kim, N. Mohammadi, Polymer for Advanced Technologies, vol. 1 (John Wiley & Sons, New York, 1990), p. 263.
5. L.W. Fisher, S.M. Melpolder, J.M. O'Reilly, V. Ramakrishnan, G.D. Wignall, J. Coll. Interface Sci., **123**(1), 24 (1988).
6. G.D. Wignall, V.R. Ramakrishnan, M.A. Linne, A. Klein, L.H. Sperling, M.P. Wai, R.A. Gelman, M.G. Fatica, R.H. Hoerl, L.W. Fisher, S.M. Melpolder, J. M. O'Reilly, Mol. Cryst. Liq. Cryst., **180A**, 25 (1990).
7. E.M. Boczar, B.C. Dionne, Z. Fu, A.B. Kirk, P.M. Lesko, A.D. Koller, Macromolecules, **26**, 5772 (1993).
8. H. Kast, Emulsion Copolymerization (Hüthig & Wepf Verlag, Basel, 1985), p. 447.
9. J. Brandrup, E.H. Immergut, Polymer Handbook (John Wiley & Sons, New York, 1989), p. 218.

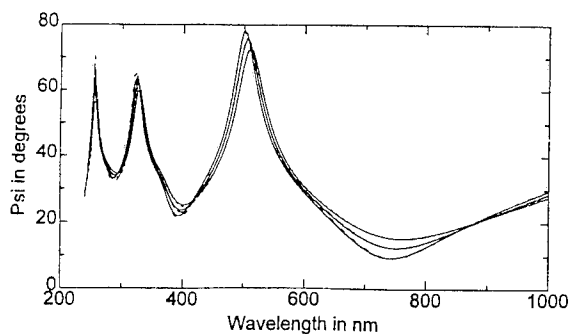


Figure 1. Psi (Ψ) vs. wavelength for Hd U-coat on silicon measured at 66° (---), 68° (—), and 70° (- - -) angle and model fits (solid line).

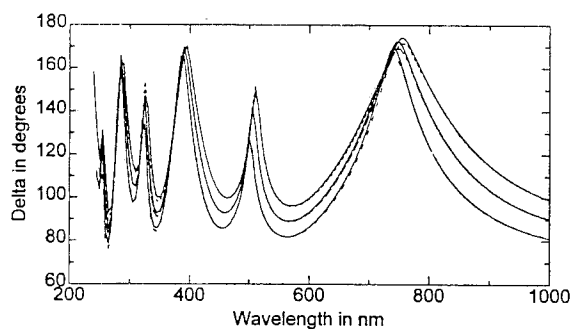


Figure 2. Delta (Δ) vs. wavelength for Hd U-coat on silicon measured at 66° (---), 68° (—), and 70° (- - -) angle and model fits (solid line).

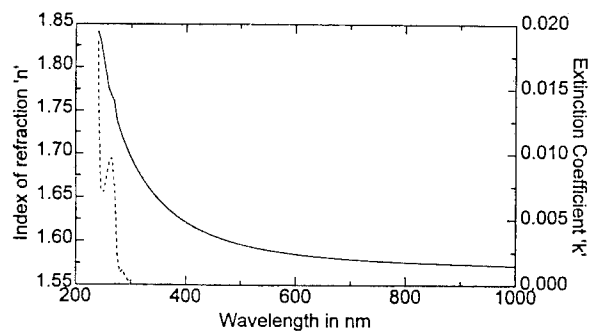


Figure 3. Optical constants vs. wavelength for PSMA; refractive index (solid line) and extinction coefficient (dashed line).

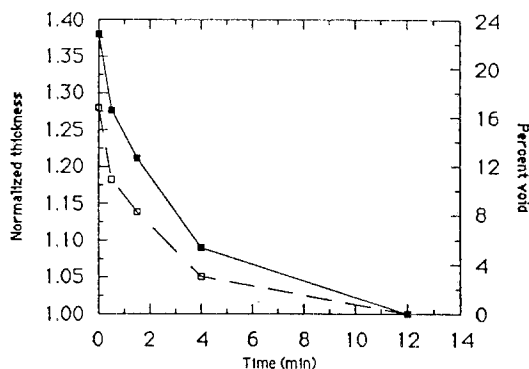


Figure 4. Normalized thickness (—□—) and void percent (—■—) vs. time at 110°C.

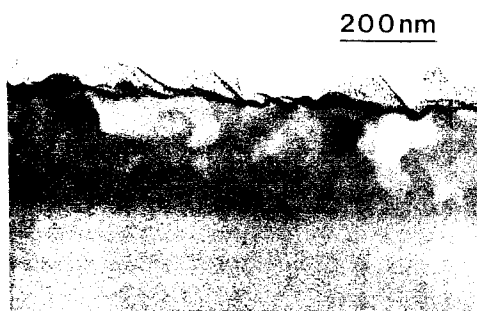


Figure 5. TEM micrograph of PSMA coating on polyester support, following 15 min at 110°C.

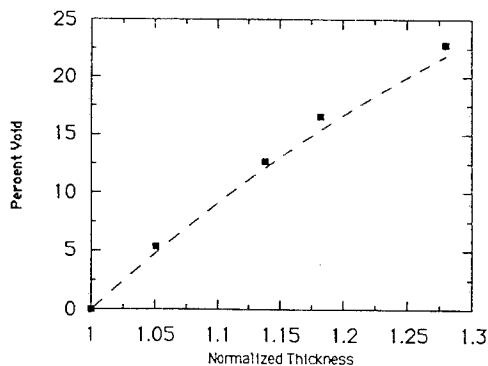


Figure 6. Percent void vs. normalized film thickness for PSMA, comparing experimental results (■) and model predictions (—).

THE WETTABILITY OF ROUGH SUBSTRATES BY VISCOUS POLYMER MELTS

S.A. Tschetter, N.E. Shephard, & J.P. Wightman

*Department of Chemistry,
Center for Adhesive & Sealant Science and
The Adhesive and Sealant Council Education Foundation
Virginia Polytechnic Institute & State University
Blacksburg, Virginia 24061-0201*

ABSTRACT

Wetting has long been recognized as a necessary but insufficient criterion for good adhesion, but little work has been reported on quantitative studies of wetting by neat polymers. Preliminary studies have demonstrated the feasibility of using model porous substrates to study the flow of neat polymers into capillaries. In this study the substrate and polymer were allowed to equilibrate at the testing temperature before coming in contact with each other. Heating was then repeated as a function of time and temperature using polystyrene of various molecular weight, including some above and below its chain entanglement length.

INTRODUCTION

Hot melt adhesives serve a variety of purposes being used in both homes as well as in industry. A main criterion for good adhesion is how well a polymer wets rough substrates. Often the topography of the substrate's surface approximates that of many capillaries. These capillaries provide the primary driving force for wetting to occur. Using a model surface with well defined capillaries, the ideal time and temperature combination needed for maximum interlocking between polymer and substrate can be ascertained.

It is the capillary driving force which makes the polymer penetrate the capillaries. When dealing with systems in which the capillaries are horizontal to the polymer, the effects of gravity are so small that they can be neglected (1). The capillary driving force arises from the fact that there is a pressure difference across the curved surface of the meniscus (1). The equation that arises from this pressure difference if θ (the contact angle) is assumed to be constant is:

$$\Delta P = \frac{2\gamma L \cos \theta}{r} \quad [1]$$

In this equation γL is the surface tension of the polymer melt, θ is the contact angle between the polymer melt and the substrate and r is the pore radius of the capillary. From this equation it is apparent that the larger r is, the smaller the capillary force will be. It is therefore desirable to have capillaries small in

diameter in order to produce large capillary forces. In addition to ΔP being large it is also desirable for the rate of the capillary flow to be large. The Washburn equation gives the rate of flow into capillaries. For the case of a single liquid displacing air the Washburn equation can be written as:

$$v = \frac{\gamma L \cos \theta}{n} \quad [2]$$

Where v is the velocity of the penetrating liquid and n is the viscosity of the liquid (1).

There is a marked difference in the viscosity of polymer's near the polymers critical chain entanglement length. For polystyrene this number is around 35000 $\langle M_n \rangle$. Above the chain entanglement length, polymers show a dramatic increase in viscosity compared to below the chain entanglement length. The change in viscosity is much more gradual before the chain entanglement length (5). The effect of chain entanglement length on the capillary flow is a main focus of this experiment.

EXPERIMENTAL

Polystyrene has a glass transition temperature of about 100°C. Three different polystyrene samples were utilized in this experiment. The first polystyrene used had a value of 42K g/mol and 3.9 for the number average molecular weight and the polydispersity ($\langle M_w \rangle / \langle M_n \rangle$), respectively. This polystyrene is called industrial quality because of its large polydispersity. These values were obtained using a Waters 150-C GPC with a ultrastrogel column and polystyrene standards. Two other polystyrene samples were produced at Virginia Tech by living anionic polymerization. Using this method of polymerization, the polymer's molecular weight is accurately targeted and possesses a low polydispersity. The two polystyrene samples produced using living anionic polymerization had molecular weights of 18K and 74K with polydispersities of 1.74 and 1.07, respectively. These molecular weights were chosen to be above and below the critical chain entanglement length of polystyrene which is known to be around 35K g/mol (5). These polystyrene samples were

called high grade because of their low polydispersities.

Alltech Anodisc™ membrane filters were used in this study. These are thin discs of aluminum oxide which have open cylindrical pores produced by anodization. Using scanning electron microscopy, the open pores were found to have a $<0.2>\mu$ diameter and a height of $<64>\mu$. A sample size of 1.5×1 cm was utilized in this experiment. The Anodisc™ filter is an ideal substrate because it is easily characterized, and because the aluminum oxide is soluble in a dilute sodium hydroxide solution. When the anodisc™ filter was dissolved away, the remaining polymer fibers were measured using scanning electron microscopy.

A procedure for heating the polymer and Anodisc™ separately in an oven to a designated temperature was designed. A special apparatus was built to allow the Anodisc™ filter and polymer sample to reach steady state temperature before coming in contact with each other. Wetting was then repeated as a function of time and temperature.

In order to expose the polymer fibers for scanning electron microscopy analysis, the Anodisc™ filter was dissolved away from the polymer using a 5 wt % solution of aqueous sodium hydroxide. The Anodisc™-polymer composite was placed in the sodium hydroxide solution with the Anodisc™ face down for 30 minutes. The residual polymer was then rinsed with room temperature deionized water. These fibers were then measured directly from the scanning electron photomicrographs to the nearest 0.1mm and averaged together to give the value used in the study. The percentage of the capillary filled was calculated using $[(L/64\mu\text{m}) \times 100\%]$ with $64\mu\text{m}$ being the height of the Anodisc™ filter and L being the measured length of the polystyrene fibers.

RESULTS & CONCLUSION

The rate in which the capillaries were filled over the temperature range is markedly different (fig.1). At 175°C the percent capillary filled over a twenty minute interval starts very low and continues until the capillary is filled. At 200°C the capillary is nearly filled in seconds after contact with the polystyrene. From these initial times and temperatures it is evident that temperature is the more effective variable compared with time when trying to maximize polymer flow.

When the polymer is below its chain entanglement length and its molecules act relatively independent of each other (fig.2). This makes the polymer less viscous and able to penetrate the capillary at a faster rate than a polymer above its chain entanglement length which is more hindered.

In conclusion this research has effectively established the protocol necessary for polymer and substrate to equilibrate at test temperature before being placed in contact with each other. It has demonstrated that temperature is the more important variable

compared to time when using hot melt adhesives over the range of temperature and time studied and capillary driving forces were related to the viscosity of polystyrene.

Fig. 1

42K $<M_n>$ FLOW INTO CAPILLARIES AT 150, 165, 175 & 200°C

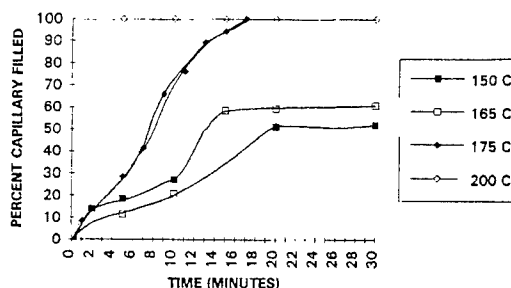
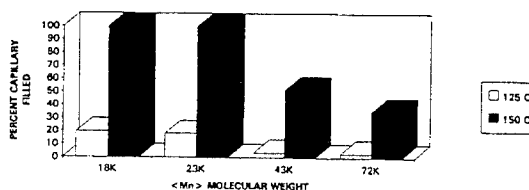


Fig. 2

FLOW OF 4 DIFFERENT $<M_n>$ POLYSTYRENE SAMPLES INTO CAPILLARIES AFTER FIVE HOURS AT 125°C & 150°C



REFERENCES

1. Adamson, Arthur W. *Physical Chemistry of Surfaces* 5th ed. New York: John Wiley & Sons, Inc., 1990. p. 4-49.
2. Heisey, C.L., Books, L.C., & Wightman, J.P. *Effect of Temperature and Flow Time on the Wetting of Rough Surfaces by a Polymer Melt* VPI & SU 1993.
3. Hiemenz, Paul C. *Polymer Chemistry The Basic Concepts* New York: Marcel Dekker, Inc., 1984. p. 1-132.
4. Levine, Ira N. *Physical Chemistry* 2nd ed. New York: McGraw Hill Book Company., 1983. p. 342-365.
5. Porter, Roger S. & Johnson, Julian F. *The Entanglement Concepts In Polymer Systems* R.L. Shriner (Ed.), Chemical Reviews, 66 (1966). p. 1-27.
6. Shaw, Duncan J. *Introduction to Colloid and Surface Chemistry* 3rd ed. Boston: Butterworth & Co. Ltd., 1980. p. 127-143.

Effect of Adherend Type upon the Adhesive Mode-I Fracture Energy of DCB Joints

A.J. Bell, A.J. Kinloch and Y.Wang

Department of Mechanical Engineering, Imperial College of Science, Technology and Medicine, London, SW7 2BX, UK.

T. Shimizu

Chemical and Insulation Material Section, Toshiba Corporation, Fuchu-city, Tokyo 183 JAPAN.

1. ABSTRACT:

Mode I tests were performed to calculate the adhesive fracture energy, G_{IC} , of an epoxy adhesive bonding steel and carbon fibre reinforced plastic (CFRP) double cantilever beam specimens (DCB). Although cohesive fracture in the adhesive layer was always observed, a dependence of G_{IC} upon adherend material was found to exist. Finite element analysis (FEA) was conducted to investigate the effect of the longitudinal, E_L , and transverse modulus, E_T , upon the stress field at the crack tip. This study shows a dependence of stress field, plastic zone size and hence G_{IC} on E_T . Consideration must therefore be given to the type of adherend employed when selecting materials for DCB specimens.

2. INTRODUCTION:

Structural adhesives are playing an ever increasing role in modern engineering and with this comes a need for a greater understanding of their fracture properties. Fracture mechanics is an approach widely applied to the characterisation of adhesive failure. This approach must not only produce accurate results but also be applicable to in-service conditions of the adhesive system. A major feature of fracture mechanics is that the value obtained for the adhesive fracture energy, G_c , when cohesive failure is observed should be independent of the test specimen employed, and hence represent a true material property. During an experimental study of an epoxy adhesive it was evident that the mode I fracture energy, G_{IC} , was dependant upon the test specimen employed. Various factors possibly affecting G_{IC} were investigated,

including crack velocity, adherend and adhesive thicknesses but these did not appear to be affecting the fracture energies obtained. A finite element analysis (FEA) was therefore performed with the aim of relating the fracture energy to the stress field and plastic zone size in the adhesive layer.

3. EXPERIMENTAL STUDY:

The adhesive studied was a single-part rubber-toughened epoxy (Permabond ESP110). Figure 1 shows the double cantilever beam (DCB) configuration used to evaluate G_{IC} ; a 40mm length of foil acted as a starter crack. Two adherend materials were employed, steel and a unidirectional carbon fibre epoxy resin system. The CFRP adherends were produced in two thicknesses. Tests were performed using an Instron tensile test machine, and the crack growth was measured using an optical microscope.

It has been shown for the DCB test [1-3] that the value of G_{IC} may be obtained from:

$$G_{IC} = \frac{P^2}{2B} \frac{\partial C}{\partial a} \quad (1)$$

where: P is the load at crack propagation, B is the width of the specimen, a is crack length and C is the compliance; where $C = \delta/P$ and δ is the displacement.

Experiments were undertaken to check the validity of a linear-elastic fracture-mechanics approach to the present DCB joint specimens. Table 1 gives the mean results from replicate tests for each adherend type. It can be seen that

CFRP adherends give approximately the same G_{IC} value, while steel adherends give a 50% greater G_{IC} value. The difference in measured fracture energies is much greater than the scatter of the replicate tests.

TABLE 1 - Experimental Specimens.

Adherend	h (mm)	t_a (mm)	B (mm)	L (mm)	G_{IC} (J/m ²)
Steel	4	0.4	20	130	1063
CFRP	5	0.4	20	130	660
CFRP	1.5	0.4	20	130	740

3.1. Crack velocity:

Andrews and Kinloch [4-6] and Gent and Kinloch [7] defined a relationship between G_{IC} and crack velocity. Crack velocities were calculated for the specimens in Table 1 but no velocity relationship was evident. For example the 5mm CFRP and steel specimens have similar velocities but different fracture energies.

3.2. Adhesive thickness:

Several workers [8-10] have shown that there is a complex relationship between bondline thickness, t_a , and G_{IC} ; with G_{IC} passing through a maximum at a critical adhesive thickness. The specimens tested in this study possessed a constant adhesive thickness. This effect does not, therefore, account for the G_{IC} differences.

3.3. Adherend thickness:

An influence of adherend thickness upon G_{IC} has been previously noted [11,12]. However, in the present work 1.5mm and 5mm CFRP specimens produced similar fracture energies, and hence there is no marked thickness affect.

3.4. Adherend constraint:

A width effect upon G_{IC} has also been shown by Kinloch and Shaw [8]. This is due to the constraint of the substrate which affects the stress field around the crack tip and increases the amount of plasticity and energy dissipation ahead of the crack. This change of stress field has been highlighted by other workers [13-14] and requires a finite element analysis to be conducted to study this effect in detail.

4. FINITE ELEMENT ANALYSIS (FEA):

FEA was used to model three specimens from the experimental study, the adhesive layer was considered to be linear elastic/plastic with a yield point of 58MPa and the adherends to be elastic.

TABLE 2 - FEA Results

Adherend	h (mm)	t_a (mm)	B (mm)	Expt. G_{IC} (J/m ²)	FEA G_{IC} (J/m ²)
Steel	4.02	0.40	19.95	1080	1075
CFRP	5.19	0.41	19.20	621	642
CFRP	1.50	0.36	19.92	664	677

4.1. Plastic zone size:

Figure 2 shows the region for which the Von Mises stresses are plotted. The Von Mises equivalent stress indicates a large plastic zone within the adhesive layer of the steel joint, Figure 3. "Thick" and "thin" CFRP adherends produce plastic zones of equal size, Figures 4 and 5, but the zone is much smaller than for the steel specimen.

4.2. Stress field:

Plots of tensile opening stress versus distance ahead of crack tip show that the steel adherend produces larger stresses, while the CFRP specimens have similar but lower stress values within the adhesive layer.

5. MODULUS EFFECTS:

The influence of adherend transverse modulus, E_T , upon elastic stresses was studied by Crews, Shivakumar and Raju [13]. To determine modulus effects in this current study, finite element models with varying modulus properties were analysed, see Table 3. The thickness of each adherend is such that they have equal bending modulus and equal loads were applied to each model.

TABLE 3 - Equivalent Bending Modulus Specimens.

Adherend	E (GPa)	h (mm)	t_a (mm)
Steel	210	4.0	0.4
CFRP	$E_L=140$ $E_T=9.5$	4.83	0.4
CFRP	$E_L=140$ $E_T=140$	4.48	0.4
CFRP	$E_T=9.5$ $E_T=9.5$	11.3	0.4

Two "theoretical" CFRP specimens with equal longitudinal, E_L , and transverse modulus, E_T , were also modelled to ascertain whether the value of E_T affected the stress field at the crack tip.

5.1. Plastic zone size:

The plastic zone size of the steel and CFRP ($E_L=140$, $E_T=140$) were of equal size. The plastic zone of the CFRP ($E_L=140$, $E_T=9.5$) and CFRP ($E_L=9.5$, $E_T=9.5$) were of equal size but much smaller than that of the above case.

5.2. Stress field:

The observed stresses within the steel and CFRP ($E_L=140$, $E_T=140$) were greater than that within the CFRP ($E_L=140$, $E_T=9.5$) and CFRP ($E_L=9.5$, $E_T=9.5$).

6. CONCLUSIONS:

It has been shown that the adherend type used has a significant effect upon the plastic zone size and stress levels within the adhesive layer. In particular the transverse modulus, E_T , plays a dominant role. Adherends with a higher value of E_T produce a larger plastic zone size and greater stresses within the adhesive layer. This in turn gives a greater G_{IC} value. This result is a further dramatic indication of the effect of the specimen geometry upon the local stress-field ahead of the crack tip, which in turn controls the energy dissipated in the plastic, or damage, zone ahead of the crack; and so affects the measured value of G_{IC} .

7. ACKNOWLEDGEMENTS:

The authors would like to thank the support of Toshiba (Japan), and in particular the support of Mr. Goto.

8. REFERENCES:

1. Mostovoy, S., Crosley, P.B. and Ripling, E.J. (1967) *J. Mater.* **2**, 661.
2. Mostovoy, S., and Ripling, E.J. (1966) *J. Appl. Polymer Sci.* **10**, 1351.
3. Crosley, P.B., Mostovoy, S., and Ripling, E.J. (1971) *Eng. Fract. Mech.* **3**, 421.
4. Andrews, E.H. and Kinloch, A.J. (1973) *Proc. Roy. Soc.* **A332**, 385.

5. Andrews, E.H. and Kinloch, A.J. (1973) *Proc. Roy. Soc.* **A332**, 401.
6. Andrews, E.H. and Kinloch, A.J. (1974) *J. Polymer Sci. Symp.* **46**, 1.
7. Gent, A.N. and Kinloch, A.J. (1971) *J. Polymer Sci.* **A2**, 659
8. Kinloch, A.J. and Shaw, S.J. (1981) *J. Adhesion* **12**, 59.
9. Bascom, W.D., Cottingham, R.L., Jones, R.L. and Peyser, P. (1975) *J. Appl. Polymer Sci.* **19**, 2545
10. Bascom, W.D. and Cottingham, R.L. (1976) *J. Adhesion* **7**, 333
11. Hojo, M. and Aoki, T. (1993) *ASTM STP 1156*, 281
12. Mangalgiri, P.D., Johnson, W.S. and Everett, R.A., Jr. (1987) *J. Adhesion* **23**, 263
13. Crews, J.H., Jr., Shivakumar, K.N. and Raju, I.S. (1988) *ASTM STP 981*, 119
14. Wang, S.S., Mandell, J.F. and McGarry, F.J. (1978) *Int. J. Fract.*, **14**, 39

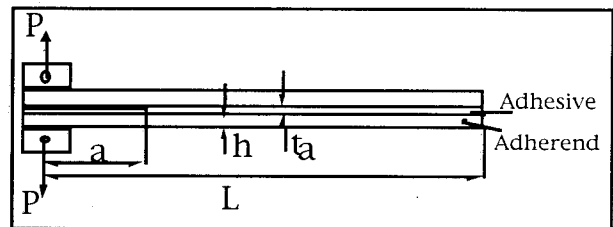


Figure 1. DCB Specimen.

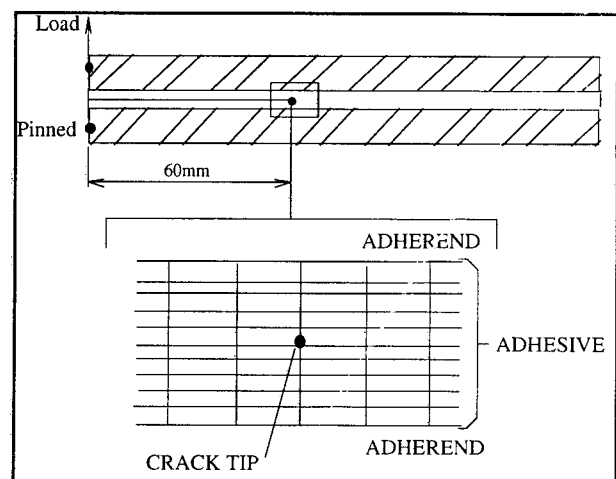


Figure 2. Von Mises Contour Region.

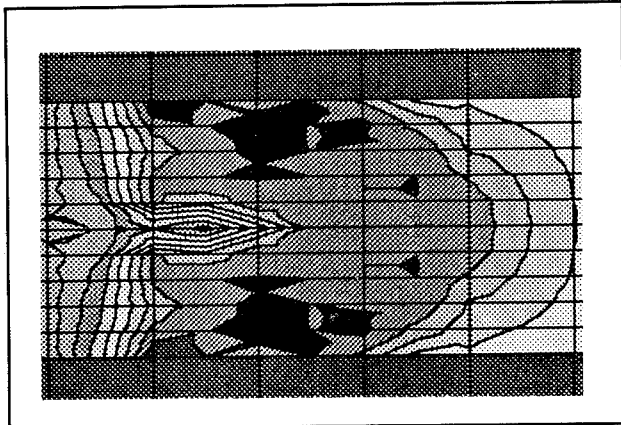


Figure 3. Von Mises Stress - Steel Adherend

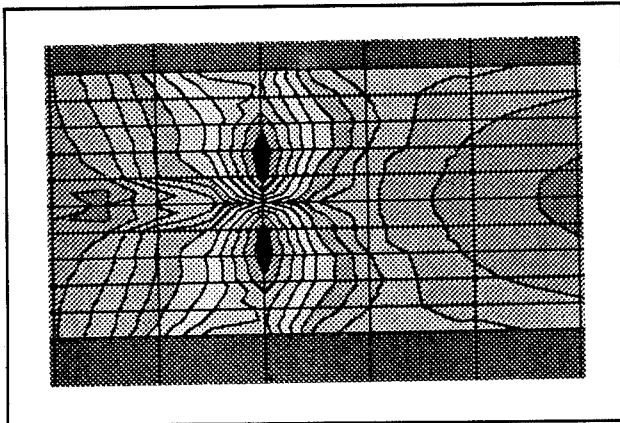
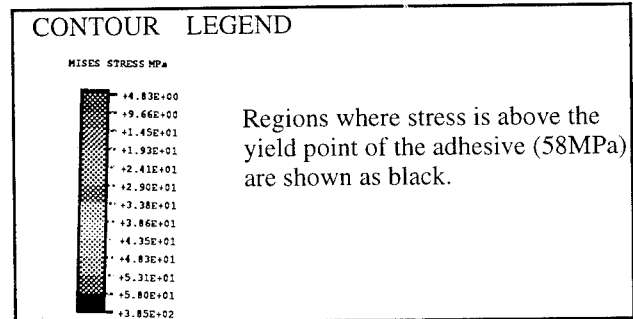


Figure 4. Von Mises Stress - Thick CFRP Adherend

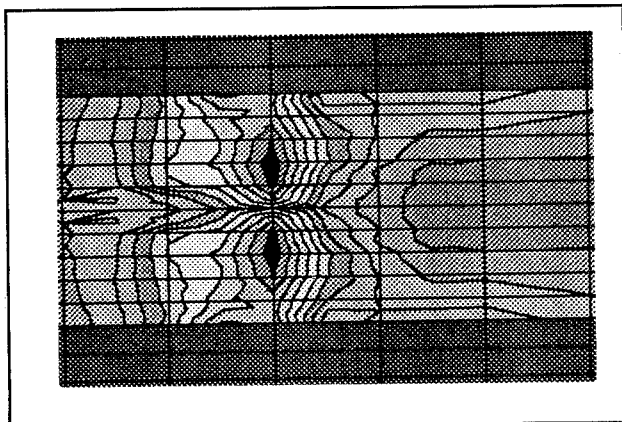


Figure 5. Von Mises Stress - Thin CFRP Adherend

POLYMERIC COUPLING AGENTS FOR ENHANCING THE ADHESION OF EPOXY TO STEEL

Karthik Vaideeswaran^{*}, James P. Bell^{*} and D.E. Nikles⁺

^{*} Polymer Science Program, Institute of Materials Science,
U-136, University of Connecticut, Storrs, CT 06269-3136

⁺ Center for Materials for Information Technology,
229, Bevill Research Bldg., Tuscaloosa, Alabama 35487-0209

Introduction

A novel method is envisaged here, wherein a polymeric coupling agent is used with a polymer topcoat (like an epoxy) to enhance bonding of the polymer to a metal (e.g., steel) and to deter corrosion of the metal. Coupling agents are di/poly-functional compounds with reactive groups which can bond a polymer to fillers or surfaces. By varying the number of reactive groups in the coupling agent, one can vary a number of interfacial properties of the same basic adhesion system [1] and have a true chemical interaction with the surfaces [2].

For optimum adhesive bonding, metals must be pretreated to remove the adsorbed impurities, weak contaminants and oxide layers. Steel and epoxies have excellent adhesion in a dry environment. In the presence of water however, displacement of epoxy by water resulting in a negative work of adhesion and localized corrosion play important roles in the strength loss of the system [2]. So, in the design of the coupling agent, it is important to take into account corrosion inhibiting effects in addition to its chemical interactions with the two surfaces to be bonded.

There are theoretical density profile calculations [3] and experimental evidence [4] for the localization of a block-copolymer at the interface between two phases. Significant entanglement of the copolymer with the matrix homopolymer chains can occur, leading to work of adhesion values much greater than those by thermodynamic predictions alone [5]. Using mean field approximations, we can calculate the volume fraction of the copolymer at the interface for an universal compatibilizer [6]. The results indicate a reduction in interfacial tension due to the block copolymer for any two compatibilized matrices. This reduction increases with increasing copolymer molecular weight and concentration.

Considering all the factors stated above, we have tested quinone-amine polyurethane block-copolymers (QAPs) for their effectiveness as coupling agents. Quinone-amine polymers adhere to steel with sufficient affinity to displace water from a rusty steel surface after chemical or thermal curing of the topcoat [7,8]. These new copolymers are also expected to be epoxy resin compatible. The QAPs used for the study were synthesized at CMIT, Univ. of Alabama, by a two step process. The first step gives a prepolymer with a hard block, to which a soft segment diol is reacted subsequently to give the block-copolymer.

Experimental

Two quinone-amine polyurethane (QAP1B&2B) block copolymers have been used as coupling agents for the epoxy-steel system. The amine-quinone monomer (AQM) was made from 1,4-benzoquinone and 2-(N-methylamino) ethanol. The QAP-1B and -2B contain 40% and 30%, respectively, of the AQM (fig.1) and stoichiometric amounts of toluene diisocyanate and Tetrathane 650 (polytetrahydrofuran of mol. wt. 650). The hard segment contents of these segmented polyurethanes were 67% and 34%. The polymers were characterized by IR spectroscopy, TGA, DSC and GPC. QAP-1B had a hard segment T_g of 73°C soft segment T_g of -35°C and a molecular weight of 14,000. QAP-2B had a soft segment T_g of -49°C.

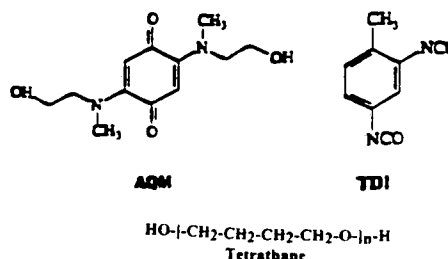


Fig.1. Chemical structures of AQM, TDI and Tetrathane.

The following surface treatment was used for the joints: The joints were immersed in a 3% citric acid aqueous solution (with its pH adjusted to 7 using ammonium hydroxide) maintained at a temperature of 70°C, followed by quick immersions in distilled water and methanol. Next, the joints were dipped in a dilute solution of the coupling agent in THF for 20 minutes. The excess QAP was washed off using THF and the joints were dried. 44 mg of a stoichiometric mixture of Epon-828 epoxy resin and methylene dianiline curing agent was used in making each modified tubular butt joint for adhesion testing. The joints were cured and tested using a torsional testing method [9], which measures the shear strength of the joint.

The surface of a steel coupon was analysed after the applying the QAP on it using methods similar to those detailed above, by IR reflectance microscopy and XPS. IR was used in the transmittance mode to study the interaction of QAPs with the epoxy.

Results & Discussion

The QAPs were found effective in very low concentrations e.g., 0.05%, 0.2% etc. by weight in THF, and caused an increase in the joint strength with increased concentration. The average (sets of seven) measured joint shear strengths of joints made using QAP-1B as the coupling agent (CA1) were:

Controls	= 60400 kPa.
0.05% CA1	= 67090 kPa.
0.2% CA1	= 67940 kPa.
0.5% CA1	= 68590 kPa.
1% CA1	= 72240 kPa.

The average measured joint shear strengths of the joints made using QAP-2B as the coupling agent (CA2) were:

Controls	= 60400 kPa.
0.2% CA2	= 68943 kPa.
0.5% CA2	= 70591 kPa.

The QAP-2B has a lower melting point and a higher soft segment content and so is much more flexible than the QAP-1B. This, probably leads to much more entanglement of chains at the interface and crack tip energy dissipation, with consequent improvement in dry joint strength.

Water durability tests also indicated that the QAP coupling agents could be used to make joints that were extremely stable in hot water (60°C) (fig 2).

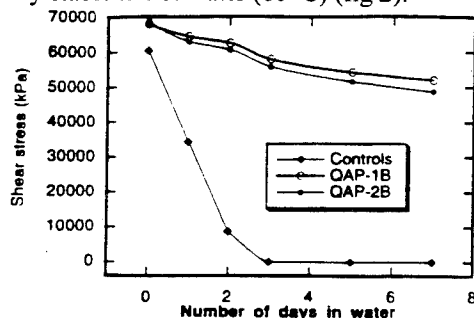


Fig. 2. Water stability comparison of QAP-1B and QAP-2B

The QAP-1B, however, outperformed QAP-2B in strength retention in water over longer periods of immersion. The reason for the initial drop in the shear stress in both the cases may be because of the plasticization effects of water at the interface, rather than any actual bond rupture. The better strength retention by the QAP-1B treated joint may be due to the inherent rigidity of QAP-1B. This higher rigidity comes from its stiffer backbone which, in turn, is a result of its greater hard segment content when compared to QAP-2B. This results in a much lower quantity of water diffusing through QAP-1B and a consequent strength retention of the joint made using this copolymer.

It was seen spectroscopically that the QAP-1B coupling agent had chemical interaction with both the steel and epoxy surfaces. IR spectroscopy in the reflectance mode was used to see interaction of the coupling agent with steel (shift in the carbonyl peak from 1622 to 1604 wavenumbers), while the transmission IR mode was used to show interaction of the coupling agent with epoxy

(disappearance of the amine peaks at 1633 and 1554 wavenumbers in the spectra of the QAP-1B, after reaction with epoxy).

XPS studies were done on the bare metal surface and the QAP coupling agent treated surface after washing with copious quantities of solvent. The QAP-1B treated surface showed Iron(II) oxide and benzoquinone like oxygen peaks in addition to a third oxygen peak. The presence of oxygen from the coupling agent indicates that it was not washed off completely from the surface by the solvent. These 3 kinds of oxygen peaks (fig.3) probably indicate the interaction of the oxygen from the quinone moiety with the steel surface. There was only a single nitrogen peak, so the amine moiety is free to react with the epoxide ring of the top coat in the system.

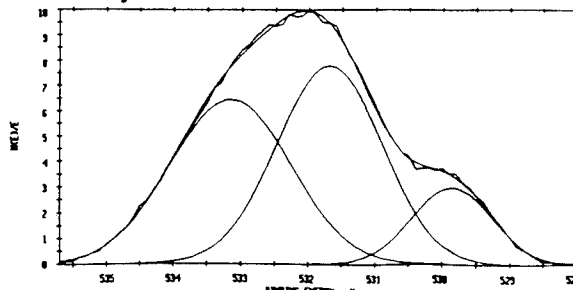


Fig. 3. The three oxygen peaks seen in the XPS of QAP-1B treated steel surface after washing with solvent.

We are investigating the effects of flexibility of the polymer chain on the bonding by using various other percentage compositions of the AQM in the Quinone amine polyurethane. Further studies using the Polymeric β -diketones and other Silanes are in progress also.

References

1. Bell. J. P, Schmidt. R. G, Malofsky.A and Mancini.D, J.Adhes.Sci. Tech., 5, 927, 1991.
2. Schmidt.R.G and Bell.J.P, J.Adhes.Sci. Tech., 3, 515, 1989.
3. Noolandi.J and Hong.K.M, Macromolecules, 15, 482, 1982.
4. Fayt.R, Jerome.R and Teyssie.P.H, J.Polym.Sci. - Polym. Letters, 24, 25, 1986.
5. Creton.C, Kramer.E.J and Hadziioannou.G, Macromolecules, 24, 1846, 1991.
6. Vilgis.T.A and Noolandi.J, Macromolecules, 23, 2941, 1990.
7. Kaleem. K, Chertok. F and Erhan. S, Prog. Org. Coatings, 15, 63, 1987.
8. Nithianandam.V.S, Kaleem.K, Chertok.F and Erhan.S, J.Appl. Polym.Sci., 42, 2899, 1991.
9. McCarvill. W. T and Bell. J. P, J.Adhesion,6, 185, 1974.

Although the research described in this article has been funded wholly or in part by the United States Environmental Protection Agency through CR 821875 to Dr.J.P.Bell, it has not been subjected to agency review and therefore does not necessarily reflect the views of the agency and no official endorsement should be inferred.

PHASE DIAGRAMS OF ACRYLIC PRESSURE SENSITIVE ADHESIVES

Hyun-Joong KIM and Hiroshi MIZUMACHI

Division of Chemistry of Polymeric Materials, Department of Forest Products Science, Faculty of Agriculture,
The University of Tokyo, Bunkyo-Ku, Tokyo 113, JAPAN

INTRODUCTION

Pressure sensitive adhesives (PSAs) have been manufactured by blending gums with resins, where gums are polymers of very low T_g such as natural rubber, synthetic rubber or block copolymer (SIS, SBS, etc), and resins are oligomeric materials such as rosins, terpene resin or some kinds of synthetic resins (C-5, C-9 resin). When these components are blends with each other, modulus and viscosity of the blends decrease extensively, and then they become very sticky. In case of acrylic pressure sensitive adhesive, tackifier resins used not to be involved in the formulation because one can produce variety of polymers by combining different comonomers. But recently there are many cases where acrylic copolymers are blended with tackifier resins in order to modify their adhesion properties. When we deal with the blended materials, it is necessary to examine to what extent the components are miscible with each other, because the miscibility must have a great influence on the phase structure, the physical properties, and also the practical performances of the materials¹⁻³. In this study the miscibility between a series of poly(butyl acrylate-co-acrylic acid) and tackifier resins of modified rosin type were investigated by means of calorimetry, dynamic mechanical measurements and visual observation, and phase diagrams could be drawn. And we have tried to analyze qualitatively the phase diagrams according to the Flory-Huggins theory on the basis of mean-field approximation.

EXPERIMENTAL

The polymers used are a homopolymer of butyl acrylate (BA) and a series of copolymers consisting of butyl acrylate and acrylic acid (AA) with varying composition ; BA/AA = 97/3, 95/5, 93/7 and 85/15 by mole percent. Tackifier resins employed are chemically modified rosins. The main components of rosin is abietic acid, and "Superester A" series are dehydroabietic acid esterified by diethyleneglycol and glycerol ("A-75"), glycerol ("A-100"), pentaerythritol ("A-115"), or pentaerythritol involving some fumaric acid ("A-125").

Acrylic polymers and tackifier resins were blends in ethyl acetate solution in various blend ratios ; 90/10, 80/20, 70/30, 60/40, 50/50, 40/60, 30/70, 20/80 and 10/90. After ensuring that the solutions are uniform and transparent for more than 24 hours, filmy samples were prepared by casting them on glass plates. In order to remove solvent from the samples, they were kept at 80°C for 24 hours and then evacuated 110°C for 48 hours.

Glass transition temperature of the blends was measured by Perkin-Elmer DSC-7 at a heating of 40°C/min. In order to get supplemental information on transition of the blends, the solutions of the blends were impregnated into filter papers, and after removing the solvent, dynamic mechanical properties of the composites were determined as a function of temperature at a frequency of 110 Hz using a Rheovibron DDV-II.

The solution of the blends were coated on glass in about 40 μ m thickness with a glass rod. After dried in a vacuum oven at 110°C for 48 hours, the films on slide glass are maintained at 20°C for 48 hours to attain phase equilibrium and then visually observed to see whether they are transparent or opaque at this temperature. Successively, the same procedures were repeated by changing the temperature in a stepwise manner up to 170°C in an air circulation oven.

RESULTS AND DISCUSSION

Phase diagrams of acrylic copolymer/Superester A-75 systems are shown in Figure 1. The phase diagrams systematically change as acrylic acid (AA) content in the copolymer increases. The blends of acrylic homopolymer NO.1 with Superester A-75 gives a phase diagrams of typical LCST type. And when content of acrylic acid is 3%,

the blends are miscible at any temperature between 20°C and 170°C, irrespective of the tackifier content. And it is interesting to notice the fact that at above 3% of acrylic acid content, phase diagram abruptly changes into UCST type. The range of miscibility of acrylic copolymer and Superester A-75 system decreases as acrylic acid content increases. And when content of acrylic acid is 15%, the range of miscibility of the blends almost disappears. Systematic changes in the phase diagrams of acrylic copolymer / dehydroabietic esters may be explained in terms of not only the specific interaction between the polymer segment and the tackifier resin, but also the bulkiness of the resin.

In this study we have tried to analyze the phase diagrams in a formal way according to the Flory-Huggins theory. Binodal curve can be expressed by the following equations⁴ :

$$\chi_{blend} = A_{blend} + B_{blend} / RT \quad (1)$$

$$1/T_{bn} = 1/T_c^{\infty} \{ 1 - 1/[2A(\phi_2' - \phi_2')] \} \{ 1/m_2 [\ln(\phi_2' / \phi_2')] - 1/m_1 [\ln(\phi_1' / \phi_1')] \} \quad (2)$$

In principle, the curve fitting can be done for the experimentally observed phase diagrams, but in this study it was rather difficult to determine the strict values of the parameters.

Figure 2 is the schematic illustration of the temperature dependence of χ_{blend} for the acrylic copolymer/Superester A-75 system. When acrylic acid content (mole fraction, y) is zero, the phase diagram is of LCST type, which means that χ_{blend} is larger at higher temperature. When $y=0.03$, the two components are miscible with each other and χ_{blend} is lower than the critical value within the temperature range of this experiments. And when y is larger than 0.03, the phase diagram of UCST type appears. If χ_{blend} is expressed by equation (1), A_{blend} must be a decreasing function and B_{blend} must be an increasing function of y . These characteristics can be qualitatively accounted for on the basis of mean-field approximation. The overall segmental interaction parameter χ_{blend} for a blend of $(A_y B_{1-y})_{m_2} / T_{m_1}$ system, where A,B, and T refers to acrylic acid, butyl acrylate and tackifier, respectively, can be expressed by the following equations⁵.

$$A_{blend} = y A_{AT} + (1-y)A_{BT} - y(1-y)A_{AB} \quad (3)$$

$$B_{blend} = y B_{AT} + (1-y)B_{BT} - y(1-y)B_{AB} \quad (4)$$

According to the data of acrylic copolymer/Superester A-75 obtained from the curve fitting method, A_{blend} and B_{blend} are approximately expressed by the following equations :

$$A_{blend} = 2900y^2 - 600y + 20 \quad (5)$$

$$B_{blend} = -4.38 \times 10^6 y^2 + 1.7 \times 10^6 y - 6.3 \times 10^4 \quad (6)$$

Then we can calculate the value of χ_{blend} at any acrylic acid content, and we can also calculate the binodal curve of the phase diagram, using equation (2). Figure 3 shows the calculated phase diagrams of acrylic copolymer / Superester A-75 system for $y=0, 0.03, 0.05$ and 0.07 . The calculated phase diagrams do not agree quantitatively with the experimentally observed ones, but the general trends are qualitatively the same. Because tackifiers used are large and bulky molecules, while acrylic polymers are long linear molecules, values of the parameters obtained according to a simple lattice model have little physical significance. If we want to have a further insight into the segmental interaction between linear polymers and bulky oligomers in a strict sense, we may have to analyze the phase diagrams according to the new Flory theory⁶, or Sanchez theory⁷ where equation of state of the component materials are needed.

REFERENCES

1. S.Naruse, H.-J.Kim, T.Tsukatani, M.Kajiyama, A.Takemura, H.Mizumachi and Y.Hatano, J.Adhesion,47,165(1994)
2. H.-J.Kim and H.Mizumachi, J.Appl.Polym.Sci., submitted for publication
3. H.-J.Kim and H.Mizumachi, J.Adhesion, submitted for publication
4. S.Akiyama, T.Inoue and T.Nishi, Polymer Blends, CMC Press, Tokyo(1981)
5. G.ten Brinke, F.E.Karasz and W.J.MacKnight, Macromolecules,16,753(1983)
6. D.Patterson and A.Robard, Macromolecules,11,690(1976)
7. I.C.Sanchez, J.Macromol.Sci.,Phys.Ed.,B17,565(1980)

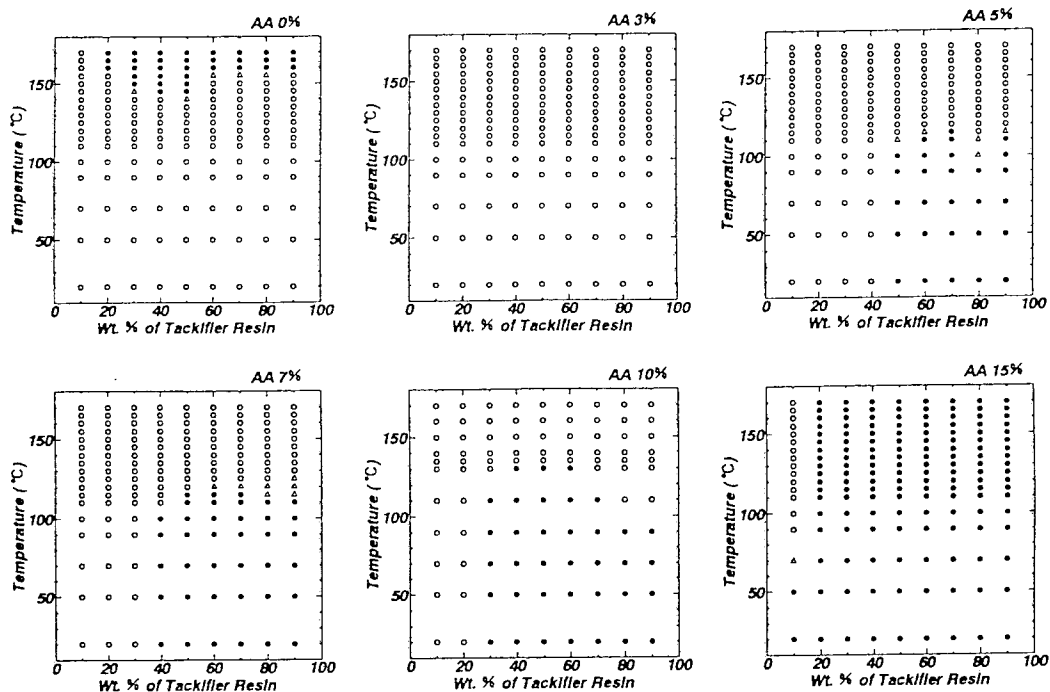


Figure 1. Phase diagrams of acrylic copolymer / Superester A-75 systems. ○ : transparent (miscible), ● : opaque (immiscible), △ : intermediate

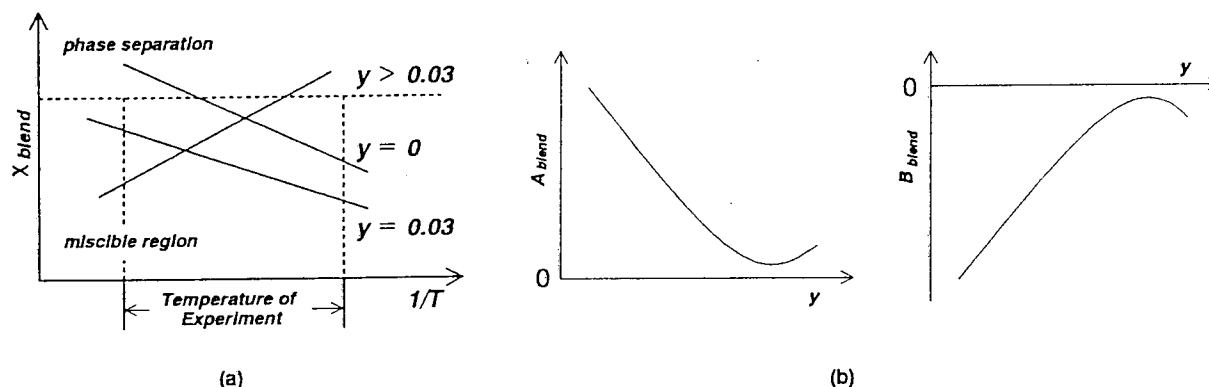


Figure 2. Schematic illustration of temperature dependence of the χ_{blend} parameter of acrylic copolymer and Superester A-75 systems. (a) Temperature dependence of χ_{blend} , (b) Composition (y) dependence of A_{blend} and B_{blend}

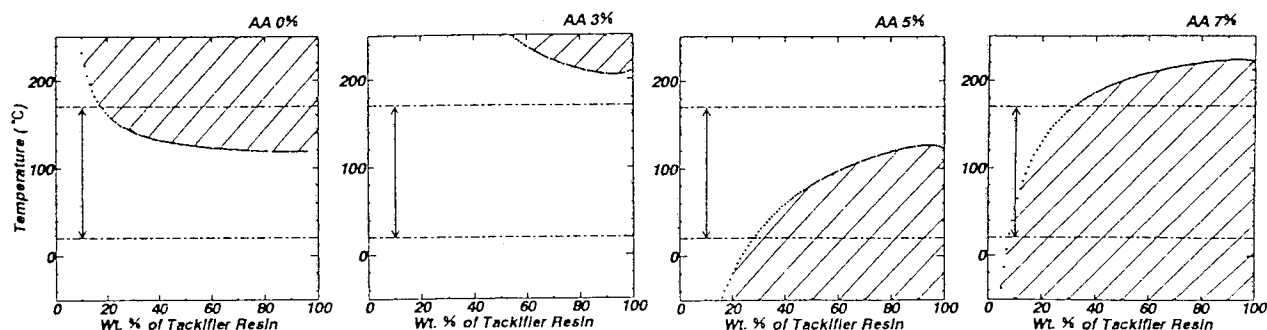


Figure 3. Binodal curve of acrylic copolymer and Superester A-75 system calculated according to eq.(1),(2),(5) and (6). The arrow line represents the range of experimental temperature and the hatchings represent immiscible region.

THE DESIGN OF COMPOSITE-TO-METAL TUBULAR LAP JOINTS FOR TORSIONAL LOADING

A. J. Kinloch and M. D. Roseman

Department of Mechanical Engineering, Imperial College of Science, Technology and Medicine,
Exhibition Rd., London, SW7 2BX, UK.

ABSTRACT

The Thick Adherend Shear Test has been used to evaluate the basic shear properties of two structural adhesives. Also, tubular single lap joints between glass reinforced epoxy tubes (53mm mean diameter) and steel end fittings have been tested under static torsional loading. As the bondline thickness increased, the joint failure torque decreased. The effect of an adhesive spew fillet was to increase the torque capacity.

INTRODUCTION

The high stiffness to weight ratio of fibre reinforced plastics make them very attractive in applications where weight or fuel saving is the requirement; for example the aircraft or automobile industries. Composite tubes subject to torsion have great advantages over their metallic counterparts due to their low rotational inertia, and ease of balancing following manufacture. Their high specific Young's Modulus (E/ρ) and material damping ensures a high natural frequency. This in many cases eliminates the necessity for two piece propeller shafts, thus reducing weight and transmitted noise still further.

In most cases the shaft is to be connected via a metallic fitting to change the drive direction or to connect to another component. The dissimilar nature of the shaft and fitting materials allow the use of an adhesive to transfer the load across the joint. The advantages over a bolted (metallic system) joint are apparent:

- load is distributed over a large area
- no holes need be drilled through the tube
- very little weight is added to the overall structure

- bearing wear is reduced in the connecting machinery
- very good fatigue resistance is apparent
- cleaner looking joint

The main disadvantage is the inability to disassemble post bonding for inspection or replacement of components.

The cheapest and most simple joint to construct is that of the single lap; this configuration however leads to rapidly changing stress gradients at the end of the adhesive layer. Progression from this leads to scarf, double lap and stepped joints.

The aims therefore for this research are to investigate the variation of joint geometry and adhesive type on the torque capacity of adhesively bonded composite to metallic tubular joints under static torsional loading.

The structural adhesives employed for this project were Permabond "E32" (two part paste epoxy) and "ESP110" (single part toughened paste epoxy). The glass fibre reinforced epoxy (grp) tubes were manufactured by Hunting Engineering Ltd.

THE THICK ADHEREND SHEAR TEST (TAST)

The TAST specimens were similar to those developed by Krieger [1]. Lengths of aluminium alloy (Dural) of width and length equal to that of the specimen were surface prepared i.e. grit blasted to give good surface topology; solvent wiped, and then etched in chromic acid for 25 minutes at 68°C. The bondline thickness was controlled by 0.5mm diameter wire insertions. After curing, slots were milled and holes drilled in each specimen as indicated in figure 1. Accuracy in the machining being paramount to

true linear loading of the specimen under testing. Five replicates were prepared for each adhesive.

Two extensometers were evaluated in the determination of shear displacement; the first being a clip gauge type (manufactured by INSTRON) which was positioned some distance from the bond line. The second (manufactured by RDP Howden Ltd.) either side and as close to the bond line as possible (see figure 1).

Figure 2 illustrates the constants attainable from the resultant shear stress/ shear strain graph.

Shear Property Results

Figure 3 shows a typical plot obtained for each of the adhesives under shear loading to failure. Typical shear properties obtained using each of the extensometers are given in table 1. The third column for each adhesive displays the shear moduli obtained from bulk specimens using Dynamic Mechanical Thermal Analysis (DMTA).

The RDP extensometer yields more representative results, as displacement due to misalignment of the specimen is not magnified as is the case for the clip gauge.

TUBULAR JOINTS

For the testing programme, glass/ epoxy tubes (6 plies of $\pm 25^\circ$) of 53mm mean diameter were wound to give a compromise between high axial stiffness and torsional strength. From the manufactures data, the final failure load of the laminate under shear loading is 188N/mm².

The failure torque (T_f) of the tube can therefore be calculated thus:

$$T_f = \frac{\tau_{\max} J}{R_2}$$

where $\tau_{\max} = 188\text{N} / \text{mm}^2$

R_2 = tube outer radius = 28mm

R_1 = tube inner radius = 25mm

J = torsion constant = 2nd moment of area of the tubular cross section

$$J = \frac{\pi}{2}(R_2^4 - R_1^4) \\ = 351907\text{mm}^4$$

Therefore

$$\Rightarrow \text{Failure torque } T_f = 2363\text{Nm}$$

Surface preparation for the grp adherend involved abrasion with "60 grade" aluminium oxide paper followed by a solvent wipe. The regime for the EN24 steel end fittings was - 1. solvent wipe 2. grit blast (fine) 3. solvent wipe 4. liquid/ vapour degrease. Bonding followed shortly afterwards, to prevent contamination or oxidation of the steel surface.

Experience has shown that in order to construct a joint of reproducible high quality with no voids (it would be unknown as to whether or not they exist once the adhesive had cured), a fail-safe bonding method must be devised (see figure 4). The silicon rubber diaphragm shown in the figure can easily be moulded to incorporate many adhesive profile shapes - in this case, spew fillet angles.

The tube and end fittings were jig assembled dry (with wire spacers of the required diameter to set the bond line thickness uniformly around the joint); followed by injection of the adhesive through a small hole drilled in the underside of the grp tube, after having oven warmed both the tube assembly (for 1 hour) and the adhesive (for 20 minutes to lower its viscosity). Once air bubble free adhesive flowed from the top hole in the tube, the joint volume was assumed to have been fully wetted. Once cured, the adhesive plugged holes in the tube limit the detrimental effect of broken glass fibres. Two replicate joint geometry's were tested for each variable.

Results of Torsional Loading

Figure 5 shows a typical loading plot for a tubular joint. The relatively linear nature of the plot is representative of the elastic shear behaviour of the composite tube and of the adhesive. The metal adherend, being of thicker wall thickness to that of the tube can be assumed to have negligible deformation to that of the other components.

The effects of changing the joint geometry are shown in table 2. Apart from the failure mode for the 0.2mm bondline thickness, failure was similar for each of the tests. This being at least 80% within the adhesive (a very thin layer remaining on the metal adherend) with the remainder being <20% block of delaminated composite in the joint region. The 0.2mm bondline thickness specimen exhibited 100% delamination failure of the composite in the joint region. After failure, all tubes showed whitening in the region of the joint when viewed from the outside, thus indicating delamination within the material. This may be due to the sudden shock release of energy at failure of the adhesive, and not to the applied torque prior to failure.

These initial results show that as the adhesive thickness is increased, the joint failure torque decreases. This is the converse to that predicted by theoretical modelling (i.e. analytical shear lag analysis), which does not normally take into account axial tensile loading and transverse compression of the joint as the twist angle is increased.

The introduction of an adhesive spew fillet results in a marked increase in torque capacity of the joint, when compared to that of the standard "base-line" joint, as the stress transfer gradient between adherends has been reduced.

A reduction in bond length shows a reduced torque capacity. The reduction is not as great as one might expect from a third smaller bond area. This implies that there is some critical length below which the joint strength is rapidly depleted.

CONCLUSION AND FUTURE WORK

The basic shear properties of two epoxy paste adhesives have been obtained through use of the "Thick Adherend Shear Test"; the shear displacements obtained using two types of extensometer. The RDP extensometer measured displacements very close to the bondline thus recording higher (and more accurate) shear moduli (1.01GPa and 2.39GPa for the two and single part epoxies respectively), the values of which will be used to characterise the adhesives when modelling the joints with finite elements.

A "fail-safe" method has been developed which ensures a reproducible void free joint, with easy control of the adhesive profile at the blind end of the joint.

Tubular joints of variable geometry have been tested under static torsional loading. The results imply that as the bondline thickness is increased, the torque capacity of the joint decreases. The converse is seen when an adhesive spew fillet shape is introduced into the design. As the bond length is decreased, so does the joint torque capacity, but not by as much as expected.

Further experimentation will include the following parameter study:

effect of :

- bond length
- metal adherend taper
- metal adherend thickness
- reversed fitting of adherends (tube outer surface bonded to metal end fitting inner surface)
- adhesive fillet angles

Parallel tests will be conducted with the single part paste epoxy.

A finite element study (using ABAQUS) will be investigated to complement the experimental programme. A comparison of this with the experimental approach is important, as an idea of the extent of axial tensile and transverse compression loading of the joint should then become apparent.

ACKNOWLEDGEMENTS

The authors would like to thank the EPSRC for funding the project; Permabond Europe, Hunting Engineering Ltd. and Turboflex Ltd. for useful advice, adhesive, tubes and end fittings. Also thanks must go to Dr. D. Tod of the DRA for carrying out DMTA on the bulk adhesive specimens.

REFERENCE

1. R. B. Krieger Jr., Adhesives Age, (1985), p.26.

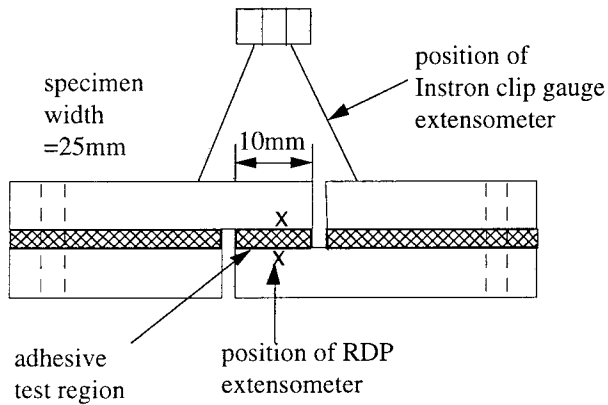


Figure 1 "TAST" specimen with alternative extensometer positioning

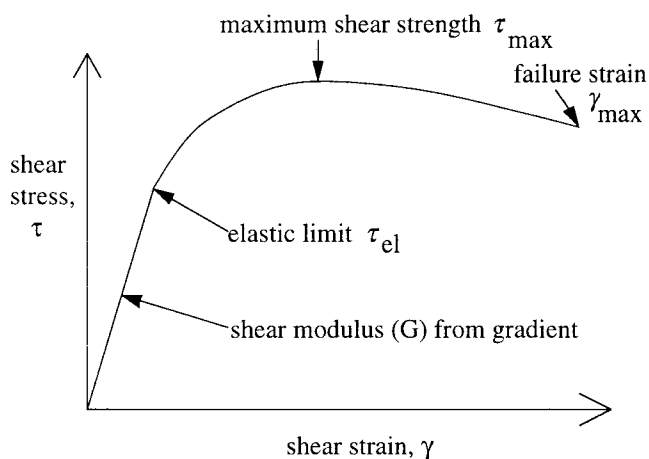


Figure 2 Constants attainable from shear stress/ shear strain plot

The following constants can be obtained from the resulting load/ displacement plot:

Shear modulus (GPa)

$$G = \frac{Ft_a}{Ad}$$

where F = arbitrary load (X) within the elastic (linear) region of the plot

t_a = average adhesive thickness

A = bonded joint area

d = shear displacement measured by extensometer at load " X ".

Elastic limit (MPa) $\tau_{el} = \frac{F}{A}$

where F = load at elastic limit

Maximum shear strength (MPa)

$$\tau_{max} = \frac{F_{max}}{A}$$

where F_{max} = maximum load endured by joint

Failure strain (%)

$$\gamma_{max} = \frac{\text{displ. at failure}}{t_a}$$

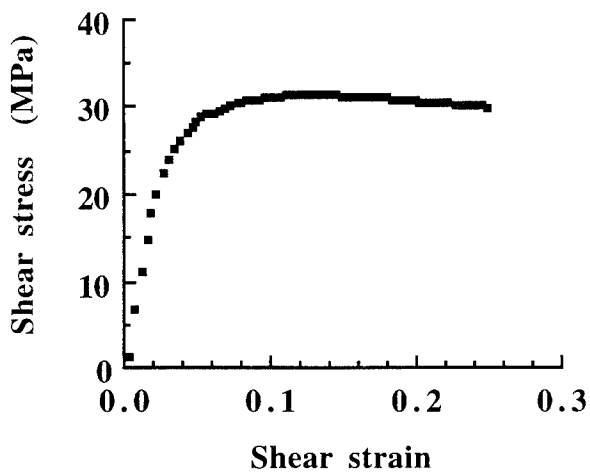


Figure 3a: Typical shear stress/ shear strain plot for E32 two part epoxy (60°C cure)

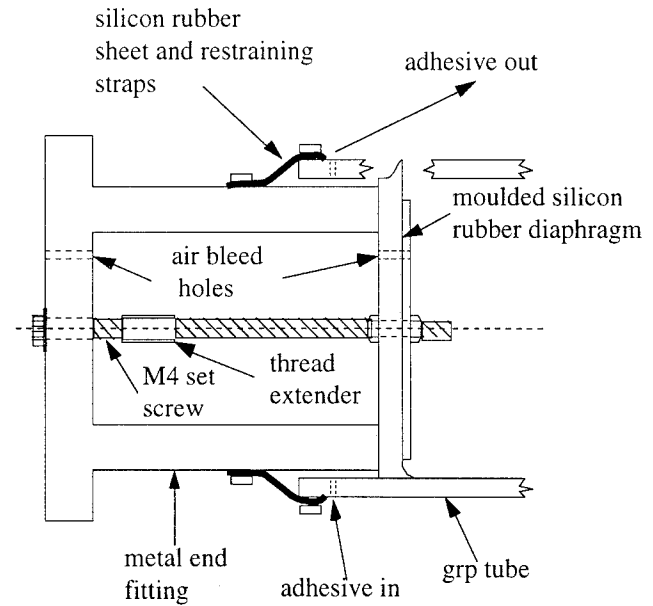


Figure 4: Adhesive injection method

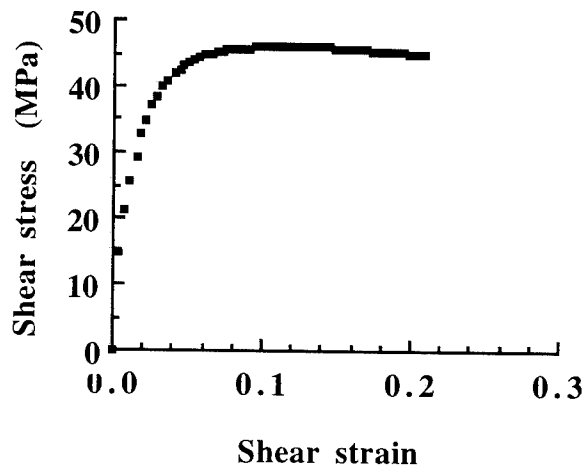


Figure 3b: Typical shear stress/ shear strain plot for ESP110 single part epoxy (150°C cure)

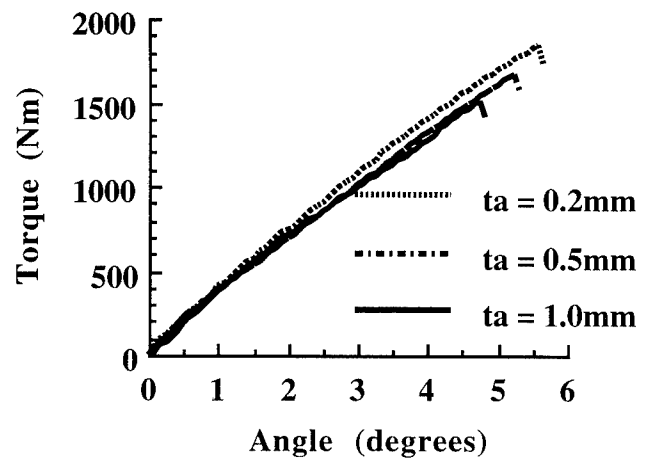


Figure 5: Typical plot for a bonded tubular joint under torsional loading

	two part paste epoxy			single part paste epoxy		
	clip gauge	RDP	DMTA	clip gauge	RDP	DMTA
G (GPa)	0.52	1.01	1.43	0.85	2.39	1.87
τ_{el} (MPa)	18.0	16.43	-----	28.7	16.66	-----
γ_{max} (%)	52.6	16.59	-----	32.3	19.29	-----
τ_{max} (MPa)	35.0	26.36	-----	51.4	42.08	-----

Table 1: Shear properties obtained using TAST and DMTA

Variable number	Variable	Failure torque (Nm)
1	adhesive thickness = 0.2mm	1679
2	adhesive thickness = 0.5mm	1612
3	adhesive thickness = 1.0mm	1418
4	bond overlap length = 10mm	1496
5	adhesive spew fillet = 30°	1654
6	adhesive spew fillet = 45°	1761

The specification shown below is the standard "base line" single lap tubular joint, to which modifications were made in the form of each of the numbered variables displayed in the table:

bond overlap length = 15mm
adhesive thickness = 0.5mm
permanent 40° spew fillet at open end of joint
no adhesive profiling at blind end of joint

Table 2: Effect of joint geometry and adhesive type on joint failure torque.

HEAT CYCLES LEAD TO IMPROVEMENTS FOR CHLORINATED POLYOLEFIN ENHANCED PAINT-TO-PLASTIC ADHESION

William L. Dechent and James O. Stoffer

University of Missouri- Rolla
Rolla, MO 65401

INTRODUCTION- Polypropylene (PP) and polypropylene blends such as thermoplastic olefin (TPO) are of interest to auto and other industries because they are inexpensive, recyclable plastics which are easy to manufacture¹. These plastics are impossible to paint unless given a surface treatment owing to 1) low surface energies, 2) insolubility, and 3) the lack of functional groups to which the topcoat could form covalent bonds. The addition of a thin layer of chlorinated polyolefins (CPO), several microns thick, to the plastic substrate is a proven method which greatly increases adhesive strength (from $< 5 \text{ g cm}^{-1}$ with no CPO treatment to $> 800 \text{ g cm}^{-1}$ for samples given either a thermal or IR treatment of the CPO coated substrate.) A layer of CPO raises the surface energy, and can be swelled and penetrated by the solvents of a paint. Previous work has shown the importance of thermal treatments of the CPO coated substrate to maximize the adhesive strength of AcrylicTM/ CPO/ TPO paint systems as quantitatively measured by Instron cloth peel tests.²⁻⁵ The current focus is on polyester/CPO/TPO paint systems with an emphasis toward the achievement of high adhesive strengths comparable to the values seen for AcrylicTM systems ($> 500 \text{ g cm}^{-1}$).

Preliminary tests of polyester systems showed adhesive strengths from 50 to 100 g cm^{-1} . This represents a 10 to 20-fold improvement over no CPO systems, and further research was directed toward achieving adhesive strengths comparable to those seen for 2K PUR AcrylicTM systems (strengths $> 500 \text{ g cm}^{-1}$.) Wide variations in adhesive strengths were observed in subsequent studies for polyester samples prepared in the same manner as the AcrylicTM systems of previous work^{3,4}; this indicated a need to develop a procedure which would assure consistent high adhesive strengths. In the new procedure, 1) the CPO coated plastic was given a heat treatment, 2) the paint was applied and 3) the samples were given two days to dry at ambient temperature, and then 4) a heat treatment was given to the

paint/CPO/plastic systems followed by 5) the peel test a day later. The second heat treatment, listed as item 4), is a new operation.

EXPERIMENTAL- The sample preparation (cutting and cleaning of the plastic) and the Instron cloth peel test were the same as in previous work⁴, with 15 samples per data point except where noted otherwise. Both waterborne CPO (CP 310w) and solvent borne CPO (CP 343-1) were used. The time and temperature for the heat treatment of the CPO coated substrate was either $140^{\circ}\text{C}/3 \text{ hr}$ (for Tables 1, 2, and 4) or $100^{\circ}\text{C}/20 \text{ minutes}$ (for Table 3.) For Tables 3 and 4, Himont 3131 thermoplastic olefin was used and the polyester topcoat was prepared from a polyester resin (Desmophen 670TM; Miles), an aliphatic polyisocyanate (Miles Desmodur N-75) and dibutyl tin dilaurate as the catalyst (FascatTM 4102; M&T.) The white (TiO_2) polyester topcoat was given two days to dry at room temperature. For Tables 1 and 2, the topcoat is a 2K PUR AcrylicTM that varies from the polyester topcoat in that AcryloidTM resin (Rohm & Haas AU-608) was used instead of a polyester resin.

The second heat treatment was applied in two different ways: 1) for Table 3, the heat treatment (variable temperature) follows a 48 hour paint dry time; 2) for Table 4, the duration of the ambient paint dry time varies (2, 4, and 6 days), and the heat treatment temperature is always 100°C .

RESULTS- Tables 1 and 2 are previously published results. Table 1 shows that the CPO treatment produced a 10-fold increase in adhesive strength; adhesion varies from sample lot to sample lot of TPO and this 10-fold increase is the minimum value observed. Table 2 shows that the heat treatment of the CPO system produces adhesive strengths 150- to 200-fold greater than no-CPO systems. All samples for Tables 1 and 2 use a 2K PUR AcrylicTM topcoat.

Tables 3 and 4 show adhesive strengths of polyester topcoat/CPO/plastic systems. The first heat treatment (of

the CPO coated plastic) was lowered from 140 to 100°C for the tests shown in Table 3. Table 3 is the first reported data of the effects of a heat treatment of a paint/ CPO/ plastic system (the second heat treatment), where a waterborne CPO is the adhesion promoter and TPO is the plastic substrate. This test differs from previous tests where CPO coated substrates were heated, but the paint cured at ambient temperature. Adhesive strength increased from 385 g cm⁻¹ to 582 g cm⁻¹ as temperature of the second heat treatment increased from 22 to 97°C. Adhesive strength values of 385 g cm⁻¹ are excellent, but previous tests of polyester systems had shown results (for ambient paint cure systems) ranging from 50 g cm⁻¹ after two days of paint cure to 100 g cm⁻¹ after ten days of paint cure. Both high (adhesive strength in the hundreds) and low (adhesive strength ~50) values have been seen repeatedly for ambient temperature cured samples (samples which were not given a second heat treatment.) As the temperature of the second heat treatment increases, the standard deviation decreases.

Table 4 shows results for both waterborne CPO and solvent borne CPO. The results for table 4 are from 7 samples per datum, rather than the usual 15, because the test was changed to split the 15 samples into two lots of 7 each, one for ambient samples, and the other for a 20 minute 100°C heat treatment. For both the waterborne CPO and the solvent borne CPO systems, samples given six days to cure before the second heat treatment show lower standard deviations than samples given less time to ambient dry.

Two types of failure mechanisms for polyester/ CPO/ TPO systems were noted. In the first, cohesive CPO failure occurred, as confirmed by ESCA analysis which showed the presence of chlorine on the underside of the paint and chlorine on the plastic. The adhesive strength values ranged from 50 to 200 g cm⁻¹, for most mechanism 1 type failures. A few type 1 failures ranged as high as 300 g cm⁻¹. In the second mechanism, cohesive plastic failure occurred at the weak boundary layer (wbl) of the TPO, with adhesive strengths surpassing 300 g cm⁻¹, as confirmed by the presence of TPO on the underside of the peel cloth.

CONCLUSIONS- Chlorinated polyolefins have been used as an adhesion promoter to increase the adhesion of paint to polypropylenes. A second heat treatment of the

polyester/CPO/TPO system assures consistent high adhesion performance with strengths greater than 500 g cm⁻¹. Without the second heat treatment, the adhesive strengths of polyester systems vary from 50 g cm⁻¹ to 500 g cm⁻¹. There is a parallel between this observation, and previous work involving acrylic samples where systems not given **any** heat treatment showed a wide range of adhesive strengths over the same range of adhesive strength values (from 50 to 500 g cm⁻¹.) For acrylic systems the first heat treatment (of the CPO coated plastic) raised the adhesive strength to from 600 to 800 g cm⁻¹.

For the ambient cured polyester tests where the samples were given 1) the same paint, 2) the same CPO, and 3) the same plastic, and 4) exposed to the same environmental conditions there is still a considerable variance in the adhesive strength (from a minimum of the 10-fold increase to a maximum of a 100-fold increase) **unless** the second heat treatment was performed.

The data in Table 4 is especially important, for all the ambient cured samples performed near the 10-fold increase level, but second-heat samples showed increases to the 100-fold increase level. This indicates that for production lots of thermoplastic olefin⁶ which would otherwise show the low end of adhesive performance (~50 g cm⁻¹), the heat treatment will increase the adhesive strength to values above 400 g cm⁻¹.

Further tests of the adhesion mechanism for polyester systems are planned because a very interesting question has been raised: why did heat cured CPO samples cohesively fail at 50 to 100 g cm⁻¹ when all other data indicates that the heat treatment raises the cohesive strength of CPO to values ~1000 g cm⁻¹? One hypothesis is that the acetate solvents of the polyester paint disrupted the crystallinity of the CPO, reverting the CPO back to an amorphous state. If this were the case, then the variance in adhesive strength for ambient cured polyester systems is an indicator of a variance in the polyester paint effect on the CPO, and the second heat treatment is a "composite healing mechanism."

REFERENCES

1. *Modern Plastics*, 86 (May 1991)
2. J. Lawniczak, C. Sass, J. O. Stoffer, W. L. Dechent, *Polym. Mater. Sci. Eng. Prepr.*, **68**, 28 (1993)
3. W. L. Dechent, J. O. Stoffer, *Polym. Mater. Sci. Eng. Prepr.*, **69**, 380 (1993)
4. W. L. Dechent, J. A. Giles, C. A. McMillan, J. O. Stoffer, *Polym. Mater. Sci. Eng. Prepr.*, **70**, 172 (1994)
5. W. L. Dechent, J. A. Giles, S. P. Sitaram, J. O. Stoffer, *Polym. Mater. Sci. Eng. Prepr.*, **71**, 617 (1994)
6. R. A. Ryntz, Q. Xie, A. C. Ramamurthy, *Twenty-First Waterborne, Higher-Solids, and Powder Coatings Symposium: Part 2*, 812 (1994)

ACKNOWLEDGEMENTS- We are pleased to acknowledge the support of the Eastman Chemical Company.

Table 1. Adhesive Strength of PUR Acrylic™/ CPO 310w/ TPO systems (no heat treatment)

Treatment	Temp.	Adhesive Strength ^a
no CPO	25° C	< 5 g cm ⁻¹
CPO	25° C	53 ± 7 g cm ⁻¹

Table 2. Adhesive Strength of PUR Acrylic™/ CPO/ plastic systems (140°C heat treatment)

CPO	Substrate	Adhesive Strength ^a
CP 310w	PP	656 ± 37 g cm ⁻¹
CP 310w	TPO	790 ± 48 g cm ⁻¹
CP 343-1	TP	957 ± 48 g cm ⁻¹

Table 3. Effect of temperature^a on polyester/ CP 310w/ TPO system on the adhesive strength where the samples were given two days to dry before the second heat treatment

Temperature ^a	Adhesive Strength
22 °C	385 ± 102 g cm ⁻¹
50 °C	388 ± 70 g cm ⁻¹
70 °C	417 ± 71 g cm ⁻¹
85 °C	532 ± 66 g cm ⁻¹
97 °C	582 ± 64 g cm ⁻¹

a) This is the second of the two heat treatments and it was 30 minutes

Table 4. Effect of time^a and temperature^b on the adhesive strength of polyester/ CPO/ TPO systems for two types of CPO

CPO	T. ^b	2 days ^a	4 days ^a	6 days ^a
310 ^c	22	—	74 ± 21	71 ± 18
310 ^c	100	—	431 ± 211	467 ± 89
343 ^d	22	49 ± 13	86 ± 35	74 ± 16
343 ^d	100	437 ± 139	550 ± 181	544 ± 85
cp ^e	22	258 ± 30	400 ± 47	430 ± 9

a) time of ambient paint dry- the time between the painting and the second heat treatment

b) temperature of the second heat treatment (°C)

c) waterborne CP 310w: no dilution; used as received

d) solvent borne CP 343-1: diluted; 5% solids in toluene

e) cp: cohesive strength of ambient cured paint as determined by a two cloth peel test where both clothes are soaked in paint

RELATIONSHIP BETWEEN THE SILICA CONTENT OF SYNTHETIC VULCANIZED STYRENE-BUTADIENE RUBBER AND ITS ADHESION PROPERTIES

A. Torró-Palau^a, J.M. Martín-Martínez^b, J.C. Fernández-García^a, A.C. Orgilés-Barceló^a.

^aINESCOP. Footwear Research Institute. 03600 Elda, Alicante. SPAIN.

^bAdhesion & Adhesives Laboratory. University of Alicante. 03080 Alicante. SPAIN.

1. INTRODUCTION

The nature and formulation of synthetic vulcanized rubber greatly determines its adhesion with different adhesives [1]. A noticeable improvement in adhesion can be obtained by surface treatment of rubber. Physical (i.e. roughening) and chemical (i.e. halogenation, carboxylic acid) surface treatments have been shown to favour adhesion on several rubbers [2-5]. It has also been suggested [5] that rubber compounding determines the effectiveness of chemical surface treatments.

Silica is generally added in the rubber compounding to provide improved mechanical properties and to decrease the production costs. The role of silica on rubber adhesion properties has not yet been stated. Therefore, the main objective of this study will be to determine the influence of the silica content of styrene-butadiene rubber formulations on their adhesion to polyurethane adhesives. The effectiveness of physical (roughening) and chemical (halogenation, fumaric acid) surface treatments to promote the adhesion of rubber will be the main discussion topics.

2. EXPERIMENTAL

Styrene-butadiene rubbers (SBR). Four synthetic sulphur-vulcanized SBR were used. The rubbers have the same formulation except for a different amount of a precipitated silica (15-47 parts in weight in respect to rubber). The nomenclature of SBR selected in this study corresponds to the capital letter **R** followed by the amount of silica in the SBR. Several physical properties of SBR were measured.

Surface treatments of SBR. Roughening was carried out to remove nearly 0.5 mm of the external surface of the rubber. Additionally, halogenation and a treatment with fumaric acid was applied to the rubber. Halogenation was carried out with 2-butanone solutions containing 2 wt% of trichloroisocyanuric acid (TCI); the time after halogenation was 18 hours and no postchlorination treatment was applied. 2 wt% fumaric acid (FA) solutions in 2-butanone: ethanol (1:1 wt%) were applied to the rubber surface; the treatment time was 18 hours. Surface-treated rubbers were characterized by IR spectroscopy, contact angle measurements (ethylene glycol, 25°C) and Scanning Electron Microscopy (SEM).

Adhesion of SBR was measured by means of T-peel tests among identically surface-treated rubbers. A solvent-based polyurethane adhesive (18 wt% of *Pearlstick 45-40/15* polyurethane - Merquinsa S.A., Barcelone - in 2-butanone), with a Brookfield viscosity of 2.6 Pa.s, was used to joint the rubber test pieces. The detailed experimental procedure used is given elsewhere [2].

3. RESULTS AND DISCUSSION

Characterization of SBR

Table 1 shows the experimental data obtained for the SBR, including the Shore °A hardness, density, abrasion resistance, tensile strength and elongation at break. Because silica is added to SBR to improve its mechanical properties, there is an increase of each of these physical properties

when the amount of silica in the rubber increases.

Roughening of SBR

Because all SBR selected in this study contain zinc stearate, there is a lack of adhesion in untreated rubbers (Figure 1). Roughening of SBR produces a noticeable increase of T-peel strength (Figure 1), which is more noticeable as the amount of silica in the rubber increases; adhesion values near 8 kN/m were obtained. The large increase in rubber adhesion produced by roughening can be ascribed to several factors.

IR spectra of unroughened and roughened R15 and R47 rubbers (Figure 2) shows the presence of zinc stearate (1540 cm^{-1}) in the untreated rubbers. IR spectrum of R47 (containing the highest amount of silica) shows a smaller intensity of C=C bands ($703, 760, 797, 910, 964\text{ cm}^{-1}$) than IR spectrum of R15. Roughening of rubber removes zinc stearate and reduces the intensity of CH_2 and CH_3 bands; the degree of effectiveness is higher in R47 rubber. Thus, roughening removes the weak boundary layer due to zinc stearate on the rubber surface.

Figure 3 shows the decrease of the contact angle in roughened rubber as the amount of silica in SBR increases. The highest T-peel strength corresponds to the smallest contact angle. Thus, the amount of silica in rubber facilitates its wettability.

Furthermore, SEM photographs (not shown here) provide evidence for the creation of roughness on the rubber surface, which should enhance the mechanical adhesion. Thus, an increase of mechanical and thermodynamical adhesion, as well as the removal of a weak boundary layer on the rubber surface due to zinc stearate, explain the improvement of adhesion in roughened SBR rubbers.

In order to explain the reasons for the increase of adhesion of SBR as the amount of silica increases, Figure 4 shows a linear relationship between the adhesion and the tensile strength at break of the rubbers. Because all T-

TABLE 1. Some properties of rubbers.

RUBBER	H (Shore °A)	D (g/cm ³)	AR (mm ³)	TS (MPa)	E (%)
R14	79	1.08	154	8.6	330
R22	80	1.11	164	10.6	431
R36	85	1.15	164	15.3	420
R47	91	1.19	168	17.5	480

H : Hardness

TS : Tensile strength at rupture

D : Density

E : Elongation at rupture

AR : Abrasion Resistance

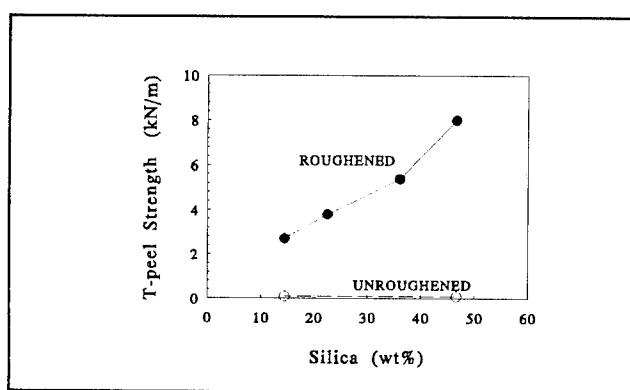


FIGURE 1. T-peel strength of SBR/polyurethane/SBR joints as a function of silica content of SBR.

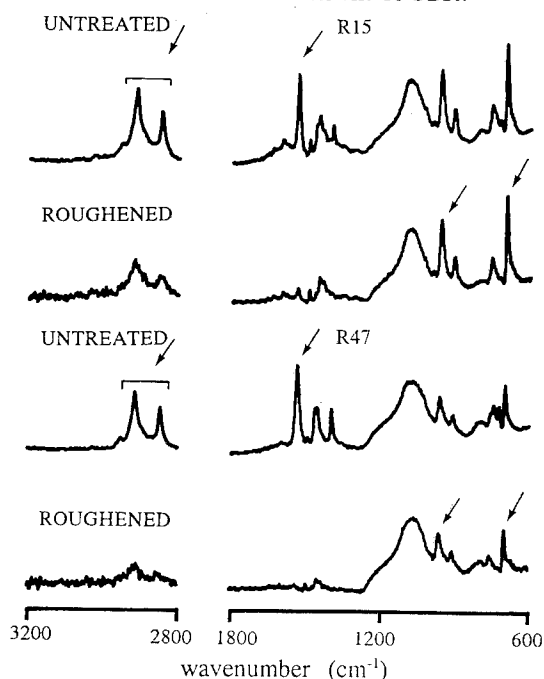


FIGURE 2. IR spectra of untreated and roughened R15 and R47 rubbers.

peel tests show adhesion failure, it can be expected that the improved adhesion of rubber should be related to the improved mechanical properties of SBR.

Chemical surface treatments of SBR

Figure 5 shows the increase of T-peel strength of SBR joints where a halogenation or treatment with FA is used. The adhesion increases as the amount of silica in roughened rubber increases. A rubber cohesive failure is found in R15, which gradually becomes adhesion failure as the amount of silica in the rubber increases.

According to Figure 6, the rubber surface treatments produce a decrease in the tensile strength at the break of the rubber, that decrease being more noticeable in the chlorinated rubber. However, the variation is not linear, perhaps indicating that the amount of silica in chemically treated rubber may influence the adhesion. In fact, although an adhesion failure in rubber R47 is obtained, a great increase in adhesion is produced.

Improved adhesion of SBR treated with TCI or FA has been widely proved elsewhere [4,5]. These chemical treatments produce roughness, improve wettability, create C-Cl and C=O species, and remove weak boundary layers on the rubber surface. Furthermore, silica content of rubber may enhance some of these effects.

No differences in wettability in R15 and R47 appear. IR spectra (Figure 7), however, show more noticeable effects due to the treatment with FA (C=O groups, reduction of intensity of CH₂ and CH₃ bands) and with TCI (C-Cl and C=O groups, reduction of intensity of CH₂ and CH₃ bands) in the rubber with the highest amount of silica (R47). On the other hand, the degree of surface modification obtained by halogenation of rubber is greater than by treatment with FA. Consequently, the adhesion should also be smaller in FA treated rubbers (Figure 5).

Although this study is still progressing, the experimental results corresponding to chemically surface treated SBR, seem to indicate that the

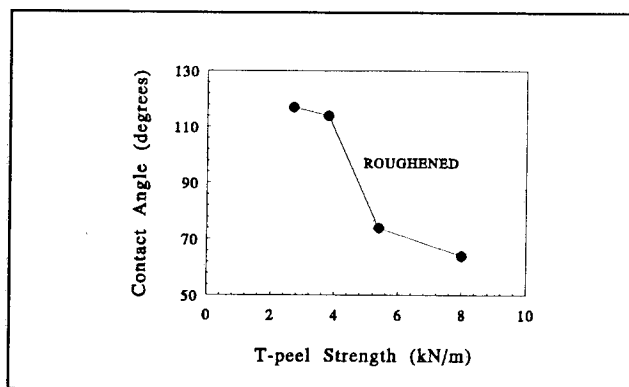


FIGURE 3. Contact angle (ethylene glycol, 25°C) of roughened SBR with different content of silica as a function of T-peel strength of SBR/polyurethane/SBR joints.

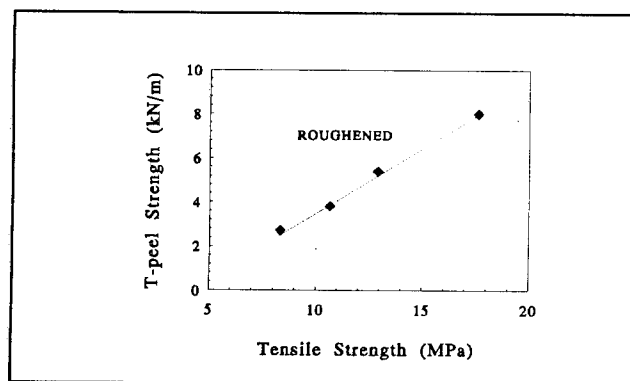


FIGURE 4. Relationship between T-peel strength of SBR/polyurethane/SBR joints and tensile strength at rupture of rubbers.

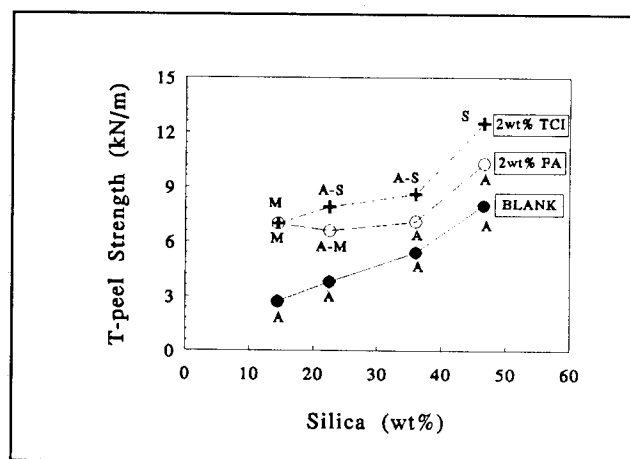


FIGURE 5. T-peel strength of surface treated rubbers as a function of their silica content.

role of the silica is to produce improved mechanical properties and, probably, to enhance the effects due to the treatment of rubbers containing greater amounts of silica.

4. CONCLUSIONS

1. The increase of silica content in SBR produced improved mechanical and adhesion properties.
2. Roughening of SBR increases its adhesion to polyurethane adhesives, this increase being more marked as the silica content increases. This improvement is probably related to the enhanced mechanical properties of rubber.
3. Chemical surface treatments of roughened rubbers greatly enhance their adhesion. Although chlorination is somewhat more effective than treatment with fumaric acid, there is an extra improvement of adhesion when the silica content of SBR is high. This improvement can probably be related to an enhancement of mechanical properties and to an influence of the silica content on the effectiveness of the surface treatment.

Acknowledgements. Financial support from CICYT (Projects. no. MAT92/0522 and MAT92/0067) is gratefully acknowledged. Authors thank CASTER (Elche, Spain) for providing the rubber samples.

REFERENCES

1. A.J. Kinloch. *Adhesion & Adhesives. Science and Technology*. Chapman, London (1990).
2. J.M. Martín-Martínez, J.C. Fernández-García, F. Huerta, A.C. Orgilés-Barceló. *Rubber Chem. Technol.* **64**, 510 (1991).
3. D. Oldfield, T.E.F. Symes. *J. Adhesion* **16**, 77 (1983).
4. M.M. Pastor-Blas, M.S. Sánchez-Adsuar, J.M. Martín-Martínez. *J. Adhesion Sci. Tech.* **9**, 1083 (1994).
5. N. Pastor-Sempere, J.C. Fernández-García, A.C. Orgilés-Barceló, R. Torregrosa-Maciá, J.M. Martín-Martínez. *J. Adhesion*, in press.

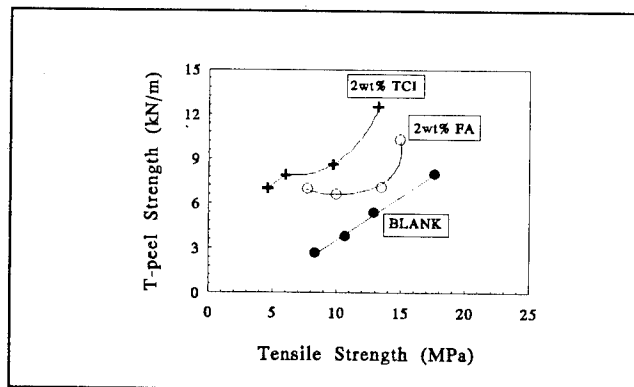


FIGURE 6. Relationship between T-peel strength of surface-treated SBR/polyurethane/surface-treated SBR joints and tensile strength at rupture of rubbers.

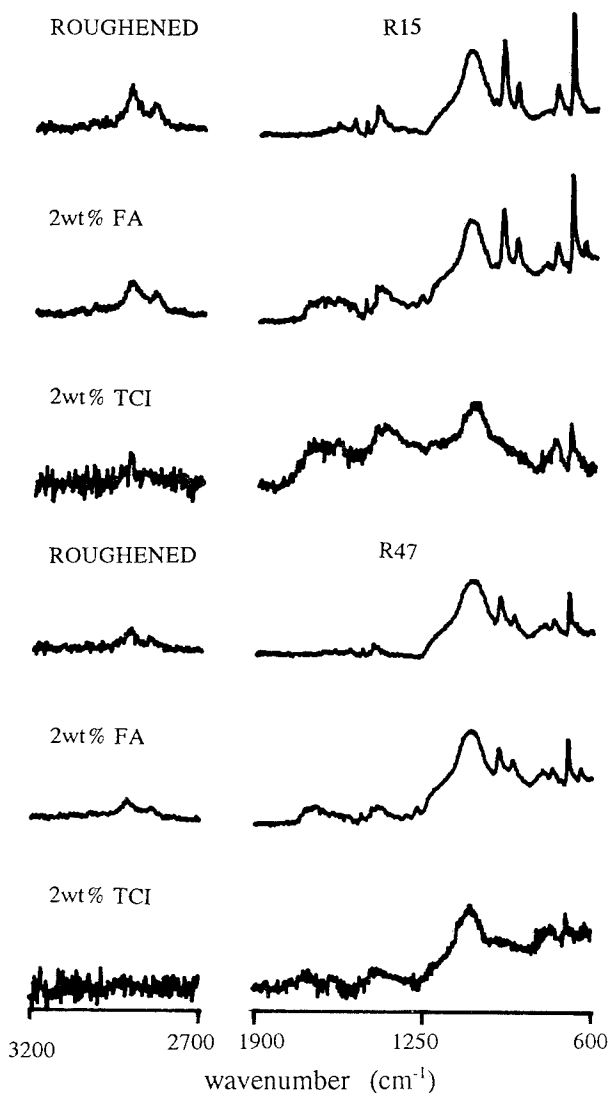


FIGURE 7. IR spectra of surface treated SBR.

DESIGN AND CHARACTERIZATION OF HIGH PERFORMANCE POLYIMIDE ADHESIVES

G. W. Meyer, J. L. Heidbrink, B. Tan, J. G. Franchina, R. M. Davis, S. Gardner, and J. E. McGrath
Virginia Polytechnic Institute and State University, Department of Chemistry,
Center for Adhesive and Sealant Science and NSF Science & Technology Center:
High Performance Polymeric Adhesives and Composites, Blacksburg, VA, 24061-0344

ABSTRACT

Soluble imide oligomers of controlled molecular weight were synthesized with phenylethynylphthalic anhydride (PEPA) and phenylmaleic anhydride (PMA) endcapping agents for use as high T_g, thermosetting adhesives. The phenylmaleic anhydride permitted a higher curing temperature (>400°C) which widens the processing window and moreover, it can be synthesized from relatively inexpensive starting materials. Commercially available monomers such as those employed in ULTEM® poly(ether imide) were investigated and it was demonstrated that both end cappers could be utilized to produce tough, ductile films that exhibited excellent solvent resistance and good adhesion to metal substrates.

INTRODUCTION

Polyimides endcapped with thermosetting groups are a major class of high performance network forming polymers. Perhaps the best known and most widely used of these systems are the ethynyl (acetylene) endcapped polyimides [1,2] such as Thermid 600 for use as high performance, high temperature curing adhesive and matrix applications. However, the major drawback in these systems is the occurrence of a curing exotherm that starts immediately after the glass transition of the polyimide has been reached. This does not allow adequate flow to occur prior to curing which can detract from proper wetting of the adherand. Our group and others have successfully addressed this problem by synthesizing polyimides endcapped with phenylethynyl groups which raises the cure temperature from ~220°C to >350°C [3]. These groups allow for a processing window which permits the fabrication of void-free specimens. We have now also explored the use of phenylsubstituted maleic anhydride as a high temperature endcapper as an alternative to the phenylethynyl based systems, to minimize cost. It was expected that the curing exotherm of the conventional maleimide sites would be increased from ~220°C to well over 300°C.

With the use of PMA as a high temperature curing endcap, polyimides may be utilized that exhibit T_g's in excess of 400°C after cure and still allow sufficient processing time before the system is fully cured. The reactive oligomers possess low melt viscosities and thermally cure without the evolution of volatile byproducts. This paper will address polyimides prepared from Bisphenol A dianhydride (BPA-DA) and 1,3-phenylene diamine (*m*-PDA) and from hexafluoroisopropylidene-2,2-bis (phthalic acid anhydride)

(6FDA) and 4,4'-oxydianiline (ODA) endcapped with 4-phenylethynylphthalic anhydride (PEPA) and phenylmaleic anhydride (PMA).

EXPERIMENTAL

Synthesis of 4-Phenylethynylphthalic Anhydride (PEPA)

Phenylethynylphthalic anhydride was synthesized by the procedure previously reported [3].

Synthesis of Phenylmaleic Anhydride

Phenylmaleic anhydride (PMA), 1, was synthesized in our laboratory by a modification of the procedures reported by Hill [4] and Paquette [5] by the reaction of phenylsuccinic with selenium dioxide using acetic anhydride as the solvent. The crude PMA was then sublimed under vacuum at ~100°C which afforded a light yellow solid. Overall yield was 92%.

Phenylethynylphthalic Anhydride-Terminated Polyimide Synthesis

Polyimides endcapped with PEPA were synthesized by a high temperature solution imidization route previously reported [3].

Phenylmaleic Anhydride-Terminated Polyimide Synthesis

Polymers endcapped with phenylmaleic anhydride were synthesized via two methods in order to study molecular weight control using PMA as the endcapping agent.

Amic Acid Chemical Imidization

The first method of polymerization was chemical imidization through the amic acid precursor of BPA-DA with *m*-PDA and PMA as the endcapping agent and *N*-methylpyrrolidinone (NMP) as the solvent. The polyamic acid was cyclodehydrated by the addition of acetic anhydride and triethylamine by reacting at 60°C for 18-24 hours. After which time the polymer isolated in methanol and dried under vacuum.

Variable Temperature Solution Imidization

The second method of polymerization was a two step method that involved forming an amine-terminated polyimide using the high temperature solution imidization ester-acid route and then endcapping the polyimide with PMA at a lower temperature. The polymer solution was lowered in temperature to 135°C from 180°C by lowering

the oil bath temperature from 180°C once imidization was complete and then the appropriate amount of PMA was added with NMP.

RESULTS AND DISCUSSION

PEPA-Terminated Polyimides

Poly(ether imides) of molecular weights ranging from 2,000 to 30,000 g/mole were successfully synthesized. In addition, copolyimides with *para* linkages displayed a semicrystalline nature as evidenced by the DSC melting endotherms, and TM values ranging from 291 to 321°C. Glass transition temperatures before curing increased with increasing molecular weight with values increasing from 192 to 218°C as shown in Table 1. Films of the imide oligomers were formed by melt pressing the polyimides between steel platens and were cured for 90 minutes at 380°C. After thermal crosslinking, the glass transition temperatures increased significantly up to a maximum of 233°C for 3,000 g/mole system and this molecular weight also displayed the largest increase in T_g after curing. The cured samples also exhibited excellent thermal stability in air as also shown in Table 1. All of the polyimide oligomers (even the 3000 g/mole system) formed tough, creasable films after curing. Soxhlet extractions were also performed on the cured samples where they were subjected to refluxing chloroform for 5 days. High (> 95%) gel fractions were obtained upon thermally curing the phenylethynylphthalic anhydride-terminated poly(ether imide) systems.

Table 1
Thermal Characterization of Phenylethynyl Terminated Polyimides

Target Mn	T _g before cure (°C)	T _g after cure (°C)	TGA 5% Wt. Loss(°C)
3,000	192	233	547
7,000	205	227	540
30,000	218	218	539

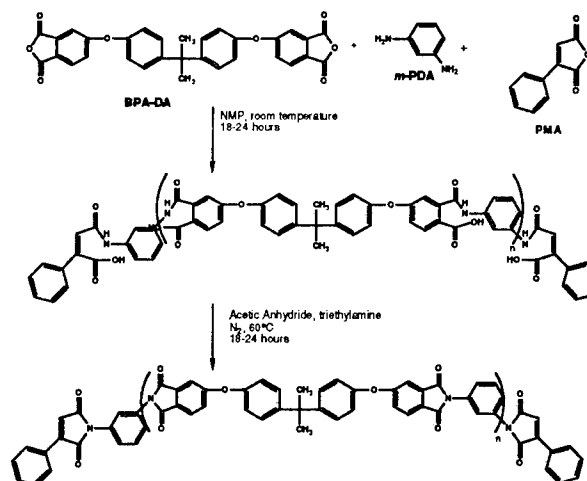
PMA-Terminated Polyimides

Phenylmaleic anhydride (PMA) was successfully synthesized in our laboratory refluxing phenylsuccinic acid in acetic anhydride in the presence of selenium dioxide for 9 hours [4,5]. The crude product can be easily sublimed under vacuum to yield pure PMA in yields of 92% or higher. PMA can also be prepared industrially from biphenyl as reported by Shier [6].

The phenylmaleic anhydride terminated polyimide matrix resins based on 6FDA and ODA and BPA-DA and *m*-PDA have been synthesized using two routes which were targeted to a number average molecular weight of 2,000 to 15,000 g/mole.

The first route employed in the synthesis of PMA endcapped polyimides involved chemical imidization

techniques. Scheme 2 illustrates the general synthetic scheme for phenylmaleic anhydride terminated polyimides.



Scheme 2. Synthesis of Phenylmaleic Anhydride-Terminated Polyimides

Molecular weight control was achieved utilizing phenylmaleic anhydride as a endcapping agent and chemical imidization techniques. This route afforded an intrinsic viscosity value of 0.18 dL/g that corresponded very well with 3,000 g/mole 6FDA/ODA polyimide systems and values of 0.18 to 0.34 dL/g for the BPA-DA/*m*-PDA systems that ranged from 2,000 to 15,000 g/mole for the theoretical number average molecular weight. Glass transition temperatures for the 6FDA/ODA system increased from 245°C before curing to 290°C after curing at 350°C for 45 minutes which is consistent with the T_g of the high molecular weight linear systems. A curing study was performed at various temperatures and times in a convection oven. After curing for 30 minutes at 310°C in a nitrogen atmosphere, the system was completely soluble in chloroform. After 30 minutes at 350°C the system was mostly crosslinked or insoluble, but still had a soluble portion as seen by the coloration of chloroform indicating a sol portion. However when cured at 350°C for 45 minutes, the system was completely insoluble. The 5% weight loss was seen at 526°C before curing, indicating thermal stability, and at 558°C after cure. The thermal stability of the 3,000 g/mole oligomer synthesized by chemical imidization was subjected to an isothermal TGA scan at 350°C for 6 hours. Only 0.36% weight was lost, indicating no volatiles were released during the curing process.

The second route employed to synthesize PMA terminated polyimides was a two step route where an amine-terminated polyimide was first formed and then subsequently functionalized with PMA. The amine-terminated oligomer was formed in NMP/*o*-DCB at ~180°C and then reaction temperature was lowered to 135°C and the PMA was added and allowed to react for 6 hours. Again, the intrinsic viscosity value of 0.18 dL/g

confirms that molecular weight was achieved. In addition, proton NMR confirmed the presence of the protons of the amine endgroups in the first step and the disappearance of amino protons after PMA functionalization.

The melt flow properties of these systems was also examined by parallel plate rheology studies. The polymer was held isothermally at 350°C and exhibited a melt viscosity below 5 PaS for approximately 30 minutes at which point the viscosity began to increase indicating curing (Figure 2). A dynamic scan from 225°C to 470°C also showed that after the T_g, the viscosity dropped to below 10 PaS and at approximately 440°C, the viscosity began to increase indicating curing (Figure 3). These measurements indicate a wide curing window of ~200°C.

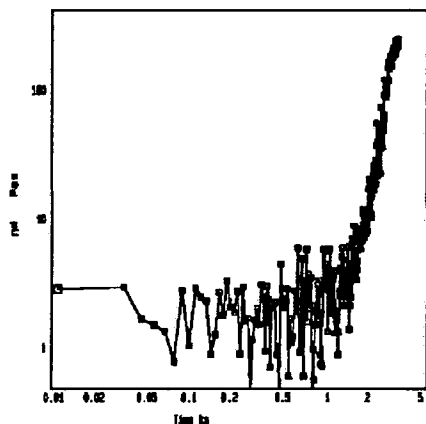


Figure 2. Isothermal melt viscosity of 3,000 g/mole PMA terminated polyimide held at 350°C under nitrogen.

CONCLUSIONS

Polyimide controlled molecular weight oligomers endcapped with phenylethynylphthalic anhydride or phenylmaleic anhydride can be synthesized. Upon curing, insoluble, crosslinked

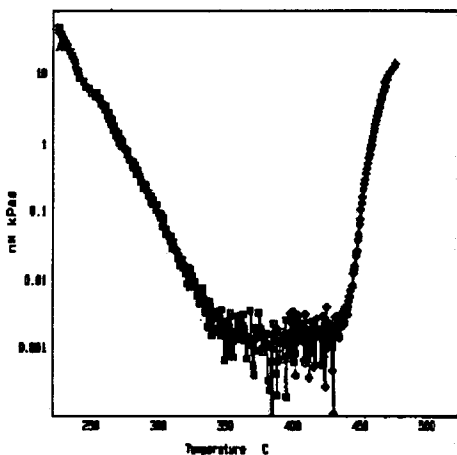


Figure 3. Influence of temperature on melt viscosity of 3,000 g/mole PMA endcapped polyimide.

films with the anticipated T_g values were obtained that exhibit good thermooxidative stability, and high gel contents. Oligomers capped with PMA are easily processable and have a wide curing window of ~200°C, indicating that phenylmaleic anhydride appears to be a viable alternative for phenylethynyl systems and a possible efficient alternative for many polyimide adhesive systems.

CURRENT AND FUTURE STUDIES

Efforts are currently directed at the manufacture of specimens made from the BPA-DA/*m*-PDA PMA capped polyimide systems for mechanical and adhesion testing to compare with phenyl-ethynyl capped systems. In addition studies aimed at following the cure cycle using solid state Magic-Angle ¹³C Nuclear Magnetic Resonance are ongoing.

ACKNOWLEDGMENTS

The authors would like to gratefully acknowledge the National Science Foundation and Technology Center for partial support under contract DMR-912004. In addition, a fellowship from the Adhesive and Sealant Council and generous support from the Gencorp Foundation is greatly appreciated.

REFERENCES

1. S. Alam, L. D. Kandpal, I. K. Varma, *J. M. S.-Rev. Macromol. Chem. Phys.*, C33 (3), 291-320, 1993.
2. P. M. Hergenrother, Acetylene Terminated Prepolymers, *Encyl. Poly. Sci. and Eng.*, Volume 1, 61-86, 1985.
3. G. W. Meyer, T. E. Glass, H. J. Grubbs and J. E. McGrath, *Polym. Prepr.*, 35 (1), 549, 1994; *J. Poly. Sci.* (accepted), 1994.
4. L. A. Paquette, J. M. Gardlik, K. J. McCullough, R. Samodral, G. DeLucca and R. J. Ouellete, *J. Am. Chem. Soc.*, 105 (26), 7649, 1983.
5. R. K. Hill, *J. Org. Chem.*, 26, 4745, 1961.
6. G. D. Shier, U. S. Patent 3,919,259 (to Dow Chemical) 1975.

THE FRACTURE EFFICIENCY OF TESTS FOR ADHESIVE BONDS

Yeh-Hung Lai and D. A. Dillard

*Engineering Science and Mechanics Department, Virginia Polytechnic Institute and State University
Blacksburg, VA 24061-0219*

INTRODUCTION

Over the years, a large number of fracture tests for measuring the fracture properties of adhesive bonds have been developed [1]. Most of the analysis methods reported for the current fracture tests are based on the assumption that the adherends are loaded within the elastic range. These analyses become invalid when yielding occurs in the adherend and the error of using these elastic analyses depends on the extent of yielding. Only a small fraction of the literature for adhesive fracture tests has addressed the analyses of fracture specimens with a large extent of yielding. Although it is possible to determine the fracture properties using elastic-plastic analyses when the adherend yields during the debonding process, it may be preferable to design a test that allows the specimen to be debonded without yielding, thus permitting the use of elastic analyses. Since fracture along the bondline and yielding/rupturing in the adherends are subject to different criteria, to determine a proper specimen design that can avoid excessive yielding or rupture, requires the knowledge of the relationship between the quantities associated with these two different criteria in the same specimen. Recently, Lai and Dillard [2] proposed a simple quantity called the fracture efficiency parameter to study this relationship and reported the comparison between the standard and island blister tests.

In this paper, the concept of "fracture efficiency" will be extended to other test geometries. Since yielding/rupturing is probably one of the greatest obstacles in the coating adhesion measurement, the fracture efficiency of coating will also be studied in detail. It is believed that similar methodology can be applied to other test categories such as the laminated beam specimen.

FRACTURE EFFICIENCY PARAMETER

The fracture efficiency parameter, defined as

$$T_e = G/\sigma_{\max}^2 \quad (1)$$

represents how much energy release rate, G , a certain specimen design can produce along the bondline for a given maximum non-singular stress σ_{\max} in the adherends. A test specimen design with a high fracture efficiency is more likely to cause debonding without yielding/rupturing. Alternately, yielding/rupturing is more likely to occur if the fracture efficiency is low, and therefore, the measured bond fracture strength may be in error if yielding is not properly accounted for. By comparing the fracture efficiency parameter, one can determine an appropriate specimen design to reduce the likelihood of yielding/rupturing.

THE MOST GENERAL COATING DELAMINATION TEST

In this section, a general coating delamination specimen as shown in Fig. 1 is considered. In this problem, a coating is adhering to a substrate with a bending rigidity much larger than the coating and is subjected to a combined loading of axial force and bending moment. The energy release rate for the plane strain case based on Ref. 3 is given by:

$$G = \left[(P - \sigma_0 h)^2 + 12M^2 / h^2 \right] (1 - \nu^2) / (2Eh), \quad (2)$$

where P and M are the axial force and bending moment, respectively, per unit width in the coating at the debonded side, σ_0 is the prestress in the coating, E and ν are the Young's modulus and Poisson's ratio, respectively, of the coating. The fracture efficiency parameter for this general coating delamination specimen is given by

$$T_e = \min \left\{ g / \left(\left| \frac{6M}{Ph} \right| + 1 \right)^2, g / \left(\frac{\sigma_0 h}{P} \right)^2 \right\}, \quad (3-1)$$

$$\text{where } g = \frac{h}{E(1-\nu^2)} \left[\left(1 - \frac{\sigma_0 h}{P} \right)^2 + 12 \left(\frac{6M}{Ph} \right)^2 \right]. \quad (3-2)$$

From Eq. (3), the fracture efficiency parameter is a function of three parameters, the nondimensional bending moment M/Ph , the nondimensional prestress $\sigma_0 h/P$, and the thickness to modulus ratio $h(1-\nu^2)/E$.

Figure 2 and 3 illustrates the nondimensional fracture efficiency parameter, $Te(E/h)/(1-\nu^2)$, versus nondimensional bending moment for the most general coating delamination problem with positive and negative nondimensional prestresses, respectively. The discussions of Fig. 2 will be further subdivided into the cases with a nondimensional prestress of 0 to 1 and 1 to ∞ . The results in these figures cover all possible results for coating delamination test geometries, such as peel tests, blister tests, indentation tests, etc.

In Fig. 2, the cases with a nondimensional prestress of 0 to 1 have a nondimensional fracture efficiency parameter between 0 and 0.5. This category includes all existing peel and blister tests with a coating prestress in tension and is probably the most commonly encountered configuration. The case with a nondimensional prestress of 1 corresponds to the specimen with such a high prestress that the stress induced by the external load is negligible compared to the prestress at the debonded side. In this family of curves, the maximum nondimensional fracture efficiency parameter of 0.5 is found at the zero prestress and the zero bending moment. The minimum fracture efficiency parameter of 0 is found at the zero bending moment and the normalized prestress of 1. All curves converge to a nondimensional fracture efficiency parameter of 0.167 at very large nondimensional bending moments.

In Fig. 2, the nondimensional fracture efficiency parameter of several typical blister and peel tests are also marked, which include the peel tests of 0° , 90° , and 180° peel angles and the standard blister[4], island blister[5], and pull-off [6] tests. In these tests except for the 90° peel test, the

nondimensional fracture efficiency parameter decreases as the prestress increases. The results in Fig. 2 suggest that when the prestress is very small, the peel tests with very small angles may be preferable because of the relatively high fracture efficiency parameter. However, when the prestress is relatively large, the 90° peel test may be preferable.

The other family of curves shown in Fig. 3 is the one with a nondimensional prestress from 1 to ∞ . In this category, two peaks are observed, which correspond to the shift of location of maximum stress from the debonded side to the bonded side and then back to the debonded side of the coating. The nondimensional fracture efficiency parameter in this nondimensional prestress range also varies between 0 and 0.5. This nondimensional prestress range represents cases where the membrane stress in the debonded side has the same sign but smaller magnitude compared with the prestress. A typical example of this case is the buckle-driven delamination of thin films [3]. For cases with a infinite nondimensional prestress, the nondimensional fracture efficiency parameter is 0.5, which corresponds to prestress induced self delamination problem [7].

Figure 3 illustrates the nondimensional fracture efficiency parameter for cases with a nondimensional prestress of $-\infty$ to 0. This nondimensional prestress range represents that the axial stress at the debonded side has an opposite sign as the prestress. The tests with this nondimensional prestress range may include the peel/blister specimen with compressive coating prestresses or indentation specimens with tensile coating prestress. One peak is seen for curves with a nondimensional prestress of 0 to -1. The peak value increases from 0.5 to 2 as the nondimensional prestress decreases from 0 to -1. Two peaks are seen for curves with a nondimensional prestress of -1 to $-\infty$. The peak value decreases from 2 to 0.5 as the nondimensional prestress decreases from -1 to $-\infty$. At a very large nondimensional bending moment, the nondimensional fracture efficiency parameter also converges to 0.167.

From Figs. 2 and 3, it is found that the nondimensional fracture efficiency parameter of 2 is the theoretical limit of all possible coating

delamination specimens. Although this theoretical limit may be achieved with the combination of a nondimensional prestress of -1 and a nondimensional bending moment of 0 , this combination may merely be a coincidence since if one does not obtain debonding at this prestress and loading combination, one has to increase the load which would then cause the fracture efficiency to decrease.

SUMMARY AND CONCLUSIONS

The fracture efficiency of the most general coating delamination specimen is investigated in this paper. A theoretical limit of fracture efficiency is found for a given coating thickness. The results suggest that unless the coating thickness can be increased significantly, yielding or rupture in the coating may not be avoided no matter which test configurations is used. Therefore, experimental or analytical techniques considering the inelastic energy dissipation may be needed.

ACKNOWLEDGMENTS

The authors would like to acknowledge the financial support of the National Science Foundation's Science and Technology Center on High Performance Polymeric Adhesives and Composites at Virginia Tech (Contract DMR 9120004), the Center for Adhesive and Sealant Science at Virginia Tech, and the ALCOA Foundation.

REFERENCES

1. H. F. Brinson, *Adhesives and Sealants, Engineered Materials Handbook*, Vol. 3, ASM International, (1990).
2. Y. H. Lai and D. A. Dillard, *J. Adhesion Sci. Technol.*, **8**, 663 (1994).
3. J. W. Hutchinson and Z. Suo, *Adv. Appl. Mech.*, **29**, 63 (1992).
4. A.N. Gent and L. H. Lewandowski, *J. Appl. Polym. Science*, **33**, 1567 (1987).
5. M. G. Allen and S. D. Senturia, *J. Adhesion*, **25**, 303 (1988).
6. A.N. Gent and S.Y. Kaang, *J. Appl. Polym. Science*, **32**, 4689 (1986).
7. R. J. Farris and C. L. Bauer, *J. Adhesion*, **26**, 293 (1988).

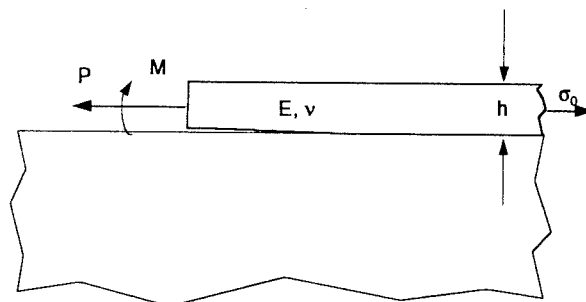


Figure 1. General coating delamination specimen.

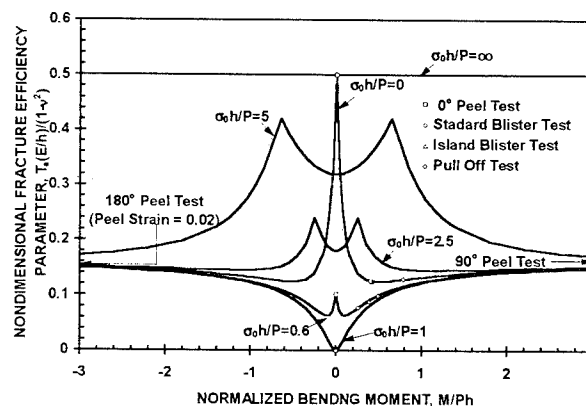


Figure 2. Nondimensional fracture efficiency parameter versus nondimensional bending moment with positive nondimensional prestresses in a general coating delamination configuration.

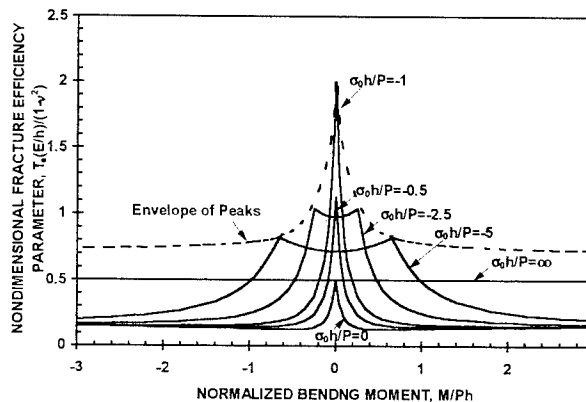


Figure 3. Nondimensional fracture efficiency parameter versus nondimensional bending moment with negative nondimensional prestresses in a general coating delamination configuration.

SURFACE-MODIFICATION OF STYRENE-BUTADIENE COPOLYMERS AND THEIR ADHESION TO COPPER AND GOLD

P. D. Mumbauer and G. S. Ferguson*

Department of Chemistry, Lehigh University, Bethlehem, PA 18015

INTRODUCTION

Chemical interactions at interfaces of interest for adhesion depend strongly on the type of functional groups present [1]. We have investigated the adhesion to metals of unmodified and surface-modified, linear and branched copolymers of styrene and butadiene (styrene-butadiene rubber, SBR). Strong chemisorption between organosulfur compounds and the coinage metals has been used successfully in the past for the formation of self-assembled monolayers [2], as well as for controlling adhesion [3,4] and adsorption of polymers from solution [5]. By analogy to this work, we have investigated the influence of thioacetate and thiol (or disulfide) groups upon the adhesion of SBR polymers to gold and to copper [4,6]. The results reported here extend previous work in our laboratories involving the adhesion of syndiotactic 1,2-polybutadiene (PBD) to the same metals [4].

MATERIALS

The polymers used in these studies were: a linear, styrene-butadiene-styrene triblock copolymer (^lSBR) with a styrene/butadiene ratio of 28/72 (wt %); and a branched copolymer (^bSBR) with a styrene/butadiene ratio of 21/79 (wt %) [7]. Photochemical addition of thioacetic acid to the butenyl groups at the surface of the SBR copolymers was achieved using ultraviolet light in the presence of an initiator [4,8] and provided thioacetate groups in the interfacial region (SBR-SCOCH₃) (Scheme 1). Attenuated total reflectance-infrared spectroscopy confirmed the presence of these groups, whose carbonyl stretching band

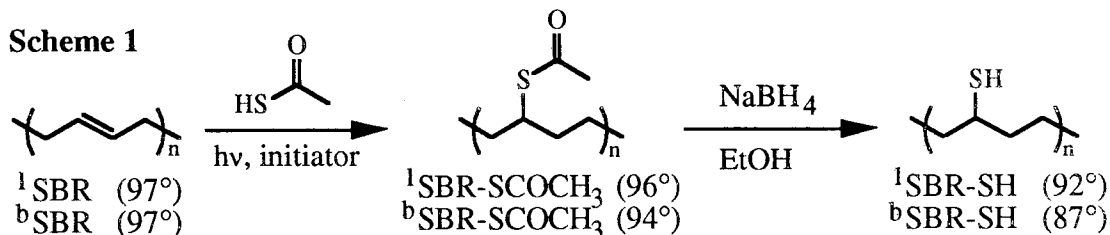
appeared at 1692 cm⁻¹. Treatment of SBR-SCOCH₃ with sodium borohydride in ethanol converted the groups to thiols (SBR-SH), and as a result, the carbonyl band diminished to ~10 % of its original intensity (Scheme 1). Our previous work with a similar polymer surface (PBD-SH) indicated that such surfaces are susceptible to oxidation by atmospheric oxygen to give disulfides and/or sulfonates [4].

The advancing contact angles of water on surfaces of SBR, SBR-SCOCH₃, and SBR-SH are shown in parenthesis in Scheme 1. The advancing contact angles of water on the thioacetate surfaces were essentially the same as those on the unmodified polymers, and conversion of the thioacetate to thiol groups caused only a small decrease. These similarities may reflect either rapid reconstruction of the surfaces of the functionalized polymers to lower their interfacial free energy [9], or a significant concentration of polystyrene (unreactive in the derivatization reactions) at the surface of these polymers.

ADHESION EXPERIMENTS

A tape-peel test gave qualitative information about the adhesion of evaporated films of copper (40 nm) or gold (30-70 nm) to ^lSBR and ^bSBR and their surface-modified derivatives. The samples having interfaces of metal against the unfunctionalized polymers visually appeared to fail at the polymer/metal interface. Those involving the surface-modified polymers, in contrast, visually appeared to fail at the tape/metal interface, indicating strong adhesion at the metal/polymer interface.

Quantitative adhesion measurements



were performed for ^bSBR and its derivatives against copper foil. In these experiments, we measured the maximum yield strength of adhesion (180° peel, 10 mm/min) for samples heated at 70 °C under a pressure of 13 ± 2 kPa for 12 h (Figure 1). Since these tests involved viscoelastic dissipation of energy within the polymer, the measured values are useful only for qualitative comparisons between these samples. For the ^bSBR-SCOCH₃/copper system, failure occurred cohesively within the polymer for all samples. For ^bSBR/copper and ^bSBR-SH/copper, adhesive failure at the polymer/copper interface visually appeared to dominate. One sample of ^bSBR-SH/copper displayed a small area of cohesive failure, possibly due to incomplete conversion of thioacetate to thiol groups for this sample.

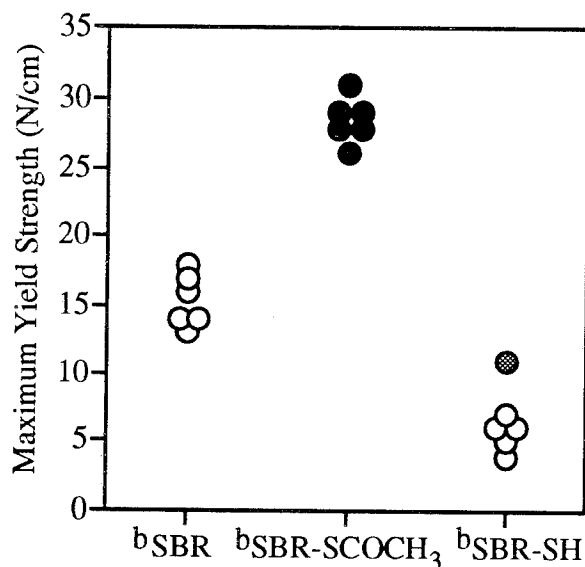


Figure 1. Maximum adhesion yield strengths measured in 180° peel tests for surfaces of unmodified branched SBR and its thioacetate- and thiol-derivatives that had been pressed and heated against copper at 70 °C for 12 h. The symbols represent cohesive failure (●), adhesive failure (○), and mixed-locus failure (◐) as determined by visual inspection.

The ^bSBR-SCOCH₃/copper interface developed approximately twice the yield strength of the unmodified ^bSBR/copper interface. Since the ^bSBR-SCOCH₃/copper system failed cohesively within the polymer, the measured yield strength gives only a lower limit for the adhesive strength of this interface. The low adhesion of copper to ^bSBR-SH, relative to ^bSBR-SCOCH₃ and the unmodified

polymer, was interesting given the prior literature in the area of self-assembled monolayers [2]. Neither of these results, however, were surprising because we found similar behavior in the adhesion of PBD-SCOCH₃ and PBD-SH to copper and provided evidence for its chemical basis [4].

CONCLUSIONS

Tape-peel tests showed that the presence of thioacetate or thiol groups in the interfacial region of SBR copolymers enhanced their adhesion to evaporated films of gold and copper. In quantitative peel tests of ^bSBR against copper foil, the presence of thioacetate groups increased adhesion at this interface, relative to that for unmodified ^bSBR/copper. In this case, failure was cohesive within the polymer. Although alkanethiols form self-assembled monolayers on copper, the adhesion of copper foil to ^bSBR-SH was weaker than for the unfunctionalized ^bSBR itself. The behavior of these surfaces mirrored previous studies in our laboratories with 1,2-polybutadiene [4].

ACKNOWLEDGEMENTS

Acknowledgement is made to the donors of The Petroleum Research Fund, administered by the American Chemical Society, for partial support of this research. Additional funding for this research was provided through the Department of Chemistry and the Polymer Interfaces Center at Lehigh University, and the Semiconductor Research Corporation. PDM acknowledges the International Society for Hybrid Microelectronics for an ISHM Educational Foundation Grant. We acknowledge Shell Chemical Company for the gift of the copolymers used in these studies.

REFERENCES

1. *Adhesion Aspects of Polymeric Coatings*; K. L. Mittal, Ed. (Plenum, New York, 1983). R. J. Good, *J. Adhesion Sci. Technol.*, **6**, 1269 (1992). A. J. Kinloch, *J. Mater. Sci.*, **15**, 2141 (1980). A. J. Kinloch, *J. Mater. Sci.*, **17**, 617 (1982). S. Wu, *Polymer Interface and Adhesion*;

- (Dekker, New York, 1982). J. J. Bikerman, *The Science of Adhesive Joints*; 2nd ed. (Academic, New York, 1968).
2. A. Ulman, *An Introduction to Ultrathin Organic Films: from Langmuir-Blodgett to Self-Assembly*; (Academic, Boston, 1991). R. G. Nuzzo, L. H. Dubois, and D. L. Allara, *J. Am. Chem. Soc.*, **112**, 558 (1990). G. M. Whitesides and P. E. Laibinis, *Langmuir*, **6**, 87 (1990). P. E. Laibinis, G. M. Whitesides, D. L. Allara, Y.-T. Tao, A. N. Parikh, and R. G. Nuzzo, *J. Am. Chem. Soc.*, **113**, 7152 (1991). P. E. Laibinis and G. M. Whitesides, *J. Am. Chem. Soc.*, **114**, 9022 (1992). P. E. Laibinis and G. M. Whitesides *J. Am. Chem. Soc.*, **114**, 1990 (1992). Y. Yamamoto, H. Nishihara, and K. Aramaki, *J. Electrochem. Soc.*, **140**, 436 (1993).
 3. D. L. Allara, A. F. Hebard, F. J. Padden, R. G. Nuzzo, and D. R. Falcone, *J. Vac. Sci. Technol. A*, **1**, 376 (1983). S. R. Wasserman, H. Biebuyck, and G. M. Whitesides, *J. Mater. Res.*, **4**, 886 (1989). G. S. Ferguson, M. K. Chaudhury, G. B. Sigal, and G. M. Whitesides, *Science*, **253**, 776 (1991). C. A. Goss, D. H. Charych, and M. Majda, *Anal. Chem.*, **63**, 85 (1991).
 4. P. D. Mumbauer, D. H. Carey, and G. S. Ferguson, submitted for publication.
 5. J. M. Stouffer and T. J. McCarthy, *Macromolecules*, **21**, 1204 (1988). T. J. Lenk, V. M. Hallmark, J. F. Rabolt, L. Häussling, and H. Ringsdorf, *Macromolecules*, **26**, 1230 (1993). F. Sun, D. W. Grainger, D. G. Castner, and D. K. Leach-Scampavia, *Macromolecules*, **27**, 3053 (1994). F. Sun, D. W. Grainger, and D. G. Castner, *J. Vac. Sci. Technol. A*, **12**, 2499 (1994).
 6. For other approaches to controlling polymer/metal adhesion, see: P. S. Ho, P. O. Hahn, J. W. Bartha, F. K. Rubloff, and F. K. Legoues *J. Vac. Sci. Technol. A* **3**, 739 (1985). J. J. Ball, H. W. Gibbs, and P. E. R. Tate *J. Adhesion* **32**, 29 (1990). J. M. Park and J. P. Bell in *Adhesion Aspects of Polymeric Coatings*, K. L. Mittal, Ed.; (Plenum, New York, 1983), p. 205. A. Mochizuki, T. Teranishi, and M. Ueda *Polymer* **35**, 4022 (1994). K. W. Paik, H. S. Cole, R. J. Saia, and J. J. Chera *J. Adhesion Sci. Technol.* **7**, 403 (1993). H. Schonhorn, R. F. Roberts, and N. D. Hobbins, *J. Adhesion* **36**, 151 (1991). A. B. Silberman, V. E. Archireev, and V. L. Vakula, *J. Adhesion* **34**, 241 (1991). P. S. Ho and F. Faupel, *Appl. Phys. Lett.* **53**, 1602 (1988). R. C. White, R. Haight, B. D. Silverman, and P. S. Ho, *Appl. Phys. Lett.* **51**, 481 (1987). Y. S. Chang, C. Y. Lin, S. M. Ma, J. F. Chang, C. H. Chen, and F. H. Huang, *Mater. Chem. Phys.* **27**, 251 (1991). C. W. Miller and P. C. Laberge, *J. Vac. Sci. Technol. A* **7**, 1818 (1989). A. J. Kinloch and M. L. Yuen, *J. Mater. Sci.* **24**, 2183 (1989). H. Ishida and K. Kelley, *J. Adhesion* **36**, 177 (1991). A. J. Kinloch and M. L. Yuen, *J. Adhesion* **30**, 151 (1989). B. J. Love and P. F. Packman, *J. Adhesion* **40**, 139 (1993). W. J. Van Ooij and A. Kleinhesselink *Appl. Surf. Sci.* **4**, 324 (1980).
 7. The copolymers (^lSBR and ^bSBR) were Kraton® D Rubbers (D-1102 and D-1116), donated by Shell Chemical Company.
 8. D. H. Carey and G. S. Ferguson, *Macromolecules*, **27**, 7254 (1994).
 9. For reviews, see G. S. Ferguson and G. M. Whitesides, in *Modern Approaches to Wettability*; M. E. Schrader, and G. I. Loeb, Eds.; (Plenum, New York, 1992), Chapter 6. *Polymer Surface Dynamics*; J. D. Andrade, Ed.; (Plenum, New York, 1988).

A THERMOPLASTIC POLYETHERIMIDE ADHESIVE

Terry L. St. Clair, Donald J. Progar, Alice Chang*
NASA Langley Research Center
Hampton, VA 23681-0001

INTRODUCTION

LARCTM-IA (Langley Research Center - Improved Adhesive) is a cost-effective linear, aromatic, thermoplastic polyimide that was developed in the late 1980's initially as a high temperature adhesive. Other end use forms of LARCTM-IA, later developed, include molding powder, composite matrix resin, melt extruded films, and melt extruded shaped forms. [1-4]

Because of the unusual meta- and para-bond linkages in the diamine [3,4'-oxydianiline (3,4'-ODA)] from which it is prepared, LARCTM-IA exhibits an intrinsic molecular weight control which makes it highly processable via hot-melt techniques. To date, no other fully aromatic linear polyimide exhibits the level of melt flow at such a low temperature (300 - 350°C) as does LARCTM-IA. Adhesive properties are similar no matter whether the material is used as a solvent-based adhesive to form scrim cloth or the impregnation is accomplished via a hot-melt technique.

EXPERIMENTAL

Polymer Synthesis

The various versions of LARCTM-IA were prepared as previously reported [1] in solvents such as diglyme and N-methylpyrrolidone with stoichiometric offsets in favor of the diamine to control molecular weight. Excess amine groups were always endcapped with phthalic anhydride. Powders were prepared from the polymers at Imitec, Inc. (Schenectady, NY) via a proprietary process. Films of the polymer were prepared by one of two methods. In the first case, the powder was placed in matched-metal-die mold and was heated to a temperature in the

300-350°C under low pressure (~0.1 MPa) to affect consolidation. In the second case, the LARCTM-IA powder was converted into film using a single-screw extruder (Brabender, Plasti-Corder).

Characterization

Inherent viscosities were measured at 25°C on 0.5% solutions of the poly(amide-acid) in N-methylpyrrolidone (NMP) or N,N-dimethylacetamide (DMAc). The glass transition temperatures (T_g) were determined on a Shimadzu DSC-50 calorimeter at a heating rate of 20°C/min. The T_g was taken at the inflection point in the heat flow versus temperature curve.

Adhesive Scrim Cloth Preparation

The adhesives were converted into scrim by one of three methods. First, solutions of the poly(amide-acid)s were brush coated onto 112 E-glass (A-110 Finish) and allowed to air dry in a chemical fume hood after each of several applications. After each coat, the cloths were heated in a forced-air oven to 225°C to eliminate most of the solvent and to convert the poly(amide-acid) to the polyimide. This procedure was repeated several times in order to build up a scrim cloth thickness of 0.02 - 0.03 cm.

The second preparation involved first coating the 112 E-glass (A-1100 finish) with some poly(amide-acid) solution of the LARCTM-IA to serve as a primer. After drying and heating the cloth to 225°C, LARCTM-IA polyimide powder was placed in a matched-metal-die mold (7.62 cm x 15.24 cm); the primed glass cloth was placed on top of the powder and an equal amount of LARCTM-IA powder was placed on top of the cloth. The mold was then assembled and placed in a hydraulic press and heated to 350°C and held at that temperature under ~2 MPa for one hour. After cooling to ambient temperature the scrim cloth was removed. In the third case, the primed glass cloth was

*On-site contract employee of Lockheed Engineering and Sciences Company

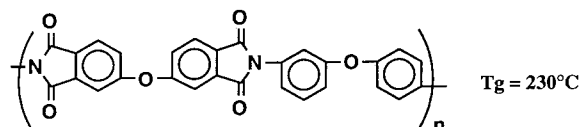
placed between two pieces of LARCTM-IA film that had been prepared via melt extrusion. The film was 0.012-0.015 cm in thickness. This assembly was placed in the matched-metal-die mold and heated to 350°C under ~2MPa and held for one hour. Again, after cooling to ambient, the scrim cloth was removed.

Adhesive Bonding

Titanium (Ti-6Al-4V) panels were lightly grit blasted and treated with Pasa-Jell 107TM to form a stable oxide surface. The surfaces to be bonded were always primed with a solution of the poly(amide-acid) solution. The titanium panels (4-fingered configuration) were bonded together in a hydraulic press equipped with heated platens at temperatures in the 340-375°C range under pressures of 0.1 to 2.1 MPa. Bonded samples were tested at room temperature, 177°C or 204°C according to ASTM-1002.

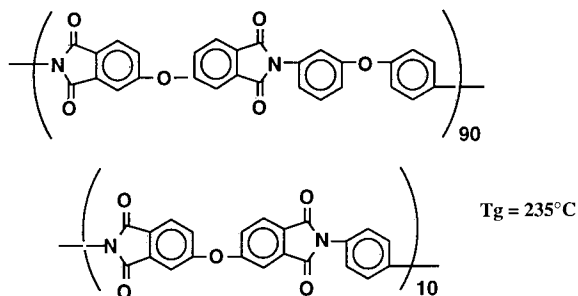
Results and Discussion

The chemical structure of LARCTM-IA is shown in Figure 1.



LARCTM-IA
Figure 1

This polyetherimide has been previously reported to exhibit excellent melt-flow properties [2]. By controlling its molecular weight, melt-flow properties can be controlled. As expected, higher molecular weight versions exhibit much less flow than lower molecular weight versions. The comparison in Figure 2 is of three different molecular weights and three different forms of LARCTM-IA. The LARCTM-IAX is a slightly modified version of LARCTM-IA where 10 mole percent of the 3,4'-oxydianiline monomer has been replaced with p-phenylenediamine. Its chemical structure is illustrated in Figure 3. When the bonded adherends from Figure 2 were thermally aged at 204°C, their performance is shown in Figure 4. These adhesives performed



LARCTM-IAX
Figure 3

exceptionally well up to the 5000 hours of exposure that had been logged at the time of this article. The performance of one version of the LARCTM-IA-bonded specimens after exposure to various solvents is illustrated in Figure 5.

SUMMARY

The novel polyimide, LARCTM-IA, is a thermoplastic polyetherimide with Tg of 230°C which exhibits a high degree of melt flow in the temperature range of 340-375°C. Several versions of this polymer have been evaluated as adhesives and they have all performed very well when exposed to elevated temperatures and to harsh solvents.

REFERENCES

1. D. J. Progar and T. L. St. Clair, *J. Adhesion Sci. Technol.*, Vol. 4, No. 7, pp. 527-549 (1990).
2. T. L. St. Clair and D. J. Progar, NASA Langley Research Center, "Polyimide Molding Powder Coating, Adhesive, and Matrix Resin," U.S. Patent No. 5,147,966.
3. T. L. St. Clair, D. J. Progar, E. J. Siochi, and D. C. Working, "LARCTM-IA Polyetherimide Adhesive," Proceedings of the 39th International SAMPE Symposium and Exhibition, pp. 3206-3211, April 11-13, 1994.
4. T. H. Hou, N. J. Johnston, and T. L. St. Clair, "Processing and Properties of IM7/LARCTM-IA Polyimide Composites," Proceedings of the 39th International SAMPE Symposium and Exhibition, pp. 573-687, April 11-13, 1994.

Figure 2 **LAP SHEAR STRENGTHS OF LARC™-IA**

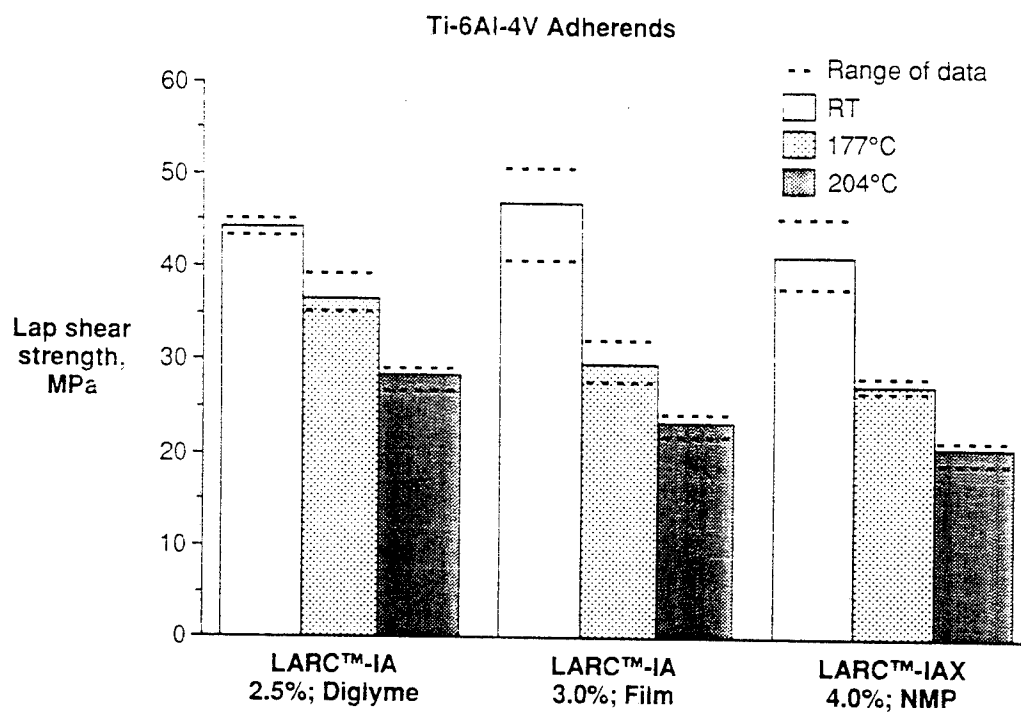


Figure 4 THERMAL EXPOSURE AT 204°C

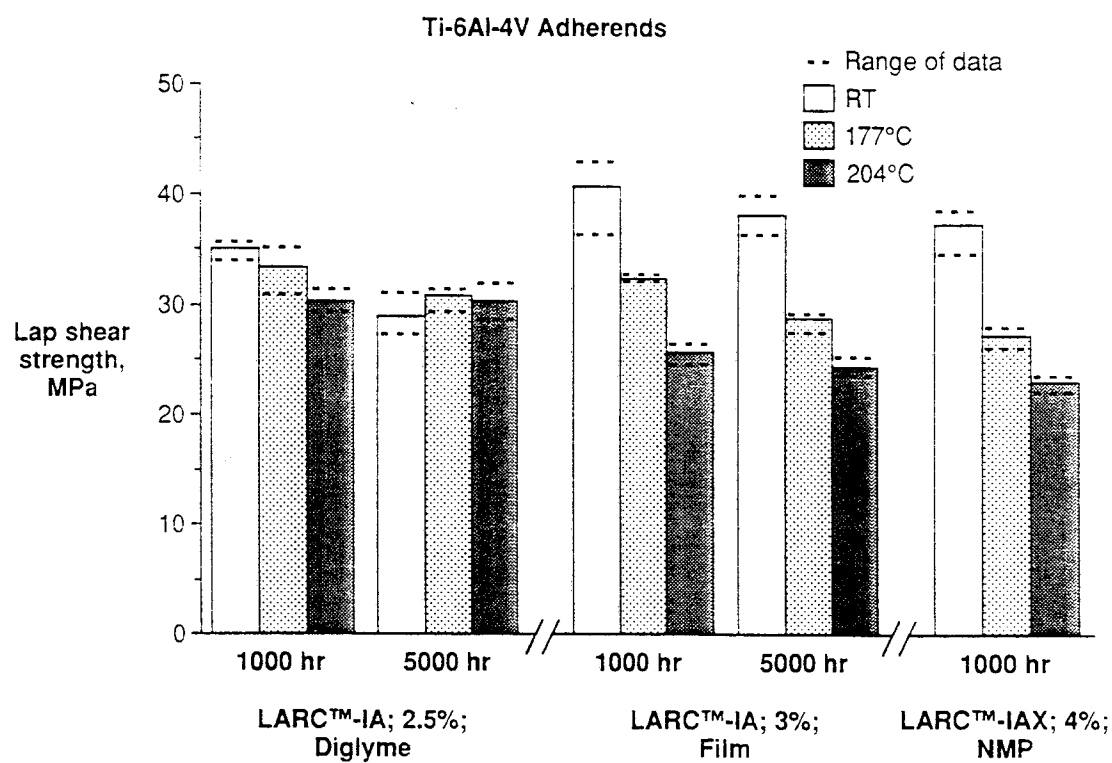
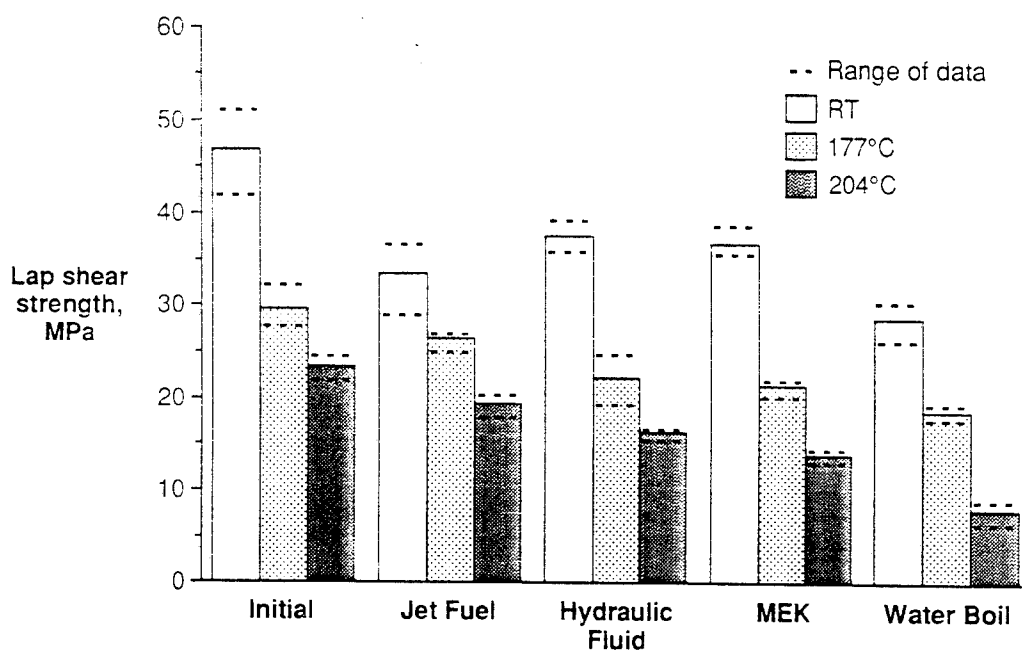


Figure 5

THREE DAY SOLVENT EXPOSURE FOR LARC™-IA; 3%; FILM

Ti-6Al-4V Adherends



Bonding conditions: 0.10 MPa (15 psi), 371°C. held 1 hr.

NEW COUPLING AGENTS FOR BONDING POLYMERS TO ALUMINUM

Stephanie L. Nesbitt*, J.P. Bell*, and D.E. Nikles**

*Department of Chemical Engineering and Polymer Science Program
University of Connecticut
191 Auditorium Road
Storrs, CT 06269

**Center for Materials For Information Technology
229 Bevill Research Building/Box 870209
Tuscaloosa, Alabama 35487-0209

ABSTRACT

Two new coupling agents, a β -diketone and a quinone-amine, have been evaluated as potential replacements for chromic pretreatments for aluminum. Internal reflectance Fourier Transform Spectroscopy and XPS both indicate chemical interaction between the coupling agent and the aluminum oxide surface. Modified tubular butt joints were utilized to measure joint strengths and joint durability after exposure to water. Joint strengths and durabilities showed significant improvement as compared to untreated controls.

INTRODUCTION

Use of polymeric coupling agents offers a practical alternative and improvements to chrome etching pre-treatments presently utilized on aluminum [1, 2]. From the environmental aspect, the elimination of the chrome etching process would greatly reduce a source of toxic hexavalent chromium. Polymer coupling agents offer a wide range of advantages beyond the environmental issue. Of primary interest is that coupling agents can be tailored to be system specific, depending on the functionalities of the metal substrate and polymer substrate which are to be bonded. In addition, the functionalities and their relative concentrations on the coupling agent backbone can be tailored to optimize interaction with the substrates and improve environmental resistance to bond failure. The porous nature of the oxidized aluminum surface permits both mechanical interlocking and chemical (ionic or covalent) bonding to active surface moieties. Another advantage of polymeric coupling agents is that they are able to absorb and distribute mechanical and thermal stresses within the bond thereby reducing internal stress concentrations which could result in bond failure.

In contrast to "primers", coupling agents form a true, verifiable chemical (ionic or covalent) bond, whereas primers typically enhance wetting. A true coupling agent is optimal at about 150Å thickness, contrary to primers

which are typically applied in layers at least microns in thickness [2].

Investigations of two potential polymeric coupling agents, a β -diketone and a quinone-amine polymer are presently in progress. β -diketones have been shown to form stable chelates with metals and metal oxides [3, 4]. These metal β -diketonates behave as inner complexes, showing predominantly covalent behavior [4]. Figure 1 shows the general structure of an oxygen-bonded β -diketone. Low molecular weight β -diketones have also been shown to exhibit corrosion resistance and improve coating adhesion on aluminum substrates [3]. Quinone-amine polymers have recently appeared in the literature. They have been shown to adhere strongly to metals and alloys and greatly improve corrosion resistance of iron particles due to the presence of reactive -NH-, -OH, and =O functional groups that can function as moisture resistant adhesion promoters [5, 6]. A significant example is that they have been shown to displace water from wet, rusty steel surfaces [5].

EXPERIMENTAL

Modified torsional shear joints, Figure 4, were degreased in methanol for 30 minutes, wiped with a methanol soaked, lint-free cloth, and air dried [7]. The joints were then soaked in a 0.2 wt% coupling agent solution for ten minutes at room temperature and air dried. 44mg \pm 1 of epoxy resin (Epon 828 and 4,4'-methylenedianiline, 28phr) was applied to the raised annulus of the torsional joint, the joint halves bonded together and the entire joint cured at 120°C for one hour and 150°C for two hours. Joint durability studies were conducted by immersing cured joints into 57°C water for varying lengths of time (days) and measuring the joint strength after removal from the water.

Fourier Transform Infrared Spectroscopy experiments were conducted using a KRS-5 internal reflectance crystal in contact with an aluminum bar, 6 x 1.5 cm, treated with the low molecular weight β -

diketone, benzoylacetone or the quinone-amine polymer. The aluminum bar was soaked in a concentrated solution of coupling agent and solvent, air dried, and then rinsed lightly with pure solvent to remove any unbound coupling agent.

RESULTS AND DISCUSSION

β -diketone

Investigations in our laboratory on a low molecular weight β -diketone, benzoylacetone, indicate strong, interaction of the β -diketone with an aluminum surface. Figure 3a is a portion of the spectrum of benzoylacetone on the KRS-5 crystal and Figure 3b is a portion of the spectrum of an aluminum bar coated with benzoylacetone, from a methanol solution, which is in contact with the KRS-5 crystal. The peak at 1595 cm^{-1} in Figure 1a has been assigned to the enolic form of the diketone [8]. The displacement from the traditional carbonyl region is attributed to the intramolecular hydrogen bonding of the resonance stabilized enol. The peak at 1595 cm^{-1} is also present in Figure 3b. In Figure 3b, however, an additional peak is observed at 1732 cm^{-1} . The keto form of the carbonyl and/or the unbound enolic form may result in the appearance of this peak [8]. The appearance of the peak at 1732 cm^{-1} signifies an apparent change in the electronic state of the carbonyl functionality and suggests that the β -diketone is chemically interacting with the aluminum oxide surface. Further studies on the exact nature of this interaction are underway.

Joint strengths and joint durabilities for low molecular weight β -diketone treated joints were evaluated via torsional shear experiments [9]. The joint subjects the epoxy-aluminum bond to almost pure shear with a high degree of reproducibility. Figure 4 illustrates the joint strengths of low molecular weight β -diketone treated joints in comparison to joint strengths of untreated controls. Dry strengths for the low molecular weight β -diketone treated torsional shear joints were comparable to the untreated controls. Low molecular weight β -diketone treated joints that were soaked in 57°C water for a variety of days, however, displayed improved shear strengths as compared to the untreated controls that were soaked for the same lengths of time. The presence of the low molecular weight β -diketone resulted in improvements in water durability compared to untreated controls.

Having observed chemical interaction between the β -diketone and the aluminum oxide surface and improvements in water durability for the low molecular weight β -diketone, we have synthesized a polymerizable β -diketone which is being copolymerized with a chain modifier and an epoxy reactive compound and will be evaluated to determine its potential utilization as a polymeric coupling agent. The combination of a β -

diketone and an epoxy reactive functional group within a copolymer provides a method by which chemical bonding can occur between the aluminum oxide and the epoxy adhesive, thus forming a true coupling agent.

Quinone-amine

A quinone-amine polymer is also being evaluated in terms of its potential utilization as a polymeric coupling agent. The polymer, AQPU-15, was synthesized via polymerization of the three compounds in Figure 5 in the ratio of 2:1:1. The AQPU-15 was provided by Professor David Nikles, University of Alabama, Tuscaloosa. Internal Reflectance Fourier Transform Infrared Spectroscopy experiments indicate that the quinone-amine polymer is interacting with the aluminum oxide surface. Figure 6a is a portion of the spectra of the quinone-amine polymer on a KRS-5 internal reflectance crystal. Figure 6b is a portion of the spectra of an aluminum bar that was treated with the quinone-amine polymer in contact with the KRS-5 crystal. Treatment of the aluminum bar is similar in method to that described for the β -diketone with the concentrated solution being of AQPU-15 and THF and the rinse in pure THF. Figure 6 shows the secondary amine region for both samples. The peak shifts from 3292 cm^{-1} in Figure 6a to 3270 in Figure 6b due to the presence of the aluminum bar. Thus, the amine is observed to be involved in the interaction between the quinone-amine and the aluminum oxide surface. Preliminary XPS studies also indicate amine interaction with the aluminum oxide surface.

Joint strengths and joint durabilities for the quinone-amine treated joints were also evaluated via torsional shear experiments [9]. Figure 4 illustrates the joint strengths of quinone-amine treated joints in comparison to joint strengths of untreated controls. Dry strengths for the quinone-amine treated torsional shear joints were comparable to the untreated controls. Quinone-amine treated joints that were soaked in 57°C water for a variety of days, however, displayed substantially improved shear strengths as compared to the untreated controls that were soaked for the same lengths of time. Therefore, the quinone-amine pretreatment resulted in improvements in water durability as compared to untreated controls.

LITERATURE CITED

1. J. P. Bell and R. Schmidt, U.S. Patent No. 4,812,363, (1989).
2. J. P. Bell, R. G. Schmidt, A. Malofsky, D. Mancini, *J. Adh. Sci. Tech.* **5**, 927-944 (1991).
3. V. P. Wystrach and F. C. Rauch, U.S. Patent # 3,615,888, (1971).

4. R. C. Mehrotra, R. Bohra, D. P. Gaur, Metal β -Diketonates and Allied Derivatives. (Academic Press Inc., N.Y., 1978).
5. K. Kaleem, F. Chertok, S. Erhan, J. Polym. Sci.: Part A: Polymer Chemistry **27**, 865-871 (1989).
6. J. Liang and D. E. Nikles, IEEE Transactions on Magnetism (1993) Accepted for publication.
7. J.P. Bell and C.J. Lin, J. Appl. Polym. Sci. **16**, 1721-1733 (1972).
8. R. M. Silverstein, G. C. Bassler, T. C. Morrill, Spectrometric Identification of Organic Compounds, ed. 4, (John Wiley & Sons, N.Y., 1981).
9. R. G. Schmidt and J. P. Bell, J. Adhesion **27**, 135-142 (1989).

FIGURES

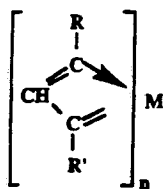


Figure 1. General structure of an oxygen-bonded metal β -diketonate.

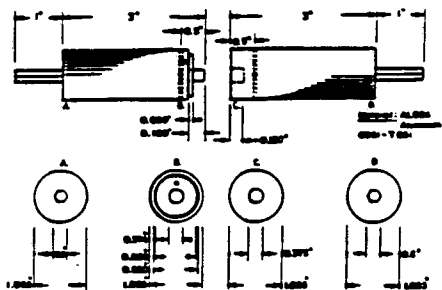


Figure 2. Schematic of the tubular butt joints developed by Bell and Lin [7].

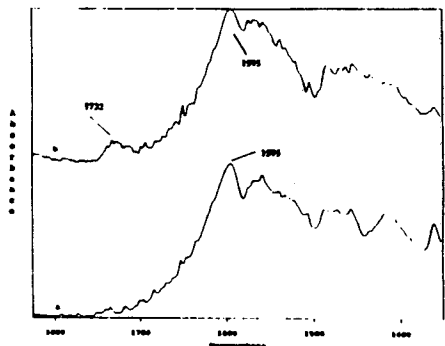


Figure 3. Internal reflectance spectra (KRS-5 45° incidence) of 3a) benzoylacetone and 3b) benzoylacetone treated aluminum bar.

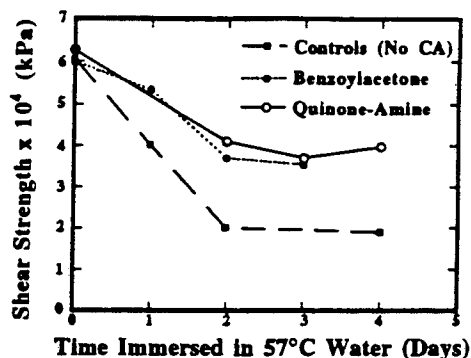


Figure 4. Comparison of shear strengths of control joints, β -diketone, and quinone-amine treated joints after immersion in 57°C water.

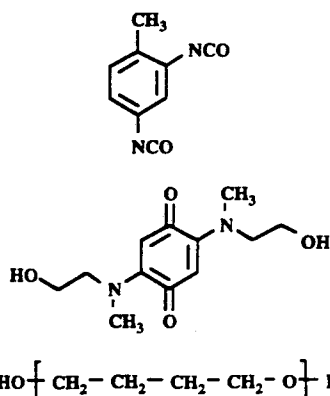


Figure 5. Chemical structures of the components of AQP-15. Ratio of 2:1:1.

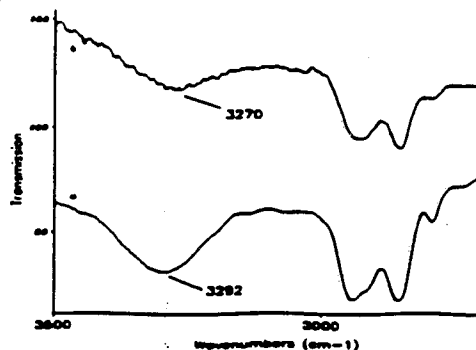


Figure 6. Internal reflectance spectra (KRS-5 45° incidence) of 6a) AQP-15 and 6b) AQP-15 treated aluminum bar.

Although the research described in this article has been funded wholly or in part by the United States Environmental Protection Agency through CR 821875 to Dr. J.P. Bell, it has not been subjected to agency review and therefore does not necessarily reflect the views of the agency and no official endorsement should be inferred.

INFRARED AND RAMAN SPECTROSCOPY OF POLYMER/METAL INTERPHASES: APPLICATION TO ADHESION

by

F. J. Boerio, I. Segall, C. E. Taylor, Y. M. Tsai, J. T. Young, and W. W. Zhao
Department of Materials Science and Engineering
University of Cincinnati
Cincinnati, Ohio 45221-0012

INTRODUCTION

The purpose of this paper is to describe the use of reflection-absorption infrared spectroscopy (RAIR) and surface-enhanced Raman spectroscopy (SERS) to determine the physical and chemical structure of polymer/metal interphases which are relevant to adhesion. RAIR can be used to characterize thin polymer films on metal substrates, to determine the orientation of functional groups of the polymer on the metal surface, and to determine the nature of reactions occurring at the interface between the polymer and substrate and between the polymer and an adhesive system. SERS can be used for in-situ, non-destructive characterization of buried polymer/metal interphases.

Several examples of the use of RAIR and SERS will be described. Included will be the use of RAIR and SERS to determine the orientation and interfacial chemistry of model polyimides adsorbed onto silver and gold substrates. The use of RAIR to characterize plasma polymerized primers on metal substrates and their reactions with model rubber systems will also be discussed. Finally, use of SERS to characterize interphases between polymer systems such as anaerobic adhesives and silver substrates will be described.

EXPERIMENTAL

Polymer films were deposited onto mechanically polished cold-rolled steel substrates by plasma polymerization of acetylene using

techniques which have been described previously [1]. The thickness of the films was determined by using a Rudolph Research Model 436 ellipsometer to examine substrates before and after deposition of films. Reflection-absorption infrared (RAIR) spectra of the plasma polymerized films were obtained using a Perkin-Elmer 1800 Fourier-transform infrared spectrophotometer.

A model "rubber" consisting of squalene (100 phr), zinc oxide (10 phr), carbon black (10 phr), sulfur (5 phr), stearic acid (2 phr), and antioxidant, DCBS, and cobalt naphthenate (each 1 phr) was used to simulate reactions occurring between natural rubber and plasma polymerized acetylene films. The components of the model system were mixed together in a beaker which was heated to 160°C while being stirred and purged with nitrogen. Steel substrates coated with plasma polymerized acetylene primers were immersed into the mixture, withdrawn at selected intervals, rinsed ultrasonically with hexane, and dried in a stream of nitrogen. The substrates were then examined using RAIR [2].

Substrates for SERS investigations were prepared by evaporating silver island films onto glass substrates at a rate of about 1 Å/sec to a final thickness of about 40 Å [3]. Gold island films were prepared similarly except that the deposition rate was 0.2 Å/sec and the final thickness was about 65 Å.

4-Mercaptophenylphthalimide (4-MPP) was synthesized as described in reference 4. Monolayers of 4-MPP were adsorbed onto gold substrates by immersing the substrates into 1×10^{-3}

M solutions in chloroform for 12 hours and then rinsing the substrates thoroughly with chloroform.

A model anaerobic acrylic adhesive system consisting of triethyleneglycol dimethacrylate (TRIEGMA) (100 phr), o-benzoic sulfimide (BS) (0.83 phr), acetylphenylhydrazine (APH) (0.70 phr), and cumene hydroperoxide (CHP) (2.78 phr) was obtained from Loctite Corporation. Thin films of the adhesive were deposited on silver island films by spin coating from dilute solutions in acetone or from the undiluted adhesive.

SERS spectra were obtained using a spectrometer equipped with a Spex 1401 double monochromator, Hamamatsu R943-02 photomultiplier tube, and Stanford Research Model 400 photon counter interfaced to a personal computer. A Spectra-Physics Model 165 argon-ion laser ($\lambda = 5145 \text{ \AA}$) and a Lexel 3000 krypton-ion laser ($\lambda = 6471 \text{ \AA}$) were used to obtain SERS spectra from silver and gold substrates, respectively.

RESULTS AND DISCUSSION

Plasma Polymerized Primers for Rubber-to-Metal Bonding

RAIR spectra of as-deposited plasma polymerized acetylene films on polished steel substrates are shown in Figure 1. The thicknesses of these films were 57, 90, 635, and 900 \AA . Peaks characteristic of hydrocarbons were observed near 2960, 2928, 2870, 1450 and 1375 cm^{-1} . The band near 3295 cm^{-1} was assigned to CH stretching in monosubstituted acetylene ($\text{R-C}\equiv\text{C-H}$). Weak bands related to $\text{-C}\equiv\text{C-}$ stretching in mono- and disubstituted acetylene were observed near 2100 and 2210 cm^{-1} , respectively. A band assigned to $\text{C}=\text{C}$ stretching was observed near 1600 cm^{-1} . The strong, sharp band near 916 cm^{-1} may be related to the CH_2 wagging mode of vinylidene groups. Bands near 758 and 700 cm^{-1} were assigned to CH and CC out-of-plane bending in monosubstituted benzene rings and bands near

3055 and 3027 cm^{-1} were assigned to CH stretching in aromatic groups. Bands near 1595, 1510, and 1495 cm^{-1} were assigned to aromatic ring stretching modes. Evidence of oxidation resulting from the reaction of trapped radicals with atmospheric oxygen and moisture was obtained. Thus, the band near 3455 cm^{-1} was assigned to O-H stretching and bands near 1715 and 1680 cm^{-1} were assigned to $\text{C}=\text{O}$ stretching.

The band near 758 cm^{-1} was very strong for 635 and 900 \AA films, much weaker for the 90 \AA film, and undetectable for the 57 \AA film. A very weak band which may be related to a surface acetylide [5] was observed near 3250 cm^{-1} in spectra of the 57 \AA and 90 \AA films but not in spectra of the thicker films.

After reaction of the polymer films with the model rubber system for 30 minutes, the band near 3295 cm^{-1} disappeared, indicating that $\text{C}\equiv\text{C}$ bonds were consumed by reaction of the films with the "rubber." New bands appeared near 2850, 1551, 1539, 1512, 1430, 1320, 1085, and 1011 cm^{-1} . The band near 2850 cm^{-1} was assigned to cyclohexane rings of DCBS. Bands near 1512, 1430, 1320, 1085, and 1011 cm^{-1} were characteristic of benzothiazole in DCBS. The band near 1539 cm^{-1} was due to zinc stearate.

4-Mercaptophenylphthalimide (4-MPP) Monolayers on gold

Results obtained from RAIR and SERS showed that 4-MPP, which is a model for polyimides, adsorbed dissociatively onto gold to form a thiolate [4]. The tilt angle between the 2-fold symmetry axis of 4-MPP and the normal to the gold surface was about 21° . The normal Raman spectrum of 4-MPP is shown in Figure 2. Several bands characteristic of the imide group were observed. The bands near 1789 and 1771 cm^{-1} were assigned to the symmetric and asymmetric stretching modes of the carbonyl

bonds, respectively, and the very strong band near 1395 cm^{-1} was assigned to the axial imide CNC stretching mode. Very strong bands near 1604 and 1100 cm^{-1} were assigned to modes $\nu(8a)$ and $\nu(1)$ of the p-disubstituted rings. The band due to the SH stretching mode was observed near 2581 cm^{-1} .

The SERS spectrum of 4-MPP on a gold substrate is shown in Figure 3. Strong bands were observed near 1595 and 1085 cm^{-1} due to modes $\nu(8a)$ and $\nu(1)$ of the p-disubstituted rings. A medium intensity band appeared near 1390 cm^{-1} due to the CNC imide axial stretching mode. The band due to SH stretching disappeared from the SERS spectrum, confirming that adsorption had occurred through the thiol group. No bands due to the C=O stretching modes were observed near 1789 and 1771 cm^{-1} .

SERS From a Model Acrylic Adhesive System Deposited on Silver

SERS spectra obtained from films of the model anaerobic adhesive spun onto silver island substrates from the neat adhesive and from 1% and 5% solutions of the adhesive in acetone all had approximately the same intensity even though the films had much different thicknesses. These results indicated that the SERS spectra were characteristic of the interface and not of the bulk films [6]. Moreover, the SERS spectra observed for the acrylic adhesive had little resemblance to normal Raman spectra of the monomer. Instead, they were similar to SERS spectra of o-benzoic sulfimide and to normal Raman spectra of salts of o-benzoic sulfimide. These results indicated that o-benzoic sulfimide in the adhesive segregated to the interface and adsorbed by dissociation to form a salt. A similar process may occur in the case of copper or iron substrates. In those cases, the metal ions in the salts may accelerate polymerization of the monomer by undergoing oxidation while CHP is reduced to form radical anions which initiate polymerization. APH may also accelerate the cure

by oxidizing while metal ions are reduced, thus enabling the oxidation of metal ions and the reduction of CHP to be repeated.

CONCLUSIONS

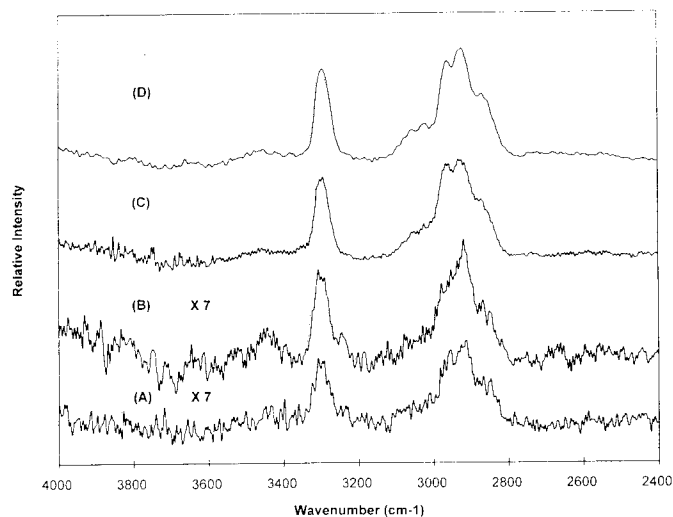
Infrared spectroscopy has many applications that are relevant to adhesion science. Included characterizing the physical and chemical structure of thin polymer films on metal substrates and determining the nature of reactions occurring at the interface between the polymer and substrate and between the polymer and an adhesive system. Raman spectroscopy, especially surface-enhanced Raman scattering, can be used for in-situ, non-destructive characterization of buried polymer-metal interphases.

ACKNOWLEDGMENTS

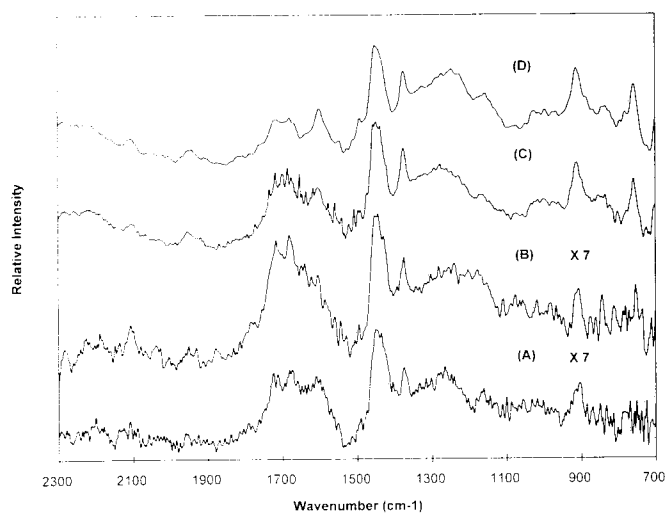
This research was supported in part by grants from the National Science Foundation, Loctite Corporation, and Office of Naval Research.

REFERENCES

1. Y. M. Tsai, U. R. Aggarwal, F. J. Boerio, D. B. Zeik, S. J. Clarson, W. J. van Ooij, and A. Sabata, *J. Appl. Polymer Sci.: Applied Polymer Symposium* **54**, 3 (1994).
2. Y. M. Tsai and F. J. Boerio, *Surf. Interface Anal.*, in press, 1994.
3. J. T. Young and F. J. Boerio, *Surf. Interf. Anal.* **20**, 341 (1993).
4. J. T. Young, F. J. Boerio, Z. Zhang, and T. L. Beck, *Langmuir*, submitted for publication, 1994.
5. C. C. Chang and R. J. Kokes, *J. Catalysis* **28**, 92 (1973).
6. F. J. Boerio, P. P. Hong, P. J. Clark, and Y. Okamoto, *Langmuir* **6**, 721 (1990).



(A)



(B)

Figure 1. RAIR spectra of plasma polymerized acetylene films on CRS substrates. The film thicknesses were (A) - 57, (B) - 90, (C) - 635, and (D) - 900 Å.

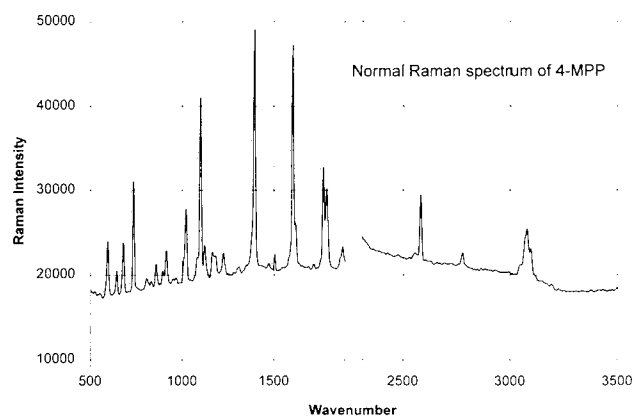


Figure 2. Normal Raman spectrum of 4-MPP.

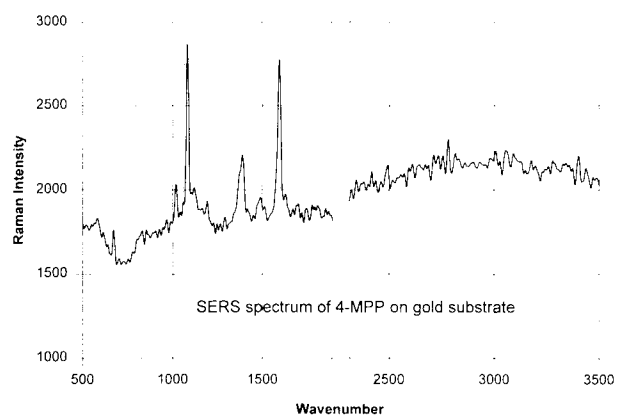


Figure 3. SERS spectrum of 4-MPP adsorbed onto gold.

Rheo-Photoacoustic FT-IR Spectroscopy and Interlayer Adhesion of Polymers

Brian D. Pennington and Marek W. Urban*

Department of Polymers and Coatings
North Dakota State University
Fargo, North Dakota 58105

Photoacoustic Fourier transform infrared (PA FT-IR) spectroscopy provides several advantages in the characterization of materials over conventional infrared spectroscopy techniques, adding a multi-dimensional character to the analytical process. For example, while the ability to obtain molecular level information without altering a specimen is one of the appealing features, determination of the stratification and degradation processes in polymers (1,2), non-equilibria processes (3,4), or crosslinking of thermosetting polymers (5,6) add another dimension.

A schematic diagram of the basic PA FT-IR experimental setup is presented in Figure 1A. In this experiment, modulated infrared light enters an acoustically isolated photoacoustic cell, and those wavelengths of incident modulated radiation which correspond to vibrational modes of chemical bonds are absorbed. As a result of reabsorption, energy is given off in the form of heat. As heat reaches the surface, pressure variations in the coupling gas over the sample are induced at the frequency of

modulated light. These pressure fluctuations are detected by the use of a sensitive microphone, and the signal is Fourier transformed into an infrared spectrum (7).

In an effort to further expand the versatility of the PA FT-IR method, our research group has introduced two new concepts to the basic PA experiment. The first involved the development of the rheo-photoacoustic (RPA) technique (8), which enables collection of the PA spectra from uniaxially elongated samples held at fixed elongations during spectral acquisition. A schematic diagram of the experimental setup is illustrated in Figure 1B, and appears to be sensitive to the interchain bonding of poly(p-phenylene terephthalamide) (PPTA) fibers. Other applications were also demonstrated (8,9). More significantly, this approach enables the determination of the strength of molecular level interactions which contribute to adhesion between polymeric materials (9-11).

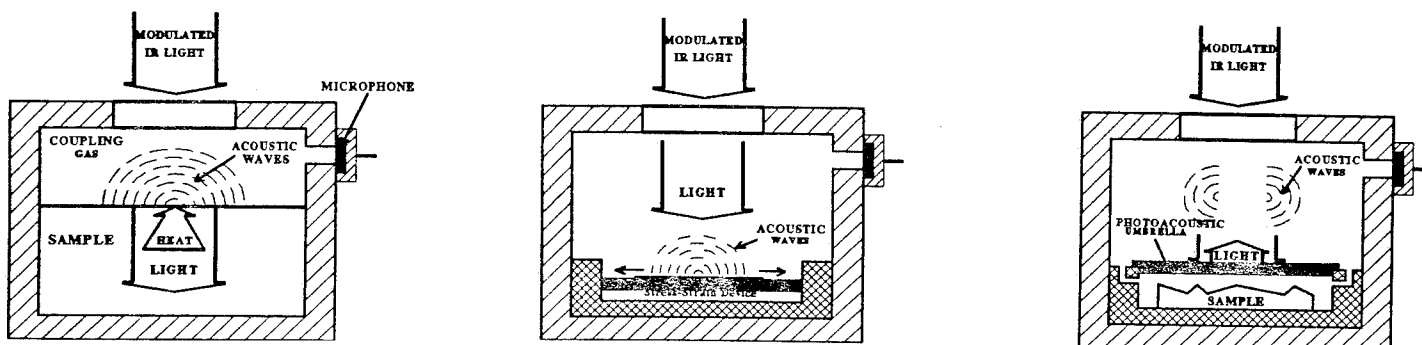


Figure 1. A schematic diagram of: A - PA FT-IR cell; B - rheo-photoacoustic (RPA) FT-IR cell; C - RPA FT-IR cell with "photoacoustic umbrella."

The RPA FT-IR setup also opened the opportunity to monitor diffusion of small molecules from polymeric materials (12-14). In this approach, an aluminum "photoacoustic umbrella" was utilized, which allows determination of the concentration of gas-phase species over a solid sample. This is depicted in Figure 1C. Because theoretical (15) and experimental details (13,16,17) were presented elsewhere, the following sections will highlight selected applications relevant to molecular level quantitative approaches in polymer-polymer adhesion.

RPA FT-IR Spectroscopy and Adhesion

Measurement of adhesion in a bilayer system is strongly influenced by physico-chemical changes at polymer interfaces. Although RPA FT-IR spectroscopy has been utilized in the

studies of polymer-polymer interfacial interactions, no correlations have been made between spectroscopic data and the work of adhesion. Using the experimental setup shown in Figure 1B, one can induce interfacial stresses in a bilayer polymer system and determine the work of adhesion. Before such correlations can be made, it is necessary to develop theoretical foundations leading to assessment of the work of adhesion.

Theoretical Considerations of Vibrational Energy Changes and Work of Adhesion

A typical bilayer experiment is designed in such a way that a substrate is stretched and an adhered top film resists deformation. Therefore, shear stresses are induced at the polymer-polymer interface. If the interfacial interactions are significant, the potential energy of bonds involved in adhesion will change. If this is the case, vibrational frequencies of chemical bonds involved will also change, and the correlation

* - to whom correspondence should be addressed

between the wavenumber changes resulting from stresses induced at the interface and the work of adhesion can be made.

The total potential energy for a bilayer system can be expressed as a sum of the following interactions

$$V_{\text{Total}} = V_{11} + (V_{\text{int}})_{12} + V_{22} \quad (1)$$

where: $(V_{\text{int}})_{12}$ is the interfacial interaction potential between a polymer substrate [1] and a top polymer layer [2], and V_{11} and V_{22} are the interaction potentials between respective molecular layers. The total force at the interface experienced by the bilayer can be determined by differentiating the total potential energy with respect to the change in bond distance to give

$$(\partial V_{\text{Total}} / \partial r_1) = (\partial V_{11} / \partial r_1) + (\partial (V_{\text{int}})_{12} / \partial r_1) \quad (2)$$

The total force is equal to the force in the unperturbed substrate molecules and the force resulting from 1-2 interactions. For example, the intermolecular potential for an outer diatomic segment of a substrate will change as a result of interactions with a top film layer. Therefore, a vibrational frequency perturbation is anticipated. Because dispersive, repulsive, dipolar orientational, and inductive interactions have a significant effect on the net potential energy, let us estimate each of the energies and establish their contributions to the work of adhesion.

The dispersion forces are created by the Coulombic interactions of electrons and nuclei in atoms. This motion produces an instantaneous dipole that induces a secondary dipole in the neighboring atoms which can be estimated using the London relationship (18)

$$V_{\text{dispersion}} = (\alpha_1 \alpha_2 / R_{12}^6) (I_1 I_2 / I_1 + I_2) \quad (3)$$

where: α_1 and α_2 are the bond polarizabilities of polymers 1 and 2 in the bilayer system, I_1 and I_2 are the bond ionization energies, and R_{12} is the "effective" interbond distance.

The interaction between two molecules at the polymer-polymer interface, one with a permanent dipole moment and another with a zero dipole moment, will result in a secondary (induced) dipole due to the electrical field existing around the first molecule. The attraction energy between the dipole-induced dipole was shown by Debye (19) to be

$$V_{\text{induction}} = (\mu_1^2 \alpha_2 + \mu_2^2 \alpha_1) / (R_{12}^6) \quad (4)$$

Another interaction is a dipole-dipole interaction, in which molecules with a permanent dipole moment interact with each other. The energy of this interaction for the dipolar orientation of species 1 and 2 can be expressed as

$$V_{\text{dipolar orientation}} = (\mu_1 \mu_2 / R_{12}^3) \varphi \quad (5)$$

where: μ_1 and μ_2 is the bond dipole moments, and φ is the orientation factor.

The repulsion component between the electrostatic charges in two interacting molecules can be determined from

$$V_{\text{repulsion}} = a \exp(-b R_{12}) \quad (6)$$

where: a and b are empirical constants. The repulsive component results from the force due to the overlap of the electronic orbital structure between the two molecules.

The force for each type of interaction can be determined by taking the derivative of each potential energy term with respect to r_1 , giving the overall force

$$F = F_{\text{att}} + F_{\text{rep}} = (V'_{\text{dis}} + V'_{\text{or}} + V'_{\text{ind}}) + V'_{\text{rep}} \quad (7)$$

As a result of perturbation, the vibrational frequency will change. At the same time, however, the bond distance, as well as the force constant, will also change. To account for these changes, one can adopt an approach similar to that proposed for solute-solvent interactions. It is assumed that the substrate frequency shift produced by the attractive and repulsive forces of the surrounding medium are proportional to the changes in the bond length (20,21)

$$\Delta v / v_0 = -a (r_1 / r_e) \quad (8)$$

$$a = r_e [-3/2(g/f) + (G/F)] \quad (9)$$

where: G is the ensemble average for the cubic force over the perturbation coordinates, and g is the cubic force constant. The proportionality constant, a , depends on the properties of the two interacting molecules. The g/f term can be determined by utilizing Badger's rule (22), whereas the G/F term can be evaluated using empirical correlation from Oxtoby (23) and Herzfeld (24).

From the above relationships, ΔW will be determined by integrating the force of interaction, F , over the limits of equilibrium bond distance to ∞ , giving the work of adhesion

$$\Delta W = -\int F dr = -\int F_{\text{att}} + F_{\text{rep}} dr = -\int V'_{\text{dis}} + V'_{\text{or}} + V'_{\text{ind}} + V'_{\text{rep}} dr \quad (10)$$

where: F is represented as the ensemble average of the quadratic force over the perturbation.

Experimental Results of RPA Analysis.

In order to set the stage for spectroscopic measurement of adhesion and correlation of spectral changes with the theoretical derivations shown above, the photoacoustic response to tensile elongation was examined. Figure 2 illustrates PA FT-IR spectra of acrylic-coated polyethylene in the 3000-2750 cm^{-1} region elongated from 0 to 6%. The bands at 2930 and 2855 cm^{-1} are due to the polyethylene C-H asymmetric and symmetric vibrational stretching modes, respectively. The spectral features at 0% elongation illustrate the initial conditions of the unperturbed state, while the spectra recorded at various increasing elongations exhibit the development of polyethylene bands. As a tensile force is applied to the substrate, the bilayer system is being stretched and becomes thinner. Should the

interfacial attractive forces be strong enough, the acrylic coating will follow the deformation of the polyethylene substrate, causing the thickness of the top layer to decrease. A linear increase in the polyethylene bands would be expected from a uniform elongation, since the sampling depth has remained constant. However, a significant increase of the polyethylene bands at 2930 and 2855 cm^{-1} with elongations exceeding 5% occur, while the C-H stretching band due to acrylic at 2959 cm^{-1} is diminished. A sudden increase of the PE bands is attributed to the presence of interfacial voids which provide a means for heat

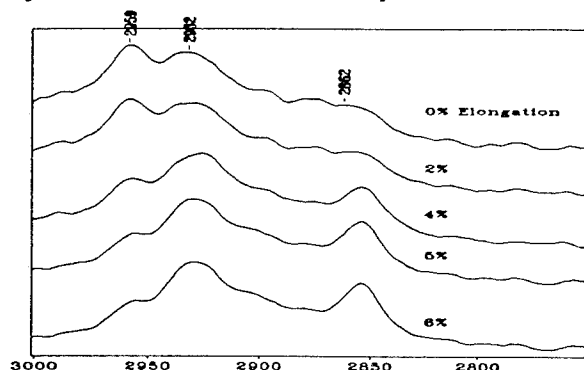


Figure 2. Acrylic / PE RPA FT-IR spectra in the 3000 to 2750 cm^{-1} region.

As the bilayer system is elongated, in addition to the intensity changes, vibrational energies of specific bands also change. As seen in Figure 2, as the acrylic-PE bilayer system is elongated, a change of the substrate vibrational energy is reflected in a shift of the bands at 2930 and 2855 cm^{-1} . The CH_2 symmetric band is shifted from 2857 to 2855 cm^{-1} , while the CH_2 asymmetric frequency changes from 2932 to 2930 cm^{-1} for elongations up to 6%. It appears that the magnitude of the wavenumber shift of the C-H stretch is affected by the degree of elongation of the substrate, adhesive properties of the bilayer, and the nature of interactions. For example, shifts up to 16 cm^{-1} were detected for a PDMS-PE bilayer (11). The apparent overlap with the acrylic C-H stretching bands is resolved by correlating the reduced intensity of the 2959 cm^{-1} band due to the thinning process. Since our previous studies (8) have shown that elongation of the substrate alone does not produce any changes in the vibrational energy (11), the effect of the interfacial forces accounts for this shift. This information can be used to quantify the data in conjunction with the theoretical considerations presented above (eqns 1-10).

Although studies of several bilayer systems showed similar trends, and the substrate bands were detected at various elongations, the full extent of interfacial failure was detected at the point where the substrate band intensity remains unchanged. In the case of epoxy-PP, this elongation occurs at 16%, epoxy-PE at 12%, acrylic-PE at 5%, and acrylic-PP at 6%.

Measurement of Bilayer Interactions with RPA FT-IR.

The effect of different intermolecular forces on the work of adhesion is of our central focus. As changes in the substrate bond length produced by elongation occur, vibrational energy changes are induced. At the same time, the potential energy

to escape without passing through the top-coat. This will result in a substantial increase of the substrate band intensities at the point where interfacial failure occurs.

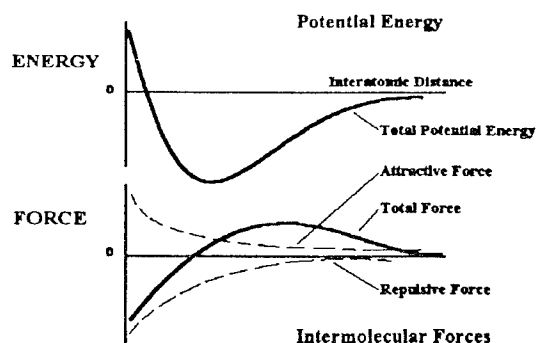


Figure 3. Interlayer energy and intermolecular forces between two molecular layers plotted as a function of distance.

changes with the bond distance. Because the most outer segments of a molecule will be affected by the surroundings, the C-H stretching vibrational energy is expected to be sensitive to environmental changes. Indeed, in all systems we studied, the C-H asymmetric stretching mode is often the most sensitive to interfacial stresses. Similar observations were accounted in the studies of solute-solvent interactions (20). If one envisions that the repulsive and attractive components of the overall work of adhesion are in a state of equilibrium, the intermolecular distance will determine to what extent each component dominates. This is shown in Figure 3. For an equilibrium situation, the attractive and repulsive forces will be equal. As external forces are imposed on the system, the bond distance decreases, and the repulsive component will dominate. In contrast, as the bond distance increases from the initial equilibrium bond distance, the attractive forces will prevail.

The experimentally measured frequency shifts can be used in eqn. 8 with the constant a to determine the change in the C-H bond distance from equilibrium. The ratio of the cubic force constant to the quadratic force constant (g/f) can be determined by Badger's rule, with the corresponding forces (G/F) from the empirical correlation expressed by eqn 9, to give the proportionality constant, a . With the corresponding potential energy, the quadratic force for each contributing component to the total potential energy function can be determined from eqn 7. In view of the above considerations, and according to eqns 3-5, there are dispersive, dipolar orientational, and inductive intermolecular forces. However, these attractive forces are not the only ones that are responsible for interfacial interactions. If substrate and film molecules approach each other, the interfacial distance (r) decreases, and at some point, the repulsive forces will counteract attractive forces. Having established each potential energy component contributing to the interfacial interactions, the actual work of adhesion can be calculated from the frequency shifts of vibrational bonds sensitive to interfacial interactions. Using the results from eqns 3-6 and combining with eqn 10, the estimated value of the work of adhesion for each bilayer system can be determined. Table I summarizes work of adhesion values obtained for selected systems. Since polymeric materials are not expected to strongly adhere, the

THE DETERMINATION OF ADSORPTION ISOTHERMS BY XPS AND ToF-SIMS

John F Watts, James E Castle, Mohamed M Chehimi*, Marie-Laure Abel*

Department of Materials Science and Engineering,
UNIVERSITY OF SURREY
Guildford Surrey GU2 5XH UK

*Institut de Topologie et de Dynamiques des Systèmes
Université Paris 7 Denis Diderot
1 rue Guy de la Brosse 75005 Paris France

INTRODUCTION

The manner in which ionic or molecular species adsorb onto solid surfaces can provide valuable information about surface properties and surface/adsorbate interactions. The traditional way of following such processes is the construction of adsorption isotherms, originally devised to study gas phase adsorption, but also derivable from solution adsorption using surface analysis methods.

The original gas phase isotherm methodology relates the reduction in gas pressure, as a result of surface adsorption, to the base pressure and amount of material adsorbed. This is plotted on orthogonal axes to form an adsorption isotherm which may take the form of any of the well known types (Langmuir 1, 2, 3, Tempkin, Freundlich etc). By the use of surface analysis methods it is possible to report the amount of material deposited onto the solid surface from the solution phase as a function of normalised solution concentration.

XPS METHODOLOGIES

This method was first reported in the literature some eighteen years ago and was used to study the adsorption of silane adhesion promoters onto hydroxylated iron surfaces [1]. The adsorption isotherms obtained in this work are shown in Figure 1.

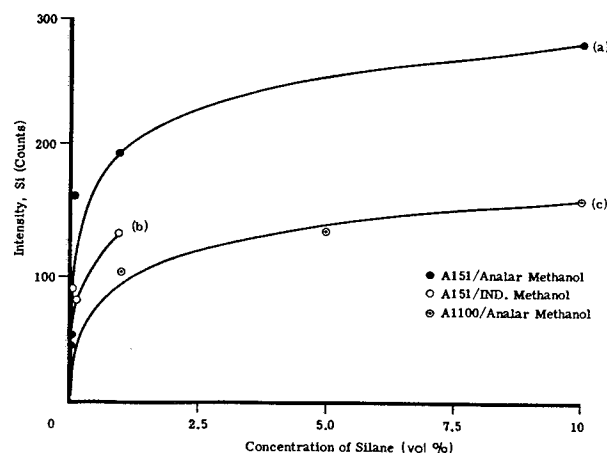


Figure 1. XPS adsorption isotherms for silane molecules on steel surfaces.

The isotherms are of the Tempkin type and a

γ -aminopropyltriethoxy silane shows reduced coverage compared with a vinyl tipped version. This can be ascribed to adsorption of the former species by either functional group, thus the surface concentration of silane molecules is reduced when compared with the vinyl version.

More recently the method has been extended to determine the acidity of carbon fibre surfaces in conjunction with devitalisation methods using Ag^+ and Mg^{2+} ions [2]. In this case the isotherms are of the Langmuir type and extraction of the monolayer coverage parameter (x_m) allowed the surface acidity to be determined by consideration of the surface oxygen concentration determined by XPS. This is achieved by plotting normalised uptake (S/surface composition of labellant) versus solution concentration (S/S_0), [where S =solution concentration and S_0 =solubility of labellant]. The x_m parameter is simply the reciprocal of the slope of the Langmuir plot determined in this manner. A Langmuir plot of this type is shown in Figure 2.

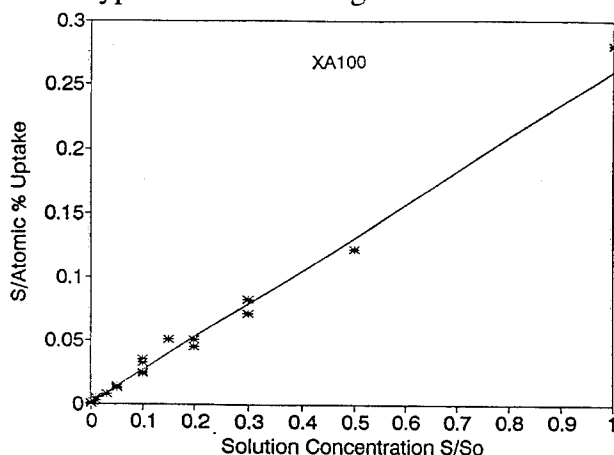


Figure 2. Langmuir plot for the adsorption of silver ions, from AgNO_3 solution on electrochemically oxidised carbon fibres.

In the analysis of polymers, however, care must be taken that the adsorbate is not also absorbed into the substrate which will lead to an erroneous result [3].

ToF-SIMS ISOTHERMS

This method has now been extended to study the adsorption of a simple homopolymer (PMMA) onto conducting polymer powders by XPS. The adsorption characteristics are strongly influenced by the choice of solvent. By plotting adsorption as a function of the solvent acid/base character a "Triangle of Fowkes" type of plot can be determined [4]. The adsorption isotherms using neutral solvents are all of a similar Langmuir type but the 'plateaux' values vary with the temperature of adsorption. It has also been possible to produce solvent effect isotherms using ToF-SIMS data, which perhaps reflects the true situation at the surface rather better [5]. A comparison of the adsorption behaviour of PMMA on hydrogen sulphate doped polypyrrole (PPy) is shown in Figure 3.

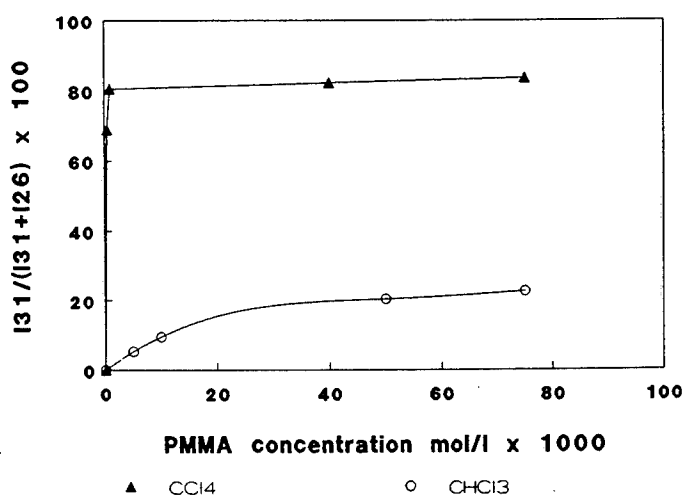


Figure 3. ToF-SIMS adsorption isotherms of PMMA on PPy from CCl_4 and CHCl_3 solutions.

The diagnostic ions used were $m/z = 31$ (CH_3O^-) for PMMA and $m/z = 26$ (CN^-) for the PPy substrate. The solvent effect is clearly seen, the PMMA deposition from the neutral tetrachloromethane solution being greater.

CONCLUSIONS

The use of XPS and SIMS in this manner provides valuable information concerning the initial interaction of adsorbate with the substrate. Such techniques can be used to ascertain the mode of interaction and may prove useful in identifying adsorption characteristics of various components in a multi-component formulation. Work is now underway to examine the extent to which some empirical observations can be correlated with computer chemistry calculations using a molecular simulations approach [6].

REFERENCES

1. R Bailey, J E Castle, J Mater Sci, 12, 4647, (1977).
2. C A Baillie, J F Watts, J E Castle, J Mater Chem, 2, 939, (1992).
3. R W Paynter, J E Castle, D K Gilding, Surf Interf Anal, 7, 63, (1985).
4. M-L Abel, M M Chehimi, Synth Met, 66, 225, (1994).
5. M-L Abel, M M Chehimi, A M Brown, S R Leadley, J F Watts, J Mater Chem, submitted.
6. S J Davis, J F Watts, Paper at this Meeting.

THE QUANTITATIVE EVALUATION OF ACID-BASE PROPERTIES BY XPS

S.R. Leadley, J.F. Watts, and G. Beamson
Department of Materials Science and Engineering
University of Surrey
Guildford Surrey GU2 5XH UK

INTRODUCTION

One of the most important properties of polymers that has enabled them to be used widely in adhesion and coatings applications is their ability to become readily adsorbed on to solid surfaces [1]. This is due to polymers having large surface areas which produce correspondingly high values of surface activity, and thus, facilitating adsorption [2] as a means of reducing surface activity, (i.e. the surface free energy of the solid).

When a single component homopolymer is cast onto a high energy substrate conformational changes may occur. Such a homopolymer that has been used as a model in studies of polymer/substrate interactions is poly(methyl methacrylate) (PMMA) [3-7]. In recent theoretical studies using a kinetic Ising model, Chakaraborty and co-workers have studied the PMMA/aluminium system [3,4]. These simulation studies have shown a near interface conformation in which the polymer chains tend to lie in a relatively flat orientation parallel to the metallic substrate. This gives a net result in which there appears to be a thin, diffuse, layer of PMMA between the bulk polymer and the substrate. This concept is shown conceptually in Figure 1.

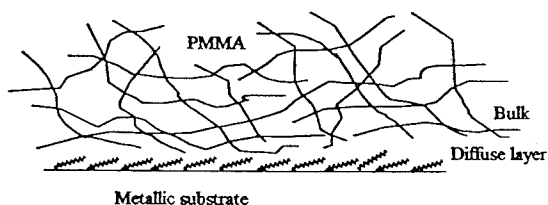


Figure 1. Schematic model indicating the formation of a diffuse interphase between aluminium and bulk PMMA [8].

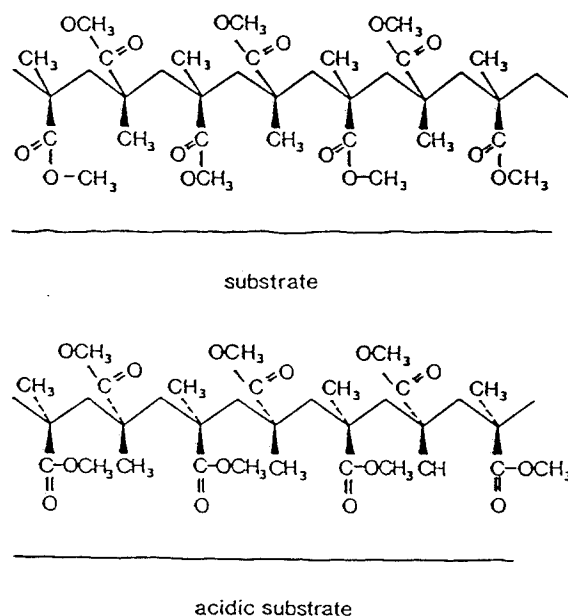


Figure 2. Schematic representation of PMMA indicating re-orientation of the carbonyl group on interaction with an acidic substrate [6].

The concept of a thin, diffuse, layer of PMMA at the surface interface can also be proposed from results of X-ray photoelectron (XPS) studies of PMMA/silicon systems [5,6]. Beamson and co-workers observed that the peak fitting of the C1s spectrum of thin PMMA films cast on to silicon wafers varied with the thickness of the polymer overlayer, and that the thicker layers yielded spectra identical to those taken from bulk PMMA [5]. This difference between thin layers and bulk PMMA was attributed to the acid-base interactions between polar carbonyl and methoxy groups with the acid substrate, the variation in the binding energy of the polar carbon species probably being manifestation of the magnitude of such acid-base interactions. In complementary work by Chehimi and Watts [6], the observation was made, by

angular resolved XPS, that acid or alkali treatment of glass and silicon substrates can lead to the reorientation of the carbonyl group of PMMA at the PMMA/inorganic interface, as shown in Figure 2 [6]. Such orientation was found to be most pronounced at low pH; ie. when acid-base interactions would be at a maximum.

The nature of the acid-base interactions occurring at the interface of PMMA/silicon systems has been investigated in an *in situ* study of using internal reflection infrared spectroscopy [7]. This study showed that the carbonyl groups of the PMMA were hydrogen bonded to silanol sites on the silicon substrate.

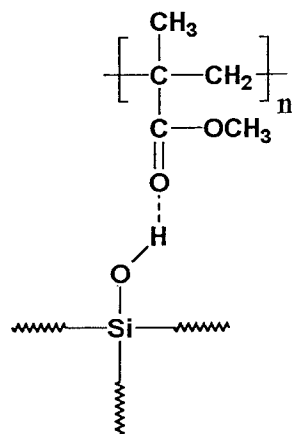


Figure 3. Schematic of the hydrogen bonds formed between the surface silanol groups and oxygen atoms in carbonyl groups on PMMA [7].

Both theoretical and experimental studies indicate that there is an interphase between bulk PMMA and the substrate on which it is cast, that is different in conformation from bulk PMMA. This work shows how XPS studies have been extended in the direct examination of the acid-base bonding of ultra-thin layers of PMMA on model substrates.

EXPERIMENTAL

XPS spectra were acquired using a Scienta ESCA300 X-ray photoelectron spectrometer,

described elsewhere [5]. Silicon substrates were used as received and after treatment with buffered sodium hydroxide solutions with a range of pH values. Thin PMMA films were prepared by spin-casting from chloroform solution on to the silicon substrates.

DISCUSSION

Figure 4 shows a comparison of the C1s spectra of a ultra thin film of PMMA on silicon as recieved and silicon treated in a sodium hydroxide solution at pH 13.4. It can be seen that the binding energy (BE) of the carbonyl species is higher on the treated silicon substrate than that of PMMA cast on the as received silicon.

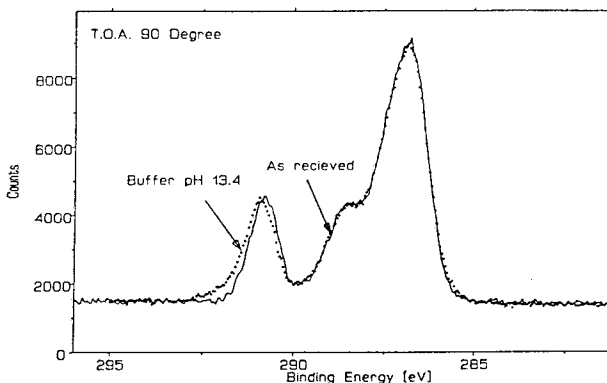


Figure 4. A comparison of C1s spectra of PMMA spin-cast on to silicon substrates as received and treated with alkaline solution.

It was also observed that the carbonyl species of the PMMA spin-cast on to the treated silicon substrate had a greater asymmetry than that observed from the PMMA spin cast on to the as received substrate. When peak fitting the C1s spectrum of PMMA it is conventional to fit four peaks [5], and when peak-fitting the C1s spectrum of the PMMA spin-cast on to the as received silicon substrate an accurate representation of the spectrum was achieved. However, fitting four peaks to the PMMA spectrum of the polymer cast on to the treated silicon substrate did not give as accurate a fit, due to the asymmetry of the carbonyl species. A more accurate fit was

achieved by fitting a fifth peak to the carbonyl species as shown in Figure 5. This indicates that some interaction is occurring between the carbonyl species and the treated substrate.

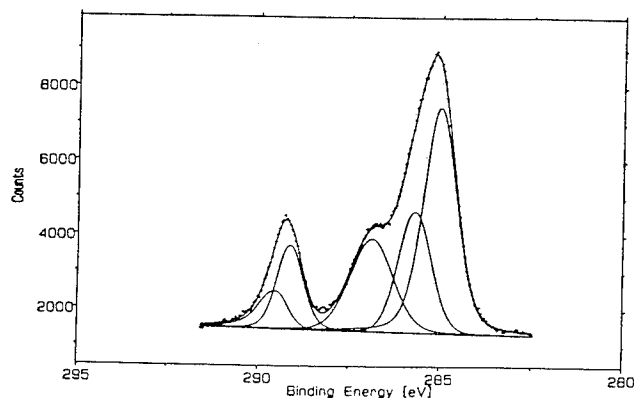


Figure 5. The C 1s spectrum of PMMA spin-cast on to an alkaline treated silicon substrate, using a peak-fitting protocol involving five peaks.

As the PMMA films became progressively thicker the asymmetry of the carbonyl species reduced and the conventional fitting procedure of four peaks was the most accurate method. This indicates that XPS has been able to examine directly the interaction between the carbonyl group and the alkaline substrate.

CONCLUSIONS

XPS has been used successfully in the direct examination of the acid-base bonding of PMMA on model substrates. The interaction between the carbonyl group of PMMA and the alkaline treated silicon substrate was not observed in thicker PMMA films, indicating that the conformational changes involved, only occur at some interphase region between the substrate and the bulk PMMA.

REFERENCES

1. R. Roe, Adhesion and Adsorption of Polymers, ed. L.H. Lee (Plenum Press, New York and London, 1980) 12B p. 629
2. A. Silberberg, Adhesion and Adsorption of Polymers, ed. L.H. Lee (Plenum Press, New

York and London, 1980) 12B p. 591

3. A.K. Chakaraborty, and P.M. Adriani, Macromol. 25, 2470 (1992)
4. J.S. Schaffer and A.K. Chakaraborty Macromol. 26, 1120 (1993)
5. G. Beamson, A. Bunn, and D. Briggs, Surf. Interface Anal. 17, 105, (1991).
6. M.M. Chehimi and J.F. Watts, J. Elec. Spectroscopy. Rel. Phenom. 63, 393 (1993)
7. L. Zazzerra, M. Tirrell and J.F. Evans, J. Vac. Sci. Technol. A 11(4), 2239 (1993)
8. J.F. Watts and A.M. Taylor, submitted to J. Adhes.

DYNAMICS OF ADHESION PROMOTERS AND THE PHYSICAL PROPERTIES OF COMPOSITES

Timothy W. H. Wang and Frank D. Blum

Department of Chemistry and Materials Research Center
University of Missouri-Rolla
Rolla, MO 65401

ABSTRACT

The differences in the behavior of composites with different adhesion promoters have been studied using NMR and mechanical property tests. The two coupling agents used were aminopropylsilane (APS, $\text{SiCH}_2\text{CH}_2\text{CH}_2\text{NH}_2$) and aminobutylsilane (ABS, $\text{SiCH}_2\text{CH}_2\text{CH}_2\text{CH}_2\text{NH}_2$). These exhibit similar chemistry, but differ in their dynamics at the interface. The use of the specifically deuterated coupling agents (DAPS and DABS) allowed them to be probed with solid-state deuterium NMR at the air and polymer interface (in a composite). A comparison of the dynamics of the two systems adsorbed on silica reveal multilayers form a graded interface with respect to molecular mobility. The layer directly in contact with the silica is the most rigid and the outermost layers are most mobile. In the outmost layers, DABS moves about 10 times faster than DAPS. To probe how differences in mobility of these interfacial layers affect the physical properties; composites of glass, coupling agent and epoxy resin were prepared. In terms of strength, modulus, and fracture toughness, it was found that either coupling agent gave improved properties. The properties of the APS system were also generally better than those in the ABS system. We postulate that these differences were due to the differences in mobility at the coupling agent/polymer interface.

INTRODUCTION

Composite materials are composed of two or more components, differing in physical and chemical properties, which have been combined to provide specific characteristics for particular uses. The interfacial region between the components may be significantly different from the nature of the components. It is extremely difficult to make a quantitative determination of the mechanical properties of this interfacial material. Yet to improve the performance of composite materials, it is useful to clarify the properties of the interface and determine its role. It is possible to relate the chemical structures of the interfacial materials to the macroscopic physical or mechanical properties of composites. In many cases, the chemical reactions of

interfacial species have been related to the physical properties of composites. However, fewer studies have focused on an understanding of the dynamics (i.e. molecular motion) of the system. Silane coupling agents are widely used as surface treatments for inorganic materials[1]. Several spectroscopic techniques [2, 3] have been used to study these interfacial materials. In our group [4, 5] we have used selectively ^2H -enriched coupling agents as probes for the investigation of the interfacial region by ^2H solid state NMR.

In present study, we have chosen two structurally-similar deuterium-labelled amino-functional silane coupling agents, namely, γ -aminopropyltriethoxysilane(APS) and γ -aminobutyltriethoxysilane(ABS). We have compared the dynamics of the coupling agent layer in these two systems. We use this information to address the relationship between the mobility of the glass/matrix interface and the resultant flexural strength and fracture toughness by comparing composites made with the two different silane coupling agents.

EXPERIMENTAL

NMR measurements

Fused silica (Cab-O-Sil grade S-17, nominal surface area $400 \text{ m}^2/\text{g}$, primary particle size 7 nm) was donated by Cabot Corp. and dried in oven for 2 days at 400°C prior to use. Deuterated γ -aminopropyltriethoxysilane (DAPS) and γ -aminobutyltriethoxysilane (DABS) were prepared from the reaction of γ -cyanoethyltriethoxysilane (CES) and γ -cyanopropyltriethoxysilane (CPS) with deuterium gas[5].

The deuterated coupling agents were hydrolyzed in acetone/distilled water (10/1) for 24 hours. Fumed silica was then added into the solution. The mixture was shaken, centrifuged, decanted and then dried in vacuum oven at 110°C for half an hour. Epoxy resin and hardener were obtained from Dow Chemical, labelled as DER331 and DEH20, respectively. Deuterated coupling agents and resin were reacted in toluene by heating at 55°C for 1 hr. Solvent was then evaporated under vacuum and then dried overnight

at 120 °C. A 10:1 epoxy/ hardener was well mixed by stirring it for several minutes before the treated silica was added.

A Varian VXR-200 NMR spectrometer was used at 30.7 MHz for deuterium using a modified quadrupole echo pulse sequence (SSECHA). The typical 90° pulse length was 2 μs and the repetition time was 0.5 s. The modified quadrupole echo pulse sequence $[180^\circ\text{-d}_2\text{-}90^\circ\text{-}\tau_1\text{-}90^\circ\text{-}\tau_2\text{-echo}]_n$ contained a 180° prepulse to reduce coherent noise and acoustic ringing. Typically 30,000-40,000 scans were taken to get an adequate signal to noise ratio.

Mechanical Tests

The heat-cleaned E-glass fiber fabrics were made by Owens-Corning Fiberglass Co. γ -aminopropyltriethoxysilane (APS) was purchased from Hüls America and used as received. γ -aminobutyltriethoxysilane (ABS) was prepared by the hydrogenation of cyanopropyltriethoxysilane (CPS) under a pressure of about 100 psi in the present of nickel catalyst at 85 °C [5].

A 2% silane coupling agent solution was hydrolyzed in acetone/distilled water (10/1) for 24 hours, along with the glass fabrics. The treated glass fabrics were washed several times with distilled water and then dried in a vacuum oven at 110 °C for half an hour.

A 10:1 epoxy/hardener mixture was well stirred for several minutes. Laminates were obtained by hand lay-up with 16 treated or untreated glass fabric layers, then cured in a hot press.

Specimens were tested for flexural strength and modulus based on ASTM standard 0790-86 [6]. The testing was done on Instron model 4204. At least, six specimens from each sample plate were used. The flexural strength, S , was calculated from the force at break, P , from:

$$S = (3PL/2bd^2) \quad (1)$$

where L is the span between two support beams, b is width, and d is depth of the specimen. The aggressive environment (wet) tests were conducted on samples which were immersed in boiling water for two hours. Excess water was wiped off the surfaces of the samples.

For the double cantilever beam (DCB) specimen, a precrack was introduced by inserting a sheet of aluminum foil between the center laminate of the composite. The critical energy release rate, G_{Ic} , was calculated by:

$$G_{Ic} = (P_c/2B)(\partial C/\partial a) \quad (2)$$

where P , B , C , a are the applied load, the specimen width, compliance and crack length, respectively. The relationship between C and a was approximated

by:

$$C(a) = Ra^n \quad (3)$$

From equation (2) and (3), the critical energy release rate is given:

$$G_{Ic} = nP_c^2 C(a)/2Ba \quad (4)$$

RESULTS AND DISCUSSION

Adsorption of multilayers (in this case the equivalent of 5 layers based on 4 silanols/nm² being a monolayer) onto silica and then reacted with epoxy are shown in Fig. 1. These measurements show that the half-height width of the spectra are less at higher temperature as expected. These spectra are the results of the superposition of spectra of more rigid materials closer to the surface and more mobile ones further away. As observed in previous studies [5] the spectra for DABS were narrower than for DAPS indicate of more mobility for DABS.

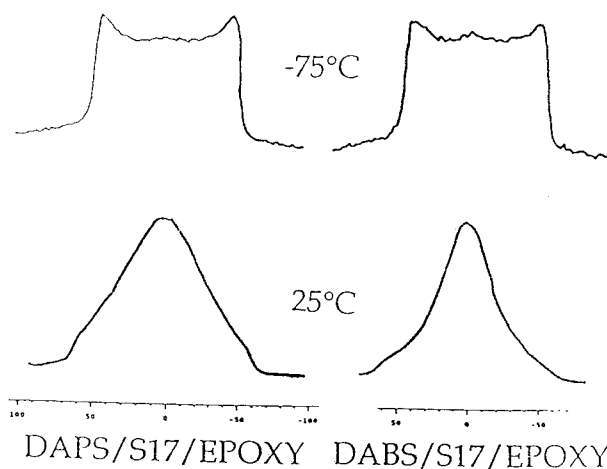


Fig. 1: ²H wideline spectra of DAPS (left) and DABS (right) treated composites at -75 °C and 25 °C.

From the load-displacement curve the compliance, C , was calculated. It was then plotted in a double logarithmic plot as a function of crack length. A typical double logarithmic plot which were based on either the point of crack initiation or crack arrest can be approximated by equation (3). By using the calculated n values in equation (3), the critical strain energy release rate is obtained. Shown in Fig. 2 are the critical strain energy release rate of the three types of composites for both wet and dry applications. G_{Ic} values were calculated at the point where the crack initiated or was arrested. For both crack initiation and arrest, the values of G_{Ic} increased in order of untreated < ABS < APS treated composites [8].

The flexural strengths for all the composites are shown in Fig. 3 for both wet and dry applications. Silane coupling-agent-treated composites are

measurably stronger and stiffer than those of the untreated specimens. Coupling agent treatment results in a bridge being built-up by the coupling agents which connects the fiber and resin. ABS treated specimens have lower flexural strengths than APS treated ones. We believe that this is probably due to the longer chain length of ABS and its concomitant higher mobility. The flexural strengths of all specimens measured dry were higher than those measured wet [9].

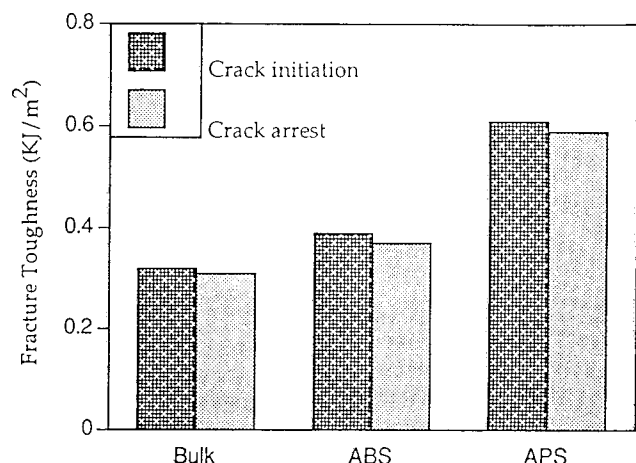


Fig. 2: Critical energy release rate of composites based on either crack initiation or arrest.

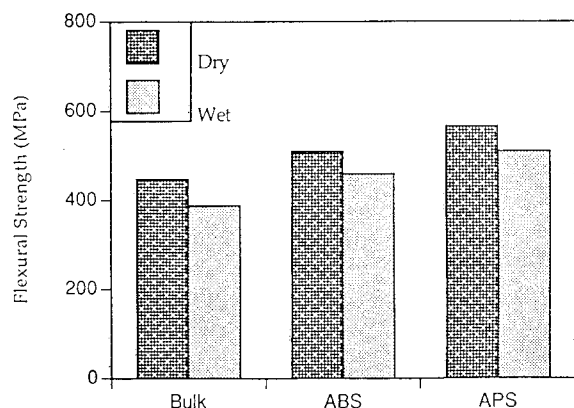


Fig. 3: Flexural strength of the composites based on the dry and wet tests.

CONCLUSIONS

Deuterium wide-line NMR has been used to probe the molecular motion of a coupling agent layer in a composite. The resonances from multilayers (5 layers) of coupling agents between the silica and epoxy shown obvious differences due to the mobility

of the coupling agents. The interlaminar fracture toughness and flexural strength of glass fiber fabric epoxy composites was also influenced by the types of coupling agents used. Untreated composites had the lowest flexural strength and fracture toughness resulting from the poor interface between fiber fabrics and resin.

The APS treated composite has the highest flexural strength and fracture toughness. This means that the coupling agent layer most effectively transferred the load between fiber and resin. The ABS treated composites behave in a manner that is between the untreated and APS-treated composites. The lower strength and modulus obtained for ABS-treated, compared to the APS-treated composite suggests a weaker interface. We believe that this is probably due to the shorter alkyl chain length of the APS which results in a less mobile material than ABS at the coupling agent/epoxy interface. This provides a better graded interface than when ABS is used.

ACKNOWLEDGMENT

We gratefully acknowledge the financial assistance of the Office of Naval Research.

REFERENCES

1. Pluddeman, E. P. 'Silane Coupling Agents' 2nd. ed. Plenum Press, New York, 1991.
2. Ishida, H. and Kumareds, G. 'Molecular Characterization of Composite Interfaces', Plenum Press, New York, 1985, p25.
3. Ishida, H. and Koeing, J. L. *J. Colloid Interface Sci.*, 1978, 64, 555.
4. Kang, H. J. and Blum, F. D. *Macromolecules* 1992, 25, 4526.
5. Kang, H. J., Meesiri, W. and Blum, F. D. *Mater. Sci Eng.* 1990, A126, 265.
6. Standard Test Methods for Flexural Properties of Plastics and Electrical Insulating Materials; Lukens, R. P.; Ed.; Annual Book of ASTM Standards; American Society for Testing and Materials: Pennsylvania, 1972, part 35, p1.
7. Blum, F. D., Meesiri, W., Kang, H. J. and Gambogi, J. E. *J. Adhes. Sci. Technol.* 1991, 5, 749.
8. Wang, T. and Blum, F. D. *Polymer Preprints* 1994, 35(2), 755.
9. Wang, T. and Blum, F. D. *Polymer Preprints* 1995, 36(1), in press.

DETECTION OF SUBADHESIVE HYDRATION OF ALUMINUM ADHERENDS BY ELECTROCHEMICAL IMPEDANCE SPECTROSCOPY

G.D. Davis and P.L. Whisnant
Martin Marietta Laboratories • Baltimore
Baltimore, MD 21227

J.D. Venables
Venables and Associates
Baltimore, MD 21204

INTRODUCTION

Moisture-induced degradation is the principal factor limiting the durability of aluminum adhesive bonds. If the joint relies solely on dispersion or secondary forces, the aluminum oxide surface will preferentially bond to the moisture and the joint will fail [1,2]. In the case of joints that also exhibit physical bonding (mechanical interlocking), the joint will remain intact until the adhesive plasticizes and disengages from the oxide or if the oxide is transformed and the resulting volume change induces high stresses at the bondline and promotes crack propagation to relieve this stress.

The mechanisms by which the physical bonding is disrupted to allow interfacial crack propagation have been the subject of much discussion. Most have concluded or accepted that the bonded aluminum oxide surface will hydrate in a moist environment [2-11]. The evidence for this mechanism includes: 1) the hydration of bare surfaces exposed to moisture; and 2) hydration of wedge test specimens near the crack tip. Because this evidence is circumstantial, some investigators [1,12,13] have questioned if hydration will occur at an intact adhesive-metal interface or only at surfaces exposed directly to moisture. They argue that hydration of the wedge test specimens occurred after the crack propagated past that point and the surface was directly exposed to moisture.

Because the two "chicken and the egg" arguments could not be resolved with previous measurements, we devised an experiment to determine conclusively if hydration can and will occur under an adhesive and if it will induce bond failure. A second aspect of the experiment was to determine if electrochemical impedance spectroscopy (EIS) can detect hydration and bond failure nondestructively.

Although EIS is often used to detect deterioration and delamination of organic coatings [14-16], it has not been used on structural adhesive joints and the effect of various differences in the two types of systems is not known.

EXPERIMENTAL

An open-faced adhesive joint was prepared by curing FM-123 adhesive (70 μm -thick) in contact with an FPL-etched aluminum disk. The specimen was mounted in a Teflon holder that isolated the edges and back from the electrolyte. The holder and support rod were coated with polyurethane to augment the isolation and prevent any contact with the electrolyte. The mounted specimen was immersed in a solution of 0.05 M Na_2SO_4 to provide sufficient conductivity for testing. Initially the solution was at room temperature, but after 1 day, the temperature was increased to 58°C to accelerate any reactions. EIS measurements were made using a PAR Model 273 potentiostat.

The data were analyzed using the Bode plots of impedance magnitude ($|Z|$) versus frequency (ν) and phase angle (α) versus frequency. From time to time, the mounted specimen was removed from the solution and examined visually. It was not removed from the fixture until the end of the experiment. XPS was then used to examine the surface chemistry at various points on the specimen.

RESULTS

Initially, the adhesive exhibited a high resistance ($\alpha=0^\circ$) of $10^7 \Omega$ at low frequencies ($\nu < 100 \text{ Hz}$) and became capacitive ($\alpha \sim 90^\circ$) at higher frequencies ($\nu > 1000 \text{ Hz}$). This behavior is typical of a protective coating on a metal. The high resistance confirms the isolation of the edges and back of the specimen from the electrolyte.

Several changes were noted with increasing exposure including a more than 100-fold decrease in the near-dc resistance and a more than 100-fold increase in the breakpoint frequency ($\alpha=45^\circ$), where the adhesive's behavior changed from being mostly resistive to mostly capacitive. The two parameters are shown as a function of exposure time in Figures 1 and 2. They exhibit trends that are the mirror image of one other. The graphs show four stages:

1. 0-10 days Very rapid change
2. 10-100 days Stabilization and little change
3. 100-150 days Rapid change
4. 150-190 days Stabilization and little change.

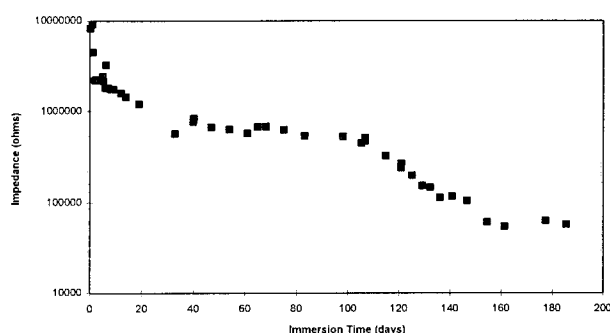


Figure 1. Near-dc impedance (measured at 100 Hz) for the open-faced aluminum bond as a function of immersion time.

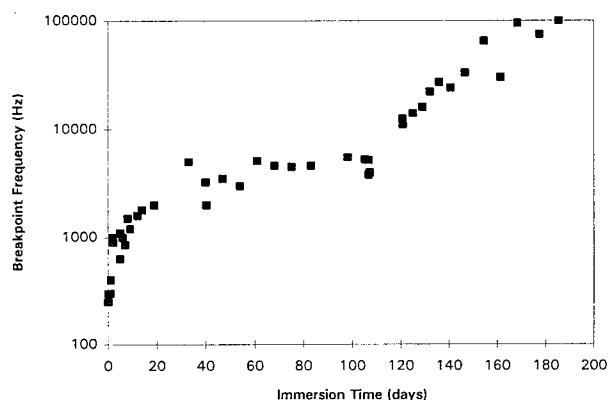


Figure 2. Breakpoint frequency for the open-faced aluminum bond as a function of immersion time.

Visual inspections showed little change in the specimen, except for a fading of the purple color of the adhesive, until Stage 3. At that point, an anomalous area was observed near the edge of the exposed region. After removing the specimen from the fixture, this region resembled white "mountains" in a sea of adhesive. These "mountains" were located where the specimen was exposed to the water, approximately 1 mm from the (protected) edge of the specimen. XPS analysis showed this material to be hydrated alumina erupting through the adhesive.

DISCUSSION

The electrochemical measurements and the long-term immersion of the open-face aluminum bond provided two very important findings: 1) hydration of an aluminum surface occurs under an adhesive; and 2) EIS measurements can detect this hydration.

The observation of hydration underneath the adhesive resolves the question of which comes first - crack propagation or hydration. This specimen had no crack and the edges were sealed from moisture. The only way moisture could reach the substrate surface was to migrate through the adhesive. Not only did the substrate hydrate, but the hydration products erupted through the adhesive. If the specimen had been an aluminum-aluminum joint, the local strength of the bond would have been reduced to zero and the growth of hydration products would generate stresses that would result in crack growth. Thus, one mechanism by which crack propagation in a moist environment is induced is subadhesive hydration of the aluminum substrate.

The detection of hydration by EIS was straightforward. We can associate the four stages of the EIS measurements with the following events:

1. Absorption of moisture into the adhesive; a thin layer of water may form at the adhesive-oxide interface
2. Incubation time for hydration
3. Hydration
4. Direct contact of the external electrolyte with the hydration products/metal.

In Stage 1, water reaching the interface preferentially bonds to the oxide thus breaking the weak secondary bonds that provide the chemical component of the interfacial bond [1,2]. If there are no physical bonds across the interface, interfacial strength is lost and delamination occurs. This is the case with most protective coatings on grit-blasted or cleaned substrates. Up to a certain point, if substrate corrosion is minimal, much of the loss of adhesion can be reversed if the system is dried so that the secondary bonds can re-form. In a properly prepared aluminum bonded structure using FPL-, PAA-, or CAA-treated adherends, the microscopically rough aluminum oxide remains intact and maintains the physical or mechanical bonding that provides interfacial strength even in the presence of moisture.

Stage 2 corresponds to the incubation time for hydration of the aluminum substrate. This incubation time depends on the stability of the surface, the amount of water present at the interface, temperature, pH of the water, and other factors. Interfacial strength is maintained during this period.

Hydration occurs during Stage 3. The second decrease in impedance and increase in breakpoint frequency is caused by the growth of the hydration product and breaching of the adhesive film allowing moisture greater access to the metal substrate. At this point, local adhesion is lost. In a complete joint, the expansion of the oxide as it hydrates would induce local stresses and allow an interfacial crack to initiate and propagate.

In the final stage, with freer access of the moisture to the adhesive-oxide interface, hydration is expected to advance from the initial bulkhead and eventually all of the surface would hydrate. At this point, the adhesive-metal bond would be virtually nonexistent. However, further changes in the impedance and breakpoint frequency are small. These parameters are being controlled by the existing hydration products and breach of the adhesive.

SUMMARY AND CONCLUSIONS

Hydration is shown to occur under an adhesive with no moisture access to the substrate except by migration through the thickness of the adhesive.

This new evidence proves that hydration can lead to crack initiation and propagation.

EIS measurements of both near-dc impedance and breakpoint frequency detected ingress of moisture to the interface and subsequent hydration of the oxide film. Accordingly, such measurements show promise as a means to detect bond deterioration before all strength is lost and delamination occurs.

ACKNOWLEDGMENT

This work was supported by Wright Laboratory, Materials Directorate under contract F33615-93-C-5324.

¹ A.J. Kinloch, *Adhesion and Adhesives* (Chapman and Hall, London, 1987).

² G.D. Davis and D.K. Shaffer, in *Handbook of Adhesive Technology*, A. Pizzi and K.L. Mittal, eds., (Marcel Dekker, New York, 1994), p. 113.

³ J.D. Venables, *J. Mater. Sci.* **19**, 2431 (1984).

⁴ H.M. Clearfield, D.K. McNamara, and G.D. Davis, *Engineered Materials Handbook, Vol. 3: Adhesives and Sealants*, H.F. Brinson, Chairman, (ASM International, Metals Park, OH, 1990) p. 259.

⁵ D.M. Brewis, J. Comyn, and J.L. Tegg, *Intl. J. Adhesion Adhesives* **1**, 35 (1980).

⁶ G.D. Davis, T.S. Sun, J.S. Ahearn, and J.D. Venables, *J. Mater. Sci.* **17**, 1807 (1982).

⁷ J.S. Noland, in *Adhesion Science and Technology: Part A*, ed., L.H. Lee, (Plenum, New York, 1975), p. 413.

⁸ J. Comyn, in *Durability of Structural Adhesives*, ed., A.J. Kinloch (Applied Science, London, 1983), p. 85.

⁹ N.-H. Sung, in *Engineered Materials Handbook, Vol. 3: Adhesives and Sealants*, H.F. Brinson, Chairman, (ASM International, Metals Park, OH, 1990) p. 622.

¹⁰ A.J. Kinloch, *J. Mater. Sci.* **17**, 617 (1982).

¹¹ A.J. Kinloch, L.S. Welch, and H.E. Bishop, *J. Adhesion* **16**, 165 (1984).

¹² J.S. Compton, *J. Mater. Sci.* **24**, 1575 (1989).

¹³ W. Brockmann, O.D. Hennemann, H. Kollek, and C. Matz, *Intl. J. Adhesion Adhesives* **6**, 115 (1986).

¹⁴ F. Mansfeld, *Corrosion* **37**, 301 (1981).

¹⁵ J.R. Scully, *J. Electrochem. Soc.* **136**, 979 (1989).

¹⁶ T.C. Simpson, H. Hampel, G.D. Davis, C.O. Arah, T.L. Fritz, P.J. Moran, B.A. Shaw, and K.L. Zankel, *Prog. Organic Coatings* **20**, 199 (1992).

THE ADSORPTION OF SILANE MOLECULES ON YTTRIUM TREATED STEEL SUBSTRATES: A ROUTE TO IMPROVED BOND PERFORMANCE?

Stephen J Davis and John F Watts

Department of Materials Science and Engineering,
University of Surrey, Guildford, Surrey, GU2 5XH, UK.
Tel 01483 259151, Fax 01483 259508

INTRODUCTION

The use of rare earth treatments (in particular yttrium), to improve bond durability has been described by Cayless and Hazell [1]. They noted a significant increase in durability with certain adhesives, whilst initial bond strengths remained unchanged. With the addition of silane adhesion promoters further improvements to the adhesion performance of an epoxy-yttrium pre-treated steel system were obtained [1]. In this paper we explore the underpinning mechanisms of this phenomenon and present preliminary results on the use of silane adhesion promoters in conjunction with the yttrium methods.

YTTRIUM DEPOSITION

Yttrium deposits in the form of yttrium hydroxide as a result of electrochemical activity and is shown to decorate micro cathodic sites in accordance with stability criteria described in the relevant Pourbaix diagram [1]. The effect of deposition variables and local substrate structure on the yttrium deposit has been addressed elsewhere [2]. The thin (order of nanometers) yttrium hydroxide layer deposits very quickly with the maximum thickness reached after 30s from a 5×10^{-4} M solution. This deposit is not removed by washing in water and remains as an indication of previous electrochemical history. Local heterogeneities significantly affect the yttrium deposition and active sites such as inclusions result in increased deposition of yttrium at the associated cathodic site. Such local deposits are thicker than deposits on the general surface and are associated with a back deposited iron cover [2].

ADHESIVE BOND FAILURE CHARACTERISTICS

Lap shear joints were made using a two part, amine cured, filled epoxy adhesive (Ciba Geigy Araldite 2013) with a $150\mu\text{m}$ glue line thickness. The adhesive was cured at 40°C for 16 hours to produce a highly cross linked

epoxy. Prior to bonding, the iron adherends were abraded to remove a surface enriched manganese layer which resulted from the hot rolling process. After abrasion, the iron was ultrasonically cleaned using acetone. Yttrium pretreatment was then undertaken (2 min in 5×10^{-4} M $\text{Y}(\text{NO}_3)_3$). Following cure and after immersion in pure water the failure load was recorded for a series of both yttrium treated and control specimens using a JJ Lloyd tensile tester.

These initial results show that the yttrium treatment has had little affect on the failure load for these test conditions. The failure surfaces for the as-cured joints showed cohesive failure within the epoxy. After 1200 hours in water the failure surface has two clearly defined regions (Fig 1(a)) and the centre region shows cohesive

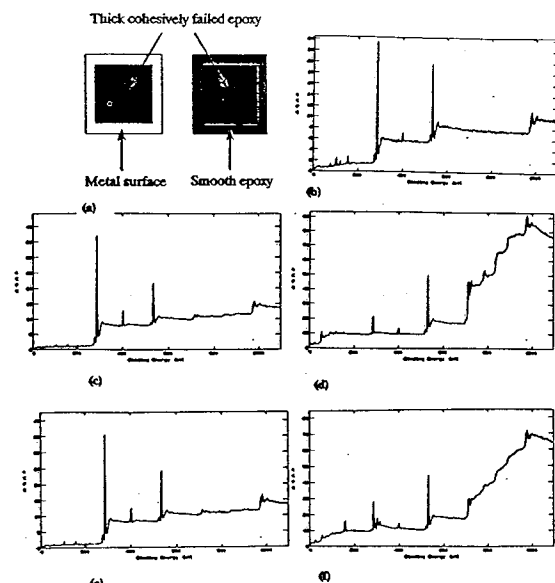


Figure 1.

(a) Schematic of failed joint, 1200 hours in water @ 30°C . SAXPS survey spectrum of the cohesively failed epoxy (b), the epoxy and metal side of the control (c d) and the epoxy and metal side of the yttrium treated (e f).

failure within the epoxy. Failure around the perimeter of the adherend overlap appears visually to be interfacial resulting in a shiny metal surface on one side and a smooth epoxy layer on the other. Small area XPS (700 μ m) was undertaken on the failure surfaces of the 1200 hour immersed sample in the outer failed region as well as the centre cohesively failed region. The survey spectrum from the centre region is given in Fig 1(b) and shows the expected peaks associated with carbon, oxygen and nitrogen (from the curing agent). There are also peaks associated with aluminium and silicon, these are likely to arise from additives used in the adhesive e.g. the filler. Results from the outer region indicate that it has failed interfacially, this is concluded by studying the survey spectra and high resolution spectra for the carbon 1s peak. The metal side of the failed samples show very low levels of carbon and a very clear iron signal, thus supporting the concept of interfacial failure. For the yttrium treated surface, there is a high yttrium signal and associated attenuation of the iron signal by the yttrium layer. The epoxy side however shows no yttrium and this confirms that a thin tenacious yttrium layer has been deposited. The shape of the background of the spectrum can also offer much information [3], following the yttrium peaks at 301 and 313eV the background has a negative post peak slope (PPS), and this is indicative of a surface phase. The nitrogen which is present on both metal surfaces could be from a polymer overlayer, however, it is more likely to have resulted from the uptake of nitrogen from water, such a phenomena is well known and has been described in previous work [4]. The low iron signal on the epoxy side is likely to result from the transfer of a small amount of iron from the metal substrate, on failure. For the yttrium treated sample, such iron must result from the regions of back deposited iron formed over the yttrium layer described above. The lack of yttrium signal on the epoxy side indicated that failure has not occurred within the iron oxide beneath the yttrium layer.

SILANE STUDIES

The combined benefit of a yttrium pre-treatment and silane coupling agents has been shown by Cayless and Hazell [1]. The use of silanes to enhance adhesive durability is the subject of much controversy, however,

their benefit when used in a well controlled manner is well documented [5]. To obtain enhanced performance it is essential to deposit a thin chemically bound tenacious silane layer. To study the adsorption process, uptake isotherms via XPS have shown to offer useful information including the type of adsorption, ie Temkin or Langmuir. Monolayer coverage can also be determined as well as the heat of adsorption [6,7]. Such isotherms have been created in this work using 3-glycidoxypolytrimethoxysilane (Union Carbide A184) from a methanolic solution for deposition onto iron. However, due to problems associated with the overlap of photoelectron peaks (The Si 2p with the Fe 3s and the Si 2s with the Y 3d), XPS could not be used to obtain adsorption isotherms on the yttrium treated sample. ToF-SIMS has been utilised to produce isotherms. Such a route has previously been used for a different system [8]. Results obtained via XPS for adsorption onto iron demonstrate the highly variable nature of silane deposition, as despite rigorous control of experimental parameters, there is variation in the nature of uptake between experimental runs (Fig 2).

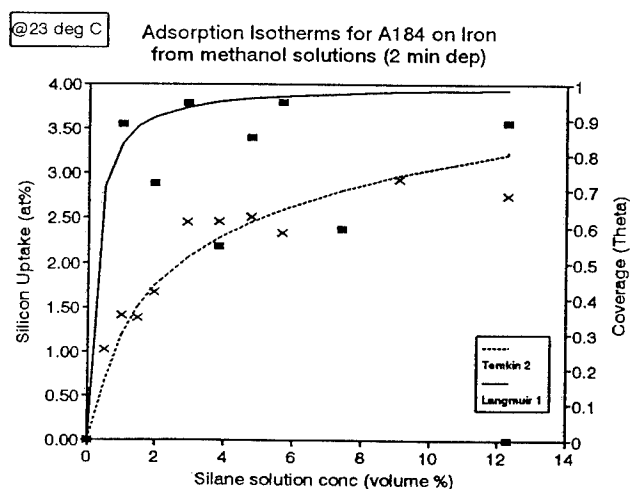


Figure 2. XPS adsorption isotherm of A184 from a methanol solution onto iron.

Initial results from ToF-SIMS isotherms are given in Fig 3. The experimental data obtained in this way is being compared with the results obtained using computer chemistry methods.

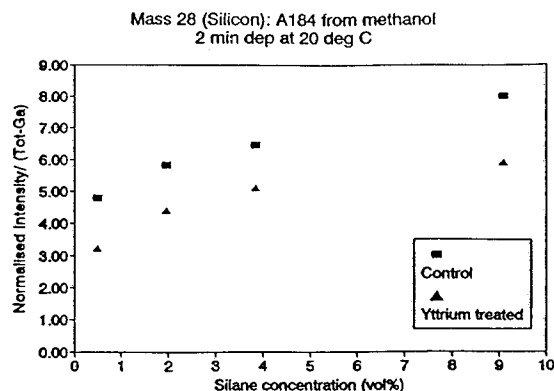


Figure 3. ToF-SIMS adsorption isotherm of A184 from a methanol solution onto iron and yttrium treated iron.

MOLECULAR MODELLING

Recent interest in molecular modelling [9] has led to the development of a number of commercial systems. Modelling the interaction between a chosen molecule (silane) and a surface can offer detailed information which can complement results from surface analytical experiments. In this study it is planned to investigate the nature of molecular alignment with the surface, and to study cooperative effects when the adsorbate is present in higher concentrations. Initial results are presented from work investigating the adsorption of A184 onto a FeOOH surface using Cerius² software (Fig 4).

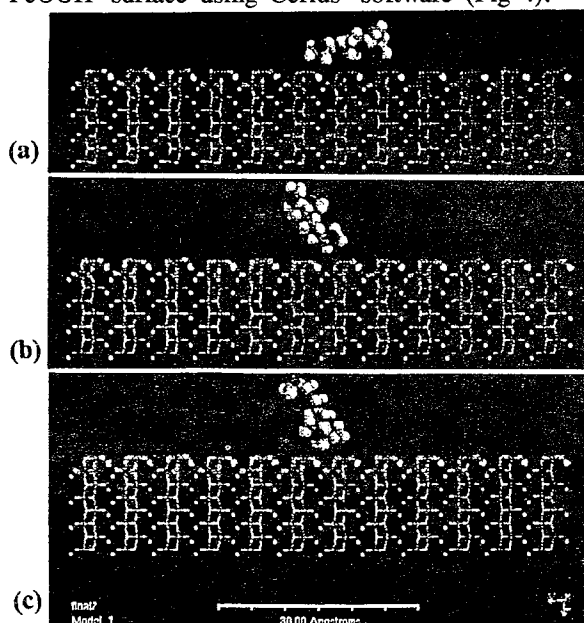


Fig 4. Initial results for the interaction between A184 and FeOOH. Energy minimisation shows that preferred orientation occurs when the silicon end is downwards. (a) 712 kcal/mol, (b) 391 kcal/mol and (c) 369 kcal/mol.

FeOOH was chosen as it has been shown to be the dominant surface phase on air passivated mild steel [10,11]. The orientation of the adsorbed molecule can be determined via energy minimisation and such information can be compared to results from angle resolved XPS (ARXPS) and depth profiles using ToF-SIMS. Initial results confirm that the silane molecule will adsorb with its silicon end towards the iron substrate. Further work will involve the calculation of adsorption sites prior to minimisation to result in a more rigorous model. The deposition of A184 onto yttrium hydroxide will also be modelled to determine the difference between uptake on the two substrates.

CONCLUSIONS

- Failure is interfacial, the rate of adhesive displacement being determined by water diffusion.
- Adsorption isotherms can be obtained using XPS and ToF-SIMS and show chemisorption, probably conforming to Langmuir type.
- Molecular modelling shows promise.
- Bond durability with a combined silane/yttrium pretreatment needs to be investigated.

REFERENCES

- 1 R.A.Cayless and L.B.Hazell. European Patent, EP 0331 284 A1 (1989)
- 2 S.J.Davis, J.F.Watts and L.B.Hazell. *Surf. Inter. Anal.*, **21**, 460 (1994).
- 3 J.E.Castle, R. Ke and J.F.Watts. *Corr Sci*, **771** (1990)
- 4 A.M.Taylor, PhD Thesis, University of Surrey (1994)
- 5 M.Gettings and A.J.Kinloch. *J.Mat Sci*, **12**, 2511 (1977)
- 6 R.Bailey and J.E.Castle. *J. Mat Sci*, **12**, 2049 (1977)
- 7 C.A.Baillie, J.F.Watts and J.E.Castle. *J. Mat Chem*, **2**, part 9, 939 (1992)
- 8 M-L.Abel, M.M.Chehimi, A.M.Brown, S.R.Leadley and J.F.Watts. Submitted to *J.Mat Chem* (1994)
- 9 M.S.Sennett, W.X.Zukas and S.E.Wentworth. *Comp Poly Sci*, **2**, 124 (1992)
- 10 J.E.Castle and J.F.Watts. In *Corrosion Control by Organic Coatings*, ed by H.Leidheiser. published by NACE, Houston, Texas, p78-86 (1981)
- 11 M.W.Roberts and P.R.Wood. *J.Elec.Spec*, **11**, 431 (1977)

PENETRATION OF SILVER INTO SELF-ASSEMBLED ORGANIC MONOLAYERS

G.C. Herdt* and A. W. Czanderna

Measurements and Characterization Branch
National Renewable Energy Laboratory
Golden, CO 80401

Abstract

The purpose of our research is to study the interactions or processes between vacuum-deposited metals (M) and self-assembled monolayers (SAMs) under controlled conditions. Metal/SAM systems are models for understanding bonding at M/organic interfaces and the concomitant adhesion between the different materials. In this work, XPS and ISS were used to characterize octadecanethiol (ODT, $\text{HS}(\text{CH}_2)_{17}\text{CH}_3$), mercapto-undecanoic acid (MUA, $\text{HS}(\text{CH}_2)_{10}\text{COOH}$), and mercaptohexadecanoic acid (MHA, $\text{HS}(\text{CH}_2)_{15}\text{COOH}$) SAMs before and after depositing up to 1.0 nm Ag at ca. 10^{-7} torr. The SAMs were prepared by self-assembly onto gold films on $\langle 100 \rangle$ silicon substrates in an ethanolic thiol solution. XPS spectra indicate that no strong interaction occurs between the deposited Ag and the COOH organic functional group (OFG) of MUA or MHA, although a stronger interaction is evident for MHA. The Ag interaction with ODT is weak. ISS compositional depth profiles (CDPs) for Ag on MHA, MUA and ODT are compared over a temperature range of 113 to 293 K. The ISS results indicate that Ag remains on the surface of MUA for up to 1 h after deposition, whereas Ag penetrates ODT in less than 5 min at 295 K. The time for Ag to penetrate into MHA is several times longer than for MUA, depending on the SAM temperature. Although Ag/OFGs are expected to have relatively weak interactions, the Ag/COOH system was anticipated to be more interactive than was found, so rapid penetration of Ag through the COOH SAM is an unexpected result.

Introduction

This paper summarizes part of recent research [1] to identify metal/organic functional group interactions at metal/self-assembled monolayers (SAM) interfaces, primarily by means of X-ray photoelectron spectroscopy (XPS), or to elucidate penetration rates of metal overlayers through the SAM using ion scattering spectroscopy (ISS). As illustrated in Figure 1a, SAMs have fulfilled a need for model systems with highly ordered organic surfaces of uniform chemical composition for studying interactions at metal or metal oxide/organic interfaces [1-11]. Chemical bonding at metal/organic interfaces plays an important role in the reliability and durability of many technological devices [12]. Until recently, bonding at metal/organic

interfaces was typically studied either by surface analysis of organic species adsorbed onto single crystal metal surfaces [13,14], or by surface analysis of metalized polymers [15,16]. The chemical environment studied in the first type of experiment bears little resemblance to that present at polymer/metal (oxide) interfaces. In contrast, the lack of structural and chemical order of polymer surfaces complicates the location and type of interactions with metal or oxide overlayers.

Less reactive metals (e.g., Ag and Cu) are frequently used as metalization coatings of polymers for mirror applications or as grid lines in photovoltaic cells, which may contain polymer/metal interfaces. For studying the stability or reactivity of interfaces, SAMs are ideal because they form highly ordered, thermally stable arrays of close-packed aliphatic chains terminated by a surface of uniform chemical functionality as originally cited in the work of Allara and Nuzzo [17]. Progress in studying alkane thiol SAMs terminated with CH_3 , OH, COOH, COOCH_3 , and CN with Ti, Cr, Cu, Ni, Al, K, Na, Ag overlayers has been summarized and critically reviewed [10].

Experimental

A detailed list and critique of the experimental measurements used to characterize SAMs is available [10]. For the typical results presented in this article, we prepared SAMs on Au of ODT, MUA, and MHA as described in detail [6]. The in situ evaporative deposition of Ag and ISS analysis of the resulting Ag/ CH_3 and Ag/COOH interfaces have also been described in detail [6]. In contrast to reactive systems, only minor XPS core level line shifts occurred between Ag and either organic functional group (OFG), indicating no strong interaction occurs.

Results and Discussion

We present and discuss in this section one type of the M/OFG combinations studied to date in which there is penetration into the SAM [10]. We also discuss typical results for the rate of penetration in the Ag/ CH_3 and Ag/COOH systems.

* Doctoral student, Materials Sci., University of Denver, Denver, CO.

Penetrating Systems: ISS CDP of Ag/CH₃ and Ag/COOH from 113 K to 293 K

ISS compositional depth profiles were obtained from 113 to 293 K to study the penetration of Ag into ODT, MUA, and MDA, as a function of temperature. For all of these experiments, 1.0 nm Ag was deposited at a rate of approximately 0.01 nm/s onto the SAM prior to depth profiling. The elapsed time after starting metal deposition and completion of the first ISS spectrum was approximately 300 s (100 s, deposition; 160 s, sample transfer; and 40 s, first ISS spectrum). Thus, 5 min elapsed for time-dependent processes to proceed before our "initial" spectrum was taken during depth profiling. An ion beam current density of 0.2 $\mu\text{A}/\text{cm}^2$ was used for all ISS depth profiles. XPS and ISS measurements were carried out on several samples at 193 K and verified that no detectable oxygen signal could be obtained from the ODT samples. These data indicate that no ice formed on the samples during low temperature experiments.

The plots in Fig. 2(a) show the *fraction* of Ag (Ag intensity divided by Ag intensity plus Au intensity) in the ISS depth profiles as a function of erosion time at temperatures from 113 to 293 K. The data are consistent with an increasing rate of Ag penetration to the ODT/Au interface at progressively higher temperatures, which results in greater Au intensities that are detected concomitantly with Ag when the Ag is at the ODT/Au interface. The time to erode through a "bare" ODT SAM to the ODT/Au interface is about 1000 s at 0.2 $\mu\text{A}/\text{cm}^2$. The plots in Fig. 2(a) are consistent with a model of Ag residing on the methyl end group of ODT at liquid nitrogen temperatures and at the ODT/Au interface at 293 K [7]. The data also elucidate the temperature regime over which the rate of penetration increases rapidly. The residual Ag signal for erosion times greater than about 2000 s, which corresponds to the location of the ODT/Au interface, indicates the presence of Ag clusters at the ODT/Au interface.

The integrated initial ISS Ag peak intensity is shown as a function of temperature in Fig. 2(b) and provides a measure of the maximum ISS Ag signal obtainable with our apparatus for 1.0 nm Ag before extensive penetration into the SAM has occurred. In contrast to Fig. 2(a), the initial ISS Ag signal decreases above and below 153 K. The reproducibility of these data was carefully checked for coverages of 1.0 nm Ag. Two additional ISS compositional depth profiles were taken for a coverage of 5.0 nm Ag at 113 K to clarify the unexpected results below 153 K. The initial ISS signal intensity at 113 K and 5.0 nm Ag coverage is approximately the same magnitude as the data taken at 153 K with 1.0 nm Ag coverage. We have not determined if the Ag peak intensity is a maximum at 153 K (1.0 nm Ag) and 113 K (5.0 nm Ag).

The data for Ag/MUA and Ag/MHA in Fig. 2(b) also show a larger initial ISS signal is obtained. Data taken that is similar to that in Fig. 2(a) show the rate of Ag penetration is slower for MUA than for ODT, and even slower for MHA. For example, the ISS peak area was measured at four different positions on the same sample for 1.0 nm of Ag on MUA and MHA as a function of time after

deposition at 295 K after waiting for about 5, 15, 35, and 65 min after deposition; a fifth ISS Ag peak intensity was measured after 900 min for both MUA and MHA. The data show that after deposition Ag remains on the surface of MUA for at least 5 min. and some Ag is on the MUA surface for more than 1 h. For MHA, Ag remains on the surface for more than 1 h (i.e., the Ag ISS intensity is unchanged), and the ISS intensity is only reduced to 68% of its initial value after 15 h, which shows that complete penetration to the SAM/Au interface is greatly retarded by the longer chain (C₁₆ vs C₁₁) MHA. By comparison, 1.0 nm of Ag penetrates ODT in less than 5 min at this temperature [Fig. 2(a)]. Ag on MUA is an intermediate case in which Ag remains on the surface for 5 to 15 min but then penetrates into the MUA, but 15% of the deposit is still on the surface after 1 h.

The time dependence of the slower Ag penetration through MUA and MHA compared with that for ODT at 295 K provides some indication of the mechanism of metal penetration through SAMs. First, weak interactions between Ag and the COOH group may retard the onset of Ag transport through MUA and MHA. We did not detect evidence for formation of a Ag unidentate complex with O, even though Ag-O interactions of 18 kcal/mol to 69 kcal/mol are known to exist. Secondly, we speculate that hydrogen bonding between surface COOH groups results in a more tightly packed SAM and makes penetration of Ag through MUA and MHA more difficult. The CH₃ group on ODT, by comparison, is in free rotation at 295 K and does not retard transport of Ag to the ODT/Au interface. The increased rate of penetration of Ag through MUA relative to that for MHA is attributed to an enhanced defect density in the less tightly packed shorter chain alkanethiol. A third possibility is that the presence of the COOH group on MUA and MHA reduces the number of pinhole defects in the SAM, so that fewer transport pathways are available in these films, again with the MHA more defect free than for MUA.

In Fig. 2(b), the initial ISS Ag peak intensities from CDPs of 1.0 nm Ag on MHA and ODT are compared for temperatures from 113 K to 295 K. The decrease in intensity below 150 K for ODT was discussed in our previous paper [6]. As is seen in Fig. 2(b), a similar decrease occurs for MHA, though below 200 K, and we think the reasons for the decrease are the same as for the Ag on ODT [6]. The initial ISS Ag peak at 295 K for 1.0 nm Ag on MHA is more intense than the most intense initial ISS peak observed for 1.0 nm Ag on ODT. This result indicates that the Ag initially remains longer on the COOH surface of MHA, the ISS may be a maximum for any given temperature. Differences in Ag coverage on ODT and MHA probably result from differences in wetting behavior (and thus clustering) as well as penetration of Ag through the two SAMs. Even though SAMs are model systems for studying interactions at metal/organic interfaces, we emphasize that the systems being studied are complex when metal penetration occurs. Factors dictating the specific structure of metal overlayers on SAMs might include metal nucleation behavior, SAM defect density and domain size, the chemical functionality of the SAM, and the available free volume between alkanethiol chains.

Acknowledgments

The authors are pleased to acknowledge support by the U.S. Department of Energy (DOE) under Contract DE-AC36-83CH10093. G. Herdt thanks Associated Western Universities/DOE for his support as a Laboratory Graduate Fellow.

REFERENCES

1. A. W. Czanderna, D. E. King and D. Spaulding, *J. Vac. Sci. Technol.*, **A 9**, 2607 (1991).
2. D. R. Jung, D. E. King, and A. W. Czanderna, *Appl. Surf. Sci.*, **70/71**, 127 (1993).
3. D. R. Jung, D. E. King, and A. W. Czanderna, *J. Vac. Sci. Technol.*, **A 11**, 2382 (1993).
4. D. R. Jung and A. W. Czanderna, *Mater. Res. Soc. Symp. Proc.*, **304**, 131 (1993).
5. G. Herdt and A. W. Czanderna, *Surf. Sci. Lett.*, **297**, L109 (1993).
6. G. Herdt and A. W. Czanderna, *J. Vac. Sci. Technol.*, **A 12**, 2410 (1994).
7. M. J. Tarlov, *Langmuir*, **8**, 80 (1992).
8. P. Zhang, Ph.D. thesis, Department of Materials Science and Engineering, Pennsylvania State University, 1993.
9. R. L. Opila, K. Konstadinidis, D. L. Allara, and P. Zhang, private communication.
10. D. R. Jung and A. W. Czanderna, *Crit. Rev. Solid State Mater. Sci.*, **19**, 1 (1994).
11. D. R. Jung and A. W. Czanderna, *J. Vac. Sci. Technol.*, **A 12**, 2402 (1994).
12. E. Sacher, J. J. Pireaux, and S. P. Kowalczyk, *Metallization of Polymers*, ACS Symposium Series, series editor, M. J. Comstock, (American Chemical Society, Washington, DC, 1990) and references therein.
13. F. P. Netzer and M. G. Ransey, *Crit. Rev. Solid State Mater. Sci.*, **17**, 397 (1992).
14. M. R. Albert and J. T. Yates, *The Surface Scientist's Guide to Organometallic Chemistry* (American Chemical Society, Washington, DC, 1987).
15. J. M. Burkstrand, *J. Vac. Sci. Technol.*, **20**, 440 (1982).
16. J. M. Burkstrand, *J. Appl. Phys.*, **50**, 1152 (1978), **52**, 4795 (1982).
17. R. G. Nuzzo and D. L. Allara, *J. Am. Chem. Soc.*, **105**, 4481 (1983), *Langmuir*, **1**, 45 and 52 (1985).

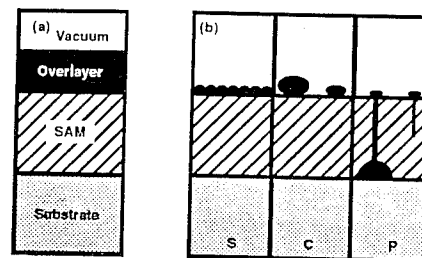


Fig. 1(a). Idealized scheme for using an organized molecular assembly to form an interface between a metal overlayer and a SAM supported on Au; (b) Cross-sections of the principally observed results to date in which there is (S) strong metal-OFG interaction, (C) weak metal-OFG interaction, and (P) very weak metal-OFG interaction. The designations S, C, and P stand for smooth, clustered, and penetrating, respectively.

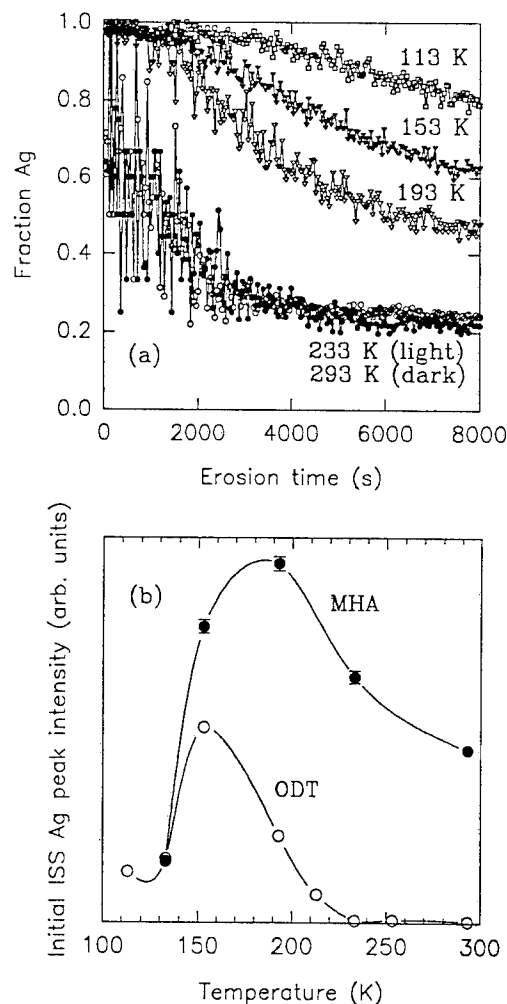


Fig. 2(a). Fraction of Ag signal (see the text) as a function of erosion time at $0.2 \mu\text{A}/\text{cm}^2$ for 1.0 nm Ag on ODT/Au at temperatures of 113, 153, 193, 233, and 293 K; (b) Initial ISS peak intensities for 1.0 nm Ag on MHA and ODT after deposition at temperatures from 113 K.

The Adhesion of Glass Particles to Silicon Substrates

R. C. Bowen, D. S. Rimai, and L. P. DeMejo
Eastman Kodak Company
Rochester, NY 14650-2151

INTRODUCTION

Adhesion induced deformations between micrometer size particles and planar substrates has been the subject of continuing investigation for over 60 years due to its importance scientifically and technologically. As has been shown in recent studies, the stresses generated by the surface forces between particles and contacting substrates can result in either elastic or plastic deformations, depending upon the mechanical properties of the materials.¹

In general the nature of the adhesion induced deformation can be determined from the power law dependence of the contact radius a on the particle radius R . This is because, in the case of an elastic deformation, the contact radius varies as the particle radius to the 2/3 power, whereas, in the case of a plastic deformation, the contact radius varies as the particle radius to the 1/2 power. Details of elastic behavior are given by theories such as those proposed by Johnson et al.² (hereafter referred to as the JKR theory) and Derjaguin et al.³

For glass particles of the sizes used in this study, any elastic deformations should be describable by the JKR theory which, in the absence of any externally applied load, predicts that

$$a^3 = 6w_A\pi R^2/K$$

where K is a function of the Young's moduli and Poisson ratios of the materials and w_A is the work of adhesion. Alternatively, if the deformation is

plastic, it can be described using the Maugis-Pollock (MP) theory, which predicts that

$$a^2 = P + (2w_A/3Y)R$$

where Y is the yield strength of the material. Once the nature of the deformation has been determined, the work of adhesion can be calculated.

EXPERIMENTAL

Soda-lime glass particles (Young's modulus and tensile yield strength approximately 72 GPa and 30 MPa, respectively.⁴ Compressive yield strength approximately 250 MPa.⁵) having radii between approximately 3.0 and 25 μm were gently deposited onto polished silicon wafers and stored for 7 days to allow strains to relax. Contact radii were measured with an SEM by viewing the particle-substrate interface at an 88° tilt angle and correcting for the effects of the 10 nm thick Au/Pd coating. This technique is referred to as the "high tilt method". Alternatively, the contact radii were also determined by evaporating aluminum onto the sample with the sample rotating at 1 rps. This permitted the aluminum to coat the substrate except on the areas where the glass particles were in actual contact with the silicon substrate. This technique is referred to as the "contact area method". Using the contact area method, the radii of various particles were measuring using SEM micrographs. The particles were then removed from the substrate and the precise areas of the substrate which had been in contact with the specific particles were re-examined. The lack of

aluminum coating under the particle created a contrast mechanism which allowed the contact radii to be determined for the specific contacting particles.

RESULTS

The power law dependence of the contact radius on particle radius was determined by linearly regressing the log of the contact radius onto the log of the particle radius. It was found that a varied as $R^{0.42 \pm 0.12}$ for the high tilt data and as $R^{0.43 \pm 0.16}$ for the contact area technique results. These results are consistent with the predictions of the MP theory, by not consistent with those of the JKR model. The average contact and particle radii are shown in Table 1, as are the specific method used to determine those radii, the number of each size particle measured, and the standard deviations about those means. As can be seen, the contact radii obtained using the two distinct measurements are, to within error, identical. It was found that the linear least squares fit lines through the data of the contact radius as a function of the square root of the particle radius intersected the origins for both techniques. This suggests that there are no appreciable applied loads, such as those arising from gravity or electron beam charging.

# of Part.	R (μm)	Std. Dev.	a (μm)	Std. Dev.	Tech.
6	2.74	0.28	0.25	0.06	tilt
5	4.25	0.64	0.29	0.07	tilt
6	21.01	0.91	0.58	0.06	tilt
7	3.39	0.48	0.24	0.11	CAM
11	11.66	1.42	0.50	0.04	CAM
8	22.62	0.97	0.56	0.15	CAM

In addition to the power law dependence of the contact radius on particle radius, the works of calculated work of adhesion can also be used to decide if the adhesion induced deformations are elastic or plastic. Specifically, if the correct deformation theory is used to analyze the data,

reasonable works of adhesion should be obtained. Assuming the validity of the MP theory and calculating w_A from the slopes of the curves, values of 0.69 and 0.55 J/m² are obtained from the high tilt and contact area methods, respectively. These values, although perhaps somewhat higher than expected are reasonable values for this system. On the other hand the value of w_A , calculated assuming that the system were described by the JKR model, as calculated using a contact radius of 0.4 μm for a 10.0 μm radius particle, is approximately 5.6 J/m². This value is unrealistically large.

The power law dependence of the contact radius on particle radius suggest that the adhesion induced deformation is plastic rather than elastic in nature. This is, at first glance, surprising considering the high value of the Young's moduli of both glass and silicon. However, if one considers that tensile interactions contribute greatly to the magnitude of adhesion induced contact radii and that the tensile yield strength of glass is an order of magnitude lower than the compressive yield strength, this observation becomes more plausible. Indeed, the adhesion induced stress on the glass particles, can be calculated using the method of Bowling,⁶ as modified by Rimai et al.¹ Accordingly, the average pressure p exerted by the substrate on the particle is

$$p = 2w_A/z_0$$

where z_0 is the separation distance between the particle and the substrate and is typically of the order of 0.4 nm. By substituting the value of the calculated work of adhesion into this equation it is found that $p \approx 1.5$ GPa, which is greater than either the tensile or compressive yield strength of the glass. Even if the work of adhesion is substantially less than that calculated from the MP model, the pressure would still be greater than the yield strengths.

CONCLUSIONS

The adhesion induced contact radii between micrometer-size glass particles and silicon substrates was found to depend on the particle radius to the 0.42 ± 0.14 power. This result is consistent with the MP model of adhesion, which assumes plastic deformation and

predicts a $1/2$ power dependence, but inconsistent with the JKR model, which assumes elastic response and predicts a $2/3$ power dependence.

¹ D. S. Rimai, L. P. DeMejo, and R. C. Bowen, J. Adhesion Sci. Technol. **8**, 1333 (1994).

² K. L. Johnson, K. Kendall, and A. D. Roberts, Proc. R. Soc. London A **324**, 301 (1971).

³ B. V. Derjaguin, V. M. Muller, and Yu. P. Toporov, J. Colloid Interface Sci. **53**, 314 (1975).

⁴ *Engineering Materials Handbook Vol. 4: Ceramics and Glasses*, ASM International, pg. 1033 (1991).

⁵ *Handbook of Engineering Materials*, pg. 4-152, Wiley, New York (1955).

⁶ R. A. Bowling, in *Particles on Surfaces I: Detection, Adhesion, and Removal*, K. L. Mittal (ed.), pp. 129-142, Plenum, New York (1988).

PARTICLE REMOVAL FROM SMOOTH AND ROUGH SURFACES UNDER SUBSTRATE ACCELERATION

Mehdi Soltani and Goodarz Ahmadi

*Department of Mechanical and Aeronautical Engineering
Clarkson University, Potsdam, NY 13699-5725*

INTRODUCTION

Developing models capable of describing the mobility of particles on a surface subjected to external forces have attracted considerable attention due to their applications in the imaging and semiconductor industries. Numerous studies concerning the particle detachment mechanism from the surface were reported in the literature. Extensive reviews of particle adhesion mechanisms were provided by Corn [1], Krupp [2], Visser [3], Tabor [4], Bowling [5], and Ranade [6]. Accordingly, the van der Waals force makes the major contribution to the particle adhesion force on a surface under dry conditions.

In this work, particle removal due to substrate acceleration is studied. The theory of rolling and sliding detachment are used and the critical acceleration needed for removing particles from a surface under different conditions are evaluated. Different adhesion models and various detachment mechanisms are used in this study. Effects of shape (spherical or cylindrical) on particle removal are studied and discussed. A comparison of model predictions with the experimental data is also presented.

ADHESION MODELS

In this section, the adhesion models for spherical particles used in this study are described. According to the JKR model (Johnson et al., [7]), the pull-off force F_{po} and the contact radius, a , of a spherical particle at the onset of detachment are given by

$$F_{po}^{JKR} = \frac{3}{4}\pi W_A d, \quad (1)$$

$$a = (3\pi W_A d^2 / 8K)^{1/3}, \quad (2)$$

where K is the composite Young's modulus given as

$$K = \frac{4}{3} \left[\frac{(1 - \nu_1^2)}{E_1} + \frac{(1 - \nu_2^2)}{E_2} \right]^{-1}. \quad (3)$$

Here, d is the diameter of the spherical particle, W_A is the thermodynamic work of adhesion, and ν_i and E_i are, respectively, the Poisson ratio, and the Young's modulus of material i ($i=1$ or 2).

For the DMT adhesion model which was described by Derjaguin et al. [8], the detachment force is given by

$$F_{po}^{DMT} = \pi W_A d, \quad (4)$$

which is 4/3 times the JKR force given by equation (1). The contact radius in the absence of external force is, $a_o = (\pi W_A d^2 / 2K)^{1/3}$, which is identical to that of a Hertzian contact. The DMT theory predicts that, at the moment of separation, the contact area is reduced to zero.

For TPL adhesion model as developed by Tsai et al. [9], the corresponding force and contact radius are given by

$$F_{po}^{TPL} = F_o \{ 0.5 \exp[0.124(\Pi - 0.01)^{0.439}] + 0.2 \Pi \}, \quad (5)$$

where the adhesion parameter, Π , is defined as

$$\Pi = \left[\frac{25A^2 d}{288 z_o^7 K^2} \right]^{1/3}, \quad (6)$$

and

$$F_o = \pi W_A d. \quad (7)$$

Here z_o is the minimum separation distance and A is the Hamaker constant. The corresponding contact radius is given as

$$\frac{a}{d} = \sqrt{\frac{K_{20} z_o}{2d}}, \quad (8)$$

with

$$K_{20} = 0.885 [\exp(0.8 \Pi^{0.5}) - 1.0] \quad \Pi \leq 1.6, \quad (9)$$

$$K_{20} = 0.735 \Pi^{0.178} + 0.52 \Pi \quad \Pi > 1.6. \quad (10)$$

The adhesion parameter, Π , for particle diameter between 0.01 to 100 μm varies from 0.01 to 5 for metals and oxides, and from 5 to 200 for polymers.

SURFACE ROUGHNESS MODEL

Consider an elastic spherical particle in contact with a rough deformable surface with randomly distributed asperity height as shown in Figure 1. Soltani et al. [10] proposed an analytical expression for the force

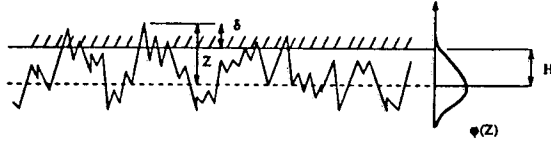


Figure 1: Contact of a Rough Deformable Surface with a Rigid Smooth Surface

needed to detach the particle from rough surfaces. Accordingly, the total pull-off force for a rough surface given as

$$F_M = \pi a^2 N f_{p0} \exp[-0.6/(\Delta_c)^2], \quad (11)$$

where f_{p0} is the maximum force which can be sustained by adhesion before separation of individual asperities, a is the contact radius, and N is the number of asperities per unit area. The standardized variable Δ_c is defined as

$$\Delta_c = \delta_c / \sigma, \quad (12)$$

where σ is the standard deviation of the height distribution, and δ_c is the maximum extension of the tip of an asperity above its undeformed height before the adhesion breaks. According to the JKR adhesion theory

$$\delta_c = \left[\frac{f_{p0}^2}{3K^2\beta} \right]^{1/3}, \quad (13)$$

where β is the radius of an asperities. Note that $\Delta_c^{-1} = \sigma/\delta_c$ is an appropriate measure of surface roughness.

The contact radius of a spherical particle attached to a rough surface is not known. Here the contact radius is estimated base on the JKR theory with an adjusted pull-off load. i.e.,

$$a = (F_M d / 2K)^{1/3}. \quad (14)$$

PARTICLE DETACHMENT

The substrate acceleration causes an effective inertia force to act on the particle parallel to the surface. Particles are removed when this force overcomes the adhesion force and the weight of the particle. The acceleration of the base may be generating by vibration (ultrasonic and megasonic), centrifuge or impact. Figure 2 compare the critical acceleration required to

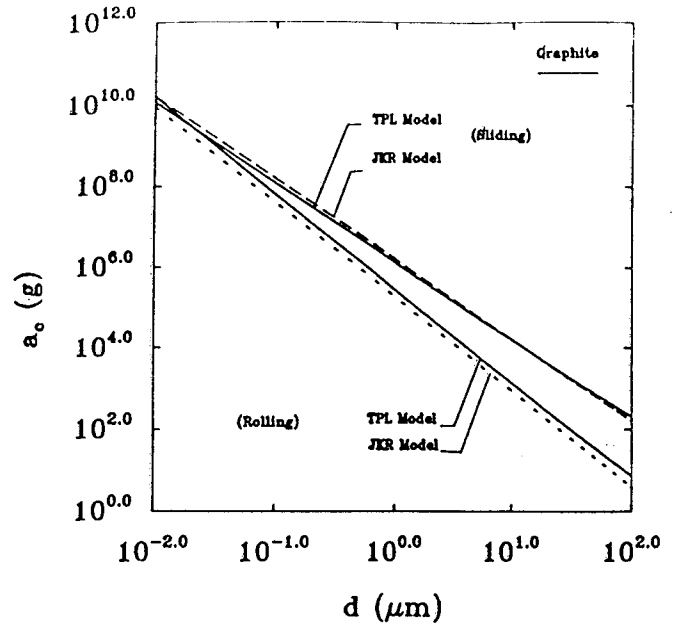


Figure 2: Comparison of the Critical Acceleration Needed to Detach Spherical Graphite Particles From a Graphite Substrate in According to Various Detachment Mechanisms and Different Adhesion Models

remove the particle from the surface for graphite in according to various detachment mechanisms. It is observed that the particle rolling detachment is much easier than particle sliding detachment. A comparison of the predicted critical accelerations for lifting detachment and the experimental data of Mullins et al. [11] for glass particles is presented in Figure 3. Additional details were described by Soltani and Ahmadi [10, 12].

CONCLUSIONS

Based on the presented results, the following conclusions may be drawn:

1. The surface topographic properties such as the number of asperities, the standard deviation of asperity height, and the radius of asperities strongly affect the strength of adhesion force on rough surfaces.
2. Relatively small surface roughnesses can reduce the adhesion force significantly.
3. The critical acceleration needed for the rolling detachment of spherical particles from rough surface is lowest when compared with sliding and lifting mechanisms.
4. The critical acceleration increases as the effective radius of asperities decreases.
5. The critical acceleration reduces as the roughness parameter ($1/\Delta_c = \sigma/\delta_c$) increases.
6. For hard elastic materials (with a high elastic modulus), small surface roughnesses (of the order of atomic scale) could reduce the critical acceleration significantly.

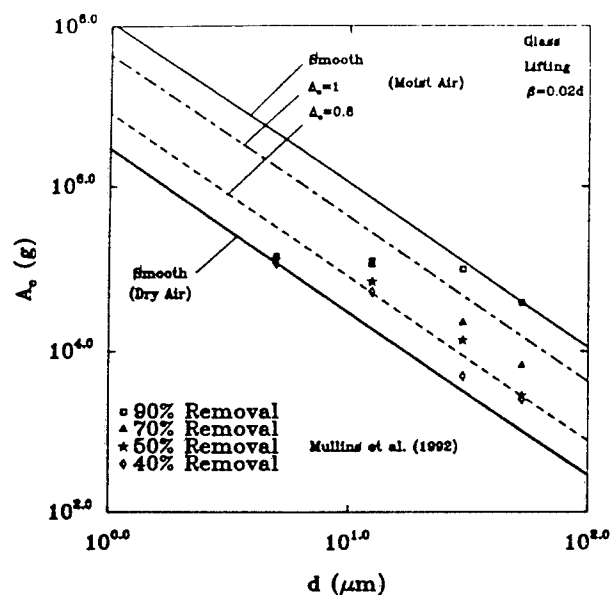


Figure 3: Comparison of the Predicted Critical Acceleration with the experimental Data of Mullins et al. [11] for Glass Particles

7. The effect of gravity on particle detachment is essentially negligible. Such effects may become noticeable as surface roughness and/or particle size increases.

8. The effectiveness of the acceleration-based surface cleaning equipment could be improved by having the force exerted in the plane tangent to the surface.

The presented results are for spherical particles and surface roughnesses which are much smaller than particle size. Studying the effect of particle geometries and surface roughnesses larger than particle size are left for future studies.

REFERENCES

1. M. Corn, in *Aerosol Science*, C. N. Davies, Ed. (Academic Press, New York, 1966, pp. 359.
2. H. Krupp, *Adv. Colloid Interface Science*, **1**, 111-140, (1967).
3. J. Visser, *Adv. Colloid Interface Sci.* **3**, 331-363, (1972).
4. D. Tabor, *J. Colloid Interface Sci.*, **58**, 2-13, (1977).
5. R.A. Bowling, *J. Electrochem. Soc. Solid State Science Technol.*, **132**, 2208-2219, (1985).
6. M.B. Ranade, *J. Aerosol Sci. and Technol.*, **7**, 161-176, (1987).
7. K.L. Johnson, K. Kendall and A.D. Roberts, *Proc. Royal Soc. Lond.*, **324**, 301-313, (1971).
8. B.V Derjaguin, V.M Muller, and Y.P.T Toporov, *J. Colloid Interface Sci.*, **53**, 314-326, (1975).

9. C.J. Tsai, D.Y.H. Pui and B.Y.H. Liu, *J. Aerosol Sci. Technol.*, **15**, 239-255, (1991).
10. M. Soltani and G. Ahmadi, *Report No. MAE-270, Clarkson University*, (1993). Also *J. Adhesion. Sci. Technol.* (In Press)
11. M.E. Mullins, L.P. Michaels, V. Menon, B. Locke and M. B. Ranade, *J. Aerosol Sci.*, **17**, 105-118, (1992).
12. M. Soltani and G. Ahmadi, *Report No. MAE-265, Clarkson University*, (1993). Also *J. Adhesion. Sci. Technol.* (In Press)

A SIMPLE MODEL FOR THE EFFECTS OF TIME ON THE ADHESION OF SUBMICROMETER PARTICLES TO SUBSTRATES

F. Zhang and A. A. Busnaina

Clarkson University, Potsdam, New York 13699-5729

and

D. S. Rimai

Eastman Kodak Company, Rochester, New York 14650

1. INTRODUCTION

The detachment of submicrometer particles from surfaces is of great significance in many industries, such as semiconductor, xerography, pharmaceutical, etc. In order to remove these particles, it is necessary to understand the adhesion and deformation between the particles and the substrate in contact. Although various theories concerning the adhesion-induced deformation have been introduced, the adhesion between two materials is still complicated if one of them deformed viscoelastically.

In this study, a viscoelastic model will be introduced. Predictions of the model will be compared with the experiments of Krishnan, Busnaina, Rimai, and DeMejo [1].

2. THEORETICAL BACKGROUND

2.1. Adhesion Forces

For small uncharged particles (diameter $d < 50 \mu\text{m}$) on uncharged substrates, van der Waals forces are assumed to be predominant [2]. Therefore, only van der Waals interaction will be considered in this study.

The van der Waals attractive force for a sphere and substrate [3] can be written as

$$F_0 = \frac{AR}{6z_0^2} \quad (1)$$

where A is the Hamaker constant, R is the radius of the spherical particle, and z_0 is the separation distance between the particle and the substrate.

Bowling [2] gave the total van der Waals force including the component due to the deformation as

$$F_a = \frac{AR}{6z_0} \left(1 + \frac{a^2}{Rz_0} \right) \quad (2)$$

where a is the contact radius between the deformed particle and surface. Tabor [4] presented a relationship between the van der Waals force for an undeformed particle on a substrate and the energy of adhesion w by:

$$F_0 = 2\pi wR \quad (3)$$

2.2. Adhesion-induced Deformation

Derjaguin [5] was the first to consider the effect of contact deformation on adhesion. Krupp [6] first suggested that an adhered particle could deform elastically in the outer annular region and plastically in the inner circular region of the contact area. The radii of the inner and outer zones were determined by Young's modulus E , and a time dependent hardness $H(t)$ which was assumed to reach a constant value H within a period of 30 minutes.

$$\pi a_0^2 = \frac{F_0}{H(t)} + \frac{1}{3} \left[\frac{\pi^{3/2} (1-\nu)^2 RH(t)}{2E} \right]^2 \quad (4)$$

$$\pi a_0^2 = \frac{F_0}{H(t)} - \frac{2}{3} \left[\frac{\pi^{3/2} (1-\nu)^2 RH(t)}{2E} \right]^2 \quad (5)$$

where a_0 represents the contact radius due to total deformation and a_1 is the contact radius due to plastic deformation.

The JKR theory [7,8] considered the contributions of the tensile interactions due to the surface energy and extended Hertz theory to the adhering contact of particles on planar substrate

$$a^3 = \frac{6w\pi R^2}{K} \quad (6)$$

where $K = 4/3 \left[(1 - \nu_1^2)/E_1 + (1 - \nu_2^2)/E_2 \right]^{-1}$ and w is the energy of adhesion, E_1 , E_2 , ν_1 , and ν_2 are the Young's modulus and Poisson's ratio of two contact materials.

Maugis and Pollock [9] (MP) generalized the JKR model to include plastic deformations and predicted that the contact area was determined by the hardness H of the deformed solid and the work of adhesion of the contact solids in the absence of applied loads.

$$a = \sqrt{\frac{2wR}{H}} \quad (7)$$

3. EXPERIMENTAL BACKGROUND

Rimai et al. [10, 11] measured the deformation radius between polystyrene particles and silicon substrate. They found that the contact radius is approximately proportional to the square root of the particle radius. They calculated the energy of adhesion using the MP model. The values of the work of adhesion w , hardness H , and Young's Modulus E are: $w = 0.32-0.72 \text{ J/m}^2$, $H = 27-32 \text{ MPa}$, and $E = 2.5-3 \times 10^9 \text{ Pa}$ corresponding to the respective periods of deposition time, one day and two weeks.

Krishnan, Busnaina, Rimai, and DeMejo [1] carried out a series of experiments to study time dependent adhesion-induced deformation of polystyrene latex particles on a silicon substrate using scanning electron microscopy. The results showed that the contact area between the particles and the substrate increased with time, reaching a constant value 72 hours later (as shown Figure 1). They found that the contact area (within one hour of deposition) was consistent with the MP model but the final contact area (after one week) was higher than that

predicted by MP model because of material creep of the polystyrene particles. The Maugis and Pollock model predicts a contact area of $0.12 \mu\text{m}^2$, which is consistent with the experimental value. The contact area predicted by the JKR model (considering elastic deformation) is too small ($0.019 \mu\text{m}^2$).

4. THE VISCOELASTIC MODEL

Krupp [6] derived his second alternative adhesion model based on the assumption [12] that the strain ϵ obtained by linear stress-strain measurements is approximately proportional to the ratio a/R of the radius of the adhesion area over that of the particle,

$$\epsilon = c \frac{a}{R} \quad (8)$$

where the proportionality constant c depends on the materials considered.

For the polymeric materials, the strain of particle/substrate might be further assumed as:

$$\epsilon = c \frac{a}{R^m} \quad (9)$$

where m is associated with different compressive and deformation conditions (elastic, elastic-plastic, full-plastic).

The mean stress σ is equal to the total van der Waals force F_a over the contact area πa^2 , where a is the radius of contact area.

Polymers often show nonelastic deformation as

$$\sigma = \frac{F_a}{\pi a^2} \quad (10)$$

experimental data showed for the PSL particles deposited on the silicon wafer [1]. Polymer solids can be considered as a class of viscoelastic materials, which means a combination of both viscous and elastic properties. The mechanical models are made of these two kinds of components: the Hooke spring $\epsilon = \sigma/E$ and the linear viscous element (represented by a damper) $d\epsilon/dt = \sigma/\eta$, where η is viscosity.

Using the Boltzmann Superposition Principle, the deformation due to a complicated stress or strain can be readily computed. Linear viscoelasticity is assumed, so the responses to the imposed stresses are additive.

A combination of a spring and a Voigt element gives the important three-element model [13,14].

$$\varepsilon = \varepsilon_e + \varepsilon_{\text{Voigt}} \quad (11)$$

or

$$\frac{d\varepsilon(t)}{dt} + \frac{\varepsilon(t)E}{\eta} = \frac{1}{E} \frac{d\sigma(t)}{dt} + \frac{\sigma(t)}{\eta} \quad (12)$$

For a constant stress in creep (elasto-plasticity) experiments we get:

$$\varepsilon(t) = \sigma_0 \left[\frac{1}{E_1} + \frac{1}{E_2} (1 - e^{-t/\tau}) + \frac{1}{\eta} t \right] \quad (13)$$

where $\varepsilon(0) (= \sigma_0/E_1)$ is the instantaneous strain and $\tau (= \eta/E_2)$ is the relaxation time. Since η is of the order of months, the last term can be neglected for short time periods. Since the initial deformation measurement is so large, $a/R \approx 30\%$ [1] that $Rz_0 \ll a_0^2$, we can neglect the Rz_0 term. Therefore, the stress $\sigma = F_0/\pi a^2(1 + a^2/Rz_0) \approx P_0 = F_0/\pi R z_0$ is approximately constant. Combining equations and neglecting the last term, we get:

$$a = P_0 R^m \left[\frac{1}{J_1} + \frac{1}{J_2} (1 - e^{-t/\tau}) \right] \quad (14)$$

where $J_1 = cE_1$ and $J_2 = cE_2$

$$a_1 = P_0 R^m \left[\frac{1}{J_1} + \frac{1}{J_2} (1 - e^{-t/\tau}) \right] \quad (15)$$

When $t = 1$ hour, combining a_1 with the MP model, we get:

$$\frac{1}{J_1} + \frac{1}{J_2} (1 - e^{-t/\tau}) = \frac{z_0}{\sqrt{2wH}} \sqrt{\frac{R}{R^{2m}}} \quad (16)$$

Since the left side of the equation depends on the material properties only, m should be equal to $1/2$. Substituting $a(t=1) = 0.138 \mu\text{m}$, $a(t=20) = 0.160 \mu\text{m}$ and $a(t=72) = 0.187 \mu\text{m}$ from [1], we get:

$$a = \frac{2w\sqrt{R}}{z_0} (C_1 - C_2 e^{-t/\tau}) \quad (17)$$

where $C_1 = 1/J_1 + 1/J_2 = 1.12 \times 10^{-13}$, $C_2 = 1/J_2 = 0.35 \times 10^{-13}$ and $\tau = 41$ hours.

5. RESULT AND DISCUSSION

The predicted values of the contact radius for deposition time after 72 hours are shown in Figure 1. The predicted values are in good agreement with the experimental data.

Further measurements of the deformation of PAL particles of different sizes are needed to verify the validity of this model with the exponent $m = 1/2$, which is associated with materials of high surface energy and large plastic deformation.

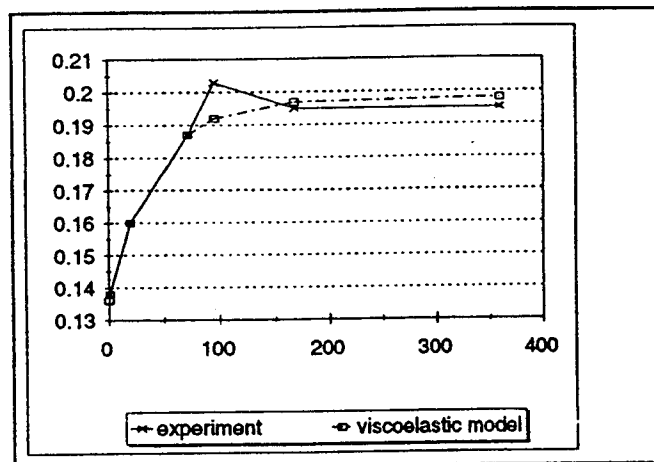


Figure 1.

References

1. Krishnan, S., Busnaina, A. A., Rimai, D. S., DeMejo, L. P., J. Adhesion Sci. Tech. (1994).
2. Bowling, R. A., Particles on Surface 1: Detection, Adhesion and Removal, K. L. Mittal (Ed.), pp. 129-142, Plenum Press, New York (1988).
3. Hamaker, H. C., Physica 4, 1058 (1937).
4. Tabor, D., J. Colloid Interface Sci., 58, 2 (1977).
5. Derjaguin, B. V., Kolloid Z. 69, 155 (1934).

6. Krupp, H., Adv. Colloid Interface Sci., 1, 111 (1967).
7. Johnson, L., Kendell, K., Robert, A. D., Proc. R. Soc. London A, 324, 301 (1971).
8. Muller, V. M., Yushchenko, V. S., Derjaguin, B. V., J. Colloid Interface Sci., 92, 92 (1983).
9. Maugis, D., Pollock, H. M., Acta Metall., 32, 1323 (1984).
10. Rimai, D.S., DeMejo, L.P., Bowen, R.C., J. Appl. Phys., 68, 12 (1990).
11. Rimai, D. S., Moore, R. S., Bowen, R. C., Smith, V. K., Woodgate, P. E., J. Mater. Res., 8, 662 (1993).
12. Tabor, D., The Hardness of Metals, Clarendon Press, Oxford (1951).
13. Aklonis, J. J., MacKnight, W. J., Shen, M., Introduction to Polymer Viscoelasticity, Wiley-Interscience (1972).
14. Krevelen, D. W. V., Properties of Polymer, Elsevier (1990).

Toner Adhesion: The Effect of Non-uniform Surface Charge Distributions

E. A. Eklund, W. H. Wayman, L. J. Brillson and D.A. Hays
Wilson Center for Research and Technology
Xerox Corporation
800 Phillips Rd. 114-23D
Webster, NY 14580

INTRODUCTION

The adhesion of charged toner particles places fundamental limits on electrophotography.[1] Despite its importance, however, the underlying physics governing toner adhesion is poorly understood. The simplest model of toner adhesion, the so-called image force model, assumes that the toner particles can be approximated by spheres with uniform surface charge density. The adhesion is attributed to the Coulombic attraction between the charged particle and its image charge in the substrate. Unfortunately, the image force model underestimates measured adhesion forces by 10 to 50 times.[2-5] In addition, predictions from other models in which short range and/or contact forces provide the bulk of the adhesion[6] do not agree with results from centrifuge and electric field detachment experiments.[2-5,7-11]

In reality, toner particles are highly irregular in shape due to the grinding process used in their manufacture. Also, toner is charged triboelectrically by mixing with larger carrier beads, a process which is expected to produce charge primarily on the areas of most intimate contact. An adhesion model which accounts for these non-uniformities in shape and charging is the charge patch model.[3,7,8] Figure 1 depicts a charged, irregularly shaped toner particle. Triboelectric charging produces patches of charge density σ on the protruding regions of the particle. It is assumed that, for a particular set of toner and carrier bead materials mixed at a certain toner concentration, the charge density σ is nearly constant. A_t is the total charged area on the particle and the sum of the charged areas in contact with the substrate is denoted by A_c . The model also assumes that the extent of a charged area in contact is much greater than the average distance between the charged surface and the substrate. For these conditions the electrostatic component of adhesion can be approximated by the expression for the force between two oppositely charged sheets. In addition, the model includes non-electrostatic contributions to the adhesion force, which also depend on the area of contact between the particle and the substrate. The total adhesion force is

$$F_a = \sigma^2 A_c / 2\epsilon_0 + W A_c = qf[\sigma/2\epsilon_0 + W/\sigma] \quad (1)$$

where $W A_c$ is the non-electrostatic component of adhesion, $q = \sigma A_t$ is the total charge on a toner particle, and $f = A_c/A_t$ is the ratio of the contact area to the total charged area on the particle. It is assumed that the force of adhesion due to the remaining charge on the particle, which is given by Eqn. (1), can be neglected in comparison to the force given by Eqn. (2). Also, since the electrostatic force has a longer range than the non-electrostatic force, the actual contact areas for the two will differ. The model assumes that the area associated with the non-electrostatic force is proportional to the area of the charge patches, A_c . For $q = 8 \text{ fC}$, $\sigma = 100 \text{ nC/cm}^2$ and $f = 0.2$ (estimated from particle morphology), the electrostatic component of the total force of adhesion is 100 nN, comparable to experimentally measured values.

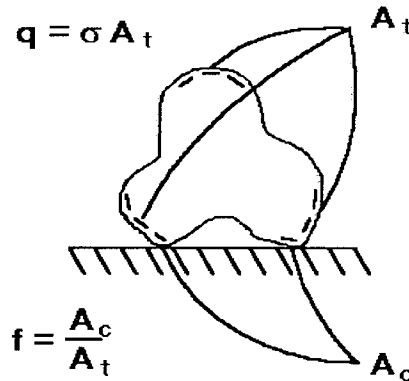


Figure 1. An irregularly shaped, charged toner particle.

Neglecting polarization, the applied force due to an external electric field is $F = qE$. Equating this to the adhesion force in Eqn. (1) gives the expression for the detachment field.

$$E_D = f[\sigma/2\epsilon_0 + W/\sigma] \quad (2)$$

Thus, according to Eqn. (1), electric field detachment probes the distribution of toner contact areas with a substrate by measuring particle adhesion.. In order to connect adhesion and contact area directly, we have added the capability of measuring particle contact area during detachment.

EXPERIMENTAL TECHNIQUE

Figure 2 is a schematic diagram of the apparatus used to measure the contact area of charged toner particles adhered to a conducting electrode. The transfer cell consists of two transparent, conducting electrodes, each possessing a sensor to detect the presence of toner.[12] The electrodes are held apart by an insulating spacer. The detection system operates on the principle of frustrated total internal reflection. A prism mounted to the back of each electrode allows an infrared light beam ($\lambda = 940$ nm) to enter and reflect from the front face of the plate. The light undergoes total internal reflection, creating an evanescent electromagnetic field just outside the surface of each electrode. Toner particles deposited on this surface allow some of the light to be transmitted into the gap, thus reducing the reflected intensity in proportion to the toner contact area. By monitoring the intensity of the totally internally reflected beam, it is possible to obtain a direct measure of the average contact area of the toner particles on each electrode as they are transferred across the gap by the applied electric field.

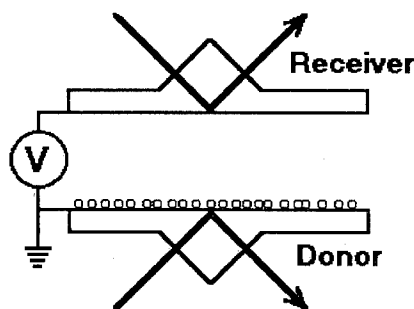


Figure 2. Schematic diagram of the transfer cell used to measure toner-substrate contact area as a function of applied voltage V .

Toner is initially deposited on the donor electrode by means of a development system in which a toner cloud is formed by an AC voltage applied to a toned roll assembly. The toner coverage is varied by changing the speed of the donor electrode as it passes over the development system, holding all other electrical deposition conditions constant. For the data presented here, the volume average particle diameter is $20\ \mu\text{m}$ and the average q/d ratio (from charge spectrograph measurements[13] of the transferred particles) is $-1.0\ \text{fC}/\mu\text{m}$. Thus q , the charge per particle, is approximately $-20\ \text{fC}$. The toner coverage was kept below one monolayer ($1.2\ \text{mg}/\text{cm}^2$) to avoid significant stacking of particles. The gap between the electrodes is $250\ \mu\text{m}$ and the maximum field possible is $18\ \text{V}/\mu\text{m}$. To avoid air breakdown, the transfer cell was evacuated to pressures below 10^{-5} Torr before applying any voltage. The electric field ramp and the acquisition of signals from the sensors

are both computer controlled, allowing simultaneous measurements of the toner contact areas on both electrodes as a function of the electric field between them.

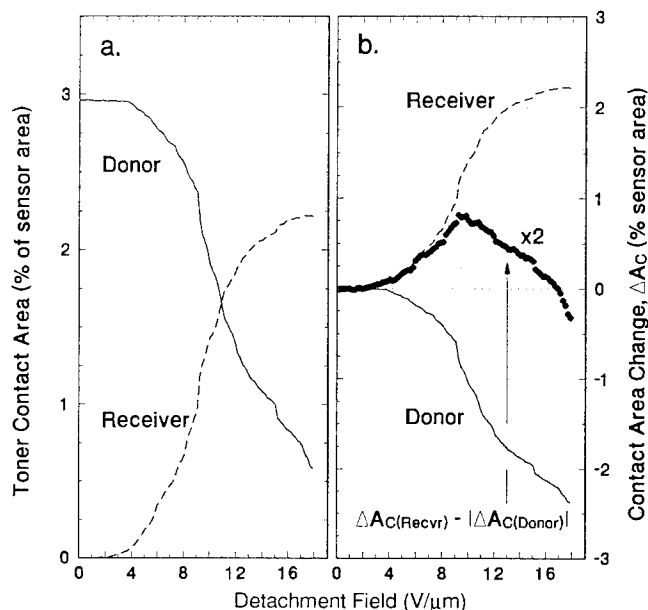


Figure 3. Changes in toner contact area on the transfer cell electrodes as a function of the applied field. In panel b, the filled circles show the difference in contact area change between the receiver and donor. The initial toner coverage on the donor electrode is $0.32\ \text{mg}/\text{cm}^2$.

Figure 3a shows plots of the toner contact areas on both electrodes as a function of the applied electric field for an initial coverage on the donor plate of $0.32\ \text{mg}/\text{cm}^2$ ($\sim 1/4$ monolayer). To allow a comparison of the data from the donor and receiver electrodes on the same scale, the results for A_c are plotted as a percentage of the total sensor area on each electrode. As expected, the contact area on the donor decreases as toner is removed and the contact area on the receiver increases as the particles are transferred. Approximately 80% of the toner initially on the donor was transferred by ramping the applied field to $18\ \text{V}/\mu\text{m}$ over a time interval of 2 min. More importantly, toner transfer occurs over a wide range of applied field values, from 4 to $18\ \text{V}/\mu\text{m}$. According to Eqn. (2), this behavior is a direct manifestation of the distribution in particle contact areas initially on the donor electrode. Figure 3b shows this same data plotted as the contact area change from the initial values at zero field. In addition, the filled circles show the difference in contact area change between the receiver and donor electrodes, amplified by a factor of 2. In all of our investigations, this change is non-zero throughout most of the applied field range, indicating that, in general, toner particles change their contact area when transferred. In Figure 3b, the relative contact area difference is positive

for fields up to $17 \text{ V}/\mu\text{m}$, implying that particles transferred in this field range have, on the average, smaller contact areas on the donor electrode than when they attach to the receiver. This is consistent with the notion that toner particles with the lowest adhesion (ie smallest areas of contact) are removed from the donor first, landing on the receiver with a new (higher) average contact area. The reverse is seen for fields above $17 \text{ V}/\mu\text{m}$, where the particles with the highest adhesion (largest contact area) were detached and transferred. The detachment process is thus selective based on contact area, while the transfer to the receiver produces a randomizing effect on a particle's area of intimate contact with the substrate. These findings are consistent with the charge patch model of adhesion.

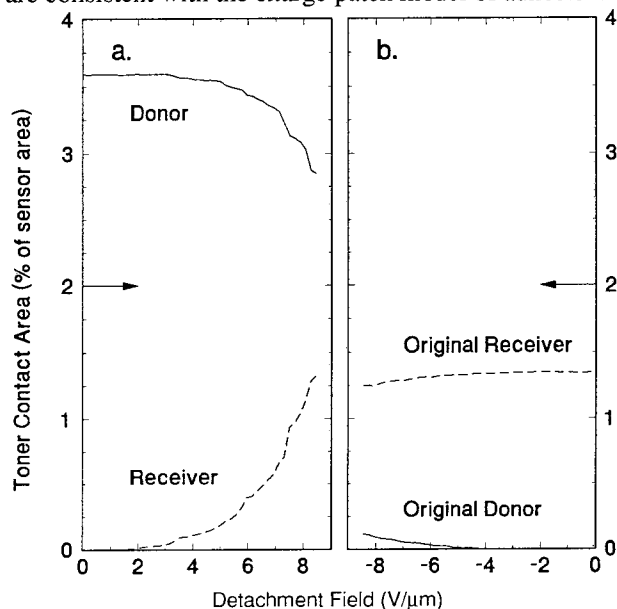


Figure 4. Toner contact area changes for (a) partial transfer and (b) back-transfer. (The original donor electrode was cleaned before the back-transfer.) The field ramp direction is indicated by the arrows.

Additional contact area was found by transferring particles from the receiver back to the original donor electrode. Results from such an experiment are shown in Fig. 4. In this experiment, particles are detached from the donor electrode (with initial loading of $0.45 \text{ mg}/\text{cm}^2$) and are transferred to a clean receiver by fields up to $8.6 \text{ V}/\mu\text{m}$. This partial transfer removes about 30% of the initial particles from the donor. From the discussion above, this transfer selects particles with the lowest adhesion, due to their low contact area. The donor electrode was then cleaned and the field ramped to the same magnitude in the reverse direction to cause transfer back to the original donor. If the toner particles had not changed their contact area, one might expect a complete (100%) back transfer efficiency. Figure 4b shows that the contact area change

for the back transfer is small, indicating incomplete transfer. In addition, weighing of the electrodes confirms that only 39% of the toner has been transferred back to the original donor electrode. This increase in adhesion is direct evidence that the toner particles have increased their contact area during the initial transfer. Thus, the contact area of a particle is not unique.

CONCLUSIONS

The charge patch model of toner adhesion accounts for the non-uniform charging expected for toner particles used in electrophotography. It predicts an enhancement of the particle adhesion forces as a result of this non-uniform surface charge distribution, in agreement with experimental results in the literature. Our experiments were designed to test the charge patch model by measuring the toner / substrate contact area, a key variable in the model, during electric field detachment of the charged toner particles. We find evidence of a distribution of contact areas in a layer of toner particles, and also that particles are detached by an electric field based primarily on their contact area. Our results emphasize the role of toner contact area in adhesion.

REFERENCES

1. D. M. Pai and B. E. Springett, *Rev. Modern Phys.*, **65**: 163-211 (1993).
2. D. K. Donald, *J. Appl. Phys.*, **40**: 3013-3019 (1969).
3. M. H. Lee and J. Ayala, *J. Imag. Tech.* **11**: 279-284 (1985).
4. M. Takeuchi, A. Onose, M. Anzai, R. Kojima and K. Kawai, *IS&T Proc., 7th Int. Cong. on Non-Impact Printing*: 200-208 (IS&T, Springfield, VA, 1991).
5. K. Noguchi, T. Wada, M. Masui, M. Takeuchi, M. Anzai and R. Kojima, *IS&T/SEPJ Proc., 9th Int. Cong. on Non-Impact Printing*: 113-116 (IS&T, Springfield, VA, 1993).
6. H. Krupp, *Adv. Colloid Interface Sci.*, **1**: 111-239 (1966).
7. D. A. Hays, *Particles on Surfaces I: Detection, Adhesion and Removal*, 351-360, ed. K. L. Mittal (Plenum, NY, 1988).
8. D. A. Hays, *J. of Adhesion Sci. and Technol.*, (in press).
9. H. Akagi, *SPIE Proc., Color Hard Copy and Graphic Arts*, **1670**: 138-145 (1992).
10. M. H. Lee, T. C. Reiley and C. I. Dodds, *IS&T Proc., 6th Int. Cong. on Non-Impact Printing*: 196-206 (IS&T, Springfield, VA, 1990).
11. N. S. Goel and P. R. Spencer, *Adhesion Sci. and Technol.*, **9B**: 763-829, ed. L-H. Lee (Plenum Press, NY, 1975).
12. C. Snelling, *Automatic Developability Sensing in Electrophotographic Printing*, US Patent 4,431,300 (1984).
13. R. Lewis, E. Connors and R. Koehler, "A Spectrograph for Charge Distributions on Xerographic Toner," *4th Int. Conf. on Electrophotography*, Washington, D. C. (1981).

RELATIONSHIPS BETWEEN PARTICLE ROUGHNESS, PARTICLE-SURFACE ADHESION, AND PARTICLE CHARGING

H. A. Mizes, M. L. Ott, E. A. Eklund, and D. A. Hays

Wilson Center for Research and Technology
Xerox Corporation
800 Phillips Rd. 114-23D
Webster, NY 14580

INTRODUCTION

Particles used as toners in xerographic printing are irregularly shaped and therefore their adhesion to surfaces will differ from the idealized theoretical descriptions of sphere-plane adhesion. In the Derjaguin approximation of sphere-sphere attraction, the adhesion depends on the local radii of curvature.[1] With atomic force microscopy (AFM)[2], we have mapped the topography of a variety of toners and the surfaces with which they come into contact.

An AFM image contains quantitative three-dimensional information of the surface topography. On the computer, we bring the digital representations of the toner particle into contact with the digital representation of a substrate at many different orientations. At each point of contact, the curvatures and thus the relative adhesion can be found. After performing a large number of simulated contacts, the distribution of adhesions for the irregularly shaped particle can be found.

In addition, the fraction of the toner surface accessible for contact can be determined. Transferred charge from contacts may reside only on these portions of the toner. The charge patch model of toner adhesion uses the number of charged regions as a parameter for electric field required to remove a toner from a surface[3].

EXPERIMENTAL TECHNIQUE

The $\sim 10\text{ }\mu\text{m}$ particles to be imaged were attached with Tempfix[®] epoxy to a silicon substrate. The particles were probed with commercially available microfabricated cantilevers. We used those that have a $2\text{ }\mu\text{m}$ high square pyramid on a cantilever beam $\sim 100\text{ }\mu\text{m}$ long. The presence of the cantilever at the base of the pyramid allows imaging of only the top of the toner. For a $10\text{ }\mu\text{m}$ diameter particle, a solid angle of 0.8π can be imaged, corresponding to 20% of the surface. This is sufficient for our data analysis.

The adhesion of toner to carrier beads must be overcome in xerography in order to develop an image on a photoreceptor. The carrier beads are magnetic spheres greater than $60\text{ }\mu\text{m}$ in diameter with a polymer coating. The coating is quite smooth. The carrier bead surface is flat on the scale of the toner and is easily imaged without artifacts with AFM.

We imaged two different toners of the same material intentionally made with two different surface roughnesses. From images of 13 different toners, we found the rough toner has a median RMS roughness of $0.130\text{ }\mu\text{m}$ and the smooth toner has a median RMS roughness of $0.089\text{ }\mu\text{m}$.

ADHESION DISTRIBUTIONS FROM SIMULATED CONTACTS

A visual representation of how the two surfaces are brought into contact is shown in fig. 1. The top surface is a perspective view of the smooth toner particle. The flat

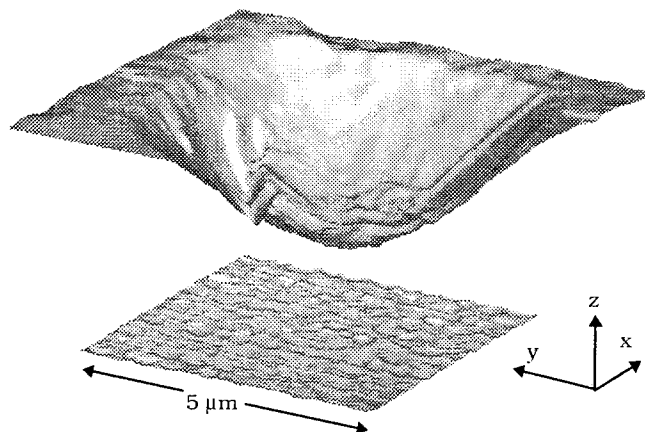


Fig. 1: Three-dimensional rendered image showing how a toner particle (top) can contact a section of a carrier bead (bottom).

area surrounding the protrusion is an artifact due to regions of the toner inaccessible to the pyramidal probe. The bottom surface is a section of a carrier bead.

A simulated contact is performed as follows: The bottom surface is translated a random amount in the x and y direction. The surface is rotated so that the surface normal, originally pointing along the z axis, points to a random direction in space. The points on the toner surface and the substrate surface that are closest to each other after these transformations are identified. These are the points that would first touch if the toner dropped vertically to the substrate.

The particle adhesion for long-range attractive interactions depends on the geometry at the point of contact. If at the point of contact the protrusions on the particle and the substrate are spherical, then the adhesion F_A is given by the Derjaguin approximation

$$F_A = W \left(\frac{R_p R_s}{R_p + R_s} \right)$$

where W is the energy per unit area for two planar contacts, R_p is the radius of curvature at the point of contact on the particle, and R_s is the radius of curvature at the point of contact on the substrate[1].

The experimental image is a square grid of pixels with the value at each pixel element corresponding to the height

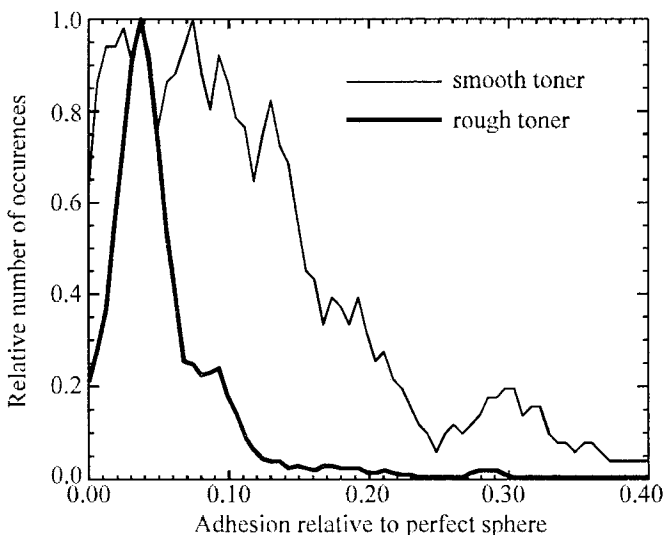


Fig 2: Simulated adhesion distribution for smooth and rough particles to a carrier bead.

of the surface. The radii of curvature in the x and y directions at the contact point are found by calculating the radius of the circle that goes through the 3 neighboring pixels in the x direction and the circle that goes through the 3 neighboring pixels in the y direction. The averages of these radii for each surface are used in the Derjaguin approximation.

The adhesion of an irregular particle depends on how it contacts a substrate. Because the rough particle may have protrusions of a different size compared to the smooth particle, the distribution of adhesions may be different.

We simulated 500 contacts between the smoother particle and the carrier bead, and also between the rougher particle and the carrier bead. The adhesion distributions are shown in fig. 2. The y axis is the relative probability that value of adhesion along the x axis will occur for a random contact. The adhesion is expressed in terms of a fraction of what it would be if the toner was perfectly spherical contacting a flat substrate. The thick line is the distribution for the rough toner and the thin line for the smooth toner.

From fig. 2 one can observe that the Van der Waal adhesion is much smaller than what is expected for a perfect sphere. Contacts occur from protrusions on the particle, which have a smaller radius of curvature than the average radius of the particle. The rough toner has much smaller protrusions than the smooth toner, so its median adhesion is 4.0% of a perfect spherical contact. The smooth toner protrusions are not so small and its median adhesion is 7.6% of a perfect spherical contact.

CONTACTABLE AREA DISTRIBUTION

A charged particle will have higher adhesion because of its attraction to its image in the surface. The adhesion depends on the distribution of charge across the surface. The distribution depends in part on regions of the toner that can come into contact with a surface. Crevices in the toner cannot be easily contacted because the ridges on either side prevent any substrate from making contact.

Two approaches can be used to determine areas of a particle that can be contacted. One way is to note the contact point after each simulated contact. However, a large number of simulated contacts must be made to discover if every possible region of the toner has been contacted. Another approach is to calculate for each point on the particle whether it is possible to touch a plane to the

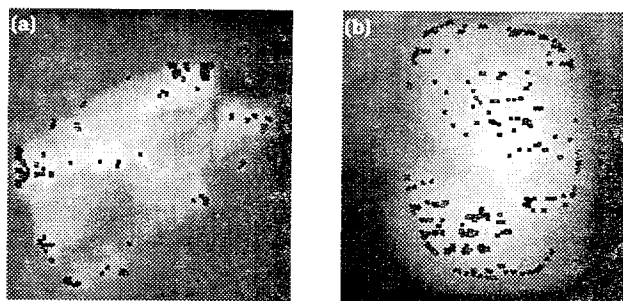


Fig 3: Topographic image of a rougher particle (a) and a smoother particle (b). The smoother particle can be contacted at more points.

point on the particle whether it is possible to touch a plane to the point. This method is much more efficient in determining the areas of the particle that can be contacted. Numerically this is done by seeing if a plane exists that goes through the test point and has all other points on the toner lying on the same side of it.

We applied the plane contact algorithm to the set of smooth and rough particles. The presence of the artificial flat area surrounding the toner in the algorithm would cause possible contact points to be rejected if the plane contacting the test point passes only through the flat area and not anywhere else on the toner. To remove this problem, the true particle image was digitally clipped from the image and analysis was only done for this portion of the image.

Fig. 3 shows an AFM scan of two of the particles analyzed. The image on the left is of a rougher particle and the image on the right is of a smoother particle. The gray level is proportional to the height of the particle. The black to white height is $2.7\text{ }\mu\text{m}$ for the rough particle and $3.1\text{ }\mu\text{m}$ for the smoother particle.

The black dots indicate the regions of the particle that can contact a plane. For both particles there is a ring of contacts points around the edge of the protruding particle. These points outline where the particle was clipped from the image. Most of these points are not truly accessible, since the portion of the particle outside the imaged region would prevent these points from being contacted. The points inside this ring are regions that can be contacted by the plane. One observes that the smooth particle can be contacted in many more areas than the rough particle.

CONCLUSIONS

The topography of a particle and the substrate to which it is adhering is an important parameter that determines its adhesion. We have developed a procedure that can determine the distribution of adhesions from an AFM measurement of the topography of both surfaces. We have illustrated the application of this procedure by determining the adhesion of two toners with different surface roughnesses to a carrier bead. With a simulated adhesion distribution, one can describe not just the force required to remove an average particle, but the force required to remove a given percentage of particles.

REFERENCES

1. J. N. Israelachvili, "Intermolecular and Surface Forces," Academic Press, London, 1985, p. 130-133.
2. D. Rugar and P. Hansma, *Physics Today*, October 1990, p. 23-30.
3. D. A. Hays, "Particles on Surfaces 1: Detection, Adhesion and Removal," p. 351-360, ed. K. L. Mittal (Plenum, NY, 1988).

HUMIDITY SENSITIVITY OF THE ADHESION OF TONER PARTICLES TREATED WITH SURFACE-MODIFIED SURFACE ADDITIVES

Mary L. Ott and Scott M. Silence

Xerox Corporation
800 Phillips Road , 139-65B
Webster, New York, 14580

ABSTRACT

Silicas and titanias have long been used as surface additives on toner particles for xerographic applications. These surface additives alter particle flow and charging ability. In addition, the additives have a strong influence on the particle adhesion to various polymeric surfaces. The silicas and titanias can be rendered hydrophilic or hydrophobic depending upon which surface treatment is performed on the additive. We have measured the adhesion of toner particles with both hydrophilic and hydrophobic silicas and titanias on the surface and we will report on the RH sensitivity of the particle adhesions for both types of additive surface modifications.

INTRODUCTION

The control of the adhesion of the toner particle to various surfaces within a photocopier (other toner particles, carrier beads, photoconductor, paper) is of importance for proper clog-free and dust-free operation of the copier. Image quality and clarity on the output document is controlled by the particle adhesion and electrostatic charge. Since copiers must function year round in a variety of environmental conditions, toner flow, adhesion and triboelectric charging properties must be as insensitive to temperature and humidity changes as possible. The aim of the current research is to measure the effectiveness of additives on tailoring toner adhesion as a function of RH.

EXPERIMENTAL

We use a Park Scientific Instruments Atomic Force Microscope for toner adhesion measurements. The toner particle is attached to the cantilever and brought into contact with an organic photoconductor surface. From a loading curve [1], the topography of the underlying surface and the adhesion of the toner to that surface are measured simultaneously. For this series of experiments, the AFM was positioned in a temperature and RH controlled enclosure.

The silicas under investigation in this study are an untreated hydrophilic silica and two hexamethyl disilazane (HMDS) treated hydrophobic silicas of low (50 m²/g) and high (200 m²/g) BET surface area. The titanias under investigation in this study are an untreated hydrophilic titania and two titanias rendered hydrophobic by two different silane treatments. Toner particles were coated at 50% and 100% additive surface coverage and subsequent toner adhesion measurements were made under various RH conditions - 70° F at 50% RH, 70° F at 20% RH, and 70° F at 6% RH. Toner adhesion measurements were also made as a function of toner contact time under these various RH conditions.

RESULTS AND DISCUSSION

Figure 1 shows adhesion in nanonewtons of toner particles coated with 50% and 100% surface coverage of the low BET HMDS treated hydrophobic silica to the photoconductor at 70° F, 50% RH as a function of position on the photoconductor. Each data point represents an average adhesion from 32 measurements made over an 80 micron scan to capture microscopic variations. Distances between positions on the photoconductor are on the order of millimeters. At 50% surface coverage, the toner adhesion is high with an overall average near 586 nN. At positions 2, 4, and 15-19 the adhesion populations are distinctly different, with the average adhesion near 197 nN. At 100% surface coverage, the adhesions are very uniform around an average of 559 nN. We have previously shown [1] that additives decrease toner adhesion by reducing the effective contact area of the toner to the photoconductor. The large changes in toner adhesion at low additive surface coverage suggest a very non-uniform distribution of additive on the toner surface. This is supported by SEM observation.

Figure 2 shows the measured values of adhesion of a toner particle with 100% surface coverage of the hydrophilic silica at two different

levels of RH- 50% and 20%. At 50% RH, the adhesions are fairly consistent with an average of 423 nN, with two positions on the photoconductor showing lower adhesion values at 120 nN. This may be attributable to an uneven distribution of additive on the surface of the particle or to variability in the amount of adsorbed moisture on the photoconductor. When the adhesion measurements were repeated at 20% RH, the average adhesion dropped significantly to 202 nN. Position 3 on the photoconductor showed a bimodal distribution of adhesion values at 20% RH. In the 80 micron scan, a third of the adhesion population was considerably higher than 202 nN, averaging 575 nN. This would suggest that the additive is responding to microscopic variability in adsorbed moisture on the photoconductor surface over the 80 micron scan.

Figure 3 shows the measured values of adhesion of a toner particle with 50% and 100% coverage respectively of the high BET hydrophobic silica. Adhesion measurements were made at 70° F and 20% RH. For the 50% surface coverage, bimodal adhesion distributions were observed at 4 of 8 positions on the photoconductor with high averages around 375 nN and low averages around 214 nN. The high averages represent 67% of the data at each position. The behavior is reversed at 100% surface coverage. Bimodal distributions are observed at 2 of 6 positions, with 67% of the data at the lower value of adhesion (158 nN) compared to a high average of 357 nN. Lower adhesion at higher surface additive concentration is expected.

Comparing hydrophobic silica toner adhesions at high (50%) and low (20%) RH, it is seen that adhesions are significantly reduced as RH is reduced - by 25% at 50% surface coverage and 68% at 100% surface coverage. This same behavior is observed in the presence of a hydrophilic silica. Adhesions drop by 50% as RH drops from 50% to 20%.

The adhesion behaviors of the toners with titanias as surface additives are in marked contrast to the behaviors of the toners with silica external additives. Figure 4 shows the adhesion of a toner with 100% surface coverage of a hydrophobic titania at 70 °F, 50% RH as a function of contact number for sub-second contacts, 4 second contacts and 8 second contacts. Here each data point represents a single contact at a single location. Each subsequent contact is made at the same location on the photoconductor. For sub-second contacts, the adhesion starts very high (880 nN) and

exponentially decays to an equilibrium value of 175 nN. When the toner contact time is increased to 4 seconds, the exponential decay is no longer observed and adhesions are stable at 715 nN. When the contact time is increased further to 8 seconds, adhesions remain stable at an even higher value of 760 nN. During sub-second contacts, moisture may be forced out of the contact region between the titania and the photoconductor surface with each successive contact, thus lowering the toner adhesion with each contact. When the contact time is increased to 4 seconds, however, the moisture interlayer has time to conform to the contact area and form a uniform bond, thus increasing the adhesion considerably. Figure 5 shows that this effect of increased adhesion with increased contact time is common to both hydrophobic titanias. The adhesion decay phenomenon for hydrophobic titania coverage is highly RH sensitive. At lower RH values (6%), the decay phenomenon is not observed and the adhesion is constant with contact number. Presumably, the water interlayer has diminished with decreased RH.

The behavior of the toner with 100% surface coverage of hydrophilic titania is in marked contrast to the hydrophobic titania behavior. Figure 2 shows titania adhesion behavior similar to the high RH hydrophobic silica case with adhesion being very high (734 nN average) and constant with contact number. No adhesion decay with contact number was observed. According to additive product literature [2], the weight percent adsorption of moisture by the titania at 50% RH is 3%. This is in contrast to values of 0.9% adsorption of moisture by hydrophobic titania, and hydrophobic and hydrophilic silicas at 50% RH. Thus, regardless of the number of contacts made by the toner with hydrophilic titania additive, the moisture layer at the interface cannot be displaced and the adhesion remains at a high value.

CONCLUSIONS

We have measured the adhesion of toners, with various hydrophobic and hydrophilic titanias and silicas as surface additives, to photoconductor surfaces, under a variety of RH conditions and at a variety of additive surface coverages. Hydrophobic silicas at low surface coverages and high RH give erratic adhesion values due to uneven surface coverage of the additive on the toner. Toners coated with both hydrophobic and hydrophilic silicas show an increase in adhesion to the photoconductor with increasing RH.

Adhesion behaviors of titania coated toners are in marked contrast to behaviors of toners with silica coatings. Toners coated with hydrophobic titanias show an adhesion decay to an equilibrium value with successive contacts, along with an increase in adhesion with increased contact time.

REFERENCES

1. M.L. Ott and H.A. Mizes, Atomic Force Microscopy Adhesion Measurements of Surface-Modified Toners for Xerographic Applications, to be published, Colloids and Surfaces, July 1994.
2. Technical Bulletin Pigments, Degussa Product Literature, No. 18

Figure 1: Adhesion of toner with low BET ($50 \text{ m}^2/\text{g}$) hydrophobic silica at 70° , 50% RH at 50% surface coverage (solid circles) and 100% surface coverage (solid triangles).

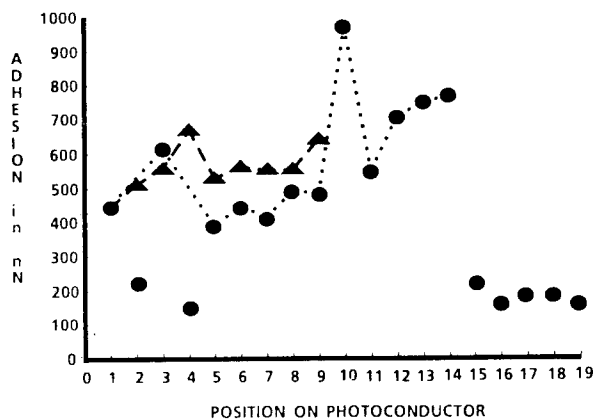


Figure 2: Adhesion of toner with 100% surface coverage of hydrophilic silica at 70° , 50% RH (solid circles) and 70° , 20% RH (solid triangles). Adhesion with 100% surface coverage of hydrophilic titania at 70° , 50% RH in solid squares.

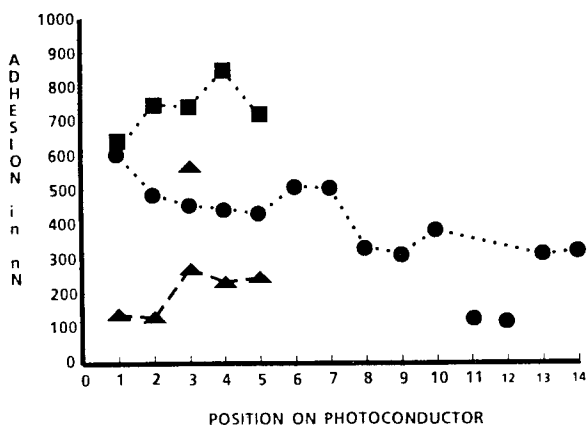


Figure 3: Adhesion of toner with high BET ($200 \text{ m}^2/\text{g}$) hydrophobic silica at 70° , 20% RH at 50% surface coverage (solid circles) and 100% surface coverage (solid triangles).

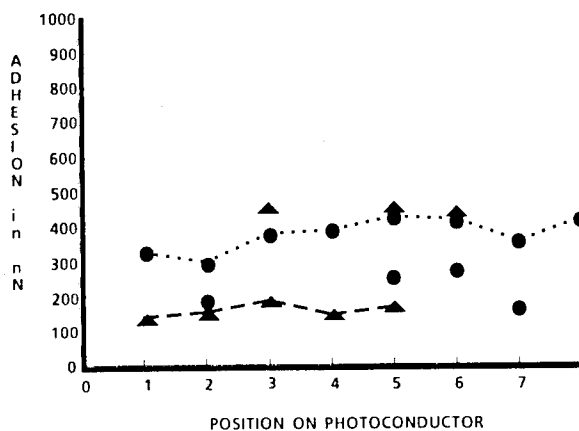


Figure 4: Adhesion of toner with 100% surface coverage of hydrophobic titania at 70° , 50% RH.

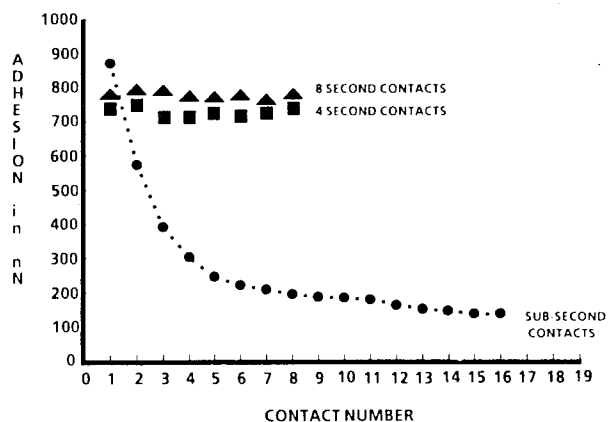
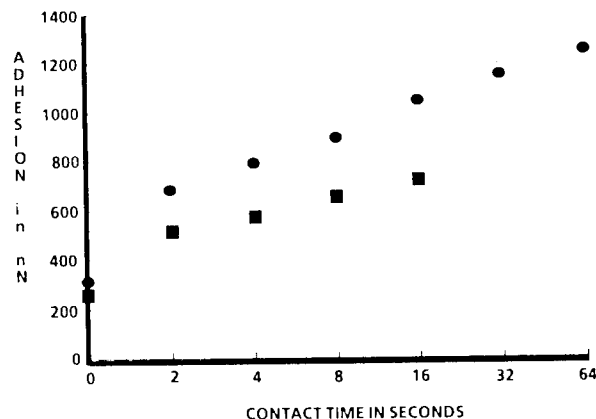


Figure 5: Adhesion increase as a function of contact time at 70° , 50% RH for toners coated with 100% surface coverage of hydrophobic titanias.



MEASUREMENT OF A WET ADHESION COATING SYSTEM ON STEEL: AN EQUIVALENT CIRCUIT MODEL

P. J. Moreland

Zeneca Resins, Runcorn, Cheshire, England

INTRODUCTION

For more than a decade, waterborne coatings have sought to replace solvent-borne coatings as the latter have come under increasing regulatory pressures based on health and safety and environmental issues. The acceptance of waterborne coatings, however, has been slow and generally has been attributed to the poorer anti-corrosive performance offered by these coatings. There are exceptions to this behaviour as discussed for a chlorine-containing vinyl acrylic polymer [1]. However, the selection of the polymer, e.g. a chloropolymer, with its excellent oxygen and water barrier properties, and system design for colloid stability and barrier property retention is critical for such performance.

Adhesion to metal substrates by the above and other waterborne polymers is often provided through the incorporation of carboxylic acid functionality. It is evident that such polar but hydrophilic functionality seems inconsistent with the need for hydrophobic properties of the polymer for water barrier properties [2]. Such dilemmas and trade-offs are not uncommon in examination of system properties for anti-corrosive performance [3]. Adhesion, and more specifically "wet adhesion" is considered by many to be a crucial factor in anti-corrosive performance [4].

In the development of our next generation, waterborne, anti-corrosive paint coatings both good wet adhesion to steel substrates and demonstrated protection in ASTM salt fog testing are being examined as some of the key requirements in the assessment of candidate acrylic polymer coatings. Such acrylic based coatings generally have poorer barrier properties

than chloropolymers but can still demonstrate good anti-corrosive performance, which needs to be understood for the design of further improved coating systems.

CONTENT

This paper presents preliminary studies of some waterborne non-pigmented acrylic polymer coatings. Principally, the systems selected are those which demonstrate differentiated, i.e. good and poor, wet adhesion to steel. The adhesion has been found to be dependent upon such factors as either the presence or absence of an adhesion promoting epoxy ester resin, the choice of co-solvent and the cleanliness of the substrate surface. The wet adhesion of the 60-70 microns coatings is assessed by the cross-cut tape test after typically 24 hours exposure to distilled water or 5% NaCl solution. These same wet adhesion promoting chemicals are associated with improved ASTM salt fog performance but this is not true for all additives showing improved wet adhesion. The differentiated performance has offered an ideal opportunity to examine the role played by these factors in the adhesion and salt fog behaviour.

One approach has been to examine the significance of water vapour permeability properties of the coatings and water entry into the coatings as determined by traditional transmission methods on free films as well as more modern Electrochemical Impedance Spectroscopy (EIS) measurements on exposed coated panels. The latter technique has allowed accepted and extended equivalent circuit models, using the B. A. Boukamp software package [5], of the coated panels to be examined. The models allow comparison of the changing

electrical coating parameters film capacitance C_f , film or pore resistance R_p , and metal interface corrosion process parameters R_{corr} and C_{corr} with the water entry, as evaluated through C_f , and measured wet adhesion rating on the same panel.

Such analyses have been conducted at room temperature, ASTM salt fog temperature (35°C) as well as 5-6°C with awareness of the significance of polymer coating properties such as MFFT and T_g in the behaviour of the coatings. It should be noted that the differentiated adhesion measured in these studies is not accompanied by visual degradation such as blistering or water blushing.

In one coating system (A) of differentiated wet adhesion at RT with epoxy ester adhesion promotion, the equivalent circuit models for good and poor coatings were virtually identical; both coatings had high impedance ($> 1 \text{ E}11 \text{ ohm cm}^2$). Good wet adhesion was obtained, however, with or without adhesion promoter, at 35°C near the T_g of the coatings. The water pickup of both coatings was much higher than at RT. The coating without epoxy ester had decreased in film impedance ($4 \text{ E}7 \text{ ohm cm}^2$) relative to that ($4 \text{ E}11 \text{ ohm cm}^2$) for the coating having adhesion promoter but indicated the same good wet adhesion. At 5°C both coatings showed poor adhesion and lower water pickup than at RT. The equivalent circuits were virtually identical with high film impedance ($1 \text{ E}11 \text{ ohm cm}^2$). In all cases "dry" adhesion was excellent, even at 5°C, and coatings giving poor wet adhesion showed good "dry" adhesion on drying out at RT.

It is possible that EIS lacks sufficient sensitivity to detect small areas of disbondment through changes in R_{corr} and C_{corr} in these coatings, hence the equivalent circuits remain identical. Or is there perhaps no electrochemical disbondment related process in these coatings? Does the cross-cut tape test contain some mechanical features of a peel test? In this case, perhaps the relative values

of the cohesive forces in the films versus the adhesion to the substrate with change of film temperature determines the failure mechanism in the test. Is then the adhesive modulus of the coating decreased with increase of film temperature, and more so with the adhesion promoter present, such that the bearing load is large and the apparent bond strength high [6]? Adhesion would then be exhibited as good with increasing film temperature exposure, as evidenced. But why is "dry" adhesion good in all cases?

Another coating system (B) has exhibited differentiated wet adhesion, with or without the epoxy ester adhesion promoter, in coatings which are naturally cured at RT for 10-11d. Both coatings oven dried under accelerated conditions at 60°C give good wet adhesion. The equivalent circuit models in the latter case are virtually identical with high film impedance ($2 \text{ E}12 \text{ ohm cm}^2$) values. In the former case, both film impedances are still high at $\text{E}9$ to $\text{E}11 \text{ ohm cm}^2$. However, the poor wet adhesion coating shows upon exposure a decreasing pore resistance R_p and corrosion resistance R_{corr} with an increasing C_{corr} (actually Q_{corr}). This electrochemical response is consistent with a model of disbondment at the interface through a defect structure, and by which the area of disbondment can be monitored by the breakpoint frequency at 45 degrees in the Bode plot [7-8]. This type of electrochemical response has generally been reported under conditions of visual blister formation and low film impedance but similar detection on high impedance epoxy coatings has been previously reported [9].

The above approach of examining wet adhesion in relation to an electrochemical model of disbondment would be ably supported by direct physical evidence of disbonded areas. Results of Scanning Acoustic Microscopy (SAM) studies will

be presented together with associated surface features using Atomic Force Microscopy (AFM).

Metal surface contamination, as revealed by X-Ray Photoelectron Spectroscopy (XPS) techniques, was one constant source of poor wet adhesion if solvent cleaning of panels was used, this led to the use of the clean as-received panels.

Upgraded wet adhesion could be obtained in one coating system (A) by change of cosolvent in the absence of the epoxy resin adhesion promoter. Such behaviour, and also the significant influence of drying temperature and time on performance, led to the examination of film property changes with time, including before and after wetting out. Surface (rocker) hardness measurements proved a sensitive means of monitoring film changes. Though plasticisation by, for example, water ingress could be readily demonstrated there was no clear evidence of a relationship between the extent of plasticisation and subsequent wet adhesion.

The data are preliminary and still being developed but it is intended to attempt to analyse the relationship between polymer design and coalescent design in the above wet adhesion and salt fog behaviour.

REFERENCES

1. P. J. Moreland, J. C. Padget and Y. K. Lim, Corrosion Asia '94 Conference, Singapore, (NACE International, Houston, 1994), Paper No. 1042.
2. C. E. Rogers, Polymer Permeability, (Elsevier, Barking, Essex, 1985), J. Comyn, Ed., p. 62.
3. W. Funke, Polymeric Materials for Corrosion Control, R. A. Dickie and F. L. Floyd, Eds., ACS Symposium Series No. 322, (Am. Chem Soc, Washington D.C., 1986), p. 222.
4. W. Funke, J. Coat. Technol., **55**, 31, (1983)
5. B. A. Boukamp, Equivalent Circuit Users Manual, (University of Twente, Enschede, The Netherlands, 1989)
6. A. Hardy, Aspects of Adhesion, D. J. Alner, Ed., (Univ. London Press, London, 1965), p. 47
7. S. Haruyama, M. Asari and T. Tsuru, Proceedings of Corrosion Protection by Organic Coatings, M. W. Kendig and H. Leidheiser, Eds., (Electrochem. Soc., Pennington, 1987), p. 197.
8. F. Mansfeld and C. H. Tsai, Corrosion, **47**, (12), 958, (1991)
9. E. P. M. van Westing, G. M. Ferrari and J. H. W. de Wit, Corros. Sci., **36**, (6), 979, (1994).

ACKNOWLEDGEMENTS

The author gratefully acknowledges the provision of SAM facilities through Dr D. Knauss at the Dept. of Materials, Univ. of Oxford and the valued inputs of G. Hill and E. Jones at Zeneca Resins.

A STUDY OF THE EFFECTS OF MOISTURE DIFFUSION ON THE STRENGTH AND FATIGUE RESISTANCE OF EPOXY BONDED ADHESIVE JOINTS

J. A. Harris† and P A Fay‡

†MERL Limited, Tamworth Road, Hertford, Herts SG13 7DG, UK

‡Ford Motor Company Ltd, Research and Engineering Centre, Laindon, Basildon, Essex SS15 6 EE, UK

INTRODUCTION

The strength properties of adhesive joints can be degraded by the effects of moisture ingress throughout the adhesive layer either by loss of interfacial strength and/or by a reduction in the cohesive strength properties of the adhesive. For epoxy adhesives, it has been suggested that interfacial failure occurs when the moisture concentration in the adhesive exceeds a critical local value which can only occur in an environment above a certain critical relative humidity [1 - 3]. Water that diffuses into epoxy adhesives can be molecularly dispersed resulting in a reduction in the glass transition temperature (T_g) by as much as 30 - 40°K [4], it may also exist in clusters that can form micro cracks in the adhesive [5].

In this study, the changes in strength properties in an adhesive joint due to moisture ingress were investigated. Joints were immersed in a standard sea water solution at ambient temperature (20°C) and also at temperatures of 38°C and 55°C, in order to assess the use of elevated temperature as a means of accelerating the degrading mechanisms. The adhesive used was a commercial flexible epoxy of the hot melt type, designed for automotive applications (Ciba-Geigy XB 5318). Joint properties were measured on single lap joints 40 mm wide with a 15 mm overlap, manufactured with sheet mild steel substrates 0.9 mm thick. There was no surface preparation of the steel which was coated with a process oil. An adhesive layer thickness of 1.7 ± 0.2 mm was maintained throughout, which is in the range expected for automotive applications. A thick adhesive layer enables changes in adhesive properties to be more readily seen as changes in joint properties. Joints were cured for 30 min. at 180°C in a hot press. Any adhesive fillet at the edges of the overlap was removed prior to testing. The strength properties of interest were the ultimate strength of the joints, which were measured 'statically', and the fatigue resistance, which was assessed by measuring the number of cycles to failure with a fatigue load that was varied between 0 and 2000 N at a frequency of 30 Hz. It was known from previous work that this force range would give a fatigue life of about 2.5×10^5 cycles for initially dry joints [6]. The changes in the distribution of moisture in the adhesive layer with time of immersion are governed by

the diffusion properties of the adhesive. The diffusion coefficient (D) and equilibrium mass uptake for the primary diffusion process (M'_∞) were obtained from mass uptake experiments on 'neat' adhesive samples at the three temperatures of interest, assuming Fickian behaviour.

RESULTS

Diffusion Properties of the Adhesive

Values for $D(\theta)$ and $M'_\infty(\theta)$ were derived from mass uptake measurements at the various temperatures of interest (θ). The results are summarised in Table 1. There was some tendency for there to be further mass uptake beyond that related to the primary process due to secondary processes that were evident in the longer term. At the lower temperatures this is attributed to the behaviour of the adhesive as a two phase system whilst at 55°C, where the secondary rate is much higher, chemical changes may occur. On the basis of Fickian diffusion, the distribution of moisture concentration through the adhesive layer depends on the product $D(\theta).t(\theta)$. Since M'_∞ does not vary significantly with temperature, then, for the same concentration profile $D(\theta).t(\theta) = D(20).t(20)$. Thus, at an elevated temperature of θ , the diffusion process is accelerated by the factor $D(\theta)/D(20)$ the values of which are given in Table 1. The times at elevated temperature may be equated to the time at 20°C as $t(\theta).D(\theta)/D(20)$. Joint property changes may therefore be compared on the basis of equal moisture concentration profiles using these 'reduced' times.

On a simplified basis the distance of penetration of moisture through the adhesive layer $x = (4 t(\theta).D(\theta)/\pi)^{1/2}$. For complete saturation of the overlap in the joint, $x = 7.5$ mm, giving times of 93, 456 and 1544 days, for temperatures of 55°C, 38°C and 20°C respectively.

Table 1 Summary of adhesive diffusion data.

Temperature, θ (°C)	M'_∞ (%)	$D(\theta)$ (m ² /s)	$D(\theta)/D(20)$
20	1.8	3.31×10^{-13}	1
38	2.0	1.45×10^{-12}	4.4
55	2.0	5.49×10^{-12}	16.6

Changes in Joint Strength Properties

Strength property measurements were made on batches of 5 joints after various times of immersion at the three temperatures. All measurements were made at 20°C.

Static strength. Typical force/deflection curves from pull to failure tests after various times of immersion at 55°C are compared in Fig. 1. With increasing time the joints apparently become more ductile in their response, and, except during the initial period of immersion, the ultimate strength of the joint decreases. These changes are consistent with the expected changes in the adhesive properties due to moisture ingress. Moisture plasticizes the adhesive leading to a reduction in modulus, yield strength and failure stress, but an increase in failure strain. In the initial stages of moisture penetration, only the edge region of the adhesive layer is affected, and the local property changes are advantageous to the strength of the joint since the stress concentration at the edge of the overlap is reduced. However as more of the adhesive layer is affected, the extent of yielding and plastic flow in the adhesive layer prior to failure increases, but since the yield strength of the adhesive is lower, the maximum force attained is reduced. Without the ingress of moisture, fracture occurs rapidly at the peak force before visible cracks are formed. After immersion, cracks form at the edges of the overlap in the adhesive prior to failure of the joint which is less rapid. Similar trends in behaviour were obtained at the lower immersion temperatures, however the changes were less rapid because of the lower rates of diffusion.

Fatigue resistance. During the fatigue tests, the maximum deflection that occurs in the fatigue cycle was monitored. Since this reflects the creep behaviour of the adhesive layer it has been termed here as the 'dynamic creep displacement'. Typical behaviour during fatigue tests after various times of immersion at 55°C are shown in Fig. 2. For 'dry' joints there is apparently little creep in the adhesive layer during the fatigue cycling to failure. However after immersion, the rate of dynamic creep increases with the time of immersion, and, except for an initial period, is accompanied by reductions in fatigue life. The increased amount of dynamic creep is again a result of the effects of moisture on the adhesive properties and the extent of the penetration through the adhesive layer.

Joint Properties Changes on a Reduced Time Basis

Figs. 3 and 4 show the static strength and fatigue life changes respectively, plotted on the reduced time basis with a reference temperature of 20°C. In the main, failure of the joints was by cohesive failure of the adhesive. Where this was the case, the data from the three

immersion temperatures follow the same trend. Thus the changes in strength properties reflect the changes in the concentration profile and cohesive properties of the adhesive. Shorter times of immersion at elevated temperature can equate to longer times at ambient. Since the changes in the properties of the adhesive are limited by the equilibrium mass uptake condition, changes in joint properties are limited by the saturation condition in the adhesive layer which at 20°C is of the order of 1500 days.

In some cases either partial or complete interfacial failure of the joint was observed. When this occurred, the strength and fatigue life were lower than with cohesive failure as indicated in Figs. 3 and 4. Although this occurred in some joints after immersion at 20°C and 38°C, a major change was seen at 55°C after about 100 days immersion, where complete interfacial failure occurred, leaving a clean and shiny metal surface. This change in failure mode took place after the whole of the adhesive layer had become saturated.

CONCLUSIONS

When the mode of joint failure is cohesive in the adhesive, changes in joint properties due to the ingress of moisture depend in the main on the distribution of moisture in the adhesive layer, thus elevated temperatures can be used to increase the rate of diffusion and hence accelerate the rate at which the changes occur.

For the commercial flexible epoxy tested, moisture ingress leads to a reduction in modulus and yield strength and an increase in creep rate, resulting in reductions in joint strength and fatigue resistance. This suggests that the T_g of the adhesive is shifted sufficiently closer to the test temperature of 20°C to produce these changes.

Interfacial failure is associated with larger and less predictable reductions in strength properties. There was little evidence to suggest that interfacial failure occurred at a critical level of moisture concentration. Other factors that govern this mode of failure include: the local stress levels in the regions of high moisture content, the initial level of adhesive strength, stability of interfacial bonds, and the time and temperature for which high moisture levels exist at the interface. The avoidance of such failures is critical to the successful long term integrity of adhesive joints for critical load bearing structures.

REFERENCES

1. R. A. Gledhill, A. J. Kinloch and S. J. Shaw, *J Adhesion* **11**, 3 (1980).

2. D. M. Brewis, J. Comyn, A. K. Raval and A. J. Kinloch, *Int. J Adhesion and Adhesives* **10**, 247 (1990).
3. D. R. Lefebvre and V.R. Raju in proceedings of *Adhesion 90*, (Cambridge 10-12 Sept 1990).
4. J. Comyn in proceedings of *Polymers in a Marine Environment* (Inst. Marine Eng. London 1987).
5. R. A. Dickie and K. N. Morman, *Poly. Eng and Sci.*, **30**, 4 (1990).
6. J. A. Harris and P. A. Fay, *Int. J Adhesion and Adhesives* **12**, 97 (1992).

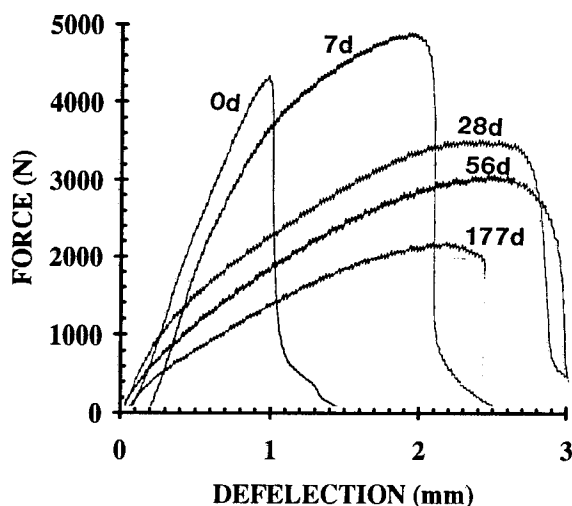


Figure 1 Static pull to failure on lap joints after various times of immersion at 55°C.

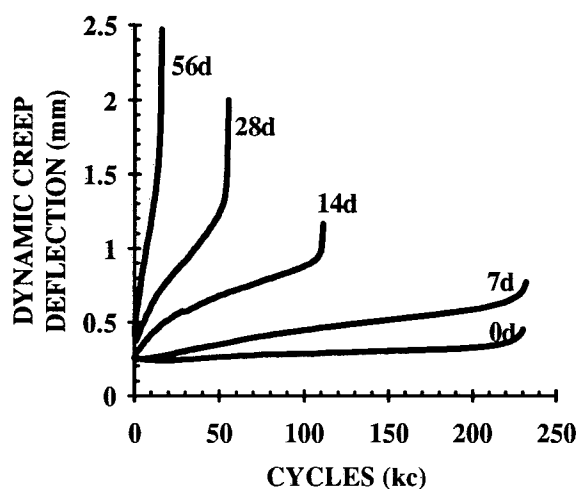


Figure 2 Dynamic creep deflection during fatigue tests on lap joints after various times of immersion at 55°C.

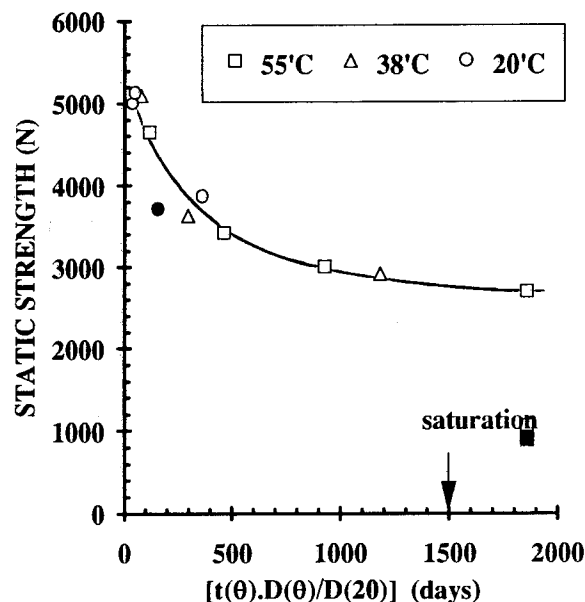


Figure 3 Static strength after various times of immersion at various temperatures, on a reduced time basis with a reference temperature of 20°C. (Filled symbols - partial or total interfacial failure).

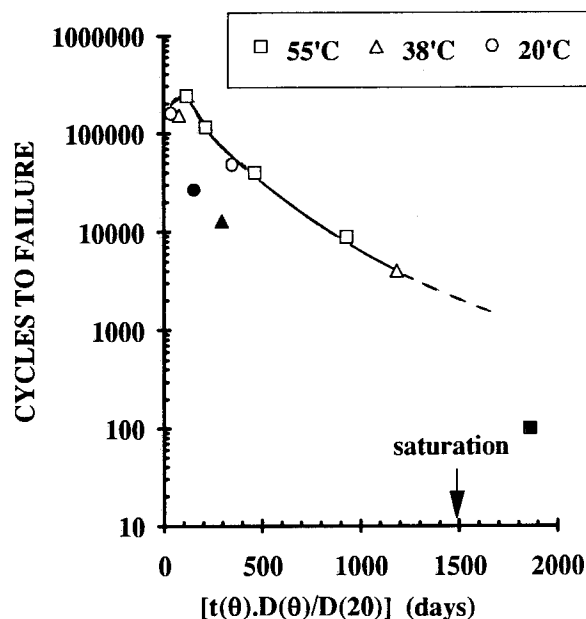


Figure 4 Fatigue life after various times of immersion at various temperatures on a reduced time basis with a reference temperature of 20°C. (Filled symbols - partial or total interfacial failure).

RELATION BETWEEN ADHESION LOSS AND WATER AT THE POLYMER/SUBSTRATE INTERFACE

Tinh Nguyen, Eric Byrd, David Alsheh, and Dale Bentz

National Institute of Standards and Technology
Gaithersburg, MD 20878

INTRODUCTION

The buildup of water many monolayers thick at the coating/substrate interface is the major cause of adhesion loss when an organic-coated substrate is exposed to water or high relative humidities [1,2]. Until now, it has not been possible to correlate the buildup of the interfacial water layer with adhesion loss because there has been no method available to quantify the water layer at the coating/substrate interface or the adhesion loss of coated substrates. In this study, the thickness of the interfacial water layer and the adhesion loss of several organic film/substrate systems exposed to water were measured and analyzed to establish the correlation between water at the interface and the adhesion loss of organic-coated materials.

EXPERIMENTAL SECTION

Specimen Preparation

For measuring water at the coating/substrate interface, specimens of solvent-free and water-reducible epoxy coatings on untreated and silane-treated 50x10x3mm Si prisms and of asphalts on untreated 50x10x3mm Si prisms were prepared. For measuring adhesion loss, untreated and silane-treated, 100 mm-diameter Si wafers were coated with the epoxy coatings while the asphalts were applied on untreated granite plates. Complete descriptions of solvent-free epoxy, water-reducible epoxy, and asphalts are given in References 3, 4, and 5. Si wafers and prisms were cleaned with acetone followed by methanol, and dried with hot air before use. The surfaces

of these Si substrates had an SiO₂ layer about 2.5 nm thick (as measured by an ellipsometer). Under the conditions used in this study (24°C and 45% relative humidity), these surfaces are expected to be covered with hydroxyl groups [6]. The SiO₂-covered Si prisms and wafers are referred to as Si substrates. Silane-treated substrates were prepared by immersing cleaned Si prisms and wafers for 30 minutes in an acidified (pH=4) water solution containing 0.1% aminoethylaminopropyltrimethoxysilane. The treated substrates were dried for 10 minutes at 110°C before applying the organic coatings. Epoxy coatings were applied on Si prisms and wafers using the drawdown technique, similar to that described in Reference 3. The thickness of the solvent-free epoxy coating was in the 130-150 μ m range and that of the water-reducible epoxy was in the 120-135 μ m range. Specimen preparations of asphalts on Si prisms and granite plates are given in References 5 and 7, respectively.

Measurement of Adhesion Loss and Water at the Interface

The specimen configuration and the FTIR-multiple internal reflection (FTIR-MIR) procedure used for determining the amount and thickness of the water layer at the coating/substrate interface are described in Reference 3. The measurements of the adhesion loss of epoxy coatings on Si wafers as a function of exposure in water were conducted using a wet peel adhesion method presented in Reference 8. Twelve specimens on two wafers were tested and the results averaged. The adhesion loss of asphalts on a granite substrate was measured

using a pneumatic pull-off adhesion tester combined with a porous stub, as described in Reference 7. Here, the results were the average of six measurements.

RESULTS AND DISCUSSION

Figure 1 presents the results on the mass and thickness of the water layer at the coating/substrate interface as function of exposure time in water for solvent-free (1a) and water-reducible (1b) epoxy coatings on untreated and silane-treated Si substrates and for asphalts (1c) on untreated Si substrates. Essentially, no water entered the interface of the solvent-free epoxy/silane-treated substrate specimens, but about 10 monolayers (one monolayer of water is approximately 0.3nm thick) have gathered at the interface of the untreated substrates.

For the water-reducible epoxy (Figure 1b), substantial water built up at the interface for both silane-treated and untreated specimens after a short exposure time. Indeed, silane treatment of the substrate surface did not appear to reduce the uptake of interfacial water for the water-reducible epoxy. Figures 1a and 1b also show that much more water has accumulated at the interface of the water-reducible epoxy specimens than that of the solvent-free epoxy specimens. For asphalt systems, the quantity of water at the interface for specimen AAD was substantially greater than that of specimens AAM and AAG.

Figure 2 gives the results on the adhesion loss as a function of time exposed to distilled water for the same coatings on Si wafers and asphalts on a granite substrate. Silane treatment had little effect on the adhesion loss of the water-reducible epoxy but greatly reduced the adhesion loss of the solvent-free epoxy specimens. Further, the water-reducible epoxy specimens lost most of their adhesion at much shorter time than solvent-free epoxy ones. For asphalt systems, specimens AAD and AAG lost their adhesion much faster than specimen AAM.

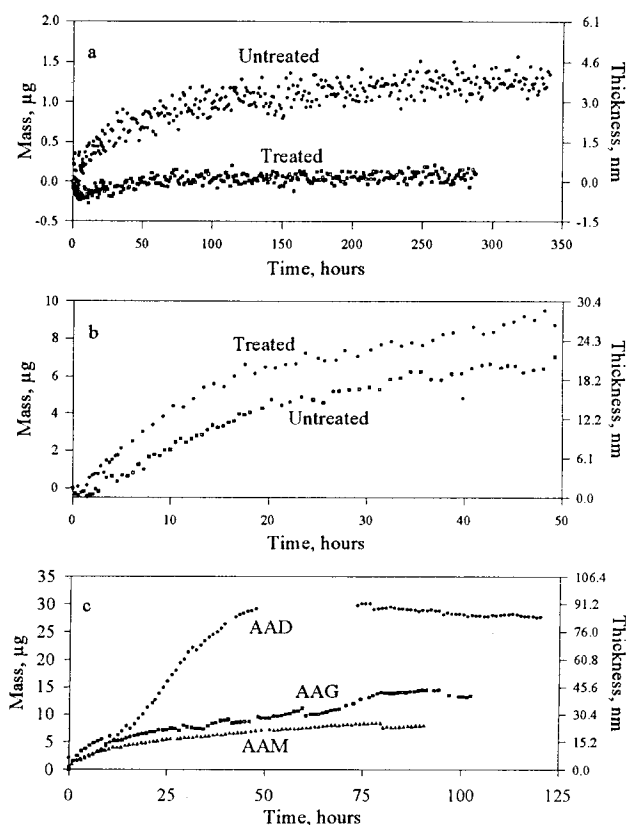


Figure 1. Amount and thickness of the water layer at the coating/Si substrate interface: a) solvent-free epoxy, b) water-reducible epoxy, and c) asphalts.

Except for the water-reducible epoxy specimens that need further investigation, the results presented here indicate that larger amounts of water at the coating/substrate interface generally correspond with greater adhesion loss. Additional data and further analysis are needed to determine more precisely the range of the amount of water at the interface corresponding with the range of the adhesion loss for a variety of coating systems. Once this kind of relationship is well established, the FTIR-MIR technique could be used for studying the adhesion loss at the molecular level.

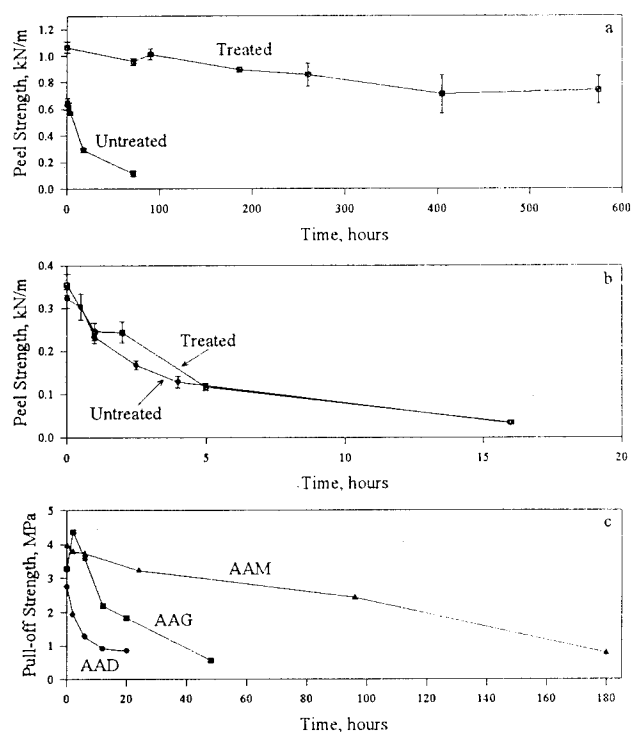


Figure 2. Adhesion loss of coated substrates in water: a) solvent-free epoxy/Si wafer, b) water-reducible epoxy/Si wafer, and c) asphalt/granite.

SUMMARY AND CONCLUSIONS

The buildup of a water layer many monolayers thick at the coating/substrate interface is the major cause of adhesion loss when an organic-coated substrate is exposed to water or high relative humidities. This study investigated the relationship between the adhesion loss and the amount of water accumulated at the interface. Except for the water-reducible coating system, there was, in general, a correlation between the amount of water at the coating/substrate interface and the adhesion loss of an organic coating.

ACKNOWLEDGMENTS

This work is supported in part by the Transportation Research Board, National Academy of Science. We thank Dr. Robert Brady of Naval Research Laboratory for providing the water-reducible epoxy coating.

REFERENCES

1. H. Leidheiser and W. Funke, *J. Oil & Color Chemists' Assoc.*, **70**, 121(1987).
2. D.R. Lefebvre, K.M. Takahashi, A.J. Muller, and V.R. Raju, *J. Adhesion Sci. Technol.*, **5**, 204(1991).
3. T. Nguyen, D. Bentz, and W.E. Byrd, *J. Coatings Technol.*, **66**, 39 (1994).
4. T. Nguyen, D. Bentz, and W.E. Byrd, *J. Coatings Technol.*, in press.
5. T. Nguyen, E. Byrd and D. Bentz, National Institute of Standards and Technology Internal Report NISTIR 4783, March, 1992.
6. T. Nguyen, E. Byrd, and D. Bentz, *J. Adhesion*, **48**, 169(1995).
7. T. Nguyen, E. Byrd, and J. Seiler, National Research Council NCHRP-IDEA Annual Progress Report 1, Dec. 1994, p.18.
8. D. Alsheh, T. Nguyen, and J.W. Martin, Proceedings, Adhesion Society Conference, February, 1994, p. 209.

EFFECT OF PRECURE MOISTURE EXPOSURE ON A STRUCTURAL EPOXY ADHESIVE

S.M. Ward, M.A. DeBolt, G.L. Westerbeek and R.A. Dickie
Ford Research Laboratory
Dearborn, MI 48121-2053

INTRODUCTION

The use of adhesives in the automotive industry is increasing in an effort to improve vehicle stiffness and reduce potential fatigue damage to spot welds in weld-bonded applications. It is important that structural adhesives maintain their integrity during manufacturing and vehicle service. Process conditions such as humidity exposure of the uncured adhesive can affect the adhesive's ultimate performance.

The deleterious effects of humidity exposure on uncured structural adhesives have been well documented in the aerospace industry. These effects include changes in rheological properties, cure temperatures, gel times, cured morphology and poor T-peel performance at low temperatures [1-2]. Modification of adhesive formulations to reduce adhesive sensitivity to precure humidity exposure has resulted in limited success, for example see Reference 3. Another approach is to minimize humidity exposure of the uncured adhesive by controlling manufacturing conditions, which is the general approach in the aerospace industry. Unfortunately, typical automotive stamping and assembly facilities do not have climate control capabilities. Therefore, it is necessary to determine how precure humidity affects adhesive chemistry and adhesive bond performance to define acceptable process conditions.

The chemical and physical effects of precure humidity exposure to a high performance one component structural epoxy adhesive are examined. The effect on adhesive bond performance in lap-shear, stress-durability and impact-peel testing is also reported.

EXPERIMENTAL

The adhesive investigated was a toughened one component dicyandiamide-cured epoxy adhesive. The substrate was pretreated aluminum. Thermal analysis of the adhesive was conducted on a Mettler Thermal Analysis Systems TA3000 using a TC10A processor to monitor and collect data. The DSC scans were obtained at a heating rate of 5°C/min over a range from

25°C to 250°C in a nitrogen atmosphere. A Mattson 5000 FTIR was used to obtain absorbance spectra of the reaction of the adhesive with moisture. A thin film of adhesive was placed on a silicon polished disc from Wilmad. The disc was placed in a humidity cabinet at 84% relative humidity (RH) and 26°C and the reaction monitored periodically.

Lap-shear test specimens were prepared from 25.4 mm x 101.6 mm x 1.6 mm aluminum coupons. The overlap was 12.7 mm and the bond thickness was set at 0.25 mm with glass bead spacers. Open-bond specimens were prepared by using a robot to dispense a 3.6 mm adhesive bead on the substrates, centered on the overlap area. Specimens were exposed at 25 or 40°C; 45%, 53%, 75%, 83% or 89% RH and in either an open or closed bond configuration. After humidity exposure, glass beads were sprinkled on to the open bond adhesive and the top substrate was placed in the overlap position and clamped to the bottom substrate. The fillet area was scraped clean with a square edge spatula. The closed-bond specimens were made in the same manner as the open-bond specimens except that the adhesive was placed on the substrate as a thin film instead of a bead. All bonds were cured after humidity exposure at 180°C for 30 minutes in an air-circulating oven. Impact-peel specimens were prepared from 20.0 mm x 90.0 mm x 1.6 mm aluminum coupons. The bond length was 30.0 mm and the bondline thickness was set at 0.25 mm with glass beads. The length was set by placing 12.7 mm wide teflon tape across each of the aluminum coupons 30.0 mm from the end. Bonds were exposed to humidity, mated and cured in the same manner as lap-shear specimens.

The amount of adhesive remaining in the cured lap-shear bonds after precure humidity exposure was measured with a vision system consisting of a Dage Six Fifty camera, equipped with a 60 mm Nikon lens, a moveable stage to adjust the sample position, and Optimus data acquisition and processing software. The loads to failure of the lap-shear bonds were determined by pulling the bonded coupons to failure on an Instron Universal Test Instrument (Model 1125) at a

constant crosshead speed of 10 mm/min. The load to failure was determined from the peak load. The stress-durability test method has been described elsewhere [4 and 5]. The stress-durability fixtures were stressed at 7, 5 and 2 MPa. Stress-durability testing was done in a corrosive environment (adapted from Ref. 6). Impact peel specimens were tested on a Dynatup, General Research Corp., (Model GRC 8250) Impact Test Machine in the drop tower configuration. The method used was similar to the ISO wedge impact method for adhesives [7]. The GRC 730-I version 2.20 Instrumented Impact Test Data System was used to acquire data.

RESULTS AND DISCUSSION

It has been reported by Kibler and Creasy [8] that the temperature at which some dicyandiamide structural adhesives begin to react is lowered upon exposure of the uncured adhesive to moisture as the water may catalyze the reaction or react with the epoxy directly. In this case, the reaction onset temperature of the adhesive was not greatly affected by exposure to moisture as measured by differential scanning calorimetry (DSC). A summary of DSC results are presented in Table I.

Table I - DSC Summary

Exposure Condition	Onset Temperature	T _g (Midpoint)
No Exposure	151.2°C	102.5°C
9d 84% RH 25°C	151.1°C	104.3°C
5% H ₂ O added	150.5°C	104.5°C

The glass transition temperature of the cured adhesive was also not affected by precure exposure to moisture (Table I). It has been reported by Pike, et al. [9] for another dicyandiamide-epoxy system that precure exposure to humidity resulted in a lowering of the T_g. They hypothesize that the dicyandiamide in the adhesive reacts with water to form guanylurea. The subsequent reaction of the guanylurea with the epoxy produces a different cured state of the adhesive resulting in a system with a lower T_g. The reaction of dicyandiamide with water in dilute acidic or basic solutions has been reported to produce guanylurea [10]. It is possible that there is not a sufficiently acidic

or basic environment in this adhesive at the test conditions for the dicyandiamide to react with water.

To determine whether either dicyandiamide or the epoxy resins in the adhesive reacted with water, a thin film of the adhesive was exposed to humidity under the same conditions as performance test specimens and the progress of the reaction was monitored by FTIR. Of particular interest are the dicyandiamide absorption peaks at 2300 and 2200. There was no change in these peaks over the course of the time the adhesive was exposed to moisture. There was also no change in the epoxy spectrum, particularly in the 3500-2800 region. From the DSC and FTIR data, it appears that this adhesive does not undergo a chemical reaction with water.

The effect of precure humidity exposure on the adhesive examined appears to be largely a physical absorption phenomena rather than a chemical reaction. When the adhesive was cured, vaporized water out-gassed causing foaming of the adhesive. Precure humidity exposure of closed bonds resulted in porosity at the bondline edges whereas exposure of open bonds, i.e. adhesive bead, resulted in more uniform foaming throughout the bondline. The adhesive in both open and closed bonds foamed out of the bond to form a larger fillet than normal. The amount of adhesive remaining in the bondline after cure decreased with increasing humidity, temperature and exposure time. For example, at 84% RH, 25°C and 24 hour exposure time (a severe exposure), the specimen exposed as an open adhesive bead had only about 50% of the adhesive remaining in the bondline after cure. Exposures at mild conditions, 43% RH, 25°C for up to 24 h, had little effect on the bondline morphology as there was only an 8% increase in porosity compared to an unexposed specimen.

The effect of the resulting porosity after precure humidity exposure on the adhesive bond performance was examined in three types of tests: lap shear, stress durability and impact peel. Lap-shear test data showed a 10-20% drop in the failure load as the amount of adhesive remaining in the bondline decreased. This is not a very large drop in failure load for a bond with only 50% of the adhesive remaining; however, since the fillet (which increases with humidity exposure) dominates the tensile failure load of a lap-shear coupon, porosity within the bondline does not greatly affect the lap-shear test results. All lap-shear specimens failed cohesively.

Stress-durability testing, which measures the ability of an adhesive bond to withstand a static load in an environment, is an accelerated test ideally suited for comparing adhesive bond performance. At the highest stress level of 7 MPa (which corresponds to approximately 30% of the initial lap shear failure load of unexposed bonded assemblies), differences between bonds exposed to precure humidity and those with no exposure were quite apparent. The average time to failure decreased from 6,816 h to 96 h (approximately 1.4% of the unexposed bond lifetime) for bonded assemblies with only 50% of the adhesive remaining in the bondline. At medium stress levels (5 MPa), the average time to failure decreased from 10,848 h to 2,688 h (approximately 25% of the unexposed bond lifetime) for bonds with only 50% of the adhesive remaining. In general, the time to failure decreased as the amount of porosity in the adhesive bondline increased for both the 7 and 5 MPa stress levels. No failures have been observed for bonded assemblies stressed at 2 MPa for any humidity exposure condition ($t > 12,500$ h).

The effect of precure humidity exposure on impact peel performance was also investigated. Impact-peel specimens do not have a true fillet since teflon tape is placed at the end of the bondline and any adhesive on the edge of the bonded assemblies is removed prior to testing. Therefore, any foaming of the adhesive after precure humidity exposure (resulting in less bonded area) should more directly relate to the impact load measurement than for measurements of lap-shear specimens. This was indeed the case as shown in Table II.

Table II - Impact Peel Loads

Type of Bond Exposed	% Adhesive Remaining in Bondline	Average Load (kN)
No Exposure	98.3 ± 1.0	0.460 ± 0.013
Closed	92.3 ± 2.4	0.464 ± 0.016
Closed	81.4 ± 1.9	0.417 ± 0.014
Closed	75.6 ± 4.4	0.416 ± 0.020
Open	52.1 ± 3.1	0.328 ± 0.023
Open	49.8 ± 1.6	0.312 ± 0.017
Open	42.2 ± 4.5	0.283 ± 0.028

The impact load decreased dramatically with increasing adhesive porosity, up to a 38% decrease for bonds

with only 42% of the adhesive remaining after cure. The total energy adsorbed also followed the same trend; however, the decrease was slightly greater. The amount of scatter increases for bonds exposed to precure humidity as the adhesive foaming patterns are somewhat variable. All of the specimens tested failed cohesively.

CONCLUSION

No chemical changes were observed in the structural epoxy adhesive studied upon precure exposure to humidity. However, precure humidity exposure increased porosity of the cured adhesive from 2 percent for unexposed adhesive to about 50 percent for adhesive with severe humidity exposure. Overall adhesive bond properties decreased with precure humidity exposure; however, the severity of the effect varied with the test. Tests in which the fillet is very important, i.e. lap shear, showed only a small decrease in properties. Tests in which the amount of adhesive in the bondline is important, i.e. impact peel and stress durability, showed a large dependence on the amount of precure humidity exposure.

ACKNOWLEDGEMENTS

We thank Ron Perry, Steve Bernock and Mo Cheung for their assistance.

REFERENCES

1. M. Fragoulis, F.C. Tolan, P.J. Pearce and C.E.M. Morris, *J. Adhesion* **20**, 275, (1987) and references therein.
2. E.B. Stark, A.M. Ibrahim, T.E. Munns and J.C. Seferis, *J. Appl. Poly. Sci.* **30**, 1717 (1985).
3. C.J. Almer and A.V. Pocius, 12th National SAMPE Tech. Con., 924 (1980).
4. R.A. Dickie, M.A. DeBolt, S.M. Ward, SAE Congress, No. 950128 (1995).
5. Ford Laboratory Test Method BV101-07 (1993).
6. V. Hospadaruk, J. Huff, R.W. Zurilla and H.T. Greenwood, SAE Congress, Paper No. 780186 (1978).
7. International Standard 11343 (1993).
8. K.G. Kibler and T.S. Creasy, *27th National SAMPE Symp.* 416 (1982).
9. R.A. Pike, F.P. Lamm and J.P. Pinto, *J. Adhesion* **13**, 229 (1982).
10. J. Eloranta, *Suomen Kemistilehti* **33**, 193 (1960).

ADHESIVE BONDING OF COATED STEELS

I.A. Ashcroft, P. Basu, G. Spinks
Dept. Materials Engineering, University of Wollongong,
Northfields Ave., Wollongong, NSW 2522, Australia.

INTRODUCTION

Adhesives are currently used to bond aluminium in structural applications but their use with steel substrates has been limited. This is partly due to the stringent requirements of large industrial users of steel and partly due to the suitability of well developed welding techniques for joining uncoated steel. The last decade has seen a rapid expansion in the use of coated steels. These materials are more difficult to weld which may make adhesive bonding a more attractive alternative joining technique. Despite previous work in this area, concerns regarding material selection, joint design and joint durability have inhibited the uptake of adhesive technology. It is also clear from the often conflicting results in the literature regarding coated steels that small differences in surface chemistry or morphology can significantly affect joint performance which limits the transfer of existing knowledge to new systems without extensive testing.

The current project is part of the Co-operative Research Centre in Materials Welding and Joining. This programme involves industry, government and university research groups and is specifically concerned with industrial oriented research. The aim of the adhesive bonding project is to address the above problems by a systematic programme to assess the initial joint strength and durability for specific systems in order to isolate the controlling factors regarding joint performance. This should enable rapid assessment of new coating systems. In this paper a review of the methods currently used in the project will be reviewed and a new technique for in-situ monitoring of the rate of water absorption in adhesives will be presented.

ADHESIVE BONDING PROGRAMME

Initial joint strength is determined with the lap shear test, which is representative of engineering joints and a width tapered cantilever beam (WTCB) which enables calculation of the fracture toughness of selected joints. Durability is assessed by accelerated ageing of lap shear and wedge test sample in a 95% R.H. environment at 50°C.

As the condition of the adherend surface was regarded as critical to the durability of the joints this is characterised by Auger electron microscopy, SEM and surface roughness measurements. A sessile drop technique is used to calculate the surface energy of adherends and adhesives in order to estimate W_{ad} .

It has been found that lap shear strength is sensitive to many factors including adherend yield strength, overlap length, bondline thickness, adhesive type and the nature of the coating on the steel. The WTCB test is less sensitive to geometric factors such as the bondline thickness which affirms its use as a more intrinsic measurement of joint performance. The coating type has been seen to have a controlling influence on the durability of the joints. Acid-base characteristics of the interface (as determined by contact angle measurements) appears to be important in determining bond strength. Work is continuing to fully establish these relationships.

WATER ABSORPTION IN POLYMERS

It is well known that the strength of an adhesive bonded joint is susceptible to degradation on exposure to a high humidity environment. The mechanism of joint degradation is often complex and can involve any or all of the following: swelling, plasticization, hydrolysis or cracking of the adhesive, solution of adhesive or filler in water, hydration, oxidation or corrosion of metal substrate, breaking of bonds at the interface or replacement of adhesive by water at the interface. Whichever mechanism is responsible for joint failure it is clear that the transport of water through the adhesive or substrate or along the interface is important.

An indentation test may be able to monitor water ingress into an adhesive and provide information concerning the mechanical properties as a function of water absorption. If the adhesive is approximately homogeneous in its initial dry state then the measured hardness will be independent of indentation depth and hence, indentation at different loads will give the same

hardness value. As water begins to diffuse into the adhesive the measured hardness will be a composite value dependent on the hardness of the dry adhesive, the hardness of the saturated adhesive and the hardness of intermediate layers which are partially saturated. In this case the measured hardness will be dependent on the thickness of these layers, which will vary with time, and the depth of indentation. This is illustrated in Fig. 1, where it can be seen that the hardness with load P_1 will be that of the saturated layer (assuming negligible substrate effect) whereas at load P_2 , the measured hardness will be some value between the hardness of the saturated and the dry adhesive. If the load is increased further the apparent hardness will increase until the saturated layer contribution becomes negligible. The apparent rate of water uptake and time to saturation will, therefore, depend on the indentation load used.

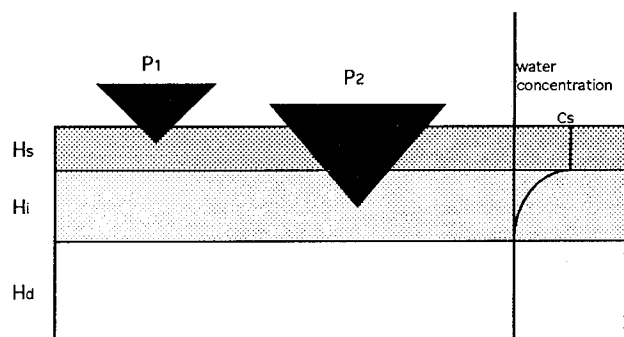


Figure 1. The effect of indentation load on the hardness of surfaces with absorbed water layers. $P_2 > P_1$, C_s is saturated concentration, H_s , H_i and H_d are saturated, intermediate and dry hardness regions respectively.

DEPTH SENSING INDENTATION

A depth sensing indentation test offers certain advantages over conventional constant load indentation tests. Since penetration depths increase for a given load as hardness decreases, constant load tests result in a different sample volume being taken depending upon the adhesive hardness and the amount of absorbed water. A fairer comparison would be made if a constant indentation depth were used or preferably a plot of hardness against depth obtained. The latter can be achieved with the use of a depth sensing indentation system which monitors force and depth as an indentation is made, allowing hardness to be calculated as a

function of indentation depth. This can be used to identify regions of different hardness through the sample thickness.

EXPERIMENTAL

The adhesive used was a commercially available, two part epoxy adhesive. A UMIS 2000 ultra micro-indentation system was used for the indentation measurements. It is well known that polymeric materials are sensitive to loading rate and therefore, the same loading regime was used for all the indentation tests. The total time for loading and unloading was 10 minutes and there were two minute pauses between indentations. Penetration depth data was also collected over a period of 100 seconds at maximum load in order to monitor the creep response. Distilled water, which had been left in the sample chamber overnight to equilibrate to the same temperature (20°C), was placed in a petri dish with the sample immediately prior to starting the indentation sequence. A series of 10 indentations with a maximum force of 100 mN were made, the entire test taking approximately 2 hours to complete.

RESULTS

Hardness calculated from the maximum load as a function of time in water can be seen in Fig. 2. Although some experimental scatter is evident, it is clear that hardness decreases as time in water increases. This is rapid initially but by approx. 80 minutes soaking time there is no further decrease in hardness within the experimental scatter.

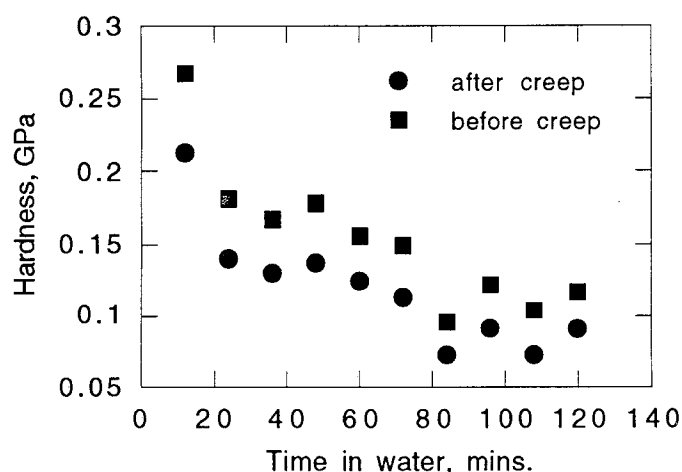


Figure 2. Variation in hardness as a function of time in water.

Fig. 3 shows the creep strain after 100 seconds as a function of time in water. The creep strain increases with time and appears to be reaching a steady value after 100 minutes.

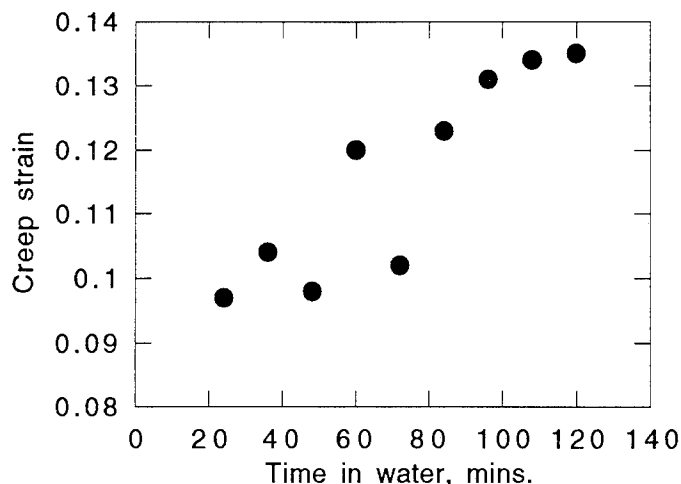


Figure 3. Variation in creep strain as a function of time in water.

Hardness as a function of penetration depth is shown in Fig. 4. After 26 minutes: the initial (low load) hardness is much lower than the final (high load) hardness and stays fairly constant with time. In contrast, the high load hardness continues to decrease until the 74 minute trace. After this time the hardness is fairly uniform with depth.

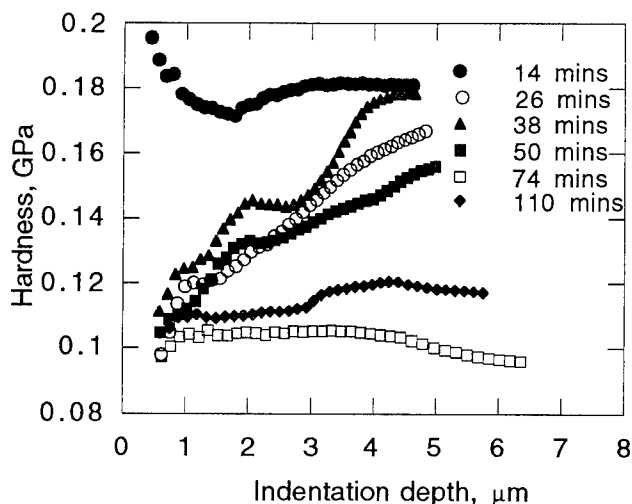


Figure 4. Hardness as a function of indentation depth.

DISCUSSION

The results observed in this study are consistent with a saturated layer of adhesive with low. The hardness measured when a layer of lower hardness is present on the surface depends on the size of the indentation and the thickness of the film. The hardness at low indentation depths quickly reaches a constant value as the surface is saturated whereas at higher loads the hardness is still a composite value between the hardness of the saturated and dry epoxy. Eventually the thickness of the saturated layer will reach a thickness where the indentation depth at the highest load is completely in the saturated film and the hardness will not vary with depth. The time taken to reach this saturation point will depend on the maximum penetration depth.

It can be seen from Figs. 2-3 that the mechanical properties of the adhesive changes significantly as water is absorbed into the surface. This means that the mechanical properties can be used as a probe to monitor the rate at which water diffuses into the adhesive. This may be more important than the actual changes in the mechanical properties of the adhesives as it is frequently the rate of transport of water to the interface which is the controlling factor in joint degradation and may be determined by the rate of diffusion through the adhesive in many systems.

The data in this study indicates that constant values of hardness and modulus with a 100 mN load are obtained after approximately 80 minutes immersion in water. This indicates that by this time the saturated layer thickness is at least as thick as the indentation depth, i.e. $>6 \mu\text{m}$. The ratio of film thickness to indentation depth at which substrate effects become negligible depends on the relative hardness of the film and substrate.

CONCLUSIONS

It has been demonstrated that depth sensing indentation systems can be used to monitor the diffusion of water through surface layers in an epoxy adhesive. Further, it has been shown that in-situ measurement of hardness as a function of indentation depth provides the most information regarding moisture penetration.

SILANE COUPLING AGENTS AS ADHESION PROMOTERS FOR BONDING THERMOPLASTIC POLYMERS TO ALUMINUM

Steven H. McKnight and John W. Gillespie, Jr.
Center for Composite Materials and the Materials Science Program
University of Delaware
Newark DE 19716

INTRODUCTION

The long-term performance of any adhesive joint is dependent on the surface preparation of the adherends prior to bonding [1]. The use of chemical coupling agents represents an alternative surface treatment to the traditional etching and anodizing of aluminum alloys. Silane coupling agents have been extensively used for promoting adhesion of thermosetting polymers to inorganic surfaces such as the hydrated oxide surfaces on metals [1-3]. However, much less research has been focused on promoting adhesion between non-reactive thermoplastic polymers to silane treated metal oxide surfaces [4]. This work further investigates the effect of silane coupling agents on the performance of thermoplastic polymers to metals.

The first portion of the study was aimed at characterizing the nature of various adsorbed silane layers. The apparent surface energy of different silane layers was assessed using dynamic contact angle measurements. This information was then used to estimate the solubility parameters of the adsorbed silanes, and predict compatibility with different thermoplastic polymers. Next the performance of polypropylene-aluminum joints was studied. The fracture toughness of the joints was measured using dual cantilever beam (DCB) and wedge-crack extension (WCE) tests, and the hot-wet durability was characterized by measuring crack extension in the wedge test specimens. Finally, the loci of failure was investigated using spectroscopic and microscopic techniques to gain insights into the adhesion promoting interactions in the interphase region.

EXPERIMENTAL

Surface Properties of Adsorbed Silane Layers

Selection of appropriate coupling agents for different polymers should be based on the nature of adhesion enhancement. Thermoset and thermoplastic polymers are believed to rely on different mechanisms for enhanced adhesion [1]. In the absence of reactivity (e.g. most thermoplastic polymers) other mechanisms must be triggered to effectively couple the polymer to the substrate. These mechanisms include the formation of semi-interpenetrating networks (semi-IPN's), which provide strength through entanglements of the thermoplastic polymer molecules and the siloxane network [1,4]. The formation of a semi-IPN requires miscibility and hence true chemical compatibility of the polymers as well as development of the network structure.

The results from simple thermodynamic interphase models suggest that in many instances, compatibility requires small differences in the solubility parameters of the two polymers [5,6]. Therefore, an estimation of the solubility parameters of

the different silane layers is important for appropriate selection. Unfortunately, the solubility parameters of adsorbed silane layers are not readily available from the literature, and are hard to measure using swelling experiments. However, it is rather straightforward to calculate the surface energies of the adsorbed layers using contact angle measurements. Additionally, the surface energies can be related to the solubility parameters using an approach outlined by Gardon [7]. This approach can be used to estimate the solubility parameters of different silane layers from measurements of the surface energies, and then used to predict compatible thermoplastic polymers.

In this work, dilute solutions of various silanes in water or methanol were used to coat cleaned glass slides. The slides were then dried for 30 minutes at 180°C; and the contact angles of different fluids on the adsorbed layer were measured immediately using a dynamic contact angle analyzer in conjunction with the Wilhelmy plate technique. A polar-dispersive analysis [8] was employed to calculate the apparent surface energies for each adsorbed silane. The Gardon approach was used to estimate the solubility parameter of the adsorbed silane films [5, 7]. The surface tension and solubility parameter values are shown in Table 1, along with values for some polymers of interest. Solubility parameters for GPS estimated here, closely agree with measured values from swelling experiments [9]. These solubility parameters can be used to select appropriate coupling agents for different polymers.

Processing Performance Relationships for Silane Treated Aluminum-Polypropylene Adhesive Joints

A processing-performance study was performed to characterize the mechanical behavior of aluminum-polypropylene joints as a function of surface treatment and processing conditions. 2008-T4 aluminum was treated using dilute solutions of various silanes in water or methanol, and drying at 50°C. Additionally, the use of a chemically modified polypropylene was investigated as an alternative means of promoting aluminum-PP bond strength [10]. (Materials are listed in Table 1.) Joints were assembled according wedge-crack extension (ASTM D-3762) and dual cantilever beam (DCB) test specimen geometries. A hot press was used to bond the thermoplastic polymers to the treated substrates. Initial processing conditions for each type of polymer were chosen on the basis of prior experience and the processing characteristics of each polymer. Wire spacers (placed in the trim areas) were used to maintain a constant bondline thickness.

Static Performance The length of the initial wedge-crack is an indication of the toughness of the polymer-aluminum bond. At a constant crack opening displacement (imparted by the wedge), shorter crack lengths are indicative of tougher bonds. To assess the effect of different adhesion promoting interactions, the initial crack lengths were compared. Figure 1 displays the initial crack lengths of the PP bonded specimen.

Two important results were obtained. First, the performance of the silane treated joints was related to the differences in solubility parameters, as evidenced by the smaller crack length observed in the CSS treated sample. The incompatibility of the GPS and PP does not allow formation of an interpenetrating network and molecular entanglements necessary for adhesion promotion [1,4]. Secondly, the performance of the MA-PP+AEAPS sample was outstanding, producing results comparable to those obtained with a toughened epoxy adhesive. This is most likely due to chemical reactions between the maleic anhydride in the MA-PP and the amino groups in the silane layer, which provide superior bonding.

The next portion of the study examined the kinetics of bond development in CSS treated aluminum-PP joints. Samples were hot-pressed at 200°C for different periods of time. The toughness of the joints was measured using DCB and wedge-crack tests. Several interesting findings can be summarized. In all DCB specimens, an increase in the critical strain energy release rate (G_{1c}) with crack length. (R-curve behavior). This was due to polymer bridging across the interface. Figure 2 shows the R-curves for two of the samples processed for 30 minutes. From these curves values of G_{1c} for initiation and propagation of the cracks could be obtained. The dependence of measured G_{1c} on process time was clearly demonstrated. Figure 3 displays G_{1c} of initiation, propagation, and values from the wedge test as a function of processing time. These results lend further support to the diffusion and semi-IPN theory of bonding for non-reactive polymers and silane layers.

Hot-Wet Durability Figure 4 displays the crack growth in 65° water for the wedge test specimen. Results for PP bonded to an anodized sample are shown for comparison [9]. The CSS treated specimens displayed the best hot-wet performance followed by MA-PP+AEAPS samples. The GPS, MA-PP, and MA-PP+CSS samples completely disbonded within 15 minutes of immersion. Thus, good static performance does not assure high resistance to hot-wet environments.

Locus of Failure Visually, the locus of failure in the CSS treated specimens visually appeared to change depending on location in joint. SEM examination shows severe PP deformation in some regions, and smooth appearance at others. Upon further examination using external and internal reflectance infrared techniques, the presence of polypropylene and silane molecules on both sides of the failure surface was detected. Figure 5 shows the reflection absorption infrared (RAIR) spectrum of the failure surfaces, and indicates both PP and CSS are present on the surface. More detailed examination using XPS is currently being performed to more accurately assess the loci of failure, and will be reported subsequently. However, these preliminary findings illustrate the ability of silane treatments to promote bonds sufficient to promote some degree of cohesive failure into the PP.

CONCLUSIONS

The use of silane coupling agents to enhance thermoplastic-aluminum adhesion was investigated. Effective adhesion promotion was shown to occur when appropriate silane selection and processing conditions were implemented. The results reported provide support to the theory that diffusion

followed by semi-IPN formation is responsible for bond improvement.

REFERENCES

- [1] A.J. Kinloch, *Adhesion and Adhesives: Science and Technology*, Chapman Hall Ltd., London, (1987)
- [2] E.P. Plueddeman, *Silane Coupling Agents*, Plenum Press, New York (1991)
- [3] Boerio, F.J. in *Treatise on Adhesion and Adhesives*; Vol. 6, Marcel Dekker, Inc; (1989)
- [4] Sung, N.H., Kaul, A., Chin, I., Sung C.S.P., *Polymer Eng Sci*, 22, 637 (1982)
- [5] Palmese, G.R., Doctoral Dissertation, Department of Chemical Engineering, University of Delaware (1991)
- [6] De Gennes, P., in *Physics of Polymer Surfaces and Interfaces*, I.C. Sánchez, ed., Butterworth-Heinemann, Boston, (1992)
- [7] Gardon, J.L., "Cohesive Energy Density" in *Encyclopedia of Polymer Science and Technology*, Wiley, New York, (1985)
- [8] Wu, S., *Polymer Interface and Adhesion*, Marcel Dekker Inc., New York, (1982)
- [9] Allen, K.W. in *Silanes and Other Coupling Agents*, K.L. Mittal, ed.; VSP BV, Zeist, The Netherlands, (1992)
- [10] J. Schultz, et.al., *J. Mat. Sci.*, 24, 4363, (1989)
- [11] McKnight, S.H., J.W. Gillespie, Jr., and C.L.T. Lambing, *Proceedings SAMPE Symposium*, (37) 1994

TABLES AND FIGURES

Table 1: Surface energies of adsorbed silane layers and corresponding estimated solubility parameters.

Silane/Polymer	γ (mN/m ²)	δ (J/cm ³) ^{1/2}	Reference
Z-6040 ¹ (GPS)	43.01	19.8-20.7	This work
GPS	-	19*	Allen
Z-6020 ¹ (AEAPS)	40.0	19.3-20.2	This Work
Z-6032 ¹ (CSS)	35.1	16.7-17.4	This Work
Epoxy Pre-polymers	45-46	17 - 21	Palmese
Amine Curing Agents	44-45	17 - 22	Palmese
Polypropylene	32-35	16-17	Wu

¹ Dow Corning ®

* Evaluated from swelling experiments on bulk silane

Table 2: Materials Used in This Study

Materials	Designation
<u>Aluminum</u>	
2008-T4	Al
<u>Polymers</u>	
Pure Polypropylene	PP
Maleic Anhydride modified Polypropylene	MA-PP
<u>Silanes</u>	
Glycidoxymethoxy silane	GPS
Cationic Styrylamine Silane	CSS
Diamino Silane	AEAPS

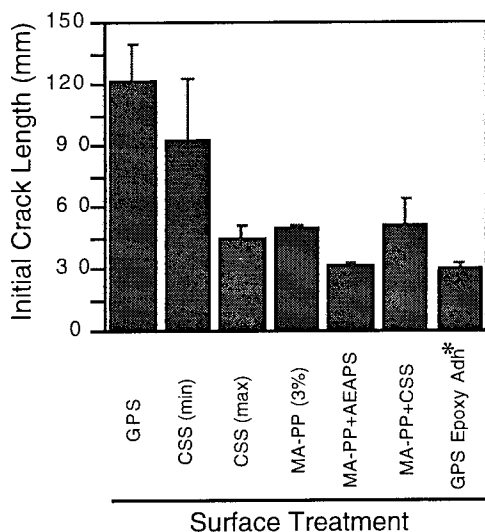


Figure 1: Initial wedge-crack lengths as a function of surface treatment. (Values for a toughened epoxy-aluminum joint are shown for comparison.)

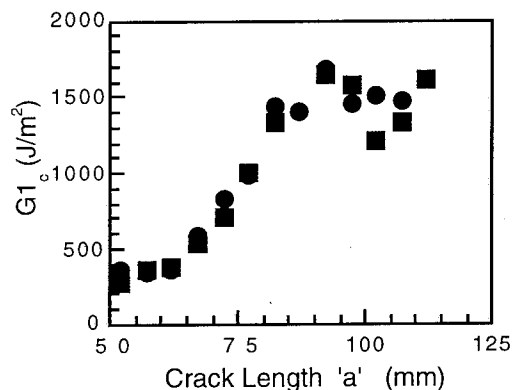


Figure 2: Typical G_{Ic} vs. crack length (R-curve) for two DCB specimens processed at 200°C for 30 minutes.

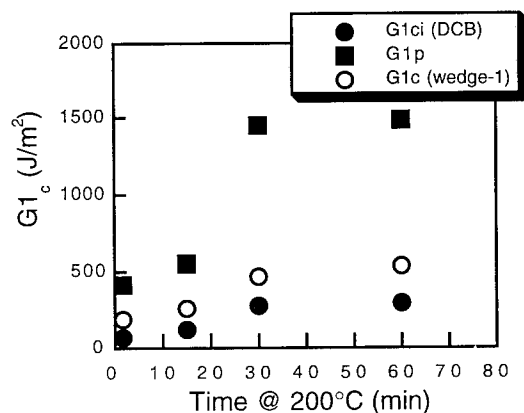


Figure 3: G_{Ic} vs. dwell time at 200°C. Values of G_{Ic} for initiation, propagation, and the values obtained from the wedge-crack test are displayed.

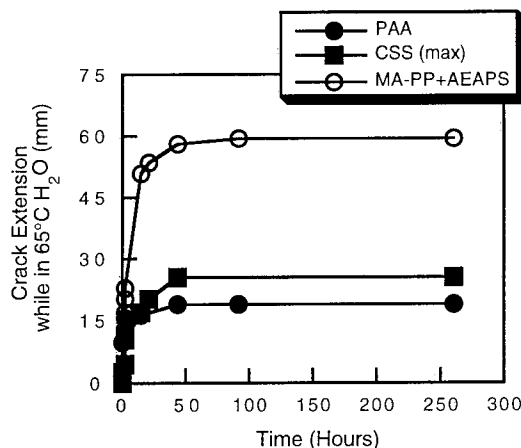


Figure 4: Crack extension (Δa) vs. exposure time (65°C H₂O) for aluminum samples bonded PP. (Note: Other treated samples had cracks which grew to full extension and are not displayed.)

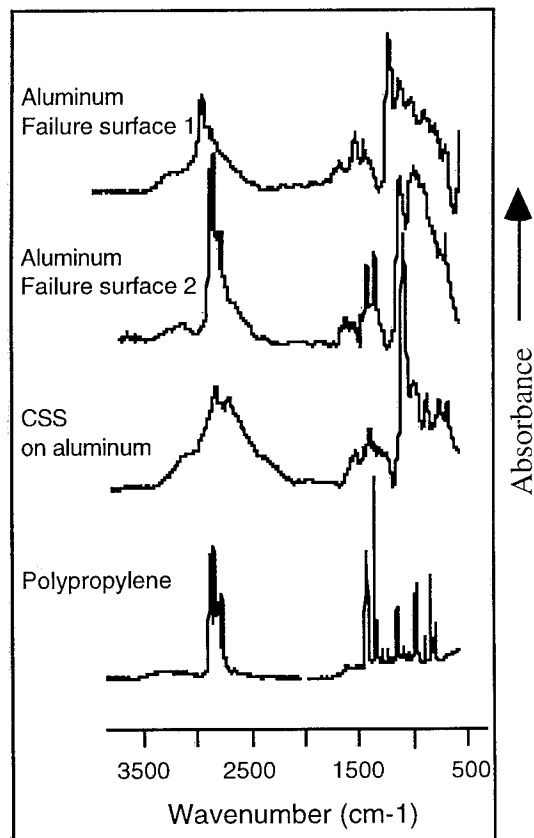


Figure 5: RAIIR spectra of two failure surfaces and CSS on aluminum; and a transmission spectrum of polypropylene.

CHARACTERIZATION OF INTERPHASES IN POLYMER/POLYMER JOINTS

M.F. VALLAT, C. SPITERI*, J. SCHULTZ, A. BELGRINE*, G. EVRARD*, A. COUPARD*

Centre de Recherches sur la Physico-Chimie des Surfaces Solides - CNRS (UPR A6601)
24, avenue du Président Kennedy - 68200 MULHOUSE (France)

*Laboratoire de Recherches et du Contrôle du Caoutchouc et des Plastiques
60, rue Auber - 94400 VITRY/SEINE (France)

INTRODUCTION

Damping rubber/metal structures are generally obtained by association of a rubber and a metal sheet through an adhesive layer. In order to reduce their weight and the corrosion problems, the metal is replaced by reinforced thermoset polymers such as epoxy resin. To eliminate the adhesive layer between the resin and the rubber, the introduction in the elastomer matrix of a functional copolymer has been proposed. The first step has been the choice of the copolymer by means of the rheometric behavior of binary blends¹. Infrared spectroscopy², differential scanning calorimetry³ and chromatography helped us to understand the interfacial interactions between the copolymer and the epoxy resin. A peel test is used to evaluate the adherence of the elastomer blends/epoxy resin assemblies. Finally, the properties of the interphase are looked for by infrared spectroscopy⁴ and mechanical measurements⁵.

MATERIALS

The epoxy resin (EP) used is a commercial diglycidyl ether of bisphenol-A monomer (DGEBA) with a low degree of polycondensation mixed with dicyandiamine (DICY) as the curing agent. The elastomer matrix is constituted by synthetic polyisoprene (IR - Natsyn 2200). The choice of the copolymer has been made using the results of the rheometric measurements on blends of resin/functional elastomer/carbon black (SAF) obtained on open mill (weight proportion 1/2/1). The comparison of the behavior of different polymers led us to choose a carboxylated acrylonitrile-butadiene copolymer (XNBR - Krynac X7.40 containing 27% CN and 7% COOH groups). Indeed, the co-crosslinking due to the

reaction between the carboxylic acid and the amine or oxirane groups is shown by the increase in the shear torque at high temperature (about 140°C) (Fig. 1). Other modifications of the properties confirm this reaction : glass transition temperature by DSC and dynamic mechanical spectroscopy, steric exclusion chromatography, infra-red spectroscopy.

ADHESIVE BEHAVIOR

The influence of two parameters :

- the degree of crosslinking of the resin before assembly,
- the mixing ratio of XNBR in the polyisoprene matrix

on the peel force (90° peel test) has been checked at room temperature and a peel rate equal to 50mm/min.

The peel energy of EP/XNBR assemblies increases when the degree of crosslinking of the epoxy resin increases up to about the gel point (40%). Then, it decreases for higher degrees. This behavior has been attributed to the reactivity of the epoxy⁶ (which increases with time) on the one hand and to the decrease of the mobility of the prepolymer⁷⁻⁸ (which prevents the diffusion of the prepolymer toward the interface) on the other hand. Moreover, the degree of crosslinking of the copolymer before assembly doesn't alter very much the peel strength. This remark is in agreement with the reactivity of the XNBR (through the carboxylic groups) and the resin which is not affected by the formation of the rubber network. It should however be noticed that ionomer formation has been observed by Mondal et al.⁹ during crosslinking of carboxylated nitrile rubber by zinc oxide. The implication of the carboxylic groups of the XNBR chains in such ionomers would retain the availability and reactivity

of these groups for further reaction with the epoxy resin during assembly at high temperature.

Fig. 2 gives the peel force as a function of the concentration of XNBR in the elastomer blend. The adherence between the elastomer matrix of IR and the epoxy resin is very small. The peel force increases suddenly when the concentration of XNBR reaches about 17-20%w/w. Moreover, the failure from interfacial becomes mixed and then cohesive in the rubber. The cohesive strength of the rubber blends goes through a minimum for 17% of XNBR in the blend

SURFACE CHARACTERIZATION OF THE RUBBER BLENDS

Two techniques have been used to show that polyisoprene and XNBR are immiscible¹⁰. Surface segregation¹¹ of XNBR in IR/XNBR blends is evidenced by wettability measurements for concentrations of XNBR between 17 and 25%. FTIR spectroscopy in ATR mode (Fig. 3) indicates that the surface of the blend is enriched in carboxylic and nitrile groups in the same domain as shown by the wettability technique.

INTERPHASE CHARACTERIZATION

FTIR microscopy in transmission mode with a 10 μ m beam diameter is performed on cross-section strata (10 μ m thick layers) of epoxy resin/XNBR assemblies normally to the interface. The diffusion of different species can then be followed. In the interphasial region, epoxy and opened epoxy ring groups due to oligomer diffusion were found to be more than 100 μ m away from the original interface. The crosslinking agent (DICY) remains very close to the interface. Consequently, the mechanical properties of the elastomer blend should be modified near the interface. The modulus of thin layers (30 to 50 μ m) of rubber cut parallel to the interface are determined on a dynamometer (Minimat) at 0.1 mm/min. On Fig. 4, are given the results obtained for EP/XNBR assemblies. As can be seen, the modulus increases drastically near the interface. Moreover, the deformation at rupture decreases showing the effect of the diffused species on the elastomer network. The thickness of the interface can be evaluated to about 200 μ m. This result confirms those obtained by infra-red

spectroscopy and also by dynamic mechanical measurements¹²⁻¹³.

CONCLUSION

By introducing a copolymer such as a carboxylated acrylonitrile-butadiene rubber in polyisoprene matrix, it is possible to built a strong bond with epoxy resin composites without any adhesive. A thick interphase (about 200 μ m) is formed due to complex diffusion processes during the elaboration of the joint. Covalent and hydrogen bonds are established between the epoxy and the carboxylic groups.

Acknowledgements : This work is supported by a grant from the French Ministry of Research and Technology. We are also grateful to Hutchinson Research Center for its technical collaboration.

REFERENCES

- 1 H.B. WANG, J. Appl. Polym. Sci., **44**, 789 (1992)
- 2 Y.S. KLYANCHKIN, V.A. TRUSHNIKOV, J. Adhesion Sci. Technol., **6**(10), 173 (1992)
- 3 J.P. PASCAULT, D. VERCHERE, H. SAUTEREAU, J. Appl. Polym. Sci., **45**, 1799 (1992)
- 4 G.T. FIELDSON, T.A. BARBARI, Polymer, **34**(6), 1184 (1993)
- 5 A.J. KINLOCH, S.J. SHAW, D.L. HUSTON, Polymer, **24**, 1355 (1983)
- 6 M.F. GRENIER-LOUSTALOT, P. GRENIER, J. Polym. Sci., **20**, 4011 (1984)
- 7 J.P. PASCAULT, J. Appl. Polym. Sci., **45**, 1799 (1992)
- 8 Y. DENG, G. MARTIN, Macromolecules, **27**, 5147 (1994)
- 9 U.K. MONDAL, D.K. TRIPATHY, S.K. DE, Polymer, **34**, 18 (1993)
- 10 P.R. COUCHMAN, Macromolecules, **24**, 5772 (1991)
- 11 S.H. ANASTASIADIS, Macromolecules, **22**, 1449 (1989)
- 12 C. SPITERI, M.F. VALLAT, J. SCHULTZ, G. EVRARD, A. BELGRINE, N. DAUBOURG, A. COUPARD, C. CARDINET, Le Vide, les Couches Minces - Suppl 268, 149 (1993)
- 13 C. SPITERI, M.F. VALLAT, J. SCHULTZ, A. BELGRINE, G. EVRARD, A. COUPARD, Proc. Euradh'94, Mulhouse September 12-14, 1994, p. 470

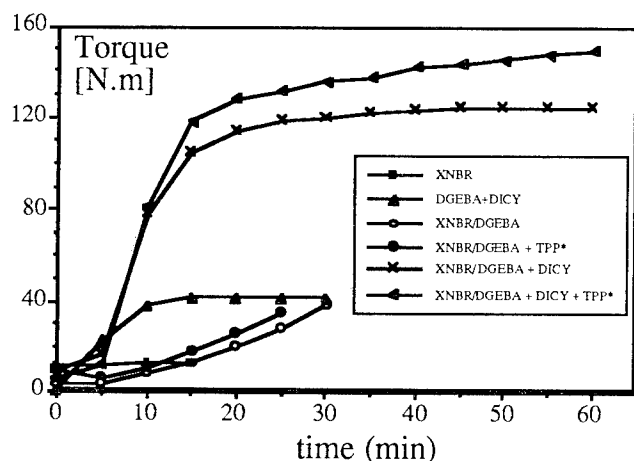


Fig. 1 : Rheometry results on EP/XNBR blends with EP crosslinking agent (DICY) and a catalyst (TPP = triphenylphosphine) of the reaction of co-crosslinking (EP-COOH)

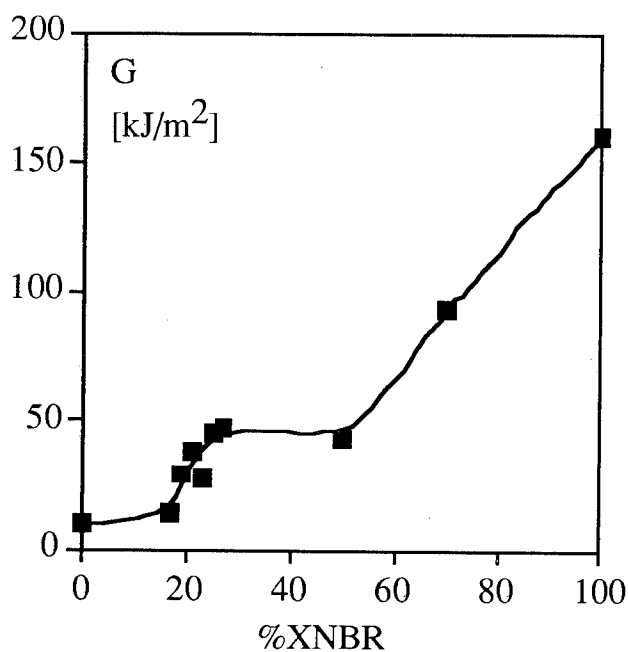


Fig. 2 : Peel energy of EP/PI-XNBR assemblies as a function of the amount of XNBR in the PI-XNBR rubber blend

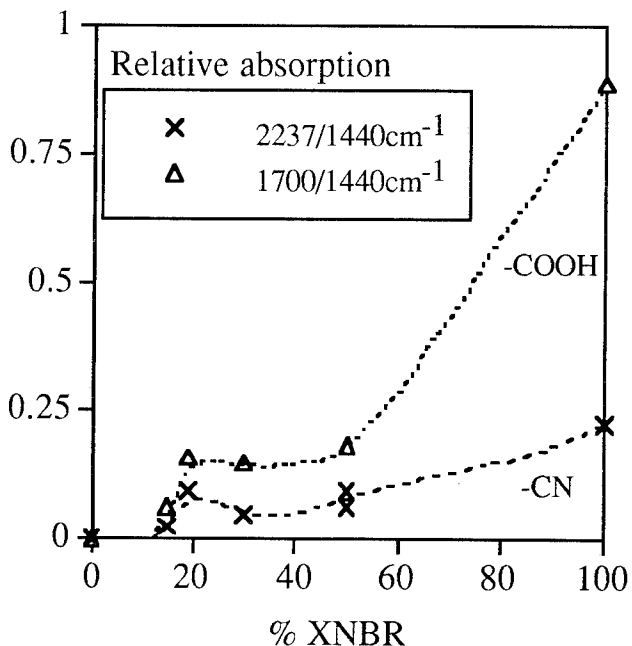


Fig. 3 : Surface functional groups by FTIR-ATR spectroscopy on PI-XNBR rubber blends

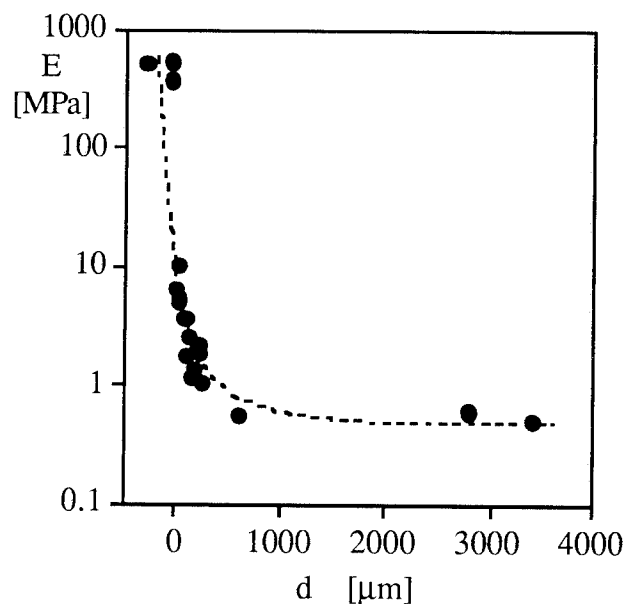


Fig. 4 : Variation of the modulus in the rubber interphase as a function of the distance from the interface

THE INFLUENCE OF SURFACE MORPHOLOGY ON THE ADHESION OF COATINGS TO THERMOPLASTIC POLYOLEFINS UNDER STRESS

Rose A. Ryntz
Ford Motor Company
Automotive Components Division
24300 Glendale
Detroit, MI 48239

INTRODUCTION

Adhesion is concerned with a situation where stress may be transmitted across the boundary between two adjacent surfaces[1]. The stress may be of several forms: tension or compression (normal to the interface); shear (parallel to the interface); peel; or a combination of these. In order to withstand stress, and prevent any considerable strain, whether across an interface or within a single coherent solid, there must be forces of resistance. The forces of resistance can be in the form of a chemical bond, or in the case of adhesion to low surface free energy plastics, the forces are those of attraction, namely secondary, van der Waals forces. These forces are comparatively weak but they are generally effective over considerably greater ranges than any of the primary forces.

In injection molded plastics, in particular where semi-crystalline polymers are involved, residual stresses can occur in the top few microns of the plastic depending upon injection molding conditions and polymer composition utilized [1]. It was reported by Schonhorn and others [1-7] that heterogeneous nucleation and crystallization of polymer melts against high-energy surfaces, e.g., metals, metal oxides, and alkali halide crystals, results in marked changes in the surface region morphology. More specifically, it was claimed that transcrystallinity [8] (transcrystallinity is reported to consist of elongated spherulites originating at the polymer surface and propagating for several microns normal to the surface) could be induced in polyethylene and polypropylene by crystallizing the respective melts in intimate contact with specially prepared aluminum and copper. Formation of a transcrystalline layer is favored by conditions which induce a high density of nuclei at the surface. A close arrangement of growth centers causes the spherulites to grow in a columnar fashion with little lateral development [9].

Microstructures of semi-crystalline polymers vary from spherulitic to lamellar and single crystals, in size of

structural units, depending upon [10]:

- molding temperature
- flow patterns
- aging and heat treatment
- nucleating agents

The distribution of spherulite sizes vary as a function of depth. In injection molded polypropylene, for example, not only does the crystal size vary but also the crystal type. Hexagonal spherulites (less perfect flat, concave boundaries) were shown to be more prominent at the surface. They were characterized by greater susceptibility to etching in SEM analysis. Monoclinic spherulites, a more crystalline, ordered arrangement, were found to occur in the bulk morphology in conical shapes. In thermoplastic olefin (TPO, a blend of polypropylene and ethylene propylene diene rubber) that had been injection molded, Bonnerup [11] found that not only was the polypropylene surface crystallinity affected but that the EPDM phase separated in the crystallization process and was present in very low concentrations at the surface.

Bikkerman [12] found that two solids in contact cannot fail exactly at the interface between them. Hence, if failure occurs at or near an interface at a relatively small applied stress a *weak boundary layer* is assumed to have been present. Weak boundary layers are believed to arise if:

- there is an incompatibility between two polymers so that they remain separate.
- the surface roughness amplitude between two similar solids is 3000 angstroms or less.
- a similar T_g for both polymers exists so that shrinkage and thermal stresses are eliminated by annealing. Fracture toughness and crack propagation are related to weak boundary layer management.

Injection molding is one of the most widely utilized methods of polymer processing. This process includes injecting molten polymer into a cold mold followed by packing under high pressure and subsequent cooling to solidification. The filling and cooling stages have an important effect on the rheological properties since the viscoelastic nature of the polymer results in development of shear and normal stresses and large elastic

deformation during filling with subsequent incomplete relaxation during the cooling stage. The resultant residual stresses, which determine the orientation in the final molded part, are dependent upon the thermal, rheological, and relaxation properties of the polymeric material as well as the processing conditions [13].

Molecular orientation in injection molding has been modeled by many researchers [14, 15] to explain the complex molecular orientation distribution observed. Most models incorporate flow and heat transfer mechanisms coupled with molecular theories. The orientation in the surface skin is related to steady elongational flow in the advancing front, whereas the orientation in the core is related to the shear flow, behind the front, between two solidifying layers [14]. Coupled with the elongational and shear-induced orientations, a molecular relaxation process takes place which is determined by the rate of heat transfer. Internal stresses that develop within the injection molded part are the result of thermal, flow, and pressure histories [16]. The melt temperature of the polymer was found to cause two maxima in residual stress (R.S.) [17]. The second one reverses from compressive to tensile. In general, most changes occur in the surface regions, while R.S. decreases with increasing melt temperature, as is the case in zones far away from the gate [17]. It was found that R.S. are compressive in the surface layers and tend to decrease upon increase in mold temperature and distance from the gate.

Residual stress can be measured by optical birefringence. Birefringence has a number of causes. The polarizability of chemical bonds change when they are stressed, giving rise to the photo-elastic response upon which measurements of residual stress may be measured. On the other hand, chemical bonds are directional and in a non-isotropic material the presence of favored bond orientations will produce birefringence, so that in an injection molded article containing frozen in molecular orientation this may provide a much larger contribution than the residual stresses [18]. The birefringence effect should be higher closest to the mold wall, dependent of course upon the heat diffusivity of the polymer and the molding conditions.

It is our intent, therefore, in this paper, to demonstrate the effect of injection molding conditions of thermoplastic olefins (TPOs) on subsequent adhesion of topcoats. The topcoats, namely two-component basecoat/clearcoat films, are made to adhere to the TPO substrates through the use of solvent-borne chlorinated polyolefin (CPO) adhesion promoters. The locus of adhesion (cohesion) failure in stressed parts is studied and the influence of alternate TPO materials is also examined.

RESULTS AND DISCUSSION

Past work [2] indicated that the morphology of TPO contained many layers of phase separated materials and that within the layers the crystallinity varied by depth into the substrate. The variance in molecular orientation within the TPO substrate was followed by optical birefringence patterns. The cross-section of the TPO, obtained by cryogenically microtoming a section of the TPO to approximately 15 microns, is mounted in Canada Balsam on a microscope slide and viewed under cross-polarized light at a magnification of approximately 50X. One can view the variation in molecular orientation near the top and bottom surfaces as thin, differently colored lines running parallel to the surfaces.

In order to differentiate whether the main contribution to birefringence was due to molecular orientation or stress, the same TPO material was injection molded as well as compression molded. Cross-sections of the molded plaques were then viewed under optical cross-polarized light. The compression molded sample showed no evidence of birefringence near the surface of the cross-section, therefore it is believed that the main contributor to the birefringence is flow induced stress.

Crystallinity variations in the TPO as a function of depth and injection molding conditions were also evident, as determined by Differential Interference Contrast (DIC) microscopy. The size of crystallites became larger going from the top and bottom TPO surfaces (size approximation < 0.5 microns) to the middle (size approximation < 50 microns). The density of these layers, however, was found to vary significantly based on microfocus x-ray fluorescence data. The top and bottom surfaces of the TPO substrate were very dense, closely packed regions, while the center, or bulk, of the TPO was less dense².

Further analysis of the TPO surface regions (the top 5-10 microns) as obtained by microtoming sections of the surface and analyzing by differential scanning calorimetry (DSC) and fourier transform infrared spectroscopy (FTIR) revealed that the amount of polypropylene (PP) to ethylene propylene rubber (EPR) varied as a function of depth into the surface as well. In the DSC analysis of skin vs. bulk TPO, not only does the melting behavior of PP vary in the skin (broad melt at 164.01°C , indicative of hexagonal form of PP crystals) vs. the bulk (sharper melt at 168.32°C , indicative of monoclinic crystal formation) but the amount present (as ratioed by the heats of fusion of PP with polyethylene (PE)) also increases in the skin. The FTIR analysis of the skin vs. bulk TPO material also indicates higher concentrations of PP in the skin vs. bulk as determined by

the ratio of the PP C-H stretch (at 1458 cm⁻¹) to the PE C-H bend (at 1166 cm⁻¹).

Since it has been demonstrated that boundary layers do exist within TPO and past literature suggests that applied stress can induce failure within boundary layers, we undertook a study to examine the effects of stress on painted TPO. In order to understand the relationship between boundary layers and the cohesive integrity of the substrate once painted (nominal thickness for CPO adhesion promoter, two-component isocyanate basecoat/clearcoat) the sample was exposed to a thermal stress as follows:

- The painted sample was immersed in a water bath maintained at 38°C for 4 hours, following which it was transferred to a -30°C freezer for a period of at least 3 hours.

- Within 60 seconds after removal from the freezer, the sample was scribed with an "X" with a utility knife, and then subjected to a high pressure mix of steam and water from a steam cleaner for a period of 30 seconds.

The temperature of the steam/water mix was approximately 90°C, at a discharge pressure of 38 KPa measured 2.5 cm from the nozzle tip. The steam/water jet contacted the plaque at the intersection of the scribe lines, from a distance of 7 cm and at an angle of 45 degrees to the plaque, on an area of approximately 100 mm². The sample was inspected visually for any delamination of paint or substrate. This analysis, done under the same conditions described for cross-polarized birefringence above, was performed on the delaminated area. The delamination occurs from the X-scribe into the top surface of the TPO. The delamination appears to be cohesive in the top boundary layer of the TPO.

The TPO was also subjected to impact by a "designer stone" and analysis of impact damage proved to also occur in the top TPO boundary layers [19] as viewed visually and as determined by numerical simulation.

In order to understand the cohesive integrity of the TPO substrate we undertook a study of the "peel strength" of the boundary layers within the substrate as measured by a modified Hesimeter. In this test method, a sample is placed horizontally on top of the translational stage of the Hesimeter and the blade is placed perpendicular to the top surface of the substrate on a side cut edge, a fixed depth below the top surface through use of a micrometer depth guide on the blade fixture. The blade then translates at a constant force across the substrate measuring the energy required to cohesively "rip" the boundary layers within the substrate from the bulk material.

Before attempting to measure the "cohesive energy" required to separate boundary layers within a

variety of TPO substrates, we developed a hypothesis on how to strengthen so-called weak boundary layers. In essence, we believed that if we could increase the compatibility of rubber phases or domains with the polypropylene matrix in the TPO substrate we would increase the cohesion. In attempts to delineate the amount of compatibility that exists between a rubber and a polypropylene we utilized a Modulated DSC (differential scanning calorimetry) technique on thin microtomed layers of the substrate itself. Our premise in measuring the thermal transitional behavior of the sectioned stated:

If compatibility between PP and EPR increased, the ability of the PP to phase separate and crystallize would be diminished. The smaller the crystallite size of PP at the surface of a TPO, therefore, should be indicative of compatibility assuming that all injection molding conditions and cooling conditions were equal. We therefore injection molded plaques of varying compatibilities of EPRs and PPs, microtomed off the top and "bulk" layers of the substrate, and measured the "reversible" and "non-reversible" behavior of the PP crystallinity (melting endotherm heat capacity). The reversible (complex heat capacity) melt relates to the ability of the polymer to undergo reversible thermal events such as T_g, whereas the non-reversible (kinetic) melt truly relates to the irreversible aspects of the polymer, e.g., evolution of moisture, decomposition, curing, and crystallization, and is only minimally dependent upon time. If we normalize all samples for amount of material being melted and take the difference between the heats of fusion (H_f) of reversible melt vs. the H_f of non-reversible melt we can use this quantity as a measure of compatibility, assuming that the crystallization effects obtained by the irreversible melt are a true indication of the "normalized" crystallinity within the sample. A smaller difference in this value should be indicative of a more compatible sample, while the more negative the difference should be indicative of smaller crystallite fractions. An ideal, perfectly compatible material should have a value of zero.

Table 1 lists the quantification of "compatibility" as measured by the modulated DSC technique described above vs. the ability of the topcoated panel to pass the Thermal Shock test methodology. In the Thermal Shock test, the value of "20" indicates no paint or substrate removal while a value of "0" is indicative of gross failure. Ratings are listed in increments of 0.5 units, with each unit representative of 0.5 mm² in failure. The reported ratings in the Thermal Shock test are the average of 10 samples baked at the corresponding bake temperature listed. It can be seen in the tabulated data, that the samples listed as finer dispersion, more compatible materials afford smaller modulated DSC "compatibility"

values and far superior Thermal Shock performance, regardless of bake temperature. It is believed that since these materials are more compatible, that the PP crystallinity is "fixed" after molding and subsequent bakes of 121°C (the topcoat bake for a duration of 30 minutes) have little effect on recrystallization (the recrystallization temperature for PP is between 112 and 121°C). The incompatible materials, however, can continue to phase separate and recrystallize in subsequent bakes and thereby strengthen their top boundary layers. In the case of incompatible, poorly dispersed PP/EPR blends, the topcoat bake temperature can have profound effects on strengthening the subsequent cohesion of the substrate.

The effect of amount and type of EPR utilized to compound a TPO should have a profound effect on the resultant cohesion of the substrate. As we discussed *vide supra*, the compatibility influences the "cohesion" of the boundary layers. Theoretically, the greater the amount of rubber contained in a TPO substrate, the more energy should be required to "rip" apart consecutive boundary layers (assuming equivalent compatibilities). This is justified by assuming that the cohesive "rip" that occurs in the TPO boundary layers is a result of cavitation of a PP-rich layer from a EPR-rich layer. If a greater quantity of EPR is present to elongate to its tensile yield prior to break or cohesive loss, then a greater amount of cohesive energy should be required to delaminate the layers. We measured this effect through Hesiometer peel test measurements. The two TPO substrates contained the same PP and the same EPR. The injection molding and cooling conditions utilized to prepare the plaques were identical. The sample with the higher EPR content, regardless of depth to which a cut was performed, displayed higher cohesive strength in the material.

The effect of injection molding conditions on the same two TPO materials (same EPR and PP with varying amounts of EPR) as above versus cohesive strength is shown in Figure 1. Samples were taken near the gate and as far from the gate as possible (termed "ungate" for these demonstrations). It can be seen that the rubber content is now not the only factor that determines cohesive integrity of the substrate. The effect of position from the gate on cohesive strength of the TPO now plays a vital role. It appears from the Figure that the samples far away from the gate, regardless of the EPR content, exhibit greater cohesive strength. This can be explained in terms of the resultant boundary layer formation described in the introduction to this paper. Residual stresses in the substrate are known to decrease as one proceeds farther from the gate. The degree of packing and crystallinity of the material also changes as a function of distance from the gate. Therefore, the findings are not surprising.

Hesiometer peel strengths were also measured on TPO blends containing varying PP tacticities and EPRs with varying levels of ethylene content. It is assumed that as the ethylene content increases in the EPR it becomes less compatible with the PP. Therefore, those materials containing low ethylene content EPR (Figure 2) should be more compatible than the TPOs containing high ethylene content EPR (Figure 3). The effect of PP tacticity (high isotacticity, approximately 70% crystalline, vs. medium tacticity, approximately 50% crystalline) and rubber content are compared vs. the cohesive strength of varying layers within the substrate. It can be generalized that higher crystallinity in the PP affords more cohesively strong materials when formulated with a low ethylene content EPR (Figure 2). In these examples lower EPR content in the formulation affords greater peel strengths. In Figure 3 the opposite holds true. Those samples with lower crystallinity PP generally afforded greater substrate cohesiveness while the EPR content made much less significant a contribution. The information attained in these experiments lends support to the hypothesis that crystallinity, as well as the compatibility of the PP/EPR phases (which in effect controls crystallinity in the molded sample), plays a significant role in controlling the cohesive strength of boundary layers within injection molded TPO samples.

The final set of experiments performed were those involving compatibility of EPR and PP in TPOs. The samples that were judged as "compatible" and "less compatible" through modulated DSC experiments were subjected to the Hesiometer peel test methodology. It can be seen in Figure 4 that the samples classified as "compatible" generally require a greater amount of energy to "rip" boundary layers apart, regardless of depth into the substrate, than those deemed "less compatible". The same trend holds true as discussed above that the higher the EPR content generally the greater the cohesive strength within a given set of compatibilities between the EPR and PP.

Conclusions

Injection molding conditions, e.g., melt temperature, aging and heat treatment, surface geometry, etc., have been shown to be significant in determining the final cohesive strength of a TPO substrate. The crystallinity and phase separation that occurs in a TPO sample once molded can be controlled to some degree based on the molding history. The degree of cohesive strength in a TPO sample, however, seems to be a direct result of the blends of EPR and PP that are chosen. Although we have not fully defined the formulation parameters required to attain a robust TPO material

system, i.e., impact resistance, paintability, cohesive integrity, etc., we believe that we have undertaken some fundamental studies in terms of defining measurements of compatibility within them. We will continue to relate the material properties of the TPO to the ability of the TPO to accept automotive grade topcoats. Our experiments now focus on understanding the role of diffusion related events, such as the ability of a solvent-borne CPO adhesion promoter to promote paint adhesion, on subsequent paint adhesion and cohesive strength within TPO composites as related to material properties, such as compatibility, crystal size, and induced shear stresses.

REFERENCES

1. Allen, K.W. Analytical Proceedings, 1992, 29, 389.
2. Ryntz, R.A. "The Effects of Thermoplastic Olefin (TPO) Morphology on Subsequent Paintability and Thermal Shock Performance", J. Coating Technology (in press) (1994).
3. Schonhorn, H. Macromolecules, 1(2), 145 (1968).
4. Kwei, T.K., Schonhorn, H.L., and Frisch, H.L. J. Appl. Phys. 38 (6), 2512 (1967).
5. Schonhorn, H. J. Polymer Phys., B 5, 919 (1967).
6. Schonhorn, H. and Bryan, F.W. J. Polym. Sci., A-2 6, 231 (1968).
7. Schonhorn, H. J. Polym. Sci. B 2, 465 (1964).
8. Sharples, A. Introduction to Polymer Crystallization, St. Martin's Press, New York, 1966, p. 21.
9. Fitchmun, D.R. J. Polym. Sci. Part B 7 (4), 301 (1969).
10. Bartosiewicz, L. and Mencik, Z. Internal Ford Communication (1974).
11. Bonnerup, C. and Gatenholm, P. J. Polymer Sci. Part B 31 1487 (1993).
12. Bikkerman, J. J. The Science of Adhesive Joints 2nd Edition, Academic Press, New York, 1968, Chapter 7.
13. Isayev, A. I. and Hieber, C. A. Rheol. Acta 19 168 (1980).
14. Tadmor, Z. J. Applied Polym. Sci. 18, 1753 (1974).
15. Flaman, A. A. M. Polymer Eng. and Sci. 33 (4), 193 (1993).
16. Hastenberg, C. H. V., Wildervanck, P. C., and Leenen, A. J. H. Polymer Eng. and Sci. 32 (7), 506 (1992).
17. Siegmman, A., Buchman, A., and Kenig, S. Polymer Sci. and Eng. 22 (9), 560 (1982).
18. White, J. R. Polymer Testing 4, 165 (1984).
19. Ryntz, R. A., Ramamurthy, A. C., and Mihora, D. J. "A Numerical Simulation of Impact Induced Failure in TPO Substrates" J. Coating Technology (in press) (1994).

Table 1 Compatibility Assessment of Varying PP/EPR Blends

PP/EPR Composition	Modulated DSC Quantity (H_f rev - H_f non-rev)	Thermal Shock Performance 80°C	
		Bake	121°C Bake
Control	-0.146	16.1	19.8
More compatible, finer dispersion	-0.076	20	20
Less compatible	0.122	16.9	19.9

Figure 1 The Effect of Molding Position on the Cohesive Strength of TPO

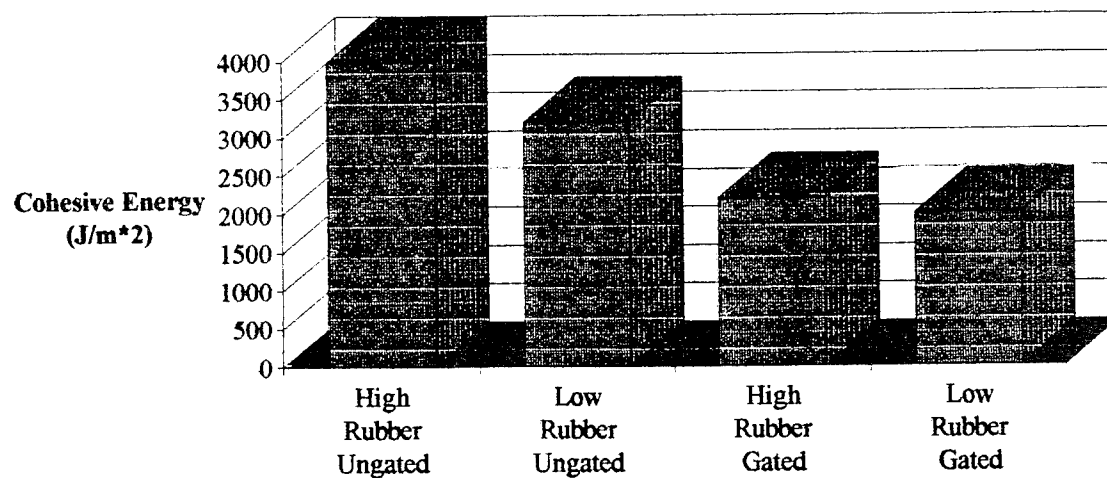


Figure 2 The Effect of PP Tacticity on the Cohesive Strength of Low Ethylene Content Rubber TPO

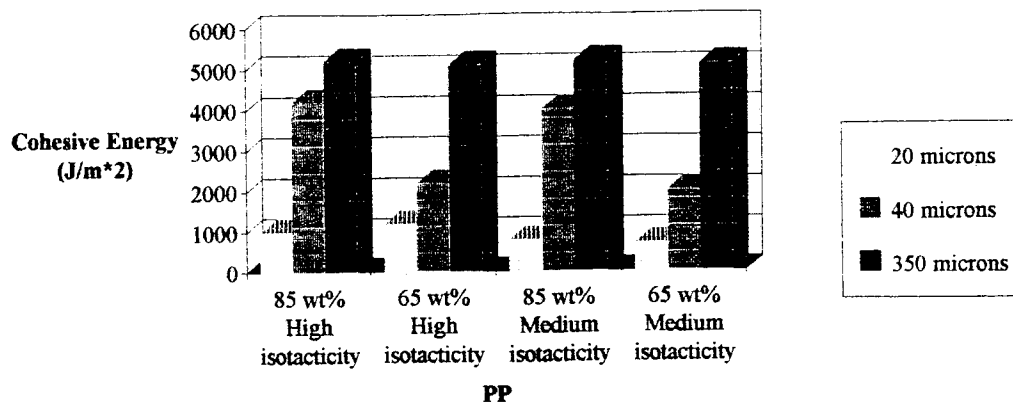


Figure 3 The Effect of PP Tacticity on the Cohesive Strength of High Ethylene Content Rubber TPO

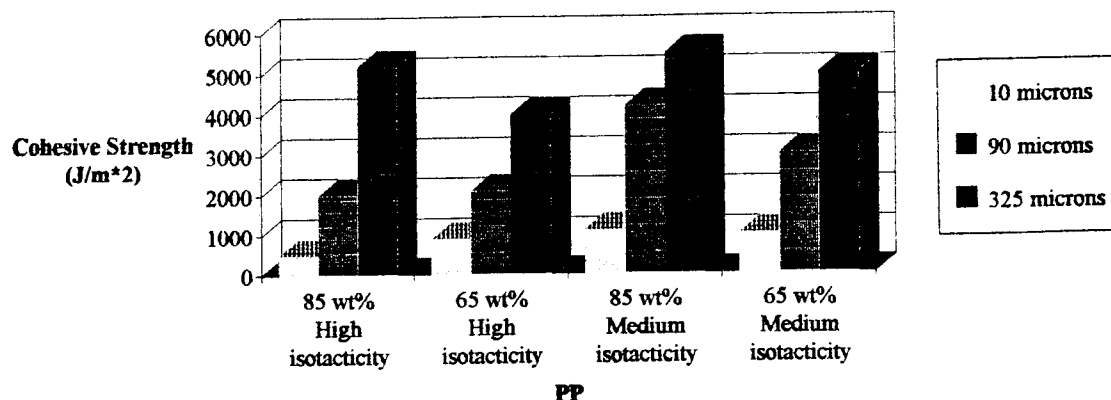
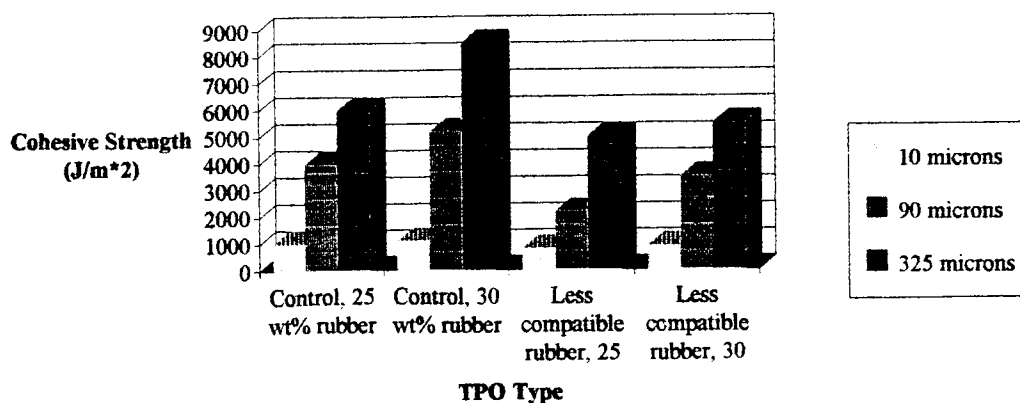


Figure 4 The Effect of Rubber Compatibility on the Cohesive Strength of TPO



work of adhesion values are expected to be small in relation to other systems, for example polymer-metal interfaces.

In summary, RPA FT-IR spectroscopy, with a proper experimental setup, can be utilized to monitor diffusion processes in polymers, morphology changes, and interfacial interactions induced in bilayer polymer systems. With proper

calibration curves, RPA FT-IR can be used for quantitative analysis of processes at the ppm level. Monitoring changes on the molecular level during substrate elongation allows attractive and repulsive interfacial forces to be related to changes in the substrate bond distance and utilized in the measurement of work of adhesion.

Table I
Calculated Work of Adhesion Values

	V(dis) ergs * 10 ¹⁶	V(rep) ergs * 10 ¹⁰	V(or) ergs * 10 ¹⁸	V(ind) ergs * 10 ¹⁵	W _A (total) J/m ² * 10 ⁴
ACRYLIC/PE	1.13	1.41	0	3.02	9.82
ACRYLIC/PP	1.10	1.39	4.17	3.77	8.56
EPOXY/PE	1.12	1.45	0	2.98	7.49
EPOXY/PP	1.09	1.44	4.14	3.71	4.68

References:

- Salazar-Rojas, E.M.; Urban, M.W. *J. Polym. Sci.: Polym. Chem. Ed.* **1990**, *28*, 1593.
- Urban, M.W. *Prog. Org. Coat.* **1989**, *16*, 371.
- Huang, J.B.; Urban, M.W. *J. Chem. Phys.*, **1993**, *98*, 5259.
- Huang, J.B.; Urban, M.W. *J. Chem. Phys.*, **1994**, *100*, 4509.
- Urban, M.W.; Gaboury, S.R. *Macromolecules* **1989**, *22*, 1486.
- Gaboury, S.R.; Urban, M.W. *ACS Proc. PMSE* **1989**, *60*, 875.
- Urban, M.W. In *Structure-Property Relationships in Polymers*; Urban, M.W.; Craver, C.D. Eds.; Am. Chem. Soc.: Washington, D.C., 1993.
- McDonald, W.F.; Goettler, H.; Urban, M.W. *Appl. Spectrosc.* **1989**, *43*, 1387.
- Urban, M.W.; Goettler, H. U.S. Patent 5,036,708, 1991.
- Urban, M.W. *Vibrational Spectroscopy of Molecules and Macromolecules on Surfaces*, Wiley & Son, New York, 1993.
- McDonald, W.F.; Urban, M.W. *J. Adhesion Sci. Technology* **1990**, *4*, 751.
- Pennington, B.D.; Urban, M.W. *J. Adhesion Sci. Technology* **1995**, in press.
- Ludwig, B.W.; Urban, M.W. *Polymer* **1992**, *33*, 3343.
- Ludwig, B.W.; Urban, M.W. *Polymer* **1993**, *34*, 3376.
- Ludwig, B.W.; Urban, M.W. *Polymer* **1994**, *35*, 5130.
- Huang, J.B.; Urban, M.W. *J. Chem. Phys.* **1993**, *98*, 5259.
- Ludwig, B.W.; Urban, M.W. *J. Coatings Technology* **1994**, *66*, 59.
- London, F. *Trans. Far. Soc.* **1937**, *33*, 8.
- Debye, P.J.W. *Phys. Z.* **1920**, *21*, 178.
- Zakin, M.R.; Herschbach, D.R. *J. Chem. Phys.* **1985**, *83*, 6540.
- Zakin, M.R.; Herschbach, D.R. *J. Chem. Phys.* **1986**, *85*, 2376.
- Herschbach, D.R.; Laurie, V.W. *J. Chem. Phys.* **1961**, *35*, 458.
- Oxtoby, D.W. *J. Chem. Phys.* **1979**, *70*, 2605.
- Schwartz, R.N.; Slawsky, Z.I.; Herzfeld, K.F. *J. Chem. Phys.* **1952**, *20*, 1591.

IN SITU FTIR STUDY OF THE REACTION OF ORGANOSILANES AT THE FLAT SILICA SURFACE.

M.J. Azzopardi and H. Arribart

Laboratoire CNRS/Saint-Gobain
Surface du Verre et Interfaces
BP 135 ; 93303 Aubervilliers Cedex ; FRANCE

INTRODUCTION

Organosilanes are widely used to improve the durability of adhesion between silicate glasses and polymers [1]. For this purpose, the surface of glass is commonly coated with an organosilane layer from an aqueous solution of a trihydrolyzable silane (general formula RSiX_3 , where R is an appropriate organic group and X is a hydrolyzable group such as $-\text{Cl}$, $-\text{OC}_2\text{H}_5$, $-\text{OCH}_3$...). Several reactions may occur when the silane solution is in contact with the glass surface : hydrolysis and condensation in solution, bonding to the glass surface, growth of a polymerized layer. Reactivity of silanes in solution [2] and with high specific area silica powders has been extensively studied [3], but the mechanisms of the interaction with surface sites of flat substrates and the formation of the polysiloxane layer remain a challenging area of adhesion science.

In the present study we focus on the in-situ investigation of the reactions at the interface between an organosilane solution and a flat silica surface. The experimental technique that we have used is infrared spectroscopy. High sensitivity has been achieved by using the attenuated total reflection (ATR) technique in a liquid flow cell. The ATR crystal, either silicon or germanium, is covered with a very thin silica layer. We report two experiments obtained with model systems : triethylsilanol and diethylchlorosilane interacting with the silica surface in an organic solvent.

EXPERIMENTAL METHODS

Specimen preparation and FTIR-ATR analysis have been previously described [4]. Here the internal reflection element (IRE) is a germanium crystal ($50 \times 10 \times 0.5 \text{ mm}^3$) covered with a silica thin film, typically 100 \AA thick, prepared by RF sputtering.

To monitor the chemical conditions of the surface reaction, the pure solvent, CCl_4 , or the silane solution are allowed to circulate through the ATR flow cell. The experimental set-up is maintained under a N_2 gas flow in order to avoid moisture. A fresh solution of silane in CCl_4 is prepared and checked by IR transmission spectroscopy. After preparation of the IRE, the flow cell is immediately assembled and aligned in the purged sample compartment of the spectrometer. A background spectrum is collected once the cell is filled with the solvent. Then the silane solution is pumped into the cell. Spectra are collected during the reaction until no change can be detected. Finally, pure solvent is circulated through the cell to remove the molecules which have not reacted with the surface and spectra are collected, again until no change occurs.

Spectra are calculated in absorbance unit per reflection.

RESULTS AND DISCUSSION

Submonolayer grafting : reaction of triethylsilanol with silica

The reaction of monohydrolyzable silanes with silica surface can lead to the formation of at most one monolayer of grafted molecules. Therefore, these reagents permit to probe the chemical reactivity of surface sites. In order to avoid any ambiguity about the hydrolysis state of the reagent, we have chosen to start our study with triethylsilanol, $(\text{C}_2\text{H}_5)_3\text{SiOH}$.

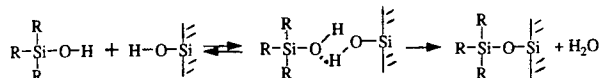
The first results obtained for the reaction of triethylsilanol with a thin film of silica on a silicon crystal have been previously published [4]. We have shown that some surface silanols were consumed but, as the characteristic Si-O-Si absorption band is outside the spectral window of silicon, it was not possible to directly detect a siloxane bond. As illustrated in the following example, this could be achieved by using a germanium IRE.

Fig. 1a and 1b display the spectrum obtained using our ATR experiment with a germanium IRE, after having rinsed the reagent by circulating the pure solvent and leaving it in the cell. The evanescent wave is sensitive to the grafted molecules only. The positive band around 1060 cm^{-1} is attributed to the siloxane bonds formed between the silica and the reagent, $\nu_{\text{as}}(\text{Si}_2\text{O-Si})$. A negative band is observed near 3660 cm^{-1} and is attributed to the surface silanols which have reacted with the reagent, $\nu(\text{Si}_2\text{O-H})$. In CCl_4 medium, this frequency corresponds to both the isolated/geminal surface silanols and the pairs of adjacent silanols H-bonded to each other [6]. The intensity of the CH_3 absorption band, $\nu_{\text{as}}(\text{CH}_3)$ at 2955 cm^{-1} , allows us to determine the amount of grafted molecules, with respect to the band intensity of non grafted molecules and taking into account the intensity distribution of the evanescent wave inside the solution [4] : grafted molecules form a submonolayer of less than one molecule per 1.5 nm^2 .

Fig. 2 shows the result of the subtraction between the spectrum obtained at the end of the reaction and the spectrum obtained after having rinsed the reagent. For the spectrum obtained at the end of the reaction, where the cell is still being filled with the silane solution, the evanescent wave probes both the molecules grafted on the silica surface and the unreacted ones in solution. Therefore, the positive bands are due to the species that are eliminated when rinsing. We observe that not only the molecules of triethylsilanol in solution but also those hydrogen bonded to the surface ($\nu(\text{O-H bonded})$ near 3200 cm^{-1}) are eliminated when rinsing with pure solvent. The negative band near 3660 cm^{-1} is attributed to the surface silanols that have been restored by the elimination of the hydrogen bonded molecules of the reagent when rinsing.

Fig. 3 shows the evolution during the reaction of the intensity of the following bands : $\nu(\text{Si}_2\text{O-H})$ near 3660 cm^{-1} , $\nu(\text{C-H})$ near 2900 cm^{-1} , $\nu_{\text{as}}(\text{Si}_2\text{O-Si})$ near 1060 cm^{-1} . We observe that both the C-H band of the reagent and the band of the silanol sites of the silica surface reach a plateau after few minutes of reaction : a rapid adsorption occurs on the surface silanols. As we have shown before (fig. 2), when rinsing with pure solvent, non-grafted molecules of reagent and molecules H-bonded with surface silanols are eliminated. Correlatively, the formation of the siloxane bond is relatively slow : it takes about one hour to reach a plateau.

According to these observations, our interpretation of the reaction is that triethylsilanol molecules adsorb rapidly on the surface silanols via hydrogen bonding and then, a small part leads to the formation of a covalent bond. We suggest that, the silanol sites which are involved in the covalent bonding are different from those reacting through hydrogen bonding. The reaction may be depicted as follow :



Monolayer grafting : reaction of diethylchlorosilane with silica

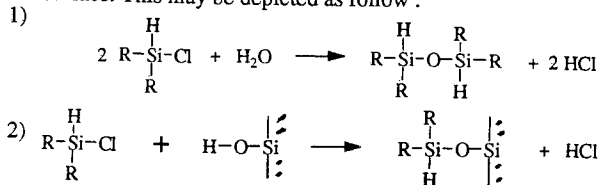
We have studied the case of diethylchlorosilane, $(C_2H_5)_2(H)SiCl$, in order to illustrate the formation of a dense monolayer of silane. This particular reagent has been chosen with regard to the high reactivity of Cl groups and the rich potential of information which can be drawn from the Si-H infrared band. Indeed, the absorption frequency of the $\nu(Si-H)$ band is very sensitive to the electronegativity of the substituents on the silicon atom [7]. Therefore, we have shown that the $\nu(Si-H)$ band is observed at 2152 cm^{-1} in diethylchlorosilane and at 2110 cm^{-1} in tetraethylsiloxane, the condensed derivative. The frequency of the $\nu(Si-H)$ band gives information about the hydrolysis or condensation state of the reagent.

Fig. 4a, 4b and 4c display three spectra obtained using our ATR experiment with a germanium IRE, where the cell is still being filled with the silane solution, during the reaction. The evanescent wave probes both the molecules grafted on the silica surface and the unreacted ones in solution. As for the precedent case (fig 1), the formation of siloxane bonds between the silica and the reagent is evidenced by the $\nu_{as}(Si_3O-Si)$ band around 1060 cm^{-1} in fig. 4c and a consumption of surface silanols, both isolated/geminal surface silanols and pairs of adjacent silanols H-bonded to each other, is evidenced by the negative $\nu(Si_3O-H)$ band near 3660 cm^{-1} . We observe furthermore the consumption of chains of surface silanols H-bonded to each other and to water and of surface water, which is seen by the negative broad band near 3350 cm^{-1} in fig. 4a attributed to $\nu(Si_3O-H\dots)$ and $\nu(HOH)$. The negative band near 1625 cm^{-1} in fig. 4c due to $\delta(HOH)$ confirms that some surface water is eliminated during the reaction. On the other hand, the formation of siloxane bonds between the reagent and the silica surface is confirmed by the emergence of a shoulder on the low frequency side of the $\nu(Si-H)$ band in fig. 4c. Indeed, the $\nu(Si-H)$ band is observed at 2155 cm^{-1} in diethylchlorosilane and near 2140 cm^{-1} for the grafted molecules (ATR spectrum obtained after having rinsed with pure solvent, not shown here).

The result of the subtraction between the spectrum obtained at the end of the reaction and the spectrum obtained after having rinsed the reagent (not shown here) is similar to the spectrum of the reagent in solution. Therefore, only the molecules of diethylchlorosilane remaining in solution are eliminated when rinsing with pure solvent.

Fig. 6 shows the evolution during the reaction of the intensity of the following bands : $\nu(Si_3O-H)$ near 3660 cm^{-1} , $\nu(O-H\dots)$ near 3350 cm^{-1} , $\nu(C-H)$ near 2900 cm^{-1} , $\nu(Si-H)$ in diethylchlorosilane near 2155 cm^{-1} , $\nu(Si-H)$ in grafted molecules near 2140 cm^{-1} , $\nu_{as}(Si_3O-Si)$ near 1060 cm^{-1} . We observe that the isolated/geminal surface silanols and the pairs of adjacent silanols H-bonded to each other disappear more rapidly than the chains of surface silanols H-bonded to each other and to water. On the other hand, the intensity of the C-H band allows us to determine that grafted molecules form a dense monolayer.

According to these observations, our interpretation of the reaction is that diethylchlorosilane reacts through the formation of siloxane bonds, rapidly with the isolated/geminal surface silanols and the pairs of adjacent silanols H-bonded to each other and more slowly with the chains of surface silanols H-bonded to each other and to water. We assume that some water molecules adsorbed on the silica surface are involved in the first step of the reaction to form a by-product, the tetraethylsiloxane, which is eliminated from the surface. This may be depicted as follow :



CONCLUSION

We have demonstrated that the grafting of triethylsilanol and diethylchlorosilane on the silica surface occurs through the formation of siloxane bonds, the progressive built up of the organosilane layer being monitored in situ by means of a sensitive FTIR-ATR experiment. We have shown that the reaction of triethylsilanol with silica leads to the formation of a submonolayer whereas the reaction of diethylchlorosilane leads to the formation of a dense monolayer. As the reactivities of the organosilanes studied are very different, it has also been possible to identify different silanols sites of the silica surface.

REFERENCES

1. E.P. Pluedemann, *Silane Coupling Agents* (Plenum Press, New York, 1982)
2. H. Ishida, *Polym. Comp.* **5** (2), 101 (1984)
3. E.R. Pohl and F.D. Osterholtz, in *Silanes and Other Coupling Agents*, K.L. Mittal ed. (VSP, Utrecht, 1992) or *Journal of Adhesion Science and Technology*, **6** (1), 127 (1992)
4. C.P. Tripp and M.L. Hair, *Langmuir* **8**, 1961 (1992) and literature cited
5. M.J. Azzopardi and H. Arribart, *Proceedings of the 16th Annual Meeting of the Adhesion Society, Williamsburg, 1993*, p. 310
6. M.J. Azzopardi and H. Arribart, *J. Adhesion*, in press
7. F.M. Mirabella Jr. and N.J. Harrick, *Internal Reflection Spectroscopy : Review and Supplement* (Harrick Sc. Corp., New York, 1985)
8. W.D. Bascom, *J. Phys. Chem.* **76** (22), 3188 (1972)
9. E.J. Heilweil, M.P. Casassa, R.R. Cavanagh and J.C. Stephenson, *J. Chem. Phys.* **82**, 5216 (1985)
10. A.L. Smith, *Spectrochimica acta* **16**, 87 (1960)
11. A.L. Smith and N.C. Angelotti, *Spectrochimica acta* **15**, 412 (1959)
12. R.N. Kniseley, V.A. Fassel and E.E. Conrad, *Spectrochimica acta* **15**, 651 (1959)

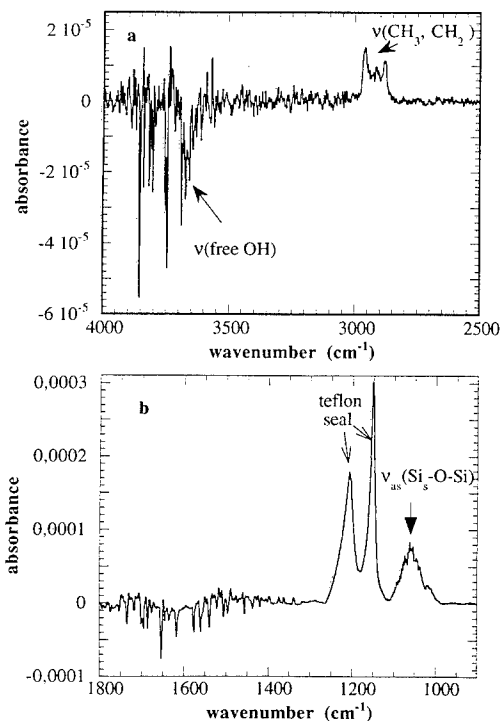


Fig. 1.a) and b) Attenuated total reflection spectrum after reaction of triethylsilanol + CCl_4 with the cell filled with the solvent CCl_4 .

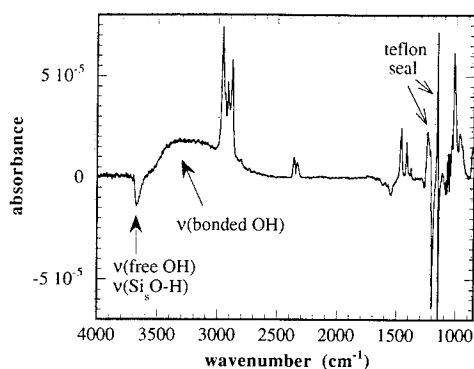


Fig. 2 Result of the subtraction between the spectrum obtained at the end of the reaction of triethylsilanol + CCl_4 and the spectrum obtained after having rinsed with CCl_4 .

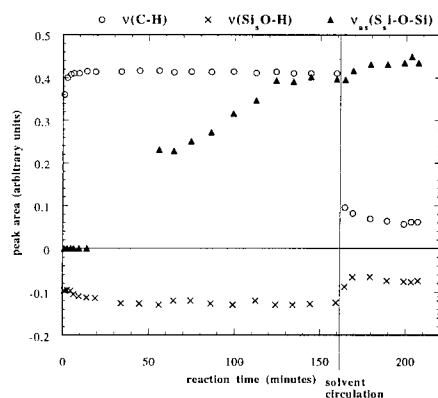


Fig. 3 Evolution during the reaction of triethylsilanol + CCl_4 of the intensity of the following bands : $\nu(\text{Si}_3\text{O-H})$ near 3660 cm^{-1} , $\nu(\text{C-H})$ near 2900 cm^{-1} , $\nu_{\text{as}}(\text{Si}_3\text{-O-Si})$ near 1060 cm^{-1} .

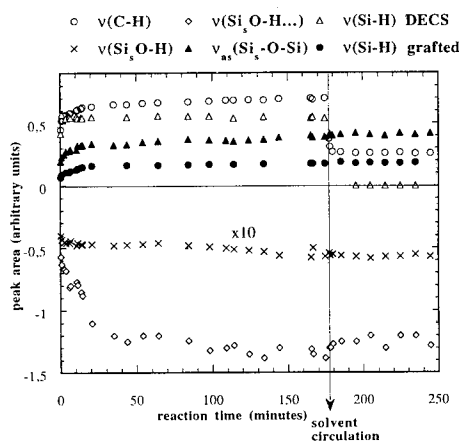


Fig. 5 Evolution during the reaction of diethylchlorosilane + CCl_4 of the intensity of the following bands : $\nu(\text{Si}_3\text{O-H})$ near 3660 cm^{-1} , $\nu(\text{O-H...})$ near 3350 cm^{-1} , $\nu(\text{C-H})$ near 2900 cm^{-1} , $\nu(\text{Si-H})$ in diethylchlorosilane near 2155 cm^{-1} , $\nu(\text{Si-H})$ in grafted molecules near 2140 cm^{-1} , $\nu_{\text{as}}(\text{Si}_3\text{-O-Si})$ near 1060 cm^{-1} .

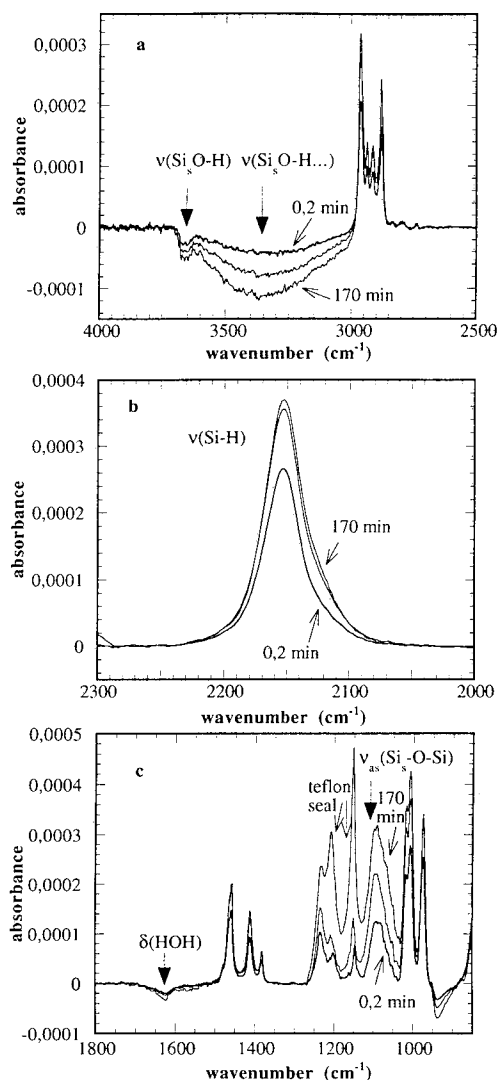


Fig. 4.a), b) and c) Attenuated total reflection spectrum during the reaction of diethylchlorosilane + CCl_4 with the cell filled with the reagent solution.

ADHESION BETWEEN SEMI-CRYSTALLINE POLYMERS

E. Boucher, J. P. Folkers, H. Hervet, L. Léger

Laboratoire de Physique de la Matière Condensée

Collège de France

11, place Marcelin Berthelot 75231 Paris Cedex 05, FRANCE

U.R.A. C.N.R.S. 792

INTRODUCTION

Because of their potential use in a wide range of applications, assemblies containing two (or more) different polymers have been widely studied. In general, however, the two polymers are incompatible, and the corresponding composites have poor mechanical properties. A third component, or "compatibilizer", is often added to avoid interfacial failure between the polymers in multilayer structures and blends [1]. For two-component systems of glassy polymers, copolymers of the two components have been shown to be efficient compatibilizers, and the mechanism of action for diblock copolymers has been thoroughly elucidated in recent studies [2, 3].

In this study, we report results on a system of two incompatible, semi-crystalline polymers, polypropylene and polyamide-6, that is strengthened by *in situ* formation of diblock copolymer at the interface. We have evaluated the energy of adhesion (G) by measuring the strain energy release rate (G_c) using an asymmetric double cantilever beam (ADCB) test. X-ray Photoelectron Spectroscopy (XPS) proved to be a reliable method for determining the amount of copolymer at the interface. Using ADCB, XPS, and Scanning Electron Microscopy (SEM), we have studied the kinetics of adhesion and the mechanism of dissipation.

EXPERIMENTAL

Materials.

We used commercial-grade polyamide-6 (PA6) and polypropylene (PP). For PA6, M_n was 17000 g/mol with $M_w/M_n \approx 2$. The PA6 chains had an average of one NH_2 end per chain. In the case of PP, M_n was 57000 g/mol and M_w was 275000 g/mol. The PP was 95% isotactic and had less than 1500 ppm of additives (mainly anti-oxidants). The functionalized polypropylene (PP_s) was prepared by ELF ATOCHEM and had an average of one succinic anhydride group per chain. PP_s chains were diluted in pure PP at a weight fraction of 5 %, giving a product denoted here as PP^* . All materials were available as films with thicknesses of approximately 600 μm .

Preparation of Samples.

Joints between PA6 and PP^* were created by the formation of copolymer at the interface through the reaction between a succinic anhydride group of PP_s and an NH_2 end of PA6 (Figure 1). Samples were made by clamping sheets of PA6 and PP^* together under slight pressure in a mold that was heated in a temperature-controlled furnace between 185 °C and 220 °C.

Measurement of Adhesion Energies.

Because the mechanical properties of PA6 are very sensitive to the water content in the polymer, all samples

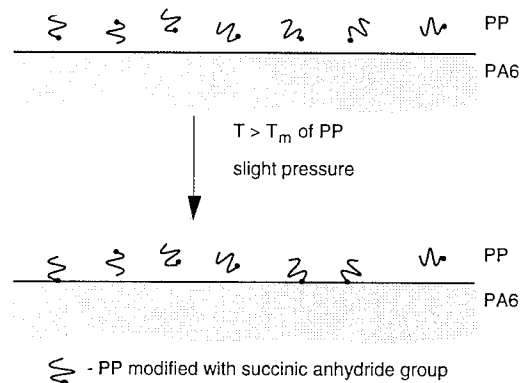


Figure 1: Formation of copolymer at the interface.

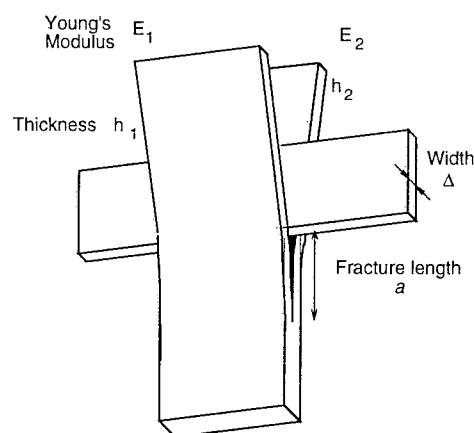


Figure 2: Fracture test geometry.

were stored in an atmosphere of controlled humidity for at least 24 h prior to measurement of the fracture toughness by the ADCB test [4]. Details of the measurement are shown in Figure 2: a blade of width Δ was inserted at the interface between PP^* and PA6, and was pushed into the sample at a speed of 3 $\mu\text{m/s}$. The critical strain energy release rate is

$$G_c = \frac{3 \Delta^2}{8 a^4} \frac{E_1 h_1^3 E_2 h_2^3}{E_1 h_1^3 \alpha_2^2 + E_2 h_2^3 \alpha_1^2}$$

where α_i is a correction factor given by

$$\alpha_i = \left(1 + 1.92 \frac{h_i}{a} + 1.22 \left(\frac{h_i}{a} \right)^2 + 0.39 \left(\frac{h_i}{a} \right)^3 \right) / \left(1 + 0.64 \frac{h_i}{a} \right)$$

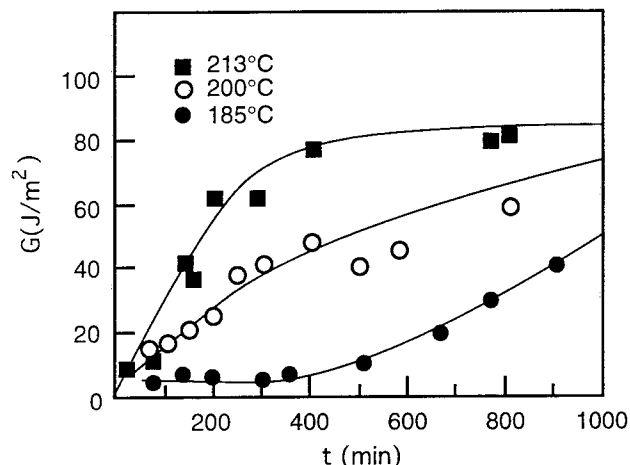


Figure 3: Energy of adhesion G as a function of time for three different temperatures.

Images of the region ahead of the blade were recorded by a video system for every millimeter that the blade advanced. The fracture length and its standard error were determined from at least 10 images.

X-ray Photoelectron Spectroscopy (XPS).

Bulk PA6 was removed from an uncleaved sample using a three-step process. The majority of the bulk PA6 was dissolved in several washes with formic acid; these washes were, however, not able to remove all of the free chains, because of hydrogen bonding between free and grafted chains. To eliminate the hydrogen bonds, the remaining PA6 was reacted with trifluoroacetic anhydride, after which remaining free chains could be easily rinsed away in a non-polar solvent. The grafted chains were then hydrolyzed to restore the original chemical composition.

XPS spectra were collected on a Surfaces Science SSX-100 spectrometer using a monochromatized Al K_{α} source ($h\nu = 1486.6$ eV). All binding energies were referenced to the peak due to hydrocarbon in the C 1s region at 284.8 eV. To check for contamination of the interface, survey scans were initially taken between 0 and 1100 eV on each sample. Spectra for the 1s peaks of carbon, nitrogen, and oxygen near 285 eV, 400 eV, and 530 eV, respectively, were then collected on a clean part of the sample. The reproducibility of the measurement on a given sample was $\pm 10\%$.

RESULTS

G as a Function of Time and Temperature.

Samples were made at relatively low operating temperatures (185–220 °C) in order to control the density of copolymer and to be able to vary G over two orders of magnitude (1–100 J/m²). Figure 3 presents G as a function of the time of reaction at three temperatures. At 213 °C, the energy of adhesion saturated near 80 J/m² after 500 min. Lowering the temperature to 200 °C decreased the rate of growth of G , and saturation was not observed before 900 min. Decreasing the temperature further to 185 °C significantly changed the behavior: the interfacial toughness increased rapidly to 6 J/m², remained at this value for approximately 400 min, and then began to increase at a rate similar to that at 200 °C.

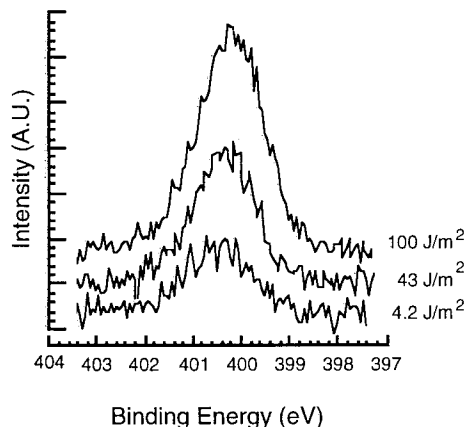


Figure 4: Normalized nitrogen 1s region of XPS for three different energies of adhesion.

Analysis of Cleaved Surfaces.

We investigated fractured joints with SEM and XPS to elucidate the mechanisms of dissipation. SEM showed that the roughness of the PP* side of the cleaved joint increased with increasing energy of adhesion. On the micron scale, the roughness appeared to be due to broken fibrils, implying crazing in the PP*. On the PA6 side of the joint, however, the roughness of surface did not change as a function of the adhesion energy.

XPS showed no nitrogen on the PP* side of fracture over a wide range of G . The nitrogen signal on the PA6 side, however, decreased relative to that of pure PA6, implying attenuation of the signal due to the presence of PP_s on this side. These results imply that the fracture occurred on the PP* side of the joint.

To support the conclusions from SEM and XPS, we attempted to reform joints for two gently delaminated samples whose energies of adhesion were 5 and 100 J/m² (the latter having been made at 220 °C). The PA6 side from each sample was put in a mold with *pure PP* and heated briefly at the same temperature as that used to make the original joint. In the case of the weaker joint, the initial adhesion energy was recovered, as expected if the grafted PP_s chains had been pulled out of the PP* during delamination. For the stronger joint, we measured an energy of 20 J/m² on the reformed joint, suggesting partial rupture of the PP_s chains during the initial separation.

Evaluation of the Density of Copolymers by XPS.

To understand polymer-polymer adhesion with diblock copolymers, it is essential to determine the density of copolymer at the interface (Σ). Because we were able to remove the bulk PA6 from an adhered sample, the nitrogen signal in the XPS spectrum could be attributed to grafted chains of PA6 on the PP*. Since there was only one succinic anhydride group per PP_s, it was possible to assume that the amount of grafted PA6 was equal to the amount of copolymer. Figure 4 presents representative XPS spectra in the nitrogen 1s region for samples with various values of G . The signals have been normalized by the carbon counts for the sample. For each sample, only one peak for nitrogen is present at approximately 400 eV. These data also clearly show that the amount of PA6 increases with G , implying an intimate relationship between these two parameters.

We determined Σ from the normalized N 1s counts (N/C) in the following way:

$$\Sigma = -(N_a \rho / M_n) \lambda \ln \left(1 - \frac{(N/C)}{(N/C)_\infty} \right)$$

In this equation, N_a is Avogadro's number, ρ is the mass density of PA6, M_n is its number average molecular weight, λ is the escape depth of the electrons (estimated to be 19 Å, including the geometry of the instrument), and $(N/C)_\infty$ is the normalized nitrogen counts for PA6. In Figure 5, we present G as a function of the density of copolymer at the interface. These data are best fit by an equation of power 2, in agreement with a model based on stress concentration in the fibrils near the crack tip [5].

DISCUSSION

Kinetics of Grafting.

From the data in Figures 3 and 5, we can estimate the initial rate of formation of copolymer at the interface and observe the influence of the temperature of sticking. If we assume that diffusion of PP_s to the interface is the rate limiting step in the formation of copolymer (i.e., that the chemical reaction is fast relative to diffusion, a reasonable assumption given the rates for similar reactions, and that all of the available NH_2 ends of PA6 are close to the interface), we can relate Σ to time using a standard diffusion equation: $\Sigma = 2c_0(\Sigma_\infty a^2)^{1/2} \sqrt{Dt/\pi}$, where c_0 is the concentration of succinic anhydride and a is the monomer size of PP. Since we have assumed that the available NH_2 ends are close to the interface, we can choose Σ_∞ as the highest density measured by XPS. Using these assumptions, we estimate the diffusion constant D for PP_s in bulk PP to be $9.5 \times 10^{-12} \text{ cm}^2\text{s}^{-1}$ and $4.3 \times 10^{-12} \text{ cm}^2\text{s}^{-1}$ at 213 °C and 200 °C, respectively, in agreement with previous measurements for polyethylene [6]. At 185 °C, we can estimate that $D = 2 \times 10^{-12} \text{ cm}^2\text{s}^{-1}$ from the data taken after 400 min. From these data, we calculated an activation energy for diffusion of $E_a = 21.5 \pm 2 \text{ kJ mol}^{-1}$ from the equation: $D = D_\infty \exp[-E_a / R(T - T_g)]$, where T_g is the glass-transition temperature for PP. Although difficult to determine accurately from three data points in a small region of T , we estimate D_∞ to be on the order of $5 \times 10^{-6} \text{ cm}^2\text{s}^{-1}$.

Mechanism of Fracture.

From the results presented in this paper, we can begin to assemble a mechanism of failure for joints of PP and PA6, two semi-crystalline polymers, reinforced with diblock copolymers. The present interpretations are based on the large amount of work that has been done on joints between glassy polymers.

The first conclusion is that dissipation of energy occurs predominantly in the PP^* . The SEM results showed that the concentration of fibril-like deformations increased with increasing fracture toughness on the PP^* side of joints; no changes, however, were observed on the PA6 side of the joints. These results suggest craze formation on the PP^* side of the fracture, in agreement with the lower yield stress for PP relative to that of PA6.

The second conclusion is that plastic deformations are concentrated at the tip of the fracture. One of the most important results of this study is the square-law relationship between the energy of adhesion and the density of copolymer at the interface. Originally developed to model

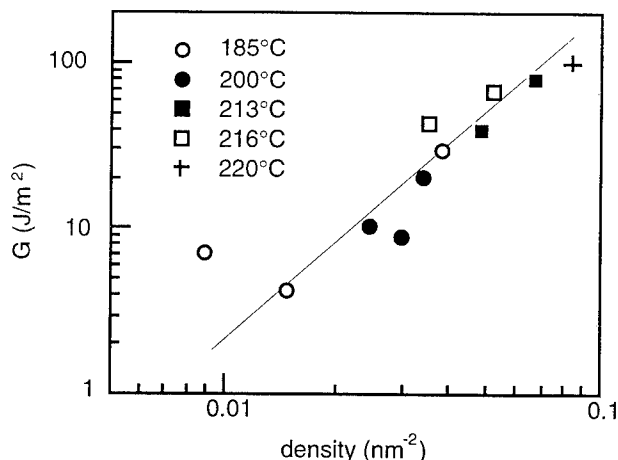


Figure 5: Energy of adhesion G as a function of the density of grafted chains Σ .

craze failure in glassy polymers, the theoretical explanation of such a relationship is based on two main assumptions: first, the stresses from the fracture are concentrated in a small region around the tip of the fracture, and second, the plastic zone of deformation is continuous [5]. The main consequence of this relationship for our system is that the polymer chains are capable of bearing the load at the crack tip. The structure they adopt is probably that of fibrils similar to those in glassy polymers, although it must be stressed that the existence of crazes in our system has not been explicitly shown.

The third conclusion is that the fibrils probably fail by chain breakage at high energies of adhesion. For low energies of adhesion ($G \sim 5 \text{ J/m}^2$), the mechanism of failure appears to be craze-like formation followed by chain pull-out of the grafted PP_s chains, because joints between pure PP and the PA6 side from a delaminated joint could be reformed at the same energy of adhesion. At higher energies, the chains deteriorated partially, and the initial energy of adhesion could not be restored, implying either that the grafted PP_s chains were shorter after fracture or that their concentration was lower. The former implies a mechanism by which chains break during the failure of fibrils.

In summary, the experiments presented here have begun to explain polymer-polymer reinforcement with diblock copolymers in semi-crystalline systems. We have shown that the behavior of the system is similar to those with glassy polymers. The role of crystallites in the adhesion, however, remains to be studied on the microscopic level.

References:

- [1] V. J. Triacca, S. Ziace, J. W. Barlow, H. Keskkula and D. R. Paul *Polymer* **32**, 1401 (1991).
- [2] E. J. Kramer, L. J. Norton, C. -A. Dai, Y. Sha and C. -Y Hui, *Faraday Discuss.* 1994, in press.
- [3] C. Creton, E. J. Kramer, C. -Y Hui and H. R. Brown, *Macromol.* **25**, 3075 (1992).
- [4] H. R. Brown, *J. Mater. Sci.* **25**, 2791 (1990).
- [5] H. R. Brown, *Macromol.* **24**, 2752 (1991).
- [6] J. Klein, *Nature* **271**, 143 (1978).

Acknowledgments: We thank ELF ATOCHEM for advice, materials, XPS experiments, and financial support.

CHARACTERIZATION OF INTERFACES BETWEEN VACUUM-DEPOSITED SILICONE DIOXIDE FILMS AND POLYMETHYLMETHACRYLATE SUBSTRATES

W. H. Tsai*, J. T. Young, Y. M. Lian, and S. L. Liao
Polymer Analysis and Characterization Department
Union Chemical Laboratory, ITRI
Hsinchu, Taiwan 300, R. O. C.

INTRODUCTION

Polymethylmethacrylate (PMMA) is by far the most widely used optical plastic. A variety of coatings on PMMA substrates are available for meeting different optical response. One of the simple ways to reduce surface reflection is to coat the PMMA surface with a single layer of silicone dioxide (SiO_2). However, poor adhesion is frequently observed between vacuum-deposited SiO_2 films and PMMA optics since the property of the SiO_2 is greatly different from that of PMMA in nature. In order to improve adhesion, some type of surface treatment of the polymer prior to the deposition of SiO_2 is usually employed.

In that regard, plasma treatment is an effective and promising method for the modification of polymer surfaces. It has many advantages over conventional methods, including superior adhesion to other materials, environmentally safe, uniform treatment for large parts, etc.

Generally speaking, exposure of a polymer to the plasma of a reactive or inert gas would result in oxidation, crosslinking, and ablation at the polymer surfaces. Based on these processes occurred during the plasma treatment, several mechanisms has been proposed for the improved adhesion between plasma-treated polymers and subsequently deposited inorganic layers. These include chemical bonding, the elimination of weak boundary layer (WBL), mechanical interlocking, and electrostatic attractions [1,2]. However, the exact mechanism is still not well understood.

In order to further understand the SiO_2 -PMMA interaction mechanisms and thus to improve the adhesion, we are interested in using multiple surface-analysis techniques to characterize interfaces

between vacuum-deposited SiO_2 and plasma-treated PMMA substrates. In this paper, X-ray photoelectron spectroscopy (XPS), atomic force microscopy (AFM), and contact angle measurement were utilized to examine the PMMA surfaces. XPS was also used to determine the locus of failure after tape tests and to analyze the depth profile of thin SiO_2 films deposited onto PMMA substrates. The correlation between plasma effects, adhesion mechanisms, and adhesion tests were also determined.

EXPERIMENTAL

The PMMA substrates were first rinsed ultrasonically in a 1% detergent solution and then in deionized waters. After that, PMMA substrates were dried at 50° for 15 hours. Plasma treatments were conducted in a commercial APS B-0006 plasma reactor which was powered by a R.F. generator (13.56 MHz). The plasma power and operation pressure were 100 watts and 300 mTorr, respectively. PMMA samples were treated with O_2 or air plasma for 60 seconds. In some cases, thin SiO_2 layers were vacuum-deposited onto PMMA substrates.

A Perkin-Elmer model 5400 spectrometer with Al $K\alpha$ X-ray was used to generate survey and high-resolution XPS spectra of PMMA. Mg $K\alpha$ radiation was used for the depth profiling analysis. Ion beam sputtering was performed using 4 KeV argon ions. The take-off angles were 15° and 70° which correspond to 26 Å and 94 Å sampling depths, respectively.

Contact angle measurements were determined according to a contact angle goniometer (FACE CA-

A), with water being used as the test liquid. AFM images were obtained using a Park Scientific Instrument model AutoProbeTM LS atomic force microscopy.

The adhesion of films to PMMA substrates was evaluated using tape test. The peel strength of tape test with a peeling angle of 90° was measured via a digital tensiometer. The recorded values represented the relative adhesion strength.

RESULTS AND DISCUSSION

A. X-ray Photoelectron Spectroscopy (XPS)

The XPS atomic concentrations for PMMA substrates before and after O₂ or air- plasma treatments are summarized in Table I. Sampling depths were calculated to be 26 and 94 Å for the corresponding 15° and 70° take-off angles. When the take-off angle is 70°, the O/C ratio was approximately the same for all three cases (38.1-38.9%). These results indicated that the bulk of the PMMA was not affected by the O₂ or air plasma.

However, when the take-off angle was 15° (26 Å sampling depth), significant differences in O/C ratio were observed. In the case of unmodified PMMA, the O/C ratio was 38.7% for 15° take-off angle which was very close to the value for 70° take-off angle. This result indicated that the surface and bulk composition of unmodified PMMA substrates were very similar.

When the PMMA was treated with O₂ or air plasma, the O/C ratios (15° take-off angle) changed dramatically. This indicated that plasma modification was very effective in the near surface region. The greatest degree of modification occurred in the topmost surface layer (~20 Å). At the depth of about 90 Å, the O/C ratio approached the value of unmodified PMMA.

In some cases, plasma-treated PMMA samples were left in the vacuum system for varying time periods before XPS analysis. The atomic concentrations obtained from these experiments are also listed in Table I. Again, when the take-off angle was 70°, the XPS signals were mostly contributed from the bulk PMMA. The O/C ratio was therefore

independent of the exposure time in vacuum for all samples.

However, differences were observed when the take-off angle was 15°. The O/C ratio for PMMA surfaces was about 45.1 % right after the O₂-plasma treatment. This value started to decrease as the exposure time increased. After 168 hours in vacuum, the O/C ratio was only 39.1% which was very close to the value of unmodified PMMA. This observation was probably attributed to the degradation of PMMA during the O₂-plasma treatment. The degradation resulted in formation of low molecular weight species on the PMMA surface which were volatile enough to be pumped off in vacuum. Low molecular weight species might form a weak boundary layer between SiO₂ and PMMA, causing the loss of adhesion. Even though the H₂O contact angle for O₂-plasma treated PMMA was lowered to about 44° (see Table II), the tape test results (described below) indeed showed that the relative adhesion strength decreased after O₂-plasma treatment.

These phenomena were not observed in the case of air-plasma treated PMMA. The O/C ratio (15° take-off angle) for air-plasma treated PMMA did not change as the exposure time increased. A new component which was assigned to the O-C-OH groups was observed near 287.3 eV in the XPS C(1s) spectra of air-plasma treated PMMA. The appearance of this component indicated that OH groups were incorporated into the PMMA surface after the air-plasma treatment. Similar results were also observed by Vargo et. al. who investigated the O₂/H₂O plasma modified PMMA surface [3]. Incorporation of polar groups increased the surface free energy of PMMA (as evidenced from the low H₂O contact angle, see Table II) and enhanced the SiO₂-PMMA interactions. The adhesion was therefore improved significantly after the air-plasma treatment (see below).

B. Relative Adhesion Strength (Tape Test)

The relative adhesion strength of SiO₂ deposited onto PMMA substrates are summarized in Table III. The adhesion strength for SiO₂/unmodified PMMA samples was about 230

g/cm. The relative strength for SiO₂/O₂-plasma-treated PMMA samples decreased to about 150 g/cm, while the relative strength of SiO₂/air-plasma-treated PMMA samples increased to about 550 g/cm.

According to the tape test and XPS results, it can be concluded that the loss of adhesion between SiO₂ and O₂-plasma treated PMMA was due to the formation of weak boundary layers. Whereas, air-plasma treatment introduced polar functional groups onto the PMMA surface, enhanced the SiO₂-PMMA interactions, and thus improved the adhesion. These results indicated that interfacial interactions and the elimination of weak boundary layers were probably the dominant adhesion mechanisms for the case investigated here.

C. Atomic Force Microscopy (AFM)

Another possible bonding mechanism, i.e. mechanical interlocking, was also investigated by AFM in the present study. AFM images obtained from unmodified, O₂-plasma treated, and air-plasma treated PMMA are shown in Figures 1 to 3, respectively. All three photographs were very similar, indicating that the topography (i.e., roughness) of polymer surfaces was not the major factor affecting the adhesion for the case studied here.

D. Locus of Failure and Depth Profiling

SiO₂ thin films were delaminated from PMMA substrates via tape test. The failure surfaces were then examined by XPS. In the case of unmodified PMMA, Si was clearly observed at the tape side of failure surfaces, while only C and O were detected at the PMMA side of failure surfaces. These results revealed that the failure occurred at the interface between SiO₂ and unmodified PMMA.

The depth profile analysis of SiO₂/PMMA samples was also performed using XPS. As the sputtering depth increased, faster and greater changes in Si concentration were observed for the SiO₂/unmodified PMMA samples relative to the SiO₂/air-plasma-treated PMMA samples. This indicated that more SiO₂ particles were distributed in the air-plasma treated PMMA matrix, as compared to the unmodified PMMA matrix. In other words, a sharp interface between SiO₂ and PMMA was observed for the case of unmodified PMMA.

However, a broader interfacial zone was observed for the case of air-plasma treated PMMA. These results implied that SiO₂ was more compatible with the air-plasma treated PMMA than the unmodified PMMA. As a result, one can expect stronger interactions and thus better adhesion between SiO₂ and air-plasma treated PMMA.

SUMMARY

Summarizing results presented here, it was concluded that air-plasma treatment improve the SiO₂-PMMA adhesion quite significantly, while O₂ plasma treatment exhibited the opposite effect. The loss of adhesion after O₂-plasma treatment was attributed to the formation of weak boundary layers between SiO₂ and PMMA. On the other hand, air-plasma treatment introduced polar groups onto the PMMA surface, and thus enhanced the interfacial interactions and the adhesion.

A sharp interface between SiO₂ and PMMA was observed for the case of unmodified PMMA. However, a broader interfacial zone was observed for the case of air-plasma treated PMMA. This implied that SiO₂ was more compatible with the air-plasma treated PMMA than the unmodified PMMA. These results were in good agreement with XPS and tape test results.

ACKNOWLEDGMENTS

This research was supported in part by a grant from The Ministry of Economic Affairs (MOES). Authors would also like to thank Mr. John Newman of Evan Centrals for performing the XPS experiments.

REFERENCES

1. E. M. Liston, L. Martinu and M. R. Wertheimer, *J. Adhesion Sci. Technol.* **7**, 1091 (1993).
2. L. J. Gerenser, *J. Vac. Sci. Technol.* **A8**, 3682 (1990).
3. T. G. Vargo and J. A. Gardella, *J. Polymer Sci.: Part A: Polymer Chem.* **27**, 1267 (1989).

Table I. Atomic concentrations for PMMA substrates before and after O₂ or air plasma treatments(100w, 300 mTorr, 60 sec)

Samples	Take-off Angle(°)	Atomic Concentration(%)			O/C (%)
		C(1s)	O(1s)	Si(2p)	
Cleaned PMMA	15	72.1	27.9	-	38.7
	70	72.4	27.6	-	38.1
O ₂ -plasma, 0hr	15	68.9	31.1	-	45.1
	70	72.0	28.0	-	38.9
O ₂ -plasma, 24hr	15	69.8	30.2	-	43.3
	70	72.3	27.7	-	38.3
O ₂ -plasma, 48hr	15	70.6	29.4	-	41.6
	70	72.5	27.5	-	37.9
O ₂ -plasma,168hr	15	71.9	28.1	-	39.1
	70	72.4	27.6	-	38.1
Air-Plasma, 0hr	15	76.0	23.7	0.3	31.2
	70	72.2	27.7	0.1	38.3
Air-Plasma, 24hr	15	75.8	24.0	0.2	31.7
	70	72.1	27.8	0.1	38.6
Air-Plasma,48hr	15	76.1	23.7	0.2	31.1
	70	72.0	27.9	0.1	38.8
Air-Plasma,168hr	15	75.9	24.0	0.1	31.6
	70	72.2	27.8	-	38.5

Table II .Contact angle measurements for unmodified, O₂-plasma, and air-plasma treated PMMA substrates

Sample	Unmodified	O ₂ -plasma	Air-plasma
Contact Angle	PMMA	PMMA	PMMA
θ	69°	44°	52°

Table III .Relative adhesion strength of SiO₂ films deposited on unmodified, O₂-plasma, and air-plasma treated PMMA substrates

Sample	Unmodified	O ₂ -plasma	Air-plasma
Adhesion Strength	PMMA	PMMA	PMMA
Relative Strength(gcm ⁻¹)	230	150	550

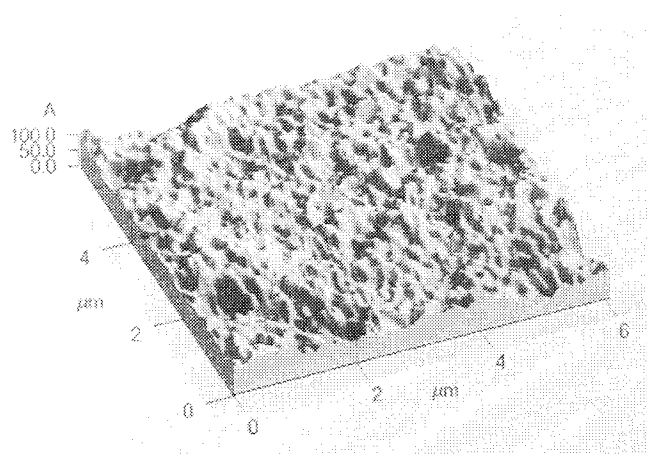


Figure 1 AFM image of unmodified PMMA surfaces

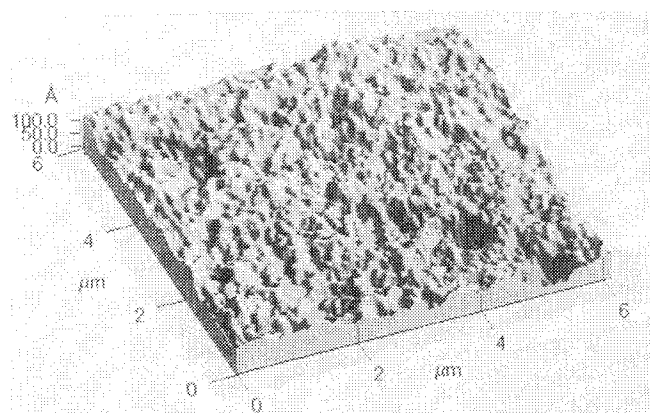


Figure 2 AFM image of O₂-plasma treated PMMA surfaces

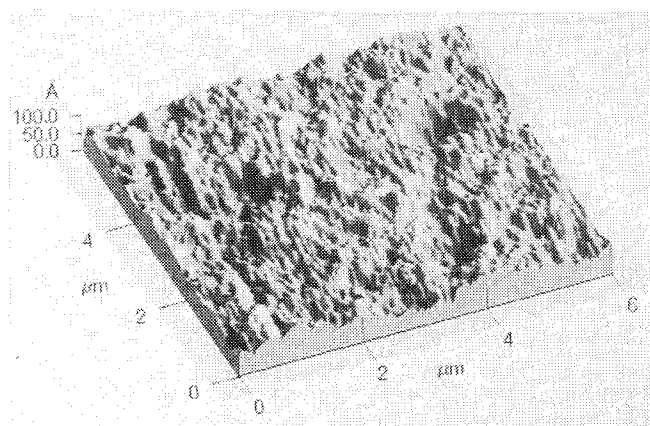


Figure 3 AFM image of air-plasma treated PMMA surfaces

ADHESION MECHANISMS OF POLYURETHANES TO GLASS SURFACES

R. K. Agrawal and L. T. Drzal

Department of Chemical Engineering
Michigan State University, East Lansing, MI 48824-1326

INTRODUCTION

Glass/polyurethane adhesion has become increasingly important in the automotive and other industries in a variety of applications including laminated windshields, reaction injection molded modular windows for automobiles, long and short glass fiber reinforced thermoplastic and thermoset composites, etc. In all of these applications, good adhesion between the glass and the polyurethane is imperative. However, polyurethane compositions can vary over a wide range with a resulting change in their mechanical properties for a given application. It would be very advantageous to the adhesion scientist and engineer to know the relationship between polyurethane composition and adhesion to glass surfaces.

In our previous studies on glass/polyurethane adhesion^(1,2) we found that polyurethane to glass adhesion is greatly influenced by the modulus of the polymer in the interphase. We also found that along with modulus, phase separation in polyurethane also influences its adhesion to glass. An interphase region was found between the polyurethane matrix and the glass substrate of our previous studies which had a composition intermediate to that of the matrix and the glass surface. The composition and the thickness of this interphase region was found to be related to the phase separation in the matrix.

In the present study, we have investigated the physico-chemical interactions at the polyurethane/ glass interface. Surface free energies of the various polyurethane formulations were evaluated using theoretical and experimental techniques, and the dependence of the surface free energies on the surface composition and/or the phase separation has also been studied. The thermodynamic work of adhesion to the glass surface has been evaluated for the various phase-mixed and phase-separated polyurethanes and compared with the experimental adhesion data reported earlier⁽¹⁾. The role of chemical interactions at the polyurethane/glass interface has been explored by coating the glass surfaces with an alkyl silane to make the surface chemically "inert" prior to the adhesion testing.

EXPERIMENTAL

Materials. The polyurethanes used in this study were based on caprolactone polyols available from Union Carbide under the trade name "Tone." Hard segments were made from a 80%-20% mixture of toluene 2,4-diisocyanate and toluene 2,6-diisocyanate (TDI, Aldrich Chemical Co.) and 1,4-butanediol

(BDO, Aldrich Chemical Co.) as the chain extender. The various polyurethane formulations (Table 1) had the same chemistry and reactive groups, but differed only in their

Table 1. Urethane Formulations at Isocyanate Index of 1.0

No.	Polyol (Tone)			B D O Mol %	T D I Mol %	Hard Seg wt %
	301	305	310			
10A	-	-	X	0	60	22
10B	-	-	X	22	56	37
10C	-	-	X	31	54	47
10D	-	-	X	34	53	60
10E	-	-	X	41	52	67
5B	-	X	-	7	58	37
5C	-	X	-	20	56	47
5D	-	X	-	31	54	59
5E	-	X	-	36	53	67
1C	X	-	-	0	60	47
1D	X	-	-	18	57	59
1E	X	-	-	26	55	67
HS	-	-	-	50	50	100

stoichiometry and hard segment contents which produced different shear moduli that varied by two orders of magnitude. The air side of annealed soda-lime float glass plaques was used as the adherend. A 2.0 weight percent solution of methyltrimethoxysilane, available from Dow Corning under the trade name Z6070, and a 2.0 weight percent solution of trimethyl chlorosilane, available from Aldrich Chemical Co., were coated on the air side of the glass samples for some of the studies. 1/4" x 1/4" x 1/4" blocks of the formulated polyurethanes were cast on the air side of the glass plaques and the adhesion was determined by measuring the shear strength. The details of polyurethane mixing and adhesion sample preparation can be

found in our previous study⁽¹⁾.

Measurements. The surface free energy of the samples was obtained from the experimental determination of contact angles for sessile drops using a Rame-Hart Model 100 goniometer. All experiments were conducted at room temperature ($\sim 23^\circ\text{C}$). The surface tensions of the various caprolactone-based polyols were measured using a Cahn DCA-322 dynamic contact angle analyzer. Rectangular bars (30 mm x 4 mm x 1.5 mm) of polyurethane samples were used for dynamic mechanical analysis on a Polymer Laboratories MK III DMTA system. Elastic storage modulus (E') at various temperatures was obtained in a single cantilever bending oscillation mode of deformation at 1 Hz fixed frequency. The temperature was varied from 10°C to 50°C at $5^\circ\text{C}/\text{min}$. Subsequent to adhesion testing, failed glass surfaces were analyzed using a Perkin-Elmer PHI5400 x-ray photoelectron spectrometer.

RESULTS AND DISCUSSION

Physical Interactions. The surface free energies of the various model polyurethanes were determined from the contact angle measurements of several liquids with different surface tensions and chemical functionalities. Figure 1 shows the γ^p versus hard segment content for Tone 301 and Tone 310 based polyurethanes. Also shown is the data point HS for the 100% hard segment content polyurethane (containing only BDO and

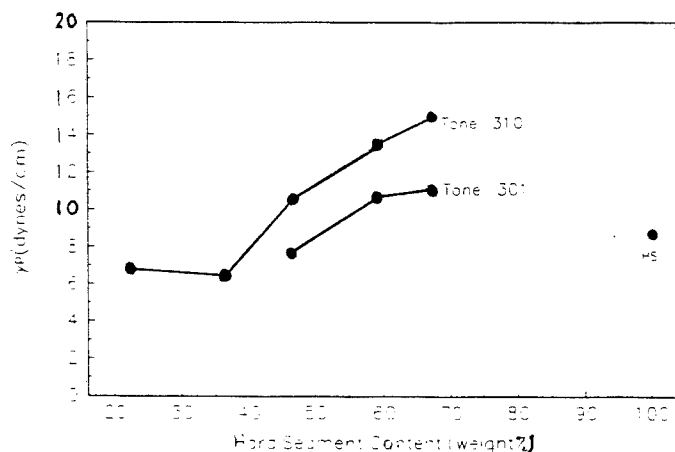


Figure 1. Variation in Polar Component of Surface Free Energy of Polyurethanes

TDI). The data shows that the γ^p values increase with increasing hard segment content in both the 301 and 310 series polyurethane samples. The γ^p values for the 1 series are in general lower than that for the 310 series for the same hard segment contents. A sharp increase in the γ^p value occurs for sample 10C and the trend continues with the samples 10D and

10E. This observation can be explained by noting that with increasing hard segment content, phase separation increases in higher molecular weight polyol (Tone 310) based polyurethanes^(1,2). The phase separation in the lower molecular weight polyol (Tone 301) based polyurethanes is not as significant and thus the γ^p values for these polyurethanes are lower than the 310 series polyurethanes.

The adhesion values of these polyurethanes to soda-lime glass surface were determined and are shown in Figure 2. Polyurethane to the glass adhesion improves with phase separation in the matrix and also with the modulus of the matrix. A plot of the adhesion values as a function of γ^p shows a linear relationship between the γ^p and the adhesion values.

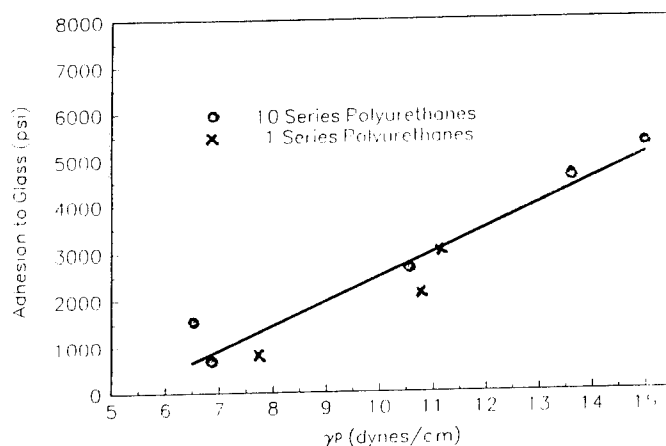


Figure 2. Shear Strength of Polyurethanes to Glass as a function of Polar Component of Surface Free Energy

The above observations suggest that in the samples exhibiting good adhesion to the glass, the interphase region between the polyurethane matrix and the glass surface consists of a larger concentration of higher polar free energy components than the bulk and the components are butanediol type species which could hydrogen bond to the glass surface.

To further explore the role of the hydrogen bonding and other polar interactions between the polyurethane surface and the glass surface, selected polyurethanes with varying surface γ^p values (and thus with varying surface BDO content) were bonded to the bare soda-lime glass plaques and to glass plaques coated with 2% (weight) layer of BDO from acetone. The samples were tested for adhesion in shear. The results indicated that the adhesion values of the polyurethanes with low γ^p values can be significantly improved by coating the glass surface with BDO, or in other words, by making their surface rich in the higher γ^p component, BDO. Analysis of the failed glass surfaces using XPS confirmed the presence of a polyurethane

peak in the BDO coated glass surface indicating a polyurethane rich surface compared to the glass surface without BDO coating.

To determine the mechanical properties of the butanediol rich interphase region, polyurethane rectangular bars were prepared with 5% and 15% (by total weight) excess of 1,4 butanediol and were tested for elastic storage modulus using Dynamic Mechanical Analysis. Excess BDO was incorporated into the urethane composition by addition to the homogeneous stoichiometric mixture of polyol, BDO, and isocyanate.

The elastic storage modulus of polyurethane 1D with 5% BDO is about 10%-12% higher than for the stoichiometric composition 1D. Since the interphase formation in BDO coated glass plaques is expected to be similar in comparison, we can conclude that the localized interphase modulus in the BDO coated 1D adhesion sample is higher than that of in the 1D adhesion sample without any coating. The higher interphase modulus should result in higher adhesion values which is in agreement with the adhesion data obtained with BDO coated glass plaques. This observation suggests that the preferential segregation of BDO type species to the interphase region in polyurethane/glass samples influences its adhesion not only through increased polar interactions and hydrogen bonding but also by increasing the modulus of the interphase region.

Chemical Interactions. Glass surfaces are known to be rich in isolated, vicinal, and geminal silanol groups. In addition to the physical interactions between the surface silanols and the polyurethane matrix, there could be various chemical interactions. To investigate the chemical interactions such as covalent and ionic bonding, the glass surfaces were treated with prehydrolyzed methyltrimethoxysilane and trimethyl chlorosilane prior to the adhesion testing. The purpose of the silane treatment was to make the otherwise hydroxylated glass surface chemically inert towards any subsequent covalent bond formation with polyurethanes.

These samples were tested for adhesion. A comparison of this data with adhesion data for the bare glass surface reveals that the methyltrimethoxysilane and trimethyl chlorosilane coatings on the glass surface had little influence on the adhesion values within experimental error. Similar adhesion data is obtained from the treated glass surfaces. This suggests that the adhesion mechanism of the polyurethanes to the glass surface is not due to covalent or ionic bonding in the interphase region. The locus of failure seems to be between the silane layer and the polyurethane matrix, through the interphase region.

The preferential segregation of BDO at the interphase region observed in this study is not inconsistent with the previously reported studies. Hearn et al ⁽³⁾ and Vargo et al ⁽⁴⁾ have reported the enrichment of air/polyurethane interface in low molecular weight polyether polyol components. The glass/polyurethane

interphase of this study is expected to be different than the air/polyurethane interface studied by the above mentioned researchers. The high surface energy (56.77 dynes/cm) and especially the polar nature of the glass surface ($\gamma^P = 37.59$ dynes/cm) will have a significant influence on the interphase composition. This reasoning is further supported by the studies reported by Deng and Schreiber⁽⁵⁾ discussing orientation phenomena at polyurethane surfaces in contact with different media.

CONCLUSIONS

Phase separation in polyurethanes significantly affects its adhesion to glass surfaces. Polyurethane phase separation influences the composition and the thickness of the interphase region by causing a preferential segregation of high polar surface energy components to the interphase region. Chemical bonding in the form of covalent and ionic bonding does not contribute to the overall glass/polyurethane adhesion.

Physical interactions are the most important factors in controlling glass/polyurethane adhesion. The polar surface free energy of the various polyurethanes correlated well with the XPS results regarding the BDO enrichment of the interphase regions in the phase separated polyurethanes. Although the work of adhesion between the polyurethanes and the glass surface was found to be a poor predictor of the actual adhesion behavior, a linear relationship between the polar surface free energy and the observed adhesion values was found emphasizing the role of polar interactions in polyurethane adhesion.

The modulus of the interphase was found to be higher than that of the bulk matrix due to the preferential segregation of butanediol at the glass-polyurethane interphase. This increase in modulus was relatively small and determined not to be an important factor for the superior polyurethanes. The most important mechanism affecting adhesion between the polyurethanes and the glass surface of this study is the formation of hydrogen bonds between the butanediol rich interphase region and the hydroxylated glass surface.

REFERENCES

1. R. K. Agrawal and L. T. Drzal, *J. Adhesion*, 1995. (in press)
2. R. K. Agrawal and L. T. Drzal, *J. Adhesion Science and Tech.*, 1995. (in press)
3. M. J. Hearn, B. D. Ratner, and D. Briggs, *Macromolecules*, **21**, 2950-2959, 1988.
4. T. G. Vargo, D. J. Hook, J. A. Gardella Jr., M. A. Eberhardt, A. E. Meyer, and R. E. Baier, *Applied Spectroscopy*, **45**, No. 3, 448-456, 1991.
5. Z. Deng and H. P. Schreiber, *J. Adhesion*, **36**, 71-82, 1991.

SURFACE AND INTERFACIAL STRUCTURE OF RELEASE COATINGS FOR PRESSURE SENSITIVE ADHESIVES

D. J. Kinning
3M Company, St. Paul, MN 55144

INTRODUCTION

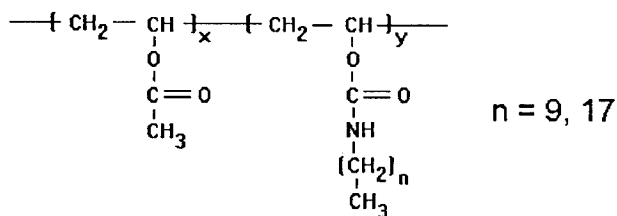
Most pressure sensitive adhesive (PSA) products require the use of release coatings in one form or another. For example, the backing in a roll of tape is often coated with a release material to provide a controlled unwind or peel force. In addition, it is desirable that the peeling force does not change appreciably with aging time and temperature. It has been shown that the work needed to peel a PSA from a substrate can be written in the form [1,2]:

$$\text{Work to peel} \approx W_a F$$

where W_a is the thermodynamic work of adhesion, describing the attractive strength of the chemical interactions between the PSA and the substrate, and F is a function which describes the energy dissipated in irreversible deformation of the adhesive and adherends. Then in order to maintain a constant peeling force between a PSA and a release coating upon aging, the work of adhesion should be kept constant. However, if there are favorable specific interactions between chemical groups in the PSA and release coating, and there is sufficient segmental mobility within the PSA and release coating, a restructuring or reorganization at the PSA/release coating interface can occur upon aging. Such restructuring of interfaces has been shown to occur in a number of multicomponent or multisegment polymeric systems. [3-6] This restructuring can lead to higher adhesion forces (i.e., larger W_a) and increases in the force necessary to peel the PSA from the release coating. This talk will focus on our studies characterizing the affect of release coating surface structure and PSA/release coating interfacial structure on peel strength, using polyvinyl N-alkyl carbamate release coatings [7] to illustrate the general principles.

EXPERIMENTAL

Polyvinyl N-octadecyl carbamate (PVNOC) and polyvinyl N-decyl carbamate (PVNDC), the structure of which are shown below, were synthesized by reacting a partially



hydrolyzed poly(vinyl acetate) with octadecyl isocyanate and decyl isocyanate, respectively. The reactions were carried out at 30% solids in refluxing xylene. Samples for DSC, DMTA, and x-ray scattering were prepared by casting 1mm thick films onto a silicone release liner. Samples for surface analysis, by XPS, static SIMS, and contact angle measurements, as well as for adhesion measurements, were prepared by diluting the PVNOC and PVNDC solutions to 2 wt% with toluene, and then coating the solutions onto PET film using a #6 Mayer rod, resulting in a coating thickness of about 0.1 micron. A tape having an alkyl acrylate PSA containing 4.5 wt% acrylic acid was used for the adhesion measurements. The 180° peel force was measured at a peeling rate of 90°/min after aging for various times and at various temperatures.

RESULTS AND DISCUSSION

Bulk Structure of Polyvinyl N-Alkyl Carbamates

X-ray scattering experiments indicate that the PVNOC exhibits a layered structure with a spacing of 34 Å. In addition, a sharp reflection is observed at a spacing of 4.18 Å which can be attributed to the 100 reflection of hexagonally packed octadecyl side chains. [8] When examined by DSC, the PVNOC exhibits an endothermic transition between 50 and 70 °C, which can be attributed to the loss (melting) of the hexagonal packing of the octadecyl side chains. The PVNOC can be classified as having a Smectic B type liquid crystal structure. In contrast, the PVNDC shows a broad reflection at 4.4 Å in the x-ray pattern, indicating an amorphous packing of the decyl side chains. Indeed, the DSC trace of PVNDC shows only a glass transition centered at 45 °C. Figure 1 shows the shear modulus vs temperature data obtained via DMTA for PVNDC and PVNOC. The PVNDC starts to soften at temperatures above about 20 °C, and has a lower modulus (i.e., higher segmental mobility) than the PVNOC at temperatures between 20 and 70 °C. The PVNDC starts to soften at temperatures above about 40 °C, and the modulus drops rapidly between 50 and 70 °C.

Surface Structure of Polyvinyl N-Alkyl Carbamates

The advancing contact angles of water and methylene iodide on the PVNOC and PVNDC coatings are listed in Table 1, from which the dispersive and polar contributions to the surface energy of the coatings were

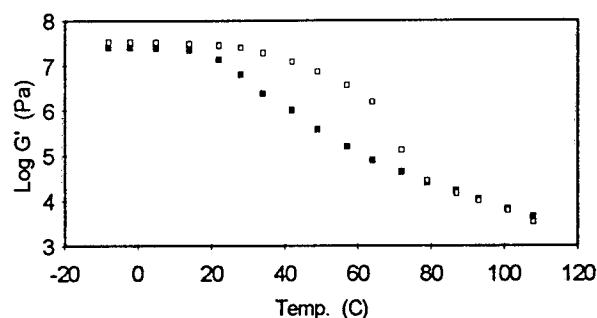


FIGURE 1 DMTA Results for PVNOC (open squares) and PVNDC (filled squares).

TABLE 1 Advancing contact angle analysis

Coating	H ₂ O ± 2°	CH ₂ I ₂ ± 2°	γ^d (dyne/cm)	γ^p (dyne/cm)
PVNDC	109°	72°	21.8	0.1
PVNOC	110°	72°	21.8	0.1

calculated using the geometric mean equation. For both coatings the surface energy is 21.9 dyne/cm, being almost entirely dispersive. These results are consistent with an overlayer of the alkyl side chains at the coating surface, and more specifically, a high concentration of the methyl end groups.

The atomic concentrations determined from angle resolved x-ray photoelectron spectroscopy (XPS) for the PVNDC and PVNOC coatings are given in Table 2. For both coatings the concentration of oxygen and nitrogen decrease and the concentration of carbon increases as the takeoff angle (sampling depth) is decreased. Note however, that the changes in atomic composition with sampling depth are more pronounced in the case of octadecyl side chains, which would indicate that the average hydrocarbon overlayer thickness is larger in the case of PVNOC.

TABLE 2 Atomic conc. vs takeoff angle, from XPS

Coating	Takeoff Angle	%C ±1	%O ±0.2	%N ±0.1
PVNDC as cast	15	87	9.2	4.2
	30	83	12	5.1
	90	80	15	5.3
PVNOC as cast	15	94	4.5	1.5
	30	91	7.1	2.3
	90	86	11.0	3.1
PVNOC, aged 45 sec at 60 °C against PSA	15	91	7.5	1.7
	30	90	8.1	2.4
	90	85	12.2	3.1

Based on modeling of the angle resolved XPS data, wherein the photoelectron mean free paths were

assumed to be 30 Å [9], alkyl side chain overlayer thicknesses at the coating surface were determined to be about 5 and 15 Å for PVNDC and PVNOC, respectively, compared to the fully extended alkyl side chain lengths of 11.4 and 21.6 Å, respectively.

The positive and negative ion static secondary ion mass spectroscopy (SIMS) spectra for the PVNDC coating are shown in Figure 2. The spectra for the PVNOC

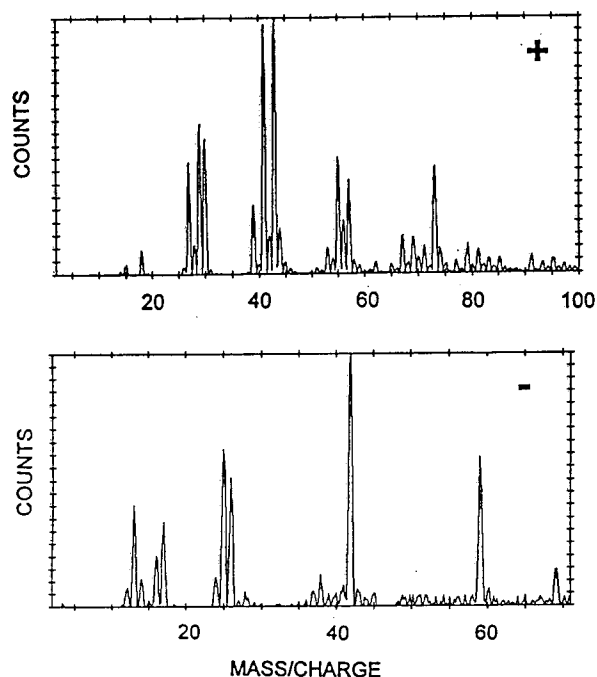


FIGURE 2 Positive and Negative Static SIMS Spectra for PVNDC Coatings.

coating were similar, except that the relative magnitudes of the various fragments were somewhat different. The positive spectra show the characteristic envelope of hydrocarbon mass fragments, and an additional fragment at 30 amu attributable to either $\text{N}=\text{O}^+$ or $\text{CH}_2=\text{NH}_2^+$ fragments from the urethane groups. The dominant mass fragments in the negative spectra appear at 42 and 59 amu, and can be assigned to $\text{N}=\text{C}=\text{O}$ from urethane groups and CH_3COO^- from acetate groups, respectively. Table 3 lists the intensities of these fragments for the different coatings, relative to the intensity of the 41 amu positive fragment and the 25 amu negative fragment. Note that the relative intensities of the 30 amu positive fragment and the 42 and 59 amu negative fragments are significantly greater for the PVNDC coating, indicating a greater concentration of the urethane and vinyl acetate groups in the surface region probed by static SIMS (10–20 Å) in the case of decyl side chains. These results are consistent with the angle resolved XPS analysis.

TABLE 3 Relative intensities of Static SIMS fragments

Coating	Int ₃₀ /Int ₄₁ (pos)	Int ₄₂ /Int ₂₅ (neg)	Int ₅₉ /Int ₂₅ (neg)
PVNDC	0.54	1.59	0.95
PVNOC	0.22	0.40	0.61

Adhesion of PSA Tapes

The peel adhesion of the alkyl acrylate PSA tape to the PVNDC and PVNOC coatings, as a function of dwell time and aging temperature, are shown in Figure 3. Note that the initial (30 sec dwell) adhesion is similar, and low, for both PVNDC and PVNOC coatings. This observation is consistent with the contact angle analysis, which indicated that the top molecular layer of both coatings consisted largely of the low energy methyl end groups. There is a large difference, however, in the way the adhesion of the tape changes with aging time and temp-

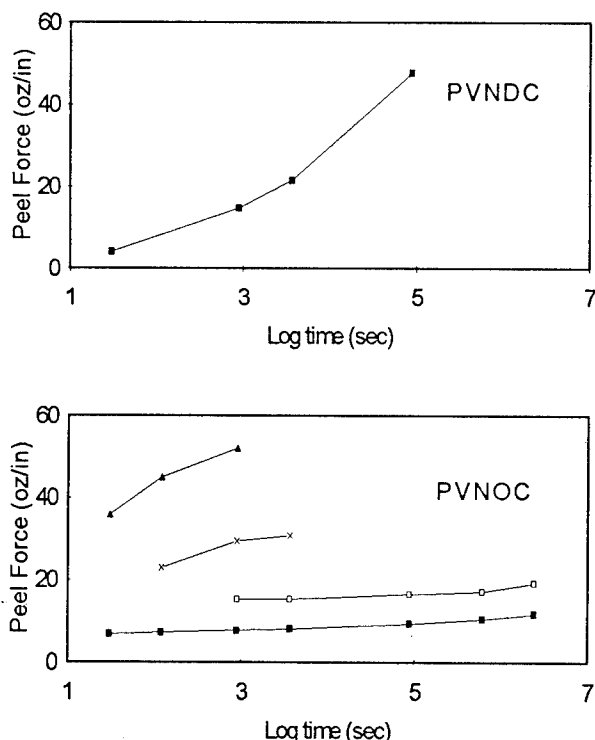


FIGURE 3 Peel Force vs Log of Aging Time for Aging Temperatures of 21 °C (filled squares), 47 °C (open squares), 54 °C (X), and 60 °C (filled triangles).

erature for the PVNDC and PVNOC coatings. In the case of decyl side chains, the peel adhesion increases dramatically with aging time, even at 21 °C. Aging at higher temperatures resulted in a cohesive split within the PSA after only 15 minutes dwell time. In contrast, the peel adhesion from the PVNOC coating increases only

slightly with time at temperatures below about 50 °C; only at higher temperatures does the adhesion increase significantly with time. It is proposed that the build in adhesion can be attributed, in large part, to a restructuring near the PSA/release coating interface. If the segmental mobility within the release coating is sufficient, and energetically favorable specific interactions can occur between components in the PSA and release coating which are not initially in contact, then segmental rearrangements can occur at the interface leading to stronger attractive forces and higher adhesion. For the systems discussed here, polar or acid-base interactions can occur between the acrylic acid group in PSA and the urethane and vinyl acetate groups in the release coating. The different aging behavior seen for PVNDC and PVNOC coatings can be attributed to 1) larger concentrations of urethane and vinyl acetate groups in the near surface region of the PVNDC coatings, and 2) higher segmental mobility within the PVNDC coating, at least at temperatures between 20 and 70 °C. Note that the aging temperatures at which the adhesion to the PVNOC coating increases significantly (≥ 50 °C) correspond to the temperature at which the hexagonal packing of the octadecyl side chains begins to be disrupted and the modulus starts to drop off (i.e., the temperature at which the segmental mobility increases).

Analysis of Interfacial Restructuring

Two approaches have been taken to assess the validity of the interfacial restructuring hypothesis. The first approach was to analyze the surfaces of the PSA and release coating both before and after aging and peeling apart. As an example of this type of experiment, consider the case where the PSA tape was aged against the PVNOC coating for 45 seconds at 60 °C, and gave a peel adhesion of 39 oz/in. The atomic concentrations obtained by XPS for the PVNOC coating after peeling off the tape are given in Table 2. A slight increase in nitrogen and a more significant increase in oxygen content are seen upon aging, at the shallowest depths probed. The PSA surface after peeling was indistinguishable, by XPS, from the initial PSA surface. Similarly, no changes in the SIMS spectra of the PSA are seen upon aging. However, significant increases in the relative intensities of the 42 amu (from 0.40 to 0.57) and 59 amu (from 0.61 to 1.54) fragments in the negative SIMS spectrum of the PVNOC coating are seen upon aging. In addition, it should be noted that no increases in the relative intensities of the mass fragments associated with the acrylate PSA are seen by SIMS on the PVNOC coating. The XPS and SIMS results demonstrate that 1) the failure mode during peeling is indeed interfacial (at least for peel forces less than 55 oz/in; higher peel forces resulted in cohesive failure within the PSA), and 2) a restructuring does occur within the PVNOC coating near the interface with the PSA, whereby more urethane and vinyl acetate groups come into contact with the PSA, causing a build in adhesion.

The receding contact angles of water on the PVNOC coatings were also measured before and after aging of the PSA against the coatings. Aging was done at temperatures between 21 and 65 °C for various periods of time in order to obtain a wide range of peel forces. Figure 4 shows a plot of the measured peel adhesion versus the cosine of the water receding contact angle on the PVNOC coating subsequent to peeling of the PSA tape. The peel adhesion is seen to increase systematically as the water receding contact angle decreases. Based on the XPS and SIMS results, the decrease in water receding contact angle can be

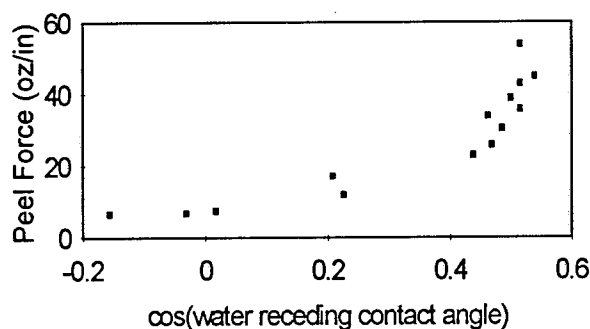


FIGURE 4 Peel Adhesion vs Cosine of the Water Receding Contact Angle on PVNOC Coating.

attributed to higher concentrations of urethane and vinyl acetate groups at the coating surface. Thus, the receding water contact angle measurements provide further evidence for a restructuring within the PVNOC coating near the interface with the acid containing acrylate PSA. It should be mentioned that the changes in the surface composition of the PVNOC coating are reversible if the coating is exposed as a free surface and sufficient segmental mobility is provided by heating of the coating.

Another approach which can be used to study the susceptibility for restructuring of the release coatings is to measure the receding contact angle of water as a function of water dwell time and temperature. Decreases in receding water contact angle with increasing water dwell time and/or increasing temperature can be taken as evidence for restructuring. For example, Figure 5 shows the results for PVNOC coatings. The water contact angle, at 21 °C, decreases only slightly during the first few minutes of contact, and remains fairly high, indicating that relatively little restructuring of the coating took place. Similar behavior is observed at 40 °C, although the receding water contact angle decreases slightly more than at 21 °C. In contrast, at 50 °C, the receding contact angle decreases markedly during the first few minutes of water contact, indicative of a significant restructuring. At 65 °C, the water receding contact angle is quite low, even when measured at very short dwell times, suggesting that

the restructuring occurs rapidly at this temperature. Note that the stability in water receding contact angle as a function of temperature is mirrored in both the stability of the PSA adhesion provided by the PVNOC coating as a function of aging temperature and the segmental mobility within the PVNOC coating as a function of temperature. The ability of the PVNDC coating to maintain a high water receding contact angle, even at 21 °C, is significantly less than that of the PVNOC coating, consistent with the build in adhesion seen for the PVNDC coating at 21 °C.

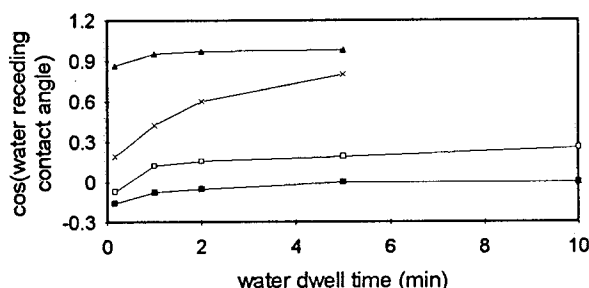


FIGURE 5 Cos(water receding contact angle) vs water dwell time for PVNOC coating, at 21 °C (filled squares), 40 °C (open squares), 50 °C (X), and 65 °C (filled triangles).

REFERENCES

1. A. Gent and J. Schultz, *J. Adhesion* **3**, 281 (1972).
2. G.J. Lake, *Proc. Int. Adhesion Conference (The Plastics and Rubber Institute, London, 1984)*, p. 22-1.
3. T. Yasuda, T. Okuno, K. Yoshida, and H. Yasuda, *J. Polym. Sci.:Part B* **26**, 1781 (1988).
4. Y. Tezuka, T. Ono, and K. Imai, *J. Coll. Int. Sci.* **136**(2), 408 (1990).
5. Z. Deng and H.P. Schreiber, *J. Adhesion* **36**, 71 (1991).
6. K. Lewis and B.D. Ratner, *J. Coll. Int. Sci.* **159**, 77 (1993).
7. C.A. Dahlquist, J.O. Hendricks, and W.E. Sohl, U.S. Patent 2,532,011 (1950) (assigned to 3M).
8. N.A. Plate' and V.P. Shibaev, *J. Polym. Sci.:Macromol. Rev.* **8**, 117 (1974).
9. M.P. Seah and W.A. Dench, *Surf. Int. Analysis* **1**(1), 2 (1979).

STRUCTURE-PROPERTY-PERFORMANCE RELATIONSHIPS IN EMULSION PRESSURE SENSITIVE ADHESIVES: EFFECT OF MATERIAL AND FORMULATING PARAMETERS.

Krishan C. Sehgal and David R. Bassett
UCAR Emulsion Systems
Union Carbide Corporation
Cary, NC, USA

Pressure Sensitive Adhesives (PSA) are soft ductile materials which in the dry state (i.e., free of solvent or water), are permanently tacky at room temperature and adhere to a variety of surfaces under only slight pressure. Their compositions are inherently soft with low glass transition temperatures and low to medium molecular weight. They exhibit a balance of adhesive and cohesive strength depending upon the viscoelastic/surface nature of the adhesive and the performance requirements of the particular end use. These adhesives are being increasingly used in consumer, automotive and construction markets as tapes, labels decals, floor tiles, wall coverings, wood grain films and protective maskings. Commercial systems are available as solvent-borne, water-borne and hot melts. Due to environmental, health and economic reasons, a rapid evolution from solvent - borne to water-borne and hot melt systems has been taking place. PSAs, generally copolymers, are derived from acrylic, vinyl acetate, ethylene, styrene, butadiene and isoprene monomers. In many cases, they are formulated with tackifiers, plasticizers and curing agents to enhance adhesive properties. Water-borne systems are modified with surfactants, defoamers and rheology modifiers to enhance application properties. A good monograph on PSA technology is available(1).

Peel, tack (quick stick) and shear (holding power) adhesion are three major performance properties of the dry adhesive. Adhesive with high peel or tack generally possesses low shear properties and vice versa. These properties are controlled by surface/rheological and bulk/viscoelastic contributions which in turn depend on the material and formulating components of the adhesive system. An empirical relationship has been found (2) to exist between peel(interfacial) and shear(cohesive strength) adhesion.

A perusal of the literature shows that information on the fundamental knowledge on structure-property-performance relationships

in water-borne systems is scanty. Only a few studies, mostly on solvent borne systems, have been reported (3,4,5,6,7). The variables that effect the properties of PSAs can be collected into two groups--polymer structure and formulating factors. This paper describes the results of fundamental studies which have been carried out in our laboratories on the effect of these variables on the performance properties of emulsion Pressure Sensitive Adhesives.

The latex adhesives were prepared by emulsion polymerization and tested as described earlier(8).

1. Polymer structure: Fundamental molecular properties such as the Tg, molecular weight/distribution, polarity and polymer branching/crosslinking affect the adhesive /interfacial and cohesive characteristics which determine the performance properties.

Glass Transition Temperature: PSAs are low Tg materials which are required to develop high strength of adhesion to a wide variety of surfaces under mild bond formation conditions above their Tgs. Acrylic adhesives are typically based on higher chain monomers like butyl, 2-ethyl and octyl acrylates whose long, nonpolar side chains provide internal plasticization . Small amounts of higher Tg monomers, like styrene, methyl methacrylates, vinyl acetate to impart cohesive strength ; and functional monomers like those containing acid, hydroxyl, nitrogen to impart specific adhesion, are added. For example calculated Tg of about -45°C can be achieved through compositions such as n-butyl acrylate/methyl methacrylate in a ratio of 98/2 or 2-ethylhexyl acrylate/methyl methacrylate in a ratio of 80/20. A series of polymers encompassing a range of -54 to + 8° C were prepared by varying the ratio of the major monomers while keeping other aspects constant and the effect on tack and shear was studied in detail. The effect on peel was shown in a previous publication (5). The divergent influence of polymer Tg on adhesive(tack) and

cohesive(shear) characteristics was seen. Tack decreased and shear increased with increase in Tg. A -15°C Tg was selected as the practical upper limit for tack. A high tack (like the peel) value requires intimate contact between polymer segments (high mobility) and the substrate. Shear adhesion on the other hand requires high cohesive strength which, unlike tack/peel, is favored by stiff polymer segments, inter and intra-chain associations, chain entanglements and actual crosslinks. The manner in which the polymer Tg was varied had a strong effect on the shape of Tg vs. tack or Tg vs. shear curves. Monomers with the same Tg which lower or raise Tg equally but differed in bulkiness and side group modified the shapes of the curves in different ways.

In synthesizing a PSA special attention must be given to molecular weight in addition to Tg because of their interplay with the mobility of the polymer molecules.

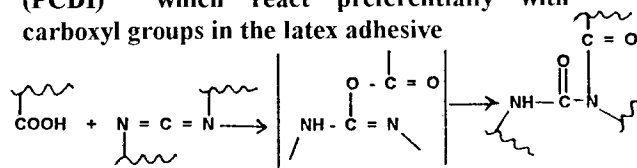
Molecular Weight and Distribution:

Under constant monomer composition and polymerization conditions, the molecular weight was altered by changing the concentration of the chain transfer agent (CTA) from 0 (high molecular weight) to 1.0% (low molecular weight), and the distribution was altered by process conditions. The effect on peel strength and holding power (shear) is shown in FIG. 4a and b respectively. The peel curve shows three distinct regions. In region 1, the peel force increases with increase in molecular weight (decrease in CTA concentration). The mode of failure was cohesive on a macroscopic scale indicating sufficient mobility and deformation characteristics favorable for the formation of a good bond and insufficient cohesive strength to withstand the stresses applied during the debonding process. In region 2, the peel force attains a maximum value but the failure mode is still cohesive. The increase in peel strength appears to be arising out of the increase in cohesive strength due to increase in the molecular weight. In region 3, peel strength decreases with increase in molecular weight, the failure mode shifts from cohesive to adhesive on a macroscopic scale. An increase in cohesive strength takes place to a degree which markedly restricts the flow and deformation behavior of the polymeric adhesive and inhibits the achievement of maximum number of contacts at the interface required for the formation of stronger interfacial bond. The

shear adhesion (Fig. 4b) shows a continuous increase with increase in the molecular weight which is due to the increase in the cohesive strength. The curve shows a steady increase initially followed by a sharp increase. Altering the molecular weight distribution through process variations considerably enhanced the adhesive properties balance, (higher peel and tack for a given level of CTA) thus allowing a greater latitude for polymer design.

Functional Groups: Several polar functional groups such as carboxyl, hydroxyl, and nitrogen containing are incorporated into the acrylic adhesive polymer to enhance specific interaction with organic and inorganic surfaces. In addition, functional groups like the carboxyl can also enhance the stability of the latex. The effect of the level of carboxyl groups on peel and shear adhesion is also shown in Fig. 2a and b. The shear adhesion increased with increase in the carboxyl content. The peel adhesion showed two different behaviors in the molecular weight range studied. In the moderate to high molecular weight range, increasing the level of carboxyl groups causes a decrease in peel adhesion. It appears that dipole-dipole interactions due to the carboxyl groups result in an increase in cohesive strength. Thus a modification in the rheological properties, as observed by an increase in Tg and elastic modulus with increase in the carboxyl content, takes place (5). In the low molecular weight range, the peel strength increases with increase in the carboxyl content due to increase in the cohesive strength as explained earlier. Thus different peel behaviors in the molecular weight range are consistent with the offered explanation.

Functional acrylic latexes with carboxylic functionality can be crosslinked to increase their shear resistance. Crosslinking studies reported here were done by post-addition of polyfunctional carbodiimides (PCDI) which react preferentially with carboxyl groups in the latex adhesive



Two sets of crosslinking experiments were done with PCDI(UCARLINK 29 SE). In the first set, the effect of different levels of PCDI on the adhesive properties of a model

system containing 3 % carboxyl monomer was studied and the data are presented in Table 2.

Table 2: Effect of different levels of PCDI on peel and shear

PCDI Level (meq/100 meq COOH	Peel (g./cm.)	Shear (hr.)
0	516	5
0.9	400	7
1.8	305	54
9.0	361	>200
36	332	>200
54	198	>200
99	152	>200

It can be seen that several conflicting trends caused by the reaction resolve themselves into a smooth decrease in peel and a quantum jump in shear. The carboxyl/carbodiimide reaction seems to be quantitative in nature. The formulator can design to a narrow peel /tack range while maintaining high shear strength.

In another set of experiments, the effect of dwell time (residence time between stainless steel substrate and the adhesive before testing the bond), varying from immediate to 168 hours, on adhesive properties was studied. In the presence of PCDI, the peel strength rose from about 321 to 714 g/cm and the shear resistance rose from 1 to 36 hours in 168 hours period. In the absence of PCDI, the peel strength increased from 411 to 804 g/cm, but the shear resistance showed only a slight increase from 0.8 to 1.5 hours. The retention of high peel strength along with improved shear resistance perhaps indicates that under these experimental conditions crosslinking by PCDI takes place in the bulk and not in the surface layers.

The effect of rate and temperature, during the formation and rupture of the bond on the adhesive properties of various systems on different substrates, was also studied in details (9) . Such studies have enabled us to predict the performance of the adhesive assembly over long and short time intervals and to evaluate the contributions of the interfacial and bulk properties- essential information to modify the surface, elastic and inelastic components of the adhesive to develop new systems with enhanced performance.

2. Formulation components: The adhesive systems are formulated to modify the adhesive

and application properties. In PSAs, tackifiers and plasticizers are used to adjust the adhesive properties and surfactants, defoamers and rheology modifiers are used to adjust the applications properties for water-borne systems.

Tackifiers and Plasticizers: The work done in our labs has shown that several polymers manufactured by Union Carbide Corporation can be readily modified with various rosin ester or hydrocarbon tackifier dispersions to yield systems with higher peel-tack than the original latexes and without appreciable loss in shear. Depending on the adhesive properties requirements, the concentration of the tackifier to be used lies in the 20-35 % range. At concentrations greater than 40 % , drop in peel-tack properties takes place in most cases. This behavior has been explained in terms of the " Two Phase " and " Modulus " theories. Usually a minimum increase of 50 % in peel-tack of a given latex is observed after compounding with 30 % of a given tackifier. The loss in shear depends on the initial shear of the base latex and the type of tackifier used. Higher the softening point of the tackifier and initial shear of the base latex , lower is the loss in shear of the compounded latex. The advantage of using tackifiers is that, unlike plasticizers(which can also be used to improve peel-tack), they do not have significant adverse effect on the shear adhesion properties. Tackifiers, which are low molecular weight and high Tg materials, modify the rheological and viscoelastic properties of the base latex by increasing Tg and reducing modulus at low rates and increasing modulus at high rates. This accounts for their unique behavior.

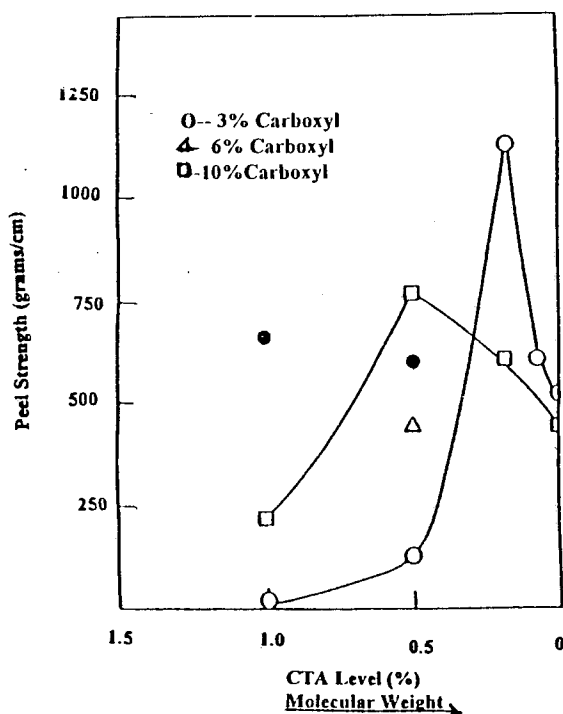
Surfactants, Defoamers and Rheology Modifiers: From a practical point of view, a carefully designed/compounded water-borne PSA requires extensive adjustment for wetting, foam control and rheology to coat on different machines varying in speed and coating heads. Effective wetting of face stocks and backings, which differ widely in surface energies (e.g., 18-100 mJ/m²), is a primary requirement. For most difficult substrates like silicone release liners and polyethylene, surfactants are usually added during compounding to lower the surface tension of the latex close to that of the to be coated substrate. However, post-added and process surfactants can cause excess foaming. Defoamers are used to counteract this tendency.

Since defoamers are "antisurfactants" they can harm wettability. Rheology modifiers are used to improve flowing and leveling. The consequential increase in viscosity can help wetting. However, in some cases they can increase the foaming tendency. These effects of surfactants, defoamers, rheology modifiers on applications properties are listed below

System	Wetting	Foam	Flow/ Control	Leveling
Latex	Poor	Poor	?	?
Latex+ Surf.	Good	Poor	?	?
Latex+Surf.+ Defoamer	Good	Good	?	?
Latex+Surf.+ Defoamer+Rheol. Modifier	Good	Good	Good	Good

Conclusions: This paper has attempted to further the understanding of the combined role of key material and formulation parameters which govern the performance of acrylic PSA emulsions. Such studies have provided useful leads for optimizing the adhesive and application properties of emulsion adhesives and led to the development of unique PSA Latex systems.

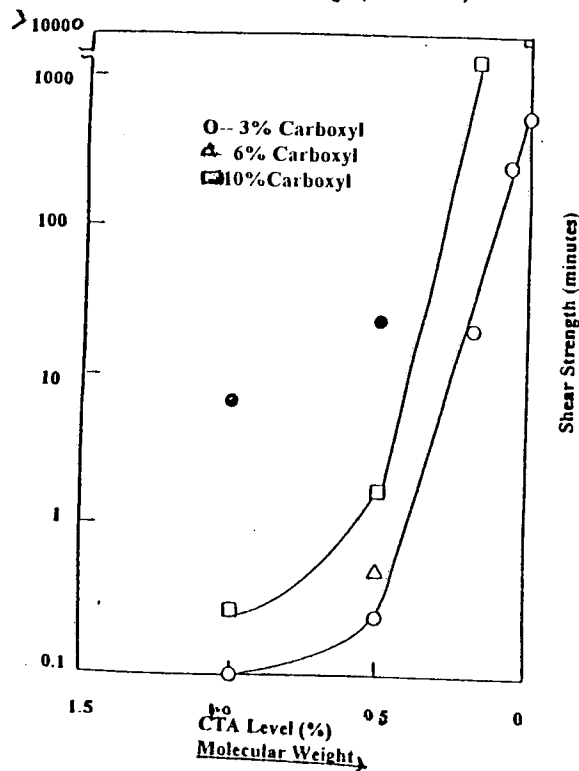
Figure 1a: Peel Strength vs. Molecular weight(CTA level)



References:

1. D. Satas, "Handbook of Pressure Sensitive Adhesive Technology", Van Nostrand Reinhold Company, New York, (1989)
2. K. C. Sehgal, 67th Annual Colloid and Surface Science Symposium(ACS) Toronto (1993)
3. D. W. Aubrey, and S. Ginopsatis, J. Adhesion, **12**, 189 (1981)
4. M. Toyama, T. Ito, and h. Nukatsuka, J. Appl. Polymer Science, **17**, 3495 (1973)
5. K. C. Sehgal, and M. A. Sherwin, PSTC Proceedings (1992)
6. D. Satas, Adhesive Age, October,19(1972)
7. Huang-Kong Chan and G. J. Howard, J. Adhesion, **9**, 279(1978)
8. K. C. Sehgal, PSTC Proceedings, 1987
9. K. C. Sehgal and D. R. Bassett, To be published

Figure 1b: Shear vs. Molecular Weight(CTA level)



Imaging the Bonding and Debonding of Pressure Sensitive Adhesives

Robert K. Galkiewicz
3M Company, Saint Paul, Minnesota 55144

INTRODUCTION

Although pressure sensitive adhesives (PSAs) have been in use for over half a century, we have not yet obtained a detailed understanding of the mechanisms involved in their bonding and debonding. One major element needed to obtain insight and predictive ability into these phenomena is the ability to *visualize* the processes. This visualization is often beyond our reach due to reasons such as small feature sizes, fast rates, or low contrast. Through a straightforward application of video-recording, light microscopy, illumination techniques, and computer image analysis, one can dramatically improve this visualization.

We catalog our visualization techniques into three general areas. In order of chronological development, we have imaged the dynamic debonding of tapes in peel ("external imaging"), the bonding of tapes as a function of formulation, topology, rolldown, and time ("static wetout"), and the dynamic debonding local to the tape/substrate interface ("dynamic wetout"). This latter technique is actually a combination of the first two methods.

EXPERIMENTAL

All three of the above techniques share some common equipment. The image magnification is provided by an Olympus™ SZH-ZB Stereo-microscope. This microscope possesses a 7.5 - 64X zoom setting, and we use planar objectives of 0.5X, 1X, and 1.5X. Mounted onto the microscope are an Olympus™ photo-tube (SZH-PT), TV Camera Adapter (MTV-3-AD), and a solid-state TV camera (COHU™ 4815-5000). The output of the camera can be directed to either of two different devices. For the case of dynamic measurement, where rapid time evolution must be archived, we employ a Panasonic™ video-cassette recorder (AG-7500) and use the S-VHS mode whenever possible for best image resolution. For the case of static and quasi-static measurements, we employ an Imaging Technology's PCVisionPlus™ digitizing board, currently installed in an HP-Vectra™ QS/20 computer; the imaging monitor is a Sony™ PVM-1342Q. We use either Jandel's JAVA™ or BioScan's OPTIMAS™ software packages to analyze the digitized images. We employ a Schöly 150H Fiberoptic light source with dual gooseneck guides for sample illumination. When examining wetout we use an Olympus™ TL2 vertical coaxial illuminator. Finally, 90° peel tests are performed on an Instron™ 4501 tester at 0.3m/min at 50%RH and 22C.

EXTERNAL IMAGING

This technique is not new. Dahlquist [1] has described photographic images of tape peeling from a wheel by Paul Stredry at 3M; these were recorded as early as 1959. In addition, peel imaging work was performed in Japan by Fukuzawa [2] in 1966.

The peeling tape may be imaged either from the front or the side of the peel nip. The schematic of figure 1 shows a typical setup for imaging the peel nip from the front.

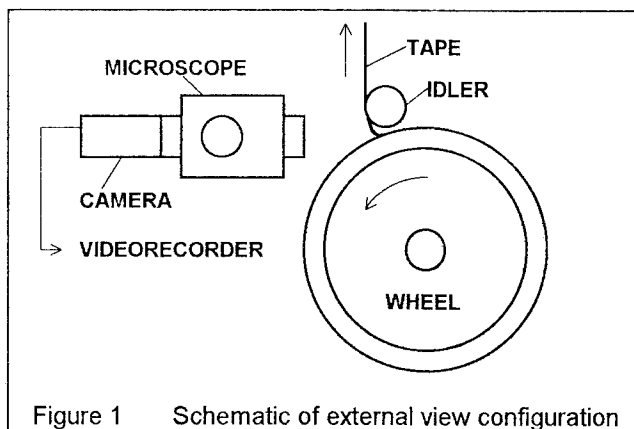


Figure 1 Schematic of external view configuration

Here, a tensile testing machine pulls tape in applied rate peel from a free-rolling peel wheel which typically consists of either polished aluminum or quartz glass. Tape is applied to and peeled from the outer surface and is pulled around a small idler roller to localize the peel nip with respect to the microscope. If peeled from the side, then care must be taken to prevent viewing artifacts associated with adhesive edge ooze. The appearance of the peel nip can be quite different depending on cohesive strength, peel rate, and surface roughness.

At low speeds, the peel front can best be described as a series of vertical, parallel ribs extending out of the nip. These ribs are roughly equidistant, and when some perturbation acts to create or remove one of them, the nip adjusts to restore the periodic spacing. These ribs are generally thought to be a manifestation of "meniscus instability" created by a competition between the viscoelastic and surface stresses within the adhesive [3,4].

As the peel rate is increased, the rate at which the ribs are perturbed increases. At high enough rates the perturbations dominate the process and periodicity of the ribs is lost. The resulting appearance of the peel nip is very complex, and might best be described as a foam.

The question of what actually perturbs the ribs at higher rates will be addressed in the dynamic wetout section below. The change in peel nip appearance does not seem to be singularly correlated with peel force. That is, we do not typically observe a dramatic change in peel force corresponding to a dramatic change in the appearance of the peel nip.

Because the nip topology is so complex, it resists quantitative analysis. Even with image capture techniques, the question of what aspect of the external view of the image to quantify is open. The existence of evenly spaced ribs allows us to measure average rib spacing, thickness, and height, but current theory is not developed to a state to allow us to use this information advantageously. When the ribs evolve to a complex, perhaps chaotic nip, the analysis question becomes even more problematical.

The examination of these images - especially from videotape, where one can slow, freeze, and even reverse the motion - can and does provide a *qualitative* perspective. The image shown in figure 2 indicates that the PSA deformation is not usually simple uniaxial extension. An element of adhesive at the leading edge of the nip is generally connected back to the undeformed layer and buttressed by a sheet of adhesive that has ill-defined shape and stress. There is strong biaxial displacement, and often triaxial stresses. This likely indicates that any peel model utilizing a uniaxial approach will be hard-pressed to produce quantitative agreement with experiment.

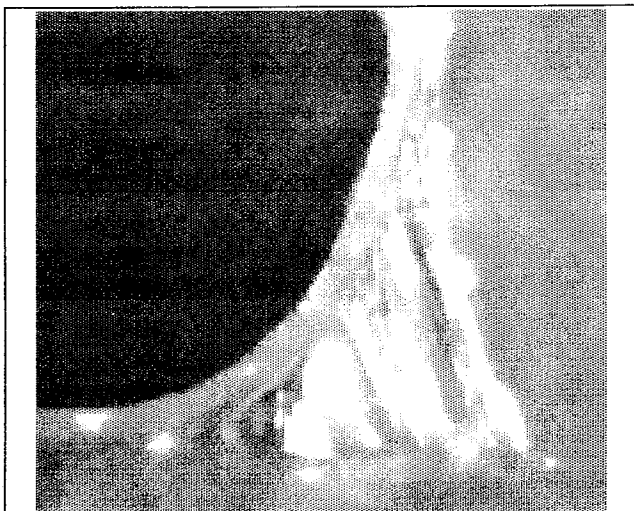


Figure 2 External view of rib formation. The PSA used for this example is a thermoplastic consisting of a co-polymer of isooctyl acrylate, acrylic acid, and meth-acrylate-terminated polystyrene polymeric monomer. The width of the image represents 0.7mm.

STATIC WETOUT

The debonding performance of a pressure sensitive adhesive is a strong function of the bonding behavior. While this fact seems obvious, it is often overlooked in practical applications. The bonding behavior is itself a function of chemical, physical, and topological characteristics of the adhesive and target substrate. The chemical characteristics are usually addressed by the surface free energy. Molecular rearrangements within both surfaces and the flow properties of the adhesives are examples of physical effects. If either the adhesive or the target substrate, or both are rough then the topological characteristics can be important.

The topological facet of wetout can be examined and quantitated through the use of image analysis. A schematic of our apparatus is shown in figure 3. Here, the stereo-microscope is inverted to facilitate i) sample handling, ii) the ability to apply a deadload pressure to the bond for time studies, and iii) the ability to apply zero load over the entire bond area. A bond is made by applying the PSA to a substrate that is transparent and flat. The bond is then viewed through the substrate. If bond area and magnification used permits, we generally select six different areas of the bond to image in order to obtain a measure of the standard deviation of the wetout. These

areas are chosen as objectively as possible within a constraint of no overlap of images.

Of importance in the optimization of contrast is the coaxial vertical illuminator and analyzer. This combination serves to contrast those areas of the substrate which are wet by the PSA with those that are not. Wet areas appear dark due to the small normal-incidence reflectivity coefficient associated with two dielectric interfaces (for instance glass and PSA) possessing fairly equal indices of refraction. Non-wet areas appear brighter because the reflectivity is higher from an interface (glass and air) with relatively different indices of refraction. The illuminator/analyzer combination essentially eliminates the reflection of light from the microscope side of the glass plate and so helps to enhance the contrast from the bond side. It is important to note that while good image contrast is *desired* for external imaging, it is *required* for quantitative analysis of wetout images, especially those with uneven background lighting.

Since visible light is being used as a probe, the lateral and vertical resolution of this technique is measured on a scale of 10^{-7} m, whereas true wetting would be measured in units of 10^{-10} m. Rigorously then, this technique cannot validate that the dark areas are 100% wetout. We do proceed on the assumption that this is so, at least for an optically flat surface (we have measured RMS roughnesses of 1-2 nm for our plate glass) and a viscoelastic liquid, for the purposes of this analysis.

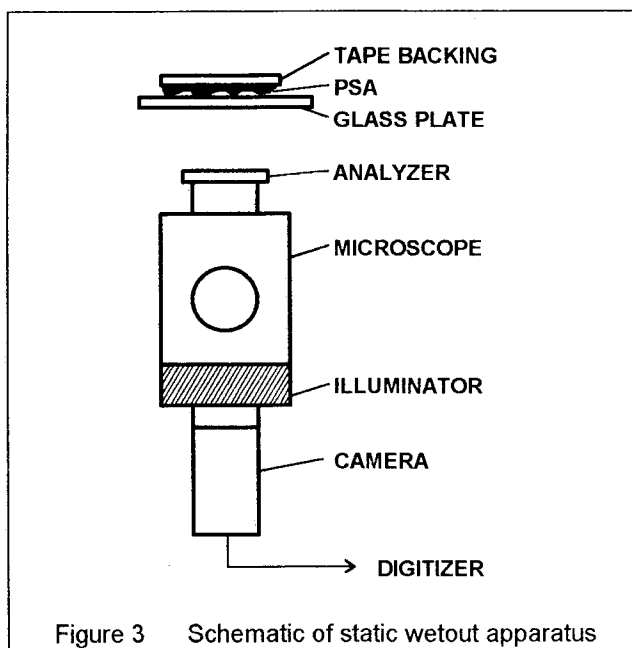


Figure 3 Schematic of static wetout apparatus

With this assumption in mind, static wetout can be used to study several different facets of bonding. The first and simplest is the percent of the image viewed that is wetout. Additionally, one can obtain the number of wet areas and their absolute sizes. This information can then be obtained as a function of formulation, topology, rolldown, and dwell time for any given substrate.

Formulation

The dependence on formulation usually amounts to a variation of both i) surface affinity between the PSA and

target substrate and ii) deformation properties (rheology) of the PSA. Of course, both of these properties are critically important for all PSAs in debonding as well as bonding, and so formulation is typically the prime variable in product development studies.

Topology

This topic is of interest when either the PSA or the target substrate is rough. The scale of the roughness, both in the vertical and lateral dimension can be very significant. Vertical scales significantly smaller than the thickness of the PSA lead to increased (and often almost total) wetout with time. Scales of the order of the adhesive caliper can preserve initial wetout values. In addition, the vertical shape of the roughness (that is, its cross-sectional profile) is important. For profiles with steep walls, wetout does not change significantly with rolldown load or time. Also of importance is the type of roughness feature. Positive features (such as hill projecting out of the adhesive surface) allow air to escape during rolldown and also during subsequent wetout with dwell. Negative features (holes in the adhesive surface) tend to trap air and to prevent total wetout during rolldown.

Rolldown

For a topological adhesive, rolldown is a key variable with respect to subsequent adhesive response. Typically, the wetout and adhesion increase with increasing rolldown. For very tacky adhesive/target substrate combinations - where the peel compression zone [5] dominates the applied rolldown - the correspondence between the rolldown and peel is complex. Rolldown can also be moderated by the dwell time effect discussed below. Figure 4 shows both wetout and peel force plotted against rolldown for an acrylate adhesive similar to that of figure 2 but with higher polystyrene polymeric monomer content and patterned with a microstructured surface consisting of a periodic array of cube-corners 125 μm high as positive features. The substrate was plate glass. The low peel value at 35 Nt/dm is unexplained.

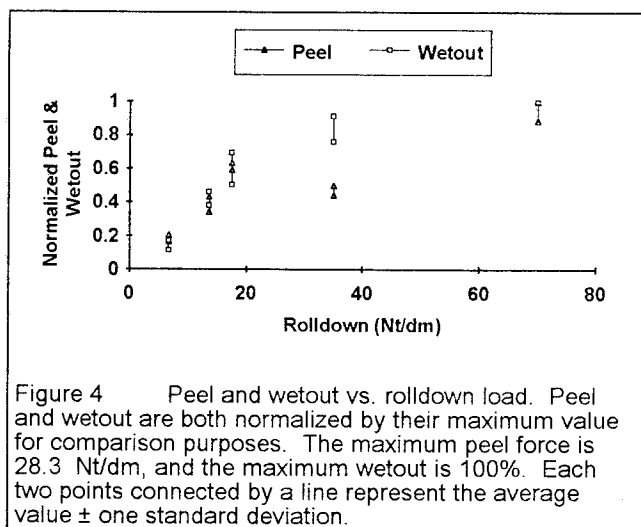


Figure 4 Peel and wetout vs. rolldown load. Peel and wetout are both normalized by their maximum value for comparison purposes. The maximum peel force is 28.3 Nt/dm, and the maximum wetout is 100%. Each two points connected by a line represent the average value \pm one standard deviation.

Dwell Time

The change in the bond state with dwell time can be controlled by modifying the surface affinity, the PSA rheology, and the topological structure. With the proper combinations of the above three variables, one can create adhesive constructions that increase bond wetout with

time, maintain it at a roughly constant level, or decrease bond wetout with time. An example of this latter behavior is shown in figure 5 where the peel force and wetout are plotted against time for the patterned adhesive of figure 4. The dramatic decrease in both properties in time is due to the elastic recovery forces within this PSA overcoming the capillary forces derived from the surface affinity between the PSA and glass substrate. The microstructure on the PSA surface which has been deformed by the roll-down essentially pushes itself from the surface in an attempt to restore its undeformed shape.

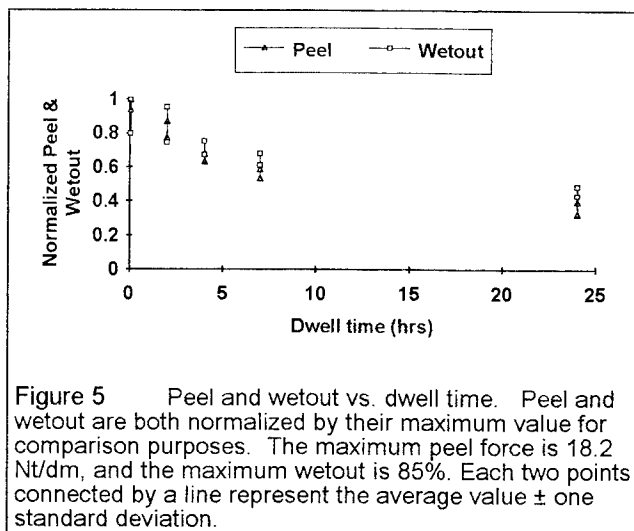


Figure 5 Peel and wetout vs. dwell time. Peel and wetout are both normalized by their maximum value for comparison purposes. The maximum peel force is 18.2 Nt/dm, and the maximum wetout is 85%. Each two points connected by a line represent the average value \pm one standard deviation.

DYNAMIC WETOUT

This technique is similar to a method described by Miyagi et. al. [6]. That work in turn was an extension of work performed by Urahama [7] who employed an apparatus consisting of an optical microscope and still camera to record tape separating at low rates from glass in applied load peel.

Our work utilizes a peel wheel in a manner similar to that indicated above for external imaging. The quartz glass wheel is used exclusively in order to view the footprint of the peeling tape through the rim from below. As shown in figure 6, the optic axis of the camera/microscope is aligned parallel to the axis of rotation (but inside the circle of the rim) and a small dental mirror is used to reflect the axis radially out the rim. This arrangement, in combination with the illuminator/analyzer pair, produces images of wetout directly under the nip of a peeling tape as the wheel rotates. The wetout footprint can be viewed over the entire circumference of the wheel (0.3 m). By increasing the illumination with a light source from above (outside the rim), the emphasis of the view can be changed from the footprint itself to a view corresponding to that of the naked eye. An example of this effect is shown in figure 7, where the lower image was taken 0.1 seconds after the upper at a peel rate of 12.7 mm/min. (The adhesive is that of figure 2.)

Using this arrangement, one can view the process of rib perturbation described earlier. Seen in this light, the ribs are disturbed by the creation of voids in the wetout. As the nip approaches, the voids (which are more or less

stationary) grow and form a bridge across the leading edge of the nip. An example of this is shown in figure 8. The formation of the voids might be attributed to i) intrusions of the meniscus deep into the nip and ii) enlargement of intrinsic flaws (either within the adhesive or at the interface) due to high levels of triaxial stress. As peel rate increases, the voids become more numerous along the peel front until there exist about as many voids as ribs. By this point the rib pattern is totally destroyed and the nip area acquires the appearance of a foam or, when seen in time sequence, a boiling liquid.

This viewing technique also allows us to view the importance of the peel compression zone, both for smooth tapes with trapped air bubbles and for rough tapes. The behavior with rough tapes can be very enlightening. We have found that tapes microstructured with negative features (holes) resist complete wetout via the peel compression zone. Conversely, tapes microstructured with positive features (hills) can experience stresses capable of inducing complete wetout within the zone.

CONCLUSIONS

A straightforward application of video-recording, light microscopy, illumination techniques, and computer image analysis dramatically improves the visualization of the bonding and debonding of PSAs. The value of external imaging lies in its ability to enhance our intuitive understanding and perspective of peel, especially the time evolution of features as a function of peel rate. Static wetout provides quantitative data on the completeness of bonding (rolldown and subsequent wetout) and allows us to correlate bonding with peel force. Finally, dynamic wetout allows us to study the PSA-substrate interface more completely, and provides information on the effect of the peel compression zone and the evolution of features in the nip as a function of formulation and peel rate.

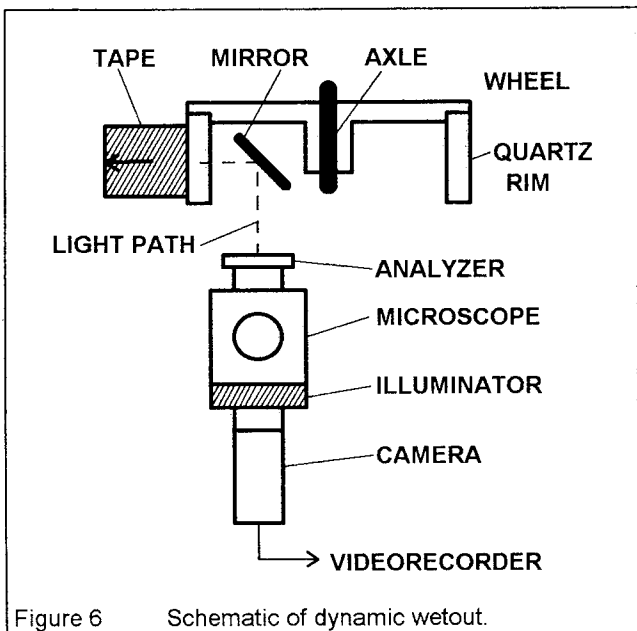


Figure 6 Schematic of dynamic wetout.

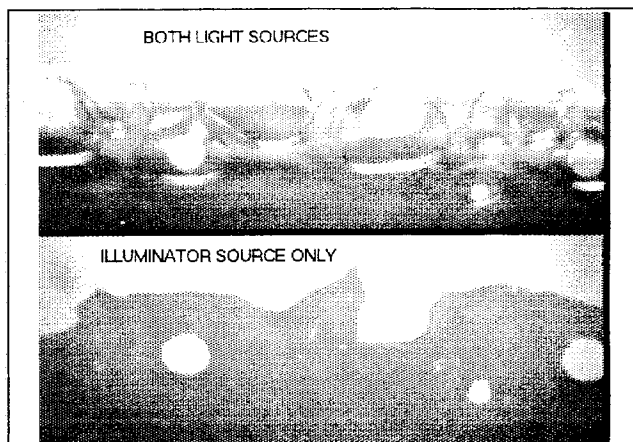


Figure 7 Comparison of dual lighting for the PSA of figure 2. The total width of the image represents 2.5 mm.

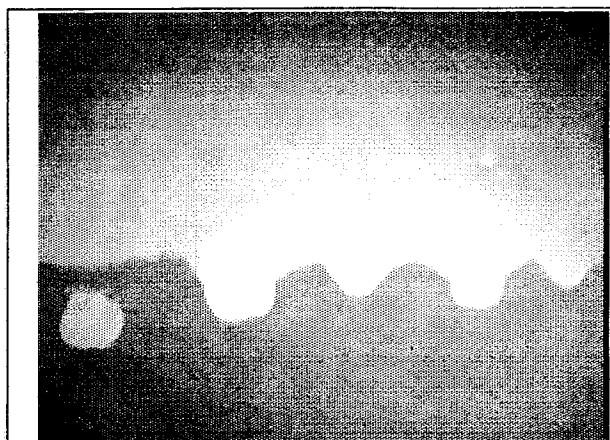


Figure 8 Example of a void (far left) creating a bridge along the peel front. This is the PSA of figure 2. The total width of the image represents 1.9 mm

ACKNOWLEDGEMENTS

The author is grateful to J.R. Manore for assistance with data collection and for many helpful suggestions. Thanks are also due Dr. S.F. Silver for initial guidance into this research area, and to the management of the 3M Adhesive Technologies Center for their continuing support.

REFERENCES

1. C.A. Dahlquist, *Tech XI - Advances in Pressure Sensitive Tape Technology* (Proceedings of the Pressure Sensitive Tape Council's 11th Annual Technical Seminar), May 4-6, 1988, pp. 19-46.
2. T. Fukuzawa, *J. Adhesion Soc. Japan*, 8, 160 (1966).
3. McEwan, A.D. and Taylor, G.I., *J. of Fluid Mech.*, 26, 1 (1966).
4. H. Koguchi and T. Yada, *J. of Applied Mechanics*, 57, 769 (1990).
5. D.H. Kaelble, *Trans. Soc. of Rheology*, IV, 45 (1960).
6. Z. Miyagi, M. Koike, Y. Urahama, and K. Yamamoto, *Int. J. Adhesion and Adhesives*, 14, 39 (1994).
7. Y. Urahama, *J. Adhesion* 31, 47, (1989)

RATE-TEMPERATURE DEPENDENCE OF THE AUTOHESION OF CARBON BLACK FILLED STYRENE-BUTADIENE RUBBER

G.R. Hamed and P.S. Wu

Maurice Morton Institute of Polymer Science
College of Polymer Science and Polymer Engineering
The University of Akron
Akron, Ohio 44325-3909

Introduction

This paper is the fourth in a series 1-3 dealing with the time-temperature dependence of the tack and cohesive strength of uncrosslinked elastomers measured by a peeling geometry. In the first paper¹, it was shown that the cohesion and autohesion after brief contact of a cold-emulsion SBR determined at various rates and temperatures could be time-temperature superposed to form mastercurves using shift factors in accord with the universal WLF equation. In the second paper², autohesion of the same SBR was determined for various contact times. Samples contacted for up to 15 minutes exhibited a sharp decrease in relative autohesion at intermediate rates, while, for contact times exceeding 180 minutes, relative autohesion increased continuously with rate, reaching a limiting value of unity, which was maintained up to the highest reduced rates. Studies of autohesion and cohesion were extended in the third paper³ to include other elastomers: butadiene rubber, natural rubber and two isopropyl azodicarboxylate modified polybutadienes. Relative autohesion for these elastomers as a function of rate and temperature was qualitatively similar to that found previously for SBR. In the present paper the effect of carbon black on the autohesion and cohesion of SBR is discussed.

Materials and Experimental

The elastomer employed was a cold-emulsion SBR 1502, containing 23% bound styrene. Carbon black N330 was obtained from the Cabot Corporation. The backing cloth was a woven cotton fabric with a thickness of about 1.2 mm. An internal mixer with 250 mL capacity and a two-roll mill were used to mix the rubber. After the rubber had cooled for two hours, 20 g were cut to test the Mooney viscosity at 100°C. The ML/1+4/100°C value was 75±4.

Sample Preparation and Testing

After rubber strips with cloth backing had been contacted under controlled pressure and time, they were peeled apart in a T-peel geometry, Figure 1. Peel tests were done at various peeling rates and temperatures. Cohesive strengths also were determined using the T-peel geometry.

Results and Discussion Cohesive Strength

The cohesive peel strengths of the gum SBR and one containing 50 phr of N330 black increase with increasing test rate or decreasing temperature, and, in addition, data can be shifted horizontally along the rate axis to form mastercurves. Time-temperature shiftability indicates that the cohesive

strength is controlled by molecular, segmental motions. When chain mobility is high (due to high temperatures or long times), molecular strands readily slide past one another and strength is low. On the other hand, strength is high when chain slippage is hindered because of less thermal energy or when deformations are rapidly imposed.

Shift factors, a_T , for the gums are in accord with the universal WLF equation. In contrast, a_T values for the filled SBR are larger than those for the gum, although they can be fitted to the WLF form, with constants

$$C_1 = 6.57 \text{ and } C_2 = 86.6, \text{ i.e.,}$$

$$\log a_T = \frac{-6.57 (T - T_0)}{86.6 + (T - T_0)}$$

The constants were determined from linear regression of the $[(T-T_0)/(\log a_T)]$ versus $(T-T_0)$ plot. (C_1 is given by the negative inverse of the slope and C_2 by the intercept divided by the slope).

Autohesion

The gum SBR exhibits a decrease in autohesion at high test rate. Hamed and Shieh¹ found similar behavior with another gum SBR of lower molecular weight. With the same values of a_T employed to shift the cohesive strength data, mastercurves of autohesion could be constructed. Unlike the gum, the autohesion of the filled SBR at high rates behaves like its cohesive strength--reaching a near plateau.

Relative autohesion

Relative autohesion, G_r , was calculated by dividing autohesion by cohesion. Mastercurves for the gum and filled SBR are presented in Figure 2. Relative autohesion of the gum increases with reduced rate, reaching a limiting value of one over a range of intermediate rates before declining abruptly at rapid test rates. G_r is a normalized value of autohesion, but it is not a good measure of the extent of bond formation, because it is multi-valued; clearly, G_r can equal one even when the tack junction is not fully healed.

There is direct evidence from examining peeled specimens that the peel transition for the gum is associated with a change from a viscous to a more elastic response with increasing rate. At rates just less than the transition, the surface of peel specimens are rough due to large permanent deformation associated with fibril formation and rupture. There are no remnants of the original (i.e., prior to contact) surfaces. Contrarily, above the transition, peeled surfaces appear the same as before contacting--small surface imperfections and depressions which were present in the surfaces prior to contacting can still be seen after peeling--though the interface has been subjected to peeling stresses. Clearly, whatever deformation has taken place has done so in a nearly reversible way.

For the filled rubber, relative autohesion increases with test speed and, like the gum, it also reaches a limiting value of one, but at a higher critical rate. However, relative autohesion remains unity up to the highest rates tested. The black-filled SBR, although stiffer than the gum SBR,

is less elastic than the gum. The absence of an abrupt transition in the peel response of the filled SBR is consistent with the transition being associated with a viscous \rightarrow elastic response change. The filled SBR continues to behave in a manner expected for a "viscous" response up to the highest Ra_T tested.

References

1. G.R. Hamed and C.H. Shieh, Journal of Polymer Science: Polymer Physics Edition, **21**, 1415 (1983).
2. G.R. Hamed and C.H. Shieh, Rubber Chem. Technol., **58**, 1038 (1985).
3. G.R. Hamed and C.H. Shieh, Rubber Chem. Technol., **59**, 893 (1986).

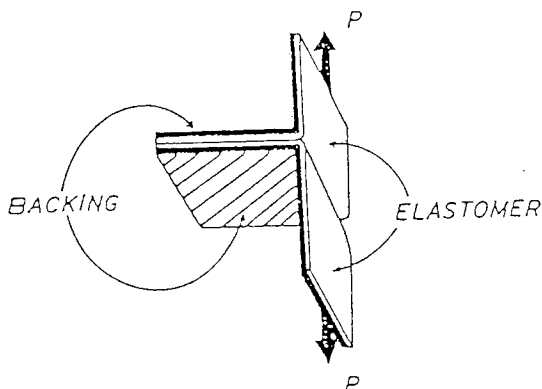


Figure 1. T-peel geometry.

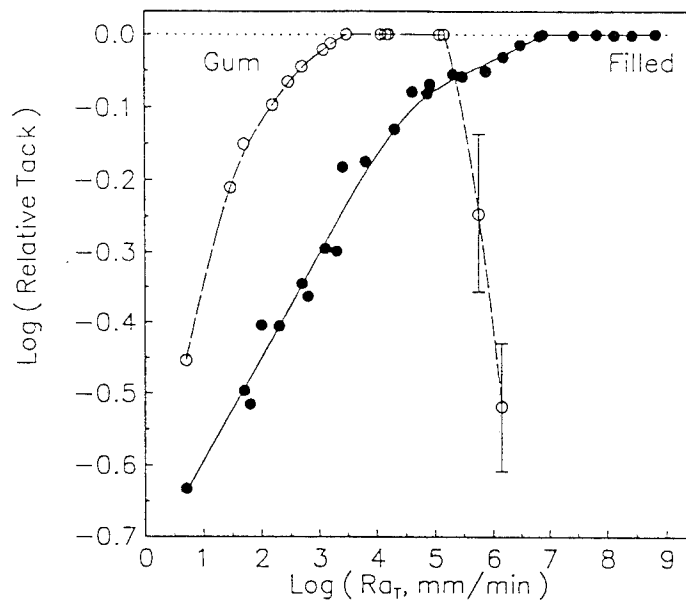


Figure 2. Comparison of mastercurves of relative tack for filled and gum SBR 1502 (contact pressure = 0.57 MPa, contact time = 90 seconds). Solid circles with solid line: filled system; open circles with dash line: gum system.

Viscoelastic Properties of Pressure-Sensitive Adhesives

E. P. Chang

Avery Research Center, Pasadena, California, 91107, U.S.A.

INTRODUCTION

It has been well established by many investigators that the performance of PSA's (e.g. peel, tack and shear) depends strongly on the bulk viscoelastic properties of the adhesives (1-15). The William Landel Ferry; WLF, superposition procedure between rates and temperatures of the tests has been applied very successfully in adhesion tests both in peel (2,3) and in other modes of debonding (4,7,8). In addition, correlations of different peel failure modes with different rheological regions of PSA's have been established and reported by Aubrey and Sherriff (16). Dale and coworkers (13), by combining the small-strain (dynamic mechanical) and high strain (stress-strain) measurements, and correlating these mechanical properties with industry standard "applications" peel and shear properties, established that the majority of the performance range shown by commercial PSA's is controlled by the bulk mechanical properties (tensile strength, storage modulus and dissipation) of the adhesive polymers. In addition, room temperature performance properties were found to correlate better with the properties measured by DMA at higher temperatures than those at room temperature, suggesting the trade-off of high strain and high temperature. Recently, Tse (14) has identified the correspondence of the adhesive performance frequencies with the deformation frequencies on the rheological master curves. He proposed that the criteria for good PSAs are low plateau modulus (satisfying Dahlquist contact criterion), and high-energy dissipation at the corresponding debonding frequency. Chu (15), by comparing the dynamic mechanical properties of commonly employed elastomers and resins, together with their blends, and showing how they can be related to PSA industry standard test methods, was able to establish that the performance of commercial PSA's can be related to the glass temperature (T_g) and plateau modulus as well as the frequency dependence of dynamic testings. Based on this principle, a viscoelastic window for good PSA's was proposed. More recently, viscoelastic windows of

different types of PSA's based on dynamic storage (G') and loss (G'') moduli at bonding and debonding frequencies have also been proposed by Chang (16). The objective of this paper is to review the use of viscoelastic properties for the correlation of pressure sensitive adhesive performance in these recent works.

DISCUSSION

Work of dale et al. (13)

Even though the time scales of the mechanical experiments were not close to those of either peel or shear, they nevertheless presented some useful correlations between the mechanical results and the standard peel and shear data. The choice of 127 deg. C is arbitrary, nevertheless it identifies the superposition of high-temperature small strain dynamic mechanical measurements with room temperature high-strain peel and shear measurements. They also recognized the decisive dissipation in peel is at high strains (closer to the tensile tests), and the caution of using $\tan \delta$ as a measure of energy dissipation because of its strain dependency (17,18).

The noteworthy features and contribution of this work are:

- *The proposed strain temperature superposition concept to reconcile or correlate the small deformation dynamic mechanical and the large deformation tensile tests.

- *The demonstration that the necessary requirements of successful PSA's are to simultaneously possess both solid-like strength and liquid-like flow behavior.

- *The use of $\log \tan \delta$ (positive and negative respectively) to delineate liquid-like and solid-like properties, and the caution of the strain.

- *The importance of the differences in energy integral for adhesive (lower boundary stress) and cohesive peel failures (utilizing full stress-strain curve) adhesives. This identifies the achievement of higher peel strength going from adhesive to cohesive failure. This also confirms that the surface adhesion serves primarily to prevent

premature separation from the substrate (2, 19-22) that results in a low peel force

*Confirmation of the major role that bulk viscoelastic properties play in PSA performance, and demonstration of the power of the tensile and dynamic mechanical methods for correlations with standard peel and shear performance tests.

Work of Tse (14)

By combining the theoretical consideration of Kinloch and coworkers (23-25), Dahlquist contact criterion(1) and the proposed bonding and debonding functions, Tse presented the PSA performance as:

$$T = P_0 BD$$

where T is the adhesion performance and P_0 is an intrinsic interfacial failure energy (either the energy required to open up a unit area of PSA-substrate interface in the absence of viscoelastic energy loss or the thermodynamic work of adhesion which is substrate dependent). B is the bonding function and assumed to be constant when the Dahlquist contact criterion is satisfied (i.e the plateau modulus is lower than 3.3×10^5 Pascals). D is the debonding function which is the viscoelastic loss component. It is strongly dependent on the characteristic debonding frequency, or the separation speed of the PSA test.

Even though viscoelastic measurements involve low strains, while PSA adhesion tests involve high strains, his study confirms many findings of earlier studies on the good correlations of viscoelastic properties with PSA adhesion. The noteworthy features and contribution of this work are:

*Separation of the bonding and debonding steps in PSA adhesion.

*Relationship between viscoelastic behavior at different frequencies and PSA performance and the identification and location of the debonding frequencies for different adhesion tests on the rheological master curves.

*The proposal of a domain disruption temperature T_{dd} which is much lower than the domain disappearance (critical) temperature; T_c , proposed by Krause and Hashimoto (26) and the "monophasic" temperature by Widmaier and Meyer (27). The absence of correlation between shear adhesion failure temperature (SAFT) and T_{dd} , suggests that the responsible mechanism for the lower SAFT observed in resin-rich systems is the lowering of the plateau modulus or narrowing of the plateau width.

* Evidence both for and against the existence of two phases (polyisoprene-rich and resin-rich) in the midblock rubber matrix. Such differences can most probably be reconciled by the different sensitivities and thermal history of the different tests (DSC versus rheological measurements).

*The inference that resin restricts segmental motion of the rubber midblock, resulting in a higher monomeric friction coefficient.

* The identified criteria for good PSAs; namely low plateau modulus to facilitate bonding and high energy dissipation at the PSA debonding frequencies and domain integrity. This is consistent with the proposed viscoelastic windows by Chu (15) and Chang (16).

Work of Chu (15)

Even though there has been earlier studies on the subject of dynamic mechanical properties of resin-rubber mixtures, Chu, nevertheless, through his systematic studies, presented a coherent picture of how the interaction of rubber with resins affects the dynamic mechanical properties, which in turn affects PSA performance. Compared to previous publications, the noteworthy features and contribution of this paper are:

*Identification of the limitation and strengths/capabilities of different Rheometrics fixtures (torsional rectangular, and different diameter parallel plates) for dynamic mechanical measurements of PSA materials. Of particular values to those not too well familiar with all the testing modes, are the caution of instrument compliance at low temperatures or measuring glassy modulus and the recommendation of different size parallel plates for different modulus range measurements.

*The testing and characteristics of resin-rubber compatibility by the criteria of : a pronounced shift in the $\tan \delta$ peak maximum temperature together with a decrease in the plateau modulus.

*The observation that rubbers with higher plateau modulus and T_g values are much more difficult to tackify than those with lower values. This criterion should compliment the matching of the solubility parameter between rubber and resin, commonly used in the PSA industries.

*The order of compatibility of different types of resins with different types of rubbers. This is particularly useful for formulation chemists who need guidance on the selection of compatible resins for these rubbers.

*The identification that good PSA systems (rubber tackified with appropriate amount of compatible resin) have a depression of modulus at low frequencies (making bonding favorable) and an elevation in the high frequency modulus (making

debonding stronger). This also demonstrates the importance of $G'_{w=100}/G'_{w=0.1}$ in achieving good PSA properties

*The proposal of room temperature modulus values at different frequencies for PSA systems. e.g. for tapes and labels, and the proposal of a viscoelastic window for good PSA tapes based on modulus requirement.

*The correlation of tack data versus dynamic mechanical data, specifically $G'_{w=0.1}$ and ratio of $G'_{w=100}/G'_{w=0.1}$. The correlation points out that low $G'_{w=0.1}$ and high $G'_{w=100}/G'_{w=0.1}$ ratio are desirable for high tack values.

*The proposal of empirical windows for various performance labels and PSA tapes based on the loci of room temperature plot of modulus and T_g values determined form the temperature at which $\tan \delta$ is a maximum.

Work of Chang (16)

Using 10^{-2} and 10^2 rad/s as the frequency window for the peel, tack and shear tests, G' and G'' values of different PSA samples at these two frequencies are measured, and their viscoelastic windows (VWs) were constructed by plotting the four coordinates : (1) G' at 10^{-2} rad/s, G'' at 10^{-2} rad/s, (2) G' at 10^2 rad/s, G'' at 10^{-2} rad/s, (3) G' at 10^{-2} rad/s, G'' at 10^2 rad/s, and (4) G' at 10^2 rad/s, G'' at 10^2 rad/s on the log-log cross plot of G' and G'' . It was found that for most PSA's, the range of G' and G'' at room temperature within the selected frequencies falls between 10^3 and 10^6 Pascals. In addition, there is a unique correlation between the adhesion performance of the PSA's versus the location of their VW's. A four quadrant concept was therefore adopted to categorize different types of PSA's. The location of different viscoelastic windows is shown in Figure 1 with their corresponding operative viscoelastic regions:

Quadrant 1: (Top left hand quadrant): High G' -low G'' ---This quadrant corresponds to high modulus, low dissipation. The bonding and debonding frequencies both occur at the plateau region of the rheological master curve. No PSA can be found in this quadrant because of the high bonding modulus and highly elastic nature (lack of flow) of the material making the bonding step unfavorable. Some elastomer and release coatings occupy this quadrant.

Quadrant 2: (Top right hand quadrant): High G' -high G'' ---This quadrant corresponds to high modulus and high dissipation. The bonding frequency corresponds to the plateau region, while the debonding frequency corresponds to

the transition in their rheological master curves for high shear PSA's. The high bonding modulus compensated by the high dissipation or flow makes the bonding marginal. Shear is high because of the high G' or high cohesive strength of the material.

Quadrant 3: (Bottom left hand quadrant): Low G' -low G'' - This quadrant corresponds to low modulus, low dissipation. The bonding frequency corresponds to the plateau region, while the debonding frequency corresponds to the onset of the flow transition in their rheological master curves for removable PSA's. Bonding is facilitated by the low modulus in spite of the low flow characteristics. Peel values are usually low because of the comparatively low debonding cohesive strength and low dissipation. Removable and medical type PSA's fall within this quadrant.

Quadrant 4: (Bottom right hand quadrant): Low G' -high G'' - This quadrant correspond to low modulus-high dissipation. The bonding frequency corresponds to the onset of flow region, while the debonding frequency corresponds to the transition in their rheological master curves for very quick or cold-stick PSA's. The low bonding modulus coupled with high flow make bonding very efficient, thus permitting the material to stick even at low temperature or very short contact time.

Central Area: Medium G' -Medium G'' - This central area corresponds to medium modulus-medium dissipation. The bonding frequency corresponds to the transition region, while the debonding frequency corresponds to the flow region in the rheological master curves (usually characterized by the absence of a distinct plateau region) of general purpose PSA's .

Acknowledgement

The author would like to thank Avery Dennison for permission to publish this work.

References

1. C.A. Dahlquist, Proc. Nottingham Conf. on Adhesion, Part III, Chapter 5, 134, Maclaren & Sons Ltd., London, (1966).
2. D. H. Kaelble, *J. Adhesion* 1, 102 (109), (1969).
3. A. N. Gent and R. P. Petrich, *Proc. Roy. Soc., (London)*, A310. 433, (1969).
4. H. K. Chan and G. J. Howard, *J. Adhesion*, 9, 279, (1978)
5. D. H. Kaelble, *Trans. Soc. Rheol.*, 4, 43, (1960)
6. G. Kraus et. al., *J. Adhesion*, 8, 235, (1977).
7. J. B. Class and S. G. Chu, *J. Appl. Polym. Sci.*, 30, 805, (1985).

8. J. B. Class and S. G. Chu, J. Appl. Polym. Sci., 30, 815, (1985).
9. J. B. Class and S. G. Chu, J. Appl. Polym. Sci., 30, 825, (1985).
10. S. G. Chu, in Chapter 8, Viscoelastic Properties of Pressure-Sensitive Adhesives, edited by D. Satas, Van Nostrand Reinhold, 1989.
11. C. W. Macosko, Adhesive Age, 35, September, (1977).
12. A. Zosel, Colloid & Polymer Sci., 263, 541, (1985)
13. W.C. Dale, M.D. Paster and J. K. Haynes, J. Adhesion 31, 1, (1989)
14. M. F. Tse, J. Adhesion Soc. Tech. 3(7), 551,, 1989.
15. S. G. Chu, , Adhesive Bonding, L. H. Lee Ed., Plenum Publishing Corp., New York, 97, (1991).
16. E. P. Chang, J. Adhesion, 34, 189, (1991).
17. E. H. Andrew, J. Polymer Sci. Symp. 72, 285, (1985).
18. E. H. Andrew, J. Polymer Sci. Symp. 46,1, (1974).
19. D. H. Kaelble, Physical Chemistry of Adhesion, John Wiley & Sons; New York, (1971).
20. R. J. Good, F. Shoraka, Amer. Chem. Soc. Symp. 287, 39, (1985)
21. R. J. Good, R. K. Gupta, J. Adhesion 26, 13, (1988).
22. F. D. Petke, in Adhesion Science and Technology, L. H. Lee, ed., Plenum: New York, 177, (1975).
23. A. N. Gent, A. J. Kinloch, J. Polym. Sci. Part A-2, 9, 659, (1971).
24. E. H. Andrew, J. Kinloch, Proc. R. Soc. Lond. Sere. A, 332, 385, (1973).
25. E. H. Andrew, J. Kinloch, Proc. R. Soc. Lond. Sere. A, 332, 401, (1973).
26. G. Kraus, T. Hashimoto, J. Appl. Polym. Sci, 27,1745, (1982)
27. J. M. Widmaierer, G. C. Meyerer, J. Polym. Sci. Phys. Ed. 18, 1237, (1980).

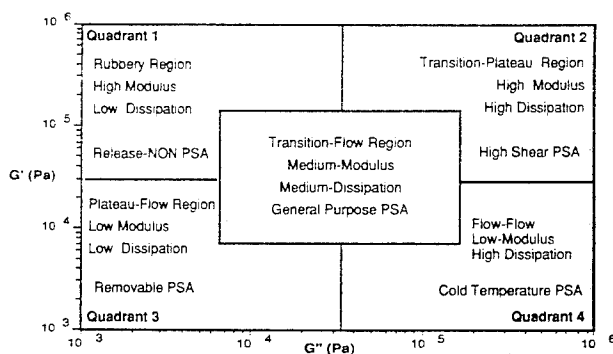


Figure 1: Viscoelastic Windows of PSA's

SILICONE PRESSURE-SENSITIVE ADHESIVES WITH ENHANCED SURFACE WETTABILITY

Shaow B. Lin
Specialty Coatings, Technology, GE Silicones
260 Hudson River Rd., Waterford, NY 12188

INTRODUCTION

High performance tape products made from silicone pressure-sensitive adhesives (PSAs) are serving applications across many industries including converting, electronic & electrical, and photographic processing. These silicone PSAs are typically made by compounding high molecular weight silicone gums with a tackifying siloxane resin in solution. By balancing the resin to gum ratio and carefully selecting the gum and resin characteristics, these adhesive properties - peel adhesion, probe tack and lap shear - are compositionally obtained over a wide range [1].

In high speed converting operations, a PSA for splicing needs to possess "high wettability" property, the ability of a PSA to instantaneously adhere to the surface of interest with the slightest of applied pressure. The establishment of this PSA-to-surface adhesion is completed within a matter of seconds. The faster the converting line speed, the shorter the available application time for splicing. This increasingly demanding industrial environment is placing a strong quest for a silicone PSA with superior wettability, and prompts this study to better understand the chemical aspects of the PSA-to-surface adhesion phenomenon.

This study investigates the adhesion characteristics of silicone PSAs to preferred substrates found in the splicing tape industry. A group of silicones with selected organic functionalities - fluoro, epoxy, vinyl and amino - are chosen as modifiers for a polydimethylsiloxane silicone PSA system. The adhesion properties characteristic of the wettability of these modified PSAs are shown.

EXPERIMENTAL

Adhesive Preparation and Testing

A silicone PSA identified as the control was made to 60 wt. % solids in toluene. The PSA was

the reaction mixture of 57 parts of SR545 resin, a silanol-containing MQ siloxane resin (by GE Silicones) with 43 parts of a silanol-stopped, high-molecular-weight polydimethylsiloxane (PDMS) gum. Silicone modifiers for this study were formulated into the control silicone PSA mixture. The type and properties of the silicone modifiers investigated are shown in Table I. The general nomenclature and shorthand of the silicones is described as follows [2]. D^F represents a trifluoropropyl methylsiloxane unit; M^E is a 2-(3,4-epoxycyclohexenyl)ethyldimethylsiloxyl unit; M^{vi} is a vinyl dimethylsiloxyl unit; D^N is a 3-(2-aminoethyl)aminopropylmethylsiloxane unit.

Table I. Silicone Modifiers for Silicone PSAs

Modifier Type	Modifier Structure	Functional Group Conc. (m. equiv./g)	Viscosity, @ 25 °C
Fluoro	MD ₃₀ ^F M	6.17	1000 cps
Epoxy	M ^E D ₁₀₁ M ^E	0.256	376 cps
Vinyl	M ^{vi} D ₄₂₅ M ^{vi}	0.063	3600 cps
Amino	MD ₂₄₀ D ₁₀ ^N M	0.80	2500 cps

Silicone PSA mixtures were catalyzed with benzoyl peroxide (BPO), then coated over 1 mil polyester film, to give a 1.5 - 2 mil dry adhesive build. The coated films were flash dried for 90 seconds at 95 °C, and then cured for 90 seconds at 177 °C.

The peel adhesion property of the cured adhesive tapes is measured by performing a 180° peel against a clean steel plate. The measurement is carried out according to ASTM D3330 at a rate of 12 in./min. The probe tack adhesion is measured according to ASTM D2979-88 using a Polyken Probe Tack Tester (TMI) at a contact pressure of 14.5 psi, a probe movement rate of 1 cm/sec, and a dwell time of 1 second. The loop

tack adhesion test, which measures the extent and the strength of bonding formed between the PSA and the surface of interest, is done on a Loop Tack Tester (Chemsultants International).

RESULTS AND DISCUSSION

Adhesion Characteristics of Silicone PSAs

Using a diacyl peroxide catalyst, silicone PSAs cure to a crosslinked adhesive structure, which renders superior flexibility and thermal stability over a wide temperature range (-60 °C to 250 °C). BPO thermally decomposes to benzoyl radicals. These benzoyl radicals effectively abstract hydrogen atoms of the methyl silicone groups on the polymer chains and of the siloxane resin molecules. This results in the random formation of crosslinked bridges throughout the adhesive matrix.

The degree of cure in silicone PSAs is varied systematically by the BPO concentration. The resulting effect of BPO concentration on peel, probe tack and loop tack properties of the PSAs is investigated at concentrations ranging from 1.0 to 2.5 wt. % per total silicone solids. As the BPO concentration increases, both peel and probe tack values decrease. The loop tack responded according to the testing surface type: it decreased from 101 to 87 ounces to a stainless steel surface, and only ranged from 1.2 to 0.9 oz to a silicone-coated surface (Release International, 8714). The loop tack adhesion property therefore appeared sensitive to the wettability of PSA to surface.

Modifier Effect on the Wettability of PSAs

The effect of incorporating an organosilicone modifier on the resulting PSA properties, particularly the wettability property, was studied. Four structurally distinct, organic functionalities - fluoro, epoxy, vinyl and amino - were selected for comparison. These modifiers were individually incorporated into the control PSA mixture at a 5 parts modifier per 100 parts PSA solids level. The peel and probe tack properties were measured against stainless steel. The loop tack adhesion was measured against the silicone release paper from Release International.

Tack of a PSA is a composite property of the adhesive-adherend bonding and the viscoelastic

property of the adhesive. It is measured categorically by three types: rolling ball, probe tack, and loop tack (90 degree peel). Each test operates under different mechanical conditions, and reveals much different aspects of the tack adhesion property [3-4]. The loop tack testing is chosen for the study since it closely reflects the interface wetting behavior and the subsequent debonding force of the adhesive-to-adherend interface under a well controlled setting.

The loop tack adhesion of these modifier-containing PSAs is shown in *Figure 1*. It shows the loop tack adhesion of the resulting PSAs ranked in descending order: amino > vinyl > epoxy > fluoro > the control. The modified PSAs exhibit higher loop tack values than the control PSA. Predominantly, the surface of the cured silicone PSAs is now enriched by the organic functionalities of the modifiers, which are higher in surface energy than the silicone. The increase in surface energy leads to modified adhesives with improved wettability over that of the control silicone adhesive.

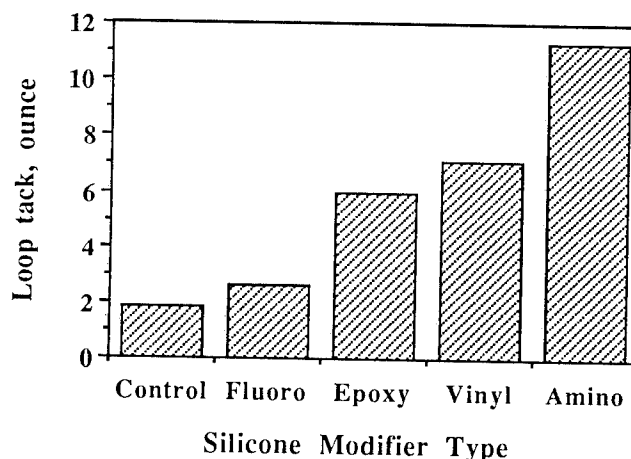


Figure 1. Effect of silicone modifier type on the loop tack adhesion (to a silicone release) of cured PSAs.

Adherend Type on the Wettability of PSAs

The effect of adherend surface type and the adhesive composition on the wettability of silicone PSAs is investigated. Many silicone release systems are found in the industrial splicing application environment. Three types of silicone release coatings are chosen for a study on how the wettability of a silicone PSA changes with the adherend surface chemistry. SS4331 is a thermally cured silicone release coating system, derived

from high molecular weight, addition-cure vinylsilicones in solvent. SL6100 is a thermally cured silicone coating, derived from solventless, addition-cure low viscosity vinylsilicones. UV9300 is an ultraviolet radiation-cured, silicone release coating, derived from iodonium-catalyzed, epoxy-containing methylsilicones. All three systems are manufactured by GE Silicones [5].

The adhesive properties of silicone PSAs to various surfaces are shown in Table II. The peel adhesion of modified PSAs are lower than that of the control, which is expected due to the dilution in resin content, from 57 to 54.3 wt. %. Yet, a "softening" effect of the modifiers on the viscoelastic property of PSAs exists in the following order: fluoro < epoxy < amino.

Table II. Modifier effect on the properties of Silicone PSAs

Modifier Type	Peel, oz/in.	Loop Tack Adhesion, ounce			
		Steel	SS4331	SL6100	UV9300
Control	47.0	87.1	1.1	4.4	38.9
Fluoro	45.5	87.9	2.1	4.2	36.4
Epoxy	40.0	80.2	3.4	30.0	34.4
Amino	35.5	65.4	5.4	21.6	21.6

Silicone PSAs exhibit a high loop tack adhesion to steel and UV9300 surfaces, and poor loop tack to SS4331 and SL6100 coated surfaces. Judging from the loop tack values, these PSAs establish a full wetting with steel surface and a good wetting with UV9300. Contrarily, the wetting and the bonding between the adhesives and SS4331 or SL6100 surfaces are poor.

By incorporating silicone modifiers into a silicone PSA, the wettability between the silicone PSA to these "difficult-to-wet" surfaces (SS4331 and SL6100) is enhanced. The wettability enhancement appears to be related to the structure of these modifiers. The amino and epoxy types are more effective than the fluoro type. As shown, the aminosilicone modifier improved the loop tack adhesion of the control PSA to these surfaces from a negligible reading to a noticeable level.

Contrastingly, a decrease in loop tack adhesion to the "ready-to-wet" surfaces (steel and UV9300) is noted upon modification. This is attributed primarily to the softening or plasticization effect on the viscoelastic adhesive properties.

CONCLUSION

This report studies the adhesion characteristics of peroxide-cured silicone PSAs as a function of the extent of cure in the adhesive matrix. As the cure in PSA increases, the peel, probe tack and loop tack adhesion to steel decrease correspondingly.

The wettability of silicone PSAs to difficult-to-wet surfaces is enhanced by incorporating an organofunctional silicone into the silicone PSA mixture. The wettability enhancement corresponds to the type of organofunctionality present in the modifiers in the order: amino > vinyl > epoxy > fluoro.

Contrastingly, when measured against ready-to-wet surfaces the modified silicone PSAs exhibit lower loop tack adhesion values than that of the unmodified PSA. This is attributed to the softening on the viscoelastic adhesive properties.

ACKNOWLEDGMENTS

The author thanks Robert Rowland for experimental assistance, Michael O'Brien for release coating discussions and Stuart Kerr for general discussions. The support of GE Silicones management is greatly appreciated.

REFERENCES

1. S.R. Kerr III and S.B. Lin; *Adhesive Age*, pp. 36 - 43 (September 1994).
2. S.B. Lin; *J. Appl. Polym. Sci.* (to appear).
3. F.H. Hammond, Jr.; Handbook of Pressure Sensitive Adhesive Technology, Don Satas Ed.), Van Nostrand Reinhold, New York, pp.38-60 (1989).
4. F.H. Hammond, Jr., ASTM Spec. Publ. No. 360, pp. 123-134 (1964).
5. GE Silicones Product Literature, "Release Coatings" (1993).

MAXIMUM PEEL STRENGTHS OF PRESSURE-SENSITIVE STYRENE-BUTADIENE LATEX POLYMERS OVER WIDE TEMPERATURE AND PEEL RATE RANGES

Jan J. Spitzer, J. Antonucci, A. Edwin Karabela, and K.P. Lok

BASF Corporation, Dispersions R&D, Charlotte Technical Center,
11501 Steele Creek Rd, Charlotte N.C. 28273

INTRODUCTION

One of the key application properties of elastomeric pressure-sensitive adhesives is their peel strength. There are usually two performance "desirables" of importance related to peel strength: (i) to obtain maximum possible peel strength, and (ii) to maintain large peel strength performance over a wide range of peel rates and temperatures. In this paper we focus on the first "desirable", the maximum possible peel strength, by asking how the maximum peel strength (under any conditions of peel rates and temperatures) depends on the molecular weight and on the glass transition of the polymer, while maintaining reasonable pressure-sensitive properties (Dahlquist criterion).

EXPERIMENTAL

Synthesis. Five polymers were synthesized by the usual continuous monomer addition emulsion polymerization process, yielding latexes with particle size of about 165 nm and total solids content of about 50%. These latices were adjusted to pH of about 7 with concentrated ammonia and

stripped of residual monomers by a combination of chemical stripping and steam distillation.

Peel Strength Measurement. The samples for peel strength measurements were prepared by direct coating of thickened latexes onto 1 mil polyester film with an automatic bar coating machine. A pressure-sensitive adhesive film of about 20 microns thick was obtained when this polyester film was dried at 90°C for 3 min. These films were conditioned at 23°C and 50% R.H. for about 24 hours. Then one-inch strips were glued to cleaned stainless steel plates with a 4.5 lb roller, and the 180° peel strength determined using a Syntech tensile machine equipped with a constant temperature chamber. The measurement was performed as soon as the temperature reached the set temperature. Each measurement was repeated three times, the standard deviations varying from 3% to 20%, depending on the mode of failure (in the region where the mode of failure changed, the errors were relatively large). Large number of data were obtained in the temperature range of -55°C to +50°C at peel rates of 0.12, 1.2 and 12 in/min.

RESULTS AND CONCLUSIONS

Characterizations. The first three polymers under the heading "Molecular Weight" in Table 1 have the same stabilization system and the same glass transition temperature, the only difference being their molecular weight, which is characterized by their gel content. The remaining two polymers under the heading "Glass Transition" have a different stabilization system from the first three polymers, which is reflected in their water-sensitivity. These two polymers have different glass transition temperatures but approximately the same gel content. These polymers were additionally characterized by DMA, showing the expected trend for the storage modulus and $\tan\delta$ with the gel level (molecular weight variations), and the approximate constancy of these values for the constant gel polymers (glass transition variations).

Peel Strengths. The dependence of the peel strength on temperature and peel rate is shown in Figures 1. - 5. for all five polymers. From these graphs the maximum peel strength and the corresponding temperature was determined for each peel rate. These

results are also summarized in Table 1, showing that the maximum peel strength depends on the peel rate (the lower the peel rate, the lower the temperature of maximum peel strength). The temperature of the maximum peel strength depends on the gel level of the polymer: the lower the gel level, the lower the temperature of the maximum peel strength. Rather remarkably, and perhaps unexpectedly, the actual values of the peel strength do not depend on the gel level (molecular weight) of the polymer, at least within these ranges of variables. The same conclusion can be drawn from the comparison of the two polymers of different glass transition temperature. It may be noted that the maximum peel strength generally occurs in the range where the adhesive mode failure changes to the cohesive mode of failure (either by changing temperature or peel rate). In other words the maximum peel strength is defined by the approximate equality of the cohesive and adhesive strength, which are the function of the peel rate and temperature. In the design of high peel strength adhesives, it is then necessary to increase both the adhesive and the cohesive strength of emulsion polymers in approximately the same proportion.

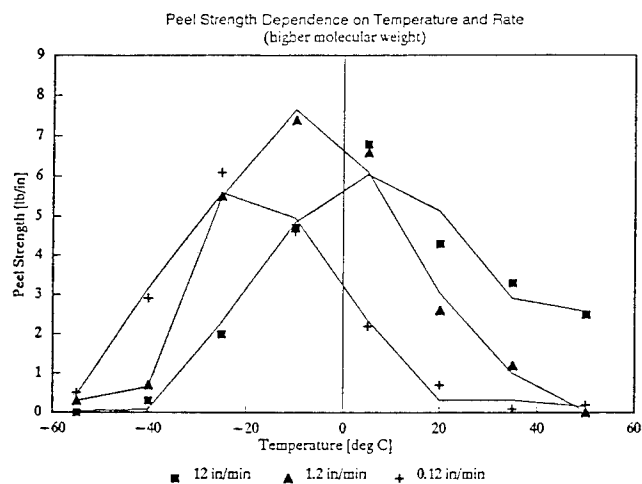


Figure 1

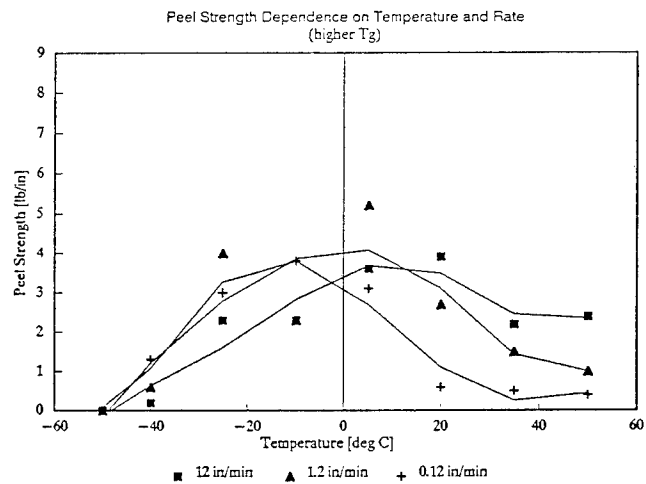


Figure 4

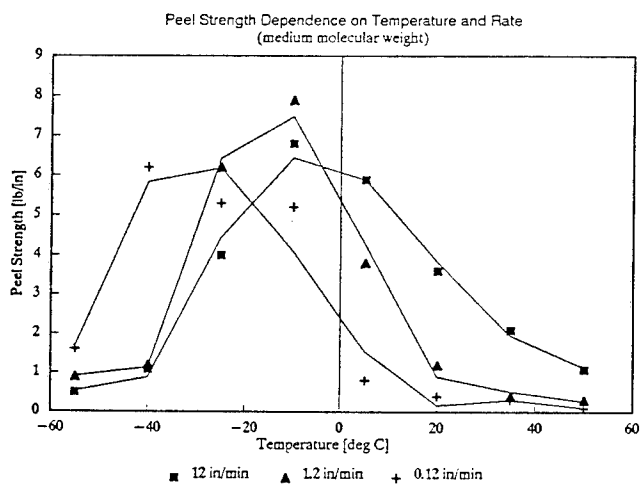


Figure 2

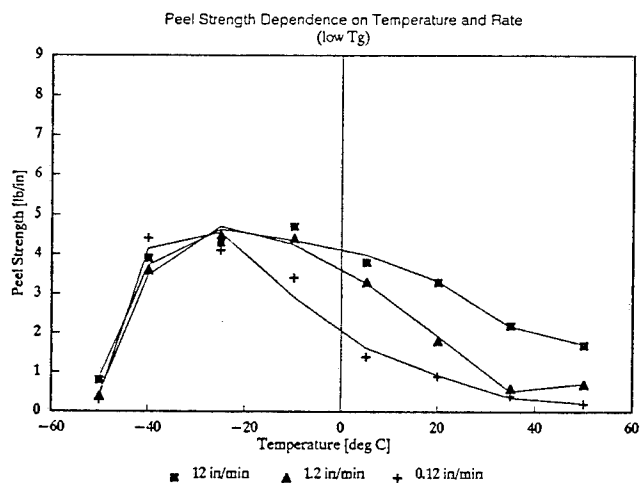


Figure 5

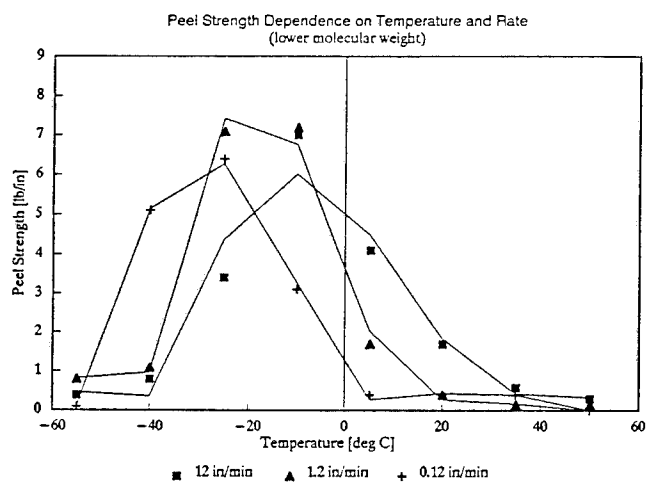


Figure 3

Table 1. Characterization Data and the Maximum Peel Strength

	Molecular Weight			Glass Transition	
	Higher	Medium	Lower	Higher	Lower
T _g (DSC) [°C]					
Onset	-44	-46	-45	-	-
Midpoint	-39	-41	-39	-39	-51
Gel [%]	41	26	15	47	47
G'/100000 [dyn/cm ²]	7.5	4.3	1.9	18	12
tanδ	0.56	0.75	1.03	0.58	0.52
Max. Peel Strength [lb/in]	6-7	6-7	6-7	4-5	4-5
● 12 in/min ● T [°C] =	17	-2	-8	20	-10
● 1.2 in/min ● T [°C] =	8	-15	-20	5	-15
● 0.12 in/min ● T [°C] =	-20	-25	-30	-10	-30
Water-sensitivity	Medium	Medium	Medium	Large	Large

* Strain @ 30%, frequency @ 1Hz, temperature @ 30°C

WATER WICKING RATE OF AN ABSORBENT PAPER LAMINATED BY PRESSURE SENSITIVE ADHESIVE

Tahua Yang and Robert J. Nelson

Abbott Laboratories, Diagnostic Products Division
Abbott Park, Illinois 60064

ABSTRACT

An interfacial model is proposed in conjunction with Lucas-Washburn equation to illustrate the water wicking phenomena in an absorbent paper, which is laminated by a pressure sensitive adhesive (PSA). Several key variables based on the equation and interfacial model have been studied. Larger pore sizes and rougher surface of the absorbent paper cause decrease of the wicking time. A thicker adhesive layer slows the wicking flow due to reducing the imperfection at the diffuse interface. Higher conversion pressure provides more intimate contact between the PSA and absorbent paper, which increases the water wicking time.

INTRODUCTION

Wicking through an absorbent paper or a porous membrane bound by a pressure sensitive adhesive (PSA) is widely used in the medical diagnostic industry. Since the reaction kinetics of these diagnostic devices are controlled by the wicking, it is important to understand the basics of this phenomenon and the parameters that affect the wicking flow.

Numerous studies of the wicking flow through a porous medium have been published [1-3]. The Lucas-Washburn equation [4,5], $l = (R\gamma\cos\theta/2r^2\mu)^{1/2}(t)^{1/2}$, is a well-known theory of the wicking flow. l is the distance traveled by the liquid, while l_r is the actual traveling distance, where r is tortuosity factor. R , γ , θ , μ , and t are radius of capillary, surface tension of liquid, contact angle of solid medium, viscosity of liquid, and time, respectively. This equation is derived from Laplace and Young's capillary pressure and Poiseuille laminar flow theory. Many modifications have been done to correct the assumption of capillary flow due to observed deviations [6-8]. Other formats of the equation for different flow patterns have also been proposed [9].

In the present investigation, the simple Lucas-Washburn equation was used to describe the wicking flow. In the real situation, the pore geometry of the absorbent paper is less structured and interconnected, so the wicking flow normally deviates from the model of a cylindrical tube proposed by the Lucas-Washburn equation. However, the qualitative relationships between wicking flow and all related parameters in the equation still exist. The radius of a capillary is quantitatively associated with the porosity of an absorbent paper. The contact angle, θ , in the equation exhibits the combined effect of the porous fiber matrix and PSA wall. The diffuse interface, which is described in the Interfacial Model Section, plays an important role in addressing the effect of the contact angle.

INTERFACIAL MODEL

Figure 1 shows a hypothetical interfacial region between an absorbent paper and a PSA. The diffuse interface is a thin layer interface with small amount of penetrated PSA. Contact angle changes from the region of the absorbent paper to that of the diffuse interface, where θ_1 and θ_2 are contact angles for the absorbent paper and the diffuse interface, respectively. θ_2 is larger than θ_1 due to more hydrophobic nature of the PSA. In fact, θ_2 is a conceptual contact angle that depends on the formation of the diffuse interface. More intimate contact or more PSA penetration causes higher θ_2 .

EXPERIMENTAL

The absorbent paper used for this study was a saturating base obtained from the Fletcher Paper Company. The basis weight of the paper is 15 lb/1300 ft² with a caliper of 4 mils. The porosity and surface roughness of the paper are the parameters investigated in this study. Porosity measurements were obtained using a Gurley Densometer (ASTM D726-58). The Sheffield method (TAPPI T538) was used to measure the surface roughness. The porosity could be adjusted by refining the cellulose fibers during pulping. The surface roughness was controlled by a calendering process.

The adhesive is a copolymer of acrylic and vinyl acetate from Adhesives Research, Inc. It is a solvent-based self-crosslinking system. The finished adhesive has a very low level of residual solvent. 0.7 mils thick adhesive was produced by reverse roll coating. But in thickness study, handsheet samples were prepared by draw-down method.

The wicking measurement was performed on an Abbott abused-drug diagnostic device, which is pictured in Figure 2. The device consists of seven tracks arranged in a radial pattern with open channels at the front and the absorbent Fletcher paper at the end of the tracks. Measurements were done by dispensing 200 microliters of water in the center well and starting the timer. The wicking time is recorded when the wave front reaches the end of the tracks. The time for water front to travel through the open channels is less than two seconds. Therefore, the wicking time for the device is the time consumed for water wicking through the laminated absorbent paper. Twenty-one tracks were measured for each wicking experiment.

RESULTS AND DISCUSSION

Figure 3 shows the wicking time for an aging experiment in ambient conditions for 19 days. The ranges of slowest and fastest wicking time are plotted to show the precision of the experiment. The wicking flow slows down after aging process. In fact, the water wicking rate of an absorbent paper laminated by a PSA is similar to the peel strength of a PSA joint. The stress is built up suddenly during

lamination process. One way to relieve the stress is to push the soft and mobile adhesive into the interface for more intimate contact with its substrate. Therefore, at the diffuse interface of the interfacial model, the contact angle, θ_2 , becomes higher. The trend of observed wicking flow agrees with the prediction based on the Lucas-Washburn equation.

Absorbent Paper

The porosity of an absorbent paper plays an important role in the Lucas-Washburn equation. Figure 4 shows a plot of water wicking time versus Gurley porosity. Note that smaller Gurley number indicate larger pore size. First three samples show that the wicking time increases with reduced pore size. The trend agrees with the Lucas-Washburn equation. The last sample with Gurley porosity of 8.0 shows abnormal decrease. During the wicking experiment, delamination of the adsorbent paper from PSA was observed. It is obvious that a weak boundary layer was created by less PSA penetration into smaller pore sizes. Weak boundary layer results in gaps and channeling flow at the interface instead of wicking flow in the absorbent paper.

The effect of surface roughness of the absorbent paper was also investigated. The information from this study reveals the critical aspect of the diffuse interface in the interfacial model. Figure 5 shows the subtle difference of the wicking time for rough surface of $S=310$ and smooth surface of $S=210$. Smoother surface shows slightly longer wicking time due to more intimate contact, thus higher θ_2 , at the interface of the absorbent paper and PSA.

PSA

Another parameter investigated was the effect of PSA thickness on the wicking flow (See Figure 6). The trend for the effect of adhesive thickness on wicking time is similar to that on other properties such as peel or probe tack strengths. A thicker adhesive provides a better contact interface, or higher θ_2 , which increases the wicking time. However, there was one exception to this observed trend. The wicking time for 0.5 mils PSA was longer than that of 0.7 mils PSA sample. An explanation for this observation has not been formulated.

Conversion Pressure

Conversion pressure becomes an important factor when the pore sizes of the absorbent paper are large and the lamination pressure is high. In this instance, a thicker diffuse interface is formed due to more PSA penetration. Consequently, the material has a higher contact angle, θ_2 , which translates into a slower wicking flow. In Fig. 7, higher conversion pressure contributes to higher θ_2 and increases the wicking time.

CONCLUSIONS

It is possible to control the wicking rate of an absorbent paper laminated by a PSA by altering the pore size and surface roughness of the absorbent paper, the thickness of PSA, and lamination pressure. A qualitative analysis for the wicking flow of a laminate can be explained based on the

Lucas-Washburn equation and the interfacial model.

REFERENCES

1. A. Marmur, J. Coll. Int. Sci. **122**, 209 (1988).
2. A. Marmur, J. Coll. Int. Sci. **129**, 278 (1989)
3. D. Danino and A. Marmur, J. Coll. Int. Sci. **166**, 245 (1994).
4. R. Lucas, Kolloid. Z. **23**, 15 (1918).
5. E.W. Washburn, *Phys. Rev. 2nd Ser.*, **12**, 273 (1921).
6. L.R. White, J. Coll. Int. Sci., **90**, 536 (1982).
7. Y-W. Yang, G. Zografi, and E.E. Miller, J. Coll. Int. Sci., **122**, 24 (1988).
8. Y-W. Yang, G. Zografi, and E.E. Miller, J. Coll. Int. Sci., **122**, 35 (1988).
9. A. Borhan and K.K. Rungta, J. Coll. Int. Sci., **158**, 403 (1993).

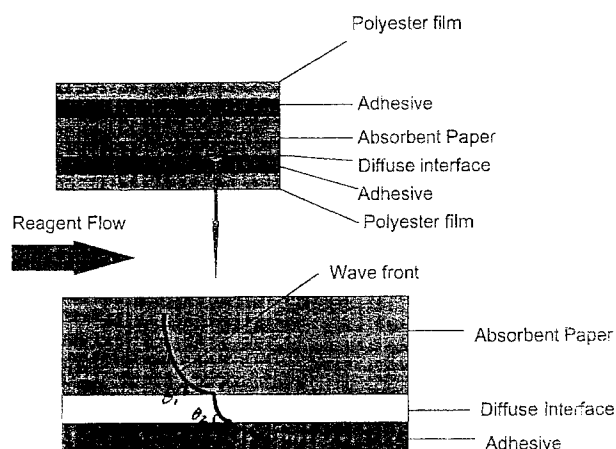


Figure 1. Interfacial model for reagent flow. Note that the contact angle, θ_2 , is higher than θ_1 .

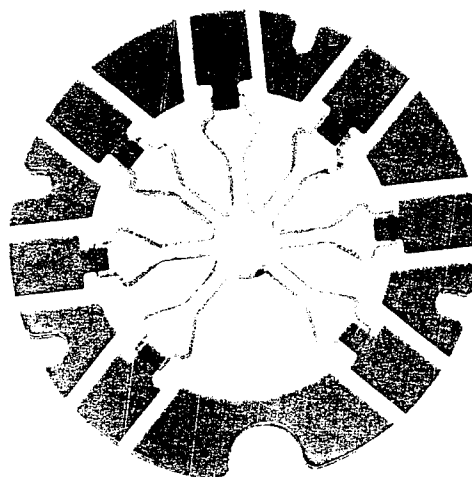


Figure 2. Abbott diagnostic device with seven tracks. The dark areas at the end of the tracks are the laminated absorbent paper.

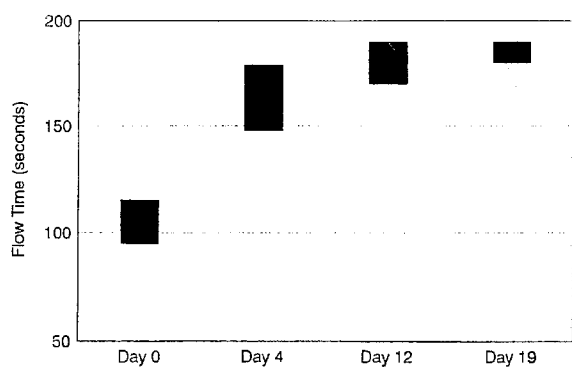


Figure 3. Wicking time for aged devices. The trend is mainly controlled by the pressure sensitive adhesive.

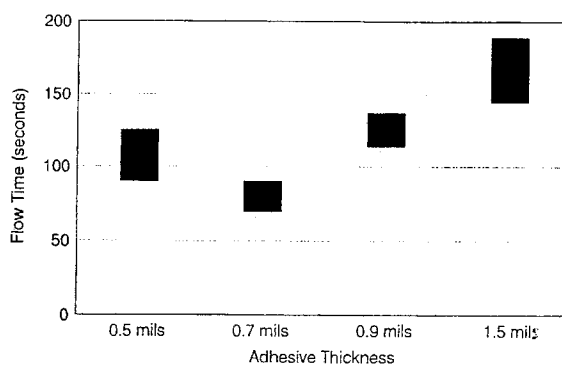


Figure 6. Effect of adhesive thickness on the flow time.

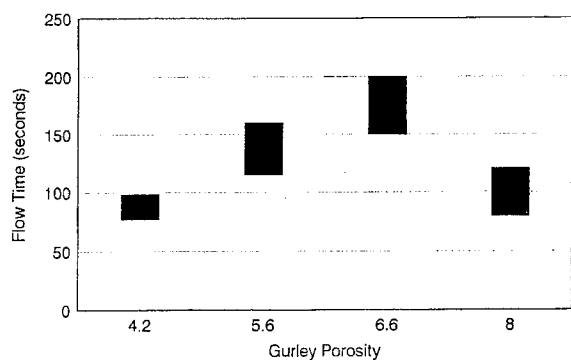


Figure 4. Effect of Gurley porosity on the flow time. Note that a larger Gurley number indicates smaller pore size.

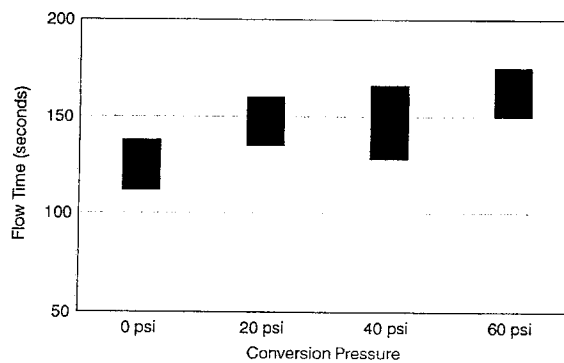


Figure 7. Effect of conversion or lamination pressure on the flow time.

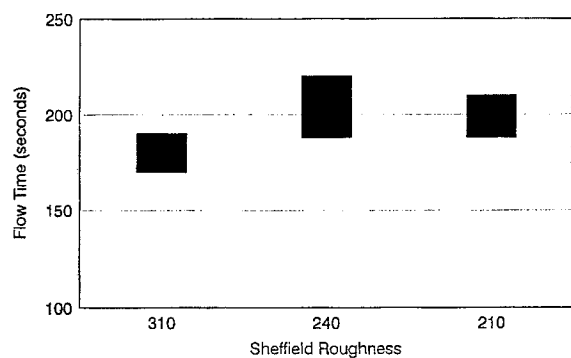


Figure 5. Effect of surface roughness on the flow time. Rougher surface has larger Sheffield number.

HERTZIAN INDENTATION TEST FOR MEASURING THE FRACTURE ENERGY OF POLYMER/GLASS INTERFACES IN SANDWICH GEOMETRIES

J. E. Ritter, T. J. Lardner, G. Bao⁺, and P. Juntawongso

Department of Mechanical Engineering
University of Massachusetts, Amherst, Massachusetts

⁺The Johns Hopkins University, Baltimore, Maryland

INTRODUCTION

A major research challenge is to access accurately the fracture energy of bimaterial interfaces. Recent research has shown that a simple indentation test can be used to measure interfacial fracture energy of coatings. For polymer coatings on glass substrates [1,2], the indentation test consists of loading a coated surface with an indenter, e.g., ball or Vickers. The polymer coating underneath the indenter is deformed and displaced laterally. This lateral motion of the coating results in stresses at the interface which, at sufficiently high indenter loads, causes an interfacial crack to initiate and subsequently propagate with increasing indenter load. For thin refractory coatings, e.g., m-ZrO₂ between two plates of sapphire [3], the top sapphire plate was indented with a ball at a load sufficient to propagate a Hertzian cone crack through the sapphire and into the interface. In both these indentation tests finite element analysis was used to relate indentation load and the debond crack size to the critical energy release rate, G_c .

The purpose of this research was to use the Hertzian cone crack test [3] to measure the fracture energy (or critical energy release rate) of polymer glass interfaces.

EXPERIMENTAL

The specimens consisted of two annealed glass plates (1 mm and 3 mm thick) approximately 25 mm x 25 mm in size bonded together with an epoxy adhesive (DGEBA, Devon Corp.). The epoxy adhesive was $25 \pm 10 \mu\text{m}$ thick. The epoxy adhesive was cured for 24 h in ambient air. After curing, the edges of the sandwich specimen were polished to eliminate excessive adhesive that had squeezed out between the plates.

The specimens with the 1 mm thick glass plate on top were indented using an Instron testing machine with a 12.5 mm diameter WC-6% Co sphere. A thin teflon film was placed between the surface and the indenter to minimize frictional effects. The

indentations were made in the center of each specimen with a fixed crosshead speed during loading and unloading of 0.01 cm/min under ambient conditions. The preselected indentation load was held for 25 sec before unloading. It was observed that the Hertzian cone cracks nucleated in the indented surface and propagated stably down and into the interface (see Fig. 1) as the load was increased. No debond crack growth was observed on unloading. Eight to ten samples were tested per indentation load.

RESULTS AND DISCUSSION

A series of cone crack experiments was first carried out in bulk glass specimens of 3 mm thickness. In these experiments the cone crack diameter $2R$ was measured as a function of the indentation load P . It was found that the parameter $P/R^{3/2}$ was constant and equal to $28.3 \text{ MPa } \sqrt{\text{m}}$ and that the angle the cone crack makes with the top surface was 22° , which agrees well with the results of [3].

At low indentation loads it was found that the interfacial debond crack would sometimes form under elastic indentation (see Fig. 2). As indentation load increased the probability of a debonded crack forming increased, as well as the occurrence of radial cracks around the indent site, see Fig. 3. It is evident from Fig. 3 that inelastic deformation occurred underneath the indenter, resulting in the formation of radial cracks that attained their final size on unloading. Above an indentation load of 1962 N, all samples debonded and showed radial cracks, emanating from the indent site. Figure 4 compares the probability of occurrence of radial cracking to that of debonded cracking. Since radial cracks initiated and grew after the cone-interfacial crack formed, radial crack formation and growth is not thought to have an influence on the growth of the cone-interfacial crack. Thus, it is believed that the formation of the cone-interfacial crack can be modeled assuming elastic contact.

The elastic, Hertzian cone crack test was analyzed using a finite element procedure based on the ABAQUS code. The finite element mesh is illustrated

in Fig. 5. Consistent with experimental results, the cone crack angle β was taken to be 22° . The ratio of the crack dimension a to the indentation dimension a_0 was taken to be 1.2 and the contact pressure distribution was assumed to be parabolic with the peak pressure (p_0) given by 1.5 times the mean pressure [4]. Figure 6 summarizes the finite element results where a normalized energy release rate $\pi^2 EGR^3/P^2$ is plotted as a function of the normalized crack size R/h where E is elastic modulus, G is energy release rate, and h is the thickness of the top plate. It should be noted that the finite element model analyzed in this study (see Fig. 5) differs significantly from that of Davis *et al.* [3]. Davis *et al.* assumed that the Hertzian cone crack intersected the surface at the symmetry axis underneath the applied load P . This model is not realistic in terms of the Hertzian cone crack geometry and the load distribution applied by the ball indenter.

Based on the results in Fig. 6, the critical energy release rate G_c (or fracture energy) of the epoxy/glass interface could be determined from the indentation load/crack radius data. Table I summarizes these results where the average G_c for the epoxy/glass interface is $2.4 (\pm 0.9) \text{ J/m}^2$. This compares favorably to the value $(3.4 \pm 1.6) \text{ J/m}^2$ that we measured using a four-point flexure test.

In summary, it is believed that the Hertzian cone crack test provides a very simple, convenient, and accurate means of measuring the fracture energy of polymer/glass interfaces in sandwich geometries. As such it could be used in quality control to quickly assess the polymer/glass interfacial fracture energy in such products as laminated safety glass.

ACKNOWLEDGMENT

This research was supported by NSF Grant DMR-9301761.

REFERENCES

1. L. G. Rosenfeld, J. E. Ritter, T. J. Lardner, and M. R. Lin, *J. Appl. Phys.*, **67**, 3291 (1990).
2. J. E. Ritter and L. G. Rosenfeld, *J. Adhesion Sci. Technol.*, **4**, 551 (1990).
3. J. B. Davis, H. C. Cao, G. Bao, and A. G. Evans, *Acta Metall. Mater.*, **39**, 1019 (1991).
4. L. Yingzhi and D. A. Hills, *ASME J. Appl. Mech.*, **58**, 120 (1991).

Table I. Fracture Energy G_c of the Epoxy/Glass Interface Using the Hertzian Cone Crack Test

Indentation Load (N)	Debond Crack Radius (mm)	Fracture Energy (J/m^2)
1570	3.2	3.28
1766	3.6	2.46
1962	3.8	2.36
2158	4.5	1.02
2354	3.9	2.98

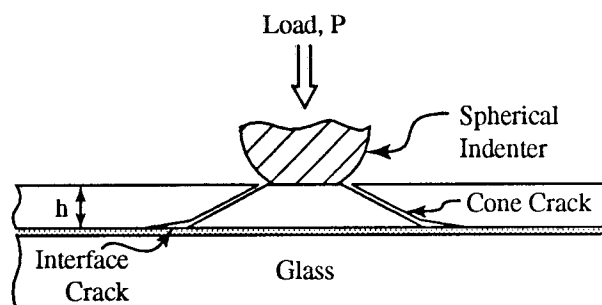


Figure 1. Schematic of the Hertzian cone crack test.

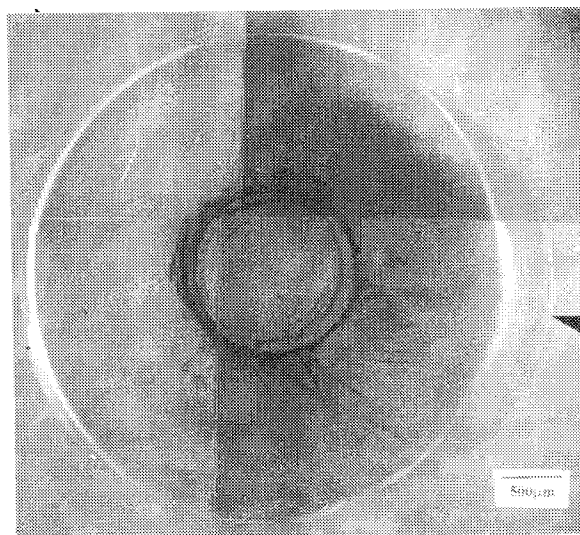


Figure 2. Micrograph of delamination crack formed under elastic indentation ($P = 1569 \text{ N}$) of a glass/epoxy/glass sandwich specimen.

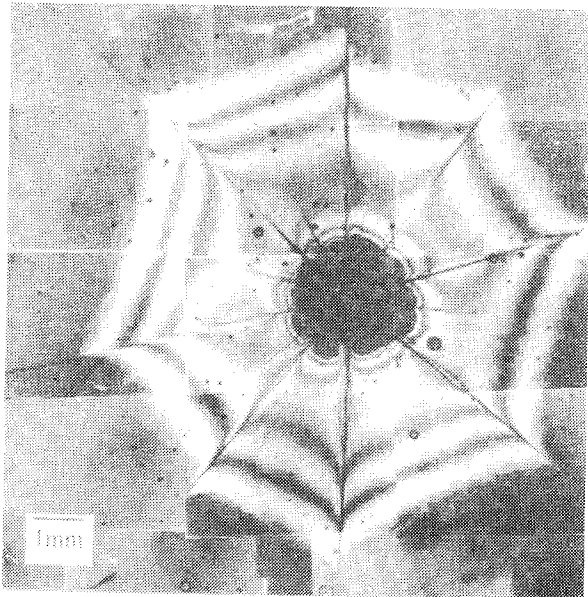


Figure 3. Micrograph of delamination crack formed under elastic/plastic indentation ($P = 2158 \text{ N}$) of a glass/epoxy/glass sandwich specimen.

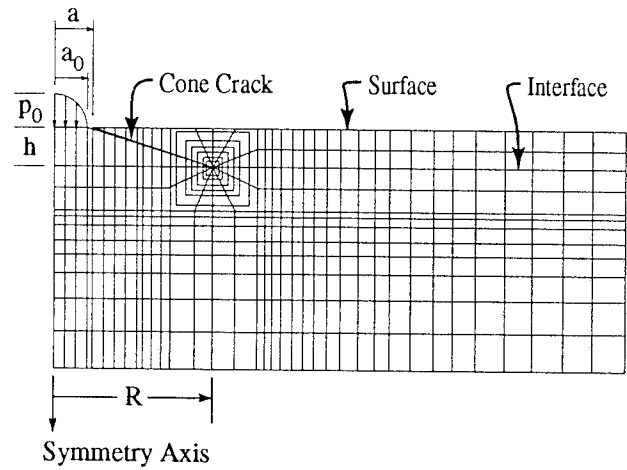


Figure 5. Finite element mesh used to compute the energy release rate G .

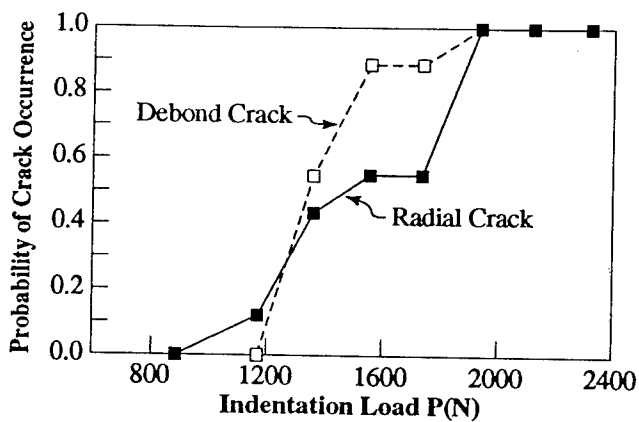


Figure 4. Comparison of probability of occurrence of radial and debond crack formation.

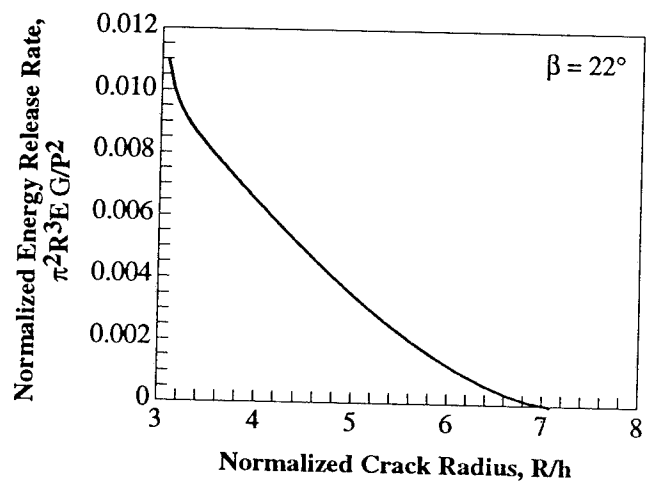


Figure 6. Finite element results of the normalized energy release rate as a function of normalized crack radius for the Hertzian cone crack test.

INTERFACIAL CRACK GROWTH IN POLYMER/GLASS SANDWICH SPECIMENS

J. E. Ritter, T. J. Lardner, G. C. Prakesh, and A. J. Stewart

Department of Mechanical Engineering
University of Massachusetts, Amherst, Massachusetts

INTRODUCTION

Preventing delamination of the interface is of critical importance in the successful application of polymer adhesives. Interfacial failure can occur when the driving force for interfacial crack growth reaches a critical value (G_c) or when environmental factors such as moisture causes slow crack growth at a driving force G less than G_c . Environmentally-assisted crack growth is most important from a design standpoint since crack growth can occur at a relatively low G and lead to delayed failure. It is moisture-assisted crack growth that is the focus of this research.

Moisture-assisted crack growth in epoxy-glass interfaces was measured as a function of the applied G using a four-point flexure test coupled with an inverted microscope [1,2]. The specimens consisted of two glass plates bonded together with epoxy adhesive (see Fig. 1). It was found that the cracks grew on both interfaces if the glass interfaces were both smooth; however, roughening the surface of one of the glass plates increased the fracture resistance of this interface sufficiently so that crack growth would occur only on the "smooth" interface (#1 or #2). Thus, the specific objective of this research was to understand the choice of the interface for crack propagation in terms of fracture mechanics principles.

RESULTS AND DISCUSSION

For the cases where cracks formed and grew exclusively on either interface #1 or #2, the crack growth rate was constant, i.e., crack length varied linearly with time. When both interfaces were smooth, thus having the same fracture resistance, cracks would form and grow on both interfaces. Figure 2 shows a schematic of cracks forming and growing on both interfaces. In this case, two edge cracks are initiated on interface #2 and then grow across the width of the sample; however, in some instances only one edge crack would form and grow across the sample. It is important to emphasize that the crack on interface #1 did not jump to interface #2; hence, the epoxy adhesive always remained intact

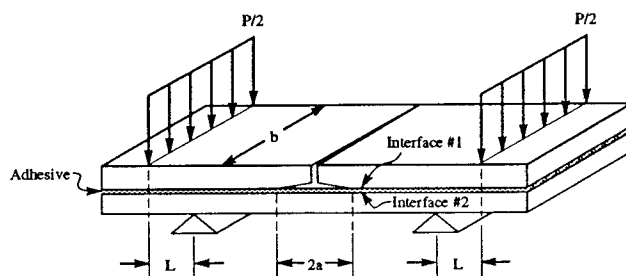


Figure 1. Schematic of four-point flexure adhesive specimen.

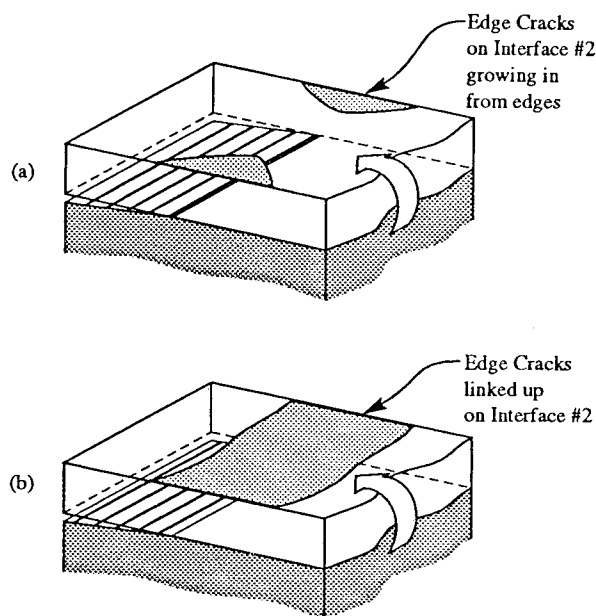


Figure 2. Comparison of crack growth rates in an epoxy/glass system.

between the two cracks on the different interfaces. As the edge crack grew across the width of the sample, it would advance at about the same rate as the crack on interface #1. Once the crack on interface #2 had propagated across the width of the sample, it continued to propagate ahead at a constant rate while the crack on interface #1 arrested.

To provide a fundamental mechanics background for understanding the experimental results of the various interfacial crack geometries, an elastic finite element analysis using ABAQUS (Hibbitt, Karlson, and Sorenson, Inc.) was carried out. The results are summarized in Table I for the specimens involving only a single interfacial crack and Table II for the specimens involving dual interfacial cracks. For these finite element calculations, the elastic modulus and Poisson's ratio of the glass were taken to be 70 GPa and 0.3, respectively, and the corresponding values for epoxy were 2.8 GPa and 0.3. The 4-point flexure dimensions were an inner span of 22.23 mm and outer span of 31.75 mm. The glass dimensions were 40 x 8 x 1 mm and the thickness of the epoxy adhesive was 40 μ m. The applied load for all cases was $P = 2$ N. The characteristic length used to calculate the phase angle Ψ was taken to be equal to the thickness of the adhesive layer, 40 μ m.

For the cases involving a single interfacial crack, Table I, all the finite element results were independent of crack size from $a = 1.0$ to 4.75 mm and were independent of thickness of the adhesive layer from 20 to 80 μ m. For specimen 1 the finite element results agree well with analytical results for a two-layered specimen given by [1,2]

$$G = \frac{(PL)^2}{8Eb} \left[\frac{1}{I_2} - \frac{1}{I_c} \right]$$

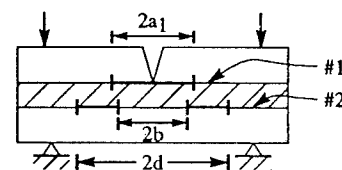
where L and b are defined in Fig. 1, E is elastic modulus of glass, I_2 and I_c are the moments of inertia of the lower glass plate and composite specimen, respectively. Specimen 2 shows that the presence of an adhesive layer has a negligible effect on G but decreases Ψ by 11°, in agreement with the asymptotic limit prediction of Suo and Hutchinson's analysis [3]. Comparison of specimens 2 and 3 shows that for the same applied load, G is reduced about 45% for an interfacial crack solely on interface #2 and the phase angle is reduced by 57%. Thus, the presence of the unbroken polymer ligament limits the energy release rate and decreases the crack tip shear stress that tends to drive the crack out of the interface. These factors

have opposing effects on the growth of a crack on interface #2.

Table I. Finite element analysis results of single crack geometries.

Specimen	G (J/m ²)	Ψ
1	1.53	41°
2	1.55	30°
3	0.83	13°

Table II. Finite element analysis results for dual crack geometries.



$a_1 = 2$ mm and $d = 4.75$ mm

b (mm)	G_1	G_{2I} (J/m ²)	G_{2O}	Ψ_1	Ψ_{2I}	Ψ_{2O}	
0.00	0.10	-	1.50	70°	-	54°	Overlap
0.75	0.14	0.06	1.41	70°	-70°	54°	
1.43	0.47	0.32	1.35	70°	-70°	54°	
2.26	2.54	0.98	0.04	43°	-74°	-76°	No Overlap
2.61	1.79	0.18	0.01	33°	-70°	-76°	
3.25	1.57	0.02	0.00	30°	-70°	-70°	
4.75	1.55	0.00	0.00	30°	-	-	

The decrease in G decreases the crack driving force but the decrease in ψ indicates a more opening mode stress at the crack tip that would tend to promote crack growth especially under subcritical crack growth.

For specimens with cracks on both interfaces of the laminated specimen (Table II), several important observations can be made relative to the dual crack observations discussed above. For no overlap of the two cracks, G for the crack on interface #2 is considerably less than that for the crack on interface #1 (G_1) and the ψ for the crack on interface #2 indicates the presence of considerable shear at the crack tips. Both of these effects would suggest that the crack on interface #1 would grow, leading to an overlap with the crack on interface #2. Then with overlap between the cracks on interface #1 and #2, G for the crack on interface #1 is now considerably less than the G for the outer crack tip on interface #2 (G_{20}) and ψ is greater. For the inner crack tip G_{21} is much less than G_{20} and ψ_{21} indicates considerable shear at this crack tip. Thus, these finite element results correctly predict the dual crack growth experimental observations discussed above. First, when cracks form on both interfaces #1 and #2, they always form with some degree of overlap. Second, the cracks on interface #2 do not grow toward the center of the specimen but instead only the outer crack tip grows outward. Thirdly, crack growth on interface #1 is arrested once the crack on interface #2 becomes fully developed. Finally, additional finite element results show that for a fixed overlap (10 times the thickness) G_{20} is relatively constant at a value of about 10% less than that given by Eq. (1).

Figure 3 compares moisture-assisted crack growth rates for crack growth solely along either interface #1 of #2 (specimens 2 and 3 in Table I) to that for a crack growing on interface #2 in the presence of a crack on interface #1 (specimen in Table II). This data was taken from different sets of samples made over several months. The applied G for crack growth solely on interface #1 was calculated from Eq. (1) and that for crack growth solely on interface #2 was reduced by 45% of the value given by Eq. (1) in accordance with the finite element results in Table I. For crack growth on interface #2 with a crack on interface #1, G was taken to be 10% less than the value given by Eq. (1). The relatively large amount of experimental scatter in Fig. 3 is thought to be due to the intrinsic nature of interfacial crack growth and batch to batch variability. Nevertheless, it is clear that within experimental scatter that the crack growth rates

for these specimens are similar for the different crack geometries. This agreement indicates that the primary driving force for moisture-assisted crack growth at the epoxy/glass interface is the applied G at the crack tip and that the phase angle difference between 13° and 54° has a negligible effect on crack growth. This latter result is in agreement with those of Liechti and Chai [4] who measured no significant effect of phase angles from 0° to 70° on fracture toughness (G_c) of an epoxy/glass interface.

ACKNOWLEDGMENT

This research was supported by NSF Grant DMR-9301761.

REFERENCES

1. K. M. Conley, J. E. Ritter and T. J. Lardner, J. Mater. Res., 2, 2621 (1992).
2. J. E. Ritter and K. M. Conley, J. Adhesion and Adhesives, 12, 245 (1992).
3. Z. Suo and J. W. Hutchinson, Mater. Sci. & Eng., A107, 135 (1989).
4. K. M. and Y. S. Chai, ASME J. Appl. Mech. 58, 680 (1991).

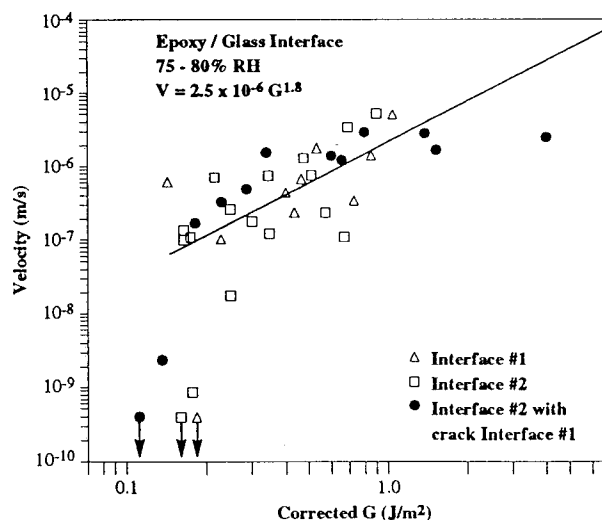


Figure 3. Comparison of crack growth rates in an epoxy/glass system.

RATE DEPENDENT INTERFACIAL AND COHESIVE FRACTURES IN CONVENTIONAL DOUBLE CANTILEVER BEAM SPECIMENS

M. D. Rakestraw, M. W. Taylor, Y. H. Lai, T. Chang and D. A. Dillard

*Center for Adhesion and Sealant Science, Virginia Polytechnic Institute and State University
Blacksburg, VA 24061-0219*

INTRODUCTION

Since most adhesives are viscoelastic polymers, their performance characteristics can be sensitive to both temperature and loading rate. For example, when testing adhesives below the glass transition temperature, lower fracture energies are usually obtained when using lower temperatures and higher testing rates. This paper will focus on investigating this rate effect for model epoxy adhesive bonds. Time dependent fracture observations and data will be used to propose a model for rate sensitive fracture. In order to report these results, an appropriate means for determining the effective loading rate for standard double cantilever beam (DCB) fracture specimens will also be discussed. The model will be shown to be useful in predicting the maximum value of strain energy release rate in double cantilever beam specimens loaded at a constant crosshead rate. Finally, this technique will also be shown to be capable of predicting changes in failure locus from adhesive to cohesive behavior.

MATERIALS

Five model epoxy systems with various amounts of rubber-toughener were used as the adhesives for this study. The model epoxy systems were composed of a liquid bisphenol A-type resin, a curing agent, a curing accelerator, a filler, and an epoxy-terminated toughener. The epoxy resin used was D.E.R. 331^{®1}. This is a "standard" low molecular weight liquid bisphenol A-type resin available from The Dow Chemical Company. The curing agent used was dicyandiamide which is often referred to as "dicy". Dicy is a latent, solid curing agent, which, when milled into liquid epoxy resins, provides one-package stability for up to six months at ambient temperatures. Curing occurs with heating. A tertiary amine accelerator is necessary if rapid cures are desired for dicy/epoxy systems. Therefore, 3-phenyl-1,1 dimethyl urea, or PDMU, was used to reduce cure times.

The use of 2-3 parts per hundred reduces the curing temperatures of such systems from 177°C to about 121°C. Simultaneously, the curing time is reduced. Finally, a filler was used to suspend the dicy evenly throughout the adhesive, thus producing a more homogeneous final product. The filler used was M-5 SILICA which is a slightly acidic, hydrophilic fumed silica produced by the Cabot Corporation. It has a surface area of 200 (± 25) m²/g, a density of 0.0812 g/cm³, and a particle diameter of about 0.014 microns. The toughener used was Kelpoxy G272-100, a concentrate of an epoxy-terminated elastomeric copolymer designed by Reichhold Chemicals as an additive or modifier to toughen epoxies, epoxy novalacs, and PVC plastisols. Epoxy resin blends containing Kelpoxy exhibit elastomer particles of .01-10 micron diameter which impede the propagation of cracks. The epoxide equivalent weight is approximately 340 g/cq.

EXPERIMENTAL RESULTS

Figure 1 shows some typical results for a double cantilever beam (DCB) specimen. A constant crosshead rate was imposed until debonding initiated and the load began to drop. The crosshead was then stopped, and the debond allowed to propagate under fixed displacement conditions. As the debond equilibrated, the load was removed in order to check for linearity. The specimen was then reloaded at the original crosshead rate. This process was repeated until debonding approached the end of the beam. These simple tests revealed a number of peculiar fracture trends. For example, although the initiation and arrest strain energy release rates (SERR's) remained relatively constant, the maximum attainable SERR's consistently decreased as the crack lengths increased. Also, if the crosshead displacement rate was sufficiently increased, then the mode of failure would make a transition from interfacial failure to cohesive fracture within the adhesive layer. By using several different "adhesive systems" and testing rates, it was possible to make some correlation between the rate of testing and the failure characteristics of the joint being tested. It was found that, although the "global"

¹D.E.R. is a registered trademark of The Dow Chemical Company

crosshead displacement rate (or loading rate) which is used to control a test may be kept constant, the DCB specimen's *crack tip loading rate* can vary by more than an order of magnitude as the specimen debonds, and significantly affect the results of the tests.

ASTM D 3433 [1] seeks to eliminate this dependence on crosshead rate and debond length by adjusting the crosshead rate in a prescribed manner. Rather than taking this approach, we sought to try to utilize the data obtained to develop a model for the time dependent processes which occur.

RATE-DEPENDENT MODEL

Time dependent crack growth has been approached in a variety of ways. A great deal of experimental results have been presented in terms of the rate of crack growth [2]. For example, Fig. 2 shows typical da/dt vs. G data plotted on log scales. This data represents information collected during the time dependent crack growth while the crosshead is being held fixed. Unfortunately, data plotted from successive load cycles on the same specimen show considerable variation. Although da/dt is convenient for several reasons, it also has other disadvantages as well. For example, while the load is being increased and the crack remains stationary, da/dt is zero, and cannot be used to quantify the rate at which the crack is being loaded. In an effort to avoid some of these problems, an alternative approach was sought. The time rate of change of the stress intensity factor has been used to characterize crack tip loading rates for monolithic materials [3]. For bonded joints, the SERR is more appropriate, so we have proposed that the time rate of change of the SERR be used to characterize the response of adhesive bonds. One initial advantage seems to be more consistent results between the loading cycles, as shown in Fig. 3.

The model based on dG/dt was formulated around a displacement control scenario, and recognizes that the rate of change of G is based on two components: 1) the external loading (crosshead displacement rate), and 2) the reduction in SERR as the crack propagates. The first term may be easily calculated by analyzing the test geometry and knowing the applied force (or displacement) and the crack length. The second term represents the "natural" failure process in the adhesive bond. For slow crack growth in our specimens, this process was always what appeared (to the eye) to be an interfacial failure. Based on the data in Fig. 3 the "natural" SERR unloading rate was proposed to be

$$\frac{dG}{dt} = -AG^z$$

Using this form, one may predict how the maximum SERR will decrease with increasing debond length for constant crosshead testing, as shown in Fig. 4. Here a single loading cycle from Fig. 1 was used to obtain A and z for the adhesive bond system. This information was then used to predict the maximum observable SERR for several different crosshead rates. Finally, the maximum SERR from Fig. 1 were plotted as points to show the excellent agreement which was obtained.

Further considerations have also led to the development of a mode transition envelope which predicts when the mode of failure will switch between adhesive and cohesive behavior. Depending on the amount of rubber toughener in the adhesive, different A and z values were obtained. Further characterization of the adhesive at higher displacement rates has allowed us to superimpose adhesive and cohesive behavior in order to predict mode conversion, as shown in Fig. 5.

The proposed model does appear to be useful in characterizing the time dependent debond growth characteristics of model epoxy systems in laboratory environments. The A and z parameters were found to be dependent on the amount of rubber toughener, suggesting that these parameters may be useful in comparing various adhesive bond systems. Several advantages to the model exist, although the usefulness of the model for long term characterization is not clear. Further work is needed to better understand the potential of this approach.

SUMMARY AND CONCLUSIONS

Variations in measured values of maximum strain energy release rates for a uniform double cantilever beam with crack length under constant crosshead loading conditions suggest rate dependent fracture processes at the interface of epoxy/steel bonds. An empirical model based on the time rate of change of the strain energy release rate was proposed to predict such behavior. Initial comparisons with experimental data seem promising, although further study is needed. By incorporating a adhesive / cohesive failure transition envelope with the model, estimates are obtained for what combination of loading rate and crack length will result in changes in failure mode.

ACKNOWLEDGMENTS

The authors would like to acknowledge The Dow Chemical Company, the Adhesive and Sealant Council, and the Virginia Institute for Material Systems for financial support of this work. We also appreciate the support of the Center for Adhesive and Sealant Science

and the National Science Foundation Science and Technology Center: High Performance Polymeric Adhesives and Composites, contract DMR 9120004.

REFERENCES

1. A A Khalil and M R Bayoumi, *Eng. Frac. Mech.*, **39**, 1037, (1991).
2. D. Maugis, *J. Mater. Sci.*, **20**, 3041, (1985).
3. *Annual Book of ASTM Standards*, Vol. 15.06 Adhesives, ASTM, Philadelphia, (1994).

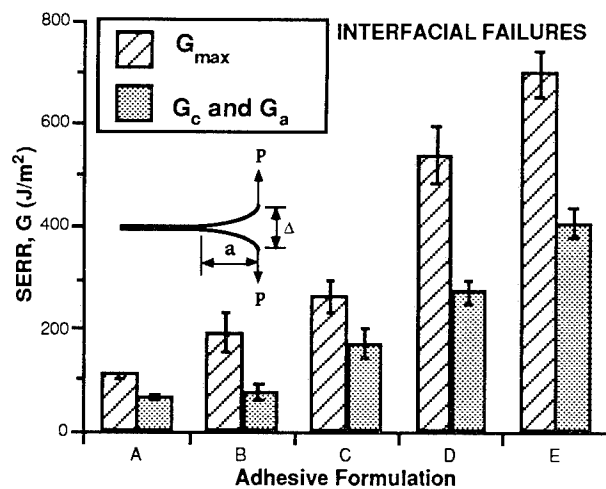


Fig. 1: Quasi-static DCB results (1mm/min testing speed).

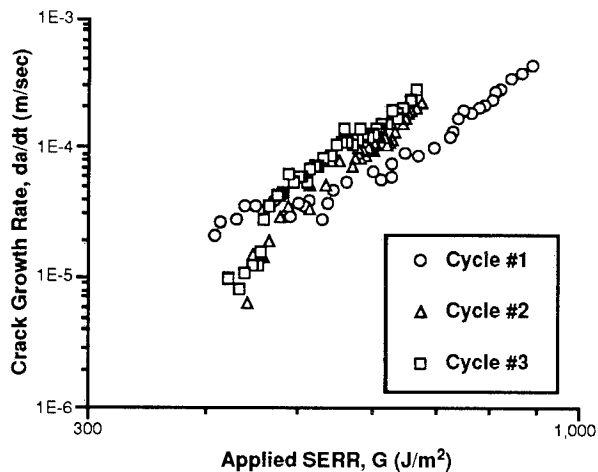


Fig. 2: Crack growth rate as a function of crack tip loading level while the crosshead was held constant (Adhesive E).

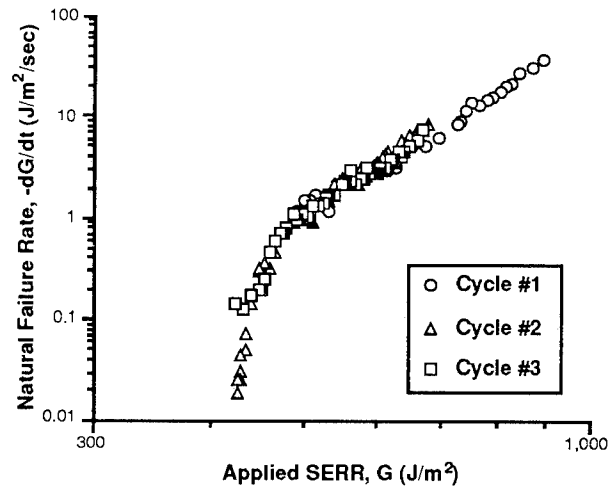


Fig. 3: Crack tip unloading rate due to crack growth, $\left. \frac{dG}{dt} \right|_a$, as a function of crack tip loading level (Adhesive E). Data corresponds to that of Fig. 2.

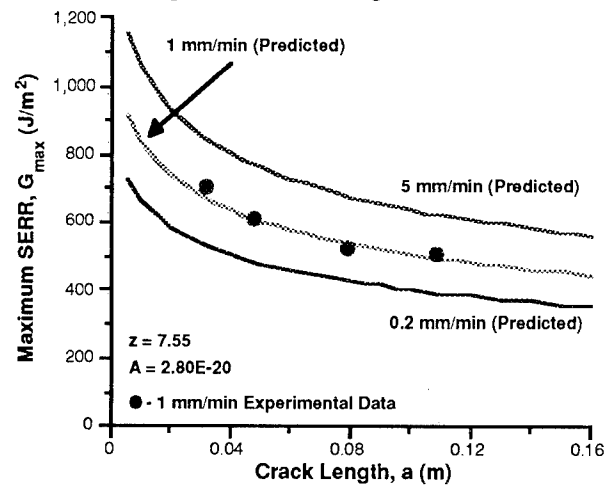


Fig. 4: Predicted and experimental maximum strain energy release rate values as

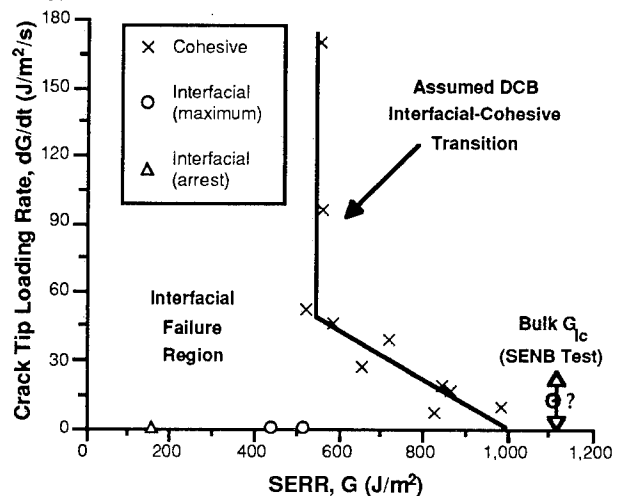


Fig. 5: Fracture energies as a function of crack tip loading rate (Adhesive C).

STUDY OF EFFECT OF THICKNESS ON MECHANICAL PROPERTIES OF ADHESIVE MATERIAL BY SIEM

Y.Y. Wang, Q. Wang and F.P. Chiang

Department of Mechanical Engineering
State University of New York at Stony Brook
Stony Brook, NY 11794-2300

INTRODUCTION

The extreme and often contradictory demands on the materials in use today has made joining of dissimilar materials a necessary. The performance of a structure or a material is critically dependent on the behavior of any adhesive joints it contains. Although the chemical nature and mechanical performance of different adhesives have been extensively studied, there is still a lack of knowledge about the adhesive micro-mechanical properties. One of the issues is the thickness effect, on which several contradictory results have been published. While some report that the adhesive material has different mechanical properties when tested in a thin-film form and a bulk form [1], others obtain good agreement between thin-film and bulk properties [2]. One of the reasons for these conflicting conclusions is due to the inaccuracies of the experimental techniques. The test on an adhesive material in its thin-film form is difficult, especially when the bond line is only a few micron thick. In this study, a technique so called SIEM (Speckle Interferometry with Electron Microscopy) is applied to measuring the displacement field of the adhesive layer at a micron level. Elastic moduli of the adhesive material in thin-film form are to be determined.

EXPERIMENTAL TECHNIQUE AND PROCEDURE

Three joints with different thicknesses of the adhesive layer are made first and then six specimens, one normal and one oblique, are cut from three joints as it is shown in Fig.1. The materials of the adhesive and the adherend are so selected that the ratio of the nominal Young's moduli of the adherend and the adhesive is about 14, and the Poisson's ratios are 0.36 and 0.42 respectively. The thickness of the specimen is about 2.50 mm. Since the measurement is on the surface of the specimen, we simply take the assumption of plane-stress although the stress state in the adhesive layer is more suitable to plane-strain problem. The surface of the specimen is finely polished and suitable particles are deposited on the surface to generate speckles. Fig.2 is the speckle pattern of a specimen.

Speckle Interferometry with Electron Microscopy (SIEM) [3] combines the speckle interferometry, electron microscope and digital image processing techniques. It can precisely measure a whole field displacement at a micro-scale level. The specimen is loaded inside the vacuum chamber of a scanning electron microscope by a spatial loading frame. The force is measured by a load transducer. A sequence of images in the same area are recorded and digitized during the test until the specimen

is broken. The digitized image consists of 512×512 pixels with gray value from 0 to 255. Each image is first segmented into 32 subimages and then the average displacement of each subimage is calculated by Computer Aided Speckle Interferometry [4].

STRESSES IN BUTT AND SCARF JOINTS

The stress analysis of an axially loaded butt joint has been analyzed [5-7]. For a plane-stress analysis [5], the horizontal stress parallel to the bond plane is not reported. The horizontal stress is discussed in a plane strain analysis [6,7]. This horizontal stress is significant in the adhesive layer if the difference of the Poisson's ratios of the adhesive and the adherend is large. By following Parks' [6] procedure, the horizontal stress σ_h in the adhesive layer is obtained as,

$$\frac{\sigma_h}{\sigma_o} = \frac{E_a}{E_s} \cdot \frac{E_s \nu_a - E_a \nu_s}{E_s - E_a}, \quad (1)$$

where, σ_o is the nominal stress that equals to the load divided by the section area, E and ν are tensile moduli and Poisson's ratio, and the subscripts s and a denote the substrate and the adhesive respectively. This analysis is based on assumptions that σ_h is only caused by the unequal Poisson's effect of the adhesive and the adherend, it is uniformly distributed over the whole of both interfaces, the shear stresses that exist near the free edge of the joint are ignored, and both materials of the adhesive and the adherend are isotropic. As the horizontal stress and the nominal stress are so defined, the normal strains in the center area of a butt joint are,

$$\epsilon_{22,a} = \frac{\sigma_o}{E_a} \cdot \left[1 - \nu_a \frac{E_s \nu_a - E_a \nu_s}{E_s - E_a} \right], \quad (2)$$

$$\epsilon_{11,a} = \frac{\sigma_o}{E_a} \cdot \left[\frac{E_s \nu_a - E_a \nu_s}{E_s - E_a} - \nu_a \right], \quad (3)$$

in which, 2 is in the load direction and 1 is in the transverse direction (see Fig.1).

Stress distribution in a plane scarf joint has been given by Chen [5]. It is claimed that the stresses distribute uniformly in a scarf joint when the scarf angle α is,

$$\alpha = \tan^{-1} \sqrt{\frac{E_s \nu_a - E_a \nu_s}{E_s - E_a}}. \quad (4)$$

The scarf angle of the studied specimen is so selected according to eq.(4).

RESULTS AND DISCUSSIONS

Fig.3 shows displacement contours of a butt joint and a scarf joint. Since the adhesive is softer than the adherend, naturally most contour lines lie in the adhesive layer. The displacement of the butt joint along the loading direction is not uniformly distributed in the adhesive layer. The gradient of the displacement (Fig.3 (b)) near the interfaces is higher than at the center of the adhesive layer and elsewhere. There exists a region of high strain concentration between the adhesive and the adherend, which is due to the three dimensional stress state at interfaces. The u-field on Fig.3(a) is abnormal. The displacement contour is parallel to the bond line instead of perpendicular to it as expected from theoretical consideration. The proper explanation could be the imperfect alignment of specimen. It may infer that the direction of the principal stress at adhesive is extremely sensitive to the specimen configuration and loading geometry. The residual stress in the adhesive layer may also contribute to this phenomenon. Fig.3(d) shows the v-field of a scarf joint. Obviously in the area far from the adhesive only normal strain exists because contour lines orient along x direction. But in the adhesive very large shear strain appears, which is also found on u-field from Fig.3(c). This is again contrary to the theoretical prediction. Since there is no contour line in loading direction on u-field, the Poisson shrinkage of adherend is very small compared with the shear deformation. The nominal strain obtained from v-field displacement is plotted against nominal stress in Fig.4. The Young's modulus of the adherend is about the same as calibrated from another test. The modulus of the adhesive is higher than the value provided by manufacturer. The nominal strain of the adhesive is the average strain calculated from the displacement between two interfaces and uniaxial stress state is presumed. The strain in the center of adhesive is different, which is clearly displayed on Fig.5.

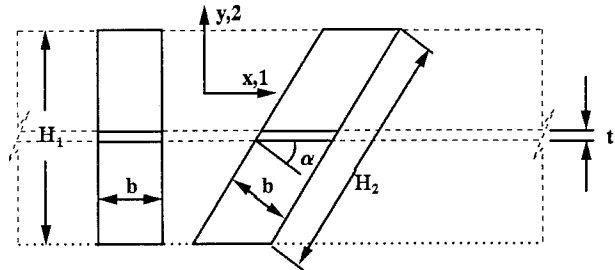
Unlike the standard optical methods, the SIEM utilizes the digital signal processing technique which accuracy depends on the sampling rate. From all the displacement plots of different specimen under different loads, it is found that contour lines are smooth and consist with each other. The experimental results is reliable. Moire interferometry is employed to verify the results from the joint with thick bond layer and SIEM is used to test the joint with a bond layer of several microns.

ACKNOWLEDGEMENT

The sponsorship of AFOSR, No.F496209310218 and ONR, No.N0001491J1380 is greatly acknowledged by authors.

REFERENCES

1. D. Peretz, J. Adhesion, 9, p.115, (1978).
2. L. Lileheden, Int. J. adhesion and Adhesive, 14, p.31, (1994).
3. Q. WANG, and F.P. Chiang, Proceedings of the American Society for Composites 9th Technical Conference, p.948, (1994).
4. D.J. Chen and F.P. Chiang, Applied Optics, p.1839, (1993).
5. D. Chen, and S. Cheng, J. Applied Mechanics, 57, p.79, (1990).
6. V.J. Parks, Experimental Mechanics, , p.77, (1988).
7. A.J. Kinloch, J. Material Science, 17, p.617, (1982).



	H ₁	H ₂	b	t
Joint 1	33.5	38.6	6.35	0.006
Joint 2	33.5	38.6	6.35	0.050
Joint 3	33.5	38.6	6.35	0.370

Fig.1 Specimen geometry. The dimension in the figure is in mm.

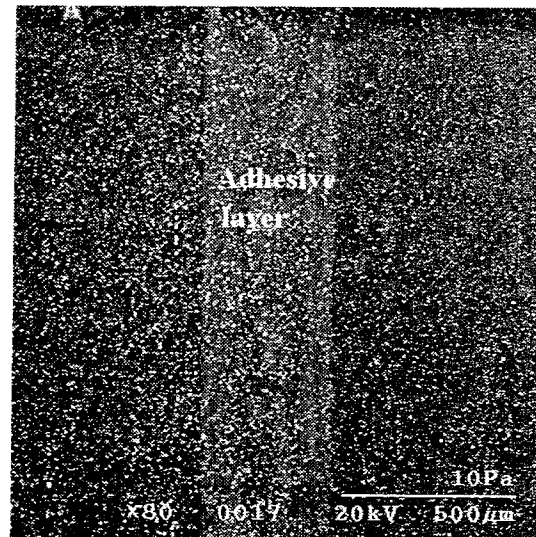


Fig.2 Speckle pattern of a specimen.

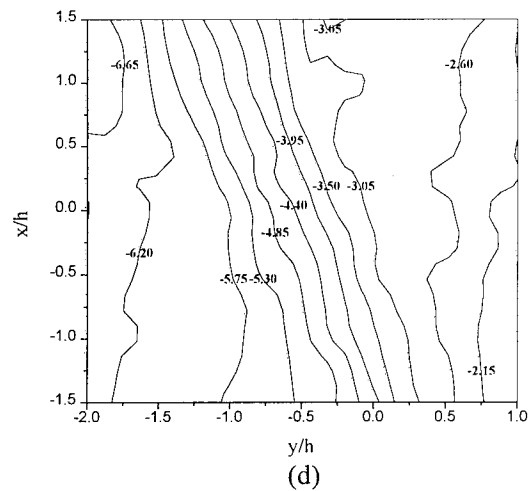
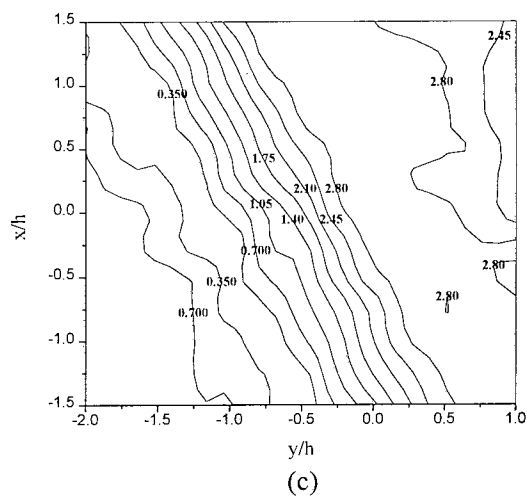
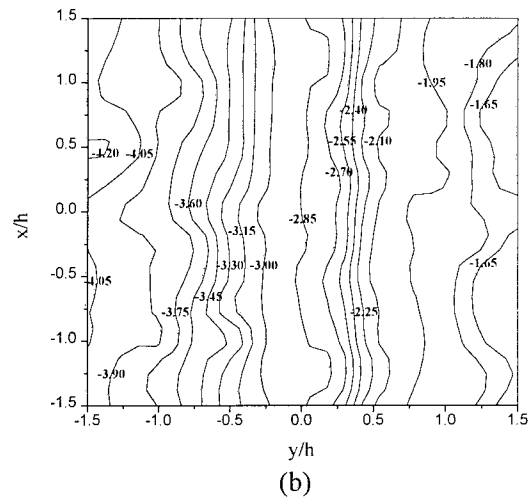
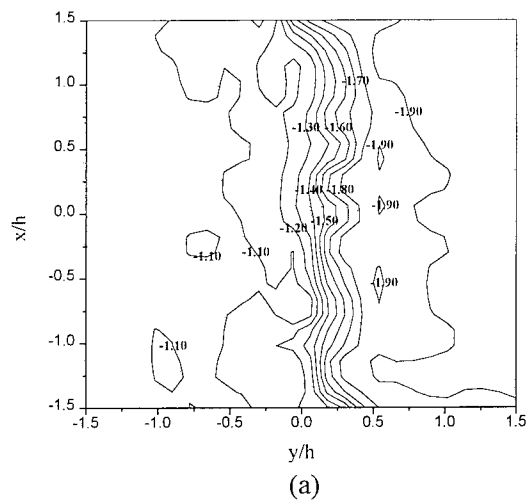


Fig.3 Displacement contours of a butt joint and scarf joint. (a) U-field of butt joint, (b) v-field of butt joint, (c) u-field of scarf joint and (d) v-field of scarf joint.

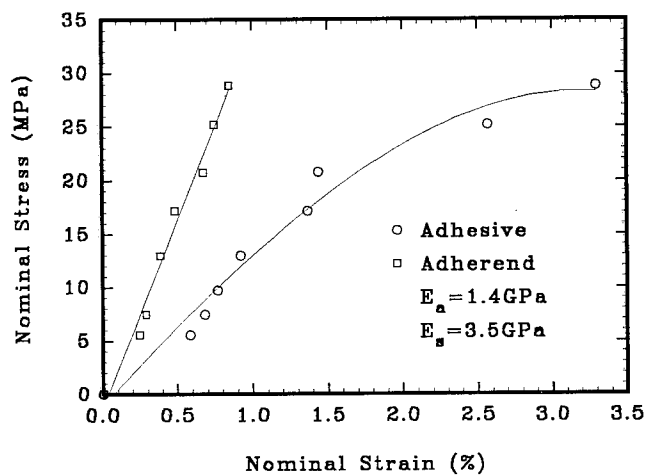


Fig.4 Nominal stress-strain relation of a butt joint.

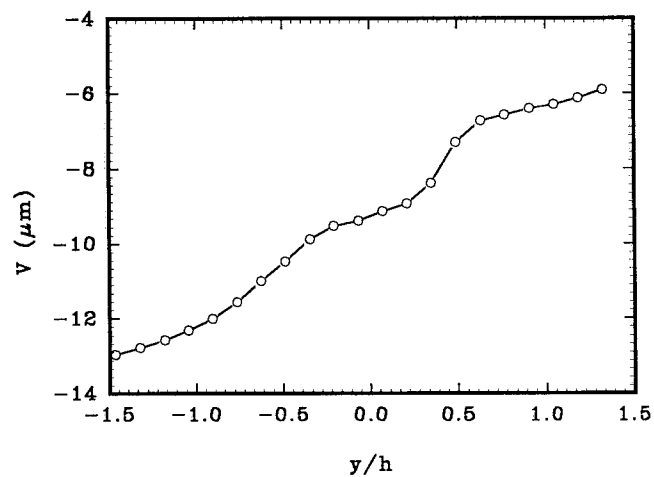


Fig.5 Displacement in y direction across the adhesive layer.

TOPOGRAPHY AND CAPILLARY BONDING OF WET POLYETHYLENE SURFACES

S.C. Colbeck,

U.S. Army Cold Regions Research and Engineering Center, Hanover, NH

J.B. Rossacci, E.M. Shipulski, C.A. Brown,

Mechanical Engineering Department, Worcester Polytechnic Institute, Worcester, MA

INTRODUCTION

The objective of this work is to improve the understanding of the mechanism of interaction of topography with capillary bonding. We would like to know how to measure and characterize the topography of a surface to predict the capillary bonding, and to design topographies to control the capillary bonding. The ability to acquire and manipulate large topographic data sets has advanced significantly in recent years. Topographic characterization methods can be developed in consideration of the mechanism of interaction on a fundamental scale. The reliance on statistical approximations of topographic features can be reduced. However, the scales of the data acquisition and analysis need to be considered in the characterization of the topographic data (Brown et al. 1993).

There has long been an interest in wetting and capillary bonding of surfaces which comes from areas such as waterproofing, friction on snow and disk-slider stiction in magnetic media. The smoothest ski bases are not the fastest; similarly the sliders on the smoothest magnetic media disks can have the greatest stiction. The character of the roughness, as well as the magnitude, appears to be critical in both cases. The roughness of the surface influences the wetting angle (Dettre and Johnson 1964), yet the commonly used Ra (arithmetic average) alone is not sufficient to predict the contact angle of water on rough surfaces, even when the surfaces have been prepared by similar processes.

In this work a theory is examined which has been proposed to describe the adhesion of a grooved polyethylene surface to ice (Colbeck 1994). In this theory the ice is assumed to be completely wet and flat with a contact angle of 0° , and the adhesive force is determined mainly by the product of the water tension and the wetted area on the polyethylene. When the tension in the water exceeds a critical level, the area of contact varies with the tension. The critical level of the water tension and the nature of the variation of the area of contact depend on the roughness of the polyethylene. An experimental apparatus which allows the adhesive force to be measured as a function of the level of tension in the water is presented. The results of measurements are discussed and further experimentation and roughness characterization are proposed.

METHODS

The experimental apparatus shown in Fig. 1 is used to measure the force necessary to rupture the capillary bond (F) as a function of the bulk water tension level (T). The porous ceramic serves to transfer the bulk water tension to the wetted contact surface with the polyethylene. The porous ceramic has a relatively smooth surface that is completely wet. In the procedure the polyethylene is placed on the wet ceramic surface and the bulk water tension level is adjusted for that test. The bulk water tension level is the bulk pressure in the water below atmospheric pressure. The vertical load on the polyethylene is increased in small increments, allowing the time for the water tension to equalize through the porous ceramic after each incremental increase, until the polyethylene separates from the porous ceramic. The bond force is the force at the final increment. The fractional area (A_f) is determined by comparing the bond force and bulk water tension level with the projected area of the polyethylene (A_p):

$$A_f = F / (T A_p) \quad (1)$$

Equation (1) counts only the contribution of the bulk tension in the water to the bond force and ignores the contribution of the surface energy, or tension, between the liquid and the air in the meniscus between the polyethylene and the porous ceramic. It can be shown that, at conditions of complete wetting, the contribution of the surface tension to the bond force is relatively small, approximately 5% of the total force. This is about the same as the resolution of the force-measuring device used in these experiments.

RESULTS AND DISCUSSION

Over repeated tests at different bulk tensions the bond force increases with an increase in the water tension level to a maximum then decreases with further increases in bulk tension. Since the bond force is assumed to be the product of the wetted area and the bulk tension, decreases in bond force with increases in bulk tension indicate that the wetted area is decreasing. Calculating the fractional area according to equation (1) the fractional area is plotted versus the bulk water tension level in mm of water in Fig. 2. At the highest bulk tensions Fig. 2 shows that the apparent fractional areas tend to increase with subsequent measurements.

A simple theory has been developed to explain, based on the roughness of the polyethylene, the decrease

in wetting with increasing bulk tension below the maximum bond force (Colbeck 1994). The theory assumes that the topography of the polyethylene is composed of a series of long v-shaped grooves. The water will wet the side of a groove to a depth which depends on the water-polyethylene contact angle, the angle of the groove and the bulk tension in the water. The deeper that the grooves are wet, the greater the fractional area. There is a distribution in the depth and angle of the grooves, so that each groove, according to its geometry, can have a different critical tension for dewetting. The distribution of the groove geometries indicates that there should be a gradual decrease in the overall wetted area as the bulk tension in the water is increased. The wetted area and thereby the bond force should decrease gradually as the bulk tension is increased, as shown in Fig. 2. Based on the measurements made by the apparatus in Fig. 1 the measured force can be used to surmise the distribution of the groove geometries which contribute to the dewetting. This theory is not developed to explain the increase in fractional area with subsequent measurements, nor can it be used to predict the capillary bonding behavior based on a knowledge of the topography.

Fig. 3 shows how the relative areas of ground polyethylene can increase as the scale of measurement decreases (Brown et al. 1993). The relative areas are the measured areas, which depend on scale and take into account the topography, divided by projected area. Although the laser sensor (Cyberscan), which acquired the topographic data on which Fig. 3 is based, cannot detect topographic features smaller than about $300\mu\text{m}^2$, it is evident from the slope of the plot at the finest scales that significant topographic detail continues to finer scales. At the largest scales, above approximately 0.01mm^2 , the surface appears smooth, since the relative areas are close to one. At these scales the slope of the surface is zero. For the relative areas to increase at finer scales, the slopes of finer scale facets, or v-grooves, on the surface must also increase.

The tendency of the first tests shown in Fig. 2 can be interpreted in using the description of the topography shown in Fig. 3. At the smallest tensions, where the fractional area is close to one, the capillary bonding sees the polyethylene surface as smooth. At higher tensions the capillary becomes more sensitive to the fine scale topographic details and the greater slopes of these details. This may be the same as saying that the smaller grooves must have steeper angles than the larger. The surface can be seen as a collection of smaller grooves on larger grooves, i.e., it has a fractal character, over some range of scales below 0.003mm^2 .

There are two interpretations we propose for the greater fractional areas, at a given bulk tension, calculated from the subsequent tests in Fig. 2. One, the contact angle between the water and the polyethylene decreases with time. This could be a purely chemical effect. Two, the finest grooves on the surface were not wet for the first series of tests, only with time did the water penetrate into the finest grooves. This incomplete wetting might also be interpreted as a topographical component of the time-dependent wetting, thereby contributing to the first interpretation, above.

Further work is required to advance the understanding of the topographic dependence of capillary adhesion. Based on a model suggested by the above theory, we propose to simulate wetting of surfaces, and the resulting bond forces as a function of bulk tension, using actual topographic data acquired by scanning microscopy. Experimental curves, similar to Fig. 2, would be compared with those resulting from the simulation for a wide variety of topographies. This further work would help determine the critical scales and topographic feature types for capillary bonding.

REFERENCES

- C.A. Brown, P.D. Charles, W.A. Johnsen, S. Chesters, *WEAR*, 161 (1993) 61-67.
- S.C. Colbeck submitted for review (1994)
- R.H. Dettre, R.E. Johnson in "Contact Angle, Wettability and Adhesion," Am. Chem. Soc. Washington, D.C. (1964) 136.

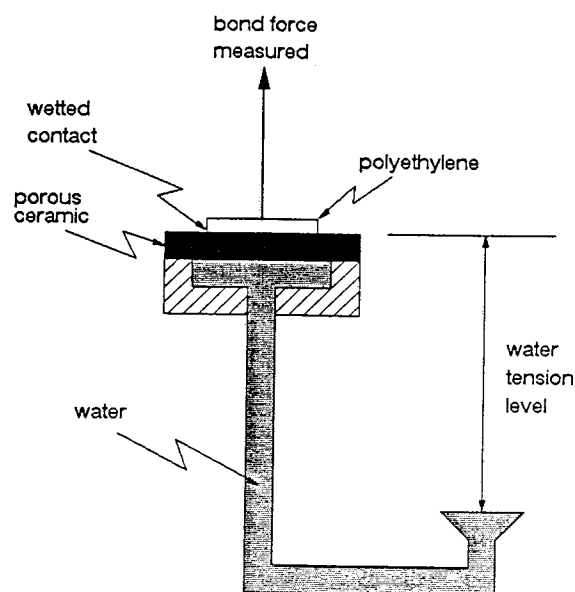


Fig. 1. Apparatus for measuring the capillary bond force between a polyethylene block and a wet, porous ceramic as a function of tension in the water.

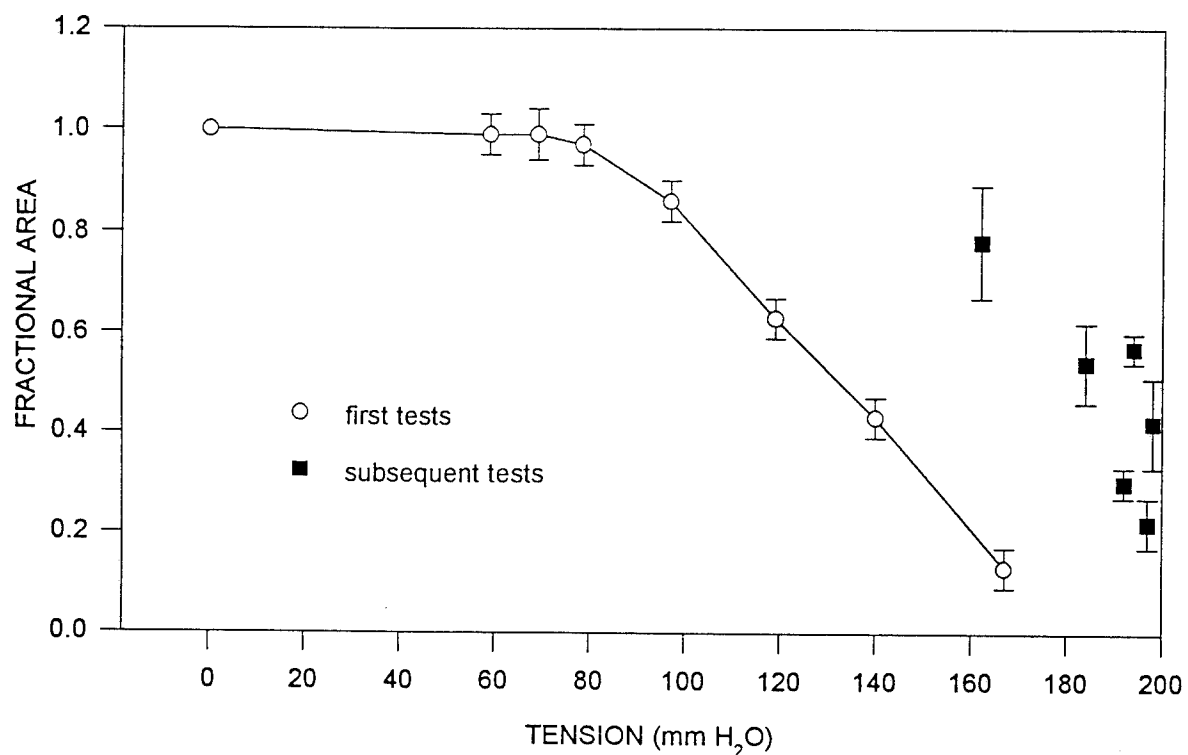


Fig. 2. The fractional area for wetting as a function of the bulk tension level in the water. The fractional area is calculated from the bond force, bulk tension and projected area, as shown in Eq. (1).

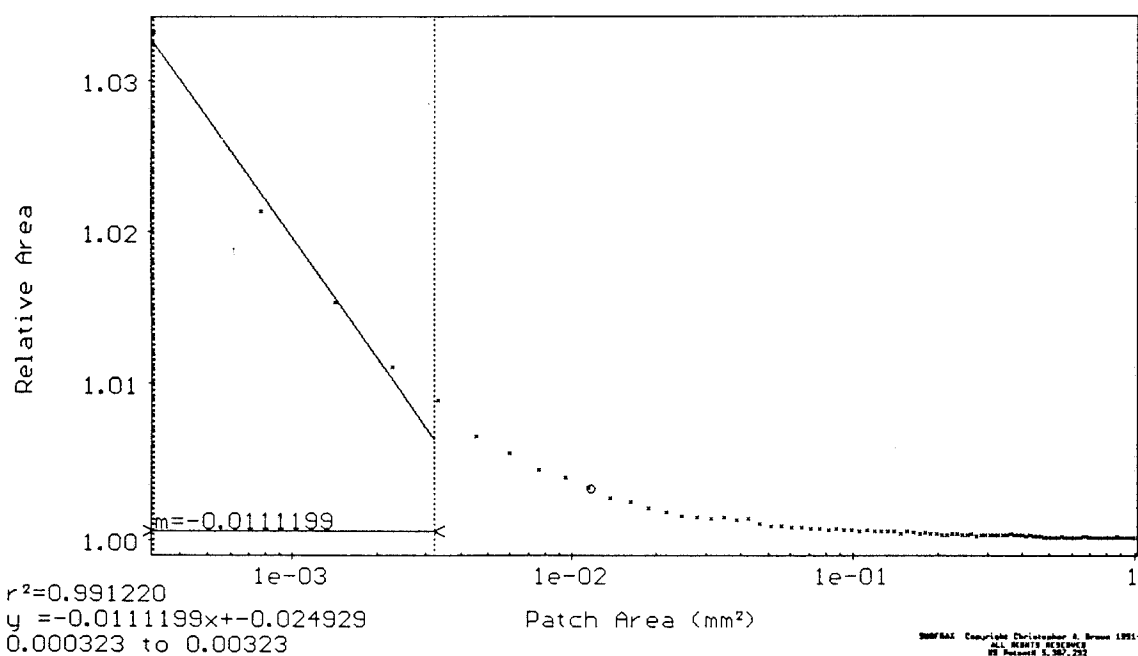


Fig. 3. Relative area as a function of patch area, or scale of measurement. The relative area is the measured area, which is determined by tiling the surface with triangular patches of a certain size, divided by the projected area (Brown et al. 1993). The surface is represented by topographic data, elevations on a regular grid, acquired by scanning laser profilometry.

Fracture of an Adhesive-Substrate Interface in Sandwich Specimens

J. G. Swadener and K. M. Liechti

Engineering Mechanics Research Laboratory
Department of Aerospace Engineering and Engineering Mechanics
University of Texas at Austin, Austin, Texas 78712-1085

INTRODUCTION

The common occurrence of interfacial fracture in composites, microelectronics devices and adhesively bonded joints motivates this experimental and numerical study of stationary and growing interfacial cracks. The thickness of an adhesive layer has been shown by Chai [1,2] to be a significant factor in the cohesive fracture toughness of adhesively bonded joints and has been shown by Tvergaard and Hutchinson [3] to affect interfacial toughness. A number of studies have determined that interfacial toughness is a function of fracture mode-mix. In this regard, Liechti and Chai [4,5] and Liang and Liechti [6] have considered the widest range of mode-mixes in bimaterial specimens. In reporting interfacial toughness, several studies made use of more complex specimens where one of the materials was sandwiched between stiffer substrates [7,8]. However, the effect of the thickness of the constrained layer was not considered. This work determines NCOD for a glass/epoxy interface crack in glass/epoxy/aluminum sandwich specimens. Unusual asymptotic behavior is seen in these results. The results also indicate a weakening of the interfacial toughness with decreasing epoxy height.

EXPERIMENTAL PROCEDURE

For the specimens shown in Fig. 1, the epoxy height, h_2 , ranges from 0.130 to 0.355 mm. The specimens are pre-cracked along the glass/epoxy interface. Displacements (u, v) are applied to the specimen via steel grips in both the bond-tangential (x -) direction and the bond-normal (y -) direction in the same manner as described by Liechti and Chai [4]. Crack growth is maintained along the interface. NCOD are measured using crack opening interferometry [9].

Interference fringes produced by crack opening interferometry are recorded using a video camera for later analysis. This allows collection of data for stationary cracks during application of ramped displacements and for slowly growing cracks under appropriate fixed displacements. One such recorded image is shown in Fig. 2. Spatial resolution of the video cassette recorder is 5 μm at the magnification used (200X). A digital image analyzer makes possible determination of NCOD to 1/100

of a fringe order which gives a resolution of 3 nm. However, uneven reflections from the aluminum adherend cause greater scatter in the results.

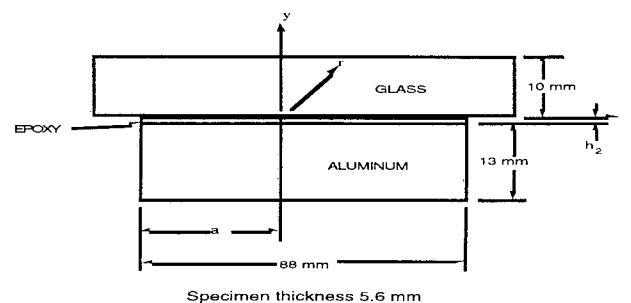


Fig. 1 Specimen Geometry

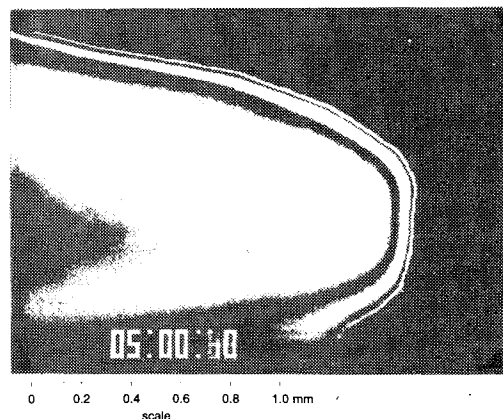


Fig. 2 Crack opening interferometry fringe pattern of a crack growing along a glass/epoxy interface

RESULTS, ANALYSIS AND DISCUSSION

As seen in Fig. 2, the crack front is curved. NCOD are determined for a line parallel to the x -axis through the center of the crack front. NCOD results for a stationary crack under bond-normal loading are plotted versus the distance from the crack tip, r , on a log-log scale in Fig. 3. The experimental results match the predictions in the far field region, $r > 300 \mu\text{m}$, but lie significantly below the predictions in the near field region, $r < 50 \mu\text{m}$. The differences are not due to plasticity (e.g. HRR fields) as plastic yielding would cause a deviation in the opposite direction [10,11]. Fig. 4

shows similar results for a growing crack with bond-tangential applied displacements in the direction which causes the crack to open near the crack front. The solid lines in these figures are finite element predictions for a straight crack front under the condition of plane strain.

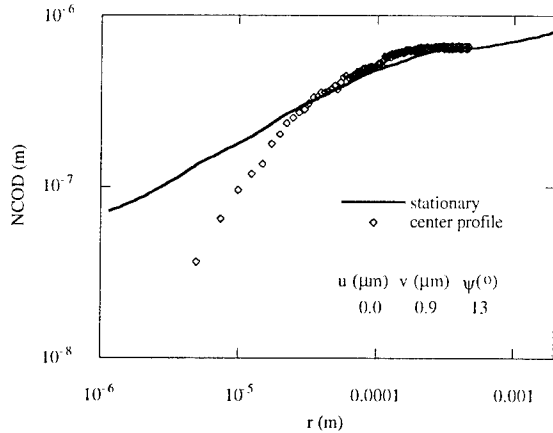


Fig. 3 Experimental and numerical NCOD results for a stationary crack

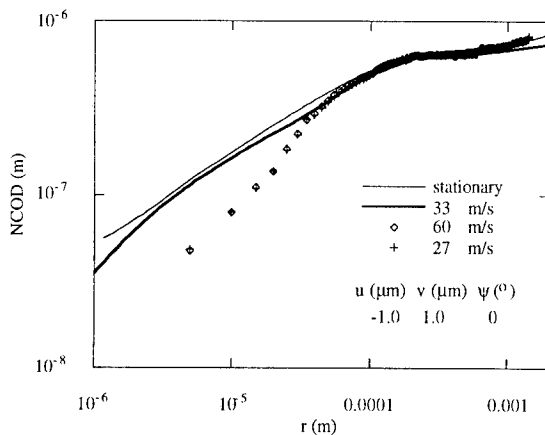


Fig. 4 NCOD for a growing crack with closing shear displacement

Finite element calculations are computed using ABAQUS finite element software [12]. Glass and aluminum are modeled as elastic materials. The extended Drucker-Prager plasticity model of ABAQUS with strain rate dependence is used for the epoxy. Material data come from compression and shear test results [13]. If the epoxy is modeled without strain rate dependence, the finite element calculations of the NCOD of a growing crack differ slightly from the from the stationary computations due to residual deformations in the plastic wake. However, including strain rate dependence increases the yield strength of the epoxy near the crack tip where strain rates are high. This greatly reduces the plastic deformation and hence also the residual deformation in the plastic wake. Thus the growing crack analysis agrees closely with the stationary crack analysis as shown in Fig. 4. The analysis with rate dependence also gives the extent of

plastically deforming epoxy, the plastic zone. For the applied displacements shown in Fig. 4, the plastic zone is found to extend from 2 μm behind the crack tip to 3 μm ahead of the crack tip and 4 μm perpendicular to the interface. The size of the plastic zone varies with load, but is within a factor of 2 for the loads studied. This agrees with the lack of any observation of plastic behavior even as close as 2.5 μm behind the crack tip. Quasi static analysis is justified for these cases because the crack speed is very slow compared to wave speeds in the epoxy.

The effect of crack front curvature was examined using a 3D finite element model. It was found that the NCOD results from the 3D analysis lay on or above the plane strain straight crack results. Thus, 3D effects do not account for the deviation of near field NCOD results.

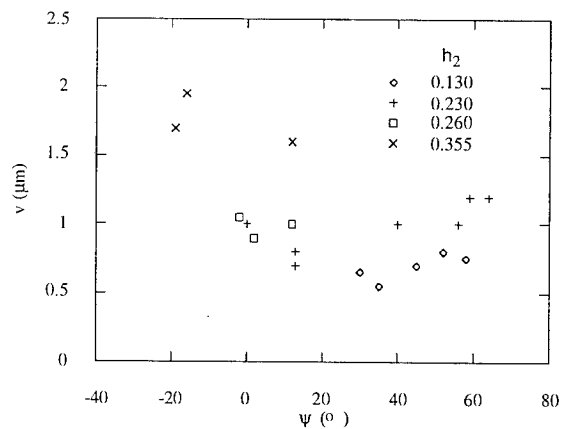


Fig. 5 Far field NCOD versus mixity

The applied bond-normal displacements, v , required to obtain steady crack growth are shown in Fig. 5 as a function of mixity ψ , where the angle ψ represents the mixture of Mode I (opening) and Mode II (shear) stress intensity factors, K_1 and K_2 respectively. The mixity ψ is given by:

$$\psi = \tan^{-1} \left(\frac{K_2}{K_1} \right) + \epsilon \ln \left(\frac{\hat{l}}{h_2} \right),$$

where ϵ is the bimaterial constant and \hat{l} is a length parameter chosen to be 100 μm . The applied displacements are seen to be a function of both h_2 and ψ . The dependence on h_2 occurs despite the fact that plastic zone sizes are small compared to the epoxy height. We define the displacement v_0 to be the applied bond-normal displacement with no bond-tangential displacements. If the applied bond-normal displacements are normalized by v_0 , the h_2 dependence is removed. The normalized displacements are then plotted versus crack speed in Fig. 6. These normalized displacements are seen to be independent of crack speed. The global energy release

rates, G_{ss} , for these tests are compared with bimaterial results [5,6] in Fig. 7.

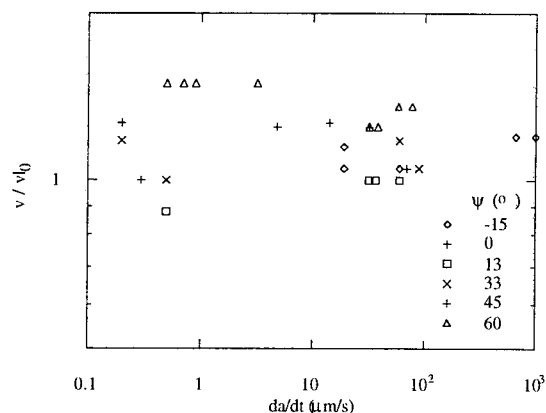


Fig. 6 Normalized far field NCOD versus crack speed for various mixities

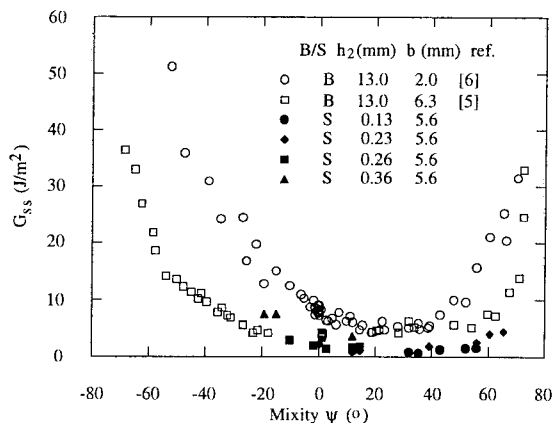


Fig. 7 Variation of interfacial toughness with mode mix for bimaterial (B) and sandwich (S) specimens

A measure of the strength of the singularity in the vicinity of the crack tip is found by approximating the near field NCOD as $NCOD = Ar^\lambda$. For the growing crack experiments where the near field NCOD can be accurately determined, this gives the value for λ shown in Fig. 8. The value of λ is not a strong function of mixity and its mean value is found to be 0.88 ± 0.15 (95%). In a similar manner, the mean value of λ for stationary crack experiments is found to be 0.87 ± 0.13 (95%). This differs significantly from the finite element results which give asymptotic slopes ranging from 0.5 to 0.6 with increasing values of ψ .

CONCLUSIONS

In brief, near field NCOD test results lie below predictions. Both stationary and growing cracks show the same asymptotic behavior which is not explained by plasticity, time dependent behavior or 3D effects. Liang and Liechti [6] have shown that long range cohesive

tractions (possibly due to electrostatic effects) could account for a similar disparity in bimaterial specimen results, however this requires further study. The energy release rate for a sandwich specimen decreases with bond thickness and shows a toughening behavior with mode mix which is similar to bimaterial specimens.

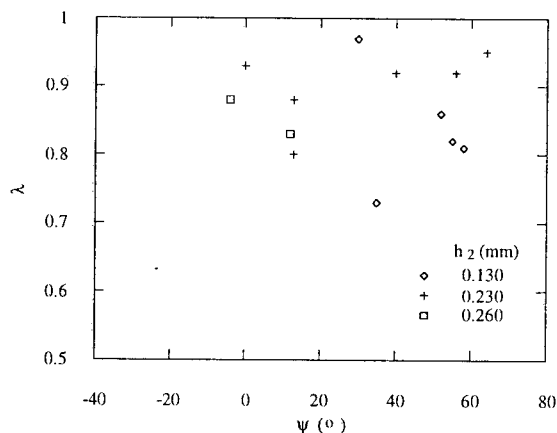


Fig. 8 Parameter λ versus mixity for growing cracks

REFERENCES

1. H. Chai, Composite Materials: Testing and Design (Seventh Conference), ed. J. M. Whitney, (ASTM STP 893, 1986) p.209.
2. H. Chai, *Int. J. Fracture*, **37**, 225 (1992).
3. V. Tvergaard and J. W. Hutchinson, Harvard University Report MECH-230 (1994).
4. K. M. Liechti and Y.-S. Chai, *J. Appl. Mech.*, **58**, 680 (1991).
5. K. M. Liechti and Y.-S. Chai, *J. Appl. Mech.*, **59**, 295 (1992).
6. Y.-M. Liang and K. M. Liechti, *Int. J. Solids and Structures*, in press
7. H. C. Cao and A. G. Evans, *Mechanics of Materials*, **7**, 295 (1989).
8. J.-S. Wang and Z. Suo, *Acta Metall. Mater.*, **38**, 1279 (1990).
9. K. M. Liechti, Chapter 4 in Experimental Techniques in Fracture, ed. J. S. Epstein (1993).
10. J. W. Hutchinson, *J. Mech. and Phys. Solids*, **16**, 13 (1968).
11. J. R. Rice and G. F. Rosengren, *J. Mech. and Phys. Solids*, **16**, 1 (1968).
12. Hibbitt, Karlsson and Sorensen Inc., ABAQUS User's Manual, (Pawtucket, RI, 1992).
13. Y.-M. Liang, EMRL Report No. 93/12 (The University of Texas at Austin, 1993).

Elasto-Plastic, Three-Dimensional Stress Analysis of the Peninsula Blister

by
A. Shirani and K. M. Liechti

Engineering Mechanics Research Laboratory
Department of Aerospace Engineering and Engineering Mechanics
University of Texas at Austin
Austin, Texas 78712-1085

INTRODUCTION

Several studies have been conducted to examine delamination mechanisms in layers. Blister specimens have been used for that purpose since the early works of Dannenberg [1], Williams [2], Takashi *et al* [3] and Erdogan and Arin [4]. For very thin films (Hinkley [5] and Allen and Seninturia [6]), or sandwiched layers (Liechti and Liang) [7], bursting or extensive yielding can be a problem. The peninsula blister configuration [8] shows more promise due to the relatively low delamination pressure levels, the fact that it is a constant energy release rate configuration and plastic zone sizes are small [9]. The purpose of the work reported here was to examine the effect of non-linearity of the mechanical behavior of the delaminating layer in a peninsula blister when thin films must be used. The analysis was based on stationary as well as slowly growing cracks.

ANALYSIS

The geometry of the specimen is shown in Figure 1. In this case, a copper layer had been deposited on polyimide which, in turn, had already been deposited on a silicon substrate. A delamination was placed between the copper and polyimide layers. The delaminating layer in peninsula blister has the rectangular planform of length, l , and span, $2c$. It is essentially attached to polyimide layer along $y=\pm c$, along $x=0$ for $y \leq c$ and along $x \geq a$ for $|y| \leq b$. A delamination span to length ratio $c/a=0.5$ and the peninsula width to span $b/c=0.2$ were considered.

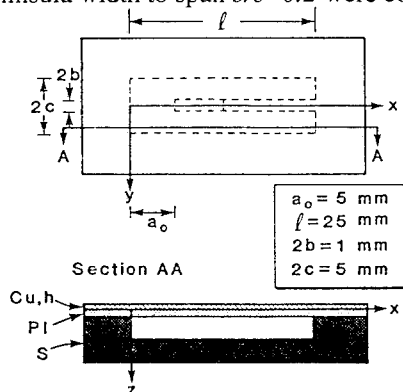


Fig 1 Peninsula Blister Specimen Geometry.

Under certain conditions [8], delamination will only progress along the length of the peninsula, increasing the delamination length a . The layer of copper was considered to be rigidly clamped along the boundary of the delamination, essentially ignoring any deformation in polyimide layer, since most of the strain energy available to produce fracture is stored in copper layer.

In previous work [9], nonlinear Von Karman plate theory was considered in the analysis the response of the delaminating layers, covering the two extremes of linear plate and membrane behavior. The material behavior was taken to be elastic, but the stresses exceeded the yield strength for large aspect ratios a/h . This led us to consider the elasto-plastic behavior of the copper in addition to the geometric non-linearity. A Raleigh Ritz procedure was employed to take advantage of the principal of virtual work and formulate the problem properly. The analysis made use of J_2 flow theory along with a Ramberg-Osgood fit to the elasto-plastic stress/strain behavior of the copper which was assumed to be pure with a relatively low yield stress (Table 1). The energy release rate due to delamination growth along the peninsula was extracted from the Von Karman plate theory solutions for the stresses and displacements in the regions behind and ahead of the crack front. Two and three-dimensional finite element analyses were also conducted using the ABAQUS code [11] and the material response described above. In addition to providing a consistency check for the Von Karman plate theory analyses and insights into the three-dimensionality of the problem for stationary cracks, the finite element analysis was used to model steadily growing cracks in order to determine plastic dissipation rates and to examine various criteria for delamination growth.

RESULTS

First, the value of the central deflection and the energy release rate was evaluated as a function of pressure. Then the delamination of the copper from an interface with a toughness of 100 J/m^2 was considered throughout the study as a main debonding parameter, in order to find the critical pressure for delamination and compare stress levels and distributions in a layer of copper by itself and later in a composite layer with chromium.

The central deflection of the specimen with a single copper layer is shown in Figure 2 as a function of applied pressure.

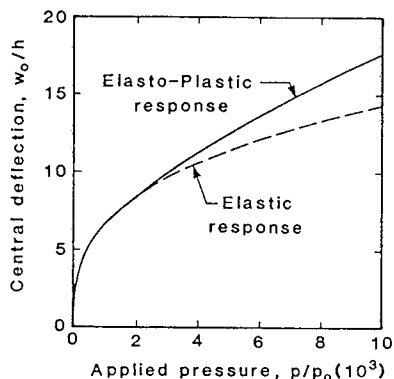


Fig. 2 Central Deflection of the Peninsula Blister Specimen

The larger deflections obtained from the elasto-plastic analysis are expected due to the lower stiffness after yielding. Consequently, lower critical pressures result for a given resistance to delamination (Fig. 3). The results shown in Figure 4 indicate that, for interfaces with a toughness of 100 J/m^2 and the aspect ratios $10 \leq a/h \leq 2500$, there are no plasticity effects and linear elastic fracture mechanics procedures should be sufficient. However, in the proposed delamination experiments and many microelectronics applications, the copper thickness ranges from $0.1 \mu\text{m} \leq h \leq 2.0 \mu\text{m}$, which for a 5 mm delamination gives rise to $2500 \leq a/h \leq 50000$ and large scale yielding will most likely have to be considered. The critical pressure curves drawn in Figure 3 were obtained from Raleigh Ritz analyses for a delamination length $a = 5 \text{ mm}$ and 120 values of h ranging from $0.5 \mu\text{m} \leq h \leq 100 \mu\text{m}$. Critical pressures obtained from three-dimensional finite elements for the same thickness considered above agreed with those obtained from Raleigh Ritz analysis to within 9%.

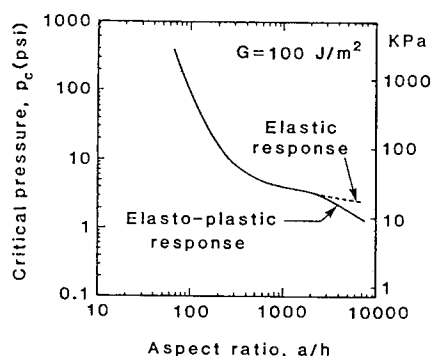


Fig. 3 Critical Pressure in Peninsula Blister Specimen.

The advantage of the finite element analysis was that the fully three-dimensional geometry of the peninsula blister could be modeled. This led to the determination of the plastic zone shapes as a function of the through-thickness location. Von Mises effective stress contours for the worst case, the bottom of the delaminating layer, are

shown in Figure 4. Yielding in the copper was taken to occur at $\sigma_y = 68.9 \text{ MPa}$, which is the white contour line. It can be seen that yielding occurred around the crack front $x = a$ and near $x = a/2$, where the maximum deflection occurred.

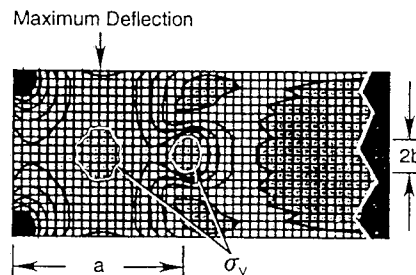


Fig. 4 Von Mises Equivalent Stress Contours.

The plastic zone extended approximately two elements ahead of and one and half an element behind the crack front and two elements laterally from the plane of symmetry. The yielding zone around $x = a/2$ was about 50% larger. Each element was $250 \times 250 \mu\text{m}$, and the layer thickness was $1 \mu\text{m}$. Clearly, large scale yielding is involved for the conditions cited above. Thus if such conditions prevail, analyses of the type presented are required. These are large and very intensive and a simpler solution was therefore considered.

A scheme for preventing excessive yielding was considered in the form of a stronger, stiffer layer bonded to the $1 \mu\text{m}$ copper. As an example, chromium was considered as a potential top layer with a thickness of 1 or $2 \mu\text{m}$ obtained through electroplating. A similar three-dimensional finite element analysis was conducted for these conditions. By using the composite material, stress levels in the copper decreased to such an extent that even $1 \mu\text{m}$ of chromium decreased the stresses below the copper yield strength. Thus, the chromium layer can indeed function as a yielding inhibitor and increase the potential for thin film delamination tests to be conducted on the basis of linear elastic fracture mechanics.

All of the analyses that have been described up to this point have been for stationary delaminations. It is well known that the stress distributions for running cracks can differ appreciably and so the next step that was taken was to consider a quasi statically growing crack. In ABAQUS, there are several methods for prescribing the debonding criterion. If two-dimensional analyses are used, then the crack growth rate, or a maximum cohesive stress criterion can be selected. On the other hand, if three-dimensional conditions apply, then a "contact pressure" criterion can only be used, where the contact pressure refers to the load in interface elements placed between the copper and the rigid substrate. Three-dimensional stress analyses were conducted to check the possibility of using simple two-dimensional plane strain analyses. However due to the narrowness of the peninsula, it quickly became clear that two-dimensional conditions do not prevail. In order to

narrowness of the peninsula, it quickly became clear that two-dimensional conditions do not prevail. In order to determine the amount of yielding in the composite layer while the crack was running, it was first necessary to calibrate the contact pressure required to cause one element to debond at an overall energy release of 100 J/m^2 . The critical value (0.25 MPa) was then used as the condition for node release in order to simulate crack growth.

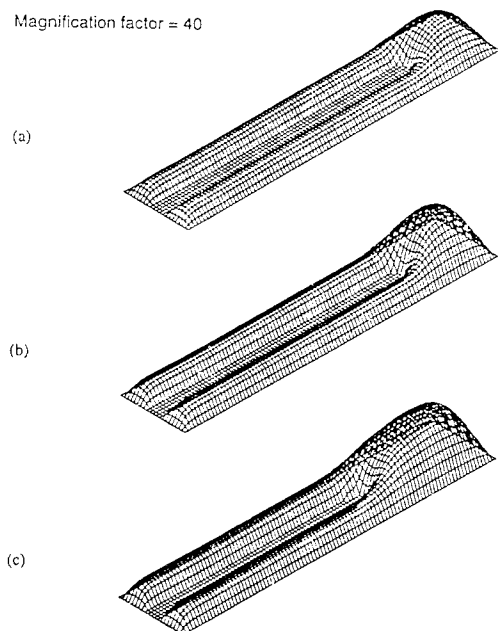


Fig. 5 Deformed Configuration of the Peninsula Blister Specimen. a) Before Delamination. b) At the Initiation of Delamination. c) Growing Delamination.

The deformed configuration at the three different times is shown in Figure 5. As predicted by Dillard *et al* [8], the delamination grew along the peninsula (in the x - direction) rather than across it (in the y - direction). Furthermore, it was found that stresses in the delaminating layers were higher for the growing crack than for the stationary crack. However, the stiffness and strength of the 1mm chromium layer was still sufficient to prevent any yielding in the copper. A $2 \mu\text{m}$ chromium thickness decreased stress levels even more. In all cases, the stresses were highest at the original and current crack fronts in addition to the location of the maximum deflection.

CONCLUSIONS

A peninsula blister specimen with copper delaminating from a layer of polyimide on a silicon substrate was stress analyzed using a Raleigh Ritz procedure and finite element methods. In both cases, the elasto-plastic behavior of the copper was considered and, in the latter, a fully three-dimensional analysis was made for stationary as well as growing cracks. For an interfacial

toughness of 100 J/m^2 , it was found that plasticity effects are important for delaminating layer length to the thickness ratios of $a/h \geq 2500$, commonly encountered in microelectronic structures. It was also found that the stress distribution is highly three-dimensional.

A composite layer made of chromium deposited on the copper was also considered for stationary and growing cracks. In both cases, the stiffer and stronger chromium layer eliminated any plastic deformation in the copper, thus simplifying the extraction of toughness values from tests.

TABLE 1 Mechanical properties of Delaminating Layers

Material	Young's Modulus, E (10^6 psi/GPa)	Yield Stress, σ_y (ksi/MPa)	Power law constant, n
Copper	16/110.2	10/68.9	3
Chromium	35/248.2	120/827.2	9

REFERENCES

1. Dannenberg, H., *J. Appl. Polymer Sci.*, **5**, 125-134 (1961).
2. Williams, M.L., *J. Appl. Polymer Sci.*, **13**, 29-40, (1969).
3. Takashi, M., Yamazaki, K., Natsume, T., and Takebe, T., *21st Japan Cong. on Mat. Res.- Non-Metallic Mat.*, 260-264 (1978).
4. Erodgan, F., and Arin, K., *Int. J. Eng. Sci.*, **10**, 115-125 (1972).
5. Hinkley, J. A., *J. Adhesion*, **16**, 115-125 (1983).
6. Allen, M. G. and Senturia, S. D., *J. Adhesion*, **25**, 303-315 (1988).
7. Liechti, K. M. and Liang, Y-M, *Int. J. Fracture*, **55**, 95-114 (1992).
8. Dillard, D. A. and Bao, Y., *J. Adhesion*, **33**, 253-172 (1991).
9. Liechti, K. M., and Shirani, A., *Int. J. Fracture*, **67**, 21-36 (1994).
10. Timoshenko, S., and Woinowsky - Kreiger, S., *Theory of Plates and Shells*, McGraw-Hill, New York, 2nd Edition 1987.
11. ABAQUS, version 5.2, Copyright 1992 Hibbit, Karlsson and Sorensen.

RF CURING IMPLEMENTATION IN AUTOMOTIVE PRODUCTION

Kimberly A. Chaffin, Chi Li, and Ray A. Dickie
Ford Research Laboratory
P. O. Box 2053, Dearborn, Michigan 48121

ABSTRACT

The implementation of radio-frequency (RF) heating processes to cure adhesive joints within plastic components results in reduced cycle times and improved product quality. In addition, utilization of RF curing has provided strong evidence that the processing of low volatile organic content (VOC) adhesives can be technically viable and economically competitive. Implementation challenges result when bondlines deviate from the two dimensional, ideal case, in which parallel plate electrodes can be utilized. The feasibility of using RF curing for parts with both complex three dimensional bondlines and inaccessible joints has been demonstrated in production. Additional processing challenges are part variability and standing electrical waves. We have proven that with careful process design these variables can be accommodated, eliminating them as factors in a successful production application.

BACKGROUND

Radio-frequency electronic heating, also called dielectric heating, is an efficient way to convert electromagnetic energy to thermal energy for heating materials possessing a high dielectric loss at radio frequencies. The RF heating process has been widely employed for processing thermoplastics, especially embossing vinyl, in automobile trim parts manufacturing. However, dielectric heating as an industrial process dates many years, with many patents dealing with various aspects of the technology. For example, Blessing [1] describes the cure of a composite plywood structure for the manufacture of wooden aircraft propellers. The advantages cited [1] are the same as those we recognize today: a rapid more even cure of an adhesive bondline within an insulating material.

More recently, research in the area of RF curing has focused on the high volume processing of plastic components with complex bondlines [e.g. 2]. Technical issues being addressed for current applications are the effects of RF field strength on the adhesive cure, the heating rates, the cooling rates, the effects of low VOC adhesives, and the electrode design.

FUNDAMENTALS OF RF CURING

RF curing is very effective in curing adhesive between insulating materials because of the high dielectric loss of the unreacted adhesive relative to the dielectric loss of the substrate. The dielectric loss is a measure of the molecular

mobility of a material under an oscillating electric field. Because the uncured adhesive will have many polarizable species such as monomers, oligomers, ions, and polar chain ends, the dielectric loss of most adhesives tends to be much larger than that of the substrates they are joining.

Under the oscillating electric field charged molecules of these high loss materials will try to orient themselves with the field. These molecular motions, on the order of 10 million to 100 millions times per second in the RF range, induced by the electric field result in frictional heat generated within the high dielectric material. Quantitatively, the heat generated per unit volume of adhesive within the RF field can be determined as follows:

$$\frac{\partial H}{\partial t} = |E_a|^2 2\pi f \epsilon_a'' \quad (1)$$

where E_a is the electric field strength over the adhesive and ϵ_a is the dielectric loss of the adhesive [3,4]. A similar equation can be written for the substrates, however, if the dielectric loss of the substrate is much smaller than that of the adhesive, then the heating rate of the bondline due the RF field (q_r) can be simplified to just include the adhesives contribution, thus can be written as:

$$q_r = \frac{\partial H}{\partial t} = |E_a|^2 2\pi f \epsilon_a'' \quad (2)$$

Because of the strong dependance of dielectric loss upon the heating rate, RF heating offers significant rate advantages over conventional heating methods for low VOC adhesives. In the case of water based systems, the polar nature of the water molecule increases the dielectric loss of the adhesive resulting in significant improvements in process cycle times. These resulting short cycle times make low VOC adhesives a viable option for trim applications which require the short process cycles times (20-35 seconds), typically only obtained with high solvent adhesives.

RF HEATING VS. ALTERNATIVE HEATING

In RF heating the intense temperature rise of the adhesive in the joint is due to the conversion of electromagnetic energy and chemical reaction energy into thermal energy. Quantitatively, the temperature rise in the adhesive joint can be calculated by solving the set of energy equations which

describe the heat generation and transport for a given joint geometry as follows:

$$\rho C_p \frac{\partial T}{\partial t} = k \nabla^2 T + q_r(T,t) + q_c(T,t) \quad (3)$$

where the density (ρ) and the heat capacity (C_p) are independent of temperature, while $q_r(T,t)$ and $q_c(T,t)$ are the rates of heat generation by RF dielectric field and chemical reaction, respectively. The conduction term for an adhesive joint under RF heating represents the heat loss to the substrate from the adhesive.

Convection heating can also be described by equation (3). However, in convection heating $q_r(T,t)$ is zero, and the conduction term represents the heat transient from the outside of the bondline inward to the adhesive.

This fundamental difference in the conductive heating term in the heat transient equation (3) is responsible for explaining the short cooling cycles experienced with RF when compared to conventional heating methods. The driving force for heat loss is the change in temperature across the substrate. In the case of RF curing, the temperature of the adhesive is much greater than that of the outer surface of the substrate, providing a driving force for cooling away from the bondline. In the case of conventional heating, where the heat is provided from the outside of the bondline inward through the substrate, the temperature of the outside surface of the substrate is going to be much hotter than the adhesive temperature. In this case, the adhesive will not cool until the substrate cools below the adhesive temperature, providing a driving force for cooling rather than for heating.

Because the temperature distribution for the RF cured joint results in the maximum joint temperature in the adhesive layer, substrate temperatures never need to approach their distortion temperatures for effect cure of the adhesive. This phenomena allows for a larger cure window, thus more aggressive cure temperatures can be used, resulting improved produce quality.

IMPLEMENTATION OF RF CURING

RF dielectric heating technology can be applied to many manufacturing process such as bonding composite structures [5, 6], automotive lamps [7], and interior trim panels [2]. The critical issue is designing the electrodes to focus the RF electromagnetic energy into the bondline. In the simplest case, the electrodes would be flat parallel plates which could easily access the bondline. However, most real applications have complex, three dimensional, inaccessible bondlines.

The RF electric field can be illustrated using lines of force.

For a joint accessible with parallel plate electrodes, the lines of force are very dense, traveling from in a straight line, perpendicular to both electrodes. This parallel plate electrode configuration provides a uniform field, maximizing the electric field strength (E_a) in equation (1), thus maximizing the heating rate.

For parts with bondlines which are inaccessible to parallel plates electrodes, fringe field can be directed into the bondline, providing the electromagnetic energy required for adhesive activation. Fringe field, found at the ends of parallel plate electrodes, can be represented by circular lines of force which are perpendicular to the electrode ends. Fringe field is non-uniform and lower in intensity than parallel plate heating, thus requires higher voltages to match the heating rates obtainable with a parallel configuration. However, fringe field heating has proven effective in heating bondlines which are difficult to access from both sides [7].

For three dimensional complex bondlines, the electrodes must follow the contour of the part, thus the electrodes must be cast or machined to maintain a local parallel plate configuration. If these three dimensional bondlines are coupled with inaccessible portions, then fringe field heating can be utilize. However, for a given voltage:

$$|E_a|_{fringe} < |E_a|_p \quad (4)$$

therefore the parallel plate portions of the bondline will heat more rapidly than the fringe field portions of the bondline. One approach to dealing with the non-uniform heating is to use a two component room temperature cure adhesive. The RF heat serves to initiate the chemical reaction, developing handling strength within 10 to 20 seconds, depending upon the adhesive formulation. After this green strength is achieved, the part can move on to subsequent processing before curing is complete [6].

Part variability is common concern for injection molded plastic components. Using the electrodes to provide compression to the bondline minimize misfit and warpage. Compression with the electrodes reduces the distance between the electrodes and the bondline, focusing the RF energy into the bond and maximizing the voltage across the adhesive, thus optimizing the heating rate of the bondline.

RF BONDED EDGEFOLDING IN PRODUCTION

Door trim panel edgefolding an bonding will be used as an example to illustrate the implementation of RF bonding technology [2]. In the manufacturing of automotive trim panels, a soft PVC skin is laminated to a rigid thermoplastic resin panel either by vacuum forming or by low pressure injection molding. The excess skin is folded and bonded to

the back side of the thermoplastic panel using a laminating adhesive. Conventionally, a solvent based adhesive is sprayed or brushed onto the panel and the edgefolding process immediately follows. The folding operation can be automated by mechanical means such as using an edgefolding press.

The process cycle time for the folding and bonding operation is largely determined by the speed of the adhesive's strength development. The implementation of RF heating to directly heat the adhesive in the edgefolding and bonding process dramatically reduces the cycle time, making the use of low VOC adhesives in such trim operations technically feasible.

An existing edgefolding press was modified to incorporate the necessary electrodes for RF heating. Two electrodes, a RF electrode and a ground electrode acting as an antenna and receiver, respectively, are required to incorporate the RF energy into the bondline. The aluminum nest which holds the door panel during the edgefolding acts as the RF electrode. The nest was insulated electrically from the rest of the press by using high density polyethylene (HDPE) blocks. Eight folding elements, two for the bottom flange, two for the right side, one each for the left side and the corners sections, slide inward and drop down to fold the vinyl skin around the plastic panel. The aluminum folding elements act as ground electrodes and as electromagnetic shields which prevent the RF energy from escaping the press. The RF electrode was connected to a generator via a series of co-ax boxes and brass ribbons, a number of leads were used to eliminate potential standing waves in the long bondline of the door panel. The ground electrodes were connected to the frames of the press and then to the ground terminal of the generator which was positioned beneath the aluminum nest. The internal capacitance and inductance of the transmission line and the electrodes must be tuned to the output circuits of the generator such that a proper level of power is transferred to the bonding area.

In this process, the panel is placed into the electrode nest. The folding elements move inward, pushing with them the excess vinyl for the edgefold. Next, these ground electrodes move downward and inward completing the edgefold. The two electrodes form a parallel plate configuration through which the RF field acts. One of the key design issues is the electrode design. Process optimization of the electrodes allows for a 30 second cure time for the edgefold of the door panel with a water base, environmentally friendly adhesive.

Using RF energy to cure the bonded edgefold on the interior trim panels offers many advantages over conventional curing methods. RF curing allows for the efficient use of a water based adhesive for the edgefold due to the increased

dielectric loss as a result of the polar water molecules. The low glass transition temperature (T_g) and thermal conductivity of the door panel materials lead to many processing problems when considering convective methods of curing the bondline, however, the RF heating process is compatible with the low T_g of the vinyl, as well as, with the low thermal conductivity of the plastic resin panel.

CONCLUSION

RF heating is an efficient method for curing bondlines within plastic components. However, when implementing RF curing in a production process care must be taken in designing the electrodes to maximize the heating rate such that the real process can approach the efficiencies of the theoretical calculations. Real parts have three dimensional complex, and potentially inaccessible bondlines. These deviations from a parallel plate configurations will reduce the process efficiency if the bonding system is not carefully designed. Electrodes can accommodate three dimensional bondlines by carefully contouring the electrodes to the part, creating locally, the affect of a parallel plate configuration. Fringe field heating can also be utilized to access hidden bondlines. In the edgefolding process, moving electrodes mechanically form the edgefold and supply the electromagnetic energy to cure the adhesive. The result is an efficient and robust bonding process.

REFERENCES

1. G. W. Blessing, "Composite Structure", United States Patent Office #2,372,929; April 3, 1945.
2. C. Li, K. A. Chaffin and A. P. Thakore, "RF Dielectric Heating and Low VOC Adhesives for Automotive Trim", *Adhesives Age*, **37** (7), 18 (1994).
3. N. Hill, W. Vaughan, A. Price, and M. Davis, "Dielectric Properties and Molecular Processes", van Nostrand, London, 1969.
4. C. Li, "Time Resolved Temperature Distribution in Adhesive Joints During RF Bonding", *Proc. 1992 Adhesion Society Annual Mtg.* 1992, p. 99.
5. K. A. Iseler, "Method and Apparatus for Bonding a Cured Fiber Reinforced Plastic Part to a Reinforcement Member", European Patent Office 0 339 493; Feb. 11, 1989.
6. C. Li. and R. A. Dickie, "Bonding Adhesive Joints with Radio-Frequency Dielectric Heating", *Int. J. Adhesion and Adhesives*, **11** (4) 241 (1991).
7. C. Li, R. A. Dickie, and F. G. Oblinger, "Method and Apparatus for Dielectrically Heating an Adhesive", United States Patent Office #5,223,684; June 29, 1993.

GUIDED WAVES FOR METAL TO COMPOSITE ADHESION BOND INSPECTION

Joseph L. Rose, Krishna M. Rajana, Semyen Pelts

The Pennsylvania State University
Engineering Science and Mechanics Dept.,
227 Hammond Building,
University Park., PA, 16802.

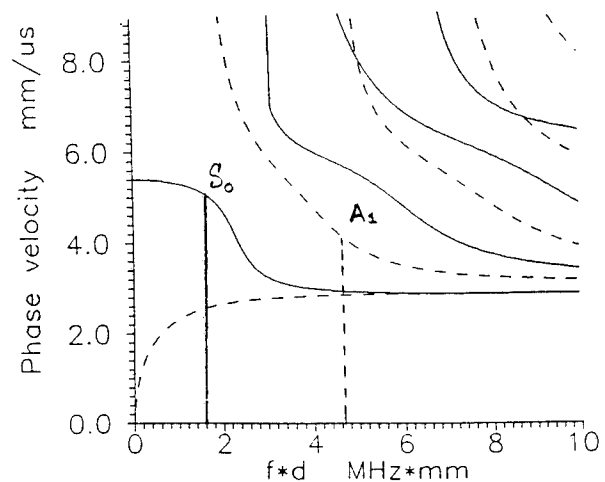
INTRODUCTION AND BACKGROUND

The use of adhesively bonded aircraft structures of all sorts has increased considerably. Skin panels with adhesively-bonded stiffeners are preferred over riveted or other mechanical fasteners due to the fact that the former offered improved stability. The load carrying capacity under axial compression or shear loading is improved considerably when adhesive bonding is used. The stringent requirement for ensuring quality of the bond has led to the development of several nondestructive testing techniques as a part of regular aircraft maintenance [1]. Due to mechanical damage during manufacturing or in-service, a repair or panel replacement might be called for. Great progress has been made in tackling the bond inspection problem between two metals. Conventional point by point test methods, though time consuming, proved to be effective for disbond detection. Presented here is a global ultrasonic guided wave approach with sensitivity for detection of interfacial weakness, delamination, corrosion attack, and cracking [2]. In particular the use of guided waves to evaluate the adhesion quality between aluminum substrate and a composite repair patch is studied.

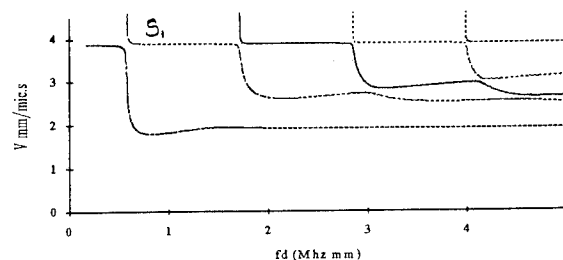
Guided wave propagation resonance tuning concepts have been successfully applied to aging aircraft structures in examining the integrity of lap splice joints and tear straps. Phase velocity and frequency tuning have allowed us to consider the bonding of any two unknown geometrical structures [3]. Presented in this paper is an extension of these basic ideas to a composite structure joined to a metal, typical of those found in composite patch repair in many military and commercial aircrafts. Tuning concepts can allow us to overcome anisotropic and nonhomogenous situations associated with composite materials. Both theoretical and experimental aspects of the problem are also considered.

Lamb waves offer a great inspection possibility due to the availability of a whole host of propagating modes each with its characteristic distributions [3]. With aluminum being isotropic, the dispersion curves can be obtained after solving for the roots of relatively simple

equations known as the *Rayleigh-Lamb equations*. The loci of the roots, i.e., phase velocity plotted as a function of the fd (frequency times the thickness d product) is termed as phase velocity dispersion curves. Theoretical dispersion curves for an aluminum layer (with longitudinal and shear wave velocities of 6.3 and 3.1 mm/ μ sec respectively) are shown in Figure 1a. Each point in this phase velocity dispersion curve represents a resonance state with a specific displacement, stress and power distribution across the thickness of the structure. Analysis of the wave structure will provide information about their sensitivities to certain types of defects.



(a)



(b)

Figure 1. Phase velocity dispersion curves for a) an aluminum plate and b) Boron epoxy plate (only symmetric case shown)

For a sample experimental problem, dispersion curves were theoretically obtained for a boron epoxy plate. The boron patch used in this study has fibers in only the 0° direction, and hence can be completely characterized by 5 elastic constants as in transversely isotropic material. Similar to the analysis in an isotropic material, anisotropic materials can also be solved using *Rayleigh-Lamb type equations*, which are relatively complex [4]. The elastic constants used for solving the dispersion curves are shown in Table 1. Presented in Figure 1b are the symmetric family of dispersion curves for a transversely isotropic boron epoxy plate. It may be noted that the phase velocity is fairly constant (~ 4.0 mm/ μ sec) for a fd range of 1 to 2 mm. MHz along the S_1 mode. This feature was used in the experiments.

Table 1: The elastic constants for the boron epoxy plate

C_{11}	C_{33}	C_{13}	C_{55}	ρ
30.1	2.7	0.6	70.0	2

Resonance Matching

Every point on a dispersion curve represents a resonance state of the structure in which it is excited. In the present work, a known mode is excited in aluminum and received via angle tuning either on an aluminum-boron epoxy overlap region or on the boron epoxy plate alone. The peaks in the received Amplitude vs. Reception Angle (ARA) plot represents overlap points on the dispersion curve of both systems for an appropriate fd product. This resonance matching concept can be used to characterize the adhesion quality while inspecting structures with unknown structural characteristics across the bond.

BOND INSPECTION

It was documented [2] that received or reflected amplitude showed good sensitivity to bond quality. A schematic of the specimen and scan protocol is shown in Figure 2a. The thickness of the aluminum plate and boron epoxy plate are 1.0 mm and 1.3 mm respectively. The overlap is 2.0" with a centrally planted through delamination of 1.0 inch. Tests are performed in both a pulse echo and a pitch catch configuration. In the first set of experiments, the A_1 mode at a phase velocity of 4.17 mm/ μ sec and fd product of 4.62 mm.MHz was utilized in a pulse echo configuration. This point has very interesting field distributions. The out of plane component of displacements are maximum at the surface while the in-plane displacements are close to zero [3]. A continuous scan was performed and the reflected amplitude was

monitored as a function of the transducer position. Presented in Figure 2b is an echodynamic profile of the reflected amplitude normalized by the peak which was obtained at the center of the delamination.

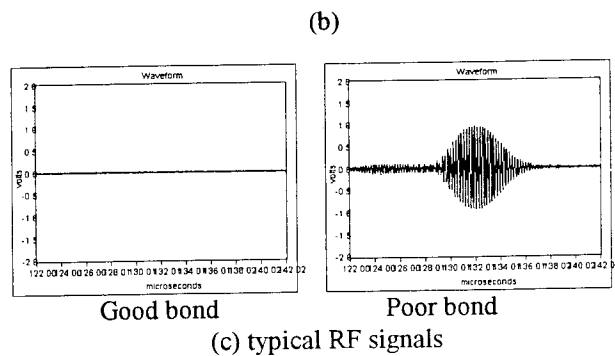
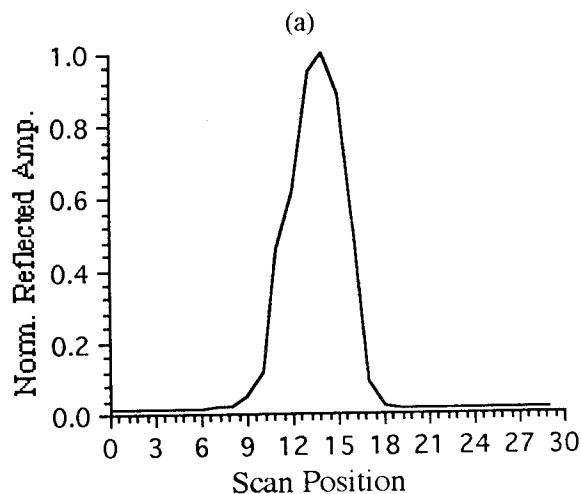
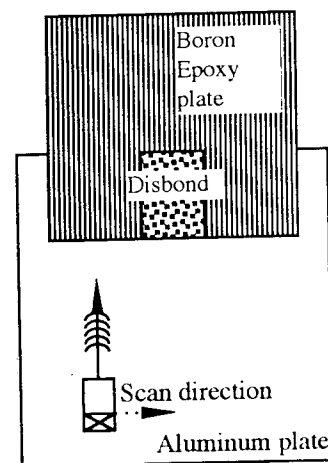


Figure 2. a) Pulse echo configuration b) Echodynamic profile obtained using A_1 at 4.62 MHz.mm. c) typical RF signals

In the second set of experiments, the concept of angle tuning was implemented. The experimental configuration was shown in Figure 3a. A fundamental symmetric mode at an fd product of 1.67 mm.MHz was excited in the aluminum plate and received using a variable angle beam transducer as shown in Figure 3a. Since the system is unknown, the bond quality can be accessed via angle tuning. If the bond quality were poor, there would be no received signal regardless of the reception angle. However, if the transducer were placed on or along a good region of the bond, peaks will be seen in the ARA plot. Shown in Figure 3b is the amplitude of the signal plotted as a function of the reception angle. The solid line indicates the results when the receiver was placed on the overlap region alone and the dotted line was when the receiver was placed on the composite alone. Shown in a dark broken line in Figure 3b is the response seen by the transducers when placed on or across a disbond. Another interesting observation is that the peaks in the ARA plots obtained when the receiver is on the boron epoxy plate alone, agrees with the theoretical dispersion curves. The agreement will be close if the finite size of the source is taken into account [3].

CONCLUSIONS

The ease of global ultrasonic guided waves to detect and characterize the adhesion quality in patch repair was demonstrated. From a wave structure point of view the out of plane displacements showed great sensitivity for disbond detection. However, for detection of interfacial weakness, a combination of in-plane and out of plane displacement will be necessary. Delamination detection in pitch-catch requires an overlap of dispersion curves for all the three systems. Hence, a combination of wave structure and resonance matching offers a powerful tool for the NDT of adhesively bonded structures.

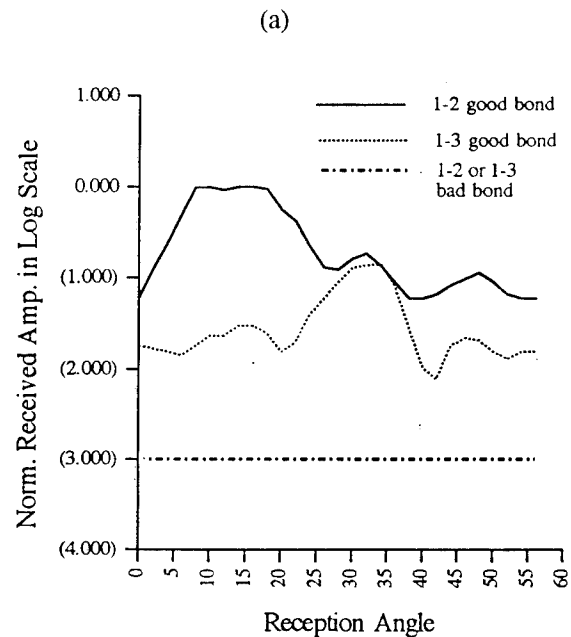
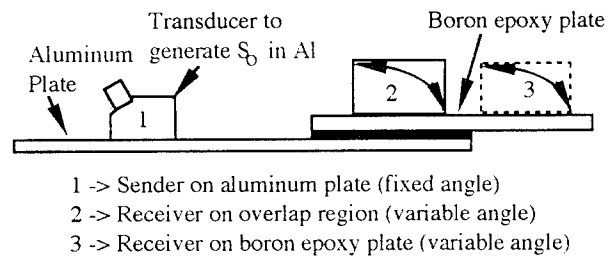
ACKNOWLEDGMENTS

Thanks are given to Mr. Dave Galella and the FAA for the financial support and technical discussions. The encouragement of Mr. Dennis Roach and Mr. Philip Walkington is also appreciated. We also acknowledge the efforts of Mr. Thomas Shahood and Mr. Bruce Bellasun, Texstran Inc. for specimen support.

REFERENCES

1. Guyott, C. C. H., Cawley, P., Adams, R. D., "The NDT of adhesively bonded structures: A review", *Journal of Adhesion*, Vol. 20, No. 2, 1986, p. 129.

2. Rose, J. L., Rajana, K. M., Hansch, M. K. T., "Ultrasonic guided waves for NDE of adhesively bonded structures", to be published in *Journal of Adhesion*.
3. Rose, J. L., Pilarski, A., Rajana, K. M., "Ultrasonic guided waves for lap splice joint inspection in aging aircraft", *QNDE*, August 1-6, 1994, Snowmass, CO., (to be published)
4. Li, Y., Thompson, R. B., "Influence of anisotropy on the dispersion characteristics of guided ultrasonic plate modes", *J. A. S. A.* Vol. 87 N0. 5, 1990, pp. 1911-1931.



(b)

Figure 3. a) Experimental configuration and b) resulting amplitude vs. incident angle plot.

INCREASED ADHESION AT THE FIBERS INTERFACE FOR POLYETHYLENE FIBER PAPERS FOLLOWING OXYFLUORINATION TREATMENT

B. Riedl and H. Chtourou

Wood Science Program
Centre for Research on Macromolecular Science and Engineering
Abitibi-Price Bldg
Laval University
Quebec Canada G1K 7P4

INTRODUCTION

There are many instances in the literature where the adhesion between two materials is increased due to the surface modification of one phase, such as plasma treatment of the reinforcing fiber. There are few cases where the adhesion is strengthened due to modification of *both* surfaces. This is not surprising since one of the components, the continuous phase, is most often a thermoplastic polymer or a thermoset resin, and these are combined with the reinforcing agent in a liquid state: thus there is no definite second surface to modify.

We have made synthetic papers from modified polyethylene (PE) fibers either by themselves or in combination with natural cellulosic fibers. Following an oxygen-fluorine treatment, adhesion between fibers was enhanced 30-50%, as estimated through standard mechanical testing of the resultant papers made with non-modified fibers. The adhesion between the fibers is a result of direct contact between the surfaces, without going through any prior liquid phase step. Hence there is no contribution due to molecular interpenetration. We have correlated the mechanical properties to acceptor-donor interactions at the interface, as obtained through inverse gas chromatography (IGC) techniques, while varying the proportion of treated PE fibers and their degree of treatment. Untreated PE fibers have a non-polar surface and do not participate in the specific adhesion. Treated fibers interact strongly

through acceptor-donor interactions. The treatment results in a very polar surface with amphoteric, i.e. combined acid-base, character. XPS surface characterization was also performed on these materials.

This case is particularly simple and such a treatment may find more application in the composite field.

EXPERIMENTAL

Material PE was from DuPont (Purplus 3850 grade). It was treated at two different levels of oxyfluorinations by a proprietary process at Air Products. Lignocellulosic fibres were of Explosion and Kraft types, from Aspen and Birch, respectively.

Apparatus XPS was done with an Escalab Mk II. IGC was done with a Hewlett - Packard 5700 GC. with different gas probes.

Paper Properties Paper handsheets, 60 g/m², were prepared according to CPPA standards methods, before they were further treated by simultaneous pressing and drying. At least 7 sheets were made for each combination of fibers. Paper was stored in a controlled humidity room (RH = 50%). Properties measured were, among others, breaking length, burst index, and tear index.

RESULTS and DISCUSSION

XPS XPS gave the intensities of different C, O, and F atoms detected at the fiber surface.

The non-treated fibre has 9% oxygen at the surface due to polyvinyl acetate and polyvinyl alcohol being added as processing aids during fiber manufacture. Oxyfluorination increases the oxygen concentration, as expected, as well as fluorine, which is absent in the non-treated fibre.

IGC From the temperature dependence of the volumes of retention of different gas probes in a chromatographic column packed with the fibres, a donor and an acceptor number, K_B and K_A , respectively, are found, typical of the fiber investigated [1].

Results [2] show that, although containing PVOH at the surface as shown through XPS, PE fibers have a both K_A and K_B of zero. This suggest the polymeric processing aid is encased in a cristalline PE matrix and is unable to interact with the gas probe molecules. Thus we expect the strength properties of PE paper to origin exclusively from fibre entanglements and fiber strength *per se*.

The oxyfluorinated fibers had a K_A and K_B number of 7.3 and 2.5, respectively, (level 1 of treatment) and 10.3 and 9.2, respectively (level 2 of treatment). These numbers are in arbitrary units, related to acceptor - donor strenghts as defined by Gutmann [3]. Thus the oxyfluorinated fibers have acquired an amphoteric surface.

For the lignocellulosic fibers, of the Explosion type, K_A and K_B were 2.4 and 12.1, respectively. This is a strongly basic surface. The surface of Kraft fiber was more weak and balanced, with K_A and K_B of 5.5 and 5.0, respectively.

Specific interactions vs. strength properties

The magnitude of the specific interaction between mixed fibers can be represented as [1]:

$$I_{SP} = K_{A1}K_{B2} + K_{B1}K_{A2} \quad (1)$$

where K_{Ai} and K_{Bi} refer to the acceptor and donor constants of fiber of type i .

We transformed Equ. (1) by introducing $Prob_{ij}$, which is the probability that a fiber i and a fiber j were close to each other in the paper. As detailed in Ref. [4], we obtained the following Equ.:

$$I_{SP} = [2(P_{PE})^2(K_A^{PE} \cdot K_B^{PE})] +$$

$$[2P_{PE} \cdot P_{lig} (K_A^{PE} \cdot K_B^{lig} + K_B^{PE} \cdot K_A^{lig})] +$$

$$[2(P_{lig})^2(K_A^{lig} \cdot K_B^{lig})] \quad (2)$$

As in Equ. (2), a value of I_{sp} can be calculated using a weighed average of the acceptor-donor contributions according to the proportions of fibers in the paper [4]. The specific interaction parameter for untreated PE is zero, that of the oxyfluorinated PE level 1 is 36.5 and that of the oxyfluorinated PE level 2 is 189.5. As a basis for comparaisn, in pure Kraft pulp and pure Explosion pulps, which have typical paper properties, I_{SP} is 55 and 58.1, respectively. We thus have relatively strong acceptor-donor properties in the treated PE fiber papers. The strength properties of PE paper, tear index (in mNm²/g), breaking length (in km) and burst index (in kPam²/g), are shown as a function of I_{SP} in Fig.1. A linear correlation is found for all three properties.

The same rationale can be applied to mixed PE/lignocellulosic fibers papers. Fig. 2 presents the strength properties of 50% PE paper with lignocellulosic fibre, Kraft or Explosion, as a function of I_{SP} , specific interaction parameter. Again, the variable is the treatment of the PE fiber as in Fig. 1. The same relationship is found.

CONCLUSION

The correlation between a specific interaction parameter, obtained from IGC measurements, and the mechanical paper properties of mixed PE/lignocellulosic fibers is strongly positive and indicative of the contribution of acceptor-donor type interactions to inter fiber adhesion in paper.

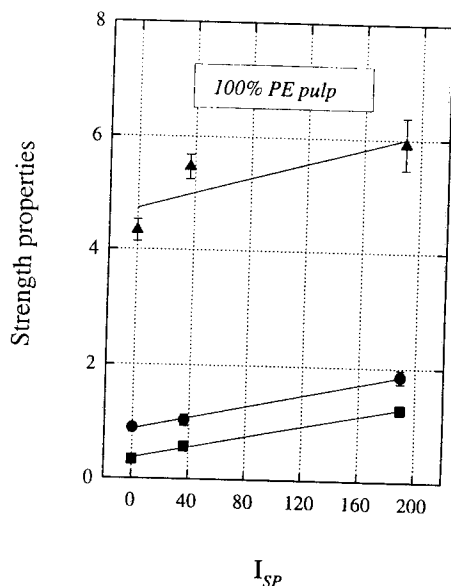


Fig. 1: Strength properties of PE paper, as a function of I_{SP} , specific interaction parameter. Tear index: ▲ ; breaking length: ● ; burst index: ■.

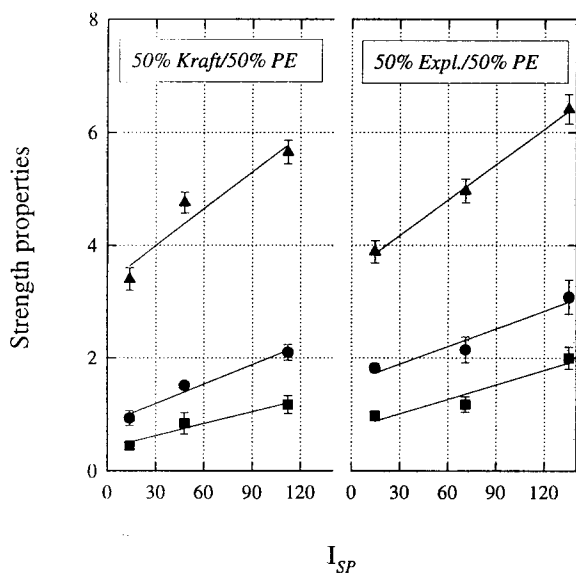


Fig. 2: Strength properties of 50% PE paper with lignocellulosic fibers, as a function of I_{SP} , specific interaction parameter. Tear index: ▲ ; breaking length: ● ; burst index: ■.

REFERENCES

1. C. Saint Flour and E. Papirer, *J. Colloid Interface Sci.*, **91**, 69 (1983).
2. H. Chtourou, B. Riedl and B.V. Kokta, *J. Adhes. Sci. Technol.*, in press 1994.
3. V. Gutmann, *The Donor-Acceptor Approach to Molecular Interactions*. (Plenum, New York, 1978).
4. H. Chtourou, B. Riedl and B.V. Kokta, *Tappi J.*, Submitted, dec. (1994).

PERFORMANCE TESTING OF COATED ALUMINUM FOOD AND BEVERAGE PRODUCTS

R. A. Haaksma

Reynolds Metals Company
Corporate Research and Development
1941 Reymet Road, Richmond, VA 23237

INTRODUCTION

The purpose of this paper is to review current methodology used to evaluate the adhesive performance of coil coated aluminum sheet used for container applications as background for discussion of needed advancements.

A number of screening tests are routinely used for quality control during the production and development of coil coated aluminum sheet which is post-fabricated into end stock and draw-redraw food cans. In the development of new surface treatments and coatings for coil container applications, candidate systems which pass screening tests are further evaluated in product shelf pack testing which lasts a minimum of six months and extends to two years for some food products.

This paper will provide a general description of the test protocol for the adhesive performance of coil coated container sheet. Examples will be provided which support the need to conduct comparison testing between different facilities, to employ methods which better reflect performance requirements in new applications and to work toward an intermediate level of testing which creates a more quantitative measure of packed product container performance without requiring months or years to complete.

BACKGROUND

The coil coating process and coated product performance requirements will be described to provide perspective on testing requirements for aluminum container products. Important factors in the design of test methodology are that system of interest is comprised of a thin polymeric coating on a surface treated aluminum substrate which is subjected to severe fabrication during manufacturing and varying degrees of environmental exposure during packing and shelf storage lifetime. Typical polymeric coating thicknesses are 2-10 μm while the thickness of the aluminum substrate is about 200-300 μm .

Steps in a typical container coil coating operation include surface preparation (alkaline cleaning, rinsing, chemical conversion coating, rinsing), coating application by a reverse roll coat process, coating bake and lubricant application. The most advanced modern coil lines run at speeds in excess of 1000 feet/minute and may have bake cycles which are shorter than 10 seconds.

Coating performance requirements include the ability to: withstand fabrication (flexibility, abrasion resistance), protect the product from the container and the container from the product (chemical resistance, barrier properties), adhere to the substrate, and provide acceptable appearance characteristics (flow properties, blush resistance). The level of performance needed depends on the service and fill environment, shelf life requirements, fabrication severity and product characteristics.

SCREENING TESTS

The first level of container screening tests are conducted on flat sheet as produced in the coil operation. Many of the tests have a common element in that they are all variations of the crosshatch tape test which are carried out following exposure to different environments. In crosshatch adhesion testing, a set of perpendicular lines are scribed in a crosshatch pattern through the coating to the underlying metal and an "adhesion" measurement is made using 3M #610 Scotch tape.

Testing on flat sheet also includes methods designed to identify sheet which will exhibit poor fabrication performance. Examples of these methods are an impact bend method called the wedge bend test and the testing conducted on Tinius-Olsen (Erchison) cups to determine coating adhesion in a draw-redraw operation. The wedge bend test is a modification of the T-bend procedure described in ASTM D 4145-83 where the adhesive performance of painted or coated metallic substrates is measured after metal is bent over onto itself at 180 degrees (0-T bend) using an impact tester. Tape is applied along

the bend using a specified procedure and any coating removal results in failure. Some procedures also call for taping perpendicular to the bend. According to the T-bend procedure, if a sample fails the 0-T bend test, the metal is bent over on itself again (1-T) and the test is repeated until no pickoff is observed. In contrast to the T-bend, a wedge bend sample is tapered and the length of paint pickoff is measured from the narrow end of the bend in one operation. Tinius-Olsen cups are made in a two step operation from blanks of flat sheet to test the effect of a two draw operation on coating adhesion. After formation, cups are taped such that the entire open end circumference is tested and performance is determined by measuring the amount of coating peel in 1/16" increments.

Fabricated product screening tests are conducted to support the development of new surface treatments and coatings for the container industry. A widely used technique is a simple electrochemical method which measures metal exposure after fabrication and is commonly known as the enamel rater test. Commercial equipment may be purchased to allow testing cans and ends of various sizes employing the same operating principle which involves using a standard electrolyte solution, making contact with the end or can, applying a constant voltage of 6.2 volts, and measuring current flow in milliamperes. [1] Enamel rater equipment is also used to determine the locus of failure by reversing the current flow and watching for gas evolution at failure sites.

The combination of exposure during the filling operation, storage requirements and product characteristics requires the use of adaptations of the above methods to assess process resistance. Acidic products which are packed in a retort fill operation represent a severe service environment for coated cans and ends. Process resistance tests which involve exposing flat sheet or fabricated products to a retort environment (250°F, 15 psi, 30-90 minutes) in a pressure cooker, autoclave, or commercial canner are standard procedures.

DISCUSSION

This section will review the testing described above and will offer an interpretation of the advantages and disadvantages of various methods. Directions for future work will also be discussed.

Crosshatch tape methods are outlined in ASTM D 3359-87 where a numerical rating of 1-5 is assigned as a measure of performance. However, in the aluminum container industry these tests are generally used as pass/fail

methods with any adhesion loss representing a failure. Attempts to utilize a numerical rating system are confounded by the number of variables in the test including the speed and angle at which the tape is removed. In general, crosshatch tape tests are operator sensitive and suffer from the same complications as other peel tests. [2] Crosshatch adhesion tests do offer a significant advantage over more quantitative methods in that they are readily conducted under conditions simulating service such as beer pasteurization conditions and retort fill environments.

One of the primary requirements in the successful development of coil coated products is acceptable adhesion after fabrication. History has shown that there is no substitute for testing an end or a can produced in a commercial operation since the complicated stress distribution developed during fabrication is impossible to reproduce in a screening test. Quality control laboratories supporting coil operations often do not have the capability of producing ends and cans. Thus, the wedge bend test has been utilized extensively as a quality control tool generating evidence that poor performance in this test can be indicative of a production problem. However, this method is not very discriminating and test results may vary widely between facilities. The use of Tinius-Olsen cups to assess coating adhesion in a draw-redraw operation is less widely practiced. The correlation between performance in this test and performance of food cans in service is not very clear. Testing of fabricated cans and ends is always preferred, where possible, and is essential in new product development.

Retort testing offers one of the most challenging types of testing to perform reproducibly and to establish conditions which allow correlation between experimenters in different locations. For example, placement of samples in pressure cookers is important since different results are often obtained when testing samples which are submerged in a test liquid as compared to samples which are exposed to the vapor phase of the test liquid. The selection of test liquids which correlate with conditions of service is also important. How relevant is exposure to a 5% (v/v) solution of acetic acid to performance of most beverage products? A striking case of lack of correlation of crosshatch tape results after exposure to a retort at 250°F for 90 minutes involves attempts to compare exposure in laboratory pressure cookers to exposure in commercial canning equipment. The commercial canning equipment provides a much more severe environment due to direct steam impingement on samples and the introduction of cold water during the quenching operation. Laboratory tests which produce conditions simulating those obtained in the

commercial canning test equipment are more discriminating than those carried out in pressure cookers.

The enamel rater methods represent an example of the use of a simple D. C. electrochemical method to assess performance in container applications. Other electrochemical tests have potential for providing additional information about mechanisms which result in performance differences. Electrochemical impedance spectroscopy (EIS) has the potential to provide performance data in testing spanning hours or days which may possibly be correlated with shelf pack data. [3,4] However, caution must be exercised to design relevant experiments which are representative of service conditions and not to oversimplify the interpretation of test results. A popular method of correlation is to attempt to relate the impedance at the low frequency limit with packed product shelf life. At this frequency limit, the applied A.C. voltage is essentially D.C. and this technique is no different than an enamel rater test. An intermediate level of testing between screening tests and shelf test data must provide more information than is available from qualitative screening experiments or it is not worth the time required to conduct more sophisticated testing.

CONCLUSIONS

A large database of results in screening tests has been developed by suppliers, coaters and customers. Confidence has been built that these results are an indicator of performance in service. Needed improvements in the application of current screening tests include more comparisons between testing conducted at different facilities to minimize variability in test results due to operator and procedural variables. As new applications for coated aluminum are developed, the screening test protocol needs to be modified to reflect new performance requirements. Work needs to be conducted to correlate the results in screening tests to performance in service.

An intermediate level of testing which goes beyond screening procedures yet does not require months or years to complete is needed to enhance future development work. Shortcomings of the current test protocol include difficulty in distinguishing between levels of performance ranging from relatively good to outstanding. While current testing identifies poor performance, no information is obtained about why performance differences exist. In developing new products, the ability to develop an understanding of the influence of chemical/physical changes on performance is critical and more quantitative measures of adhesion are important to achieving this objective.

REFERENCES

1. Wilkens-Anderson Company, 4525 Division Street, Chicago, IL, 60651.
2. N. Aravas, K. S. Kim, M. J. Loukis, Mat. Sci. and Eng., A107, 159 (1989).
3. W. S. Tait, J. Coat. Tech., 61, 57 (1989).
4. J. R. Scully, J. Electrochem. Soc., 136(4), 979 (1989).

BOND STRENGTH OF FRP-WOOD INTERFACE

Julio F. Davalos and Ever J. Barbero
Constructed Facilities Center
West Virginia University, Morgantown, WV 26506-6106

INTRODUCTION

The structural utilization of laminated wood products, such as glued-laminated timber (Glulam), is usually limited by the relatively low bending stiffness and strength of the material in relation to other products like concrete and steel. One potential solution to increase the stiffness and strength of glued-laminated timber products, particularly Glulam, is to reinforce them at top and bottom surfaces with fiber-reinforced composite materials. The study presented in this paper is part of an overall effort concerned with the eventual commercial production of wood-FRP laminates. We selected pultruded FRP as the reinforcing material, because it is the least expensive, continuous fiber, mass-produced, structural composite. We envisioned that the FRP will be bonded to wood laminates with an adhesive compatible with the operating procedures used currently in wood laminating plants. As a result of the proposed manufacturing technique, the selection, qualification, and analysis of the performance of the adhesive are critical.

In addition to sustaining the applied loads, bonded structural components are expected to perform adequately when exposed to the outside environment. Changes in environmental conditions, such as temperature and relative humidity, can significantly affect the durability of bonded assemblies. Therefore, the performance of the bond must be fully characterized before engineering applications can be implemented. In this study, the performance of the selected adhesives is evaluated on small samples, under dry and wet conditions, following a modified ASTM D-905 test procedure. Since actual applications of wood-FRP composites will

involve large components under a variety of loads and environmental conditions, analytical tools are needed to predict in-service behavior of the material.

MATERIALS

The wood material used in this study is Yellow-poplar (*Liriodendron tulipifera*), which is an abundant hardwood species in West Virginia (30 million cubic feet of standing timber), and the composite material chosen is E-glass fiber-reinforced vinylester/polyester composite (FRP) produced by pultrusion. The pultruded FRP composites can be laminated to wood laminates in a Glulam plant. Thus, the motivation for selecting pultruded FRP is the possibility of commercially producing Glulam-FRP beams in current laminating plants using an adhesive compatible with existing production operations. For this reason, three potential wood/FRP adhesives were selected for this study: (1) Resorcinol Formaldehyde (RF) (INDSPEC, Pencolite G1131), which is a wood adhesive; (2) emulsion Isocyanate (ISO) (Ashland, Iso-set WD3-C120/CX 47), which is essentially a crosslinked vinyl emulsion adhesive, and (3) Epoxy (Magnolia Plastics Magnabond 56), a strong FRP adhesive.

BOND STRENGTH

To evaluate the ultimate shear strength, bond-interface integrity, and percent wood failure, the experimental program (Gardner et al. 1994) was organized in three parts: dry shear strength test, wet shear strength test, and a 5-cycle accelerated aging test. All of these tests were performed on shear-block test specimens, as described in ASTM

D-905. The testing program followed most of the guidelines given in ASTM D-905 and some of the guidelines described in ASTM D-1101. To evaluate the significance of the experimental results, the following two requirements given by the American Institute of Timber Construction (AITC) for wood-to-wood bonded interfaces for Glulam were used: (1) a minimum dry shear strength of 1075 psi, and (2) a minimum percent wood failure of 80% under ambient conditions.

MATERIAL PROPERTIES

The equilibrium moisture content of wood with the environment is usually less than 19% by weight. If the FRP composite is bonded to wood at a certain moisture content (e.g. 12%), subsequent variations in moisture will cause shrinkage or swelling of wood. This shrinkage and swelling of wood induces strains and stresses in the wood and FRP substrates. It also results in warping of wood if the grain is oriented at an angle (cross grain) to the geometric longitudinal axis of the sample. Since wood absorbs moisture faster and swells more than the FRP composites, stresses are induced at the interface. That is, wood swelling is constrained by a stiffer FRP composite. The swelling coefficients were measured for radial and tangential directions only, as the longitudinal swelling and shrinking is small and can be neglected when compared to swelling in the other two directions. Samples were cut from selected lumber pieces without any cross grain. Using 12% as the reference equilibrium moisture content, strains were computed from the measured dimension changes due to shrinkage or swelling. Then, a linear regression equation was fit to the data, with strain as the dependent variable and the moisture content as the independent variable. The moisture-strain relationships obtained are:

$$\epsilon_T = 0.0025374 (MC) - 0.0285142$$

$$\epsilon_R = 0.001766 (MC) - 0.017936$$

where, MC is the moisture content.

The following elastic constants are needed to model each layer of the wood/FRP laminate:

three Young's moduli (E_i), three shear moduli (G_{ij}), and three Poisson's ratios (ν_{ij}). The elastic constants for wood were obtained from the literature, and the elastic constants of FRP are obtained by a combination of micromechanics and classical lamination theory. Some of the elastic constants for the composite used in this study were also determined experimentally.

INTERFACIAL STRESSES

To study the effects of moisture changes on the FRP-wood interface, a 3-D finite element modeling of the ASTM D-905 shear block specimen was analyzed using ANSYS. Solid 3-D Brick elements, with 3 degrees of freedom (3 translations) per node, and nine material properties, were used for the model. Applying the average experimental failure loads, the FEM predicts maximum stress values close to the failure shear strength of 1800 psi for Yellow-poplar reported in the literature. Within most of the bond interface region, the FEM stresses obtained by applying the mechanical load that produced failure in the dry test specimens are similar to the FEM stresses obtained by applying simultaneously the moisture and mechanical load that produced failure in the wet samples. These results indicate that the mechanical and moisture load effects can be treated approximately as linearly cumulative (Barbero et. al. 1994.) The stresses computed are closer to the shear strength values in the wood substrate than in the FRP. This result is consistent with the large percentage of wood failure observed in the experimental tests. The analysis performed is not a failure prediction analysis since no failure criterion or failure propagation theory was invoked. However, the FEM stress analysis indicates qualitatively that shear stresses due to swelling mismatch can be predicted with some confidence. Also the FEM analysis results reinforce the experimental results of the shear-block tests, since the stresses predicted are close to reported values for shear strength of Yellow-poplar.

A measure of the correlation between

experimental and numerical results is provided by the ratio of wet strength to dry strength (Table 1).

Table 1. Wet/dry strength ratio, experimental and FEM.

	Average bond strength		Wet/Dry Ratio
	Dry	Wet	
Experimental	1350	721	0.53
FEM Average Stress	1338	754	0.58
FEM Maximum Stress	2039	1190	0.56

The experimental value is computed as the quotient of the average wet failure load over the average dry failure load (wet strength = 53% dry strength). Two numerical values of the dry/wet ratio are computed from the FEM results. First, the quotient of the average stresses predicted by the Finite Element Model for wet and dry conditions. Second, the quotient of the maximum stresses predicted by the Finite Element Model. The FEM stresses for the wet test are obtained by applying the average experimental mechanical load (1442 lb over the wood layer), but without the moisture load. It can be observed that the wet/dry ratios provided by both measures of FEM results (average and maximum) are quite close to the experimental values. Also, the values of dry and wet average bond strength provided by the FEM are quite close to the experimental values shown in Table 1.

CONCLUSIONS

It is shown that the stresses developed due to swelling mismatch of wood and FRP substrates can be predicted by the Finite Element Model. The ratio of wet to dry shear strength of wood-vinylester composite combination can be predicted with confidence by the FE model. The experimental wet shear strength is 53% of the dry shear strength, while the FE model predicts 58% and 56% for maximum and average stresses, respectively. Therefore, we conclude that there is

not much deterioration of the adhesive bond due to moisture loading on the shear-block samples. Also, the FE model consistently predicted stresses in wood close to customary values for wood failure.

ACKNOWLEDGEMENTS

This project was partially sponsored by the U.S. Department of Agriculture, Forest-Service, Products Laboratory (FPL) Grant FP-91-1587 and by West Virginia University (WVU).

REFERENCES

- Gardner, D., Davalos, J. F., and Munipalle, U. (1994), Forest Prod. J., 44(5), 62-66.
- Barbero, E. J., Davalos, J. F., and Munipalle, U. M. (1994), J. Reinf. Plastics, 13(9), 835-854.

FAILURE ANALYSIS AND CHARACTERIZATION OF A PHENOLIC ADHESIVE USED TO BOND BRONZE TO A SULFUR CURED RUBBER

G. J. Dallas, E. Slagowski, W. P. Cheatle and L. Shalkowski
Research and Development Beloit Manhattan
Clarks Summit, PA 18411

Abstract

The phenolic adhesive was used to bond a shotblasted bronze with a sulfur cured rubber. The adhesive serves many purposes. They include adhesive bond strength, durability and separation of the sulfur from the bronze. A variety of analytical techniques were used to evaluate this system. They included electron microscopy, energy dispersive x-ray analysis, differential scanning calorimetry, rheology and butt joints to test the final mechanical properties of the adhesive system. The microscopy revealed that a minimum film thickness must be maintained over the shot blasted surface. The rheology and differential scanning calorimetry were used to identify mechanical transitions during the cure and the extent of cure. Butt joints representative of the above system were made and tested at different film thicknesses and cure profiles. Film thickness was found to have the greatest effect on the adhesive bond strength measurements. A minimum bond thickness of 0.002" was necessary to inhibit sulfur migration through the adhesive during the cure. Below this film thickness sulfur migration occurred and bond strength dropped linearly with film thickness.

Introduction

Roll covers are primarily 1/2 to 1" elastomeric coatings on metal cylinders. This assembly is used in paper machines for squeezing water from the wood fiber water slurry. The roll cover hardness varies, from the beginning to the end of the paper machine, from spongy to glassy material hardnesses. The roll cover that will be discussed is a suction roll. This is a roll cover towards the front end of the paper machine with intermediate hardness. This roll cover had through holes drilled in it with a vacuum assembly inside the shell. Thus, the adhesive zone is exposed to the paper making chemicals.

Electron Microscopy of Adhesive Failure Zone

Objective. Identify the structural similarities between failed bronze suction rolls coated with the phenolic adhesive.

Experimental. The samples were from failed suction rolls that ran in paper machines. The cross section was prepared by cutting the sample and sanding it smooth and finishing with 1200 grit sand paper.

A Jeol 35 C electron microscope was used in the backscattered electron imaging mode to analyze for elements of different electron density. In particular, this method was used to analyze for metal that may have migrated through the adhesive. Also, EDAX analysis was done to map the failure surface and cross sections for the elements sulfur and copper.

Results and Discussion. Electron microscopy was done on adhesion zones between bronze shell and the sulfur cured base layer. The phenolic adhesive bond line thickness was the primary focus. The cross section was photographed and a representative micrograph is shown in figure 1. Figure 1 focused on one zone where a bronze shot blasted peak nearly protruded through the phenolic adhesive. Only the relief of the bronze peak was visible in the adhesive since the debond was between the bronze and the adhesive. The film thickness over the peak was less than 0.0005". This film thickness of 0.0005" was also identified by other researchers at IBM and Lehigh as the minimum film thickness necessary to protect copper coated with epoxy and poly(methylmethacrylate) from corroding.^{1,2} Lower magnifications showed that the film thickness ranged from 0 to 0.004". The distinguishing feature of this backscattered micrograph was the dendrite (snowflake like) structure in the next adhesive layer. This dendrite was analyzed by x-ray analysis and identified as copper. This meant that at these film thicknesses the copper could migrate through the adhesive and the bronze surface was not protected from interacting with the next sulfur cured adhesive layer. This micrograph also showed the copper could not migrate through at the thicker levels of phenolic adhesive.

Conclusions. The necessary structure for a successful adhesive zone occurred when the bronze peaks were completely separated from the next sulfur cured adhesive layer or the minimum phenolic coating thickness was greater than 0.0005". A common film thickness among failed suction rolls was the average film thickness was less than 0.002"

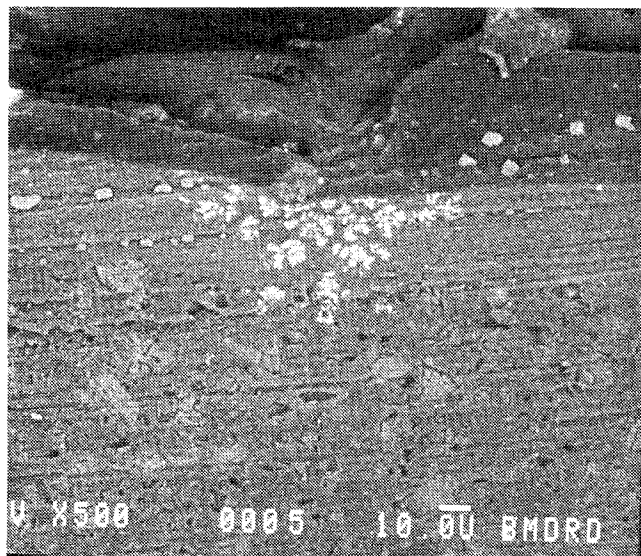


Figure 1 is a backscattered electron image of the cross section of a failed adhesive zone at 500X.

Characterization Rheology and Calorimetry

Objective. The objective of the calorimetry and rheology was to identify the cure conditions of the phenolic resin. The intent was to reduce the prebake cure cycle by increasing the processing temperature and reducing the cure time and also to insure the adhesive had gelled so it would maintain its dimensional stability through the rest of the processing steps.

Experimental. The rheology was done on a Rheometrics RDS II rheometer with either isothermal or sweep temperature conditions. The experiments were done with the 50 mm parallel plates. The strain used was 80% for the sweep temperature and 20% for the isothermal runs. A heating rate of 5°C/min was used with the sweep temperature experiment. The isothermal experiments were done at temperature 70, 75, 80, 85 and 90°C.

The differential scanning calorimetry was done on a Perkin Elmer DSC 7 in the sweep temperature mode from 40 to 250°C at 5°C/min. An uncured sample of the phenolic resin was used as a reference for the size of the exotherm. The other samples were from the isothermal rheometer experiments and the size of the residual exotherm was ratioed to the uncured material to determine percent conversion versus isothermal cure conditions.

Results and Discussion. A comparison of shear modulus versus time for the isothermal cure conditions listed above was obtained. Within each curve was an upward transition. This transition indicated when the phenolic had either gelled, formed a three dimensional network or turned to a glass. This transition was used to mark when the reaction was complete for that temperature. This data

showed that the transition could be reduced from 10 hours at 70°C to 2 hours at 90°C, with 80°C taking approximately 5 hours. The calorimetry was done to determine the extent conversion.

The differential scanning calorimeter was used to determine the extent conversion for each isothermal run. The extent conversion to form a three dimensional network for a phenolic assuming it was trifunctional is 50% [3]. A three dimensional network is important because this means that there would be dimensional stability of the adhesive during the rest of the processing steps. Table 1 shows percent conversion for each of the isothermal runs.

Table 1
Extent Conversion for Various Cures

Temperature/time	% Conversion
70°C for 16 hours	30 reference
75°C for 16 hours	35
80°C for 10 hours	35
85°C for 6 hours	50 preferred
90°C for 6 hours	50 preferred

Conclusions. The rheology experiments showed that the cure temperature could be increased from 70°C to 90°C and the reaction time reduced from 10 hours to 2 hours. The DSC data showed that not only do the higher temperatures make the reaction proceed more quickly they push the reaction to higher percent conversion. All of the tests above 80°C resulted in conversions near 50 percent. So, the elevated temperature of 85°C for 5 hours was used for the following jig experiments.

Jig Pulls

Objective. The jig pulls were conducted to determine the effect of the average adhesive film thickness on the jig's yield stress.

Experimental. The jig pulls were done with two bronze 1N butt joints. Each was approximately 2 inches in diameter and 1 1/4 inches in length. The jig side was shot blasted with GS 25 steel shot. The surfaces were cleaned with ethanol before the first coat of the phenolic adhesive. Forty to sixty minutes elapsed before the first brush coat of the phenolic adhesive. A total of four coats of adhesive were used. A drying time of 40 to 50 minutes was used between each coat. Another wait of 40 to 60 minutes was used before the one coat of a sulfur cured adhesive. Again, another wait of 40 to 60 minutes elapsed before

they were placed in the oven at 85°F for 5 hours. Three more coats of the sulfur cured adhesive were applied. The jig halves were used to sandwich two 1/8" disks of 50/50 hexane/toluene washed cookies of uncured sulfur containing hard base material. They were then put in stainless steel jig holders and vulcanized for 5 hours at 280°F. The jigs were tested on an Instron 4507 at 0.2"/min at room temperature.

Results and Discussion. The data in figure 2 showed that the jig pull yield stress was dependent upon average phenolic film thickness. These values were an average of 7 or 8 jig pulls. The errors shown were for two standard deviations. A critical film thickness of 2 mils was identified as the average film thickness necessary to have good bond strength. X-ray chemical analysis of other failed jig surfaces showed that sulfur products were formed at film thickness less than 2 mils. The error in the thickness

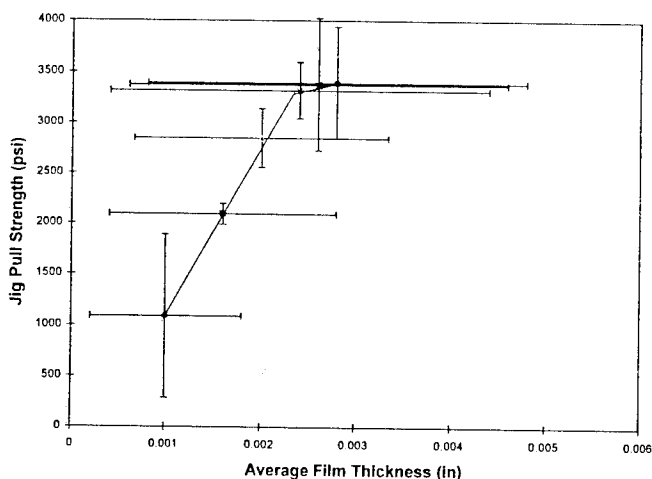


Figure 2 is a plot of jig pull yield stress versus average adhesive film thickness.

direction shows that no matter how many brush coats were applied there would always be spots that had thin zones.

Conclusions. Thus, the jig pull experiments were primarily film thickness dependent. Above a certain film thickness sulfur migration was stopped and maximum bond strength was reached.

Surface Roughness

Objective. Determine how the surface roughness of the shot blasted bronze surface related to adhesive film thickness.

Experimental. A Sunnen model SP301 was used to determine surface roughness; 8 mm and 2.5 mm stroke lengths were used. The 2.5 mm stroke length was used for Ra and Rq. The 8 mm stroke length was used for Rz and Pc.

Results and Discussion. The surface roughness ranges varied for the Ra average from 0.53 to 0.57 mils, Rq root mean square from 0.67 to 0.75 and the Rz average of the five most extreme peaks and valleys from 2 to 3.8 mils. This structure occurred with a frequency of 66 to 99 peaks per centimeter.

Conclusions. Thus, the cross sectional peak height of the shot blasted bronze ranged from 2 to 3.8 mils and a minimum 2 mil average film thickness, measured from the center line of the roughness profile, would insure the 0.5 mil of adhesive over the shot blasted peaks.

References:

1. Atkinson, J. M., Journal of Research and Development; vol. 29 , no. 1 1985.
2. Granata, R. D., A Journal of Coatings Technology; vol. 60, no. 763, 1988.
3. G. Odian, Principles of Polymerization (Wiley Interscience, New York, 1981), p. 117.

EFFECT OF CONTAMINATION AND ROUGHNESS OF STAINLESS STEEL ON THE ADHESIVE BONDING WITH A SILICONE ELASTOMER

M. Mantel⁺*, N. Shephard⁺, J. P. Wightman⁺

⁺Department of Chemistry, Center for Adhesive and Sealant Science,
Virginia Polytechnic Institute & State University, Blacksburg, Virginia 24061 USA

*on leave from Uginge Research Center, Uginge-Savoie, France

INTRODUCTION

The aim of this work is to measure the adhesion between stainless steel and a silicone sealant and to correlate fracture mechanics data obtained in air and in water with the organic contamination of the surface. We have also taken into account the roughness since all cleaning treatments will not only affect the contaminant layer, but also the roughness of the oxide film. Two surface treatments and two cleaning treatments were performed on the stainless steel to produce a different level in micro roughness and contamination. A polydimethylsiloxane was the adhesive used in order to get interfacial failures with the steel substrate. Fracture mechanics data were obtained using a 45° peel test. After peeling the samples, the steel substrates were analyzed using ESCA analysis and atomic force microscopy (AFM) in order to provide chemical and topographical information of the interfacial failure.

EXPERIMENTAL

Materials

AISI 304 stainless steel foils have a 1 mm thickness after cold rolling and annealing at 1000 °C in a N₂+3H₂ atmosphere. This annealing treatment is usually called "Bright Anneal". Under these conditions, no thick oxide scale is formed. Instead a thin passive film forms with a surface roughness of 0.02 µm. The other surface treatment performed on the samples is called "Mirror Finish" and consists in polishing the surface in

order to obtain a very smooth surface. The surface treatments and cleaning procedures are described in Table 1. The argon plasma treatment were carried out in a March I unit.

DESCRIP.	SURF. TREAT.	CLEANING TREATMENT
304 B. A.	Bright Anneal	water: rinsing in distilled water.
304 M. F.	Mirror Finish	Ar plasma: Ar plasma (50W 10min).

Table 1 Surface and cleaning treatments

45° Peel Test

Peel specimens were prepared with 12.5 mm width, 2 mm thickness and 6 cm length. A 12.5 mm wide nylon/cotton ribbon sized with γ-aminopropyltriethoxysilane was used to reinforce the peel specimens. The cure time of the PDMS sealant was greater than 21 days at ambient conditions for all samples. The crack growth rate is measured as a function of load and environment conditions. The samples were measured in air and under water immersion at room temperature.

ESCA surface analysis

ESCA analysis was performed using a Perkin Elmer PHI 5400 spectrometer employing a Mg K_α (1253.6 eV) achromatic X ray source operated at 15 kV with a power of 400W.

Atomic Force Microscopy

With a soft cantilever that generates forces smaller than inter-atomic forces, the topography of the sample can be measured without displacing the

atoms. The surface images were obtained from a Nanoscope III AFM (Digital Instruments) with a silicon nitride tip.

RESULTS

A) SUBSTRATE

The ESCA analysis of the steel samples indicated the presence of carbon, oxygen, chromium, iron, and nickel. Carbon comes from the organic contaminant layer and is significantly reduced by the Ar plasma treatment as seen in Figure 1.

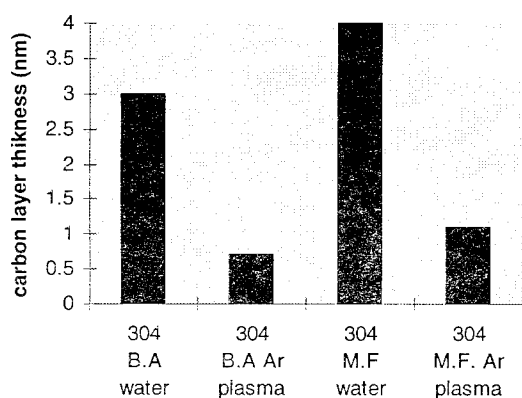


Figure 1 Organic contaminant layer thickness (nm) for different surface treatments

The small difference found between the "Bright Anneal" and the "Mirror Finish" sample can be due to the roughness that possibly affects the adsorption of contamination. Oxygen comes mainly from the oxide/hydroxide passive film and is also associated with carbon in the organic contaminant layer for the "water" samples (1). Chromium and iron are combined with oxygen in the passive film and also comes from the metal underneath for the Ar plasma treated samples.

B) INTERFACE

The observation of significant amounts of silicon using ESCA analysis is due to the presence of polymer on the metal substrates although the sealant appeared visually to have pulled away

from the stainless steel surface. The AFM images of the steel substrates before and after delamination are given in Figure 2 and 3. For the "Mirror Finish" sample an increase of the roughness is observed in Figure 2 after the delamination and the surfaces exhibit large strips. These large strips can be attributed to the sealant as shown with ESCA measurements of the silicone content. The "Bright Anneal" sample that exhibited a rougher surface shows in Figure 3 a very different failure surface. After delamination the roughness has decreased and images suggest that the polymer has filled the "valleys" of the substrate.

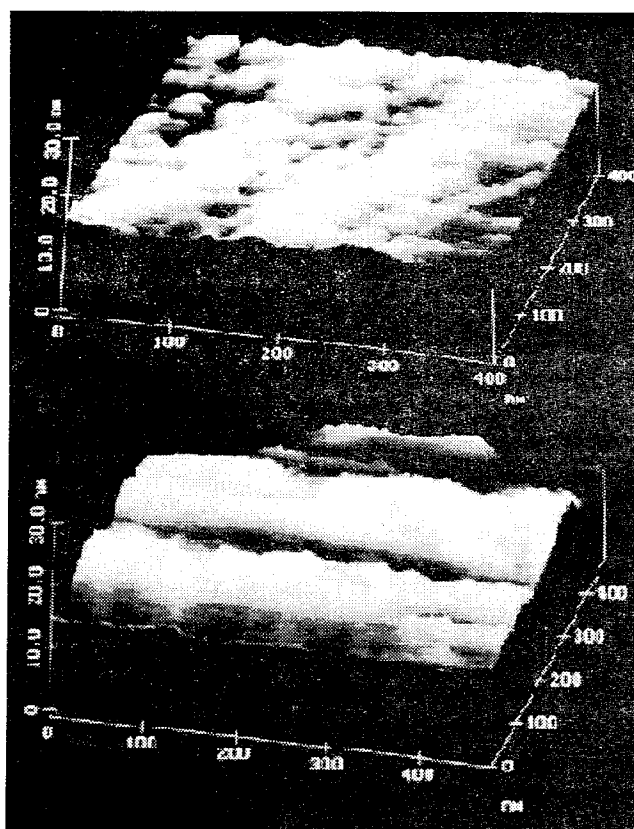


Figure 2 AFM images for the "Mirror Finish" sample after peeling in air (a top) before delamination (b bottom) after delamination.

DISCUSSION

We have plotted on Figure 4 the fracture energy at a peeling rate of 10^{-7} m/s as a function of the

contaminant layer thickness measured with XPS before bonding the steel substrates with the silicone elastomer. For all the samples, contamination results in a lower fracture energy.

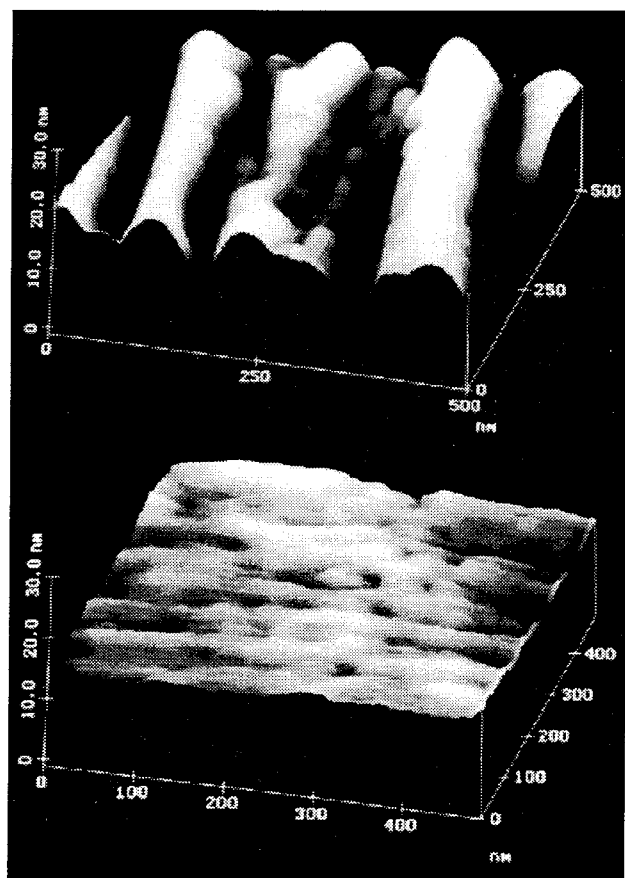


Figure 3 AFM images for the "Bright Anneal" sample after peeling in air (a top) before delamination (b bottom) after delamination.

This result can be understood with the different analysis of the substrate before and after peeling. First, it is shown that the silicone adhesive we have used is unable to displace or to ingest the organic contamination present on the substrate before bonding. As the surface energy is strongly reduced by this contamination, it will be difficult for the adhesive to achieve acceptable surface wetting. We have measured more silicon on the surface after peeling the rougher sample. It seems on AFM images that the fracture occurs above the

roughness and that the roughness can prevent the polymer to be totally peeled out from the substrate. As a result, a higher fracture energy is measured on the 304 B. A.

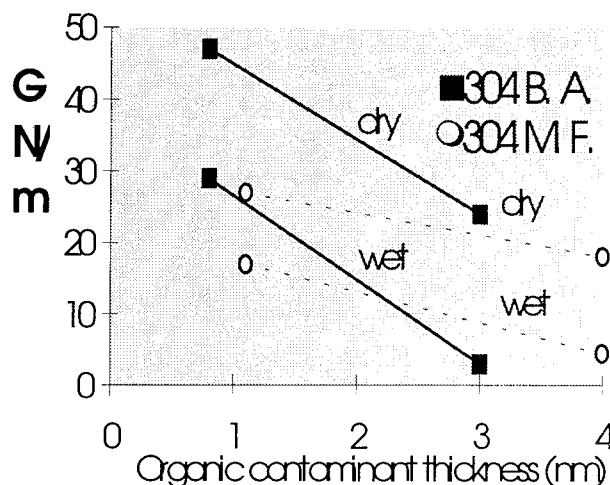


Figure 4 Fracture energy (N/m) as a function of organic contaminant thickness

The decrease in the adhesive bonding due to the contamination is more pronounced for the rougher substrate (Bright Anneal) than the smoother (Mirror Finishing). It means that the positive influence of the roughness decreased when contamination is present on the surface. The effect of water is to decrease the fracture energy measured on all the samples. ESCA measurements show that the silicone content is always less after peeling the samples in water than in air. As the passive layer should not be significantly affected by the water, the decrease of the peel strength in water is possibly due to a desorption of the organic adhesive at the interface attributed to an hydrolysis phenomena. It is interesting to plot the fracture energy for the different samples as a function of the silicone content left on the surface after peeling.

We can see on Figure 5 that the fracture energy increases with the PDMS thickness calculated from ESCA measurements. This increase of the PDMS film left on the substrate is like going from a pure adhesive failure to a cohesive one. We have

measured the fracture energy for a cohesive failure in the sealant and a value of 220 N/m was found. This value is in good agreement with the bulk fracture energy reported by Mazich, Yanyo and Gent [2-4].

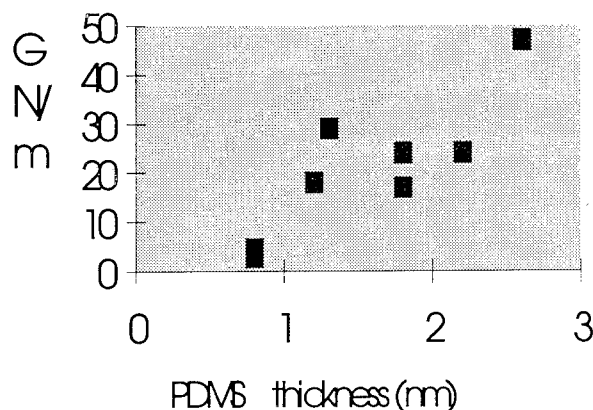


Figure 5 Fracture energy (N/m) as a function of the PDMS film thickness left on the surface after peeling.

If we assumed a linear relationship between the fracture energy and the PDMS thickness, we can extrapolate the value of the PDMS thickness corresponding to a fracture energy of 220 N/m. A value around 12 nm is found. This value can be taken as the size of the plastic zone during the crack growth and is also nearly equivalent to the distance between cross links.

CONCLUSIONS

- When the fracture is in the interphase, the fracture energy is proportional to the amount of PDMS left on the surface. The size of the plastic zone is nearly equivalent to the distance between cross links.
- Contamination is still present after peeling the sealant from the stainless steel substrate.
- Roughness increases the fracture energy and this effect is more pronounced when the surfaces are clean.

Acknowledgment

The authors acknowledge the financial support of this research by Ugine (France) and the Dow Corning Corporation. Additional support of this research by the Center for Adhesive and Sealant Science at Virginia Polytechnic Institute and State University is also acknowledged. The authors would like to thank Dr Y. I. Rabinovich for his expertise with the AFM.

REFERENCES

1. Mantel, M., Whightman, J.P., *Surf. Interface Anal.* **21**, 595-605 (1994)
2. Mazich, K. A. and Samus, M. A., *Macromolecules*, **23**, 2478 (1990)
3. Yanyo, L. C, Kelley, F. N., *Rubber Chem. Technol.*, **60**, 78 (1987)
4. Gent, A. N., Liu, G., *J. Adhesion*, **38**, 79 (1992).

EFFECT OF ELECTRODEPOSITION OF POLYAMIC ACID ON THE SURFACE PROPERTIES OF CARBON FIBERS

J. O. Iroh and W. Yuan; Department of Materials Science and Engineering, University of Cincinnati, Cincinnati, Ohio 45221-0012

INTRODUCTION

The nature of the surface of carbon fibers is of considerable relevance to the performance of fibrous composites. Even though carbon fibers possess numerous attractive properties, they are poorly wetted by the polymer matrix, resulting in low interlaminar shear strength of the composite. Tremendous efforts have been devoted so far on the modification of carbon fiber surface [1-3]. The purpose of surface treatment is to enhance the adhesion to the polymer matrix. However, one of the disadvantages of this approach is that the improvements in the interlaminar shear strength is attained at the expense of reduced impact strength. The strategy of surface coating is to insert a suitable polymer interlayer between the carbon fibers and the polymer matrix and use its properties to control the level of fiber/matrix adhesion [4-6]. In this paper the property changes that occur in carbon fibers as a result of electrodeposition of polyamic acid is reported. By adopting the electrodeposition process as a surface coating technique, it is easy to control the thickness and functionality of the coatings through selective control of processing parameters such as the solvent/precipitant ratio, acid/base ratio, solid content, current density, and pH of the medium.

EXPERIMENTAL

Unsize but surface oxidized Thornel T-650/35 and T-300 carbon fibers, from Amoco Performance Products, Inc., were used in this study. The PI2545 polyamic acid, which was prepared from pyromellitic dianhydride (PMDA) and 4,4'-oxydianiline (ODA), was obtained from E.I. DuPont de Nemours & Co. The polyamic acid was dissolved in N-methyl-2-pyrrolidone (NMP) with a solid content of 13.4%. Reagent grade dimethylformamide (DMF), triethylamine (TEA), methanol, hexadecane and formamide were purchased from Fisher Scientific Co. and Aldrich Chemical Company and used as received.

The surface properties of the coated and non-coated fibers were studied by scanning electron microscopy (SEM) and dynamic contact angle analysis (DCA).

Electrodeposition

A single carbon fiber tow was wound onto a H-shaped polypropylene frame which was covered at

both ends with aluminum foil to increase conductivity. The aluminum foil was cleaned of grease and dirt with methanol and then left in the hood for 30 minutes before it was wrapped on both ends of the frame. The frame bearing the single carbon fiber bundle was connected to the positive terminal of the Potentiostat and served as the anode. The cathode was made up of two stainless steel plates (153 x 38 x 1 mm³). Electrodeposition was carried out chronopotentiometrically. A constant current of 50 milliamperes was applied to the electrochemical cell for 1 minute. Emulsion for the electrodeposition is composed of the following: a solid content of 1 wt %, P/S ratio of 3.5:1.0, and TEA/COOH mole ratio of 1:1. The coated fibers were withdrawn from the solution immediately after electrodeposition and left to dry in the hood overnight. The coating was finally dried to constant weight at 100°C.

Dynamic Contact Angle Analysis (DCA)

All the DCA measurements were carried out with the Cahn's DCA-322 system based on the Wilhelmy technique. The uncoated and coated single fiber was first cut to about 15 - 20 mm in length. Tape was placed at one end to increase the clamping area. The fiber was then hung on the electronic balance through a clamp. The DCA analysis was performed at a speed of 20 microns/second, with hexadecane, deionized water and formamide, respectively as the wetting medium.

RESULTS AND DISCUSSIONS

Scanning Electron Microscopy (SEM)

Figures 1 & 2 show the SEM micrographs of fibers before (Figure 1) and after electrodeposition (Figure 2). The surface of the coated fibers appears quite smooth. Note the presence of longitudinal striations on the uncoated fibers (Figure 1). These striations occur during the manufacture (spinning and the surface oxidation) of the fibers. It was reported that surface treatment of fibers increase the latter's surface roughness by pitting and increased longitudinal striations [1].

The fibers are effectively covered by uniform polymer film. As the polymer film is formed, the increased electrical resistance of the coatings direct further film formation to uncoated area which are more conducting, enabling a uniform film to be built up free of pin holes. Note that the diameter of the single non-coated fiber increased from about 7 μ , to about 100 μ (Table 1) for the coated fiber. This observation suggests that the polymer coatings formed is not completely insulating and that film formation is not self-limiting. The freshly deposited polyamic acid is highly swollen, porous and conductive and permits subsequent deposition of polymer coatings directly onto conductive fiber

preform. This is especially useful when high resin volume fraction composites are desirable. Note that it is not easy to fabricate high resin content prepreg from the wet and hot melting techniques.

Surface Energy Analysis

The average values of the γ^P , γ^D , and γ^T for the non-coated T-650/35 and T-300 single fibers are about 50 mJ/m² and 60 mJ/m² respectively. The difference in γ^T of the T-650/35 and T-300 single fibers can be traced to their γ^P values. The average value of γ^P of the noncoated T-300 fiber is higher than that for the non-coated T-650/35 fiber, indicating that the T-300 fiber may have more polar chemical functional groups on the surface. The corresponding γ^T values for the coated T-300 and T-650 fibers are 52 mJ/m² (table 1, bottom) and 39 mJ/m² (table 1, top) respectively, which is about 13% and 22% lower than that for the non-coated fibers. This lowering of the γ^T values of the T-650/35 and T-300 fibers coated under the same conditions, seems to originate from their γ^D and might be due to the interaction between the wetting medium (formamide) and the deposited polyamic acid film or the difference in the orientation of the polyamic acid chains on the carbon fiber surface.

The surface energy of the T-650/35 and T-300 single fibers are compared in Figures 3 & 4. The γ^D , γ^P and γ^T for both fibers decreased after electrodeposition. Note however, that the γ^D for T-300 fiber increased after electrodeposition. The average values of the surface energies for the coated T-650/35 single fibers may represent the surface properties of polyamic acid coatings.

CONCLUSION

Electrodeposition of polyamic acid films onto carbon fibers was performed galvanostatically from non-aqueous emulsions. The surface morphology of the coatings is smooth, uniform and continuous. The diameter of the coated single fibers increased from 5.7 μ to about 100 μ , showing that high resin volume fraction in-situ composites can be formed by this technique.

The surface energy of the coated and non-coated fibers are in the range of the values reported for fibers modified by oxidative treatment. The average value of the polar component of the surface energy of the non-coated T-300 fiber is higher than that of the non-coated T-650/35 fiber. This suggests that the T-300 fibers possess more polar chemical functional groups on the surface. The total surface energy and the polar component for both fibers were found to decrease after the electrodeposition of polyamic acid.

ACKNOWLEDGMENT

This research was supported by the Engineering Foundation's "Engineering Research Initiation Grant RI-A-92-13

REFERENCES

1. D. Clark, N. J. Wadsworth and W. Watt, "The Surface Treatment of Carbon fibers for Increasing the Interlaminar Shear Strength of CFRP", in Proc. 2nd Carbon Fiber Conference, The Plastics Institute, London, pp44 (1974).
2. P. Ehrburger and J. B. Donnet, Carbon, 11, 309 (1973).
3. E. Fitzer and R. Weiss, "Surface Treatment of Carbon Fibers", in Processing of Carbon Fiber Reinforced Plastics, VDI-Verlag, pp45 (1981).
4. M. Kodama, I. Karino, and J. Kobayashi, J. Appl. Polym. Sci., 33, 361 (1987).
5. Y. Z. Wei, Z. Q. Zhang, Y. Lin, Z. H. Guo, and B. L. Zhang, Controlled Interphases in Composite Materials, H. Ishida, ed. Elsevier Science Publishing, New York, pp167 (1990).
6. R. C. Cochran, B. Okhuysen, R. E. Allred and T. M. Donnellan, "Interphase Studies in Polymer Matrix Composites", Proc. 16th Annual Meeting of the Adhesion Society, ed. F. J. Boerio, pp38 (1993).

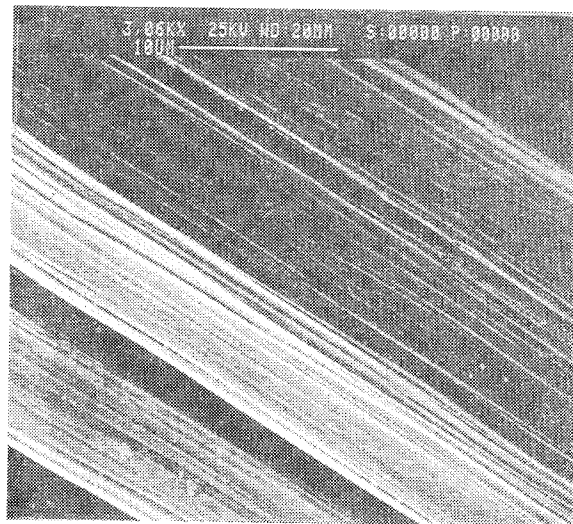


Figure 1. SEM micrographs of non-coated T-650/35 carbon fibers.

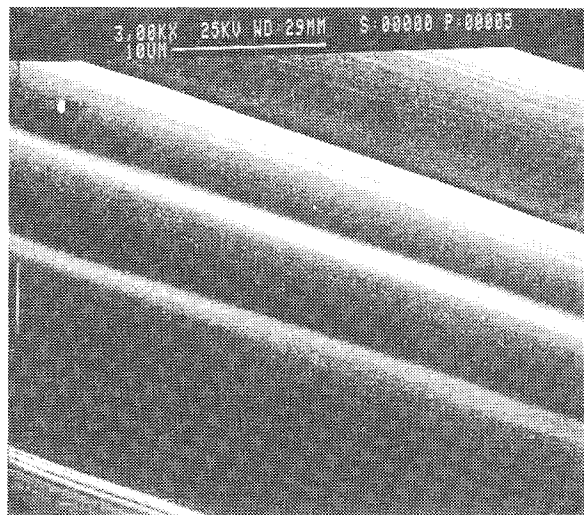


Figure 2. SEM Micrograph of T-650/35 fibers coated by electrodeposition of polyamic acid.

S/N	Diameter (mm)	γ^P (mJ/m ²)	γ^D (mJ/m ²)	γ^T (mJ/m ²)
1	151.8	9.96	28.81	38.76
2	136.4	13.17	24.18	37.35
3	121.8	18.36	17.48	35.84
4	102.2	19.08	28.00	47.08
5	129.7	12.37	23.60	35.97
Average	128.4	14.59	24.41	39.00
Std Dev	18.3	3.96	4.50	4.67

S/N	Diameter (mm)	γ^P (mJ/m ²)	γ^D (mJ/m ²)	γ^T (mJ/m ²)
1	134.8	13.30	43.20	56.50
2	124.4	21.97	25.68	47.65
3	136.5	16.08	22.11	38.19
4	104.4	5.81	68.49	74.30
5	180.1	9.59	32.90	42.50
Average	136.0	13.35	38.48	51.83
Std Dev	27.7	6.18	18.61	14.29

Table 1. Solid surface energy of T-650/35 (top) and T-300 (bottom) carbon fibers (Hamonic-mean method) coated with polyamic acid.

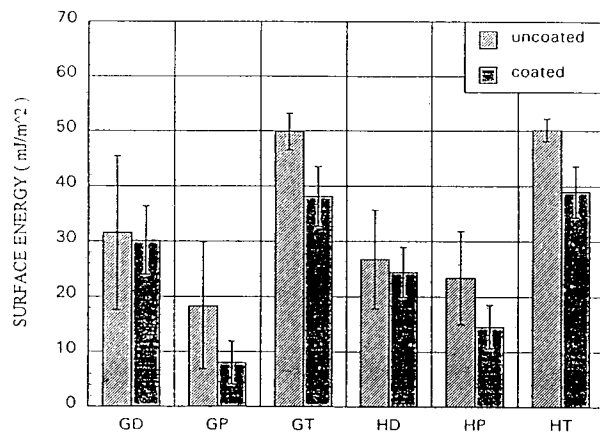


Figure 3. Comparison of the surface energy of the T-650/35 carbon fibers; D = dispersive, P = polar, T = total, G = geometric mean method, H = harmonic mean method.

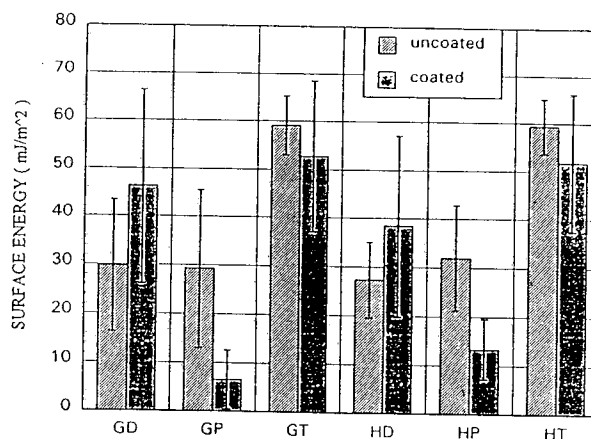


Figure 4. Comparison of the surface energy of the T-300 carbon fibers; D = dispersive, P = polar, T = total, G = Geometric-mean method, H = Harmonic-mean method.

BOND CHARACTERISTICS AT PIGMENT-POLYMER INTERFACES

J. Lara-A., Shu-de Rong and H.P. Schreiber

Department of Chemical Engineering, Ecole Polytechnique
PO Box 6079, Stn. Centre-Ville, Montreal, QC. H3C 3A7, Canada

Pigment dispersions in polymer solutions are important parts of the technology involved in the protective films industry. Dispersion stability in non-aqueous media depends on the architecture of polymer chains adsorbed on pigment surfaces [1], and this in turn depends on the balance of forces acting at the solid/liquid interface. The present paper examines the apparent roles of dispersive and non-dispersive interactions in the behavior of pigmented polymer solutions.

EXPERIMENTAL

The materials used in this research are shown in Table 1. The polymers include low density polyethylene (LDPE), a polymer interacting through dispersive (L/W) forces only; a basic ethylene-vinyl acetate copolymer (EVA, 28mole% VA) and an acidic chlorinated PE (CPE). Three variously coated rutiles, a monastral green colorant, and acid washed Chromosorb chromatographic support, were the dispersed phases. Inverse gas chromatography, frequently described in the current literature [2,3,4], determined the dispersive surface energies, (γ^d), and the acid/base interaction constants, K_a and K_d of the materials. Surface areas were obtained from BET experiments with nitrogen as the adsorbing gas. Experimental K_a and K_d data were used to compute acid/base pair interaction parameter values, I_{sp} , from:

$$I_{sp} = (K_a)_1 \cdot (K_d)_2 + (K_a)_2 \cdot (K_d)_1$$

the subscripts representing polymer and pigment components.

To evaluate the strength of bonds at the pigment/polymer interface, solvent extraction

was performed on pigments with known amounts of adsorbed polymer. Accurately weighed amounts of pigment with known adsorbed polymer were placed in a Soxhlet apparatus, and eluted under reflux with excess distilled p-xylene for up to 7 h. Aliquots of solutions were analyzed periodically for dissolved polymer. Plateau values of adsorbed polymer were obtained from Langmuir-type isotherms for pigment/polymer combinations, following the procedure of Lara and Schreiber [5]. In this, varying amounts of pigment were added to 20 mL of 1.00 wt.% polymer solutions in trichloro benzene (TCB) at 125°C and agitated for up to 6 h. The dispersions were centrifuged and the quantity of adsorbed polymer was estimated from analyses of aliquots of the clear supernatant solutions.

Experiments on dispersion stability used samples prepared by tumbling on a roll mill 10 wt.% pigment in 60 mL of 0.5 wt.% polymer solutions in TCB. Stainless steel balls (300g, 0.4 cm. diameter) were used as grinding medium and the dispersion period was 48 h. Dispersions were placed in graduated 10 mL tubes and the kinetics of deposition were followed for up to 1 week. Finally, the solutions were clarified fully by centrifugation and the volume of pigment sediment was recorded.

RESULTS AND DISCUSSION

The adsorption isotherms for pigment/polymer combinations uniformly were of the Langmuir type, and attained constant values of adsorbed polymer. The quantity of adsorbate varied considerably, however, as shown in Table 2.

Plateau values appear to be related to both the I_{sp} parameter, entered in the table, and to the surface energy of the solid. With LDPE adsorbate no acid/base interaction can take place, and plateau values on the three rutile adsorbents and on MG, are constant. A much lower value is obtained for Chromosorb, a solid with a lower $(\gamma)^d$ (see Table 1). Similarly, combinations of acidic or basic pigments and polymers (EVA/R-3 and CPE/R-2) lead to relatively low adsorption quantities, due to the tendencies of the polymers to associate with the solvent. This effect agrees with observations by Fowkes [6]. Also in accord with Fowkes, in acid/base pairs the favorable interaction balance produces higher values of plateau adsorption. In all present cases, multilayer adsorption is assumed to occur, in light of the copious amounts of available polymer.

Removal of adsorbed polymer by solvent extraction follows different paths among the pigment/polymer combinations. Initial loss rates were essentially constant, regardless of the interaction at polymer/pigment contacts. Adsorbed layers distant from the adsorbing surface seem unaffected by the presence of the solid. When L/W forces predominate (including acid/acid or base/base pairings), removal by p-xylene was close to total following ~90 min. elution, but significantly lower quantities of polymer were recovered when acid/base combinations were eluted. Evidently, the adsorbed layers close to the surface are retained by forces exceeding those of the solvating power of p-xylene under reflux. Statistical analysis gave a correlation coefficient of 0.989 between equilibrium values of eluted polymer and the I_{sp} parameter, so that these forces may be assigned to electron donor/acceptor exchanges.

The stability of pigment dispersions depends on the architecture of the adsorbed polymer

molecule as well as on the adsorbed mass. Both weak and excessively strong interfacial bonds may lead to instability due, in one case, to entanglement of adsorbed chains and flocculation, and in the other case to a collapse of the polymer molecule around the particle perimeter with agglomeration the result. Stabilization is conferred when the polymer molecule adsorbs at several particle sites and creates an entropic barrier several 10^2 \AA thick [1]. In the present work all of the solids with adsorbed LDPE deposited in periods that ranged from 4-5 h for the rutiles and chromosorb, to ~ 16h. for the high surface area MG colorant. Acid/acid and base/base combinations similarly led to solids deposition in periods that ranged from 3 - 12 h. In acid/base combinations, large variations were observed: For example, the system MG/CPE ($I_{sp}=3.7$) produced a large sedimentation volume in about 10h. The strongly interacting R-3/CPE combination ($I_{sp}=35$) produced a small volume in some 6 h, but systems such as R-1/CPE, R-3/EVA with I_{sp} values in the 20 range resulted in dispersion stability over period exceeding 7 days' observation. The qualitative conclusion is reached that preferred architecture of adsorbed polymers is attained when the acid/base forces at the interface fall into the range of $\sim 10 < I_{sp} < \sim 30$.

REFERENCES

- [1] D.H. Napper, Ind. Eng. Chem. Prod. Res. Dev. **9**, 467 (1970)
- [2] C.Saint-Flour and E. Papirer, J. Colloid Interface Sci. **91**, 69 (1983)
- [3] D.G. Gray, Prog. Polym. Sci. **5**, 1 (1977)
- [4] U. Panzer and H.P. Schreiber, Macromolecules **25**, 3633 (1992)
- [5] J. Lara, A. and H.P. Schreiber, J. Coatings Tech. **63**, 81 (1991)
- [6] F.M. Fowkes, J. Adhesion Sci. Tech. **1**, 7 (1987)

Table 1: Characterization of Experimental Materials

Material:	Surf. Area (M ² /g)	(γ_s) ^d (mJ/M ²)	Ka	Kd
Rutile R-1	9.0	45.5	3.1	3.9
Rutile R-2	8.6	44.2	5.2	1.8
Rutile R-3	10.3	50.1	3.0	5.7
Mon. Green	55	42.6	1.6	0
Chromosorb	1.1	32.5	0.9	0.3
LDPE	-	31.0	0	0
EVA	-	33.6	1.7	4.4
CPE	-	32.8	5.0	2.3

Table 2: Plateau Adsorption and Isp Values for Polymer/Pigment Pairs

Polymer:	LDPE		EVA		CPE	
Solid:	Ads. (mg/M ²)	Isp	Ads. (mg/M ²)	Isp	Ads. (mg/M ²)	Isp
Rutile R-1	2.37	0	3.11	20.2	2.95	26.6
Rutile R-2	2.28	0	4.25	26.0	2.17	21.0
Rutile R-3	2.57	0	1.90	22.9	3.72	35.4
Mon. Green	2.45	0	1.18	7.0	1.02	3.7
Chromosorb	1.20	0	1.06	4.5	0.93	3.5

Abel, M - 209
Agrawal, R - 285
Ahmadi, G - 230
Alsheh, D - 252
Anders, A - 149
Anders, S - 149
Anderson, G - 129
Andruet, R - 45
Antonucci, J - 310
Apai, G - 132
Arribart, H - 275
Ashcroft, I - 141, 143, 258
Atkinson, K - 77
Azzopardi, M - 275
Babaj-Cline, M - 151
Baborowski, J - 79
Bao, G - 316
Barbero, E - 349
Barnes, A - 112
Bassett, D - 292
Basu, P - 141, 258
Beamson, G - 262
Becker, U - 110
Belgrine, A - 264
Bell, J - 21, 167, 171, 199
Bentz, D - 252
Binns, M - 143
Blum, F - 215
Boerio, J - 92, 95, 202
Boucher, E - 278
Bowen, R - 56, 227
Brenner, D - 47
Brillson, L - 237
Brostow, W - 159
Brown, C - 328
Brown, I - 149
Busnaina, A - 233
Byrd, E - 252
Cano, R - 32
Carpenter, P - 121
Carre, A - 8
Case, S - 27
Castle, J - 209
Chaffin, K - 337
Chang, T - 100, 108, 322

Chang, A - 198
Chang, E - 303
Charbonnier, M - 79, 83
Cheatle, W - 352
Chehimi, M - 209
Chen, J - 56
Chiang, F - 137, 325
Chin, J - 11
Chtourou, H - 343
Clais, R - 112
Clark, R - 157
Cohen, C - 116
Colbeck, S - 328
Colten, R - 47
Coupard, A - 264
Czanderna, A - 224
Dallas, G - 352
Davalos, J - 349
Davis, S - 221
Davis, R - 27, 189
Davis, G - 218
DeBolt, M - 255
Dechent, W - 182
DeMajo, L - 56, 227
Deruelle, M - 66, 119
Deshayes, L - 79
Dickie, R - 95, 255, 337
Dieckhoff, S - 15, 123
Dillard, J - 24, 100, 115
Dillard, D - 45, 100, 108, 192, 322
Drzal, L - 285
Eklund, E - 237, 240
Elman, J - 162
Evrard, G - 264
Fanter, D - 15
Favro, L - 159
Fay, P - 249
Ferguson, G - 195
Fernandez-Garcia, J - 185
Fields, J - 21
Fleischer, C - 132, 162
Folkers, J - 278
Frick, G - 115
Gady, B - 145
Gaillard, F - 79, 86, 89

Galina, H - 159
 Galkiewicz, R - 296
 Gardner, S - 27, 189
 Garton, A - 21
 Gesang, T - 15
 Glassser, W - 110
 Gollapudi, S - 112
 Gonzalez, A - 27
 Grashof, H - 162
 Grube, S - 59
 Grunze, M - 5, 41
 Haaksma, R - 346
 Hamandi, R - 106
 Hamed, G - 300
 Harling, O - 62
 Harris, J - 249
 Harrison, J - 47
 Hays, D - 237, 240
 Hartwig, A - 15
 Heath, R - 121
 Heidbrink, J - 189
 Hennemann, O - 15, 123, 126
 Herdt, G - 224
 Hervet, H - 119, 278
 Hofer, R - 15
 Holmes, B - 115
 Holubka, J - 52
 Iroh, J - 359
 Ivanov, I - 149
 Jensen, B - 32
 Jones, T - 66
 Jones, C - 75, 77
 Juntawongso, P - 316
 Kaiser, R - 62
 Kander, R - 157
 Karabela, A - 310
 Kent, M - 29
 Kim, H - 173
 Kinloch, A - 167, 176
 Kinning, D - 288
 Kramer, F - 116
 Krishna, M - 340
 Krishnan, S - 59
 Kuo, P - 159
 Kwan, K - 139

Lai, Y - 108, 192, 322
Laparra, O - 59
Lardner, T - 316, 319
Leadley, S - 212
Leger, L - 69, 119, 278
Lesko, J - 27
Li, C - 337
Lian, Y - 281
Liao, S - 281
Liechti, K - 331, 334
Lin, S - 307
Linossier, I - 86
Lok, A - 310
Longhenry, J - 104
Love, B - 104, 106, 135
Mahale, A - 38
Mangipedi, V - 18, 69
Mantel, M - 355
Martin-Martinez, J - 185
McGrath, J - 102, 189
McKenna, W - 132
Meyer, G - 189
Mihora, D - 52
Mintmire, J - 35
Mizes, H - 240
Mizumachi, H - 173
Moreland, P - 246
Mourey, T - 56
Mumbauer, P - 195
Nardin, M - 147
Nelson, R - 313
Nesbitt, S - 199
Nguyen, T - 252
Nikles, D - 199
Nitowski, G - 24
O'Kell, S - 75
Ondrus, D - 95
Ooij, W - 92
Orgiles-Barcelo, A - 185
Ott, M - 240, 243
Pearson, B - 121
Peillex, E - 89
Pelts, S - 340
Pennington, B - 206
Perutz, S - 116

Perry, M - 47
Pocius, A - 18
Porter, D - 102
Possart, W - 15, 123, 126
Prakesh, G - 319
Progar, J - 198
Rakestraw, M - 100, 322
Ramamurthy, A - 52, 159
Reifenberger, R - 145
Reifsnider, K - 27
Riedl, B - 343
Rimai D - 56, 227, 233
Risch, S - 114
Ritter, J - 316, 319
Romand, M - 79, 83, 86, 89
Rose, J - 340
Roseman, M - 176
Rossacci, J - 328
Ryntz, R - 267
Saunders, R - 29
Schleef, D - 145
Schlett, V - 15, 123
Schultz, J - 1, 147, 264
Schlafer, K - 162
Schwark, D - 162
Segall, I - 95, 202
Sehgal, K - 292
Shalkowski, L - 352
Shanahan, M - 8
Shephard, N - 100, 108, 155, 165, 355
Shipulski, E - 328
Shirani, A - 334
Silbersan, P - 116
Silence, S - 243
Slagowski, E - 352
Soltani, M - 230
Spinks, G - 141, 143, 258
Spitzer, J - 264, 310
Sproat, A - 108
Srinivasan, S - 102
StClair, T - 198
Stewart, A - 319
Stoffer, J - 182
Streitz, F - 35
Strunskus, T - 5, 41

Sutherland, I - 121
Swadener, J - 331
Tan, B - 189
Taylor, C - 95, 202
Taylor, M - 45, 322
Telenkov, S - 159
Thomas, R - 159
Tirrell, M - 18, 69, 119
Tombs, T - 66
Torro-Palau, A - 185
Tsai, Y - 92, 202, 281
Tschetter, S - 165
Tudhope, A - 59
Urban, K - 100
Urnán, M - 206
Vaideeswaran, K - 171
Vallat, M - 264
Venables, J - 218
Wang, T - 215
Wang, X - 159
Wang, Y - 137, 159, 167, 325
Wang, Q - 325
Ward, S - 95, 255
Ward, T - 100, 102, 139
Watts, J - 209, 212, 221
Wayman, W - 237
Wefers, K - 24
Wesson, S - 38
Westerbeek, G - 255
Whisnant, P - 218
Wightman, J - 11, 98, 115, 151, 155, 165, 355
Williams, C - 102
Woll, C - 5, 41
Wu, Z - 159
Wu, P - 300
Yam, C - 62
Yang, T - 313
Young, J - 202, 281
Yuan, W - 359
Zhang, Y - 143, 233
Zhao, W - 202
Zhuang, H - 98